

Monographs in Electrochemistry

Series Editor: F. Scholz

Oscar Alejandro Oviedo

Luis Reinaudi

Silvana Graciela García

Ezequiel Pedro Marcos Leiva

Underpotential Deposition

From Fundamentals and Theory to
Applications at the Nanoscale



Springer

Underpotential Deposition

Monographs in Electrochemistry

Series Editor: Fritz Scholz, University of Greifswald, Germany

Surprisingly, a large number of important topics in electrochemistry are not covered by up-to-date monographs and series on the market, some topics are even not covered at all. The new series "Monographs in Electrochemistry" will fill this gap by publishing in-depth monographs written by experienced and distinguished electrochemists, covering both theory and applications. The focus is set on existing as well as emerging methods for researchers, engineers, and practitioners active in the many and often interdisciplinary fields, where electrochemistry plays a key role. These fields will range – among others – from analytical and environmental sciences to sensors, materials sciences and biochemical research.

More information about this series at <http://www.springer.com/series/7386>

Oscar Alejandro Oviedo • Luis Reinaudi •
Silvana Graciela García •
Ezequiel Pedro Marcos Leiva

Underpotential Deposition

From Fundamentals and Theory
to Applications at the Nanoscale

 Springer

Oscar Alejandro Oviedo
Departamento de Matemática y Física
Facultad de Ciencias Químicas, INFIQC
Universidad Nacional de Córdoba
Córdoba, Argentina

Luis Reinaudi
Departamento de Matemática y Física
Facultad de Ciencias Químicas, INFIQC
Universidad Nacional de Córdoba
Córdoba, Argentina

Silvana Graciela García
Departamento de Ingeniería Química
Universidad Nacional del Sur
Bahía Blanca, Argentina

Ezequiel Pedro Marcos Leiva
Departamento de Matemática y Física
Facultad de Ciencias Químicas, INFIQC
Universidad Nacional de Córdoba
Córdoba, Argentina

ISSN 1865-1836
Monographs in Electrochemistry
ISBN 978-3-319-24392-4
DOI 10.1007/978-3-319-24394-8

ISSN 1865-1844 (electronic)
ISBN 978-3-319-24394-8 (eBook)

Library of Congress Control Number: 2015957586

Springer Cham Heidelberg New York Dordrecht London
© Springer International Publishing Switzerland 2016

This work is subject to copyright. All rights are reserved by the Publisher, whether the whole or part of the material is concerned, specifically the rights of translation, reprinting, reuse of illustrations, recitation, broadcasting, reproduction on microfilms or in any other physical way, and transmission or information storage and retrieval, electronic adaptation, computer software, or by similar or dissimilar methodology now known or hereafter developed.

The use of general descriptive names, registered names, trademarks, service marks, etc. in this publication does not imply, even in the absence of a specific statement, that such names are exempt from the relevant protective laws and regulations and therefore free for general use.

The publisher, the authors and the editors are safe to assume that the advice and information in this book are believed to be true and accurate at the date of publication. Neither the publisher nor the authors or the editors give a warranty, express or implied, with respect to the material contained herein or for any errors or omissions that may have been made.

Printed on acid-free paper

Springer International Publishing AG Switzerland is part of Springer Science+Business Media (www.springer.com)

Preface of Editor

There is no need to stress the importance of underpotential deposition (upd) for electrochemistry, surface science, and physics, both with respect to fundamental and applied studies, as upd belongs to the most widely studied and applied phenomena in electrochemical systems. Thus, it was very surprising that there did not exist a single monographic treatment of upd in the world literature. Overviews were only available in review papers, and special aspects of upd were covered in some books on metal deposition and electrocatalysis, to name but two. Rather short treatments of upd are available in textbooks, but a comprehensive description of the various experimental and theoretical aspects of upd and of its use for tuning electrochemical reactions was missing. I am very happy that four authors from Argentina, Ezequiel Pedro Marcos Leiva (Córdoba), Silvana Graciela García (Bahía Blanca), Oscar Alejandro Oviedo (Córdoba), and Luis Reinaudi (Córdoba), have accepted the request to write a monograph on underpotential deposition. The authors are internationally known for their contributions to the present state of understanding upd, and I am sure that this monograph will acquire the state of a classic book which every researcher will study and refer to when entering electrochemical deposition, electrocatalysis, or fundamental and applied surface science.

Greifswald, Germany
July 2015

Fritz Scholz

Techniques and Abbreviations

AES	Auger Electron Spectroscopy
AFM	Atomic Force Microscopy
DFT	Density Functional Theory
DRS	Differential Reflectance Spectroscopy
ECALe	Electrochemical Atomic Layer Epitaxy
EDL	Electrical Double Layer
EQCM	Electrochemical Quartz Crystal Microbalance
EXAFS	Extended X-Ray Absorption Fine Structure
FTIRS	Fourier Transform Infrared Spectroscopy
GDOES	Glow Discharge Optical Emission Spectroscopy
GIXS	Grazing Incidence X-Ray Scattering
IHP	Inner Helmholtz Plane
IRS	Infrared Spectroscopy
LEED	Low Energy Electron Diffraction
M	Metal
M _{ads}	Metal Adatom
MC	Monte Carlo
MD	Molecular Dynamics
ML	Monolayer
NPs	Nanoparticles
opd	Overpotential Deposition
PAS	Photoacoustic Spectroscopy
PDEIS	Potentiodynamic Electrochemical Impedance Spectroscopy
PZC	Potential of Zero Charge
RHEED	Reflection High Energy Electron Diffraction
RRDE	Rotating Ring-Disk Electrode
S	Substrate
SDD	Surface Differential X-Ray Diffraction
SHG	Second Harmonic Generation
S/M	Substrate and Adsorbate system
S@M	Substrate and Adsorbate Core-Shell Nanoparticle System

SCE	Saturated Calomel Electrode
SEM	Scanning Electron Microscopy
SERS	Surface Enhanced Raman Spectroscopy
SHE	Standard Hydrogen Electrode
SLRR	Surface-Limited Redox Replacement
SPM	Scanning Probe Microscopy
SRS	Specular Reflection Spectroscopy
STM	Scanning Tunneling Microscopy
SSE	Saturated Sulphate Electrode
SXS	Surface X-Ray Scattering
TPD	Temperature Programmed Desorption
TPS	Thermal Desorption Spectroscopy
TTL	Twin-Electrode Thin-Layer
UHV	Ultra High Vacuum
upd	Underpotential Deposition
XPS	X-Ray Photoelectron Spectroscopy

Contents

1	Introduction	1
1.1	Underpotential Deposition: A Successful Misnomer?	1
1.2	The Magic World of Metal Underpotential Deposition	2
1.3	Pre-history and Rise of upd	9
1.4	Upd Under the Loupe: Then and Now	12
	References	13
2	Experimental Techniques and Structure of the Underpotential Deposition Phase	17
2.1	Introduction	17
2.2	Cyclic Voltammetry	18
2.3	Radiotracer Methods	23
2.4	Potential Step	26
2.5	Equilibrium-Coverage-Potential Isotherms	28
2.6	Twin-Electrode Thin-Layer	29
2.7	Rotating Ring Disk Electrode	33
2.8	Electrochemical Quartz Crystal Microbalance	37
2.9	Scanning Probe Microscopy	40
	2.9.1 Scanning Tunneling Microscopy	40
	2.9.2 Atomic Force Microscopy	47
2.10	Low-Energy Electron Diffraction, X-Ray Photoelectron Spectroscopy and Auger Electron Spectroscopy	49
2.11	X-Ray Absorption Fine Structure	52
2.12	In-Situ Surface Differential X-Ray Diffraction	53
2.13	Transmission X-Ray Surface Differential Diffraction	54
2.14	In-Situ Surface X-Ray Scattering	55
2.15	Grazing Incidence X-Ray Diffraction	55
2.16	In Situ Infrared Spectroscopy	58
2.17	Fourier Transform Infrared Spectroscopy	58

2.18	Differential Reflectance Spectroscopy	60
2.19	Optical Second Harmonic Generation	61
2.20	Surface-Enhanced Raman Spectroscopy	62
2.21	Techniques Suited to Study Alloy Formation During the upd Process	65
2.22	In-Situ Measurement of Surface and Growth Stress	68
2.23	Applications of upd as a Tool	69
2.24	Photoacoustic Technique	72
2.25	Electrochemical Impedance Spectroscopy	73
2.26	Thermal Desorption Spectroscopy	75
2.27	Glow Discharge Optical Emission Spectroscopy	77
2.28	Underpotential Deposition in Nuclear Chemistry	79
	References	83
3	Phenomenology and Thermodynamics of Underpotential Deposition	91
3.1	Phenomenology and a First Thermodynamic Approach to Underpotential Deposition	91
3.2	Introducing the Influence of Solvent in Underpotential Deposition Modeling	96
3.3	Underpotential Deposition on Single Crystal Surfaces	97
3.4	Nernstian-like Formalisms: Underpotential Deposition in the Framework of the Electrosorption Valency	100
	3.4.1 Electrical Double Layer Effects	102
	3.4.2 Solvent Effects	102
	3.4.3 Determination of the Electrosorption Valency	106
3.5	Thermodynamics of Underpotential Deposition Using the Formalism of Ideal Polarizable Electrodes	109
	3.5.1 Formalism	109
	3.5.2 Application to Sulfate Coadsorption in the Case of Cu Underpotential Deposition on Au(111)	111
3.6	Coverage Isotherms and Phase Transitions	116
3.7	A Thermodynamic Formulation Oriented to Theoretical Modeling of Underpotential Deposition as a Phase Transition, Including Ion Coadsorption, Solvent and Double Layer Effects	146
	References	156
4	Applications of Underpotential Deposition on Bulk Electrodes as a Model System for Electrocatalysis	163
4.1	Introduction	163
4.2	Catalysis of the Electrooxidation of Some C1 Molecules on Pure Pt Surfaces and Bimetallic Catalysis	164
	4.2.1 CO	164
	4.2.2 CH ₃ OH	172

4.2.3	HCOOH	180
4.2.4	The Oxygen Reduction Reaction	187
4.2.5	Hydrogen Evolution Reaction	189
4.2.6	Nitrate Reduction Reaction	193
	References	194
5	Modelling of Underpotential Deposition on Bulk Electrodes	199
5.1	Introduction	199
5.2	Application of Quantum Mechanical Methods to Underpotential Deposition	204
5.2.1	Quantum Mechanical Modeling of Underpotential Deposition Previous to the Application of Density Functional Theory	204
5.2.2	Early Applications of Density Functional Theory to Underpotential Deposition	206
5.2.3	Density Functional Theory Calculations for Underpotential Deposition Systems	209
5.2.4	Relationship Between Excess Binding Energy and Surface Energy	213
5.2.5	Density Function Theory Calculations for Expanded Monolayers	215
5.2.6	Analysis of Substrate and Adsorbate Interaction Energy	217
5.2.7	Growth of Deposits Underpotentially formed on Stepped Surfaces	218
5.3	A Statistical-Mechanical Approach to Underpotential Deposition	220
5.4	Monte Carlo Methods	226
5.4.1	Introduction and Generalities	226
5.4.2	Off-Lattice Monte Carlo	228
5.4.3	Lattice Monte Carlo	236
5.4.4	Kinetic Monte Carlo Applications	247
5.5	Miscellaneous Models Applied to Underpotential Deposition	263
5.5.1	Quantum Mechanical Semiempirical Calculations	263
5.5.2	Orientalional Ordering of Adsorbed Monolayers	264
5.5.3	Entropic Contribution to Underpotential Deposition Shift: Lattice Dynamics Analysis	266
5.5.4	Application of Molecular Dynamics and Related Techniques to Underpotential Deposition	268
	References	274
6	Underpotential Deposition and Related Phenomena at the Nanoscale: Theory and Applications	277
6.1	General Aspects	277
6.2	Kinetics and Thermodynamic Driving Force	280

6.2.1	Reduction Mechanism	280
6.2.2	Strong Versus Weak Reducing Agents	283
6.2.3	Formation Mechanism of Monoatomic Nanoparticles	284
6.2.4	Statistical Mechanic Formulation on the Stability and Metastability of Nanoparticles	290
6.2.5	Bimetallic Nanoparticles	294
6.2.6	Deposition Mechanisms at the Nanoscale	295
6.3	Towards Electrochemical Control in Synthetic Routines for Free-Standing Nanoparticles	296
6.4	Thermodynamics of Underpotential Deposition at the Nanoscale	301
6.5	Atomistic Model for Underpotential Deposition on Nanoparticles	307
6.6	Strengthening and Weakening of Underpotential Deposition at the Nanoscale. Underpotential Deposition-Overpotential Deposition Transition	309
6.7	Experimental Research	313
6.7.1	Seed-Mediated Growth	313
6.7.2	Shape Control of Nanoparticles Synthesis by Underpotential Deposition	317
6.7.3	Galvanic Replacement and Underpotential Deposition	318
6.7.4	Hollow Nanoparticles Through Galvanic Replacement	322
6.7.5	Nanoparticles Growth Inside Dendrimers	325
	References	331
7	What Is Coming Next?	335
7.1	Underpotential Deposition as a Precision Design Tool	335
7.2	Towards an Accurate and First-Principles Modeling of Metal Underpotential Deposition/Dissolution	338
7.3	Computer Experiments	340
7.4	Curvature Effects in Underpotential Deposition at the Nanoscale	341
7.5	Role of Protective Molecules in Underpotential Deposition	341
7.6	New Models of Nucleation and Growth at the Nanoscale	343
7.7	Underpotential Deposition Voltammograms: What About the Spikes?	345
7.8	The Puzzling Occurrence of Low-Density Structures and the Need to Improve the Underpotential Deposition Modeling to Consider Electrochemical Features of the System	346
	References	347
	About the Authors	349
	About the Editor	353
	Index	355

Chapter 1

Introduction

1.1 Underpotential Deposition: A Successful Misnomer?

The deposition of small amounts of metal atoms¹ on a foreign surface at potentials more positive than those predicted by Nernst equation is nowadays popularly known as underpotential deposition (upd). To denote something that involves positive quantities with the prefix under obviously appears as counterintuitive, so we devote a few lines to explain this contradictory denomination. In the fundamental field of the electrocrystallization of bulk metals, it is widely used the concept of overvoltage η , which is defined as:

$$\eta = E - E_{M_{(\text{bulk})}/M_{(\text{aq})}^{z+}} \quad (1.1)$$

where E is the actual electrode potential, and $E_{M_{(\text{bulk})}/M_{(\text{aq})}^{z+}}$ is the Nernst equilibrium potential of the reaction:



where $M_{(\text{bulk})}$ represents the bulk metallic material, and $M_{(\text{aq})}^{z+}$ stands for an ion in solution, bearing the charge number z . Due to different kinetic hindrances, it always happens in the case of bulk materials that metal deposits take place when $E < E_{M_{(\text{bulk})}/M_{(\text{aq})}^{z+}}$ so that in general the overvoltage results with the condition $\eta < 0$. Thus, in the case of bulk deposits the overvoltage results always in *negative* values of η . In the case of underpotential deposition, the reverse condition occurs, because

¹ By small amounts, we mean a number of atoms that is related to the number of atoms constituting the surface of a metal substrate. Thus, underpotential deposits usually involve submonolayers, monolayers or at the most bilayers.

metal deposition takes place for $E > E_{M_{(\text{bulk})}/M_{(\text{aq})}^{z+}}$, so that $\eta > 0$. Then, since the term *overvoltage* was already reserved for metal deposition in the $\eta < 0$ condition, the only possibility left was to denominate the situation $\eta > 0$ as *undervoltage*, from there the term *underpotential* deposition, which is usually shortened as upd.

1.2 The Magic World of Metal Underpotential Deposition

Within electrochemical surface processes, the deposition of a metal onto a foreign metal surface at underpotential opens the way to a whole universe of possibilities for preparing and designing surfaces with a variety of applications. Among them, we can mention electrocatalysis [1–5], production of compound semiconductors [6, 7], determination of metal traces by stripping voltammetry, achieving mercury-free electroanalytical procedures [8–10], design of biosensors [11–14], surface area measurement of metals [15, 16], of particular importance for metallic nanoporous materials [17, 18], design of nanoparticle shape [19–21] and composition [22, 23], fabrication of nanocables [24], nanotripods [25], microstructures with improved Surface Enhanced Raman Spectroscopy activity [26], evaluation of overpotential deposition kinetics of reactive metals [27], etc. The previous enumeration is by no means mutually exclusive, since for example nanoparticle synthesis is oriented to catalysis, and we emphasize that it is just mentioned some sample reviews or recent work.

Since upd involves the growth of a new phase in a two dimensional system, we will see along the chapters of this book that this phenomenon is by itself of fundamental importance for understanding a number of related processes involved in the formation of new phases with this dimensionality.

We illustrate with the aid of Fig. 1.1 the key advantage of electrochemical deposition of a metal concerning adsorption studies, with respect to the same processes achieved from the gas phase. Let us represent the desorption of an adatom M from a substrate S according to the reaction:



where M_{vac} represents a metal atom in vacuum. In Fig. 1.1 we show schematically the (free) energy of an atom bonded to a surface as a function of the distance from it. In the case of metallic substrate/adsorbate systems, the binding energy curve exhibits typically a minimum with values in the range $-3 \leq E_{\text{ads}}(\text{eV}) \leq -5$ with respect to the vacuum level [28], indicating that the desorption energy E_{des} must be of this order of magnitude (but with opposite sign). If we consider the thermal energy at room temperature, $k_{\text{B}}T = 0.025 \text{ eV}$, we see that the E_{des} amounts are

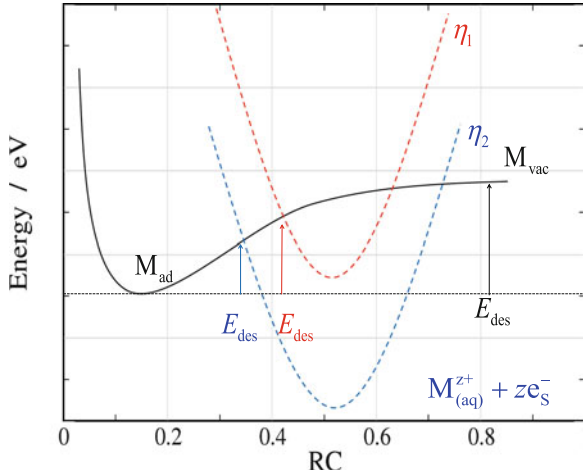


Fig. 1.1 Schematic comparison between the desorption of a metal adatom from a metal surface by physical detachment (*continuous line*) and electrochemical oxidation (*broken lines*). The *full line* illustrates the free energy curve of the adatom as function of the distance from the surface (RC reaction coordinate). The *dotted lines* represent the potential energy of the cations in solution plus the electron located in the metal for two different overpotentials, where $\eta_2 < \eta_1$. The *arrows* show the point where the potential energy of the adatom and the ion plus electron systems meet. The heights of these arrows give an idea of the activation energy for the detachment process (E_{des})

between 120 and 200 $k_B T$. Taking into account these figures we can make an estimation of the thermal desorption time of an adatom according to:

$$\frac{1}{t_{des}} = \nu \exp[-E_{des}/k_B T] \quad (1.4)$$

where the preexponential factor ν contains entropic contributions and shows a weak dependence on the temperature and E_{des} has been taken as a measure for the activation energy of the desorption process. Inserting into Eq. (1.4) the mentioned limits for E_{des} , and approximating $\nu \approx 1 \times 10^{13} \text{ s}^{-1}$, we get that the desorption times should be in the range $1 \times 10^{40} < t_{des}(\text{s}) < 7 \times 10^{73}$. This means that even if we monitor a macroscopic ensemble of adsorbed particles, let us say, of the order of $\sim 10^{23}$, we would find desorption times in the interval $1 \times 10^{17} < t_{des}^{\text{macro}}(\text{s}) < 7 \times 10^{50}$. To bring into scale the previous curves, we remind that the estimated age of the universe is $t_{\text{univ}} \approx 4 \times 10^{18} \text{ s}$. Thus, we arrive to the conclusion that the achievement at room temperature of adsorption/desorption equilibrium is not possible for most S/M metal couples, due to the fact that one of the processes (desorption) is kinetically impossible to achieve. Of course, the previous profiles may be drastically altered by increasing the temperature, but doing this would also promote other processes, like alloying, which are not wished if one is interested on

adsorption studies. What electrochemistry does, as illustrated in the red and the blue lines of Fig. 1.1 is to change reaction (1.3) into:



The dotted curves in Fig. 1.1 introduces an alternative state to that of the desorbed adatom, where now the final state is an ion in solution $\text{M}_{(\text{aq})}^{+z}$ and an electron (or the number of electrons corresponding to the valence) in the substrate electrode. Since the latter may be polarized, the free energy of electrons in the metal may be changed accordingly, and the desorption barrier may be lowered, as it is indicated by the red and blue arrows in the Fig. 1.1 for two different surface polarizations. It can be seen that the decrease of the barrier for adatom desorption, concomitantly increases the barrier for adsorption. Of course, reality is far more complex than this simple picture and a full theory able to calculate the adsorption and desorption rates accurately for metallic systems is still not available, but the figure illustrates the main idea beyond the electrochemical manipulation of substrate/adsorbate metallic systems, in comparison with a similar process in the gas phase.

From Fig. 1.1 we also visualize that in electrochemistry, the exchange rate between ions in solution and adatoms will be governed by the height of the energy barrier to be surmounted between adatoms and ions, so that it will be determined by the properties of both the metal surface and the solution. This problem has been the subject of extensive consideration in electrochemical textbooks [29] and its nature is starting to be elucidated for specific systems in very recent theoretical work [30].

As stated above, the occurrence of the upd phenomenon results in the formation of a two-dimensional phase, involving in some cases nucleation and growth processes, which take place under the influence of a potential difference [29]. Although the situation is in several aspects similar to the growth of a bulk metallic (three dimensional) phase under electrochemical conditions, there are important differences to take into account.

To go more properly into the peculiarities of upd, let us consider first the problem of the deposition of a bulk metal under equilibrium conditions. This can be described, as it is well known, by a Nernst diagram as the one depicted in Fig. 1.2a. The diagram shows the equilibrium potential $E_{\text{M}_{(\text{bulk})}/\text{M}_{(\text{aq})}^{z+}}$ for reaction (1.2) as a function of the logarithm of the activity of the cation $a_{\text{M}_{(\text{aq})}^{z+}}$, which is given by:

$$E_{\text{M}_{(\text{bulk})}/\text{M}_{(\text{aq})}^{z+}} = E_{\text{M}_{(\text{bulk})}/\text{M}_{(\text{aq})}^{z+}}^0 + \frac{RT}{zF} \ln \left(\frac{a_{\text{M}_{(\text{aq})}^{z+}}}{a_{\text{M}_{(\text{bulk})}}} \right) \quad (1.6)$$

where $E_{\text{M}_{(\text{bulk})}/\text{M}_{(\text{aq})}^{z+}}^0$ is the standard equilibrium potential, $a_{\text{M}_{(\text{bulk})}}$ is the activity of the bulk solid (generally assumed to be equal to 1), T is the temperature, R and F correspond to the gas and Faraday constants, respectively. This Figure can be

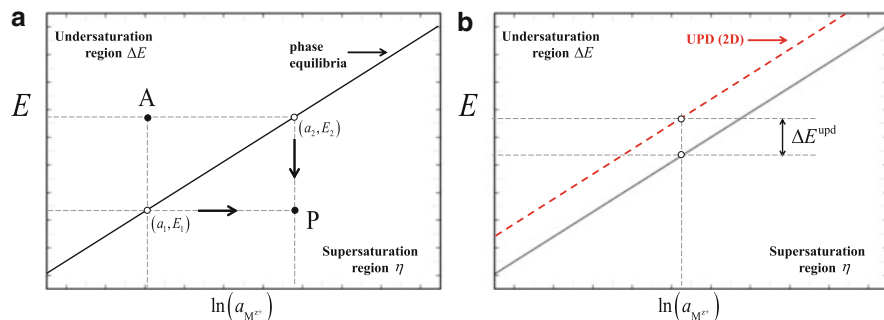


Fig. 1.2 Qualitative scheme of the variation of the equilibrium dissolution/deposition potential of a metal as a function of ion activity. (a) Case of dissolution/deposition of a bulk metal, see Eq. (1.2) in the text. (b) Case of underpotential dissolution/deposition of metal M on a foreign substrate S, see Eq. (1.5) in the text. The *continuous black curve* shows the equilibrium conditions for piece of a bulk metal, the *broken red curve* shows the equilibrium line for underpotential deposition conditions. The distance between the two curves is the underpotential shift, ΔE^{upd}

envisaged as a phase diagram, where the line denotes coexistence points of the solid phase with the ions in solution and the electrons in the metal. Points above and below the line correspond to situations where, if we force the system to be there, a non-equilibrium state will be reached. For example, if we bring the system to point A, characterized by the pair (a_1^A, E_2^A) , spontaneous metal dissolution will take place. Alternatively, bringing the system to the conditions of point P, characterized by the pair (a_2^P, E_1^P) , will result in spontaneous metal deposition. For this reason, we have denoted the previous regions as undersaturation and oversaturation regions respectively.

There are several ways to take the system into these non-equilibrium regions. Let us consider for example the two ways considered in the arrows marked in the Fig. 1.2a, to bring the system to point P, from two different initial equilibrium situations:

1. Increasing $a_{M^{z+}}^{\text{(aq)}}$ at a constant E (horizontal arrow).
2. Decreasing E , at a constant $a_{M^{z+}}^{\text{(aq)}}$ (vertical arrow).

These processes are marked in Fig. 1.2a as processes $(a_1, E_1) \rightarrow P$ and $(a_2, E_2) \rightarrow P$. Both take to the same point on the oversaturation region, leading to nucleation and growth of the bulk solid phase $M_{(\text{bulk})}$. It is interesting to note the dual way that electrochemistry provides to induce nucleation and growth of a new phase. The first path described above has been employed to induce localized electrodeposition using a STM tip [31]. Path 2 is the usual way employed to induce metal growth by a potentiostatic pulse [31, 32].

As mentioned in Eq. (1.1), the magnitude quantifying this displacement from equilibrium is the overpotential η , in such a way that $\eta < 0$ indicates oversaturation (cathodic overpotentials) and $\eta > 0$ indicates undersaturation (anodic overpotentials), while $\eta = 0$ corresponds to phase coexistence.

Although we will see that the proper thermodynamic treatment of upd involves a number of complex features, intuitive knowledge can be gained by proposing in the case of underpotential deposits an heuristic (and rough) extension of Nernst Eq. (1.6) by writing:

$$E_{(M_\theta/S)/M_{(aq)}^{z+}} = E_{M_{(bulk)}/M_{(aq)}^{z+}}^0 + \frac{RT}{zF} \ln \left(\frac{a_{M_{(aq)}^{z+}}}{a_{M_\theta/S}} \right) \quad (1.7)$$

where $E_{(M_\theta/S)/M_{(aq)}^{z+}}$ denotes the potential at which the $M_{(aq)}^{z+}$ ions are in equilibrium with the M atoms adsorbed on the surface of S at the coverage θ . $a_{M_\theta/S}$ is the activity of M adsorbed on S at the coverage θ . In the limit of multilayer adsorption, Eq. (1.7) reduces to Eq. (1.6), that is, $a_{M_\theta/S} \rightarrow a_{M_{(bulk)}} = 1$ and $E_{(M_\theta/S)/M_{(aq)}^{z+}} \rightarrow E_{M_{(bulk)}/M_{(aq)}^{z+}}$.

In the case of a bulk or surface alloy, $a_{M_\theta/S}$ decreases with the decreasing fraction of M in the alloy [2, 33]. In the case of monolayers or submonolayers, $a_{M_\theta/S}$ turns into a function of the surface coverage by adatoms. The presence of a monolayer occurring at underpotentials is equivalent to consider $a_{M_\theta/S} < 1$, so that all equilibrium potentials are shifted upwards, $E_{(M_\theta/S)/M_{(aq)}^{z+}} > E_{M_{(bulk)}/M_{(aq)}^{z+}}$, see Fig. 1.2b. As a consequence of this shift, the upd curve (red line) falls in the undersaturation region with respect to the bulk equilibrium (black line). That is, the metal M exists on the surface of S at potentials where it should not occur if we think in terms of the bulk M material!

In the case of upd, a magnitude that may be quantified is the so-called underpotential shift, denoted with ΔE^{upd} in Fig. 1.2b. Using Eqs. (1.6) and (1.7) we see that ΔE^{upd} is given by:

$$\Delta E^{\text{upd}} = E_{(M_\theta/S)/M_{(aq)}^{z+}} - E_{M_{(bulk)}/M_{(aq)}^{z+}} \quad (1.8)$$

so that $\Delta E^{\text{upd}} > 0$ indicates the presence of phases more stable than the prediction of Nernst equation.

As we will see in Chap. 3, the previous argumentation falls too short of being an accurate description, and the curves in Fig. 1.2b do not run parallel. However, we have gained an intuitive introduction to the concept of underpotential shift.

A further complication arises due to the fact that the surface of a real metal electrode is not a perfect arrangement of adsorption sites, but contains a number of imperfections like steps (one-dimensional), kinks and vacancies (zero-dimensional). These defects provide adsorption sites for the formation of deposits that are energetically more favorable than the formation of the monolayer. Thus, if we think in terms of a surface that is progressively polarized towards increasingly negative overpotentials, monolayer growth is preceded by the formation of structures of lower dimensionality [34]. Figure 1.3 shows schematically some of these structures.

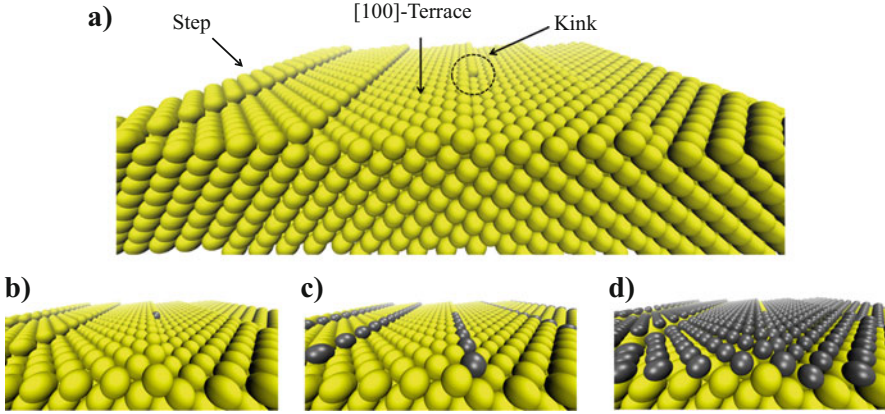


Fig. 1.3 Stepwise formation of structures of low dimensionality upon application of decreasing overpotentials: (a) defective surface, (b) kink decoration, (c) step decoration, and (d) monolayer formation

To account for the formation of metallic phases with different dimensionalities, an effective Nernst equation may be also proposed:

$$E_{(M_{iD}/S)/M_{(aq)}^{z+}} = E_{M_{(bulk)}/M_{(aq)}^{z+}}^0 + \frac{RT}{zF} \ln \left(\frac{a_{M_{(aq)}^{z+}}}{a_{iD}} \right) \quad \text{with } i = 0, 1 \text{ and } 2 \quad (1.9)$$

where $E_{(M_{iD}/S)/M_{(aq)}^{z+}}$ is the potential at which the $M_{(aq)}^{z+}$ ions are in equilibrium with M atom adsorbed on the iD -structure of S, $E_{M_{(bulk)}/M_{(aq)}^{z+}}^0$ is the corresponding standard potential and a_{iD} is an activity, function of structure and dimensionality. The concept of underpotential shift may also be extended according to:

$$\Delta E^{\text{upd}}(iD) = E_{(M_{iD}/S)/M_{(aq)}^{z+}} - E_{M_{(bulk)}/M_{(aq)}^{z+}} \quad \text{with } i = 0, 1 \text{ and } 2 \quad (1.10)$$

Figure 1.4 shows in blue the equilibrium curves corresponding to these low dimensional structures, which follow the ordering:

$$E_{(M_{0D}/S)/M_{(aq)}^{z+}} > E_{(M_{1D}/S)/M_{(aq)}^{z+}} > E_{(M_{2D}/S)/M_{(aq)}^{z+}} > E_{M_{(bulk)}/M_{(aq)}^{z+}} \quad (1.11)$$

where the upd shifts are expected to follow the ordering:

$$\Delta E^{\text{upd}}(0D) > \Delta E^{\text{upd}}(1D) > \Delta E^{\text{upd}}(2D) \quad (1.12)$$

Depending on the magnitude of these differences, several current peaks or their convolution may be present.

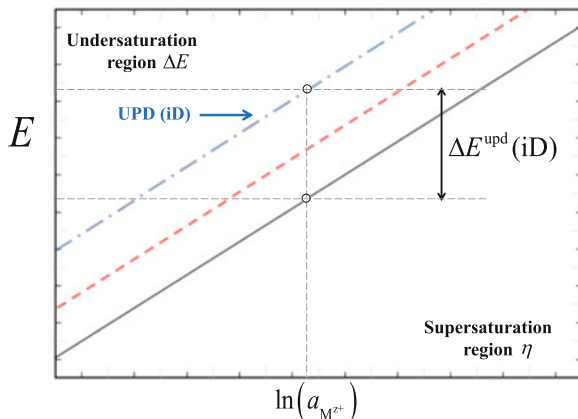


Fig. 1.4 Qualitative scheme for the variation of the equilibrium dissolution/deposition potential as a function of cation activity. The *continuous black curve* corresponds to equilibrium conditions for a bulk metal surface, the *broken red curve* shows the equilibrium line for 2D underpotential dissolution/deposition and the *blue dotted-broken line* shows the equilibrium condition for underpotential dissolution/deposition of i -Dimensional structures, with $i < 2$

The largest contribution to ΔE^{upd} is given by the magnitude of the $M - S$ binding energy, determined by the following factors [33]:

- (i) the lateral and vertical binding energies between metallic adatoms in nanostructures and the binding energy between adatoms and the substrate,
- (ii) the energetic influence of local surface defects of the substrate,
- (iii) the binding energies between solvent dipoles and the metallic substrate/ nanostructure system, and
- (iv) the binding energies of solvated anions with S and the metallic nanostructure.

While the first two factors are relatively straightforward to evaluate in terms of models taking into account the metal nature of adsorbate and substrate, the third and fourth elements involve very different interactions (i.e. van der Waals, ionic), which require approximations of considerable complexity.

Concerning effects at the nanoscale, Pliech [35] showed that the equilibrium potential of nanoparticles (NPs), $E_{M_{(\text{NP})}/M_{(\text{aq})}^{z+}}$, of a given metal shifts towards more negative potentials with decreasing size. This corresponds to an increase in the free energy of the system and the effect is consistent with an increase in the activity of the metal, that is, $a_{M_{(\text{NP})}} > 1$. This behaviour is a consequence of the increasing surface energy of the NP and/or its increasing curvature. The green curve in Fig. 1.5 shows the hypothetical $E_{M_{(\text{NP})}/M_{(\text{aq})}^{z+}}$ vs $\ln(a_{M^{z+}})$ curve, exhibiting a negative potential shift, where it is shown that the stability of the pure metal M -NP occurs in the supersaturation region. In other words, a nanoparticle of a pure metal M dissolves at potentials where this bulk metal subsists in equilibrium.

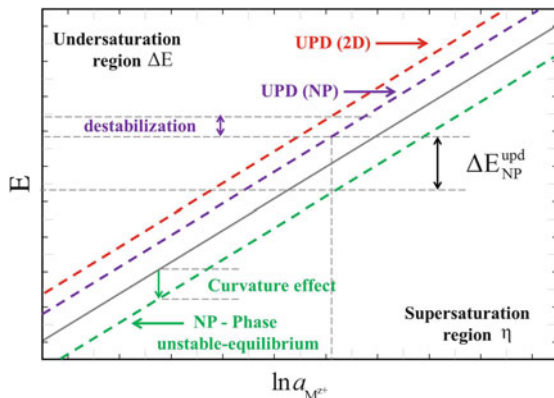


Fig. 1.5 Qualitative scheme of the variation of the deposition potential as a function of the ion activity for underpotential deposition at the nanoscale. The *continuous black curve* corresponds to equilibrium conditions for a piece of a bulk metal, the *broken red curve* shows the equilibrium line for 2D underpotential deposition, the *green broken line* shows the condition of unstable equilibrium for a metal nanoparticle and the *magenta broken line* show the underpotential deposition on a nanoparticle

However, an underpotential deposit of M on a NP made of a different metal S could in principle show the behaviour depicted by the curve in magenta in Fig. 1.5: it should be less stable than the 2D deposit of M on S (curve in red), but may be more stable than the bulk metal M (curve in black). Thus, the occurrence of upd on NPs will be the result of a delicate balance between substrate/adsorbate interaction and curvature effects, which will be in turn determined by NP size. Chapter 6 is fully dedicated to this type of problems.

1.3 Pre-history and Rise of upd

Starting from a very wide viewpoint, we can state that electrochemistry is nowadays a mature science, whose origins dates back to the work of Galvani and Volta, at the end of eighteenth and the beginning of the nineteenth centuries. Its aim is the study of the structure of the interphase between an electric conductor (denominated electrode) and an ionic conductor (denominated electrolyte), or the interphase between two electrolytes [36], and the processes that take place at these interphases. The interphase is the transition region between both phases; its properties differ significantly from those of the corresponding bulk phases. In contrast to this well established knowledge, the recognition of the fact that small quantities of metals may be deposited at potentials more positive than the Nernst reversible potential is relatively more recent. At the beginning, this phenomenon drew particular attention from electrochemists, since at that time the process of nucleation and growth of a

new phase was thought to be a rather simple phenomenon, and not a process involving different stages, as known nowadays.

The first indications for the upd phenomenon were given by Haissinsky in his research on the deposition of radioactive materials [37]. This author [38–40] argued that this phenomenon was due to lattice sites of the substrate presenting large adsorption energies (so called “active centers”). Far from the upd current denomination, at that time the process was addressed as deposition of small metal traces from extremely diluted solutions [41–43]. Shortly after this work, other authors started research on this topic, as for example Rogers [44–52], Kolthoff [53], Haenny [54, 55] and Bowles [56–61]. Current-potential curves (voltammograms) started to be used to analyze traces of Ag deposited on Pt, Cd, Zn and small amounts of Pb on mercury-plated platinum [62–64]. It was soon established that the deposition of these metal traces was very sensitive to the substrate material, and the first attempt to interpret upd through a thermodynamic model was undertaken by Rogers in 1949 [65, 66]. Up to that moment, there was a great controversy concerning the applicability of Nernst equation to describe the deposition potential of these metal traces. The work of Rogers [65] showed the need to consider all the terms in Nernst equation, including the activity of the solid, to describe this phenomenon. Based on the concept drawn by Herzfeld [67] that the activity $a_{M_0/S}$ of a metal adsorbed on a surface varies proportionally with the fraction of surface covered, θ :

$$a_{M_0/S} = f_2 \theta \quad (1.13)$$

where the proportionality constant, f_2 , is denominated activity coefficient of the metal deposit, Rogers [65] proposed a modification to Nernst equation:

$$E = E^0 - E_a - \frac{RT}{zF} \ln \left(\frac{A_e f_1}{V N_a A_a f_2} \left(\frac{C_{ox}}{C - C_{ox}} \right) \right) - \frac{bRT}{zF} \ln (C_g f_g) \quad (1.14)$$

where f_1 is the activity coefficient of the ion, C_{ox} is the equilibrium concentration of reducible ion, C is initial molar concentration of reducible (or oxidizable) ions, N_a is Avogadro’s number, A_a and A_e are cross-sectional area, in cm^2 , of an atom of deposit and area of the electrode in cm^2 , respectively. The last term in Eq. (1.14) is introduced to consider the activity of a possible complex formed by the ion. The index g denotes the complex molecule, having b ligands coordinated with the metal ion being deposited. To consider the changes in the free energy of adsorption, Rogers introduced a new term, E_a in Eq. (1.14), accounting for the difference between the deposition potential of the metal ion on a surface of similar nature and the deposition potential on a foreign one. Thus, if $E_a > 0$, the deposit should be more noble than predicted by Nernst equation. Shortly after the previous contribution, the first indication was found by Mills et al. in 1953 [68] for the dependence of the deposition potential of a given adsorbate on the chemical nature of the substrate electrode. These authors showed that Pb deposition on Au starts at 0.2 V more positive potentials than the deposition potential found on Ag surfaces.

In 1956 Nicholson [69] presented the first computational application to upd, solving numerically [70, 71] the electrochemical problem along with second Fick's law in an IBM 650 computer. This author found a good agreement between the model and experimental data for Ag and Pb deposition on Pt, but found important deviations for Cu deposition on Pt.

Concerning the relationship of upd with early ultra-high vacuum (UHV) experiments on related systems, the articles of Newman [72, 73] and Gruenbaum [74] in UHV showed the presence of a Pb monolayer (and fractions of it) on a Au(111) surface, and evidenced a layer by layer growth up to four monolayers, but the extrapolation to electrochemical systems was not straightforward.

In the 1960s, some authors started to denominate upd as “undervoltage effect” [75], and this phenomenon started to become of wider interest and deserved intensive research [76]. Table 1.1 summarizes work in the area developed in the 1960s decade.

In 1974, Gerischer, Kolb and Przasnyski [94, 95] proposed the first phenomenological theory to explain the origin of upd. Their research on the upd phenomenon showed that the potential difference between upd and bulk deposition could be related to the work function difference between substrate and adsorbate. These authors suggested that the ionic contribution of the bond between the adsorbate and the substrate, given by the partial electron transfer, is the main driving force of the phenomenon. This assumption was supported by the subsequent work of Vijn [96]. Other contributions, like the surface structure of the substrate, the effect of anions

Table 1.1 Compilation of experimental work undertaken in the 60s concerning upd

Substrate	Adsorbate	References
Pt	Ag	[77]
	Pb	[77, 78]
	Cu	[61, 77, 79–83]
	Ni	[84]
	Au	[84]
	Ce	[78, 85, 86]
	Tl	[56, 57, 61, 86]
	Bi	[61, 78]
	Cd	[61]
	Sn	[61, 60]
Graphite	Hg	[87]
	Ag	[88]
	Cu	[81, 89]
Au	Ni	[84]
	Ag	[75]
	Pb	[90, 91]
Ag	Pb	[76, 92]
	Tl	[76, 93]
Pb	Cd	[76]

and the occurrence of submonolayers or bilayers were not included in this modeling.

At the beginning of the 1970s, attention of experimentalists was focused on the charge status of adsorbates and the effect of the nature of the substrate. Schulze et al. [97–99] and Lorenz et al. [100] reviewed the state-of-the-art of the concept of electroadsorption valency at that time. While this concept will be developed in detail in Chap. 3, we advance that it is related to the flow of charge during the electroadsorption process. At difference with the Nerstian or Faradaic valence, the electroadsorption valency is generally a non-integer number. At the middle of the 1970s different authors showed the importance of performing experiments with well defined metal surfaces, the era of upd on single crystal surfaces was beginning [101–120]. The joint use of electrochemical techniques with Low Energy Electron Diffraction (LEED), Reflected High Energy Electron Diffraction (RHEED), Auger Electron Spectroscopy (AES), Ellipsometry and in situ Specular Reflection Spectroscopy (in situ-SRS) allowed to analyze surface reconstructions, deformations, thicknesses [105, 110, 111, 114, 121–123], different growth types [105, 115], expanded structures like on (100) and (111) surfaces [107, 114], including the occurrence of a second upd monolayer [103].

The study of upd on single crystal surfaces also shed light on nucleation and growth of two-dimensional structures [101, 116, 124–126]. The voltammograms showed better defined and sharper peaks than those obtained with polycrystalline surfaces, and the current-time potentiostatic transients showed possible evidence for the occurrence of first-order phase transitions, or at least the existence of attractive interactions. The possibility of studying these phenomena started to spread over the different research groups. However, the definite answer to some of the questions that arose from these studies is still pending, as we will see along Chaps. 3 and 5. The multiple peaks found in the voltammograms obtained with single crystals rapidly turned into an active subject of research [66–68, 75, 77–93, 126].

The wide research with single crystal surfaces along the 1970s showed that the correlations found by Gerischer, Kolb and Przasnyski [94, 95] could only be applied semiquantitatively to polycrystalline surfaces, since the actual situation concerning single crystal surfaces is considerably more complex [107, 127]. The concept of a binding energy only determined by electronegativity effects was found as insufficient, and the need for more complex models taking into account surface geometry and lateral interactions emerged.

1.4 Upd Under the Loupe: Then and Now

In the 1980s the study of upd was favored by the great synergy between the high degree of surface control offered by single crystals and the development of new and powerful surface techniques. The possibility of direct imaging of surfaces and the availability of structural information in direct and reciprocal space gave many answers in the upd field and opened many other ones. Chapters 2 and 3 deal with

these and other studies. The great flexibility of upd to generate surfaces with mixed properties motivated a great body of work using upd systems as model catalytic systems. Chapter 4 deals with application of upd to electrocatalysis.

The massification on computer use, the increasing computer power appearing in the 1990s, as well as the development of new software allowed performing virtual experiments (simulations) of increasing complexity for upd. Chapter 5 reports on these advances.

The advent of nanoscience in the 1990s also reached upd applications in this field, though with a decade of delay. Chapter 6 describes this emerging research area, where upd and galvanic replacement appear as a powerful tool for the design of new materials in the nanoscale.

The new trends and perspectives for upd will be described in Chap. 7.

References

1. Kokkinidis G (1986) *J Electroanal Chem* 201:217
2. Parsons R, VanderNoot T (1988) *J Electroanal Chem* 257:9
3. Jarvi TD, Stuve EM (1998) In: Lipkowski J, Ross A (eds) *Electrocatalysis*. Wiley-VCH, New York
4. Sánchez CG, Leiva EPM (2003) *Handbook of fuel cell technology*. In: Vielstich W, Lamm A, Gasteiger H (eds) Chapter 5, *Catalysis by upd metals*, vol 2. Wiley, Chichester, pp 47–61
5. Adzic RR (2007) *Electrocatalysis on surfaces modified by metal monolayers deposited at underpotentials*. In: *Encyclopedia of electrochemistry*. Wiley-VCH, Weinheim
6. Gregory BW, Stickney JL (1991) *J Electroanal Chem* 300:543
7. Wade TL, Vaidyanathan R, Happek U, Stickney JL (2001) *J Electroanal Chem* 500:322
8. Beni V, Newton HV, Arrigan DWM, Hill M, Lane WA, Mathewson A (2004) *Anal Chim Acta* 502:195
9. Herzog G, Arrigan DWM (2005) *Trends Anal Chem* 24:208
10. Herzog G, Beni V (2013) *Anal Chim Acta* 769:10
11. Aluoch AO, Sadik OA, Bedi G (2005) *Anal Biochem* 340:136
12. Noah NM, Marcellis O, Almalletti A, Lim J, Sadik OA (2011) *Electroanalysis* 23:2392
13. Li Y, Lu Q, Wu S, Wang L, Shi X (2013) *Biosens Bioelectron* 41:576
14. Ou K-L, Hsue T-C, Liud Y-C, Yang K-H, Tsai H-Y (2014) *Anal Chim Acta* 806:188
15. Chen D, Tao Q, Liao LW, Liu SX, Chen YX, Ye S (2011) *Electrocatal* 2:207
16. Shao M, Odell JH, Choi S-I, Xia Y (2013) *Electrochem Commun* 31:46
17. Liu Y, Bliznakov S, Dimitrov N (2009) *J Phys Chem C* 113:12362
18. Rouya E, Cattarin S, Reed ML, Kelly RG, Zangari G (2012) *J Electrochem Soc* 159:K97
19. Langille MR, Personick ML, Zhang J, Mirkin CA (2012) *J Am Chem Soc* 134:14542
20. Personick ML, Mirkin CA (2013) *J Am Chem Soc* 135:18238
21. Yu Y, Zhang Q, Xie J, Lee JY (2013) *Nat Commun* 4:1454
22. Jiang Y, Jia Y, Zhang J, Zhang L, Huang H, Xie Z, Zheng L (2013) *Chem Eur J* 19:3119
23. Wu Q, Li Y, Xian H, Xu C, Wang L, Chen Z (2013) *Nanotechnology* 24:025501
24. Jie-Ren K et al (2006) U. S. pattern no. 20060024438 A1, Feb 2, 2006
25. Zhang L, Choi S-I, Tao J, Peng H-C, Xie S, Zhu Y, Xie Z, Xia Y (2014) *Adv Funct Mater* 24:7520
26. Plowman BJ, Abdelhamid ME, Ippolito SJ, Bansal V, Bhargava SK, O'Mullane AP (2014) *J Solid State Electrochem* 18:3345

27. Guerra E, Kelsall GH, Bestetti M, Dreisinger D, Wong K, Mitchell KAR, Bizzotto D (2004) *J Electrochem Soc* 151:E1
28. See for example typical cohesive energies of metals in Kittel C (2005) *Introduction to solid state physics*, 8 edn. Wiley, New York
29. Budevski E, Staikov G, Lorenz WJ (1996) *Electrochemical phase formation and growth*. VCH, Weinheim
30. Pinto LMC, Spohr E, Quaino P, Santos E, Schmickler W (2013) *Angew Chem* 125:8037
31. Mariscal MM, Dassie SA (eds) (2007) *Recent advances in nanoscience*. Research Signpost, Trivandrum-Kerala
32. Lipkowski J, Ross PN (1999) *Imaging of surfaces and interfaces*. Wiley-Vch, New York
33. Oviedo OA, Mayer CE, Staikov G, Leiva EPM, Lorenz W (2006) *J Surf Sci* 600:4475
34. Staikov G, Lorenz WJ, Budevski E (1999) In: Ross P, Lipkowski J (eds) *Imaging of surfaces and interfaces – frontiers of electrochemistry*, vol 5. Wiley-VCH, New York, p 1
35. Plieth WJ (1982) *J Phys Chem* 86:3166
36. Schmickler W (1996) *Interfacial electrochemistry*. Oxford University Press, New York
37. Haissinsky M (1933) *Chim Phys* 30:27
38. Haissinsky M (1946) *Electrochimie des Substances Radioactives et des solutions extrêmement diluées*. Actual, Scient No. 1009. Hermann, Paris
39. Haissinsky M (1946) *J Chim Phys* 43:21
40. Haissinsky M (1946) *J Chim Phys* 41:21
41. Haissinsky M, Coche A (1949) *J Chem Soc*:S397
42. Haissinsky M (1952) *Ezperientia* 8:12
43. Danon J, Haissinsky M (1951) *Chim Phys* 48:135
44. Rogers LB, Krause DP, Griess JC Jr, Ehrlinger DB (1949) *J Electrochem Soc* 95(2):33
45. Griess JC Jr, Byrne JT, Rogers LB (1951) *J Electrochem Soc* 98(11):447
46. Rogers IB, Stehney AF (1949) *J Electrochem Soc* 96:25
47. Rogers LB, Miller HH, Goodrich RB, Stehney AF (1949) *Anal Chem* 21:777
48. Byrne JT, Rogers LB (1951) *J Electrochem Soc* 98(11):457
49. Byene JT, Rogers LB, Griess JC Jr (1951) *J Electrochem Soc* 98(11):452
50. Rogers LB (1955) *Rec Chem Prog* 16:197
51. Rogers LB, Merritt C Jr (1953) *J Electrochem Soc* 100(3):131
52. De Geiso RC, Rogers LB (1959) *J Electrochem Soc* 106(5):433
53. Kolthoff IM, Tanaka N (1954) *Anal Chem* 26(4):632
54. Haenny C, Mivalez P (1948) *Helv Chim Acta* 31:633
55. Haenny C, Reymond P (1954) *Helv Chim Acta* 37:2067
56. Bowles BJ (1965) *Electrochim Acta* 10:717
57. Bowles BJ (1965) *Electrochim Acta* 10:731
58. Bowles BJ (1965) *Electrochim Acta* 15:589
59. Bowles BJ (1965) *Electrochim Acta* 15:737
60. Bowles BJ, Cranshaw TE (1965) *Phys Lett* 17:258
61. Bowles BJ (1966) *Nature* 212:1456
62. Lord SS Jr, O'Neill RC, Rogers LB (1952) *Anal Chem* 24:209
63. Gardiner KW, Rogers LB (1953) *ibid* 25:1393
64. Marple TL, Rogers LB (1954) *Anal Chem Acta* 11:574
65. Rogers LB, Stelmey AF (1949) *J Electrochem Soc* 95:25
66. Griess JC, Byrne JT, Rogers LB (1951) *J Electrochem Soc* 98:447
67. Herzfeld KF (1913) *Phys Z* 13:29
68. Mills T, Willis GH (1953) *J Electrochem Soc* 100:452
69. Nicholson MM (1957) *J Am Chem Soc* 79(1):7
70. Rutledge G (1932) *Phys Rev* 40:262
71. Wagner C (1954) *J Math Phys* 32:289
72. Newman RC (1955) Ph.D. Thesis, University of London
73. Newman RC (1957) *Philos Mag* 2:750
74. Gruenbaum E (1958) *Proc Phys Soc Lond* 72:459
75. Probst RC (1968) *J Electroanal Chem* 16:319

76. Astley DJ, Harrison JA, Thirsk HR (1968) *J Electroanal Chem* 19:325
77. Nisbet AR, Bard A (1963) *J Electroanal Chem* 6:332
78. Madi I (1961) *J Inorg Nucl Chem* 22:169
79. Kublik Z (1963) *J Electroanal Chem* 5:450
80. Breiter MW (1967) *J Electrochem Soc* 114:1125
81. Breiter MW (1969) *J Electroanal Chem* 23:173
82. Napp DT, Bruckenstein S (1958) *Anal Chem* 40:1036
83. Tindall GW, Bruckenstein S (1968) *Anal Chem* 40:1051
84. Nicholson MM (1960) *Anal Chem* 32:1058
85. Madi I (1954) *J Inorg Nucl Chem* 26:2149
86. Madi I (1962) *J Inorg Nucl Chem* 24:1501
87. Perone SP, Kretlow J (1965) *Anal Chem* 37:968
88. Perone SP (1963) *Anal Chem* 35:2091
89. Vassos BH, Mark HB Jr (1967) *J Electroanal Chem* 13:1
90. Schmidt E, Gygax HR (1967) *J Electroanal Chem* 13:378
91. Schmidt E, Gygax HR (1967) *J Electroanal Chem* 14:126
92. Schmidt E, Siegenthaler H (1969) *Helv Chim Acta* 52:2245
93. Schmidt E, Wiithrich N (1967) *Helv Chim Acta* 50:2058
94. Kolb DM, Przasnyski M, Gerischer H (1974) *J Electroanal Chem* 54:25
95. Gerischer H, Kolb DM, Przasnyski M (1974) *Surf Sci* 43:662
96. Vijn AK (1974) *Surf Sci* 46:282
97. Vetter KJ, Schultze JW (1972) *Ber Bunsenges Phys Chem* 76:920
98. Vetter KJ, Schultze JW (1972) *Ber Bunsenges Phys Chem* 76:927
99. Schultze JW, Vetter KJ (1973) *J Electroanal Chem* 44:63
100. Lorenz WJ, Salié G (1977) *J Electroanal Chem* 80:1
101. Bewick A, Thomas B (1975) *J Electroanal Chem* 65:911
102. Bewick A, Thomas B (1976) *J Electroanal Chem* 70:239
103. Bewick A, Thomas B (1977) *J Electroanal Chem* 84:127
104. Bewick A, Jovičević JN, Thomas B (1977) *Trans Faraday Disc* 12:24
105. Rawlings KJ, Gibson MJ, Dobson PJ (1978) *J Phys D* 11:2059
106. Dickertmann D, Schultze WJ (1977) *Electrochim Acta* 22:117
107. Schultze JW, Dickertmann D (1976) *Surf Sci* 54:489
108. Dickertmann D, Koppitz FD, Schultze JW (1976) *Electrochim Acta* 21:967
109. Siegenthaler H, Jüttner K (1979) *Electrochim Acta* 24:109
110. Siegenthaler H, Jüttner K, Schmidt E, Lorenz WJ (1978) *Electrochim Acta* 23:1009
111. Jüttner K, Siegenthaler H (1978) *Electrochim Acta* 23:971
112. Staikov G, Jüttner K, Lorenz WJ, Budevski E (1978) *Electrochim Acta* 23:319
113. Staikov G, Jüttner K, Lorenz WJ, Schmidt E (1978) *Electrochim Acta* 23:305
114. Beckmann HO, Gerischer H, Kolb DM, Lehmpfuhl G (1977) *Faraday Symp Chem Soc* 12:51
115. Schultze JW, Dickertmann D (1977) *Faraday Symp Chem Soc* 12:36
116. Bewick A, Jovicevic J, Thomas B (1977) *Faraday Symp Chem Soc* 12:24
117. Herrmann HD, Wiithrich N, Lorenz WJ, Schmidt E (1976) *J Electroanal Chem* 68:289
118. Hilbert F, Mayer C, Lorenz WJ (1973) *J Electroanal Chem* 47:167
119. Jüttner K, Staikov G, Lorenz WJ, Schmidt E (1977) *J Electroanal Chem* 80:67
120. Schultze JW, Dickertmann D (1978) *Ber Bunsenges Phys Chem* 82:528
121. Horkans J, Cahan BD, Yeager E (1975) *J Electrochem Soc* 122:1585
122. Adzic RR, Yeager E, Cahan BD (1974) *J Electrochem Soc* 121:474
123. McIntyre JDE, Kolb DM (1970) *Symp Faraday Soc* 4:99
124. Lorenz WJ, Schmidt E, Staikov G, Bort H (1977) *Faraday Symp Chem Soc* 12:14
125. Bewick A, Thomas B (1977) *J Electroanal Chem* 85:329
126. Lorenz WJ, Herrmann HD, Wuthrich N, Hilbert F (1974) *J Electrochem Soc* 121:1167
127. Bort H, Jüttner K, Lorenz WJ, Schmidt E (1978) *J Electroanal Chem* 90:413

Chapter 2

Experimental Techniques and Structure of the Underpotential Deposition Phase

2.1 Introduction

The electrochemical deposition of metals on foreign substrates is a complex process, which includes a number of phase formation phenomena. The very initial electrodeposition stages of a metal, M, on a foreign substrate, S, involve adsorption reactions as well as two-dimensional (2D) and/or three-dimensional (3D) nucleation and growth processes. The most important factors determining the mechanism of electrochemical M phase formation on S are the binding energy between the metal adatoms (M_{ads}) and S, as well as the crystallographic misfit between the 3D M bulk lattice parameters and S. As we have shown in Fig. 1.3, when the binding energy between the depositing M-adatoms and the substrate atoms exceeds that between the atoms of the deposited metal, low dimensional i D metal phases ($i = 0, 1$ and 2) are formed onto the foreign metal substrate. This phenomenon, introduced in Chap. 1 as underpotential deposition (upd) [1–4], has been known for a long time and it has been intensively subject of study in the past decades since the 1970s. This has been demonstrated by many studies of the upd process of different metals on mono- and polycrystalline substrates as well as reviews on the subject. The understanding of the nature of this phenomenon as conceived in the middle 1990s can be found in the book of Lorenz et al. [1]. Reviews available in the literature include the works of Kolb et al., Abruña et al., Sudha and Sangaranarayanan, Aramata [5–8], and the work of Szabó [3] concerning the theoretical aspects of upd, updated by Leiva [9], and also the works of Adžić [10] and Kokkinidis [11], concerning mainly the catalytic effects of upd adatoms.

Monolayer amounts of metal adatoms obtained by upd alter the electronic properties of the substrate material itself by changing the interfacial reactivity, and therefore these systems have been the subject of a large number of studies, not only in terms of their fundamental aspects related to electrochemical phenomena (adsorption, charge transfer, nucleation and growth) but also in their technological application for corrosion inhibition or as models for the design of new electrocatalysts, between others. In addition, the study and applications of upd

processes involve now numerous disciplines apart from electrochemistry, such as chemistry, physics and materials science, as discussed in the remaining of this book.

Many electrochemical and surface characterization methods have been employed to study the upd phenomenon. Whereas electrochemical techniques provide valuable information on the kinetics and mechanisms of processes occurring at the metal/solution interface, the molecular specificity required to give unequivocal identification of species formed at electrode surfaces are obtained by a number of in situ and ex situ spectroscopies. These spectroscopic methods have been applied to augment electrochemical approaches and provide information on the elemental and molecular composition, the atomic geometry, and the electronic structure of the interface. The great progress that has been made in the development of new in-situ techniques allowed to obtain important information on electrode processes at the molecular and atomic level. In this Chapter, different techniques used for characterization of upd layers will be discussed briefly and illustrated by appropriate, representative examples.

2.2 Cyclic Voltammetry

Cyclic voltammetry has been and still is the most important routine method for characterizing the upd of a metal M on a foreign metal substrate. This technique consists of scanning linearly the potential of a stationary working electrode with a constant scan rate (dE/dt) between two chosen limits, one or more times, while the current is continuously monitored. The obtained cyclic current-potential curves offer a rapid location of redox potentials of electroactive species and provide a convenient evaluation of the effect of media upon the redox process. Any reaction at the electrode surface will usually be detected as a current superimposed to the base current due to double-layer charging.

The upd process is reflected in cathodic and anodic current density peaks at different potentials, indicating the deposition and dissolution of the metal adsorbate, respectively. The occurrence of distinct adsorption peaks in the cyclic voltammetric measurements indicates that the formation of 1–2 monolayers at underpotentials takes place in several energetically different adsorption steps.¹ The peak structure is found to depend strongly on the crystallographic orientation of the substrate and the density of crystals imperfections [1]. The number of these peaks and positions also depend on the substrate and the crystal plane on which the adsorption takes place as well as on the nature of the electrolyte. The peaks are not well-pronounced for polycrystalline electrodes whose surface presents different

¹To learn more on the relationship between the peak potential and the energetic properties of the monolayer see Chap. 3.

crystallographically oriented domains and a high density of crystal imperfections (e.g. steps, kinks, vacancies) as compared with single crystals.

Some representative examples illustrating what can be achieved with cyclic voltammetry will be presented here.

Gold has been extensively used as electrode material in fundamental electrochemistry and therefore it is interesting to evaluate its behaviour related to M upd. Ag adatoms are attractive to study on such surfaces because they present strong M-S interactions and negligible M-S misfit (the corresponding lattice parameters are $d_{0,Au} = 2.8840 \text{ \AA}$, $d_{0,Ag} = 2.8895 \text{ \AA}$) [12].

Figure 2.1 shows cyclic voltammograms for Ag upd in the systems Au(100)/Ag⁺, SO₄²⁻ (Fig. 2.1a) and Au(111)/Ag⁺, SO₄²⁻ (Fig. 2.1b) [13]. In the case of Au(100) substrates, three different adsorption-desorption (A_i/D_i) peaks are observed in the potential range $15 \leq \Delta E(\text{mV}) \leq 720$. In these experiments, the lower potential limit was kept higher than the bulk deposition potential to prevent alloying processes. For Au(111) substrates, the voltammogram displays two characteristic adsorption/desorption peaks in the upd range studied.

The deposition of Ag on Au(111) in sulphuric acid has been studied by different groups and some discrepancies in the reported voltammetric curves have been found, depending on the surface state of the substrate, which plays a critical role in the initial stages of metal deposition [13–17]. Yang et al. [18] have revisited these previous results and demonstrated that potential cycling in the upd region introduces some surface defects. They proposed that this procedure gradually transforms the surface into a surface alloy phase, leading to the appearance of another Ag upd peak located at 80 mV more positive than the first upd peak associated with the deposition of Ag on Au terraces.

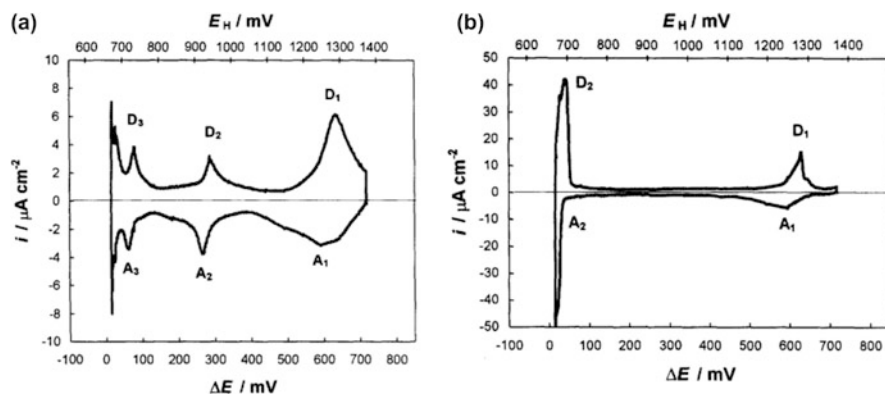
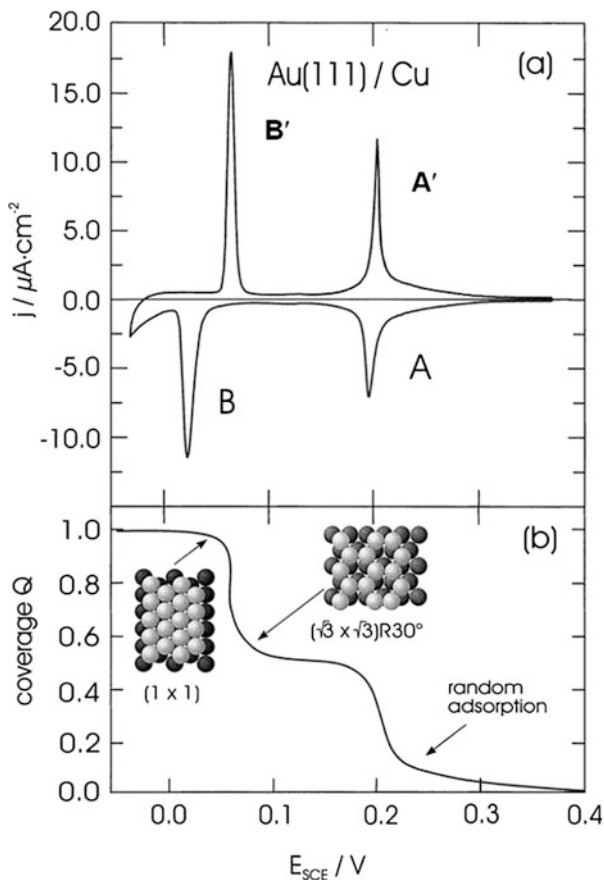


Fig. 2.1 Cyclic voltammograms for the upd of Ag in $5 \times 10^{-3} \text{ M Ag}_2\text{SO}_4 + 0.5 \text{ M H}_2\text{SO}_4$ solution at $T = 298 \text{ K}$ on (a) Au(100) and (b) Au(111) substrates. A_n and D_n with $n = 1, 2, 3$ denote cathodic adsorption and anodic desorption peaks, respectively. $|dE/dt| = 7 \text{ mV s}^{-1}$. The upper scale corresponds to the hydrogen normal electrode, while the lower is referred to the bulk Ag deposition potential (Reprinted with permission from Ref. [13])

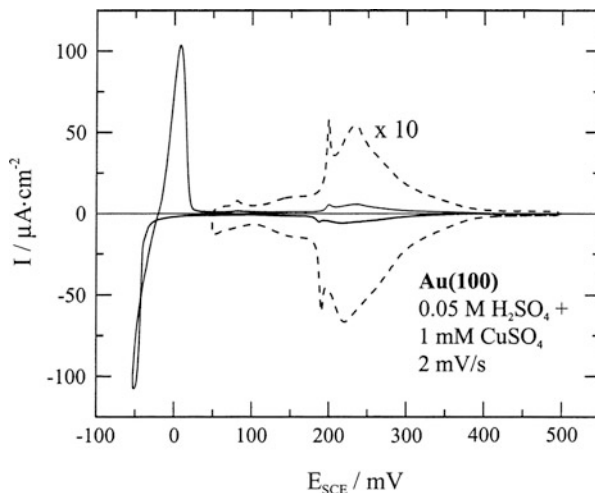
Fig. 2.2 (a) Cyclic voltammogram for the upd of Cu on Au(111) in 1 mM $\text{CuSO}_4 + 0.05 \text{ M H}_2\text{SO}_4$ solution. $|dE/dt| = 1 \text{ mV s}^{-1}$. (b) Adsorption isotherm corresponding to (a), with a schematic view of the proposed Cu structures formed on Au(111) (Reprinted with permission from Ref. [39])



Cu upd on polycrystalline and single crystal gold surfaces, in particular on Au(111), is certainly one of the few systems that has been studied with a wide variety of in-situ techniques including electrochemical ones [19–28], Scanning Tunneling Microscopy [23, 29–31], Atomic Force Microscopy [32], Spectroscopic Methods [33–36] and Quartz Crystal Microbalance [25, 37], and Ex-Situ Techniques such as Low Energy Electron Diffraction, Auger Electron Spectroscopy and Reflection High Energy Electron Diffraction [21, 22, 38].

A typical cyclic voltammogram for Cu upd on Au(111) in sulphuric acid solution is shown in Fig. 2.2a [39]. It is clearly seen that the deposition of a Cu monolayer takes place in the potential region between 0.35 V and 0 V vs SCE, before starting the bulk deposition. The present phenomenon involves two energetically distinct steps, reflected by two pronounced adsorption (A, B)/desorption (A', B') peaks pairs. The corresponding charge isotherm and the schematic view of the structures $(\sqrt{3} \times \sqrt{3})R30^\circ$ and (1×1) , related to the first and second peaks respectively, are shown in Fig. 2.2b [39]. These structures were associated hitherto to the Cu deposit at a medium coverage ($2/3$ Cu monolayer) and at a full Cu

Fig. 2.3 Cyclic voltammogram of Au(100) in 0.05 M H₂SO₄ + 1 mM CuSO₄ solution showing Cu deposition in the underpotential and overpotential region. $|dE/dt| = 2 \text{ mV s}^{-1}$ (Reprinted with permission from Ref. [40])



monolayer. The broad shoulder at potential values more positive than 0.2 V was assigned to a random adsorption of Cu atoms.

Different voltammetric features appear in the case of Cu upd on a Au(100) substrate. Figure 2.3 shows the cyclic voltammogram in 0.05 M H₂SO₄ + 1 mM CuSO₄ solution including also the Cu overpotential region [40]. A Cu monolayer formation was found in the region between 100 and 350 mV and two current density peaks pairs (corresponding to the Cu adsorption/desorption) were observed. The voltammogram obtained in the upd range between 50 and 500 mV is enlarged by a factor of 10 for clarity (dashed curve in the Figure). The charge under the upd peaks was about 400 $\mu\text{C cm}^{-2}$, which is the expected value for a Cu monolayer formed from divalent cations.

The results obtained by Behm et al., introducing chloride anions in the electrolyte, are shown in Fig. 2.4 [41]. For the sake of comparison, the Cu upd on Au(100) was studied by cyclic voltammetry in both pure sulfate and chloride containing solutions (Fig. 2.4). The voltammetric response was characterized, in agreement with other results [29, 42], by a broad adsorption peak with a small extra structure in solutions free of chloride anions (which splitted into two for lower sulfate concentrations and sweep rate [42]), related to the uptake of a full Cu monolayer. In contrast, the Cu upd in solutions with 10^{-4} M HCl was characterized by a very sharp current peak at 0.3 V. This sharp spike was correlated with the formation of an ordered adlayer superstructure. The location of the corresponding peak due to desorption indicated a reversible adsorption process.

Schiffirin and coworkers [43] have studied Cu upd on several Au surfaces with different single crystal surfaces to demonstrate the effect of step density and step orientation on this process. Figure 2.5 exhibits Cu upd cyclic voltammograms for Au(332), Au(775) and Au(554) surfaces. With the Au(332) surface, two broad, overlapping peaks in the first adsorption/desorption region are observed at 0.52 and 0.56 V vs RHE respectively (Fig. 2.5a). The relative intensity of the peak centered

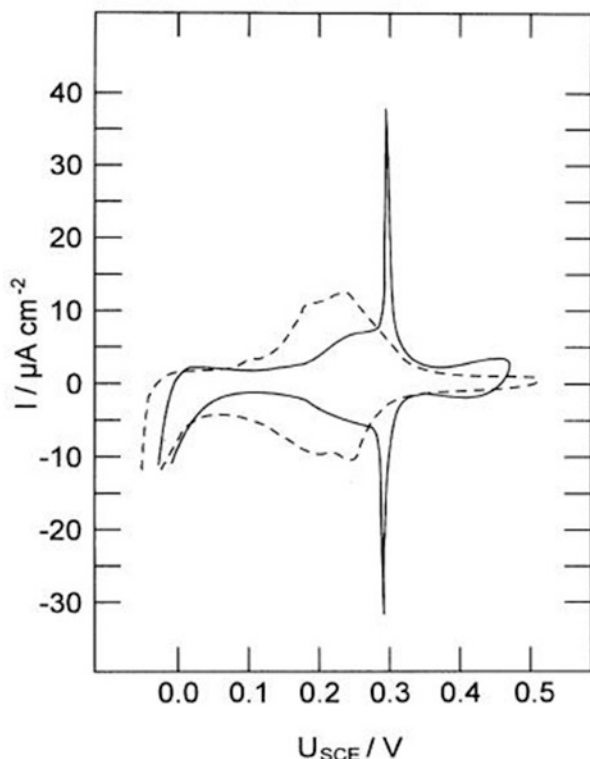


Fig. 2.4 Cyclic voltammograms for Cu upd on Au(100) in 0.01 M H_2SO_4 + 10^{-3} M CuSO_4 solution without (*dashed line*) and with 10^{-4} M HCl (*solid line*). $|dE/dt| = 2 \text{ mV s}^{-1}$ (Reprinted with permission from Ref. [41])

at 0.56 V decreases with decreasing step density (Fig. 2.5b, c). The peak at 0.52 V, on the other hand, was assigned to the formation of the $(\sqrt{3} \times \sqrt{3})\text{R}30^\circ$ structure on the (111) terraced regions, which becomes more clearly defined as the (111) terrace width is increased in the order Au(332), Au(775), Au(554), respectively. In summary, on the basis of the comparison with voltammograms for the Au(111) and Au(110) low index surfaces, these two peaks were assigned to Cu deposition on the (110) step sites and the formation of a $(\sqrt{3} \times \sqrt{3})\text{R}30^\circ$ phase on the (111) terraces, respectively. The second upd peak in the region of 0.34–0.40 V was assigned to the $(\sqrt{3} \times \sqrt{3})\text{R}30^\circ \rightarrow (1 \times 1)$ phase transition, which occurs at the most positive potentials on the most stepped surface, Au(332). The increase in step density and the corresponding reduction in (111) terrace width favours this transition and shows the influence of structural or electronic effects on the energetics and/or kinetics of the phase transition.

The structure of the metal adlayer may also be found to be strongly dependent on the anion species of the electrolyte, as mentioned before, something that was

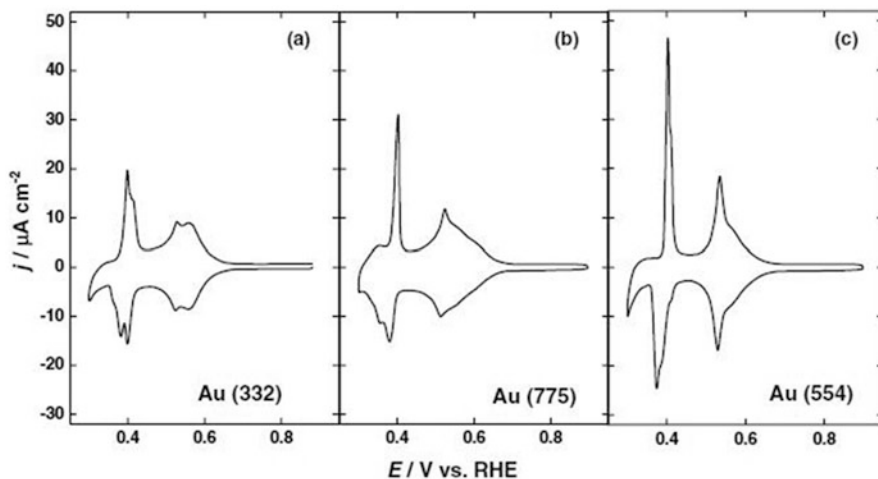


Fig. 2.5 Cyclic voltammograms of Cu upd in 0.05 M H_2SO_4 + 1 mM CuSO_4 on different stepped surfaces. (a) Au(332), (b) Au(775) and (c) Au(554). $|dE/dt| = 5 \text{ mV s}^{-1}$ (Reprinted with permission from Ref. [43])

initially evidenced from cyclic voltammograms and later confirmed by direct structural information from ex-situ and in-situ experiments. We will return to this point below when addressing the study of Cu upd on Au(111) by in-situ Scanning Tunneling Microscopy.

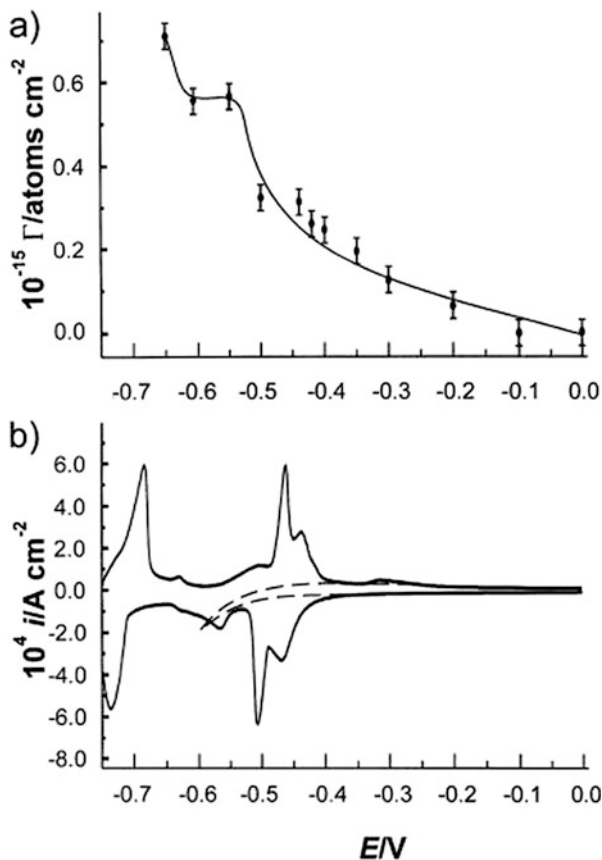
In early times, upd of metal adatoms was studied on polycrystalline inert metals, such as Pt and Au, using radiotracer measurements.² Some of these works are those from Bowles, who investigated the adsorption on Pt of the following metal adatoms: Tl [44, 45], Sn [46], Cu, Cd, Sn, Tl and Bi [47], Cu [48], Bi [49]; and from Horányi et al. who analyzed the influence of Cu upd on the adsorption of chloride and bisulfate anions using also Pt electrodes [50, 51].

2.3 Radiotracer Methods

Radiotracer methods are particularly useful in the detection and identification of adsorbed layers on substrates surfaces. They allow to determine directly the coverage vs. current or potential relationship under steady state conditions (potentiostatic or galvanostatic) in the course of electrode processes without the knowledge of the adsorption isotherms. These methods, coupled with electrochemical techniques, provide direct in-situ measurements of surface concentrations with simultaneous control of electrochemical parameters, such as potential, current or charge. They are also used to study the adsorption of anions using radiolabeled

² See pre-history of upd in Chap. 1.

Fig. 2.6 (a) Surface concentration of Tl on Au(111) determined radiometrically, $C_{\text{HClO}_4} = 0.1 \text{ M}$, $C_{\text{Tl}^+} = 10^{-3} \text{ M}$, (b) Cyclic voltammogram for the same system (*solid line*) and in thallium free solution (*dashed line*). $|dE/dt| = 200 \text{ mV s}^{-1}$ (Reprinted with permission from Ref. [53])



species in the course of the M upd phenomenon contributing to a better understanding of the process. The radiometric methods for determining the surface concentration of adsorbed species may be precise and versatile, depending on the specific activity of the isotopes used and the signals coming from the adsorbed layer, so that the signal from solution phase can be easily separated. Further information about this technique can be found in Chap. 4 of the book *Radiotracer Studies of Interfaces*, edited by G. Horányi [52].

Some illustrative examples of the use of radiotracer techniques are discussed now.

Sobkowski et al. [53] have employed a radiotracer technique combined with cyclic voltammetry to analyze thallium upd on (111), (110) and (100) single crystal silver electrodes from perchloric acid solutions. They compared the radiometric measurements of the amount of thallium accumulated at the metal/solution interface with the voltammetric curves. Figure 2.6a, b show the Tl surface concentration on Au(111) measured radiometrically and the corresponding cyclic voltammograms for the system. They found for Ag(111) electrodes that the accumulation of the adsorbate at the interface occurred at potentials more positive than

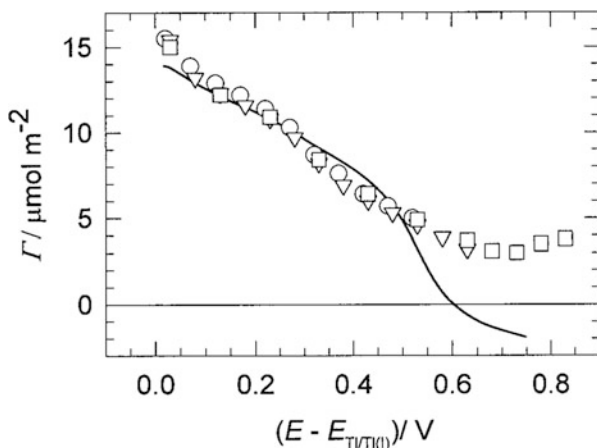


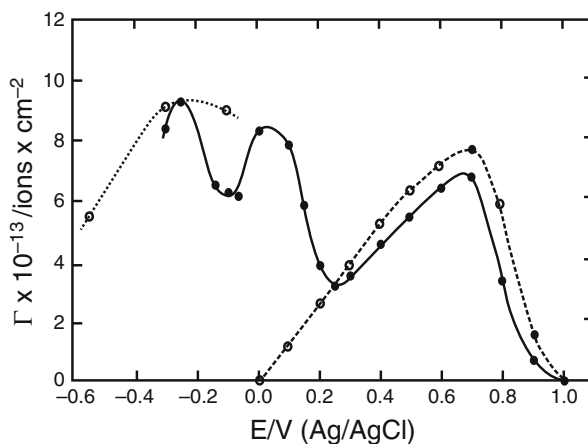
Fig. 2.7 Comparison of the positive-going potential dependence of Tl surface concentration calculated from the voltammogram (*full line*) in 1×10^{-4} M Tl^+ + 0.1 M KOH solution, $|dE/dt| = 5 \text{ mV s}^{-1}$ (*solid curve*) and measured by the radiotracer method in the same blank solution containing 1×10^{-4} M Tl^+ (○) and 1×10^{-5} M Tl^+ (□ first and ▽ third cycle of measurements). The Nernst potential for Tl/Tl^+ is -0.57 V in 1×10^{-5} M Tl^+ and -0.63 V in 1×10^{-4} M Tl^+ solutions (Reprinted with permission from Ref. [54])

those at which the voltammetric upd peaks take place, suggesting that the discharging process is preceded by the adsorption of thallium. Such an observation was possible owing to the specific feature of the radiometric method, which allows to record both the thallium deposited on the electrode surface and the accumulation of Tl species at the interface. Hence, the voltammetric peaks represent the process of discharge of thallium ions, which were earlier adsorbed. In these experiments, the monolayer surface concentration was determined to be independent of the crystallographic orientation of silver electrodes, suggesting the formation of a nonepitaxial Tl monolayer.

Poškus and Agafonovas [54] have investigated thallium upd and adsorption on polycrystalline gold in alkaline thallium solutions using radiotracer and voltammetric methods. While the radiotracer measurement allowed to obtain the total concentration of thallium atoms and ions at the electrode surface, cyclic voltammetry allowed to calculate the thallium surface concentration only due to the upd process. The authors found that in the potential region between the Tl/Tl^+ equilibrium potential and the main upd peak, both measurements are close, indicating that the thallium surface concentration is mainly due to thallium upd. However, at more positive potentials, in contrast to acidic solutions, the potential dependence of the thallium surface concentration above the main upd peak measured by the radiotracer method does not drop to zero but passes through a minimum, suggesting that the adsorption of thallium cations is induced by the specific adsorption of hydroxyl anions. This behaviour is shown in Fig. 2.7.

Radiometric studies for Cu upd on polycrystalline gold were performed by Zelenay et al. [55], to analyse bisulfate adsorption on Cu upd deposits on gold in

Fig. 2.8 Bisulfate adsorption vs E in the system Au (poly) / 0.05 M KClO_4 + 5×10^{-4} M $\text{Cu}(\text{ClO}_4)_2$ (containing 8.7×10^{-5} M Na_2SO_4) (\bullet —), as obtained from radiometric experiments. For comparison, bisulfate adsorption data for gold (\circ —) and copper ($\circ \cdot \cdot$) electrodes in 0.05 M KClO_4 are also included (Reprinted with permission from Ref. [55])



neutral perchlorate medium, i.e. 0.05 M KClO_4 + 5×10^{-4} M $\text{Cu}(\text{ClO}_4)_2$ solution containing 8.7×10^{-5} M Na_2SO_4 (^{35}S labeled). Since this method allows to measure absolute surface concentrations on smooth electrode surfaces with a detection limit of a few percent of a monolayer, it provides an insight into how anions interfere with the different stages of the M upd. Their Γ vs E measurements are presented in Fig. 2.8, showing a first maximum in the curve at potentials more positive than the Cu upd region, where no Cu deposits are present on the Au electrode. The amount of adsorbed bisulfate was however lower than that obtained for solutions without Cu^{2+} ions. Therefore, it was assumed that a possible formation of negatively charged hydroxy complexes of copper followed by their physisorption on the electrode surface cannot be excluded. The surface concentration of the anions rises sharply as the upd layer of copper is formed, indicating that the adsorption of bisulfate becomes interconnected with copper electrodeposition. A second maximum on the curve was observed when a Cu monolayer was formed on the surface until a third one appeared at more negative potentials when a few layers of bulk Cu deposit is formed. In the latter case, the behaviour of bisulfate adsorption is similar to that taking place on a solid polycrystalline copper surface. The authors also correlated the anion surface concentrations obtained through the radiometric experiments with the current-potential curves for the copper electrodeposition process.

2.4 Potential Step

The potential step technique has been applied to study the kinetics of M upd, as it is the case for example of the underpotential deposition of Cu on Au(111) in sulphuric acid solutions [56]. In these experiments, the potential was first held at a value where no copper was present on the surface for a few minutes, and then it was cycled to the desired value in the upd range. After a waiting time of 60 s, potential steps were applied and the resulting current transients were obtained in the potential

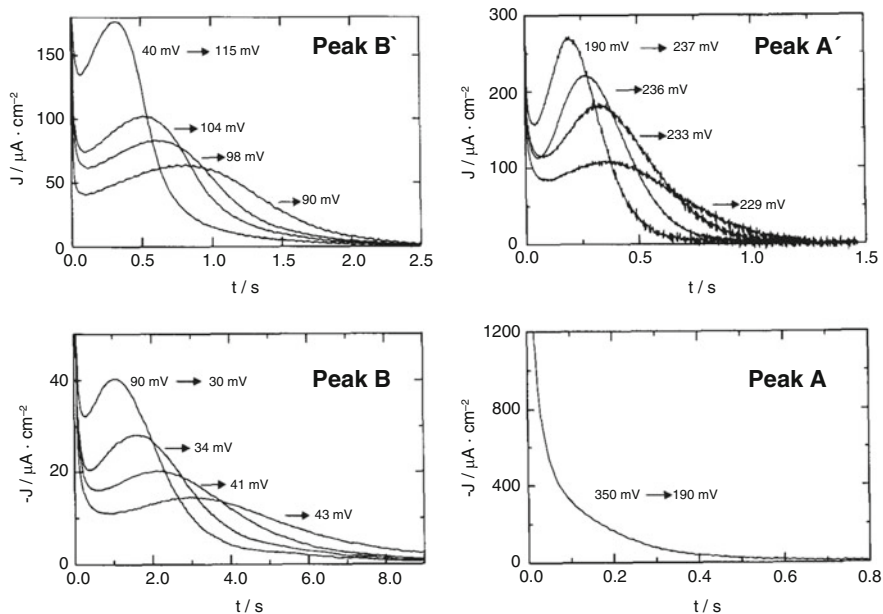


Fig. 2.9 Current transients for peaks A, A', B, B' of the cyclic voltammogram in the system Au(111)/ 1 mM CuSO₄ + 0.05 M H₂SO₄ (See Fig. 2.2). Potential steps are indicated in the figures (Reprinted with permission from Ref. [56])

regions corresponding to the four individual peaks found in the voltammogram of Fig. 2.2a, as given in Fig. 2.9. A typical shape of the current transient for the first adsorption peak A, showed after double-layer charging, a monotonic decay going to zero for long times. The experimental data were then analyzed to determine the mechanism of nucleation and growth of the Cu upd process. Linearization of the measured transient by the Cottrell equation ($I(t) \propto t^{-1/2}$) or by means of an exponential law ($I(t) \propto \exp[-kT]$), yielded nonlinear relationships, indicating that there is no pure diffusion control. The rising transients for peak B showed a current maximum, which shifted to shorter times when the overpotential increased. After long times all transients merged at a residual current value close to zero, which was associated by the authors to the side reaction of Cu⁺ formation [57]. Transients for the corresponding desorption peak B' exhibited a similar appearance to those of peak B, but in this case, the current fell to zero at longer times and no offset due to the Cu²⁺/Cu⁺ reaction was observed, as the potential was already too positive for this reaction to occur. Finally, the transients recorded for peak A' have the same shape as those of peaks B and B'. The shape of the transients for peaks B, B' and A' suggest the presence of a nucleation and growth process.³ The authors used the well known Bewick-Fleischmann-Thirsk (BFT) model for nucleation and growth [58] and found a good agreement

³ See discussion of nucleation and growth in Chap. 3.

between theory and experiment for instantaneous nucleation at long times. On the other hand, the rising parts of the transients were only poorly reproduced by the model due to its superposition with a falling transient at short times, directly after double-layer charging. They explained this discrepancy considering that adsorption at defect sites should be taken into account as a parallel reaction. Thus, they concluded that the measured current transients obtained for deposition and dissolution of Cu adlayer on Au(111) in sulphuric acid solution could be described by a model which assumes a two-dimensional nucleation and growth mechanism accompanied by an adsorption (desorption) process, with both proceeding at different electrode sites.

2.5 Equilibrium-Coverage-Potential Isotherms

Structural features of the upd layer were first derived, indirectly, from equilibrium-coverage-potential isotherms using single crystal substrates [57, 59].

Schulze and Dickertmann [57] analyzed M monolayer formation of Cu, Bi, Pb, Tl and Sb at Au(hkl) electrodes with $(hkl) = (111), (110)$ and (100) by means of their voltammetric desorption spectra, obtaining characteristic peaks that depend on the nature of the adsorbate as well as on the substrate orientation. They found that at low coverages, peak charge data obtained by integration of current/time curves yielded surface concentrations which fitted well with ordered structures. Under these conditions, a “mono-molecular” adsorption layer was found for Cu^{2+} , Pb^{2+} and Bi^{3+} .

The adsorption equilibrium isotherm provides a description of the energetics of adsorbates at the electrode-solution interface. The surface concentration of adsorbate is obtained as a function of solution concentration, electrode potential and the interactions of the adsorbate with other species.

The multi-peak structures of cyclic voltammograms in the upd range correspond to steps in the coverage-potential isotherms. This fact indicates a stepwise formation of two dimensional upd adlayers with different superlattice structures depending of substrate matrix and potential [60] as was pointed out above. The coverage can be determined by integrating the charge under the cathodic and/or anodic peaks in the cyclic voltammograms. The charge obtained can be transformed into a surface coverage assuming that the deposited metal has no partial charge, that the M layer packs into a given structure, and that the electrochemically active area of the electrode surface is known.

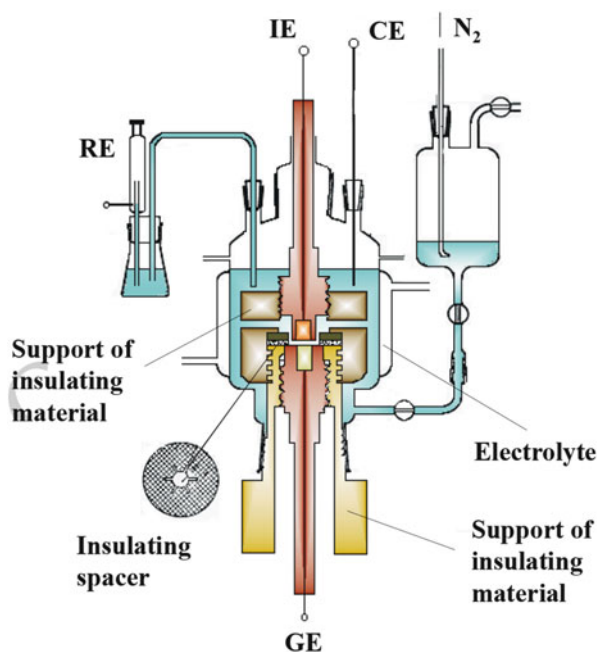
Another way to determine the adsorption isotherms is measuring the desorption of the adsorbed metal by potential steps. Figure 2.2b shows the dependence of Cu coverage (normalized charge due to Cu upd) on potential in the system Au(111)/1 mM $\text{CuSO}_4 + 0.05 \text{ M H}_2\text{SO}_4$ [39].

2.6 Twin-Electrode Thin-Layer

Another powerful tool for studying upd systems is the twin-electrode thin-layer (TTL) technique, which was introduced by Schmidt et al. using polycrystalline substrates [61, 62]. This method allows independent and precise charge density (q) and surface excess (Γ) measurements. Thus, the metal ion flux can be well separated from anion adsorption-desorption processes. Detailed design and operation of the apparatus have been described elsewhere [61–63]. A schematic view of the TTL cell is presented in Fig. 2.10. The main part of the thin layer cell consists in two planar-parallel electrodes, the working or indicator electrode (IE) and the generator electrode (GE), closely spaced by a constant distance of about 50 μm . Both electrodes are metal rods, fitted in insulating holders, e.g., Teflon, and separated at a desired distance by an insulating spacer (50 μm thickness). The small electrolyte volume between them constitutes the “thin layer”, which is separated by small capillaries from the main part of the electrochemical cell containing the counter and reference electrodes. The GE is composed of the same metal as that to be deposited on the IE, and both electrodes may be independently polarized by an appropriate bipotentiostat.

The metal ion activity ($a_{\text{M}^{z+}}(\text{aq})$) in the thin layer cell is given by the application of a constant potential to the GE according to the Nernst equation for a 3D M phase. Therefore, any $a_{\text{M}^{z+}}(\text{aq})$ changes within the thin layer due to metal ion adsorption or desorption at the IE are rapidly compensated by M dissolution or deposition at the

Fig. 2.10 Schematic view of the twin-electrode thin layer cell. Electrodes: *IE* (working or indicator electrode), *GE* (generator electrode), *RE* (reference electrode), *CE* (counter electrode)



reversible GE. The potential of the IE may be scanned at a constant rate between defined starting and final potentials, for which equilibrium conditions are adjusted. The integrals of the corresponding current-time transients in the IE circuit are related to changes in q , whereas those of the current-time transients in the GE circuit correspond directly to Γ changes at IE. q_o -values (due to the double layer charging) are determined in $M_{(\text{aq})}^{z+}$ ion-free solutions. From independent $q(E, \mu_{M_{(\text{aq})}^{z+}})$ and $\Gamma(E, \mu_{M_{(\text{aq})}^{z+}})$ measurements, the electrosorption valency⁴ can be directly determined from Δq - Γ plots with $\Delta q = q - q_o$. In the absence of specific adsorption, q_o is relatively small, and it can be assumed that γ_v (electrosorption valency) $\rightarrow z$. In contrast, if cosorption or competitive sorption processes occur in parallel with M upd at the interphase, then $\gamma_v \neq z$ gives information about the coupling between q_o and Γ .

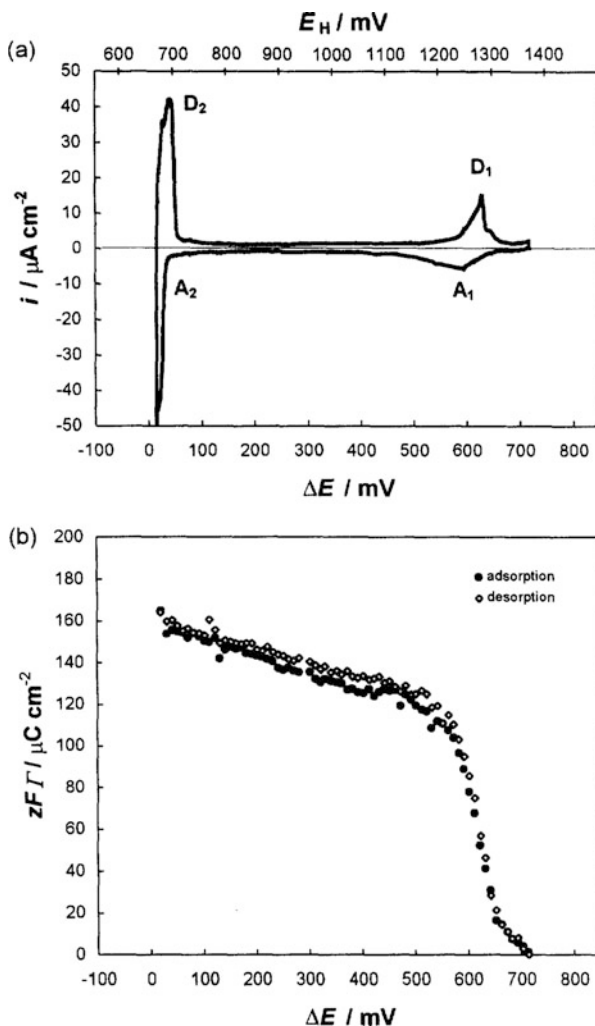
Figure 2.11a, b show the cyclic voltammogram for Ag upd on Au(111) in sulfate solutions and the Γ - ΔE isotherm determined by the TTL-technique over the entire upd range studied, respectively [13]. A charge density of approximately $130 \mu\text{C cm}^{-2}$ is obtained for the first upd peak corresponding to a coverage of $\theta_{\text{Ag}} \approx 0.58$. A total charge of about $zF\Gamma \approx 160 \pm 5 \mu\text{C cm}^{-2}$ at $\Delta E = 20 \text{ mV}$ was experimentally found, which does not correspond to the theoretical value for a complete Ag monolayer ($zF\Gamma = 222 \mu\text{C cm}^{-2}$). This fact may be attributed to additional adsorption of Ag in the upd ranges $0 \leq \Delta E(\text{mV}) \leq 20$ and $\Delta E > 720 \text{ mV}$.

For the same system, the Δq - Γ plot (Fig. 2.12) gives a value of $\gamma_v = z = 1$, suggesting the absence of anion cosorption or competitive sorption phenomena. However, Ag upd on Au(111) takes place at more positive potential values than the potentials of zero charge of Au(111) ($E_{\text{PZC}}^{\text{Au}(111)} = 470 \text{ mV}$) and Ag(111) ($E_{\text{PZC}}^{\text{Ag}(111)} = -478 \text{ mV}$) surfaces [64–66], therefore the presence of adsorbed anions cannot be excluded. A mechanism proposed by Gewirth et al. [15] for the Ag upd phenomenon is that Ag must penetrate the anion layer in order to approach the Au(111) surface, while this anion layer remains and is also present after Ag adatom formation.

A similar analysis was performed for the system Au(100)/Ag⁺, SO₄²⁻ [13]. Figure 2.1a shows the cyclic voltammogram of this system. The Γ - ΔE isotherm measured under TTL-conditions (Fig. 2.13) indicates a stepwise formation of the Ag monolayer, in agreement with the voltammetric behavior. A value of $zF\Gamma \approx 80 \mu\text{C cm}^{-2}$ is obtained for the first Ag upd peak, corresponding to a coverage of $\theta_{\text{Ag}} \approx 0.42$. At $\Delta E = 20 \text{ mV}$, the experimental value of $zF\Gamma \approx 160 \mu\text{C cm}^{-2}$ is significantly smaller than the theoretical one for a complete

⁴The concept of electrosorption valency $\gamma_v = \frac{1}{F} \left(\frac{\partial q}{\partial \Gamma} \right)_E$ is discussed in detail in Chap. 3. In the case that upd involves a straightforward full discharge of the corresponding cation, its value is equal to its valency.

Fig. 2.11 (a) Cyclic voltammogram for the upd of Ag in 5×10^{-3} M $\text{Ag}_2\text{SO}_4 + 0.5$ M H_2SO_4 solution on Au(111) substrate. A_n and D_n with $n = 1, 2$ denote cathodic adsorption and anodic desorption peaks, respectively. $|dE/dt| = 7$ mV s $^{-1}$, (b) $\Gamma(E)$ isotherm measured under TTL conditions in the system Au(111)/ 4.5×10^{-5} M $\text{Ag}_2\text{SO}_4 + 0.5$ M H_2SO_4 . $T = 298$ K (Reprinted with permission from Ref. [13])



Au(100)–(1 × 1) Ag monolayer ($192 \mu\text{C cm}^{-2}$). The authors attributed this difference to an additional Ag adsorption in the potential ranges $0 \leq \Delta E(\text{mV}) \leq 20$ and $\Delta E > 720$ mV.

Similarly to the previous system, Au(111)/ Ag^+ , SO_4^{2-} , the electroadsorption valency measurements with the Au(100) substrate (Fig. 2.14) show $\gamma_v = z = 1$, indicating that coadsorption or competitive adsorption of anions can be excluded. However, taking into account the potentials of zero charge of Au(100) ($E_{\text{PZC}}^{\text{Au}(100)} = 240$ mV) and Ag(100) ($E_{\text{PZC}}^{\text{Ag}(100)} = -648$ mV) [64–66], it could also happen that a nearly constant anion layer may be present during Ag upd.

Fig. 2.12 Determination of the electroadsorption valency, γ_v , from independent Δq and Γ measurements obtained by TTL technique. System: Au(111)/ 4.5×10^{-5} M $\text{Ag}_2\text{SO}_4 + 0.5$ M H_2SO_4 . $T = 298$ K (Reprinted with permission from Ref. [13])

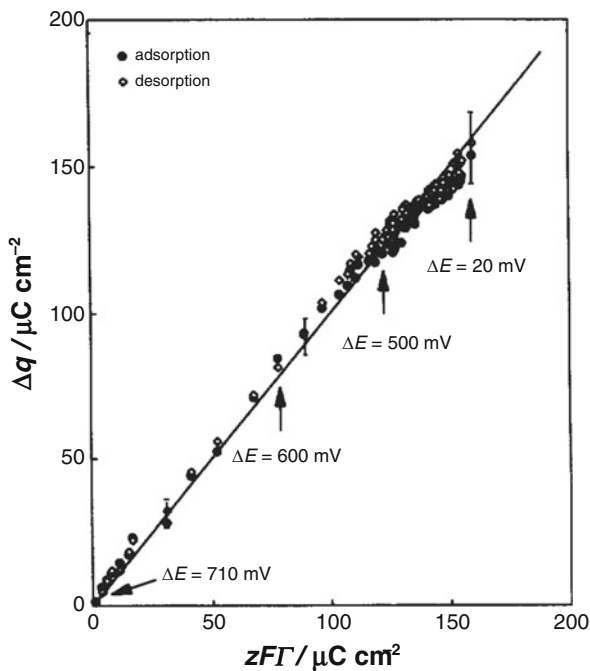


Fig. 2.13 $\Gamma(E)$ isotherm measured under TTL conditions in the system Au(100)/ 4.2×10^{-4} M $\text{Ag}_2\text{SO}_4 + 0.5$ M H_2SO_4 . $T = 298$ K. These isotherms correspond to the voltammetric profile shown in Fig. 2.1a (Reprinted with permission from Ref. [13])

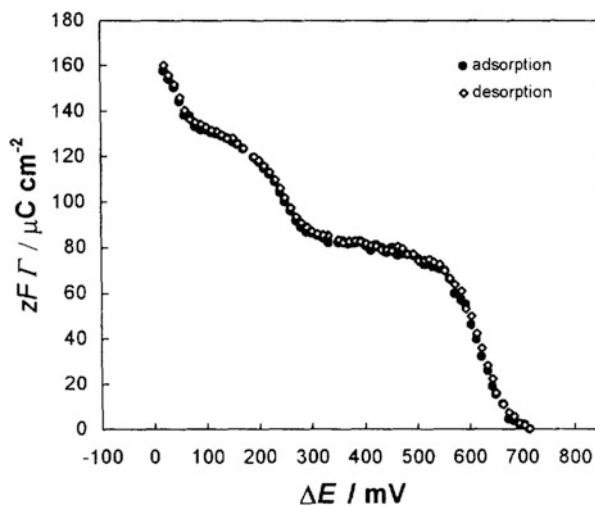
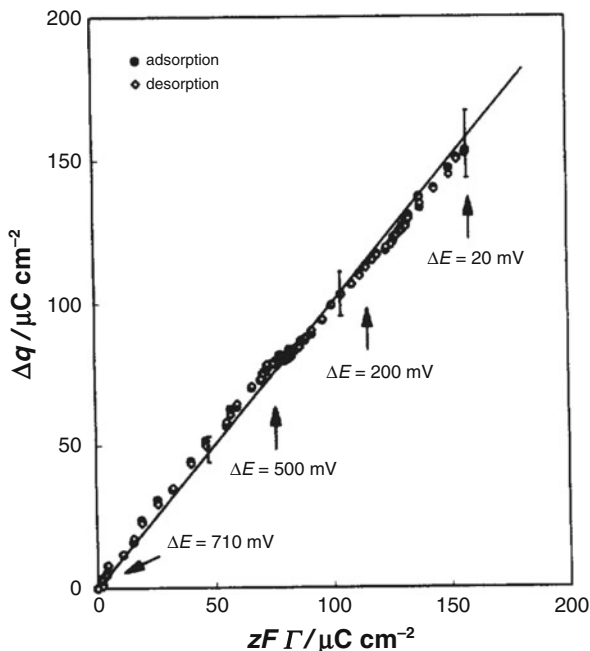


Fig. 2.14 Determination of the electrosorption valency, γ_v , from independent Δq and Γ measurements obtained by the TTL technique. System: Au(100)/ 4.2×10^{-4} M $\text{Ag}_2\text{SO}_4 + 0.5$ M H_2SO_4 . $T = 298$ K (Reprinted with permission from Ref [13])



2.7 Rotating Ring Disk Electrode

The Rotating Ring-Disk Electrode (RRDE) technique has also been used to study the upd phenomenon. In the late 1960s and early 1970s, Bruckenstein and coworkers [67–70] proved that this method was a powerful and useful tool to study adsorption processes at solid electrodes. Its main advantage is the well characterized and controlled mass transfer to the electrode through forced convection induced by electrode rotation which allows, in many cases, an easy separation and identification of mass transfer and intrinsic electrode kinetic controlling effects.

The RRDE is a disk electrode around which is placed an insulating gap made of Teflon, polyethylene or epoxy resin. A ring electrode is placed around the disk in a centrally symmetrical position. This geometry permits precise hydrodynamic control of the flux of material to and from a reacting surface. The preparation of ring-disk electrodes as well as the rigorous theory describing their behaviour together with some practical applications are described by Opekar and Beran [71].

Two types of experiments can be performed with a RRDE: collection experiments (the most common), where the species generated at the disk are detected at the ring, and shielding experiments, where the flow of bulk electroactive species to the ring is perturbed due to reaction on the disk [71, 72]. The applications of the first type of experiments to upd are explained in more detail here.

The amount of upd species deposited on the disc can be estimated using the collection mode, where the disc acts as the generator while the ring acts as the collector [73, 74]. In this case, the ring potential is held at a sufficiently cathodic potential value, which allows the massive deposition of the metal ions. When the surface of the ring is totally covered by the metal, the current stabilizes and reaches a constant value, dependent on the rotation rate, which is considered as the baseline. Then, the disc is polarized either by potential scanning or by a potentiostatic pulse to a proper potential for the deposition of one monolayer of the metal. After that, the disc potential is scanned in the positive direction to dissolve the formed monolayer. The increase of metal ions in the diffusion layer is detected as a rise in the ring current, which returns to its initial constant value after total dissolution of the monolayer. The current variation at the ring can be used to estimate the charge due solely to monolayer dissolution without any influence of surface oxidation.

Bruckenstein and coworkers have contributed a great deal to the practical application of the RRDE. They studied the kinetics and the voltammetric properties of several systems such as Pt/Cu²⁺ [68, 69], Pt/Bi²⁺ [75], Au/Pb²⁺ [76], Au/Ag⁺ [77], Au/Hg²⁺ [78], between others.

This technique has been used to separate the upd mass flux from the charge flux and thus thermodynamic data can be obtain independently from kinetic and double layer effects [73]. It can be employed to obtain both equilibrium and dynamic properties for low concentrations of depositing ions ($\leq 10^{-4}$ M). In order to obtain accurate results, other conditions are needed: the chemical nature of the ring electrode must be the same as that of the upd metal deposited on the disc, therefore plating the ring with at least ten layers of the upd metal is required; suitable rotation speed (lower rotation speeds at the higher concentrations); sufficiently negative ring electrode potential in order to ensure convective-diffusion controlled reduction of the upd species in solution at the ring electrode.

Machado and coworkers [79] have used cyclic voltammetry at stationary and rotating ring-disk electrodes in order to analyze the underpotential deposition of Cu and Ag on polycrystalline Au surfaces from sulphuric acid solutions. The charge densities obtained by the later technique were calculated by the collection mode. For a better understanding, their own voltammetric results are also presented here. Figure 2.15 exhibits the voltammetric response of the Au surface (stationary electrode) in Cu²⁺ containing solution, when holding the potential scan at 0 V vs RHE during 300 s to allow Cu deposition on the electrode surface, together with the steady state profile of the blank solution. Peak 4 is related to bulk Cu dissolution and peaks 1–3 represent the upd Cu profile. The sum of the charge densities calculated for the three upd Cu peaks reaches 405 $\mu\text{C cm}^{-2}$. The RRDE was used to separate charge and mass fluxes, allowing to estimate the charge on the disk due solely to the metal deposition reaction. The total charge values obtained for the redissolution of the submonolayers using different deposition times are shown in Table 2.1, where the charges were evaluated by two methods. In the first one, the voltammetric peaks during the potential scan on the disk were integrated to obtain the oxidation charge values. In the second method,

Fig. 2.15 Steady-state voltammetric response for the system Au/0.5 M H₂SO₄ at 1 V s⁻¹ (continuous line) and first cycle voltammogram obtained after the addition of 5 × 10⁻⁵ M CuSO₄ and holding at 0 V for 300 s (dotted line) (Reprinted with permission from Ref. [79])

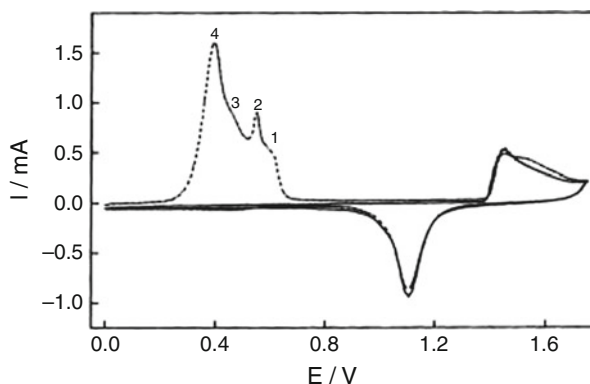


Table 2.1 Dissolution charges densities obtained for Cu upd from the two methods described in the text: cyclic voltammetry and RRDE. Cu was deposited at 0.17 V during several time intervals

$T_{\text{dep}}(\text{s})$	$q_{\text{disk}}^{(\text{v})} (\mu\text{C cm}^{-2})$	$q_{\text{disk}}^{(\text{R})} (\mu\text{C cm}^{-2})$
0	26	28
10	53	57
20	91	96
60	135	146
90	233	244
120	292	304
300	322	326
600	376	374
1200	385	386

$q_{\text{disk}}^{(\text{v})}$, disk charges calculated by the voltammetric peaks of the disk response; $q_{\text{disk}}^{(\text{R})}$ disk charges calculated through the variation of ring currents

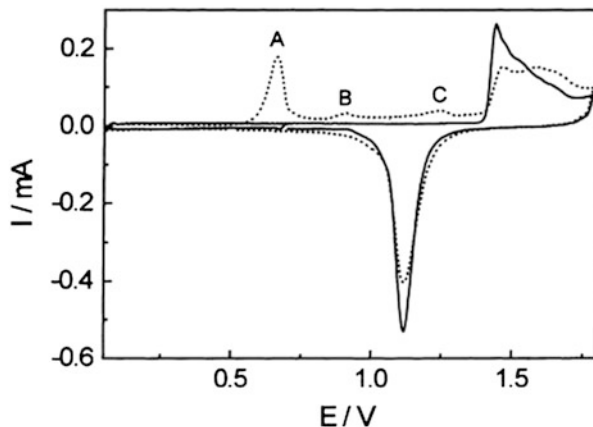
Reedited with permission from Ref. [79]

current variations observed on the ring were associated solely with the amount of Cu²⁺ which leaves the disk surface generating an increase in the ring deposition current and with the ring current after the whole Cd ML was dissolved on the disk. Both results show a good agreement between the values found using the two procedures, i.e. 386 $\mu\text{C cm}^{-2}$.

Comparing the results of charge density values related to the oxidation of a complete Cu upd monolayer, from stationary (405 $\mu\text{C cm}^{-2}$) and rotating ring-disk electrodes (386 $\mu\text{C cm}^{-2}$), very close to the theoretical value of 390 $\mu\text{C cm}^{-2}$, the authors suggested an epitaxial deposition of Cu on polycrystalline Au in a two-electron reduction process.

The same authors also investigated the Ag/Au system. The voltammetric response of the Au electrode in the solution containing Ag⁺ ions is presented in Fig. 2.16, after holding the potential scan at 0.5 V vs RHE during 600 s to allow Ag monolayer deposition on the electrode surface, together with the steady state profile

Fig. 2.16 Steady-state voltammetric response for the system Au/0.5 M H_2SO_4 at 0.5 V s^{-1} (continuous line) and first cycle voltammogram obtained after the addition of $5.6 \times 10^{-5} \text{ M AgNO}_3$ and holding the potential scan at 0.5 V for 600 s (dotted line) (Reprinted with permission from Ref. [79])



of the blank solution. Peaks B and C correspond to the dissolution of Ag upd, while the peak A is related to the bulk Ag phase. As it is shown, Ag upd occurs at a more positive potential range than that of Cu, indicating that the oxidation of the Au surface is affected by the presence of the adsorbed Ag layer. For this reason it becomes difficult to determine the charge density for a full Ag monolayer, mainly due to the possible overlapping of the Ag upd peak with Au oxidation. The authors found a value of $108 \mu\text{C cm}^{-2}$, which corresponds approximately to half a monolayer of Ag adatoms.

The RRDE measurements, which allowed to separate the oxidation charge of the monolayer from that associated to Au oxidation, indicated a value of $115 \mu\text{C cm}^{-2}$, also in agreement with that required for a half monolayer. This deposition mode is different from the Cu/Au system and the authors concluded that co-adsorption of sulfate or hydroxide anions hinder the formation of a full monolayer of Ag on polycrystalline Au.

Jüttner et al. have used cyclic voltammetry, charge isotherms and RRDE methods to analyze the upd of Cu on Au(111) surfaces in sulphuric acid solutions of different Cu^{2+} concentrations [24]. From the voltammetric measurements and charge isotherms, they concluded that the ideal metal-monolayer model was valid at low underpotentials at a high degree of adatom coverage, since the electrosorption valency γ_v is equal to the valence number z , i.e. $\gamma_v = z = 2$, indicating a full M discharge. The formation of Cu^+ ions and co-adsorption of sulfate ions produced significant deviation from the ideal behaviour ($\gamma_v \sim 1$) at higher underpotentials, where the $(\sqrt{3} \times \sqrt{3})\text{R}30^\circ$ structure was present. The authors explained this behaviour in terms of a partial discharge of Cu^{2+} to Cu^+ , the adsorption of which was stabilized by co-adsorption with sulfate ions. Charge-transfer controlled formation of Cu^+ at the interface as a reaction intermediate was detected in the transition range of underpotential and overpotential copper deposition using the RRDE measurement technique.

2.8 Electrochemical Quartz Crystal Microbalance

The electrochemical quartz crystal microbalance (EQCM) is one of the most sensitive electrochemical techniques and is particularly well suited to study underpotential deposition of metallic layers on a gold coated crystal. The technique has now become a valuable procedure in electrochemical surface science, complementary to charge evaluation procedures such as cyclic voltammetry and chronoamperometry. Usually, simultaneous cyclic voltammetry and EQCM experiments have been used in order to determine the corresponding variations of the faradaic charge and mass during the deposition process.

Immersion of a quartz crystal oscillator in an electrolyte solution, with simultaneous control of the applied potential of the overlying metallic film enables simultaneous and in-situ determination of the mass variation in relation to surface charge density associated with an electrosorption or electrodeposition process. This system is sensitive enough to detect the presence of submonolayer amounts of species on the surface, i.e. it is capable of weighing a change of mass in the charge density on the electrode surface, together with the simultaneous measurement of electric charge. Thus, the EQCM may provide information of the quantities of two species, such as adatoms and adsorbed anions, as a function of electrode potential.

The first studies on upd using a quartz crystal microbalance (QCM) were performed by Bruckenstein and Swathirajan [80], who analysed the underpotential deposition of lead and silver on polycrystalline gold in acetonitrile. In this case, they generated the monolayer deposits on the QCM and made ex-situ mass determinations. This method consisted on measurements of the resonance frequency of a piezoelectric quartz crystal upon whose faces gold electrodes had been deposited, and the crystal frequency changed as upd species were deposited. The surface coverages of underpotentially deposited species were calculated through the relation derived by Sauerbrey [81] between the frequency change of the oscillating quartz crystal and the change of the attached mass. They found a good agreement between these results and those obtained by the rotating ring disk (Ag) and rotating disk (Pb) techniques.

Later on, Bruckenstein and Shay published an important contribution on the experimental aspects of use of the QCM in solution [82] and Melroy et al. [83] were the first who evaluated in situ Pb upd deposits on Au electrodes by the EQCM technique. They obtained the electrosorption valency (γ_v) for Pb deposition onto Au, which was in good agreement with literature values, indicating the capabilities of the EQCM to be used in situ for measurement of monolayer mass changes.

Continuing on the study of upd processes with the EQCM, Deakin and Melroy [84] reported results related to the upd of several metals (Pb, Bi, Cu, and Cd) on polycrystalline Au in 0.1 M HClO₄. The coverages of the M upd layer on the Au surface were calculated from the frequency change of the QCM as a function of potential, and were in good agreement with previous values obtained using other techniques. The electrosorption valencies were calculated from the slope of the

charge versus coverage plots, which provide a sensitive measure of γ_v at any potential.

It must be pointed out that adsorbed anions may produce significant responses in the EQCM frequency changes [85] and therefore, they should be considered in the interpretation of mass changes observed in the processes of monolayer formation.

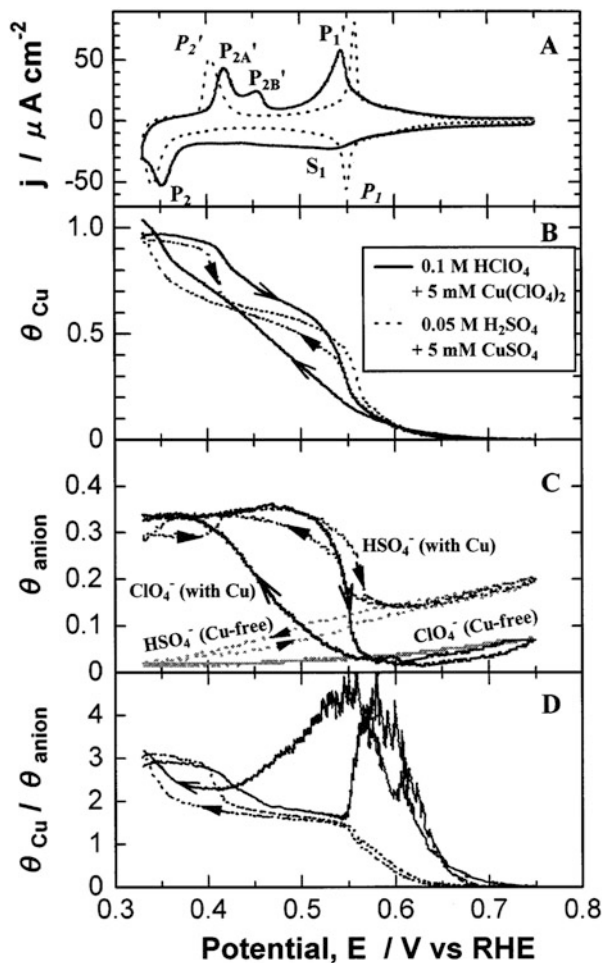
The present method was used to study the formation of copper and silver adatoms on Au(111) electrodes [16, 86, 87] and was found to provide useful information on upd processes, complementing results obtained by other techniques.

Ikeda et al. [86] showed that copper adatoms formed in the first and second upd processes on Au(111) in sulphuric acid solution are close to 2/3 of one monolayer and one monolayer respectively, and that the ratios of hydrated bisulfate anions to Cu adatoms are approximately 0.5 and 0.3, at the corresponding Cu coverages.

In a later work [87], it was found that perchlorate anions are specifically adsorbed on Au(111) and that the Cu adatoms on the surface cause an enhanced coadsorption of both sulfate and perchlorate anions. Figure 2.17 shows the cyclic voltammograms for Au(111) electrodes in both solutions and the corresponding coverages of Cu as well as those of anions. The deposition and dissolution phenomena of Cu in 0.1 M HClO₄ consisted of a two-stage deposition process characterized by S₁ and P₂ peaks, and the corresponding dissolution was characterized by P'_{2A}, P'_{2B} and P'₁ peaks (Fig. 2.17a). This voltammetric behaviour was different from that observed in 0.05 M H₂SO₄, which consisted of two sharp cathodic peaks (P₁ and P₂) and the corresponding anodic peaks (P'₂ and P'₁). The composition of the Cu adlayer (θ_{Cu} and θ_{anion} , coverages of Cu adatoms and coadsorbed anions respectively) during its formation or removal as a function of potential was determined and shown in Fig. 2.17b, c. The coverages of both anions on a Cu-free Au(111) surface, which are also exhibited in Fig. 2.17c, decrease monotonically when the potential is changed to more negative values. For the first Cu upd region, the reversible anodic and cathodic peaks of the voltammogram correspond well to the reversible changes in θ_{Cu} and θ_{anion} , producing in this deposition stage an enhancement of anion adsorption. The authors showed that the maximum HSO₄⁻ anion coverage when $\theta_{\text{Cu}} \sim 0.66$, led to a ratio $\theta_{\text{Cu}} / \theta_{\text{anion}} \sim 2$ (Fig. 2.17d), indicating a good agreement with the ($\sqrt{3} \times \sqrt{3}$) structure determined for the first Cu upd layer in H₂SO₄ solution by various methods [27, 38, 88, 89]. On the other hand, the weakly adsorbed ClO₄⁻ adsorbates (represented by a broad shoulder S₁) rearranged continuously and therefore no ordered structure was reported. In contrast, asymmetric features of the voltammograms for the second Cu upd region in H₂SO₄ and for the whole process in HClO₄ correlated with a large hysteresis in changes of θ_{Cu} and θ_{anion} , probably originating from a slow rearrangement of both species. The authors attributed these differences to the strong adsorption of HSO₄⁻ and the weak one or mobility of ClO₄⁻.

Uchida et al. [16] discussed quantitatively the composition of the Ag adlayer on Au(111) in H₂SO₄ solution including Ag adatoms and coadsorbed anions, employing the EQCM. They pursued to clarify the relation between the amount of Ag adatoms and that of adsorbed hydrated anions during the formation and

Fig. 2.17 (a) Cyclic voltammogram of the system Au(111)/0.1 M HClO₄ + 5 mM Cu(ClO₄)₂ (solid line) and Au(111)/0.05 M H₂SO₄ + 5 mM CuSO₄; (b) changes in the coverage of Cu adatoms, θ_{Cu} ; (c) changes in the coverage of anions, θ_{anion} . θ_{anion} for Cu-free Au(111) are shown by grey curves; (d) changes in the molar ratio $\theta_{\text{Cu}}/\theta_{\text{anion}}$. The results of (b), (c) and (d) stem from EQCM measurements (Reprinted with permission from Ref. [87])



removal of a Ag adlayer. They suggested that the formation of the first Ag up structure began accompanied with the desorption of anions, where the Ag adatoms were deposited at vacant sites through a “template” of adsorbed bisulfate, while in the region between the first and second up peaks, bisulfate anions tended to desorb from the Ag-free Au(111) surface. However, they found that a large amount of anions was adsorbed on the Ag adlayer on Au(111). They suggested that a rearrangement of adsorbed anions may occur at the surface resulting in, for example, an adsorption of anions on top of Ag adatoms, as proposed by an EXAFS study [90]. At the potential close to bulk deposition, the coverage of Ag increases to one monolayer, corresponding to the formation of the first close-packed Ag adlayer on Au(111). Therefore, this process involved the rearrangement of Ag atoms and adsorbed anions and the substitution of the later by Ag adatoms.

More recently, Inzelt and Horányi [91] showed that the EQCM can be also used to study alloy formation in the course of Cd upd on gold from HClO_4 supporting electrolyte. The alloy formation/dissolution processes produced the roughening of the surface, which was reflected by an increase in the total amount of adsorbed anions and adatoms, resulting in frequency changes.

2.9 Scanning Probe Microscopy

A detailed understanding of the mechanisms by which electrochemical phase formation processes take place cannot be achieved with purely electrochemical methods, but requires local information on the structural, chemical and morphological properties of the interface at the atomic scale. The analysis of the initial steps of metal phase formation has strongly benefited from the advent of the Scanning Probe Microscopy (SPM) techniques, such as Scanning Tunneling Microscopy (STM) and Atomic Force Microscopy (AFM), allowing the visualization of the deposit morphology at the atomic scale. Indeed, studies of many upd systems performed previously by conventional electrochemical techniques to evaluate thermodynamics and kinetics, were complemented by structural information of upd layers obtained by in situ STM and AFM techniques. These high-resolution microscopies have similar components but different sensing probes, and therefore various types of interaction of the tip with the surface are exploited in the different types of probe microscopes.

2.9.1 Scanning Tunneling Microscopy

Binnig and Rohrer developed the STM operating in ultrahigh vacuum in 1981 [92, 93] and later, in 1986, Sonnenfeld and Hansma demonstrated for the first time that it could be employed in electrolyte solutions [94]. This aspect is highly important since the interfacial environment of the electrochemical processes does not appear to be essentially disturbed during the structural imaging. Several works refer to the use of this technique in electrochemical systems [95–99]. In situ STM has been widely used as a powerful tool for exploring the structure of M adlayers, providing valuable insight into metal phase formation processes of different dimensionality at an atomic level. With this technique, the growth morphology of metal deposits can be followed from isolated atoms to connected films.

The most important feature of in situ STM is real-space visualization under reaction conditions of bare and adsorbate-covered surfaces at the atomic scale. This provides data on the structure of upd layers as a function of coverage, on the reconstruction and modification of the substrate caused by the electrodeposited species, on the formation of surface alloys, on possible epitaxial correlations between 2D and 3D phases, and on the mechanisms involved in all these processes.

STM is based on the phenomenon of quantum mechanical tunnelling. A sharp metal tip, often made of Pt, W or Pt-Ir, is brought close ($\leq 10 \text{ \AA}$) to the planar sample surface via a controlled approach piezo-electric motor. When the two surfaces are close enough so that their wave functions overlap, a finite probability exists that electrons will cross the barrier between the surfaces when a bias is applied between the sample and tip. The resulting tunnelling current I_{tun} , depends sensitively on the distance between tip and surface, and can be expressed by:

$$I_{\text{tun}} \approx D_S(E_{F,S})D_T(E_{F,T})V_b \exp[-2\kappa d] \quad (2.1)$$

where $D_S(E_{F,S})$ and $D_T(E_{F,T})$ are the density of states of the sample and tip at their respective Fermi level energies, d is the tip-sample separation, V_b is the bias voltage, i.e. the applied voltage difference between sample and tip, and the exponential term is the probability of tunnelling through the potential barrier [100], with κ given by:

$$\kappa \approx [2m_e\bar{\phi}/\hbar^2]^{1/2} \quad (2.2)$$

where m_e is the electron mass, $\bar{\phi}$ is the mean of the tip and sample barrier heights, and $\hbar = h/2\pi$, where h is Planck constant. Equation (2.1) is an oversimplification but sufficiently explains the operation of the instrument. The high sensitivity of the instrument, which can attain a vertical resolution of a few 0.01 nm is attributable to the strongly non linear dependence of the tunneling current on the distance between the tip and the surface.

The STM can be operated in two modes to produce images. The sample surface can be mapped in the *constant current mode* by recording the feedback-controlled motion of the tip up and down, such that a constant tunneling current is maintained at each x-y position. The structure can also be mapped in the *constant height mode* by recording the modulation of the tunneling current as a function of position, while the tip remains at a constant height above the surface. The later mode is preferred for atomic-scale images but it can only be used on very smooth surfaces. The former is required to obtain topographic images of relatively rough surfaces.

For in situ electrochemical experiments, the STM tip surface exposed to the electrolyte must be insulated by coating all but its very end with an insulator (soft glass, APIEZON wax, polymers) so that the tunneling current will not be overcome by the electrochemical background current (faradaic current) flowing through the tip. Lateral atomic resolution at metal surfaces in the electrolyte may only be achieved with optimum tunneling tips, combining ideal tip geometry with an excellent quality of the lateral tip insulation. The microscope must be coupled with a bipotentiostat, which allows that the potential of the substrate and the tip can be varied independently with respect to a reference electrode [101]. The principal limitation of the STM is that it cannot be used for non conducting samples.

An illustrative example of a surface topography showing an in situ STM image of an electrochemically polished Au(111) surface, under potentiostatic control,

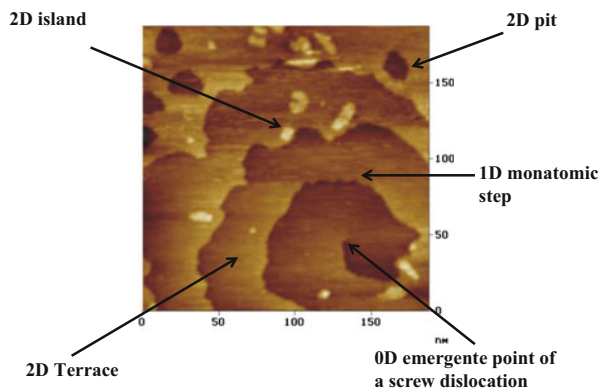


Fig. 2.18 Example of an in situ STM image showing surface defects of an electrochemically polished Au(111) surface in the system Au(111)/ 5×10^{-3} M $\text{AgClO}_4 + 0.5$ M HClO_4 at $E = 200$ mV (vs Ag/Ag^+ Nernst equilibrium potential). $T = 298$ K (Reprinted with permission from Ref. [13])

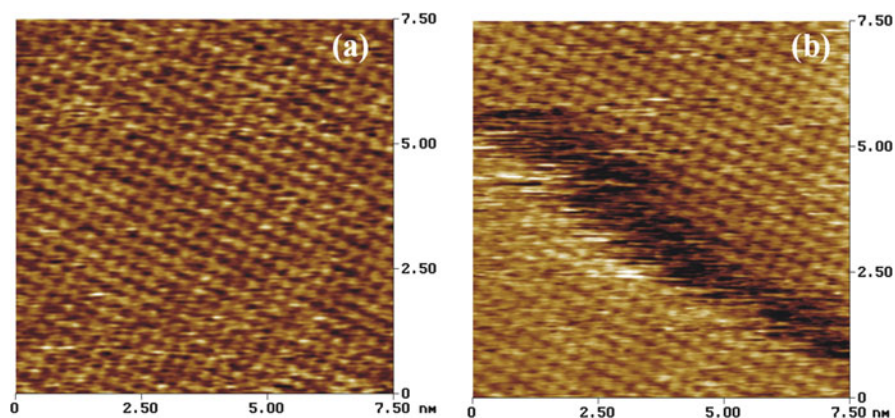


Fig. 2.19 Examples of in situ STM images with atomic resolution of an electrochemically polished Au(100) surface in 0.5 M HClO_4 at $E = 750$ mV (vs reversible hydrogen electrode). (a) on a terrace (b) on two terraces separated by a monatomic step. $T = 298$ K

with different inhomogeneities is presented in Fig. 2.18. 1D monatomic steps, 0D emergence point of a screw dislocation, 2D pits, etc., are surface defects that can be directly observed by STM and play an important role in the formation of low dimensional M phases in the upd range.

On the other hand, Fig. 2.19a illustrates an example of in situ STM imaging of a Au(100) surface in perchlorate electrolyte with lateral atomic resolution. A quadratic structure with an average interatomic distance of $d_{\text{o,Au}} = 2.8 \pm 0.1$ Å can be observed, which is in good agreement with crystallographic data of $d_{\text{o,Au}} = 2.8840$ Å [12] and previous in situ STM images [102]. Figure 2.19b

shows the atomic structure of two Au terraces separated by a monatomic step which looks frazzled in STM images. This phenomenon has also been observed at the edges of Cu islands deposited on Ag(111) [103] and has been interpreted as being due to the movement of kink sites on steps edges and, as a consequence of this movement, the STM tip finds the location of a step edge always at slightly different positions for each scan line [104, 105].

The Ag upd process on Au has also been studied by in situ STM in different electrolytes by various authors. In particular, Itaya et al. [17, 106, 107] found for annealed Au(111) substrates expanded and commensurate Au(111)–($\sqrt{3} \times \sqrt{3}$)R30° Ag and Au(111)–(4 × 4)Ag structures at relatively high underpotentials in sulphuric and perchloric acid solutions, respectively. At low underpotentials, a condensed commensurate Au(111)–(1 × 1)Ag overlayer was observed in both solutions. Gewirth et al. [14, 108] used in situ AFM, which will be addressed later, together with cyclic voltammetry to study the underpotentially deposited monolayers of Ag on Au(111) surfaces in different electrolytes. In this case the working electrode was a Au film evaporated onto mica. These authors recognized a strong anion influence on the overlayer structure and found the following structures depending on the nature of the electrolyte: Au(111)–(3 × 3)Ag (sulfate), Au(111)–(4 × 4)Ag (nitrate), Au(111)–(1 × 1)Ag (acetate) and an unassigned open structure (perchlorate). The results of Itaya and Gewirth do not agree in sulfate media. García et al. [13], using mechanically and electrochemically polished Au(111) substrates in sulfate and perchlorate solutions, found a Au(111)–(4 × 4)Ag structure. The theoretical charge for this adlayer is $zFT = 125 \mu\text{C cm}^{-2}$ ($\theta_{\text{Ag}} = 0.56$) which is in good agreement with the experimental value of $zFT = 130 \pm 5 \mu\text{C cm}^{-2}$ for the first Ag upd peak obtained by TTL-measurements. A Ag(1 × 1) structure was imaged at low underpotentials in concordance with all the authors. Later on, the in situ STM images of underpotentially deposited Ag on flame-annealed Au(111) electrodes obtained by Kolb et al. [109], revealed a series of ordered adlayer structures of increasing coverage with decreasing potential, namely ($\sqrt{3} \times \sqrt{3}$)R30°, a distorted hexagonal stripe pattern and a (3 × 3) before a close-packed (1 × 1) layer.

Changes in the atomic structures of Ag upd on Au(100) were studied by in situ STM with lateral atomic resolution in sulfate and perchlorate solutions [13]. In both cases, a quadratic structure with an interatomic spacing of $d_{\text{o,Au}} = 0.29 \pm 0.01 \text{ nm}$ was observed at relatively high underpotentials, e.g. $\Delta E = 650 \text{ mV}$, corresponding to the bare and unreconstructed Au(100) surface (Fig. 2.20a). At lower underpotentials, between the adsorption peaks A_1 and A_2 of the cyclic voltammograms (cf. Fig. 2.1a), different domains with a well ordered expanded quasi-hex Ag structure on Au(100) terraces were formed (Fig. 2.20b), that was observed in both solutions.

This expanded structure is better seen in Fig. 2.21a and could be described as a Au(100)-c($\sqrt{2} \times 5\sqrt{2}$)R45° Ag superstructure according to the model in Fig. 2.21b.

The average distance between the nearest neighbour Ag atoms was $d_1 = 4.1 \pm 0.1 \text{ \AA}$. This expanded quasi-hex structure was also reported by Ikemiya

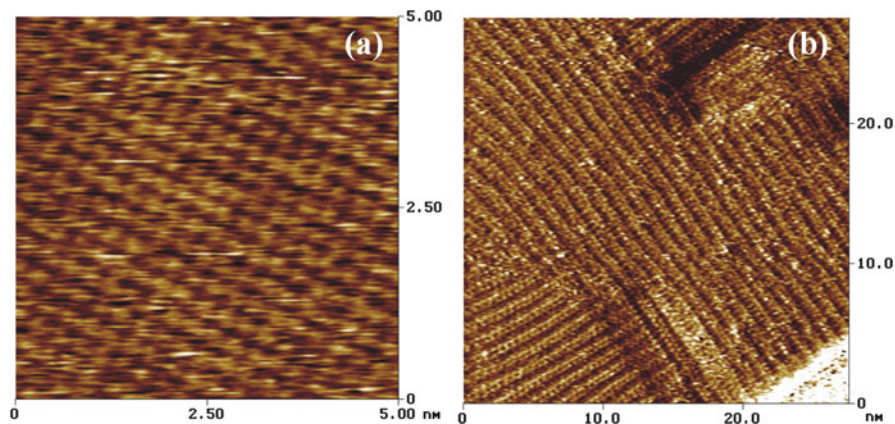


Fig. 2.20 In situ STM images with lateral atomic resolution in the system Au(100)/ 5×10^{-3} M $\text{AgClO}_4 + 0.5$ M HClO_4 at $T = 298$ K, (a) $E = 650$ mV, (b) $E = 450$ mV (vs Ag/Ag^+ Nernst equilibrium potential) (Reproduced with permission from Ref. [13])

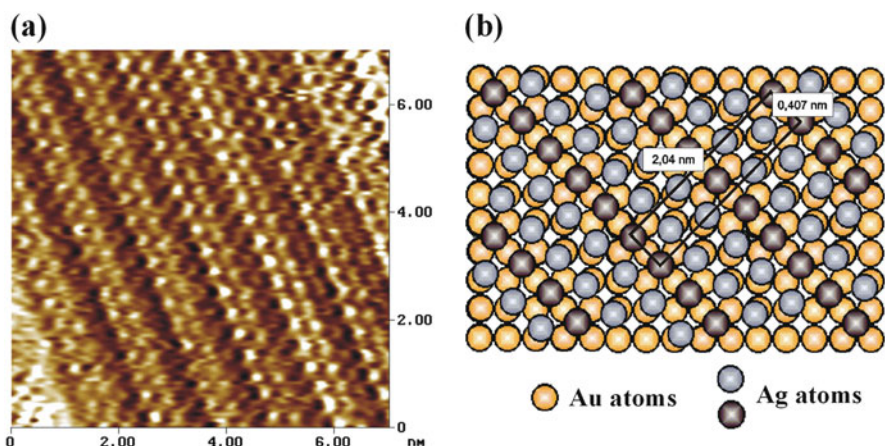


Fig. 2.21 (a) In situ STM image of the Au(100)- $c(\sqrt{2} \times 5\sqrt{2})R45^\circ$ Ag superstructure at a higher magnification, (b) schematic representation of the overlayer structure (Reproduced with permission from Ref. [13])

et al. using in situ AFM [110]. The theoretical charge value for this expanded superstructure is $zF\Gamma = 115 \mu\text{C cm}^{-2}$, whereas the experimental value was $zF\Gamma = 80 \mu\text{C cm}^{-2}$ [13, 111]. The authors ascribed this difference to the onset of Ag upd on Au(100) already at $\Delta E > 720$ mV interfering with oxygen adsorption and Ikemiya suggested that this discrepancy was caused by a partial discharge of Ag adatoms but such a claim could not be confirmed from simple charge measurements [1]. On the other hand, the expanded Ag structure correlated well with the Γ found, and therefore it appears that it was not stabilized by coadsorbed anions as it

is the case of the $\text{Au}(111)-(\sqrt{3} \times \sqrt{3})\text{R}30^\circ$ Cu structure [112], although a cosorption of anions in the Ag upd range could not be excluded.

When the electrode potential was further scanned in the cathodic direction, a condensed and commensurate $\text{Au}(100)-(1 \times 1)\text{Ag}$ phase was found. This structure was also observed in other STM work [113], although the authors could not exclude that the (1×1) structure arises as a result of alloying, i.e. it could be related to 2D upd $\text{Au}(100)-(1 \times 1)\text{Ag}$ domains or to Au-Ag surface alloy domains, which can coexist due to the onset of an inhomogeneous surface alloy formation process.

The system $\text{Au}(111)/\text{Cu}$ has been characterized by almost all electrochemical and analytical techniques. The summary of both ex situ and in situ analytical and structural studies on $\text{Au}(111)/\text{Cu}$ can be found in the review by Herrero et al. [6].

Magnussen et al. [30] obtained the first atomic images for Cu adlayers on Au (111) in a sulfuric acid solution. They found different structures before bulk Cu deposition. The first, at the most positive potentials, was the bare $\text{Au}(111)$ surface. The next structure formed, after the first upd peak, was a $(\sqrt{3} \times \sqrt{3})\text{R}30^\circ$ adlattice, which transformed into a second phase of (5×5) structure. However, subsequent work proposed that the appearance of this structure may be due to chloride contamination [29], suggesting that the upd process is extremely sensitive to anion coadsorption. Finally, a (1×1) monolayer was found just prior to bulk deposition. Figure 2.22 shows the cyclic voltammogram of the system $\text{Au}(111)$ in $0.05 \text{ M H}_2\text{SO}_4 + 1 \text{ mM CuSO}_4$ together with in-situ STM images of the structures found.

Completely different adlayer structures were reported for Cu upd in perchloric or chloride solutions [114, 115]. It was shown that instead of the structure found with sulfate-containing electrolytes, a (5×5) structure emerged due to the presence of Cl^- ions on the surface. Behm et al. [115] analysed the effect of different amounts of chloride on the adsorption behaviour and adlayer structure in Cu upd on $\text{Au}(111)$ in perchloric acid solutions. They showed that, depending on anion concentration and applied potential, two (quasi-) hexagonal adlayer structures – a commensurate (2×2) and an incommensurate (5×5) structure – with average Cu adatom spacings of 3.3 and 3.67 Å, respectively, were observed. Both structures involved cooperative adsorption of Cu and Cl^- , but the (5×5) adlattice predominated in most of the potential range and anion concentrations studied, while the (2×2) adlattice became evident at particular potentials and if anion concentration did not exceed 10^{-6} M .

More recently, Sieradski et al. [116] reported new in situ STM structural results for the upd system $\text{Au}(111)/\text{Cu}/\text{SO}_4^{2-}$. For some time the structure after the first Cu upd peak was controversial despite different studies that reported a $(\sqrt{3} \times \sqrt{3})\text{R}30^\circ$ structure, which was interpreted as a Cu adlayer with a coverage of 0.33. In some cases, this structure was found to transform into a (5×5) structure induced by the presence of chloride contamination, as pointed out above. However, EQCM and chronocoulometric results showed that the coverage of Cu at these potentials was 0.67 and that the (bi)sulfate coverage was 0.33. Later on, in situ X-ray scattering measurements [88] led to a new interpretation of the previous STM and AFM

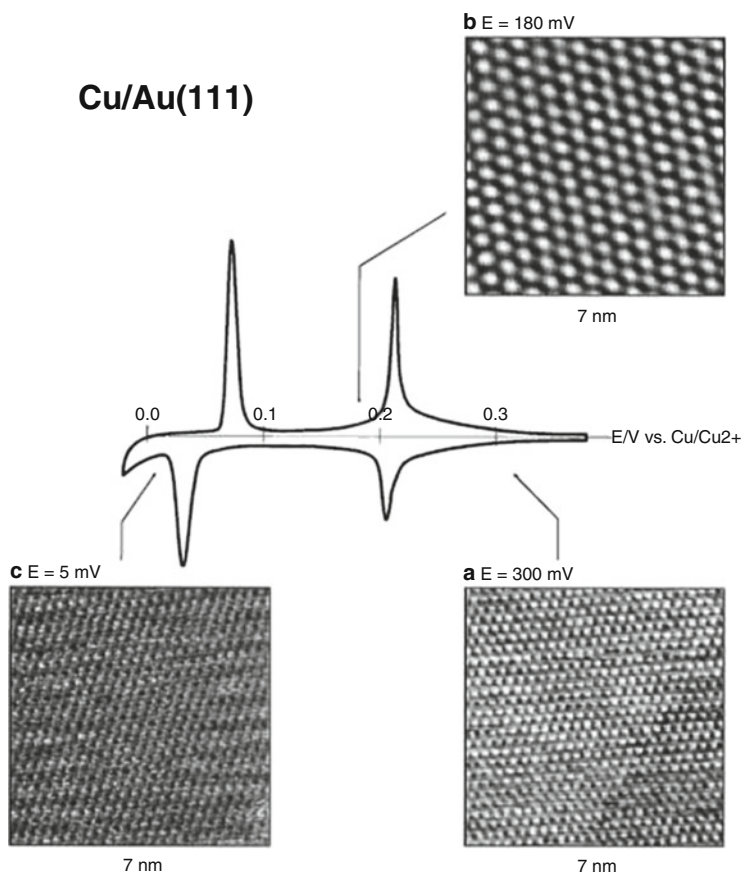


Fig. 2.22 Cyclic voltammogram in the system Au(111)/ 0.05 M H_2SO_4 +1 mM CuSO_4 ($|dE/dt|=5 \text{ mV s}^{-1}$), and in-situ STM images of the three structures observed at different potentials: (a) $E=+0.30 \text{ V}$, atomic structure of the bare Au(111), (b) $E=+0.18 \text{ V}$, ordered adlayer with the $(\sqrt{3} \times \sqrt{3})\text{R}30^\circ$ structure, ascribed to coadsorbed sulfate. (c) $E=+0.005 \text{ V}$, Cu monolayer in registry with Au(111) (Reprinted with permission from Ref. [98])

results, allowing to determine the interfacial structure of the first deposition stage: a honeycomb lattice of Cu atoms ($2/3 \text{ ML}$ coverage) with sulfate molecules adsorbed in the centers ($1/3 \text{ ML}$ coverage) above the plane of Cu atoms. Taking into account these X-ray measurements, Sieradski et al. reported not only new structural results for Cu upd on Au(111) but also showed the great capabilities of the in-situ STM technique. In Fig. 2.23, the structure of the Cu layer underneath the sulfate was possible to be imaged by manipulating the tip potential and by switching the sign of the tip bias. Namely, by adjusting the voltage of Au-coated STM tips the authors were able to image the low-density copper honeycomb structure at intermediate underpotentials.

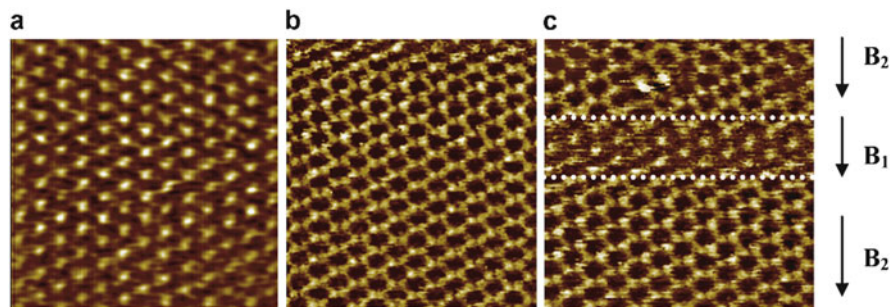


Fig. 2.23 In-situ STM images of the low-density phase in the system Au(111)/ 1×10^{-3} M Cu (ClO₄)₂ + 1×10^{-3} M HClO₄ + 3×10^{-2} M Na₂SO₄, at $E = 0.15$ V vs Cu/Cu²⁺ with different bias sign (tip potentials): (a) $B_1 = 30$ mV, sulfate ($\sqrt{3} \times \sqrt{3}$)R30° structure, (b) $B_2 = -30$ mV, Cu honeycomb structure, (c) both structures are observed as the bias is changed during the imaging scan (Reprinted with permission from Ref. [116])

2.9.2 Atomic Force Microscopy

Nowadays, the AFM, invented by Binnig and coworkers in 1986 [117–119] is the most commonly used scanning probe technique for material characterization. The major advantages of AFM are the high resolution in three dimensions and the real space visualization of both conductive and insulating samples surfaces. Therefore, a large range of topographies and many types of materials can be imaged. The latter advantage is due to the fact that AFM, unlike STM, is not based on quantum mechanical tunneling. AFM also uses a sharp tip to map surface morphology, but in this case the feedback mechanism is the force measured between the tip and the sample, not a tunneling current. The force transducer is a deflecting cantilever on which a sharp tip is mounted [120].

This microscope was developed to exploit attractive or repulsive interatomic forces between atoms in the tip and in the substrate, and operates as follows: in order to measure these forces, a sharp tip is mounted on a cantilever made of silicon or silicon nitride (both covered with a native oxide layer of 1–2 nm thickness), which deflects due to forces acting on the tip, and this vertical bending (deflection) is monitored optically by interferometry or beam deflection. That is, the cantilever bending is detected by a laser focused on its back. This laser is reflected by the cantilever onto a distant photodetector. The movement of the laser spot on the photodetector gives an exaggerated measurement of the movement of the tip, which is moved over the sample by a scanner, usually a piezoelectric element [121, 122]. However, in most instruments the sample is generally scanned instead of the tip because any cantilever movement due to scanning would add unwanted vibrations. The measured cantilever deflections are used to generate a map of the surface topography.

AFM has also provided substantial atomic-level insight into the electrode surface structure and into processes occurring on electrode surfaces. Gewirth and

coworkers [123] showed for the first time that AFM could be used to investigate electrochemical processes in situ with atomic resolution.

AFM has been used to image surfaces by probing both the attractive and repulsive forces experienced by the tip as a result of its proximity to the sample surface [100]. The most commonly used modes of operation of an AFM are: *contact mode*, *non contact mode* and *tapping mode*. In the first mode of operation, the tip is in physical contact with the surface at all times, then the probe-sample interaction occurs in the repulsive regime and the probe predominately undergoes repulsive van der Waals forces (<0.5 nm probe-surface separation). In the tapping or intermittent mode of imaging, the cantilever is allowed to oscillate at a value close to its resonant frequency. The probe lightly “taps” on the sample surface during scanning, contacting the surface at the bottom of its swing (0.5–2 nm probe-surface separation). In this way, as the probe is scanned across the surface, lateral forces are greatly reduced compared with the contact mode. In the non contact mode, the probe does not touch the sample surface, but oscillates above the adsorbed fluid layer on the surface during scanning, unless the experiment is carried out in a controlled UHV or environmental chamber. The cantilever is again oscillated as in intermittent contact mode, but at much smaller amplitude. As the probe approaches the sample surface, long-range interactions take place between atoms in the probe and the sample, such as attractive van der Waals and electrostatic forces (0.1–10 nm probe-surface separation).

The first study of Ag upd on Au(111) substrates by AFM was reported by Gewirth and coworkers [14]. They recognized different structures for Ag upd depending on the nature of the electrolyte. The AFM images showed a (3×3) structure in sulfate, a (4×4) structure in nitrate and carbonate, an incommensurate structure in perchlorate and a (1×1) structure in acetate containing solutions. The authors demonstrated that the size of the anion affected the structure of the upd adlattice, with larger anions leading to more open structures, and they ascribed this variability to differing repulsive interactions arising from anions coadsorbed with the metal adatoms. The structure of the Ag adlattice on Au(111) in sulfate containing solutions was questioned by STM studies indicating that a $(\sqrt{3} \times \sqrt{3})R30^\circ$ adlattice was formed instead, as was explained above. Other AFM studies revealed also a (3×3) structure, which corresponded to 44 % surface coverage by Ag. This structure was confirmed also by LEED, while ex-situ Auger electron spectroscopy measurements confirmed that sulfate was coadsorbed with Ag [15, 108].

For the system Au(100)/Ag⁺ in both HClO₄ and H₂SO₄ solutions, AFM studies revealed in the upd region the pseudomorphic (1×1) Ag layer for the first monolayer formed through the $c(\sqrt{2} \times 5\sqrt{2})R45^\circ$ Ag structure ($\theta = 0.6$) [110]. The latter structure was found in both electrolytes, in contrast with the Ag upd adlayers on Au(111) which depended on the anion species being in solution. It was suggested that the upd Ag adlattices on Au(100) were less sensitive to the tetrahedrally shaped anions as compared with the Au(111) surfaces. The expanded and commensurate Ag adlayer Au(100)– $c(\sqrt{2} \times 5\sqrt{2})R45^\circ$ Ag was also observed at relatively high underpotentials by in-situ STM as noted previously [13].

In relation to the Cu upd process on Au(111), the first AFM work was reported by Manne et al. [32], and they demonstrated the sensitivity of the upd adlattice structure

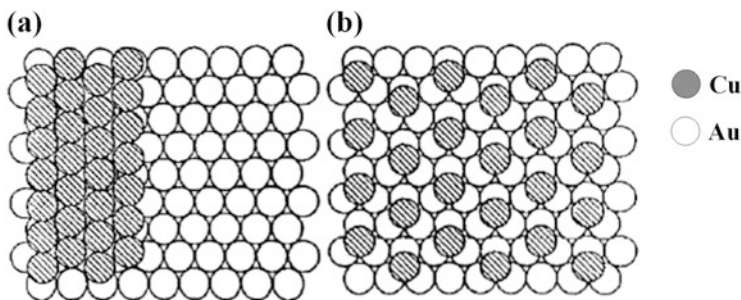


Fig. 2.24 Schematic representation of the Cu adlayer on Au(111) in (a) perchlorate solution with only part of the monolayer exhibited, (b) sulfate solution showing the $(\sqrt{3} \times \sqrt{3})R30^\circ$ overlayer structure (Reprinted with permission from Ref. [32])

to anions in solution which become coadsorbed. The Au(111) surface prior to the deposition of Cu in 0.1 M $\text{HClO}_4 + 1 \text{ mM Cu}(\text{ClO}_4)_2$ as well as in 0.1 M $\text{H}_2\text{SO}_4 + 1 \text{ mM CuSO}_4$ solutions exhibited the atom-atom spacing of the close-packed Au(111) lattice of 2.9 Å. However, for the first deposited Cu up layer in a perchloric acid electrolyte, the Cu atoms were in a close-packed lattice with a spacing of $2.9 \pm 0.2 \text{ Å}$, rotated $30^\circ \pm 10^\circ$ relative to gold, i.e. it was not commensurate with the underlying gold lattice. The authors attributed this rearrangement to the strain of incorporating Cu atoms, which show a covalent radius larger than that of Au atoms ($r_{\text{Cu}} = 1.75 \text{ Å}$, $r_{\text{Au}} = 1.42 \text{ Å}$). For a sulfate electrolyte, they were in a more open lattice with a Cu-Cu spacing of $4.9 \pm 0.2 \text{ Å}$, with a $30^\circ \pm 10^\circ$ rotation relative to the underlying Au lattice, due to stabilization of the Cu monolayer by coadsorption of SO_4^{2-} . This is equivalent to a $(\sqrt{3} \times \sqrt{3})R30^\circ$ overlayer structure. The schematic representation of both Cu structures are shown in Fig. 2.24.

2.10 Low-Energy Electron Diffraction, X-Ray Photoelectron Spectroscopy and Auger Electron Spectroscopy

The upd processes of different systems have been also investigated over the years employing several optical methods that often yielded complementary information to that provided by electrochemical analysis and non optical techniques, such as STM and AFM.

Various powerful and well established ex-situ techniques such as low-energy electron diffraction (LEED), X-ray photoelectron spectroscopy (XPS), and Auger electron spectroscopy (AES) are surface-characterization tools which have been used to analyze elements and adlattices of thin layers on substrates. Their common feature is the capability of probing the third, in-depth dimension perpendicular to a surface from the nanometer range down to monoatomic layers. However, the fact

that the experiments are not carried out in situ because the electrode is removed from the electrochemical cell and transferred into a vacuum environment (UHV chamber), together with the lack of electrode potential control, introduces some uncertainty about the relevance of the data related to the structure actually present at the interface.

LEED is based on the fact that elastically scattered electrons from a monochromatic beam of electrons incident on a surface have a spatial distribution that reflects the underlying symmetry of the surface [124, 125]. The diffracted electrons are registered using a position-sensitive detector and observed as bright spots on a screen. In this method, the energy of bombardment of the sample by electrons is low (20–200 eV) and they are diffracted to produce a pattern unique to each substrate and adsorbed layer. Therefore, it is used to study the structure and morphology of two dimensional planar surfaces. The technique may be used in a qualitative or quantitative way. In the first one, the diffraction pattern is recorded and the analysis of the spot positions gives information on the symmetry of the surface structure. In the presence of an adsorbate, the qualitative analysis may reveal information about the size and rotational alignment of the adsorbate unit cell with respect to the substrate unit cell. In the second way, intensities of diffracted beams are recorded as a function of incident electron beam energy to generate the so-called I-V curves, which through comparison with theoretical curves, may provide accurate information on atomic positions on the surface. It is also important to consider that the size and the local geometry within the surface unit cell can be obtained from the spot positions and intensities, while the spot profile, that is, the shape and width of a diffraction spot, is determined by the long-range relative arrangement of the unit cells at the surface. Vertical displacements of the surface unit cells (steps, facets) lead to splitting of the spots and changes in the spot profile as a function of electron energy [124].

The other method, AES, has widespread use in determining the elemental composition of solid surfaces. The surface to be analysed is irradiated with a beam of electrons of sufficient energy, typically in the range 2–10 keV and, after ionization, the atom can relax by either the ejection of a characteristic X-ray photon or the ejection of an Auger electron [126–128]. In AES, electron bombardment creates a vacancy in the electronic level close to the nucleus. This vacancy is filled by an electron coming from a higher electronic level, and the excess energy is then dissipated through ejection of a secondary electron (an Auger electron). The resulting energy spectrum consists of Auger peaks that are characteristic for each element. That is, as the Auger energy is only a function of atomic energy levels and therefore, each element has its own set of atomic binding energies, an analysis of Auger energies provides elemental identification. For further reading on this technique specific works are indicated [127–129].

The XPS, or electron spectroscopy for chemical analysis (ESCA), is another widely used UHV techniques and can provide complete information on chemical composition and structure both of surface and subsurface layers [130]. The information obtained is related only to surface structures or layers, due to the limited penetration of X-rays into solids (aprox. 5 nm). In this case, X-ray photons are employed to irradiate the sample that causes electron emission (photoelectric

effect). These photons interact with electrons close to the nucleus and the energy of these electrons is characteristic of the element and not of the atomic environment. Thus, as the photon energy is related to the binding energy, most elements produce XPS signals with distinct set of binding energies allowing to identify and determine the concentration of the elements on the surface.

Given that the photon energy is greater than the binding energy of the electron to the atom, the electron is then ejected from the atom with a given kinetic energy, which is the quantity measured in the experiment, and the binding energy in a particular level can be determined by subtracting the energy of the incoming photon from the measured kinetic energy of the ejected electron [131, 132]. If the incident photon is sufficiently energetic, many different levels in the sample may be ionized and thus a spectrum is produced showing all accessible energy levels as a distribution of photoelectrons with the corresponding kinetic energies of the emitted electrons. It is important to note that variations in the elemental binding energies arise from differences in the chemical potential and polarizability of compounds and therefore, they can be used to identify the chemical state of the materials being analyzed.

Some examples are presented here, where these three surface analytical probes were used as complementary techniques in studies of upd processes. Gewirth et al. [15] examined Ag upd on Au(111) in dilute sulphuric acid solutions and the possibility of coadsorption of sulfate anions, by electrochemical and ex-situ different techniques, including LEED and AES. A gold single crystal cleaned by Ar⁺ ion sputtering and annealed was used in the combined ultrahigh vacuum/electrochemistry experiments. The LEED patterns showed either a Au(111)p(5 × 5)Ag or a Au(111)p(3 × 3)Ag structure, yielding open adlattices on Au(111) surfaces. The AES measurements, which provided insight into the identity of the species at the interface, indicated that there are significant contributions from sulfate in the upd Ag adlattice and that the presence of this anion affects the ability to measure the adlattice in the LEED experiment. The authors suggested that the sulfate adlattice is present on the surface prior to the onset of Ag upd, so that Ag species must in some way penetrate the sulfate adlattice to approach the Au(111) surface. A strong anion participation was also found for the system Au(111)/Cu/SO₄²⁻ employing in-situ STM, AFM and chronocoulometry together with the thermodynamics of the so-called perfectly polarized electrode [28, 30, 32]. However, this system differs from the previous one in that essentially all the sulfate becomes removed at the onset potential for Cu adlattice formation. In contrast, the sulfate adlattice was on the surface prior to the onset of Ag upd, and the metal adlattice grew in the presence of the anion.

The early LEED and RHEED (Reflection high-energy electron diffraction) studies for the determination of the structures of Cu adlayers deposited electrochemically up to one monolayer on Au(111) were performed by Kolb et al. [21, 38]. At very low coverages no superstructure patterns were observed, while at medium coverages, ordered layers of ($\sqrt{3} \times \sqrt{3}$)R30° and (2.2 × 2.2) type were found for Cu in sulfate and perchlorate solutions, respectively, due to the specific adsorption of the anions. In a previous work [22], the ($\sqrt{3} \times \sqrt{3}$)R30° structure had also been observed by RHEED under normal vacuum for a submonolayer of Cu on Au(111).

AES measurements [21] also indicated that (bi)sulfate adsorption on Cu adlayers was stronger than that on the bare Au(111) substrate. A (1×1) structure was found for a Cu complete monolayer. However, in another work [133] employing the same techniques, it was shown that the first honeycomb structure evidenced a partial structural disorder after rinsing the electrode, leading to a loss of Cu adsorbate and to a partial rearrangement of the adlayer.

2.11 X-Ray Absorption Fine Structure

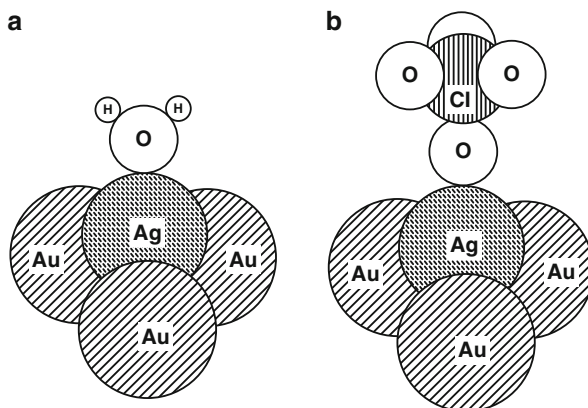
The use of synchrotron radiation and optical thin-layer cells allowed to perform in situ X-ray studies, so that another level of sophistication was achieved for in-situ determination of upd adsorbates structure on single crystal surfaces.

The use of X-rays is particularly suitable to study the electrode/electrolyte interphase because of their short wavelengths and significant penetration depth, properties that yield direct information of atomic distances and crystallographic structure [90]. Specifically, the X-ray absorption spectroscopy measures the absorption of X-rays as a function of the photon energy. The experimental data are presented as a plot of the absorption coefficient (κ) dependence on the incident photon energy, where this coefficient is determined from the decay in the X-ray beam intensity with distance ($\kappa = -d\ln I/dx$) [134]. The extended X-ray absorption fine structure (EXAFS) is related to the oscillatory variation of the X-ray absorption (expressed as absorption coefficient, κ) as a function of photon energy beyond an absorption edge. This absorption edge corresponds to a sharp increase in the absorption coefficient when the X-ray photon energy is tuned to the binding energy of some core level of an atom in the material. For atoms either forming part of a molecule or embedded in a condensed phase, the variation of the absorption coefficient at energies above the absorption edge (sufficiently high – 40–1000 eV), exhibit a complex fine structure (EXAFS) [135, 136]. Information on bond distances, coordination numbers, and atom identification can be determined. The use of synchrotron of X-ray sources provides high-intensity photon fluxes necessary to acquire sufficiently strong signals in a reasonable time, which was essential for the in situ structural analysis of the electrochemical interface. The electrochemical cell for X-ray absorption spectroscopy must be designed to minimize absorption losses at the window of the cell and the overlying electrolyte solution.

In relation with metal underpotential deposition processes, the EXAFS technique has been of great interest for studying these phenomena, since it has been able to elucidate definite structures involved in various potential regions as well as to show the occurrence of specific adsorption of ions.

An analysis of the underpotentially deposited Ag on Au(111) films on mica in 0.1 M HClO₄ containing 5×10^{-5} M Ag ions solution using EXAFS was reported by Gordon et al. [90], who pursued to investigate the local structure of the adsorbate. On the basis of the data analysis, they proposed a model, shown in Fig. 2.25, for the distribution of silver and oxygen (stemming from solution) on the

Fig. 2.25 Schematic illustration of the possible structure of an underpotentially deposited monolayer of Ag on a Au (111) substrate with either water (a) or perchlorate (b) bonded to the Ag adatoms through the oxygen, from EXAFS data analysis (Reprinted with permission from Ref. [90])



surface gold atoms, providing the data of bond lengths to gold and oxygen, suggesting that silver atoms sit at threefold sites on the gold surface with water (Fig. 2.25a) or perchlorate anion (Fig. 2.25b) bonded at a well defined distance.

Melroy et al. [137] also studied this system using sodium perchlorate as supporting electrolyte and showed that silver was on the surface on a fully reduced state. They concluded that the Ag monolayer is (1×1) commensurate with the Au (111) surface and that the Ag ad-atoms occupy threefold hollow sites, as proposed in the previous work [90]. They also observed backscattering from oxygen, presumably present in adsorbed water, which resides in either bridge or threefold hollow sites.

2.12 In-Situ Surface Differential X-Ray Diffraction

Rayment et al. [138, 139] studied the Ag upd on Au(111) in sulphuric acid media by in-situ surface differential X-Ray diffraction (SDD) in real time, using a conventional laboratory source of X-rays. Since this method has not been extensively used in the study of upd processes, only some features of SDD given by the authors will be indicated here. Basically, as X-Ray diffraction is an interference phenomenon, the adsorption of a plane of atoms on a set of diffracting planes will result in an interference, which will depend upon the spacing of the adsorbate plane with respect to the substrate planes and the atomic scattering factor of the adsorbate. The measurements consist in collecting the diffraction pattern of the bare substrate and that with the adsorbate layer on it, and then subtracting the former from the later. Thereby the change in the diffraction pattern due to the interference effect of the adsorbate on the diffraction from the substrate can be observed. Actually, a series of diffraction patterns are collected during the M upd as a function of potential, corresponding to different stages in the formation of the monolayer. Structural information such as adlayer spacing with respect to the spacings calculated for adsorption in different sites on the substrate surface, can be deduced from the characteristic interference profile.

The authors demonstrated that their SDD measurements together with cyclic voltammetry, revealed different phases of the Ag upd adlayer on Au(111) at different potentials, before the formation of the Ag(1×1) planar structure, since it was possible to monitor the adlayer spacing normal to the substrate as a function of potential. In a later work, Lee and Rayment [139] could monitor monolayer formation in situ and in real time by means of simultaneous electrochemical and structural measurements, and proved that the thin film electrode used for SDD analysis produced surface stress, which was responsible for some inconsistency in previous results. They found that Ag atoms were initially adsorbed in a mixture of bridge and atop positions, and after the completion of the upd monolayer a change in adlayer spacing was observed, which was consistent with a transition from initial adsorption in both bridge and atop sites to threefold hollow sites. They also showed that in the bulk region, there was a stepwise increase in differential intensity, with a constant adlayer spacing which is in agreement with a layer by layer growth of Ag on Au(111), as found by other authors [113].

2.13 Transmission X-Ray Surface Differential Diffraction

In order to use in-situ structural techniques under potentiodynamic conditions, Rayment and his group [140] developed the transmission X-ray surface differential diffraction technique and investigated the Ag adlayer structure on Au(111) in the underpotential region. From previous measurements using surface differential diffraction [138, 139], vertical positions of adsorbates from the substrate had been determined, but no information upon the lateral position of the adsorbate relative to the substrate was obtained. The authors demonstrated that this surface differential diffraction technique in the transmission mode allows to distinguish between different adsorption sites, resulting from the use of different anions in solution. By these experiments, it was possible to identify the adsorption site in three dimensions, confirming that Ag was adsorbed on multiple sites in a sulfate electrolyte whereas a single adsorption site (i.e. threefold hollow position) was found for acetate and fluoride solutions.

Results obtained with sulfate solutions allowed to explain the discrepancy between different Ag adlayer structures found in the literature. Summarizing, early AFM studies showed a (3×3) adlayer structure ($\theta = 1/3$) after the first deposition peak which was transformed to a (1×1) at lower underpotentials [14, 15]. The structures proposed from STM studies were a ($\sqrt{3} \times \sqrt{3}$)R 30° one for the potential range 450–200 mV versus the Ag/Ag⁺ couple, which transformed to a close packed (1×1) full monolayer at $E = 40$ mV [17]; a (4×4) open adlayer structure after the first deposition peak [13]; a ($\sqrt{3} \times \sqrt{3}$)R 19.1° structure at potentials positive with respect to the first deposition potential and a (3×3) adlayer after the first deposition peak [109]. Despite the different adlayer structures found by AFM and STM in sulfate solutions, there was agreement that a stable adlayer was formed after the first adsorption peak, which contained Ag adatoms in a mixture of sites, threefold hollow ones and possibly both bridge and atop sites.

2.14 In-Situ Surface X-Ray Scattering

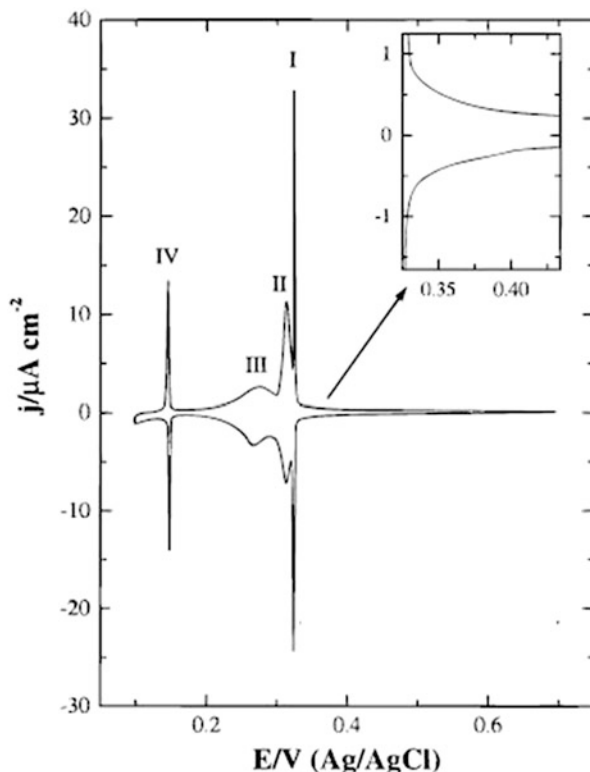
The in-situ surface X-ray scattering (SXS) technique was used to analyze also the Ag upd process on Au(111) in sulphuric acid solution [141]. This method, based on a synchrotron radiation source, is suitable to provide not only two-dimensional but also three-dimensional structural information about interphases with a very high resolution in situ. Due to the penetrating nature of X-rays, it can be used for in-situ structural studies of electrode surfaces. Basically, SXS involves measurements of the distribution of scanned X-rays in reciprocal space, and from this distribution of scattered X-rays an atomic model can be deduced and hence determination of surfaces structures may be possible [142].

In case of the system Au(111)/Ag⁺, SO₄²⁻, it was shown that initially a complete monolayer and then a “bilayer” of Ag, both with a (1 × 1) structure, were formed just before the bulk deposition started. The formation of a bilayer in the upd region was also proposed by Esplandiu et al. [109] from the charge obtained from cyclic voltammograms and STM studies, in contrast to previous works where the excess charge was attributed to the bulk deposition and the desorption of adsorbed sulfate and/or bisulfate anions during the upd process. The SXS measurements corroborated this assumption and indicated that electrochemically deposited Ag atoms both in the first and second layers were situated at the threefold hollow cubic closest packing (ccp) sites of the underlying Au and Ag layers, respectively.

2.15 Grazing Incidence X-Ray Diffraction

Grazing incidence X-ray diffraction or Grazing incidence X-ray scattering (GIXS) is another attractive tool to analyze surface structure and determine lattice spacings and atomic positions. In this case, a low angle of incidence of the X-rays upon the surface small angle (a grazing angle) enhances the electric field at the surface, thus increasing the ratio of scattering between the surface and the bulk [143]. In other words, since the refractive index of all materials at X-ray wavelengths is slightly less than unity, X-Ray beams are totally reflected for small glancing angles. Under the glancing angle condition, the electric field amplitude is doubled, resulting in an increase in scattered X-ray intensity. In addition, the background scatter originated from the bulk is reduced, since under grazing incidence conditions the penetration depth of X-rays is less than 10 nm. Therefore, this surface-sensitive technique results in an important tool to obtain microstructural information in directions parallel to the interface even on ultrathin epitaxial films [144, 145]. The cell used in this case must satisfy the same requirements as for EXAFS. Some advantages of this technique compared to EXAFS is that diffraction gives information on long-range order (not on the local environment of an element), and it is less sensitive to atomic vibrations, something which is useful when working with soft elements such

Fig. 2.26 Cyclic voltammogram of the system Au(111)/ 0.1 M HClO₄ + 1.0 mM NaBr + 1.0 mM CuO. $|dE/dt| = 1 \text{ mV s}^{-1}$ (Reprinted with permission from Ref. [147])



as lead [146]. Samant et al. demonstrated that GIXS can be used for in situ structural determination at the metal/solution interface, analyzing in situ the structure of electrochemically deposited monolayers of Pb on Ag(111) and Au(111) electrodes. They found that, when deposited on silver, Pb atoms become ordered in a hexagonal close-packed (hcp) geometry, with the lead lattice compressed 1.2 % relative to bulk lead. This layer was incommensurate with the silver substrate, with a 4.4° rotational epitaxy angle. On a Au(111) substrate, the underpotentially deposited lead monolayer was again found to order into a hcp geometry, incommensurate with the gold and compressed 0.7 % relative to bulk lead.

Later on, Herrero et al. [147] investigated the Cu upd in the presence of bromide anions employing cyclic voltammetry and GIXS together with other X-ray technique, CTR (Crystal Truncation Rod), which will not be addressed here, providing complementary information of the different interactions present. In order to understand the different structures found at different potential regions, a voltammetric profile for the system Au(111)/ 0.1 M HClO₄ + 1.0 mM NaBr + 1.0 mM CuO is shown in Fig. 2.26, which presents the four peaks characteristic of Cu upd on Au(111) electrodes in the presence of bromide.

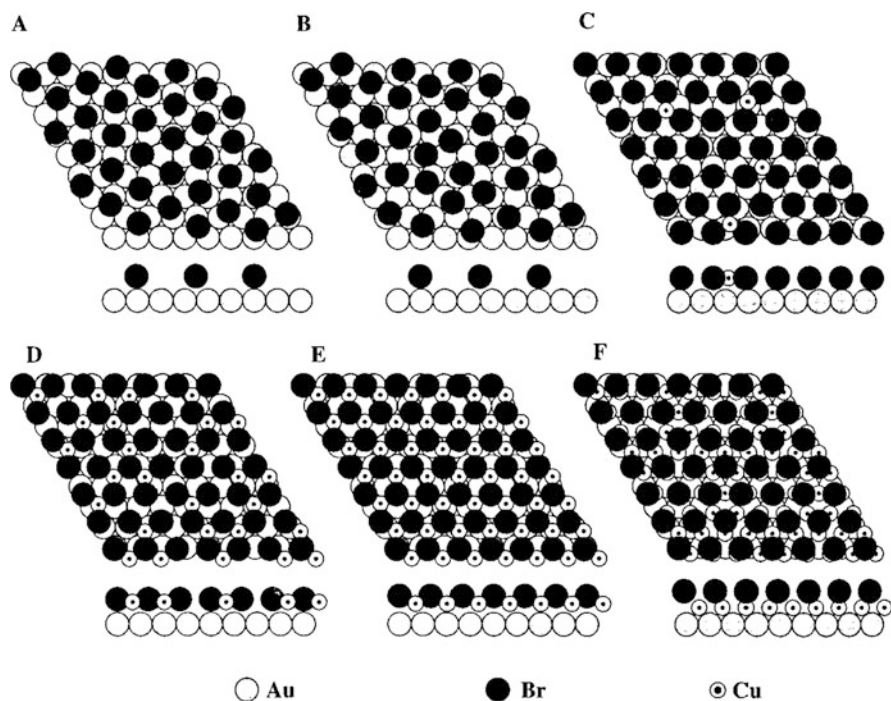


Fig. 2.27 Schematic representation of the overlayer structure of Cu deposited on Au(111) in the presence of Br^- anions at different potential values: (a) $E > +0.55$ V, (b) $+0.38 < E(\text{V}) < +0.55$, (c) $+0.32 < E(\text{V}) < +0.36$, (d) $+0.29 < E(\text{V}) < 0.32$, (e) $E = +0.29$ V, and (f) $E < +0.14$ V. For clarity, copper, gold, and bromide are not drawn to scale (Reprinted with permission from Ref. [147])

At potentials more positive than $+0.55$ V (vs Ag/AgCl), before Cu upd, bromide anions adsorb on the Au(111) surface forming an ordered and rotated hexagonal structure. The rotation angle of this structure with respect to the Au(001) direction and the Br – Br distance change with the applied potential. At potentials below 0.55 V, the bromide overlayer becomes disordered until an ordered one is formed at the beginning of Cu deposition (ca. 0.36 V) with an increase in bromide coverage. The X-ray measurements determined that Cu and bromide were mixed in the layer, with Cu atoms occupying some interstitial holes in the hexagonal bromide structure. As Cu deposition progressed (first adsorption sharp peak, I), a (4×4) bromide structure was found and then the Cu overlayer reached the Au(111) surface after lifting the anion layer. Between peaks II and III, the formation of a stoichiometric CuBr layer was observed and finally, after peak IV, there was a phase transition to give a (1×1) Cu layer with a bromide (4×4) structure adsorbed over the copper layer before bulk deposition. The schematic representation of such structures is shown in Fig. 2.27.

2.16 In Situ Infrared Spectroscopy

In situ Infrared Spectroscopy (IRS) at the electrochemical metal/electrolyte interface is a spectroscopic vibrational technique that provides information on molecular composition and symmetry, bond lengths and force constants, serving as complement of other surface-sensitive probes such as STM, EQCM, SEXAFS, etc. A better understanding of the physicochemical properties of the electrified interface can be achieved through this technique, because the obtained vibrational spectra of adsorbed species reflect the state of internal and external bonds, the lateral interactions within the adlayer, as well as the effect of the external electric field on the vibrational frequencies and intensities [148, 149]. When measuring IR reflectance spectra from a liquid/solid interface, two problems arise: one is that aqueous electrolytes are strong absorbers of IR radiation and hence the method is insensitive to changes occurring in the double layer; the other is that the sensitivity is relatively low to detect the small absorption due to a monolayer of adsorbed species. Such limitations may be overcome by using a very thin layer of solution, 10^{-4} to 10^{-3} cm, between the reflecting working electrode and the IR window, preventing the loss of IR energy by absorption in the solution. The sensitivity adequate for the detection of vibrational bands from submonolayer amounts of adsorbed species on electrodes, can be achieved by coupling of electrode potential modulation techniques to the optical signal [150].

2.17 Fourier Transform Infrared Spectroscopy

An important improvement of the IRS technique was achieved by the use of Fourier Transform instruments, because the high rate of collection of spectra in this case makes unnecessary the modulation of potential, thus giving the possibility of collecting spectra during the application of any desired potential program. This in situ – Fourier transform infrared spectroscopy (FTIRS) was used by Ashley et al. [33] to investigate the adsorption of sulfate (SO_4^{2-}) and bisulfate (HSO_4^-) ions on polycrystalline gold surfaces in sodium sulfate and also in sulfuric acid, with and without copper underpotential deposition. The authors related their findings with previous cyclic voltammetric studies obtained for a vapor-deposited polycrystalline gold substrate in a 0.5 mM CuSO_4 + 0.5 M H_2SO_4 solution. The cyclic voltammogram exhibited two adsorption/desorption peaks pairs at 0.20/0.22 V and 0.05/0.10 V, respectively, which up to that moment, were ascribed to $\text{Cu}^{2+} \rightarrow \text{Cu}^+$ for the first peak and to $\text{Cu}^{2+} \rightarrow \text{Cu}^0$ for the second peak. The PDIR (Potential-Dependent Infrared) spectra shown in Fig. 2.28, illustrated that the Cu upd exerts a strong influence on the behavior of sulfate, bisulfate and water on the interface, where the observed peaks were assigned to vibrations of surface anions.

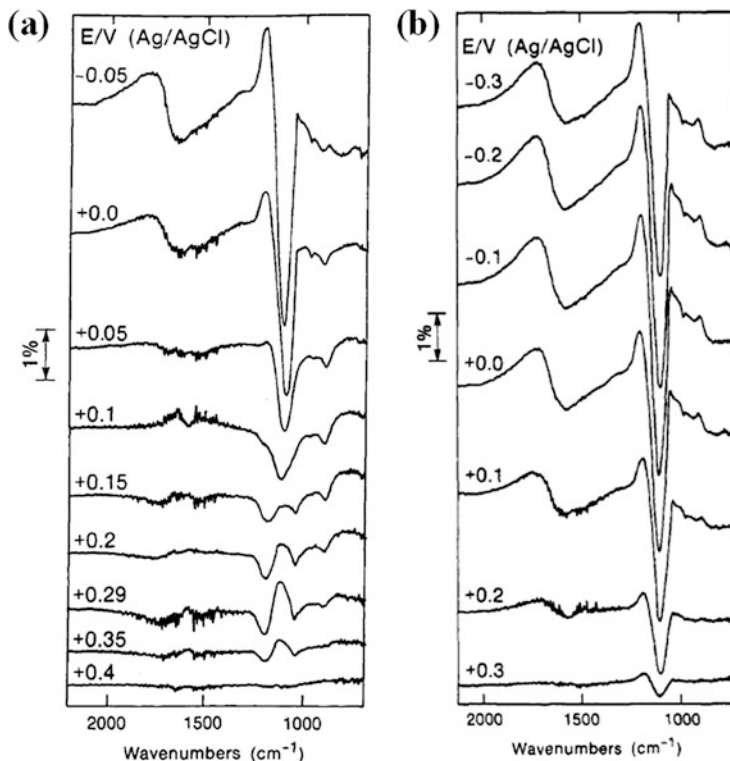


Fig. 2.28 PDIR spectra obtained on polycrystalline Au from (a) 0.5 mM $\text{CuSO}_4 + 0.5 \text{ M H}_2\text{SO}_4$ and (b) 0.5 M H_2SO_4 (Reprinted with permission from Ref. [33])

The PDIR spectra (Fig. 2.28a) obtained within the potential region where bulk Cu was deposited (e.g. 0.00 and $-0.05 \text{ V vs Ag/AgCl}$) were similar to those collected from 0.5 M H_2SO_4 on Au with no Cu present (Fig. 2.28b), where bisulfate species predominate. The results related to the Cu upd process on Au, indicated that adsorbed sulfate anion (located at $\sim 1100 \text{ cm}^{-1}$) was present on Au at more positive potentials, and its coverage increased when underpotentially deposited copper was present on the gold substrate surface (Cu^+ upd region). When the applied potential was sufficiently negative to cause full discharge of Cu upd (when deposited Cu^+ was converted to Cu^0), IR spectra showed a loss of adsorbed sulfate and an increase in surface bisulfate species (bisulfate peaks located at $-1200, 1050,$ and 900 cm^{-1}), together with a reorientation of adsorbed water molecules. The bipolar water band near 1600 cm^{-1} also appeared when Cu^0 was formed. The results were explained in terms of surface electrostatic interactions during Cu upd, and also in terms of potential-dependent pH changes at the interface. These authors demonstrated the utility of IR spectroscopy technique regarding the possibility to analyze the interfacial behavior of electrolyte and solvent during upd processes.

2.18 Differential Reflectance Spectroscopy

The properties of adsorbed metal adatoms on metal substrates can be investigated also by differential reflectance spectroscopy (DRS). This optical method is employed to elucidate the optical and hence the electronic properties of metal adsorbates. It uses photons as a probing medium (i.e. ultraviolet, visible or infrared light), and is based on the interaction of these photons with strongly absorbing materials such as metals, alloys, and semiconductors, taking place in the first 10–20 nm of the surface[151]. This important feature allows DRS to probe 50–100 atomic layers into nontransparent solid surfaces having a characteristic probing depth different from other techniques such as XPS or XRD.

In the DRS technique, the normalized reflectance change $\Delta R/R$ due to the adsorption process is measured [3, 152, 153], and is defined in a general form according to:

$$\frac{\Delta R}{R} = \frac{[R(\theta) - R(0)]}{R(0)} \quad (2.3)$$

where $R(\theta)$ and $R(0)$ are the reflectances of the adsorbate-covered and bare surface, respectively. $\Delta R/R$ can be correlated with the optical properties of the adsorbate layer and those of the substrate and the solution, using a simple three-phase model with sharp boundaries. In general, the measurements are carried out at different wavelengths with fixed angles of incidence. In all cases, the measured changes are so large that optical effects from the solution side of the double layer can be neglected. For the system Au/Cu²⁺, the reflectance change during metal deposition is mainly caused by an adsorbate induced change in the gold surface optical properties and not to absorption processes in the monolayer itself [154]. On the other hand, results from optical measurements of Cu atoms electrodeposited on Pt were presented as an example where the electroreflectance effect of Pt was negligibly small compared with the reflectance change caused by the adsorbate itself, while the influence of oxide formation or hydrogen evolution was excluded in this potential upd region. Kolb et al. [155] determined the optical constants for Cu underpotentially deposited on Pt, as a function of photon energy, angle of incidence, and adsorbate coverage, and found that the changes in the optical properties were ascribed to the Cu upd layer because the electroreflectance effect of Pt was negligibly small compared to the reflectance change caused by the adsorbate itself. It was also observed that these optical constants were quite different from those of bulk Cu, similarly to the case of Ag upd on Pt, where the deposition of 4–5 monolayers was required to obtain bulk metal properties [156]. The $\Delta R/R$ spectra (i.e. the reflectance change due to metal deposition) for a Cu monolayer on Pt single crystal electrodes revealed that the optical properties of the Cu monolayer also showed a pronounced dependence on the crystallographic orientation of the substrate. Discontinuities seen in the curve of reflectance change against coverage indicated a structural transition at such coverage.

In order to get further insight about the capabilities of this technique, Borensztein and Abelès [157] analyzed the surface reflectance spectroscopy technique and presented several application examples such as gas atoms or molecules adsorbed on metal surfaces in vacuum systems and very thin metal films deposited onto metallic surfaces, either in electrolytes or in ultrahigh vacuum. More information is available in the literature [158].

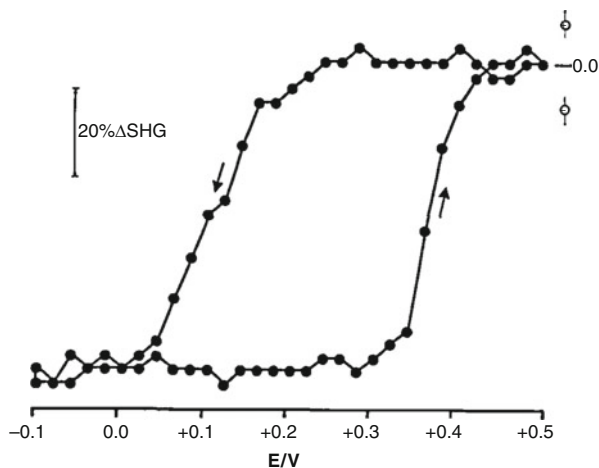
2.19 Optical Second Harmonic Generation

Optical second harmonic generation (SHG) is a non linear optical technique used to monitor surface structure in situ. In the optical methods defined above, the electrode is irradiated with light of a determined frequency and the radiation is also detected at this frequency. However, non linear optical effects can result in the appearance of radiation at twice the fundamental frequency and this phenomenon requires a non centro-symmetric medium. Therefore, SHG can be observed in a localized region (a few atomic layers) at the interface between two adjacent centro-symmetric media (such as bulk metals and solutions), where a breakdown in symmetry occurs [159–161]. The SHG signal is sensitive to species at the interface but not very effective for their identification, but together with the electrochemical analysis of the system, can be used to detect adsorbed species, reaction intermediates, and changes in the nature of the electrode surface. For a further and a more comprehensive reading, several reviews about SHG are available including principles, theory, and applications [162–166]. Typical examples for the Au/Cu²⁺ and Au/Ag⁺ systems are mentioned below in order to provide the information that is obtainable from this technique.

Ashley and coworkers [167] used SHG together with the EQCM to study copper upd on polycrystalline gold in sulfuric acid electrolyte. The second harmonic signal from a polished bulk gold substrate was observed to decrease by >60 % as a result of copper underpotential deposition on gold. The SH signals observed during copper upd, and subsequent removal of copper adlayers in a 1 mM CuSO₄ + 0.5 M H₂SO₄, are shown in Fig. 2.29. The substantial SH signal decrease during the negative potential scan was attributed to Cu upd on Au, before reaching a constant value at potentials more negative than 0.05 V vs Ag/AgCl. The authors pointed out that this decrease in SH intensity could result from an overall decrease in localized electron density at the interface when Cu became electrodeposited, until a full Cu monolayer was generated on the Au substrate, leading to a (1 × 1) commensurate structure. The SH signal remained constant on the positive scan, up to a potential of 0.3 V and then increased returning to the initial value. This observed hysteresis suggested that significant interfacial changes occurred due to the formation and dissolution of Cu adlayers, leading to different potential-dependent SHG magnitudes.

Koos and Richmond [168] have studied the structure and stability of underpotentially deposited Cu, Ag, Pb and Tl layers on Au(111) by SHG. They

Fig. 2.29 Measured SHG intensity vs potential applied to the electrode surface. Electrolyte: 1 mM $\text{CuSO}_4 + 0.5 \text{ M H}_2\text{SO}_4$. E is expressed vs Ag/AgCl reference electrode (Reprinted with permission from Ref. [167])



found similar patterns for the $\text{Au}(111)/\text{Ag}$ surface and for $\text{Au}(111)$ surface in the absence of Ag , originated by the ability of Ag adatoms to lattice match with the $\text{Au}(111)$ surface, so that the surface electronic structure was not modified. Likewise, the optical responses from the $\text{Au}(111)/\text{Cu}$ interface and the $\text{Au}(111)$ surface were consistent with the known electronic structure of the metal and the geometric structure of the overlayers. In the case of Pb and Tl electrodeposition, a strong perturbation of the anisotropic second harmonic signal was observed and the authors attributed these changes to the inability of the large adatoms to lattice match with the substrate ($r_{\text{Pb}}/r_{\text{Au}} = 1.21$ and $r_{\text{Tl}}/r_{\text{Au}} = 1.18$), causing a substantial modification of the surface electronic structure.

Later, Walters et al. [169] reported surface kinetics results of electrodeposited Ag on Au electrodes for the cases of underpotential and bulk deposition, combining potential step and optical second harmonic generation techniques. They suggested that electrodeposited silver on polycrystalline gold followed a mixed 2D-3D growth mode and found evidence that the surface structures were predominantly flat and grew at a considerable slow rate. The SHG experiments showed also the difference between the bulk Ag structures deposited on Au from those supported by a submonolayer film of Ag on Au .

2.20 Surface-Enhanced Raman Spectroscopy

With the aim of getting more information about the properties of M upd layers, Surface-enhanced Raman Spectroscopy (SERS) has also been used to this purpose. SERS is a surface spectroscopic technique that, like Fourier transform infrared spectroscopy, is based on probing molecular vibrations of the molecules adsorbed on a substrate surface. Actually, the final letter S can also stand for Scattering, emphasizing the optical effect rather than the technique. It is applicable most

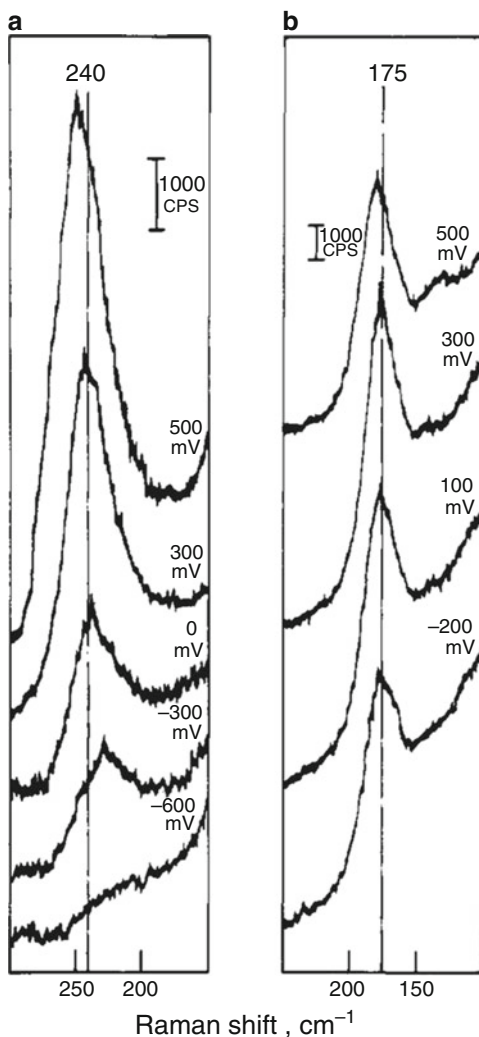
usefully to adsorption on the coinage metals, copper, silver and gold, which are highly reflective in the visible, and provides in situ information about the chemical identity of the adsorbed species, protonation/deprotonation state, molecular structure, and orientation of adsorbates at surfaces [170, 171]. The enhancement is provided by plasmon resonances (family of effects associated with the interaction of electromagnetic radiation with metals) in the metal substrate. However, a chemical enhancement involving a resonance Raman-like process associated with chemical interactions between the molecule and the metal surface can also contribute to the major SERS effect [172]. SERS mainly comes about as a combination of the two effects. Therefore, a remarkable enhancement of the scattering intensity can be observed for species that are adsorbed on, or are microscopically close to, appropriately roughened surfaces. In this case, the atomic flat surfaces commonly used in fundamental research in electrochemistry, are not suitable for SERS investigations. The roughening of the electrode surfaces usually involves the application of oxidation-reduction potential cycling in sulfate or chloride media, chemical etching in acids, electrochemical deposition of films on the substrate, etc. [173]. The inherent constraints of the technique are the limited substrate choices that exhibit localized surface plasmon resonance behaviour (Cu, Ag and Au) and the need for a roughened surface, which due to variation in the fabrication procedures can lead to inconsistent optical properties and hence, discrepant enhancement factors.

More literature about the SERS technique is available for further reading [174–176]. The use of SERS in upd systems are presented in the following examples.

Weaver et al. [177] reported surface enhanced Raman spectra for representative adsorbates, namely, halides, thiocyanate, benzonitrile, and pyridine adsorbed on upd monolayers of Ag and Cu on electrochemically roughened Au electrodes, as compared with corresponding spectra at unmodified Au and at Ag and Cu electrodes. The SER intensities on the upd surfaces were comparable to, or higher than, those observed for the bulk metal electrodes, exhibiting reversibility with respect to negative–positive potential excursions, as noted for Au substrates. Figure 2.30 shows sets of SER spectra at Ag upd on Au obtained as a function of potential for adsorbed chloride (A) and bromide (B) anions.

From the previous results, it was observed that the surface-bromide and the surface-chloride band at the most positive potentials were more intense than those typically obtained under similar conditions for conventional Ag and Au surfaces, leading to sharp decreases in the band intensities when the potential was changed to more negative values. Furthermore, these band intensities were largely recovered when the potential was reversed to the original value for anodic stripping of Ag monolayer. The same behaviour was observed for Au but not for Ag where a complete irreversible loss of SERS occurred upon such negative potential excursions. Therefore, the authors were able to infer that the stability of the SERS signals characteristic for Au substrates, was retained after the deposition of Ag upd monolayer. In this work it was also demonstrated that the surface-halide stretching frequencies and the C-N and surface-sulfur frequencies for thiocyanate on Ag upd were significantly higher than those on bulk silver electrodes at a given potential.

Fig. 2.30 SER spectra dependence on potential for: (a) chloride and (b) bromide adsorbed on an upd Ag monolayer on Au. Electrolytes: 10 mM NaCl + 0.1 M NaClO₄, and 10 mM NaBr + 0.1 M NaClO₄, respectively (Reprinted with permission from Ref. [177])



This behaviour was attributed to the greater electronic polarization of the adsorbate on the upd silver surface caused by the underlying gold substrate. Qualitatively similar, although smaller, frequency differences were seen for thiocyanate adsorbed on upd copper and bulk copper electrodes. Similar SER spectra were also seen as a function of electrode potential for benzonitrile and pyridine adsorbed on the corresponding upd and bulk metal electrodes.

Another work performed by two of the previous authors also showed the influence of modifying Au electrodes by upd layers on adsorbate-surface interactions by SERS [178]. Surface Enhanced Raman (SER) spectra were analysed for several adsorbates on underpotential deposited layers of mercury, thallium, and lead on an electrochemically roughened gold electrodes, concluding that metal

overlayers on gold provide a mean to examine adsorbate-metal bonding at surfaces which do not exhibit suitable Raman scattering enhancements.

At the same time, Fleischmann and Tian [179] found that the underpotential deposition and dissolution of monolayers of Pb and Tl on Ag roughened surfaces produced diminished surface enhanced Raman scattering, while electrodes covered by complete upd and overpotential deposited layers allowed significant SER spectra. They also probed that chloride ions were especially active in causing the loss of SERS.

2.21 Techniques Suited to Study Alloy Formation During the upd Process

In many upd systems the strong metal-substrate interaction induces place exchange processes, which lead to the formation of M-S surface alloys. This phenomenon is usually observed in systems exhibiting sufficient miscibility between the substrate and the upd metal and is usually kinetically hindered at room temperature [1]. For this reason, experiments at elevated temperature or with long-time polarization at room temperature should be carried out in order to study the formation of alloy phases. The phenomenon can be recognized by the appearance of a new desorption peak at relatively high underpotentials in an anodic linear sweep measurement and changes in the normal desorption peaks corresponding to the M upd adsorption process. STM and AFM measurements also provide detailed structural information and show clearly the drastic changes in surface morphology due 2D M-S surface alloy formation.

Interdiffusion has been observed in the following systems: Ag/Tl⁺ [180–183], Ag/Pb²⁺ [182–193], Au/Pb²⁺ [194–197], Ag/Cd²⁺ [198–203], and Au/Cd²⁺ [91, 204–211]. Typical examples are represented by the systems Au/Cd²⁺ and Ag/Cd²⁺, which were considered as model systems for the study of surface alloy formation processes.

García et al. [201, 202] analyzed the kinetics and mechanism of Cd upd on Ag (111) and the surface alloy processes involved in sulfate solutions by means of combined electrochemical measurements and in-situ STM. In relation with the surface alloy phenomenon, they showed that, at long polarization times, the condensed Cd monolayer formed via a first order phase transition undergoes structural changes involving place exchange processes between Cd atoms and surface Ag atoms. The formation of a second Cd monolayer and a significant Ag-Cd surface alloying takes place at lower underpotentials ($\Delta E < 50$ mV). The kinetics of surface alloying was studied on the basis of a diffusion model proposed by Vidu and Hara [208] for the system Ag(100)/Cd, including the relatively fast initial formation of a very thin surface alloy film and the subsequent slow alloy growth controlled by solid state diffusion. The results were in good agreement with previous measurements in the system studied [199] and suggested that at long polarization times, alloy formation occurs preferentially by the motion of Ag atoms through a

vacancy-rich surface alloy layer and the simultaneous Cd deposition at the Ag-Cd interphase. Anodic dealloying led to the appearance of a large number of 2D islands and monatomically deep pits as was observed by in-situ STM after anodic stripping. The clustering of vacancies created during removal of Cd from the surface alloy led to formation of larger pits, which disappeared by changing the underpotential to sufficiently positive values. This behaviour suggested a high mobility of Ag surface atoms at these potentials in good agreement with observations reported previously in studies with Ag(100) substrates [212].

The surface alloy process has also been observed in systems consisting in an ultra-thin Ag-Cd bimetallic layer with epitaxial arrangement on Au(111) electrodes, electrochemically deposited from separate electrolytes containing Ag^+ and Cd^{2+} ions, as well as from a multicomponent solution containing both ions [213, 214]. Anodic stripping curves obtained after long time polarization experiments demonstrated that a significant Ag-Cd surface alloying accompanied the formation of the Cd monolayer on the Au(111)/Ag modified surface, irrespective of the Ag film thickness. In the case of an extremely thin Ag layer (1 Ag ML) and taking into account the results obtained by the same authors for the Au(111)/Cd system [209], the STM images and long time polarization experiments revealed a solid state diffusion process of Cd, Ag, and Au atoms, which can be responsible for the formation of different Ag-Cd or Au-Ag-Cd alloy phases. Figure 2.31 shows a sequence of in-situ STM images corresponding to the formation of the Ag-Cd bimetallic layer onto the Au(111) substrate from a solution containing both metallic cations and its dissolution. Figure 2.31a shows the surface morphology of the bare Au(111) substrate at $E = 650$ mV vs SSE, composed of flat terraces. Figure 2.31b exhibits a Ag ML electrodeposited onto the Au(111) surface after a polarization time, $t_p = 15$ min at $E = -200$ mV (Ag overpotential deposition region). This Au(111)/Ag modified substrate was then polarized at $E = -1170$ mV producing a Cd ML (Fig. 2.31c), and also, the formation of a second Cd ML, as recognized by the presence of 2D Cd islands. Figure 2.31d displays the Au(111) surface morphology after the anodic dissolution of both Cd and Ag monolayers by polarization at $E = 650$ mV. As seen, the removal of both layers leads to the appearance of a large number of 2D islands and monatomically deep pits on the original gold terraces, indicating an alloy dissolution process. In particular, this type of behaviour was observed in the systems Au(111)/ Cd^{2+} [209, 215, 216] and Ag(111)/ Cd^{2+} [201], but was practically not observed during Ag upd on Au(hkl) [13, 113]. Therefore, it was possible to infer that in the present case, the Cd atoms reached the underlying Au surface by diffusion and/or by a place exchange mechanism with the Ag and Au atoms.

Recently, the Cd upd process in the system Au(100)/ Cd^{2+} , SO_4^{2-} and the Au-Cd surface alloy involved were investigated by the same group, by conventional electrochemical techniques and in-situ STM analysis arriving to similar conclusions [211].

García et al. [203] studied the formation of bimetallic Cd-Ag nanoparticles on vitreous carbon (VC) by conventional electrochemical techniques and ex-situ AFM. The solutions used for metal deposition were: 1 mM Ag_2SO_4 + 0.02 M

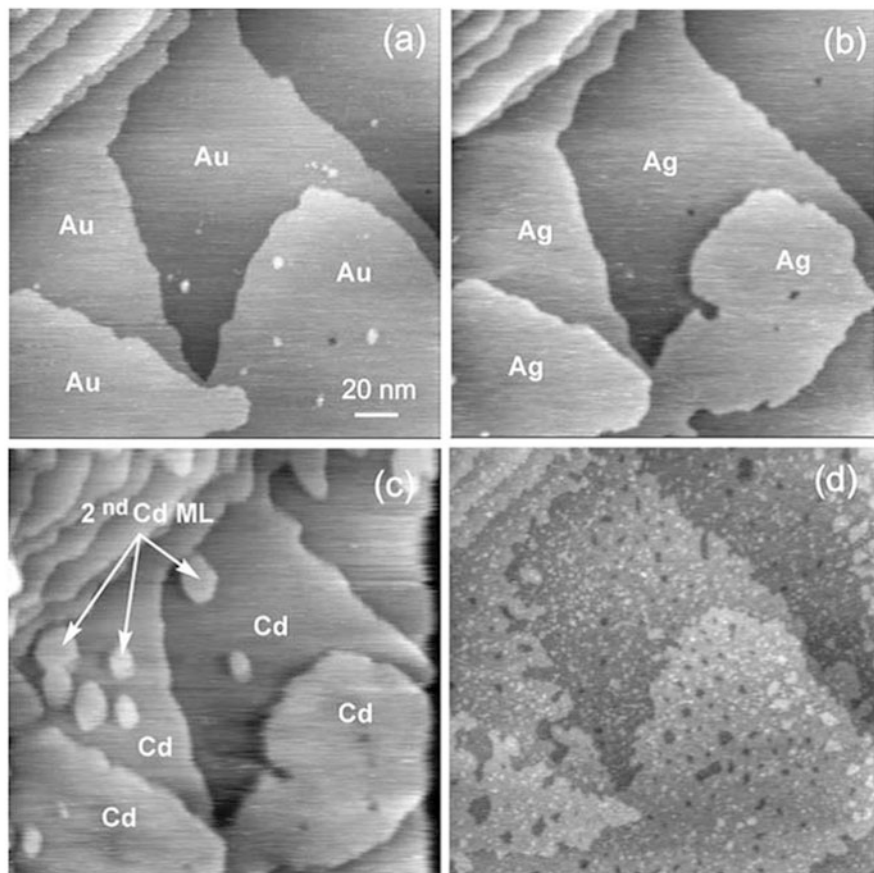


Fig. 2.31 Sequence of in-situ STM images obtained during the formation of a Ag/Cd bimetallic layer onto a Au(111) substrate under different conditions. (a) Bare Au(111) surface at $E = 650$ mV; (b) formation of a Ag ML at $E = 200$ mV; (c) formation of a Cd ML at $E = -1170$ mV; (d) surface morphology after anodic stripping at $E = 650$ mV (Reprinted with permission from Ref. [214])

$\text{H}_2\text{SO}_4 + 0.1$ M Na_2SO_4 and 2 mM $\text{CdSO}_4 + 0.1$ M Na_2SO_4 ($\text{pH} = 2.28$), whereas a 0.1 M Na_2SO_4 ($\text{pH} = 2.28$) solution was employed as blank electrolyte. The authors demonstrated that alloy formation between both metals could be inferred, which had not been previously reported using nanoparticles. They found that the alloy formation phenomena observed previously during Cd upd on bulk Ag electrodes [199, 201, 213] was also found in the case of Cd upd on Ag nanoparticles. The desorption spectra in the system Cd/Ag (nanoparticles)/VC employing different polarization times, showed three desorption peaks associated with the dissolution of the Cd overpotential deposits (opd) and upd deposits and a Ag–Cd alloy formed at low underpotentials, respectively. This phenomenon was also confirmed by performing an anodic stripping of Ag/Cd deposits to more positive electrode potentials in a blank electrolyte solution.

2.22 In-Situ Measurement of Surface and Growth Stress

Less frequently employed for studying the alloy formation process in the upd region, is the in-situ measurement of surface and growth stress, which is originated by the difference of the atomic configuration of surface atoms with regards to that in the bulk. Experimental procedures and equipment for this technique are detailed elsewhere [217]. The simplest and most widely used method involves the measurement of the deflection of a flexible cathode, typically in a direction that is perpendicular to the in-plane stress generated in the film. Interferometry, capacitance measurements, laser beam deflection and STM/AFM can be employed for monitoring the deflection. Stafford and Bertocci [217] indicated that the adsorption of species on the surface can be expected to alter the surface stress, since the local interaction of each adsorbate will modify the bond strength between neighboring atoms on the surface. Also the lattice misfit between a metal adlayer and the substrate generates surface stress, where the sensitivity of the later to both ionic and fully discharged adsorbates makes this measurement attractive for upd studies. Stafford et al. [218] investigated the voltammetric and stress response during Pb upd on textured Au(111) evaporated films in 0.1 M HClO₄ containing 10 mM Pb(ClO₄)₂ solution. Particularly, the authors analyzed the stress behaviour of the system at different sweep rates and observed initially, as shown in Fig. 2.32a, an increase in the surface stress, similar to that observed in Pb²⁺-free solution, associated with a combination of electrocapillarity and surface charge redistribution induced by anion desorption. At a potential of about -0.43 V vs SSE, a change of stress in the compressive direction was detected, under conditions where nucleation and growth of Pb islands took place [196]. Then, stress relaxation in the tensile direction occurred in a very narrow potential range after which the Pb monolayer was completed. From results reported previously [219], the surface stress was correlated to Pb coverage, obtaining an overall compressive surface stress change

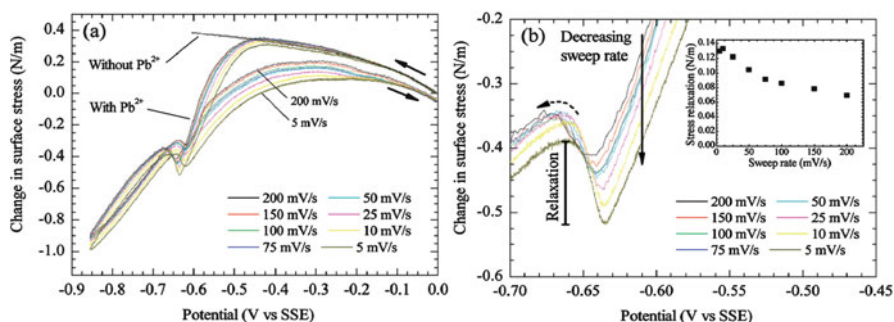


Fig. 2.32 (a) Dependence of surface stress on potential during Pb upd on a (111)-textured Au film at different sweep rates (5–200 mV s⁻¹). Solutions: 0.1 M HClO₄ with and without 10 mM Pb(ClO₄)₂. (b) Magnification of the zone where stress relaxation takes place. Only cathodic scans are shown. Inset: magnitude of stress relaxation as a function of sweep rate (Reprinted with permission from Ref. [218])

of about -1.2 N m^{-1} for the complete Pb monolayer. With further deposition, the stress moved once again in the compressive direction, as more Pb atoms were incorporated into the adlayer, causing contraction of the interatomic spacing and eventually rotation of the monolayer. Previous results obtained by Welland et al. [220] led to similar conclusions. In this case, an AFM Au-coated cantilever was used as a bending-beam sensor to measure surface stress changes, which occurred during the electrodeposition of Pb monolayer on Au(111), without considering alloy formation. This phenomenon could not be studied due to experimental conditions where fast scan rates were needed to avoid thermal drift.

The sweep rate dependence of surface stress is shown in the inset of Fig. 2.32b, indicating that at slower sweep rates, larger compressive stress was developed, something that can be explained by the occurrence of Pb-Au surface alloying, because in this case the slow sweep rate allows more time for the hcp adlayer to transform to the alloy structure. The authors concluded that the stress behavior was due to kinetically controlled surface alloying occurring at low coverages, while at high coverages the surface alloy removal took place generating a hexagonal close-packed Pb monolayer with subsequent Pb deposition. This behaviour was quite different from other systems, such as Ag(111)/Cd, in which, as mentioned above, the alloying was produced into the solid state at complete coverage and the charge required to strip Cd adatoms exceeded that of a monolayer [201]. Stafford and Bertocci also suggested that the observed stress relaxation hump could be caused by an alloying/dealloying transition. Therefore, after many cycles of Pb deposition and dissolution, the (111)-textured Au surface was roughened, as a consequence of surface alloying and dealloying processes, in accordance with the STM results reported by Green and Hanson [197].

2.23 Applications of upd as a Tool

As the M upd phenomenon is the initial stage of metal phase formation, it has often been used to modify electrodeposition processes and has been regarded as a powerful tool to modify, in a controlled way, the catalytic properties of the substrate.⁵

On the other hand, M upd has been employed to prepare ultrathin metal films. For example, a method has been developed by Brankovic et al. [221] in which an ordered metal adlayer underpotentially deposited on a substrate is replaced by a more noble metal monolayer in an electroless deposition process, producing 2D deposits uniformly covering the substrate surface. The replacement of the M upd layer takes place via an irreversible and spontaneous redox process in which this adlayer is oxidatively dissolved by cations of more noble metals, which are simultaneously reduced and deposited. The authors applied this procedure using a

⁵This application of M upd will be discussed in detail in Chap. 4

Cu upd adlayer on Au(111) as “sacrificial layer”, which was then replaced by a submonolayer of Pt, a monolayer of Pd and a bilayer of Ag in a spontaneous reversible redox process. The total amount of the deposited metal was determined by the stoichiometry of the redox reaction and the structure of the upd Cu adlayer. This method, known later as *Surface-limited redox replacement* (SLRR), refers then to a confined, in a monolayer or two, reaction where a predeposited metal layer is replaced by a more noble metal at open-circuit potential, and offers an interesting alternative approach to prepare bimetallic catalyst surfaces or uniform ultrathin 2D M films. The applicability of this procedure was also examined for the systems Au (111)/Cu and Ag(111)/Cu [222]. Two-dimensional growth of Cu up to 100 monolayers has been achieved by multiple redox replacement of monolayers of underpotentially deposited Pb used as a sacrificial metal. In this case, open-circuit potential monitoring during the replacement reaction was used to control the completion of each deposition event and the film thickness was determined by anodic film stripping. The excellent surface quality of the epitaxially grown Cu film was characterized by STM in situ and XPS analysis, which showed no traces of Pb into the Cu film.

In a recent work, Brankovic et al. [223] analyzed the stoichiometry of Pt deposition on a Au(111) substrate by SLRR employing Cu upd as intermediate, emphasizing that it was influenced by the specific experimental conditions and anions involved. The Au(111)/Cu upd was formed from a 10^{-3} M Cu^{2+} + 0.1 M HClO_4 solution, whereas the Pt deposition (redox reaction) was carried out from a 10^{-3} M $[\text{PtCl}_6]^{2-}$ + 0.1 M HClO_4 solution. The results indicated that, as the anion of the supporting electrolyte of both solutions was ClO_4^- , which does not have the tendency for complexing the Cu ions, the ligand in the depositing complex, $[\text{PtCl}_6]^{2-}$, was responsible for the final oxidation state of dissolved Cu ions as it stabilized the Cu^+ ions forming the complex $[\text{CuCl}_2]^-$. Combining the statistical STM data analysis and conventional electrochemical techniques, the authors concluded that the Cu upd adatoms oxidation to Cu(I) was thermodynamically more favorable than their oxidation to Cu(II), during the redox replacement reaction, suggesting that four Cu upd adatoms were replaced by each deposited Pt adatom.

As the electrochemical deposition method based on SLRR of underpotentially deposited sacrificial metal monolayers has gained considerable interest due to its broad applications in the preparation of catalytic materials and growth of ultrathin epitaxial films, the kinetics of metal deposition via this technique was examined by the same authors [224]. The model system was Au(111)/Pt using Pb and Cu upd sacrificial monolayers deposited on Au(111), considering HClO_4 and H_2SO_4 supporting electrolytes. The parameters of the reaction kinetics, i.e. reaction half time, reaction order and reaction rate constant, were determined. The effects on the reaction kinetics of the nature of the M upd monolayer, the transport limitation and the present anions were also investigated.

In recent years, the synthesis of multimetallic nanoclusters has been extensively studied due to their widespread applications specifically in electrocatalysis. Electrodeposition of these nanostructures can be performed by codeposition of metals from a common electrolytic bath or by sequential deposition of the involved metals. The SLRR methodology is another option for the preparation of bimetallic nanoclusters.⁶

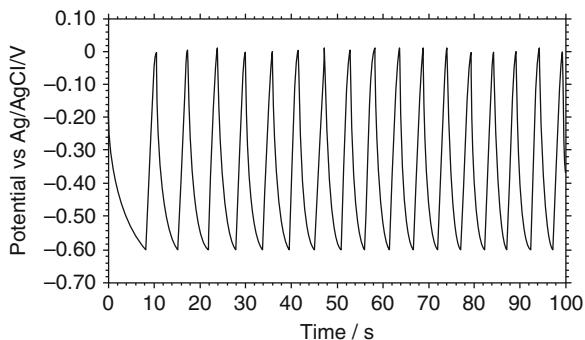
Several studies have been reported about thin composite films, using M upd layers. Particularly, the formation of nanostructures composed by compound semiconductors is of great interest because their application in optoelectronic devices. Epitaxial growth of compound semiconductors was achieved by Stickney and co-workers [225–228] using the so-called *Electrochemical Atomic Layer Epitaxy* (ECALE) method, which is based on successive upd atomic layers of different elements to form a compound. The principle is similar to that of the SLRR in the sense that both use surface limited reactions to form each atomic layer of a deposit. They developed this method for the production of II-VI compound semiconductors which are deposited epitaxially. The upd is used in order to limit deposition to a monolayer and because of the enhanced stability provided by bond formation between the II and VI elements, relative to formation of bulk elemental deposits [229]. The thin-layer electrodeposition of CdTe on a Au polycrystalline electrode was the first system studied employing the ECALE method. This deposition technique has several advantages such as the prevention of generating three-dimensional nuclei by never exceeding the monolayer regime. The control of deposition potentials is such that only deposition enough to cover the deposit occurs and the combination of each successive element with only the element previously deposited, prevents the mixing between the metals being deposited. Adequate deposition potentials and solution composition are necessary for each element being deposited. Each deposition cycle forms a monolayer of the compound, and the number of cycles determines the thickness of the deposit.

Most semiconductor compounds consist of both a metal and a main group element such as Te, Se, S, As, Sb, or Bi. At present, several compounds have been prepared by ECALE. Among them are CdTe, CdSe on polycrystalline and single crystal Au electrodes [226, 230–233]. Another groups adopted Ag(111) as substrate to prepare semiconductor compounds. For example CdTe and ZnSe deposition on Ag(111) was obtained by ECALE, alternating underpotential deposition of atomic layers of the elements making up the compound [234, 235].

Upd-based systems have been analysed in recent years for the development of electrochemical supercapacitors, which attract growing attention as electrical energy storage systems because of the high capacitance of the electrode materials resulting in higher specific power than batteries and higher specific energy than conventional capacitors. The supercapacitor processes are, ideally, 2-D and rely on faradaic processes in which a monolayer or quasi-monolayer of electrochemically

⁶ It will be discussed in detail in Chap. 6

Fig. 2.33 Chronopotentiogram of Tl upd on Ag in the presence of Br^- ions at $I = 10 \mu\text{A cm}^{-2}$. Electrolyte: 2 mM $\text{TlNO}_3 + 20 \text{ mM KBr} + 1 \text{ mM KNO}_3$ (Reprinted with permission from Ref. [237])



reactive species can be electroadsorbed or electrodesorbed with charge transfer via upd processes, e.g. Cu on Pt, Pb on Au, Bi on Au, Bi on Ag [236].

Girija and Sangaranarayanan [237] have studied Tl upd on Ag in the presence of bromide ions. They demonstrated the feasibility of upd-based systems as supercapacitors using this system as an illustrative example and estimated the specific capacitance employing voltammetric and galvanostatic charge/discharge studies. Upd-based supercapacitor systems are favorable due to the following considerations: high reversibility, large pseudocapacitance values, wide choice of the substrate and depositing species, feasibility of employing aqueous and non-aqueous solvents, specific choice of electrolytes in order to increase adsorption via pseudocapacitance. Figure 2.33 shows a typical chronopotentiogram obtained at a constant current density of $10 \mu\text{A cm}^{-2}$ over the Tl upd range, exhibiting the usually charge/discharge behaviour of supercapacitors. Furthermore, the charge curves are symmetrical to their corresponding discharge counterparts in the potential region considered, an essential criterion for the feasibility of supercapacitors, and the reversibility is maintained for $\sim 10^2$ cycles.

2.24 Photoacoustic Technique

The Photoacoustic (PA) technique has not been widely applied for upd systems but some works are found in the literature. Fujishima et al. [238, 239] reported results on the Au oxide layer and the plating of Cu on Au, demonstrating the capability of the Photoacoustic spectroscopy (PAS) to study the surface behaviour of metal electrodes in-situ. They also described the cell and the experimental procedure used for this purpose, where the current-potential and photoacoustic signal-potential curves are recorded simultaneously. Basically, PA refers to the generation of acoustic waves by modulated optical radiation. The process involves absorption of light (e.g. laser beams) in the working electrode and production of heat followed by propagation of heat-generated thermal waves to the electrode surface. Heat is then transferred into the adjacent gas, varying its pressure, which is then measured

by a microphone as the photoacoustic signal. This technique differs from the conventional ones mainly by the fact that even though the incident energy is in the form of optical photons, the interaction of these photons with the sample is studied not through subsequent detection and analysis of some of them but rather through a direct measure of the energy absorbed by the material because of its interaction with the photon beam [240, 241].

Later, Fujishima et al. [242] demonstrated that PAS is a sensitive optical method that has both sensitivity and ability to provide in-situ information about the interface electrode-electrolyte modified by upd. They were able to detect Pb upd from 0.1 M NaClO₄, +0.01 M Pb(ClO₄)₂ + 0.005 M HClO₄ solution onto Ag substrate employing PA. The clear peaks pair (deposition and dissolution) related to the Pb upd were detected in the PA signal-potential curve showing a slight increase or decrease at the potential where the peaks in the current-potential curve were evidenced. The slow transformation phenomena of Pb adsorbates on Ag(111) electrode surfaces [183–192] reported previously, was also detected as a slight fluctuation of the PA signal.

2.25 Electrochemical Impedance Spectroscopy

The potentiodynamic electrochemical impedance spectroscopy (PDEIS) is a relatively new and promising technique to study in real time the electrochemical response of metal monolayers and nanostructures on various substrates providing fast acquisition and visualisation of the interface response to ac and dc current in a single potential scan [243, 244]. In a simple experiment, the cyclic voltammogram of the system and the Nyquist and Bode plots extended to 3D as a function of potential are obtained. These later are then individually extracted from the 3D plots as orthogonal sections and decomposed by a built-in equivalent circuit analyser into the constituent responses of the circuit elements, analogous to conventional ac impedance measurements. Unlike conventional electrochemical impedance spectroscopy (EIS), which analyses frequency response in stationary states to obtain the whole equivalent circuit, PDEIS analyses the ac response in terms of equivalent electric circuit parameters dependences on the potential, allowing dynamic surface control. PDEIS appeared to be useful for nonstationary effects monitoring in upd. Different equivalent circuits were found for reversible and irreversible upd processes. For the first ones, low-amplitude ac probing generates oscillation of adatom coverage, which produces the capacitance of adsorption in the equivalent circuit, but no adsorption capacitance was found in irreversible upd systems. Moreover, PDEIS enables separate monitoring of anions coadsorption in upd processes.

Ragoisha and Bondarenko [245] demonstrated the application of PDEIS to copper underpotential deposition on polycrystalline gold in 10 mM CuSO₄ + 0.1 M H₂SO₄ and 10 mM Cu(NO₃)₂ + 0.1 M HNO₃ providing in situ investigation of anion adsorption during copper monolayer formation on gold. The dependences of the equivalent circuit parameters on potential showed different behaviours of nitrate

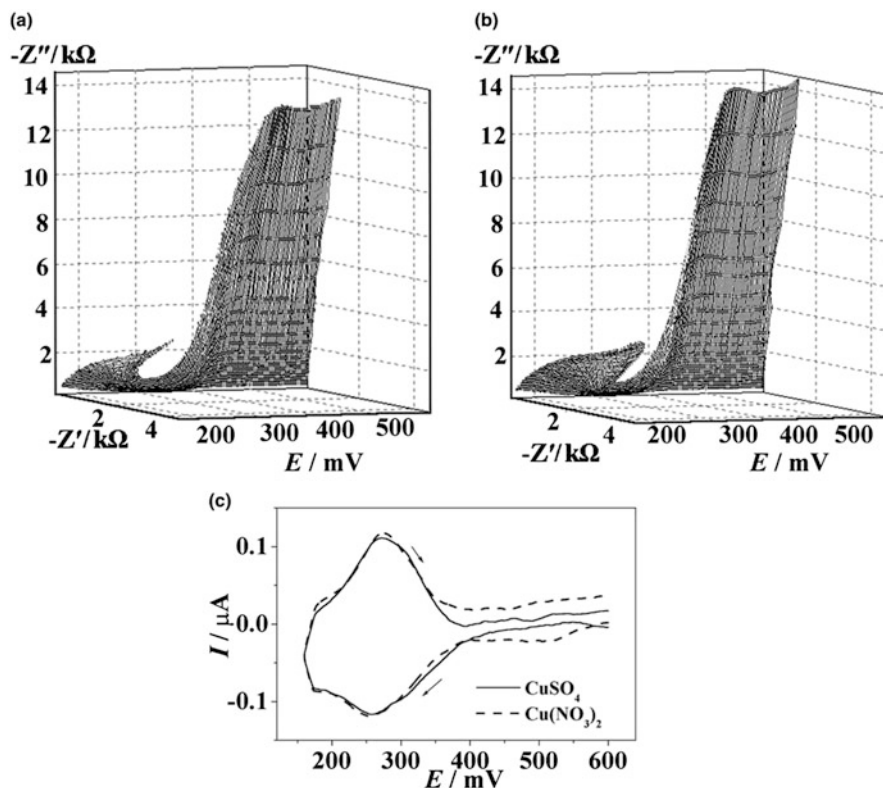


Fig. 2.34 Cathodic (a) and anodic (b) branches of the PDEIS spectrum for Cu upd on Au in 10 mM $\text{CuSO}_4 + 0.1 \text{ M H}_2\text{SO}_4$. (c) Cyclic voltammograms of Au in 10 mM $\text{CuSO}_4 + 0.1 \text{ M H}_2\text{SO}_4$ and 10 mM $\text{Cu}(\text{NO}_3)_2 + 0.1 \text{ M HNO}_3$ solutions. $|dE/dt| = 2 \text{ mV s}^{-1}$ (Reprinted with permission from Ref. [245])

and sulfate ions. The authors also indicated that the results revealed some irreversibility of the constituent processes that appeared to be reversible from cyclic voltammograms.

Figure 2.34 shows the PDEIS spectra, cathodic (Fig. 2.34a) and anodic (Fig. 2.34b) branches, for the system Au/10 mM $\text{CuSO}_4 + 0.1 \text{ M H}_2\text{SO}_4$ and the corresponding cyclic voltammogram together with the voltammetric results in the system Au/10 mM $\text{Cu}(\text{NO}_3)_2 + 0.1 \text{ M HNO}_3$ (Fig. 2.34c). Differences between the ac responses of the cathodic and anodic scans evidenced intrinsic irreversibility and non-stationary of the underlying processes. The presence of sulfate and nitrate anions for Cu upd on Au shows no pronounced changes in voltammetric results which is not the case as it is shown below. In Fig. 2.35 the best-fit equivalent circuit in each case, and the dependences of the equivalent circuit parameters on the potential are presented, such as the double layer capacitance (C_{dl}), the pseudocapacitance and pseudoresistance of Cu upd (C_c , R_c) and anion adsorption (C_a , R_a).

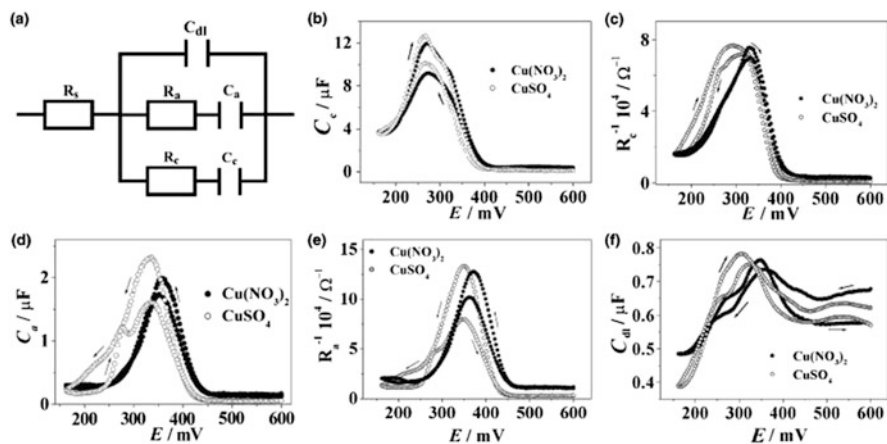


Fig. 2.35 (a) Equivalent electric circuit obtained from the PDEIS spectra for Cu upd on Au, (b)–(f) dependencies of the equivalent circuit parameters on potential (Reprinted with permission from Ref. [245])

Nitrate adsorption pseudocapacitance, and the inverse of the adsorption pseudoresistance, both exhibited peaks in a narrow range of Cu monolayer growth, while sulfate affected a wider potential range and gave two desorption peaks in the anodic scan. The complex and different potential dependences of the double layer capacitances in sulfate and nitrate solutions evidenced the anion effects during the Cu upd process on Au electrodes.

PDEIS was also used for characterisation of Ag upd on polycrystalline Pt [244], Pb upd on polycrystalline Au and on Au coated with Se atomic layer [246], Bi upd on Au [247] and Pb upd on Te [248], where no adsorption pseudocapacitances were found in equivalent electric circuit of irreversible lead upd on tellurium.

2.26 Thermal Desorption Spectroscopy

The Thermal Desorption Spectroscopy (TPS), also known as Temperature Programmed Desorption (TPD) [249, 250] is an important tool to study for example hydrogen desorption kinetics in metal hydrides, but it was found throughout the literature that it can be also applied to M upd processes, although not extensively. Briefly, TPS consists in a non-isothermic analysis of desorption kinetics and it is used to obtain information on the energetics and kinetics of adsorbed particles. It involves heating resistively via thin tantalum or tungsten wires, a sample covered with one or more adsorbate(s), following a pre-defined temperature profile (mostly

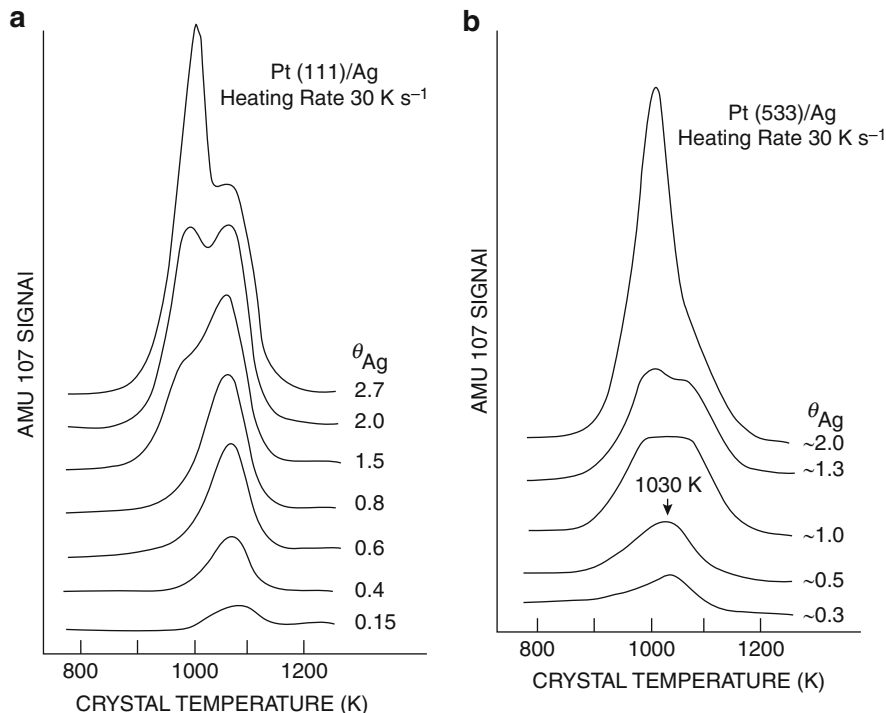


Fig. 2.36 Silver (AMU 107) thermal desorption spectra from (a) Pt(111) and (b) Pt(533) surfaces as a function of Ag coverage (Reprinted with permission from Ref. [251])

in a time-linear fashion) and simultaneously detecting the residual gas in the vacuum desorbed by the material by means of a mass analyser. The concentration of desorbing species is usually measured with a quadrupole mass spectrometer. As the temperature rises, certain adsorbed species will have enough energy to escape and will be detected as a rise in pressure for a certain mass. The experiments are performed in a continuously pumped ultra-high vacuum (UHV) chamber. With increasing temperature, the desorption rate increases, eventually goes through a maximum, and drops back to zero as the surface is depleted of adsorbate. As a result one obtains a spectrum composed of several peaks of the desorption rate as a function of temperature.

Davies et al. [251] used TDS besides AES and LEED, to analyse the growth and chemisorptive properties of Ag and Au monolayers on platinum (111) and (533) surfaces. Only the system Ag/Pt will be mentioned here. AMU 107 TDS results from Ag-covered Pt(111) and Pt(533) surfaces, are presented in Fig. 2.36. A single, desorption peak centered at 1080 K from the Pt(111) substrate was observed up to an initial Ag coverage of 1 ML (Fig. 2.36a), corresponding to the desorption of this layer. At coverages >1 ML a second, lower temperature peak is developed which becomes the dominant desorption feature at coverages >2 ML. This lower temperature peak was identified with desorption from subsequent monolayers. From these

thermal desorption studies of Ag adlayers from the Pt substrates, the authors also determined that the Ag-Pt bond in the first monolayer was $\sim 25 \text{ kJ mol}^{-1}$ stronger (278 kJ mol^{-1}) than the Ag-Ag bond (253 kJ mol^{-1}) in the subsequent monolayers. Therefore, it could be expected that the first Ag monolayer deposited on the Pt surface would spread evenly over the surface to maximize the number of Ag-Pt bonds. The growth of Ag in this case proceeded via a Stranski-Krastanov mechanism. However, the TDS spectrum for Ag desorption from the Pt(553) surface (Fig. 2.36b), shows that both peaks were detected at initial coverages below 1 ML. At 1 ML the two peaks are of comparable intensity, and at 2 ML the lower temperature peak becomes the dominant feature. These observations indicated that silver was present as multilayer 3D crystallites, as would be expected from a system followed a Volmer-Weber growth mechanism.

Stickney and coworkers [252] reported studies about the influence of the halogen layer structure on the electrodeposition of silver on a Pt(100) surface pretreated with iodine, from aqueous perchloric acid solutions, employing TPS among other techniques. They analyzed the thermal desorption from various structures formed by electrodeposition of Ag onto Pt(100) [$c(\sqrt{2} \times 2\sqrt{2})$]R45° I surface and found that the onset of atomic I desorption was retarded to some extent by the presence of electrodeposited silver and the desorption of metal deposits generally took place after most of the iodine had desorbed. The TDS spectrum for the system showed that whenever the packing density of deposited silver equaled that of a silver monolayer, silver desorption took place almost exclusively in a single, massive peak beginning near 950 K. Desorption of several silver monolayers ($\theta_{\text{Ag}} \gg 1$) and the initial stages of desorption of a silver monolayer evidently occurred in this single predominant process having a rate maximum at about 1000 K.

2.27 Glow Discharge Optical Emission Spectroscopy

Glow Discharge Optical Emission Spectroscopy (GDOES) has not been usually employed as a surface analysis technique for up-d systems, but it is suitable for chemical analysis and surface depth-profiling characterization on solid materials including ultrathin films [253]. This technique is frequently used in combination with any of the well-known surface analysis methods, such as XPS, to obtain the composition of thin films as a function of depth.

The basic principles of GDOES [254, 255] are described here briefly. The glow discharge is a kind of plasma which is created by inserting two electrodes in a cell filled with gas at low pressure (e.g. 1 Torr), commonly Ar. A potential difference (of the order of 1 kV) is applied between the flat sample to be analyzed, which functions as cathode, and the anode (copper electrode). The glow discharge plasma is thus formed and viewed by one or more optical spectrometers. Argon ions, created in the negative glow of the plasma, are accelerated towards the sample where they bombard the surface, inducing an erosion process (sputtering). The atoms, removed from the sample surface, move into the glow discharge plasma.

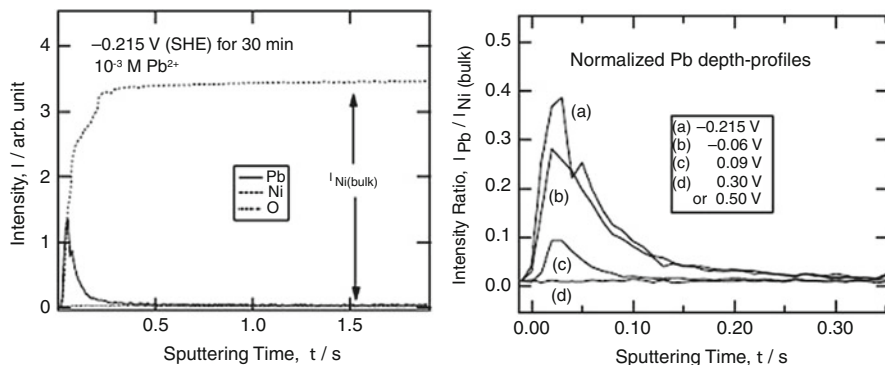


Fig. 2.37 (a) GDOES depth-profile for the Ni specimen polarized for 30 min at -0.215 V (SHE), (b) Normalized Pb depth-profiles of the Ni specimens polarized for 30 min at various potentials. Solution: 0.1 M $\text{NaClO}_4 + 10^{-2}$ M $\text{HClO}_4 + 10^{-3}$ M PbO (Reprinted with permission from Ref. [256])

Here they are excited through collisions with high energy electrons, metastable argon atoms and ions. The negative glow emits a characteristic radiation (optical emission spectrum) of the discharge gas and the elements present in the sample. This spectrum is recorded by an optical spectrometer and the concentration distribution of the different elements is deduced from the intensities of the characteristic spectral lines. Analytical applications of GDOES involve bulk elemental analysis, mostly of metals and alloys, as well as depth profile analysis of various coatings and surface-modified materials, acquiring the signal from each chemical element as a function of the sputtering time.

GDOES is a promising technique for ultrathin films analysis, including those formed by upd. Seo et al. [256] employed XPS and GDOES, together with electrochemical techniques, to confirm the evidence of Pb upd on Ni in acidic perchlorate solutions containing Pb^{2+} ions and its effect on the anodic dissolution and passivity of Ni. They reported that the upd of lead on Ni in the potential range larger than -0.215 V (SHE) corresponding to the equilibrium potential of the Pb^{2+} (10^{-3} M)/Pb electrode, was confirmed by XPS and GDOES analyses, indicating that the upd process occurred on Ni surface in the potential range of the active dissolution and active/passive transition. The GDOES results are shown in Fig. 2.37. The typical depth-profile of the Ni sample, polarized for 30 min at -0.215 V (SHE) in 0.1 M $\text{NaClO}_4 + 10^{-2}$ M $\text{HClO}_4 + 10^{-3}$ M PbO solution, evidenced the presence of lead on the uppermost surface (Fig. 2.37a). In order to compare the difference in Pb depth-profile between the Ni specimens, graphics of the intensity ratio, i.e. the intensity of Pb, I_{Pb} , normalized by dividing it with the Ni intensity in bulk, $I_{\text{Ni(bulk)}}$, vs the sputtering time were performed.

Figure 2.37b exhibits the normalized Pb depth-profiles of the Ni specimens polarized for 30 min at various potentials. It was observed that the maximum of the intensity ratio, $I_{\text{Pb}}/I_{\text{Ni(bulk)}}$, decreased with increasing polarization potential from -0.215 to 0.09 V (vs. SHE) and no Pb was detected for the Ni specimen polarized at 0.30 or 0.50 V (vs. SHE) in the passive region. Both the XPS and

GDOES results indicated that lead was present on the Ni surface in the potential region of hydrogen evolution and active dissolution, while there was no lead on the Ni surface in the complete passive region.

2.28 Underpotential Deposition in Nuclear Chemistry

Electrochemical methods for the isolation and separation of radioelements in weightless amounts are popular because of their cleanliness. The deposited radioisotopes may be desorbed from the electrodes again or may form firmly adhering uniform layers, with which radioactive energy or intensity measurements can be performed. The deposition methods are either electroless or they make use of electric current (electrolytic methods). A valuable overview on the application of electrochemical methods in radiochemistry until the middle 1950s can be found in the book of E. Broda and T. Schönfeld. [257]. The practical aspects have been summarized by Rogers [258]. This author has performed depositions in volumes of 0.01 ml. A more recent overview on theoretical aspects of this problem can be found in the article of Eichler and Kratz [259].

Due to its ability to sense very small cation concentrations, the underpotential deposition phenomenon has found application in nuclear chemistry and emerges as an interesting method for separating trace levels of a radioactive substance.

From theoretical predictions, elements with atomic number in the range 108–116 are expected to be partially very noble metals and therefore their electrochemical deposition on suitable electrode materials from aqueous solutions may be used as a possible method for their isolation [260].

Eichler and Kratz [259] have shown by means of theoretical calculations that the potential associated with the electrochemical deposition of radionuclides in metallic form from solutions of extremely small concentration is strongly influenced by the choice of the electrode material. Based on a previous work of Byrne and Rogers [261], these authors proposed a modified Nernst equation for a thermodynamic description of the electrodeposition of radiotracers in the upd range. This equation is based on physical properties (partial molar adsorption enthalpy and entropy) of the deposited metal A and the electrode metal B and lead to predictions for electrode potentials for depositions of 50 %, $E_{50\%}$:

$$E_{50\%} = E^0 - \frac{\Delta\bar{H}(A-B) - T\Delta\bar{S}_{\text{vib}}}{zF} - \frac{RT}{zF} \ln \frac{A_m}{1000} \quad (2.4)$$

Where E^0 is the standard electrode potential, $\Delta\bar{H}(A-B)$ is the partial molar net adsorption enthalpy, which corresponds to the enthalpy difference associated with the transformation of 1 mol of the pure metal A in its standard state into the state of “zero coverage”, where the interaction of A-B is strong and the interaction of A-A negligible. In the state of “zero coverage” deposition occurs in the upd range. ΔS_{vib} is the difference of vibrational entropies in the above mentioned states, and A_m is

Table 2.2 $E_{50\%}$ values, and E^0 , as defined in Eq. (2.4) for Hg, Tl, Pb, Bi, and Po at different electrode surfaces. All potentials are referred to Ag/AgCl electrode

$E_{50\%}$ (mV) Electrode	Ni	Cu	Pd	Ag	Pt	Au	E^0 (mV)
Ion							
Hg ²⁺	660	635	1145	620	965	710	595
Tl ⁺	555	315	1915	380	1425	655	-530
Pb ²⁺	-235	-380	450	-380	170	-305	-320
Bi ³⁺	300	145	790	125	585	175	120
Po ²⁺	775	330	1035	355	720	670	425
Po ⁴⁺	600	375	730	340	575	545	565

Data taken from Ref. [262]

the surface occupied by 1 mol of A atoms as a monolayer on a metal electrode B. Calculations for the deposition of elements 112–115 and their homologs Hg, Tl, Pb, Bi and Po on Ni-, Cu-, Pd-, Ag-, Pt- and Au- electrodes were carried out, confirming the influence of the nature of the electrode material on the deposition potential. Hummrich et al. [262] recalculated the $E_{50\%}$ values from [259], which are presented in Table 2.2 together with the standard electrode potentials E^0 . All the potentials are referred to the Ag/AgCl reference electrode. It is found that for Pd, and in some cases Pt or Au, particularly large, positive values of $E_{50\%}$ were calculated, larger than the standard electrode potentials tabulated for these elements. This fact indicates that these electrode materials are an excellent choice for practical applications enabling the electrochemical deposition of this kind of elements from aqueous solutions.

Hevesy and Paneth [263] performed the first studies of Po underpotential deposition on gold electrodes and introduced the quantity denominated “critical potential”, E_{crit} . This value refers to the potential at which a significant electrodeposition of a radiotracer on a metal surface occurs. The E_{crit} as well as the experimental quantity defined above $E_{50\%}$ can be considered as a measure for the strength of the interaction between the metal A and the electrode material B. These quantities are discussed in more detail below.

A specific electrolytic cell has to be designed for the present type of studies, because electrodeposition must be produced in a fast way due to the very short life of the isotopes which have to be deposited. Therefore, a small ratio of an electrolyte volume to electrode area, intensive stirring and a high temperature were considered by Hummrich et al. [262]. The electrode set-up and electrolytic cell used by these authors are depicted in Fig. 2.38. The electrolytic cell was made of polyether-etherketone with two slots for working electrodes, which were shaped in the form of foils on which the electrodeposition took place. The electrolyte volume was small, 1 mL. A large stir bar was placed between the two metal foil working electrodes, to make possible a vigorous stirring, reducing simultaneously the ratio of electrolyte volume to electrode. Electrolyte in- and outlets were provided for online experiments and were plugged in the offline experiments, and a positive temperature coefficient resistor (PCT) was mounted behind one working electrode.

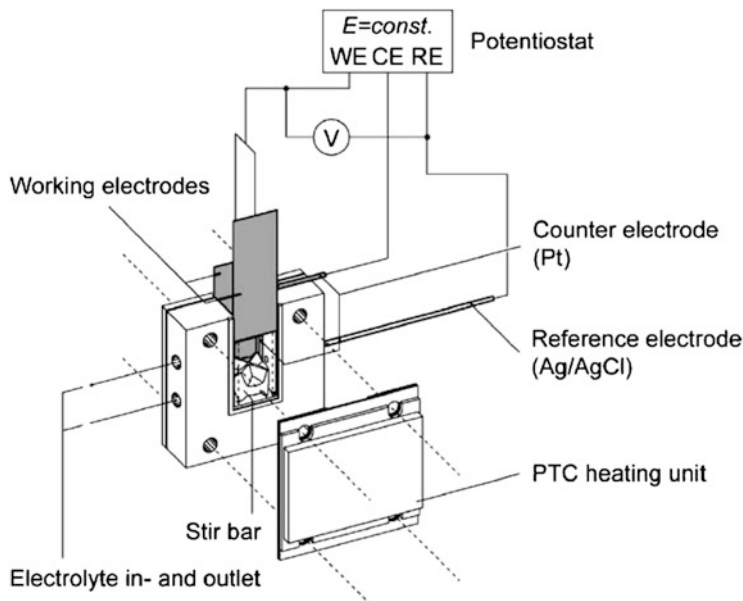


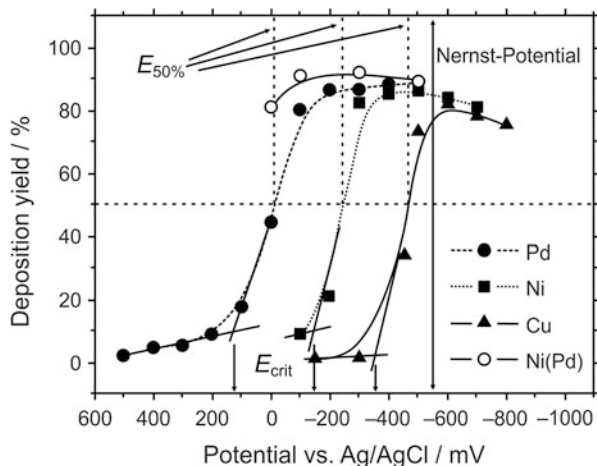
Fig. 2.38 Potentiostatic three electrode set-up and electrolytic cell for fast electrochemical deposition experiments with short-lived isotopes. WE: working electrode, CE: counter electrode, RE: reference electrode (Taken from Ref. [262] With permission)

With this set-up, Hummrich et al. [262] performed offline and online experiments. The term offline refers to experiments performed with relatively long lived homologues of the super-heavy elements, while the term online refers to experiments coupled to the nuclear facility. The first ones served to investigate the appropriate potentials for electrochemical deposition and the electrodeposition velocity of several standard radiotracers. This was achieved via measurement of the γ activity of the electrodes, which was compared with the measured count rates of a standard sample that was prepared by pipetting a definite activity on a glass fiber filter.

In Figure 2.39, the deposition yield of Pb on Pd, Ni, Cu and palladinated Ni (Ni (Pd)) surfaces is plotted versus the electrode potential, where the critical potentials E_{crit} were determined by the tangent method as proposed by Joliot [264]. In this method, the intersection of the tangent of the flat part of the curve (before deposition starts) and of the tangent that goes through the point of inflection of the gradient part of the curve, defines the E_{crit} . Starting at this potential, the deposition sets in and approaches eventually 100 %. From the potential curve, $E_{50\%}$ can be also deduced.

For the deposition of Pb on Pd the E_{crit} and $E_{50\%}$ values were +125/–20 mV, on Ni –150/–250 mV, and on Cu –350/–460 mV, respectively. Comparing these measured values with the calculated hypothetical Nernst potential (–530 mV vs. Ag/AgCl; 3 M KCl) for lead deposition on lead, it can be deduced that the

Fig. 2.39 Determination of critical potentials (E_{crit}) and $E_{50\%}$ -values for the deposition of ^{212}Pb on different electrode materials from 0.1 M HCl. A hypothetical Nernst potential for lead deposition on lead is also indicated (Reprinted with permission from Ref. [262])



underpotential deposition phenomenon is present in all cases. Especially for the deposition of Pb on Pd, the effect is more pronounced because it shows the strongest underpotential shift, namely more than 600 mV more positive than the Nernst potential. Then the electrode with the deposited product was analyzed by α -spectrometry and the results indicated that more than 97 % of the radioactivity of Pb remained on the Pd electrodes and therefore Pd should then be used as the electrode material.

Coming back to the previous studies of Eichler and Kratz [259], these authors compared theoretical $E_{50\%}$ -values with the measured E_{crit} data, and suggested that the predictions seemed to be upper limits for the “critical potentials”. In that sense, the characteristic quantities $E_{50\%}$ can be seen as useful predictions of the largely different “driving forces” for electrochemical depositions depending on the nature of the microcomponent A and on the choice of the electrode material B. On the other hand, in the work of Hummrich et al. [262] the highest measured $E_{50\%}$ values were tentatively compared with the theoretical calculations in Table 2.2. As examples, it is found that the predicted large underpotential deposition values of Pb on Pd and Pt were confirmed, although the measured values were lower than the predicted ones. The predicted $E_{50\%}$ values for the deposition on Cu and Ni were within 100 mV close to the measured values, while the calculated value for Au was much too low.

Hummrich et al. [262] also performed online experiments, which involved a set-up suited to perform electrodeposition experiments with accelerator produced isotopes. These experiments involved the following steps: (1) fast transport of the produced isotopes to the chemistry set-up, (2) transfer of the isotopes from the gas into the aqueous phase, (3) transport into the electrolytic cell, (4) electrodeposition onto the electrodes, (5) preparation of samples for decay spectrometry, (6) transport of the electrodes to a detector set-up for α -spectrometry and identification of the element by detection of its nuclear decay.

In a first type of online experiments, the electrolytic cell with the foil electrodes was used and the transport of the metal foil electrodes to detectors was performed manually. In a second type of online experiments, the working electrodes were long metal tapes which allowed for moving the spot with the deposited radioactivity very fast to a detector array, i.e. these tapes were then be pulled through the electrolytic cell in order to transport the deposited activities in front of α -detectors. This perspective was taken with the aim of developing a fully automatised system and to improve the detection probability increasing the number of detectors. Finally, these authors mentioned that a good candidate for first electrodeposition experiments in the field of the super heavy elements could be ^{270}Hs (Hassium, atomic number 108), which has a sufficient long half-life time (22 s).

References

1. Budevski E, Staikov G, Lorenz WJ (1996) Electrochemical phase formation. An introduction to the initial stages of metal deposition. Weinheim, VCH
2. Kolb DM, Przasnyski M, Gerischer H (1974) *J Electroanal Chem* 54:25
3. Szabó S (1991) *Int Rev Phys Chem* 10:207
4. Budevski E, Staikov G, Lorenz WJ (2000) *Electrochim Acta* 45:2559
5. Kolb DM (1978) Physical and electrochemical properties of metal monolayers on metallic substrates. In: Gerischer H, Tobías CW (eds) *Advances in electrochemistry and electrochemical engineering*. Wiley, New York, p 125
6. Herrero E, Buller LJ, Abruña HD (2001) *Chem Rev* 101:1897
7. Sudha V, Sangaranarayanan MV (2005) *J Chem Sci* 117:207
8. Aramata A (1997) Underpotential deposition on single-crystal metals. In: Bockris JO'M, White RW, Conway BE (eds) *Modern aspects of electrochemistry*, number 31. Plenum Press, New York, p 181
9. Leiva EPM (1996) *Electrochim Acta* 41:2185
10. Adžić RR (1984) Electrocatalytic properties of the surfaces modified by foreign metal adatoms. In: Gerischer H, Tobías CW (eds) *Advances in electrochemistry and electrochemical engineering*, vol 13. Wiley, New York, p 159
11. Kokkinidis G (1986) *J Electroanal Chem* 201:217
12. Cullity BD (1978) *Elements of X-ray diffraction*, 2nd edn. Addison-Wesley, Reading, p 506
13. García S, Salinas D, Mayer C, Schmidt E, Staikov G, Lorenz WJ (1998) *Electrochim Acta* 43:3007
14. Chen C-H, Vesecky SM, Gewirth AA (1992) *J Am Chem Soc* 114:451
15. Mrozek P, Sung Y-E, Han M, Gamboa-Aldeco M, Wieckowski A, Chen C-H, Gewirth AA (1995) *Electrochim Acta* 40:17
16. Uchida H, Miura M, Watanabe M (1995) *J Electroanal Chem* 386:261
17. Ogaki K, Itaya K (1995) *Electrochim Acta* 40:1249
18. Rooryck V, Reniers F, Buess-Herman C, Attard GA, Yang X (2000) *J Electroanal Chem* 482:93
19. Schulze JW, Dickertmann D (1976) *Surf Sci* 54:489
20. Dickertmann D, Koppitz FD, Schulze JW (1976) *Electrochim Acta* 21:967
21. Zei M, Qiao G, Lempfuhr G, Kolb DM (1987) *Ber Bunsenges Phys Chem* 91:3494
22. Beckmann HO, Gerischer H, Kolb DM, Lempfuhr G (1977) *Symp Faraday Soc* 12:51
23. Hachiya T, Honbo H, Itaya K (1991) *J Electroanal Chem* 315:275
24. Omar IH, Pauling HJ, Jüttner K (1993) *J Electrochem Soc* 140:2187

25. Borges GL, Kanazawa KK, Gordon JG II, Ashley K, Richer J (1994) *J Electroanal Chem* 364:281
26. Shi Z, Lipkowski J (1994) *J Electroanal Chem* 364:289
27. Shi Z, Lipkowski J (1994) *J Electroanal Chem* 365:303
28. Shi Z, Wu S, Lipkowski J (1995) *Electrochim Acta* 40:9
29. Magnussen OM, Hotlos J, Beitel G, Kolb DM, Behm RJ (1991) *J Vac Sci Technol B* 9:969
30. Magnussen OM, Hotlos J, Nichols RJ, Kolb DM, Behm RJ (1990) *Phys Rev Lett* 64:2929
31. Kolb DM (1994) *Ber Bunsenges Phys Chem* 98:1421
32. Manne S, Hansma PK, Massie J, Elings VB, Gewirth AA (1991) *Science* 251:183
33. Parry DB, Samant MG, Seki H, Philpott MR (1993) *Langmuir* 9:1878
34. Blum L, Abruña HD, White J, Gordon JG II, Borges GL, Samant MG, Melroy OR (1986) *J Chem Phys* 85:6732
35. Melroy OR, Samant MG, Borges GL, Gordon JG II, Blum L, White JH, Albarelli MJ, McMillan M, Abruña HD (1988) *Langmuir* 4:728
36. Tadjeddine A, Guay D, Ladouceur M, Tourillon G (1991) *Phys Rev Lett* 66:2235
37. Gordon JG, Melroy OR, Toney MF (1995) *Electrochim Acta* 40:3
38. Nakai Y, Zei MS, Kolb DM, Lempfuhr G (1984) *Ber Bunsenges Phys Chem* 88:340
39. Kolb DM (2002) *Surf Sci* 500:722
40. Randler RJ, Kolb DM, Ocko BM, Robinson IK (2000) *Surf Sci* 447:187
41. Möller FA, Magnussen OM, Behm RJ (1995) *Phys Rev B* 51:2484
42. Cappadonia M, Linke U, Robinson KM, Schmidberger J, Stimming U (1996) *J Electroanal Chem* 405:227
43. Kuzume A, Herrero E, Feliu JM, Nichols RJ, Schiffrin DJ (2004) *J Electroanal Chem* 570:157
44. Bowles BJ (1965) *Electrochim Acta* 10:717
45. Bowles BJ (1965) *Electrochim Acta* 10:731
46. Bowles BJ, Cranshaw TE (1965) *Phys Lett* 17:258
47. Bowles BJ (1966) *Nature* 212:1456
48. Bowles BJ (1970) *Electrochim Acta* 15:589
49. Bowles BJ (1970) *Electrochim Acta* 15:737
50. Horányi G, Vértes G (1973) *J Electroanal Chem* 45:295
51. Horányi G (1974) *J Electroanal Chem Interfacial Electrochem* 55:45
52. Horanyi G (2004) *Radiotracer studies of interfaces*. Elsevier B.V, The Netherlands
53. Waszczuk P, Wnuk A, Sobkowski J (1999) *Electrochim Acta* 44:1789
54. Poškus D, Agafonovas G (2000) *J Electroanal Chem* 493:50
55. Zelenay P, Rice-Jackson LM, Wiekowski A, Gawłowski J (1991) *Surf Sci* 256:253
56. Hölzle MH, Retter U, Kolb DM (1994) *J Electroanal Chem* 371:101
57. Schultze JW, Dickertmann D (1976) *Surf Sci* 54:489
58. Bewick A, Fleischmann M, Thirsk HR (1962) *Trans Faraday Soc* 58:2200
59. Jüttner K, Lorenz WJ (1980) *Z Phys Chem Neue Folge* 122:163
60. Staikov G, Jüttner K, Lorenz WJ, Budevski E (1994) *Electrochim Acta* 39:1019
61. Schmidt E, Siegenthaler H (1969) *Helv Chim Acta* 52:2245
62. Schmidt E, Wüthrich N (1970) *J Electroanal Chem* 28:349
63. Lorenz WJ, Hermann HD, Wüthrich N, Hilbert F (1974) *J Electrochem Soc* 121:1167
64. Kolb DM, Schneider J (1986) *Electrochim Acta* 31:929
65. Hamelin A (1995) *J Electroanal Chem* 386:1
66. Vitanov T, Popov A, Sevastyanov ES (1982) *J Electroanal Chem* 142:289
67. Bruckenstein S, Napp DT (1968) *J Am Chem Soc* 90:6303
68. Tindall GW, Bruckenstein S (1968) *Anal Chem* 40:1051
69. Cadle SH, Bruckenstein S (1971) *Anal Chem* 43:932
70. Tindall GW, Bruckenstein S (1971) *Electrochim Acta* 16:245
71. Opekar F, Beran P (1976) *J Electroanal Chem* 69:1
72. Bruckenstein S, Miller B (1977) *Acc Chem Res* 10:54
73. Swathirajan S, Bruckenstein S (1983) *Electrochim Acta* 28:865

74. Mascaro LH, Santos MC, Machado SAS, Avaca LA (1997) *J Chem Soc Faraday Trans* 93:3999
75. Cadle SH, Bruckenstein S (1972) *Anal Chem* 44:1993
76. Vicente VA, Bruckenstein S (1973) *Anal Chem* 45:2036
77. Riedhammer TM, Melnicki LS, Bruckenstein S (1978) *Zeit Phys Chem* 111:177
78. Sherwood WG, Bruckenstein S (1978) *J Electrochem Soc* 125:1098
79. Santos MC, Mascaro LH, Machado SA (1998) *Electrochim Acta* 43:2263
80. Bruckenstein S, Swathirajan S (1985) *Electrochim Acta* 30:851
81. Buttry DA (1991) Chapter 10: the quartz crystal microbalance as an in situ tool in electrochemistry. In: Abruña HD (ed) *Electrochemical interfaces*. VCH Publishers, Inc, New York, p 529
82. Bruckenstein S, Shay M (1985) *Electrochim Acta* 30:1295
83. Melroy O, Kanazawa K, Gordon JG II, Buttry D (1986) *Langmuir* 2:697
84. Deakin MR, Melroy O (1988) *J Electroanal Chem* 239:321
85. Deakin MR, Li TT, Melroy OR (1988) *J Electroanal Chem* 243:343
86. Watanabe M, Uchida H, Miura M, Ikeda N (1995) *J Electroanal Chem* 384:191
87. Uchida H, Hiei M, Watanabe M (1998) *J Electroanal Chem* 452:97
88. Toney MF, Howard JN, Richer J, Borges GL, Gordon JG, Melroy OR, Yee D, Sorensen LB (1995) *Phys Rev Lett* 75:4472
89. Wu S, Shi Z, Lipkowski J, Hitchcock AP, Tyliczszak T (1997) *J Phys Chem B* 101:10310
90. White JH, Albarelli MJ, Abruña HD, Blum L, Melroy OR, Samant MG, Borges GL, Gordon JG (1988) *J Phys Chem* 92:4432
91. Inzelt G, Horányi G (2000) *J Electroanal Chem* 491:111
92. Binnig G, Rohrer H, Gerber C, Weibel E (1982) *Phys Rev Lett* 49:57
93. Hansma PK, Tersoff J (1987) *J Appl Phys* 61:R1
94. Sonnenfeld R, Hansma PK (1986) *Science* 232:211
95. Siegenthaler H (1992) STM in electrochemistry. In: Güntherrodt H-J, Wiesendanger R (eds) *Scanning tunneling microscopy II*. Springer, Berlin/Heidelberg, p 7
96. Gewirth AA, Niece BK (1997) *Chem Rev* 97:1129
97. Itaya K (1998) *Prog Surf Sci* 58:121
98. Kolb DM (2000) *Electrochim Acta* 45:2387
99. Tao NJ, Li CZ, He HX (2000) *J Electroanal Chem* 492:81
100. Christensen PA, Hamnet A (1994) *Techniques and mechanisms in electrochemistry*. Blackie Academic & Professional (An imprint of Chapman & Hall), Glasgow
101. Lustenberger P, Rohrer H, Christoph R, Siegenthaler H (1988) *J Electroanal Chem* 243:225
102. Hamelin A, Gao X, Weaver MJ (1992) *J Electroanal Chem* 323:361
103. Dieterle M, Will T, Kolb DM (1995) *Surf Sci* 342:29
104. Wolf JF, Vicenzi B, Ibach H (1991) *Surf Sci* 249:233
105. Poensgen M, Wolf JF, Frohn J, Giesen M, Ibach H (1992) *Surf Sci* 274:430
106. Hachiya T, Itaya K (1992) *Ultramicroscopy* 42–44:445
107. Itaya K (1992) *Nanotechnology* 3:185
108. Chen C, Gewirth AA (1992) *Ultramicroscopy* 42–44:437
109. Esplandiú MJ, Schneeweiss MA, Kolb DM (1999) *Phys Chem Chem Phys* 1:4847
110. Ikemiya N, Yamada K, Hara S (1996) *Surf Sci* 348:253
111. García SG (1997) Ph.D. thesis, Universidad Nacional del Sur, Bahía Blanca
112. Zei MS, Qiao G, Lehmpfuhl G, Kolb DM (1987) *Ber Bunsenges Phys Chem* 91:349
113. Garcia SG, Salinas D, Mayer C, Vilche JR, Pauling H-J, Vinzelberg S, Staiikov G, Lorenz WJ (1994) *Surf Sci* 316:143
114. Batina N, Will T, Kolb DM (1992) *Faraday Discuss* 94:93
115. Hotlos J, Magnussen OM, Behm RJ (1995) *Surf Sci* 335:129
116. Vasiljevic N, Viyannalage LT, Dimitrov N, Sieradzki K (2008) *J Electroanal Chem* 613:118
117. Binnig G, Quate F, Gerber C (1986) *Phys Rev Lett* 56:930
118. Binnig G, Gerber C, Stoll E, Albrecht TR, Quate CF (1987) *Europhys Lett* 3:1281

119. Binnig G (1992) *Ultramicroscopy* 42–44:7
120. Bhushan B, Marti O (2004) Scanning probe microscopy – principle of operation, instrumentation, and probes. In: Brushan B (ed) *Handbook of nanotechnology*, 2nd edn. Springer, Heidelberg, p 591
121. Meyer E (1992) *Prog Surf Sci* 41:3
122. Butt H-J, Cappella B, Kappl M (2005) *Surf Sci Rep* 59:1
123. Manne S, Massie J, Elings VB, Hansma PK, Gewirth AA (1991) *J Vac Sci Technol B* 9:950
124. Held G (2012) Low-energy electron diffraction: crystallography of surfaces and interfaces. In: Schäfer R, Schmidt PC (eds) *Methods in physical chemistry*. Wiley-VCH, Weinheim, Chapter 20
125. Henk J (2002) Theory of low-energy electron diffraction and photoelectron spectroscopy from ultra-thin films. In: Nalwa S (ed) *Handbook of thin film materials*, vol 2: Characterization and spectroscopy of thin films. Academic, CA, San Diego, Chapter 10
126. Gallon TE, Matthew JAD (1972) *Rev Phys Technol* 3:31
127. Holloway PH (1980) Fundamentals and applications of auger electron spectroscopy. In: Marton L, Marton C (eds) *Advances in electronics and electron physics*, vol 54. Academic, New York, p 241
128. Bubert H, Rivière JC, Werner WSM (2011) Auger electron spectroscopy (AES). In: Friedbacher G, Bubert H (eds) *Surface and thin film analysis: a compendium of principles, instrumentation, and applications*, 2nd edn. Wiley-VCH Verlag GmbH & Co. KGaA, Weinheim, Chapter 3
129. Madden HH (1981) *J Vac Sci Technol* 18:677
130. Shchukarev A (2006) *Adv Col Interf Sci* 122:149
131. Venezia AM (2003) *Catal Today* 77:359
132. Fadley CS (2010) *J Electron Spectrosc Relat Phenom* 178–179:2
133. Zei MS, Nakai Y, Weick D, Lehmpfuhl G (1985) *Surf Sci* 152/153:254
134. Rehr JJ, Albers RC (2000) *Rev Mod Phys* 72:621
135. Teo B-K (1981) EXAFS spectroscopy: techniques and applications. In: Teo B-K, Joy DC (eds) *EXAFS spectroscopy: techniques and applications*. Springer Science + Business Media, New York, Chapter 3
136. Lee PA, Citrin PH, Eisenberger P, Kincaid BM (1981) *Rev Mod Phys* 53:769
137. Samant MG, Borges G, Melroy OR (1993) *J Electrochem Soc* 140:421
138. Chabala ED, Ramadan AR, Brunt T, Rayment T (1996) *J Electroanal Chem* 412:67
139. Lee D, Rayment T (1999) *Phys Chem Chem Phys* 1:4389
140. Ramadan AR, Rayment T (2001) *J Electroanal Chem* 503:28
141. Kondo T, Morita J, Okamura M, Saito T, Uosaki K (2002) *J Electroanal Chem* 532:201
142. Adžić RR, Wang JX, Ocko BM, McBreen J (2010) EXAFS, XANES, SXS. In: Vielstich W, Gasteiger HA, Lamm A, Yokokawa H (eds) *Handbook of fuel cells – fundamentals, technology and applications*. Wiley, New York, p 679
143. Chabala ED, Harji BH, Rayment T, Archer MD (1992) *Langmuir* 8:2028
144. Matsui J, Mizukil J (1993) *Annu Rev Mater Sci* 23:295
145. Segmüller A (1987) *Thin Solid Films* 154:33
146. Samant MG, Toney MF, Borges GL, Blum L, Melroy OR (1988) *J Phys Chem* 92:220
147. Herrero E, Glazier S, Abruña HD (1998) *J Phys Chem B* 102:9825
148. Miles R (1983) *Surf Interf Anal* 5:43
149. Iwasita T, Nart FC (1997) *Prog Surf Sci* 55:271
150. Bewick A (1983) *J Electroanal Chem* 150:481
151. Hummel RE, Dubroca T (2013) Differential reflectance spectroscopy in analysis of surfaces. In: Meyers RA (ed) *Encyclopedia of analytical chemistry*. Wiley, New York
152. McIntyre JDE, Aspnes DE (1971) *Surf Sci* 24:417
153. Kolb DM (1988) *Ber Bunsenges Phys Chem* 92:1175
154. Kolb DM, Leutloff D, Przasnyski M (1975) *Surf Sci* 47:622
155. Kolb DM, Kötzt R (1977) *Surf Sci* 64:698

156. McIntyre JDE, Kolb DM (1970) *Symp Faraday Soc* 4:99
157. Borensztein Y, Abelès F (1985) *Thin Solid Films* 125:129
158. Kolb DM (1988) UV-visible reflectance spectroscopy. In: Gale RJ (ed) *Spectroelectrochemistry: theory and practice*. Plenum Press, New York, p 87, Chapter 4
159. Bard AJ, Faulkner LR (2001) *Electrochemical methods. Fundamentals and applications*, 2nd edn. Wiley, New York, p 698
160. Shannon VL, Koos DA, Richmond GL (1987) *J Phys Chem* 91:5548
161. Yagi I, Lantz JM, Nakabayashi S, Corn RM, Uosaki K (1996) *J Electroanal Chem* 401:95
162. Richmond GL, Robinson JM, Shannon VL (1988) *Prog Surf Sci* 28:1
163. Richmond GL (1992) Second harmonic generation as an in-situ probe of single crystal electrode surfaces. In: Gerischer H, Tobias CW (eds) *Advances in electrochemical science and engineering*. VCH Verlagsgesellschaft, Weinheim, p 141
164. Corn RM, Higgins DA (1994) *Chem Rev* 94:107
165. Richmond LR (1991) Investigations of electrochemical interfaces by nonlinear optical methods. In: Abruña HD (ed) *Electrochemical interfaces. Modern techniques for in-situ interface characterization*. VCH Publishers Inc, New York, p 265
166. Richmond GL, Bradley RA (1995) Surface second harmonic generation studies of single crystal metal surfaces. In: Dai H-L, Ho W (eds) *Laser spectroscopy and photochemistry on metal surface*. World Scientific, Singapore, p 132, Chapter 4
167. Lakkaraju S, Bennaahmias MJ, Borges GL, Gordon JG II, Lazaga M, Stone BM, Ashley K (1990) *App Opt* 29:4943
168. Koos DA, Richmond GL (1992) *J Phys Chem* 96:3770
169. Walters MJ, Pettit CM, Roy D (2001) *Phys Chem Chem Phys* 3:570
170. Brolo AG, Irish DE, Smith BD (1997) *J Mol Struct* 405:29
171. Haynes CL, McFarland AD, Van Duyne RP (2005) *Anal Chem* 77:338A
172. Tian Z-Q, Ren B, Wu D-Y (2002) *J Phys Chem* 106:9463
173. Tian ZQ, Ren B (2003) Raman spectroscopy of electrode surfaces. In: Bard AJ, Stratmann M, Unwin PR (eds) *Encyclopedia of electrochemistry, instrumentation and electroanalytical chemistry*, vol 3. Wiley-VCH, New York, pp 572–659
174. Pemberton JE (1991) Surface enhanced raman scattering. In: Abruña HD (ed) *Electrochemical interfaces: modern techniques for in-situ interface characterization*. VCH Publishers, Inc, New York, p 193
175. Otto A (1991) *J Raman Spectrosc* 22:743
176. Sharma B, Frontiera RR, Henry A-I, Ringe E, Van Duyne RP (2012) *Mater Today* 15:16
177. Leung L-WH, Gosztola D, Weaver MJ (1987) *Langmuir* 3:45
178. Leung L-WH, Weaver MJ (1987) *J Electroanal Chem* 217:367
179. Fleischmann M, Tian ZQ (1987) *J Electroanal Chem* 217:385
180. Jüttner K, Siegenthaler H (1978) *Electrochim Acta* 23:971
181. Siegenthaler H, Jüttner K, Schmidt E, Lorenz WJ (1978) *Electrochim Acta* 23:1009
182. Schmidt E, Siegenthaler H (1983) *J Electroanal Chem* 150:59
183. Carnal D, Oden PI, Müller U, Schmidt E, Siegenthaler H (1995) *Electrochim Acta* 40:1223
184. Siegenthaler H, Jüttner K (1979) *Electrochim Acta* 24:109
185. Vitanov T, Popov A, Staikov G, Budevski E, Lorenz WJ, Schmidt E (1986) *Electrochim Acta* 31:981
186. Popov A, Dimitrov N, Velev O, Vitanov T, Budevski E (1989) *Electrochim Acta* 34:265
187. Popov A, Dimitrov N, Kashchiev D, Vitanov T, Budevski E (1989) *Electrochim Acta* 34:269
188. Dimitrov N, Popov A, Kashchiev D, Vitanov T, Budevski E (1991) *Electrochim Acta* 36:1259
189. Dimitrov N, Popov A, Vitanov T, Budevski E (1991) *Electrochim Acta* 36:2077
190. Popov A, Dimitrov N, Kashchiev D, Vitanov T, Budevski E (1993) *Electrochim Acta* 38:387
191. Dimitrov N, Popov A, Kashchiev D, Vitanov T (1994) *Electrochim Acta* 39:957
192. Popov A, Dimitrov N, Vitanov T, Kashchiev D, Budevski E (1995) *Electrochim Acta* 40:1495

193. Schmidt U, Vinzelberg S, Staikov G (1996) *Surf Sci* 348:261
194. Engelsmann K, Lorenz WJ, Schmidt E (1980) *J Electroanal Chem* 114:1
195. Green MP, Hanson KJ, Scherson DA, Xing X, Richter M, Ross PN, Carr R, Lindau I (1989) *J Phys Chem* 93:2181
196. Green MP, Hanson KJ, Carr R, Lindau I (1990) *J Electrochem Soc* 137:3493
197. Green MP, Hanson KJ (1991) *Surf Sci Lett* 259:L743
198. Schmidt E, Christen M, Beyeler P (1973) *J Electroanal Chem* 42:275
199. Bort H, Jüttner K, Lorenz WJ, Staikov G (1983) *Electrochim Acta* 28:993
200. Martins ME, Hernández-Creus A, Salvarezza RC, Arvía AJ (1994) *J Electroanal Chem* 375:141
201. García SG, Salinas DR, Staikov G (2005) *Surf Sci* 576:9
202. Staikov G, García SG, Salinas DR (2010) *ECS Trans* 25:3
203. Ambrusi RE, Staikov G, García SG (2014) *J Electroanal Chem* 728:130
204. Schultze JW, Koppitz FD, Lohrengel MM (1974) *Ber Bunsenges Phys Chem* 78:693
205. Vidu R, Hara S (1999) *Scr Mater* 41:617
206. Vidu R, Hara S (1999) *J Electroanal Chem* 475:171
207. Vidu R, Hara S (2000) *Surf Sci* 452:229
208. Vidu R, Hirai N, Hara S (2001) *Phys Chem Chem Phys* 3:3320
209. del Barrio MC, García SG, Salinas DR (2004) *Electrochem Commun* 6:762
210. del Barrio MC, García SG, Mayer CE, Salinas DR (2008) *Surf Interface Anal* 40:22
211. del Barrio MC, Salinas DR, García SG (2014) *Electrochim Acta* 130:164
212. Hirai N, Tanaka H, Hara S (1998) *Appl Surf Sci* 130–132:506
213. del Barrio MC, García SG, Salinas DR (2009) *Electrochim Acta* 55:451
214. García SG, Salinas DR (2007) Nanoelectrochemistry: 2D and 3D metal-phase formation processes. In: Mariscal MM, Dassie SA (eds) *Recent advances in nanoscience. Research Signpost, Kerala*, pp 103–122, Chapter 4
215. Lay MD, Varazo K, Srisook N, Stickney JL (2003) *J Electroanal Chem* 554:221
216. Lay MD, Stickney JL (2003) *J Am Chem Soc* 125:1352
217. Stafford GR, Bertocci U (2006) *J Phys Chem B* 110:15493
218. Shin JW, Bertocci U, Stafford GR (2010) *J Phys Chem C* 114:7926
219. Stafford GR, Bertocci U (2007) *J Phys Chem C* 111:17580
220. Brunt TA, Rayment T, O’Shea SJ, Welland ME (1996) *Langmuir* 12:5942
221. Brankovic SR, Wang JX, Adžić RR (2001) *Surf Sci* 474:L173
222. Viyannalage LT, Vasilic R, Dimitrov N (2007) *J Phys Chem C* 111:4036
223. Gokcen D, Bae S-E, Brankovic SR (2010) *J Electrochem Soc* 157:D582
224. Gokcen D, Bae S-E, Brankovic SR (2011) *ECS Trans* 35:11
225. Huang BM, Colletti LP, Gregory BW, Anderson JL, Stickney JL (1995) *J Electrochem Soc* 142:3007
226. Colletti LP, Flowers BH Jr, Stickney JL (1998) *J Electrochem Soc* 145:1442
227. Stickney JL (2002) Electrochemical atomic layer epitaxy (EC-ALE): nanoscale control in the electrodeposition of compound semiconductors. In: Kolb DM, Alkire R (eds) *Advances in electrochemical science and engineering*, vol 7. Wiley-VCH, Weinheim, p 1
228. Mathe MK, Cox SM, Flowers BH Jr, Vaidyanathan R, Pham L, Srisook N, Happek U, Stickney JL (2004) *J Cryst Growth* 271:55
229. Gregory BW, Stickney JL (1991) *J Electroanal Chem* 300:543
230. Gregory BW, Suggs DW, Stickney JL (1991) *J Electrochem Soc* 138:1279
231. Suggs DW, Stickney JL (1993) *Surf Sci* 290:362
232. Suggs DW, Stickney JL (1993) *Surf Sci* 290:375
233. Varazo K, Lay MD, Sorenson TA, Stickney JL (2002) *J Electroanal Chem* 522:104
234. Pezzatini G, Caporali S, Innocenti M, Foresti ML (1999) *J Electroanal Chem* 475:164
235. Forni F, Innocenti M, Pezzatini G, Foresti ML (2000) *Electrochim Acta* 45:3225
236. Conway BE, Birss V, Wojtowicz J (1997) *J Power Sources* 66:1
237. Giriya TC, Sangaranarayanan MV (2006) *J Appl Electrochem* 36:531

238. Fujishima A, Masuda H, Honda K (1979) *Chem Lett* 8:1063
239. Yoshihara S, Ueno M, Nagae Y, Fujishima A (1988) *Electrochim Acta* 33:1685
240. Rosencwaig A (1975) *Anal Chem* 47:592A
241. Sunandana CS (1988) *Phys Stat Sol (a)* 105:11
242. Yoshihara S, Takahashi R, Okamoto M, Sato E, Fujishima A (1991) *Electrochim Acta* 36:1959
243. Ragoisha GA, Bondarenko AS (2003) *Solid State Phenom* 90–91:103. (Proceedings of solid state chemistry, 2002)
244. Ragoisha GA, Bondarenko AS (2004) *Surf Sci* 566–568:315
245. Ragoisha GA, Bondarenko AS (2003) *Electrochem Commun* 5:392
246. Bondarenko AS, Ragoisha GA, Osipovich NP, Streltsov EA (2005) *Electrochem Commun* 7:631
247. Ragoisha GA, Bondarenko AS (2005) *Electrochim Acta* 50:1553
248. Ragoisha GA, Bondarenko AS, Osipovich NP, Streltsov EA (2004) *J Electroanal Chem* 565:227
249. Niemantsverdriet JW (2007) Temperature-programmed techniques. In: *Spectroscopy in catalysis. An introduction*, 3rd edn. Wiley-VCH, Weinheim, p 23, Chapter 2
250. Falconer JL, Schwarz JA (1983) *Catal Rev Sci Eng* 25:141
251. Davies PW, Quinlan MA, Somorjai GA (1982) *Surf Sci* 121:290
252. Stickney JL, Rosasco SD, Schardt BC, Hubbard AT (1984) *J Phys Chem* 88:251
253. Angeli J, Bengtson A, Bogaerts A, Hoffmann V, Hodoroaba V-D, Steers E (2003) *J Anal At Spectrom* 18:670
254. Bogaerts A, Gijbels R (1998) *Spectrochim Acta B* 53:1
255. Weiss Z (2006) *Spectrochim Acta B* 61:121
256. Seo M, Fushimi K, Habazaki H, Nakayama T (2008) *Corros Sci* 50:3139
257. Broda E, Schönfeld T (1955) *Radiochemische Methoden der Mikrochemie*. In: Hecht F et al (eds) *Verwendung der Radioaktivität in der Mikrochemie*. Springer, Wien
258. Rogers LB (1950) *Anal Chem* 22:1386
259. Eichler B, Kratz JV (2000) *Radiochim Acta* 88:475
260. Kratz JV (2011) Chemistry of transactinides. In: Vértes A, Nagy S, Klencsár Z, Lovas RG, Rösch F (eds) *Handbook of nuclear chemistry*. Springer Science + Business Media B.V., Springer Dordrecht Heidelberg London New York, p 925, Chapter 20
261. Byrne JT, Rogers LB (1951) *J Electrochem Soc* 98:457
262. Hummrich H, Banik NL, Breckheimer M, Brühle W, Buda R, Feist F, Jäger E, Kratz JV, Kuczewski B, Liebe D, Niewisch L, Schädel M, Schausten B, Schimpf E, Wiehl N (2008) *Radiochim Acta* 96:73
263. Hevesy GV, Paneth F (1915) *Monatshefte* 36:45
264. Joliot F (1930) *J Chim Phys* 27:119

Chapter 3

Phenomenology and Thermodynamics of Underpotential Deposition

3.1 Phenomenology and a First Thermodynamic Approach to Underpotential Deposition

As can be found from the other chapters of this book, underpotential deposition shows a wide variety of behaviors, which involve the occurrence of several surface phases, formation of submonolayers, monolayers (ML) and eventually the formation of bilayers. Adsorption may be commensurate or incommensurate, where the ML may undergo compression, and metal adatoms may coadsorb with anions to generate new phases. To start the discussion and briefly go into the history of the development of thermodynamic models for upd, we consider a relatively “simple” system, as shown in Fig. 3.1, which corresponds to Ag deposition on Pt(111) [1]. The voltammogram of this system presents three cathodic and three anodic peaks, which correspond to ML formation/desorption(3), bilayer formation/desorption(2) and bulk deposition/oxidation(1) of Ag. The peak potentials of the complementary processes do not coincide, denoting that at the present sweep rate a quasi equilibrium state has still not been reached. For the discussion below, we choose the anodic peaks, that we will denote with E_1 , E_2 and E_3 (see Fig. 3.1). At the sight of the features of this voltammogram, and although the abscissa axis *gives a measure for the electrochemical potential of electrons at the working electrode*, it may be appealing to use the position of the peaks found for this system as a measure for the stability of the different upd ad-phases being formed. In this spirit, Kolb et al. [2–4] introduced in the 1970s the concept of underpotential shift, ΔE^{upd} .

This quantity was defined as the difference in the potential of the desorption peak for a layer of a metal M adsorbed on a foreign substrate S and the potential of the peak corresponding to the dissolution of the pure metal M. In the present case, $\Delta E^{\text{upd}} = E_3 - E_1$, as marked in the red segment in Fig. 3.1.

At the time Kolb et al. developed their modeling of upd, single crystal surfaces were not available for performing electrochemical experiments, so that all the data employed by these authors were restricted to polycrystalline surfaces. On the basis

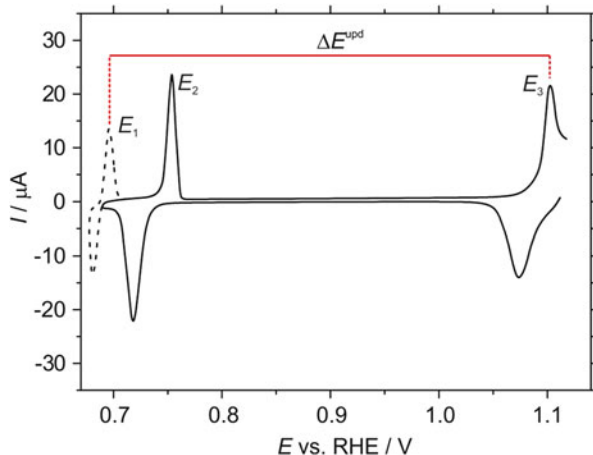


Fig. 3.1 Underpotential deposition of Ag on a Pt(111). (Taken from Ref. [1]). The peak labelled with E_1 corresponds to the oxidation of bulk Ag deposited on Pt(111). The peaks labelled with E_2 and E_3 correspond to the oxidation of underpotential deposits (Reprinted with permission from Ref. [1])

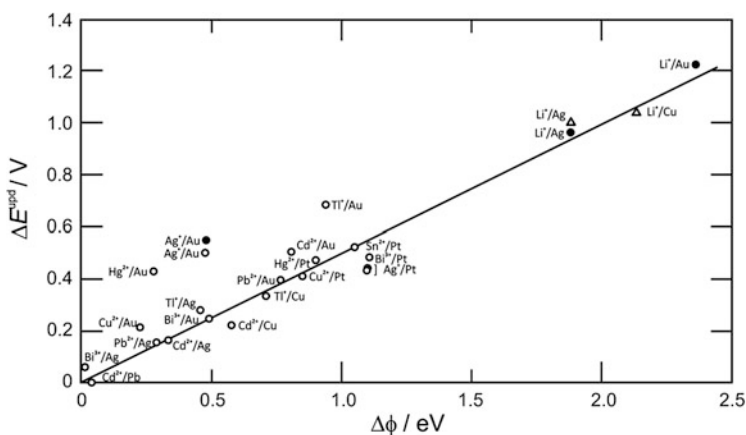
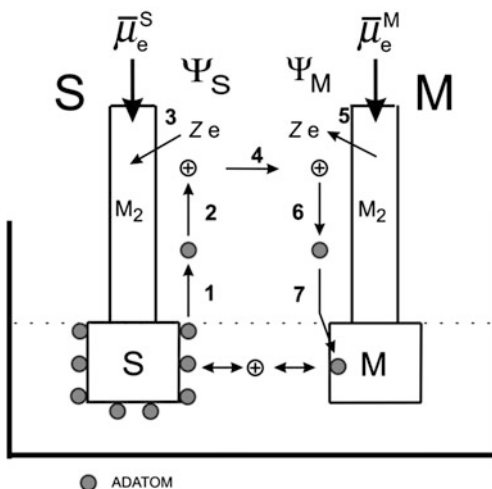


Fig. 3.2 Underpotential shift ΔE^{upd} between bulk and monolayer stripping peak as a function of the difference in work functions of substrate and adatom materials, $\Delta\phi$. The respective ions are indicated in the Figure. (O) aqueous solution; (●) acetonitrile; (Δ) propylene carbonate (Reprinted with permission from Ref. [3])

of experimental information, they found the correlation between underpotential shift and work functions difference between substrate (S) and adsorbate (M), $\Delta\phi = \phi_S - \phi_M$ shown in Fig. 3.2, where ϕ_i denotes the work function of metal i .

It must be recognized that the data in Fig. 3.2 strongly suggest that underpotential shift and work function are correlated. We now turn to analyze the arguments given to understand the present correlation. First, we explain why it is reasonable to consider the underpotential shift as a measure for the difference of

Fig. 3.3 Thermodynamic cycle employed to obtain the relationship between underpotential shift and other thermodynamic properties of the substrate/adsorbate system. S is the substrate on which underpotential deposition of metal M occurs. The electrode labeled with capital M, used here as a reference electrode, is made of the bulk metal M. A piece of the same metal M_2 is attached to both electrodes to make contact with a measuring device



free binding energies of the S/M and the bulk M system. This explanation is given in the article of Kolb et al. [2] but we give here a discussion in terms of the different quantities shown in Fig. 3.3 to clarify some points. There, we show a working electrode made of metal S covered by a monolayer of M, whose potential is measured under equilibrium conditions, with respect to a reference electrode made of the bulk metal M, which is the same as that being deposited under up conditions on S. Thus, the potential difference measured between the S and M electrodes $E_S - E_M = \Delta E^{S-M}$ can be identified with the underpotential shift defined above.¹ The solution contains the cations of the metal M being deposited at the activity $a_{M^{z+}}$, yielding the electrochemical potential $\tilde{\mu}_{M^{z+}}^{\text{aq}}$. The chemical potential μ_M^S of the M atoms deposited on S is:

$$\mu_M^S = \tilde{\mu}_{M^{z+}}^S + z\tilde{\mu}_e^S \quad (3.1)$$

where $\tilde{\mu}_{M^{z+}}^S$ represents the electrochemical potential of the ion cores of M adsorbed on S and $\tilde{\mu}_e^S$ is the electrochemical potential of the electrons in the substrate S. z denote the valence of the cation. On their side, the chemical potential of the bulk M atoms, μ_M^M , is given by:

$$\mu_M^M = \tilde{\mu}_{M^{z+}}^M + z\tilde{\mu}_e^M \quad (3.2)$$

where $\tilde{\mu}_{M^{z+}}^M$ is the electrochemical potential of the M cations in bulk M and $\tilde{\mu}_e^M$ is the electrochemical potential of the electrons in the substrate M. Since at equilibrium

¹ Although it could be argued that ΔE^{upd} is not identical with ΔE^{S-M} since ΔE^{upd} is affected by a number of experimental uncertainties like the fact that the exact position of the oxidation peak of bulk M will depend on the amount of M deposited, etc., we will assume here that $\Delta E^{S-M} \approx \Delta E^{\text{upd}}$.

the core ions are free to move from the electrodes into the solution and viceversa, we have the equilibrium condition:

$$\tilde{\mu}_{M^{z+}}^S = \tilde{\mu}_{M^{z+}(\text{aq})} = \tilde{\mu}_{M^{z+}}^M \quad (3.3)$$

Subtracting Eq. (3.2) from Eq. (3.1) and using Eq. (3.3) we get:

$$\mu_M^S - \mu_M^M = z(\tilde{\mu}_e^S - \tilde{\mu}_e^M) \quad (3.4)$$

Or equivalently:

$$\Delta E^{S-M} = -\frac{1}{ze_0}(\mu_M^S - \mu_M^M) \quad (3.5)$$

where we have used the fact that the experimental measurement of an electric potential difference corresponds to the measurement of the difference of electrochemical potentials of electrons between working and reference electrode ($\Delta E^{S-M} = -(\tilde{\mu}_e^S - \tilde{\mu}_e^M)/e_0$). In other words, the measurement of equilibrium potentials for a upd ML with respect to a reference electrode made of a bulk piece of the same metal being deposited, should deliver the difference between the chemical potential of the M atoms in the upd deposit with respect to their chemical potential in the bulk material. It is worth considering whether Eq. (3.5), formulated by Kolb et al. [2], has any restriction for its validity, besides the assumption of equilibrium. In this respect, it must be pointed out that Eqs. (3.1) and (3.2) involve the following equilibria:



where $M_{(\text{aq})}^{z+}$ denote the solvated cations in solution and M_{ads} and $M_{(\text{bulk})}$ denote the upd and bulk metal deposits respectively. *In the case where other species coadsorb (anions), they will participate in reaction (3.6) and the equilibrium potential will not be straightforwardly related to a chemical potential difference as such in Eq. (3.5).* Thus, an important approximation made in Eq. (3.6) was to assume that z electrons flowed to the S electrode for each cation being deposited on its surface. We will see below that this is not always the case, since the simple way in which we are writing this equation involves neglecting other phenomena taking place at the substrate/solution interphase upon upd.

Equation (3.5) can be derived through a thermodynamic cycle as described in Reference [5] and shown in the cycle drawn in Fig. 3.3. As stated above, the ion cores deposited on S are in equilibrium with both, the ions dissolved in solution and the ion cores constituting the M electrode. Thus, the free energy change involved in the transfer process of one of the ion cores adsorbed on S to the electrode made of

bulk M will be zero, that is, $\Delta G_{\text{tr}, M^{z+}} = 0$. This transfer may be performed alternatively by the way marked by the arrows numerated from 1 to 7, which correspond to: (1) Desorption of an M atom from the S surface, (2) Ionization of the atom M to get the M^{z+} cation and z electrons, (3) Reinsertion of the z electrons resulting in step 2 into the left electrode, (4) Transfer of the core ions from a place close² to left electrode to a place close to the right electrode, (5) Extraction of z electrons from the right electrode in order to achieve the (6) Neutralization of the M^{z+} cation, (7) Incorporation of the neutral M atom into the lattice of the M bulk electrode. Along this cycle, it comes out that the free energy changes corresponding to the following steps cancel each other: Steps 2 with 6, Steps 3 with 5. Thus, the total free energy change for the transfer of a M^{z+} core from the left to the right electrode will be:

$$\Delta G_{\text{tr}, M^{z+}} = \Delta G_1 + \Delta G_4 + \Delta G_7 = 0 \quad (3.8)$$

where we have set this equation equal to zero on the basis of the previous discussion. Let us discuss now the identity of the different terms in Eq. (3.8). ΔG_1 is the free energy change required to take a metal atom away from the electrode. This is minus the chemical potential μ_M^S of the M atoms at the substrate/adsorbate system, so $\Delta G_1 = -\mu_M^S$. Similarly, $\Delta G_7 = \mu_M^M$. The term ΔG_4 is an electrostatic work term, since it involves the transfer of an ion core from the Volta potential Ψ_S to the Volta potential Ψ_M . Thus, $\Delta G_4 = ze_0(\Psi_M - \Psi_S)$. Substitution of these contributions in Eq. (3.8) and solving upon $(\Psi_S - \Psi_M)$ yields:

$$(\Psi_S - \Psi_M) = -\frac{1}{ze_0} (\mu_M^S - \mu_M^M) \quad (3.9)$$

which is equivalent to Eq. (3.5). Of course, the latter derivation is equivalent to that of Kolb et al., but we introduced it here since it emphasizes on the physical picture that can be used to perform calculations for the present system.

It is remarkable that although Eqs. (3.5) and (3.9) involve the chemical potentials of the adatoms in the different systems, the correlation observed in Fig. 3.2 involves the work function, which is an electronic property of the materials. The explanation given by Kolb et al. for the linear correlation of Fig. 3.2 was based on two ideas: the first is that a polar bond occurs at upd deposits; the second is the fact that Pauling's electronegativity χ_P , which is a measure for the ionicity of a bond, is linearly correlated with the work function Φ as:

$$\chi_P = 0.5\Phi - \text{const} \quad (3.10)$$

² As "close" we mean at a distance close enough to the solid to be influenced by ambient electric fields in the vacuum, but far from the surface on the atomic scale.

The latter would explain the slope close to 0.5 observed in Fig. 3.2. Later on, Trasatti [6] developed a model assuming an ionic bond of the adatom to the surface, where a linear correlation was also predicted between ΔE^{upd} and $\Delta\Phi$, but with slope 1. Arguing on the basis that the picture of the ionic bond is valid for low coverages ($\theta \rightarrow 0$), Trasatti plotted the underpotential shift in this limit and also obtained a reasonably good linear ΔE^{upd} versus $\Delta\Phi$ relationship.

3.2 Introducing the Influence of Solvent in Underpotential Deposition Modeling

Sudha and Sangaranarayanan [7] have modeled upd within a thermodynamic approach, where the role of the solvent was emphasized. Figure 3.4 shows their modeling within the following scheme: (i) motion of the solvated ions from the bulk of the solution to the reaction zone, getting rid of their solvation sheath, (ii) electron transfer from the substrate to the metal ions leading to bond formation with the substrate. This process occurs after displacing adsorbed solvent molecules from the substrate.

Within the present approach, the underpotential shift was written as:

$$\Delta E^{\text{S-M}} = \theta \left(\frac{\Phi_{\text{S}}}{CN_{\text{S}}} - \frac{\Phi_{\text{M}}}{CN_{\text{M}}} \right) + \frac{(1-2\theta)\Delta G_{\text{S-H}_2\text{O}}}{z_{\text{ad}}F} + \frac{(1-2\theta)\Delta H_{\text{S-M}}}{z_{\text{ad}}FCN_{\text{S}}} + \frac{\theta\Delta G_{\text{M-H}_2\text{O}}}{z_{\text{ad}}F} + \frac{\theta\Delta H_{\text{M-M}}}{z_{\text{ad}}FCN_{\text{M}}} \quad (3.11)$$

where the first term contains the work function of the substrate (Φ_{S}) and the adsorbate (Φ_{M}), and the corresponding lattice coordination numbers CN_{S} and CN_{M} ; the

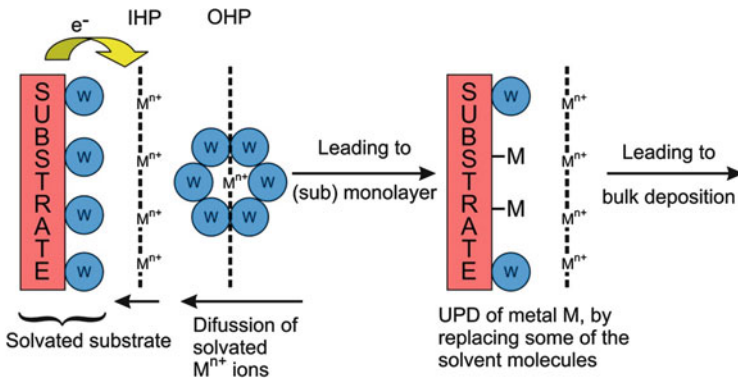


Fig. 3.4 Schematic representation of processes leading to upd of a metal M on a substrate S. IHP and OHP indicates respectively, the inner and outer Helmholtz plane. The metal ions, M^{n+} are surrounded by the solvent molecules 'w' (Reprinted with permission from Ref. [7])

second term involves the Gibbs free energy change for the substrate–water bond formation ΔG_{S-H_2O} ; the third term contains the enthalpy change of substrate–metal bond formation ΔH_{S-M} ; the fourth term is analogous to the second one, but for the solvation of the adsorbate, with the corresponding Gibbs free energy change for the adsorbate water bond formation ΔG_{M-H_2O} ; the fifth term is the analogous of the third one, but containing the enthalpy change of the M–M bond formation ΔH_{M-M} . The factor θ denotes the surface coverage of the upd metal adatoms on the substrate lattice, and it appears due to the replacement of solvent molecules by the depositing species. z_{ad} is the charge on the adsorbate. The authors estimated the underpotential shift using this equation for several upd systems, finding a good overall agreement with experimental results for polycrystalline systems. Estimations for single crystal surfaces were not made. These studies were later extended to upd in acetonitrile (ACN) and propylene carbonate [8].

3.3 Underpotential Deposition on Single Crystal Surfaces

The use of single crystal surfaces in the study of upd introduced a new element in the discussion on the modeling of this phenomenon. Schultze and Dickertmann [9] studied the formation of metallic upd adsorption layers of different metals on (111), (100) and (110) planes of gold single crystal electrodes, finding that the correlation of Kolb et al. is qualitatively valid for polycrystalline surfaces, but showed that the situation on single crystal planes is more complex. Their results are shown in Fig. 3.5. Overall, it is found that the more open face (110) yields the most stable adsorbates, while upd on the (111) yields the less stable structures, but a clearcut correlation between peak potential and work function difference can be hardly found. There are several reasons for the lack of a definite trend:

1. Upd generally shows on single crystal surfaces several voltammetric components. These are due to the occurrence of different surface structures of 2D phases. This fact was shown above in Fig. 3.1 for ML and bilayer deposition, but the situation may be more complex, even in the case of the formation of a simple monolayer.
2. A good example of the complexity that an upd system may exhibit can be found in the study of Mrozek et al. [10] concerning upd of Ag on Au(111). Since this system exhibits a negligible misfit due to the similar sizes of Au and Ag, it could be expected a priori the formation of relatively simple surface structures. However, the voltammetric results for this system already show that this will not be the case, as illustrated in Fig. 3.6, where several features are evident in the current-potential profile.

In fact, low energy electron diffraction (LEED) experiments following electrode emersion at different potentials, show an amazingly rich variety of surface structures, as shown in Table 3.1. It must be emphasized that the base electrolyte

Fig. 3.5 Peak potential (referred to the M/M^{z+} reversible deposition potential) for the desorption of upd M species from different single crystal Au surfaces. Open symbols indicate the most anodic, closed symbol the most cathodic peak. The crosses denote data from Kolb for polycrystalline surfaces (Reprinted with permission from Ref. [9])

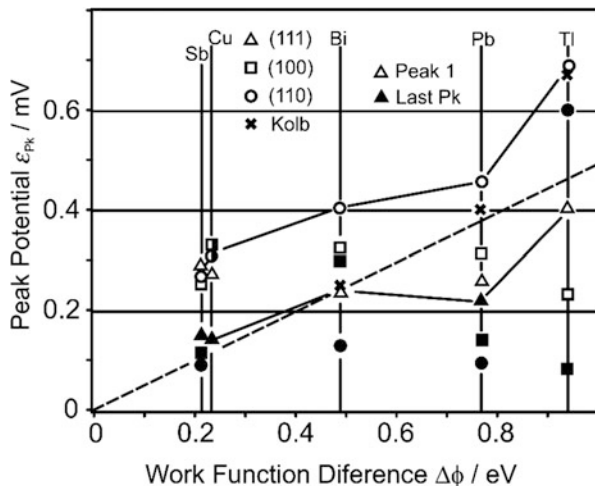
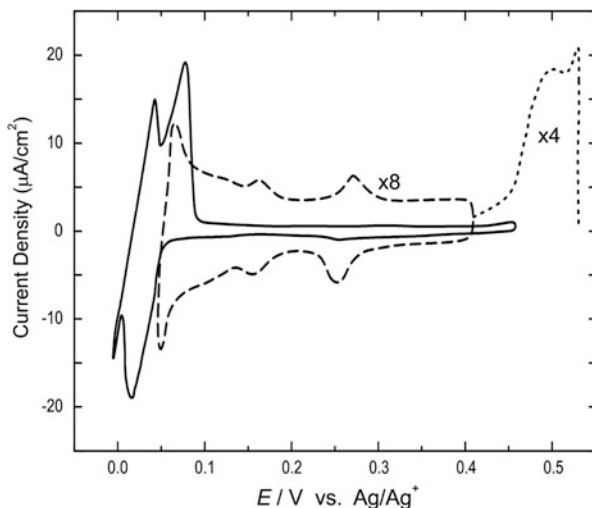


Fig. 3.6 Cyclic voltammograms for Ag upd on a Au(111) electrode in 0.1 mM HF and 0.5 mM AgF solution at 2 mV s^{-1} . Cyclic voltammograms in chosen potential ranges are shown in the same plot with different line types (Reprinted with permission from Ref. [10])



employed in these experiments was a 0.1 mM HF solution, in an attempt to minimize specific adsorption effects.

The linear correlation between underpotential shift and work function found in Fig. 3.2 was justified in terms of Eq. (3.10). However, the work functions of the single crystal surfaces of a metal spread frequently over a few hundreds of meV, making the choice of the proper value uncertain. Furthermore, Eqs. (3.5) and (3.9), which could give thermodynamic support to the observed $\Delta E^{S-M} - \Delta \Phi$ correlation, contain a term which depends on the nature of the single crystal face, μ_M^S , but also another term that is a bulk contribution, μ_M^M . To make this point clear, let us leave entropic contributions aside and think only in energetic terms. A good estimation of

Table 3.1 Surface structure as determined by LEED and electrochemically determined coverages for Ag upd on a Au(111) electrode after emersion at different potentials. Reprinted with permission from Ref. [10]

E/V vs. Ag/Ag ⁺	0.63, 0.59	0.53	0.48	0.41	0.33	0.31	0.21, 0.12, 0.09	>0.06
Coulometric coverage	–	0.34	0.61	0.69	0.75	0.76	0.82, 0.91, 0.09	>0.99
LEED structure	Non-reconstructed (1 × 1)	(3 × 3)	(5 × 5)	$\begin{bmatrix} 1 & 0 \\ -2 & 5 \end{bmatrix}$	$\begin{bmatrix} 1 & 0 \\ -2 & 4 \end{bmatrix}$	$\begin{bmatrix} 1 & 0 \\ -2 & 5 \end{bmatrix}$	$\begin{bmatrix} 1 & 0 \\ -3 & 6 \end{bmatrix}$	(1 × 1)

μ_M^S could be done by calculating from first principles the binding energy of M to the surface of S. This quantity will be certainly different if we consider, for example, an *fcc*(111) or an *fcc*(110) surface. However, the other term, μ_M^M , is a bulk term, that could be estimated from the cohesive energy of the bulk material, containing no reference to any single crystal surface. Thus, a difference of chemical potentials does not straightforwardly lead to a difference of work functions.

3.4 Nernstian-like Formalisms: Underpotential Deposition in the Framework of the Electrooption Valency

The reduction potential of a half-cell represented by Eq. (3.7), where $M_{(aq)}^{z+}$ cations are deposited on bulk M follows the venerable Nernst equation:

$$\begin{aligned} E_{M_{(bulk)}/M_{(aq)}^{z+}} &= E_{M_{(bulk)}/M_{(aq)}^{z+}}^0 + \frac{RT}{zF} \ln \left(\frac{a_{M_{(aq)}^{z+}}}{a_{M_{(bulk)}}} \right) \\ &= E_{M_{(bulk)}/M_{(aq)}^{z+}}^0 + \frac{2.303RT}{zF} \log \left(\frac{a_{M_{(aq)}^{z+}}}{a_{M_{(bulk)}}} \right) \end{aligned} \quad (3.12)$$

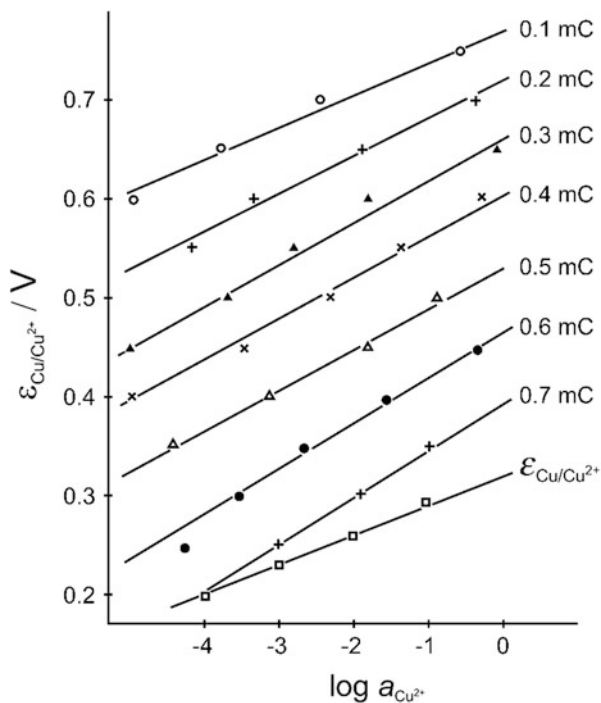
where $E_{M_{(bulk)}/M_{(aq)}^{z+}}^0$ is the standard half-cell reduction potential and the activity $a_{M_{(bulk)}}$ of metal in the solid phase is taken as unity for pure metals. The practicality of this equation suggests to propose a similar equation for the half-cell reaction (3.6):

$$\begin{aligned} E_{(M_0/S)/M_{(aq)}^{z+}} &= E_{(M_0/S)/M_{(aq)}^{z+}}^0 + \frac{RT}{zF} \ln \left(\frac{a_{M_{(aq)}^{z+}}}{a(\Gamma_M)} \right) \\ &= E_{(M_0/S)/M_{(aq)}^{z+}}^0 + \frac{2.303RT}{zF} \log \left(\frac{a_{M_{(aq)}^{z+}}}{a(\Gamma_M)} \right) \end{aligned} \quad (3.13)$$

where now $a(\Gamma_M)$ is an activity that depends on the surface excess Γ_M , $E_{(M_0/S)/M_{(aq)}^{z+}}$ is the potential at which this excess is measured and $E_{(M_0/S)/M_{(aq)}^{z+}}^0$ is the standard submonolayer potential.

It is obvious from Eq. (3.12) that $\partial E / \partial \log(a_{M_{(aq)}^{z+}}) = 2.303RT / (zF)$. Similarly, from Eq. (3.13) we have that $(\partial E / \partial \log a_{M_{(aq)}^{z+}})_{\Gamma_M} = 2.303RT / (zF)$, provided the activity $a(\Gamma_M)$ is only a function of Γ_M . Let us contrast this expectation with experiment. Figure 3.7 shows data from Schultze [14] for the electrodeposition of Cu on bulk Cu and on Pt electrodes, where the electrode potential has been plotted as a function of the concentration of Cu^{2+} for a constant charge. These constant

Fig. 3.7 Potential as a function of Cu^{2+} concentration for different coverage degrees of Cu adsorbed on a polycrystalline Pt electrode. $\mathcal{E}_{\text{Cu}/\text{Cu}^{2+}}$ denotes the equilibrium potential of a bulk Cu electrode. The number close to the different *straight lines* denote the charges obtained under galvanostatic experimental conditions (Reprinted with permission from Ref. [14])



charge conditions are supposed to represent a constant coverage, although this implies some assumptions, as discussed below.

It is remarkable that while the slope of the lines for deposition on the bulk Cu electrode has the expected $2.303RT/2F$ slope ($z=2$) in Eq. (3.13), the straight lines obtained for Cu deposition on Pt are considerably steeper. This means in the present formal scheme, a z value lower than 2. The reason for this observation is that the reaction that we wrote above in Eq. (3.6) hides a considerable complexity, far beyond the simple way in which we have written it there. The great difference between Eqs. (3.6) and (3.7) is that the latter has as a product a bulk material, while the former results in adsorbed species occurring at the electrochemical interface, which contains itself a number of complex features: an electrical double layer, a solvent, and, in some cases, other ions that may be participating in the deposition reaction. **These elements, not explicitly accounted for in Eq. (3.6), deliver a contribution to the free energy change associated with the formation of the up deposit.** Let us shortly discuss the consequences of these new ingredients for the evaluation of coverage degree of adsorbed species from the charge flowing during electrochemical experiments.

3.4.1 Electrical Double Layer Effects

In experiments yielding results like those shown in Fig. 3.7, the Cu coverage degree is evaluated from the galvanostatic charge, where the double layer contribution is subtracted using the double layer charging of a naked Pt electrode [14]. The latter involves two assumptions:

1. That the capacitance of the double layer is the same for the Cu-covered Pt electrode as it is for the Cu-free Pt electrode.
2. That the potential of zero charge is the same in both cases.

The latter is probably the more questionable assumption when the potential of zero charge of the electrodes are different. In the case of Pt and Cu the potential of zero charge (PZC) of single crystal surfaces are $PZC_{Pt(111)} \approx 1.1 \text{ V}$ [11] and $PZC_{Cu(111)} \approx -0.02 \text{ V}$ [12] vs. SHE. If we assume that the PZC of the Cu-covered Pt(111) surface is close to $PZC_{Cu(111)}$, double layer charging upon adsorbate formation at a constant potential would involve a charging of the electrode of the order $Q \approx -C_{dl}(PZC_{Cu(111)} - PZC_{Pt(111)})$. Using $C_{dl} \approx 30 \mu\text{F cm}^{-2}$ from Ref. [12], this yields $Q \approx 30 \mu\text{C cm}^{-2}$, a meaningful quantity.

3.4.2 Solvent Effects

In upd, solvent effects may be twofold, as already advanced by the model discussed in Sect. 3.2. On one side, the surface of the substrate at which the upd layer is formed may be solvated before adsorption, so that a given number of water molecules must be displaced. On the other side, the metal adatom being formed may be solvated. This effect could be particularly important in the case where the adatoms bear a partial charge. While solvent effects do not influence directly the evaluation of the coverage via the charge discussed above, solvation may influence the charge status of the adsorbate, as will be discussed in Chap. 5.

A natural attempt to generalize Eq. (3.13) would be just to say that z in this equation should be replaced by some effective valency, say γ_v , yielding [13]:

$$E_{(M_\theta/S)/M_{(aq)}^{z+}}(\Gamma_M) = E_{(M_\theta/S)/M_{(aq)}^{z+}}^0 + \frac{RT}{\gamma_v F} \ln \left(\frac{a_{M_{(aq)}^{z+}}}{a(\Gamma_M)} \right) \quad (3.14)$$

where we have written $E_{(M_\theta/S)/M_{(aq)}^{z+}}(\Gamma_M)$ to emphasize that this quantity denotes the equilibrium potential at which the surface excess Γ_M is obtained.

From the previous equation, we see that $\gamma_v = \left[\partial \ln \left(a_{M_{(aq)}^{z+}} \right) / \partial E \right]_{\Gamma_M} RT/F$, provided the metal activity is only a function of adsorbate excess. This quantity determines the shift of the (sub)monolayer equilibrium potential with change in

solution composition at constant coverage and is denominated electrosorption valency.

Schultze and Vetter [14–18] have developed a comprehensive theory of electrosorption processes including adsorption of neutral molecules without charge transfer, as well as adsorption of ions with complete discharge that take into account the two previous features. This theory is in principle also suited to be applied to the study of upd phenomena, and we discuss it shortly here. Szabó [19] adapted the formulation of Refs. [14–17] to the discussion of the upd phenomenon, and we adhere to his notation. Within this theory, the concept of electrosorption valency γ_v , introduced intuitively above, plays a fundamental role. This quantity is defined, in excess of supporting electrolyte as:

$$\left(\frac{\partial \mu_{M_{(aq)}^{z+}}}{\partial E}\right)_{\Gamma_M} = -\left(\frac{\partial q_m}{\partial \Gamma_M}\right)_E =: \gamma_v F \quad (3.15)$$

where $\mu_{M_{(aq)}^{z+}}$ is the chemical potential of the $M_{(aq)}^{z+}$ cations in solution, E is the electrode potential, q_m is the electrode charge and Γ_M is the surface concentration of specifically adsorbed metal. The excess of supporting electrolyte is necessary to warranty that all changes in the electrode potential are translated into changes of the potential difference across the compact double layer. We will assume this condition to be valid all along the present discussion. For a more general discussion without this assumption, we recommend reading of the original articles [14–17].

The definition given in on the l.h.s. of Eq. (3.15) can be rationalized in terms of writing Eq. (3.14) as:

$$E_{(M_0/S)/M_{(aq)}^{z+}}(\Gamma_M) = E_{(M_0/S)/M_{(aq)}^{z+}}^0 + \left[\frac{\mu_{M_{(aq)}^{z+}} - \mu_{M_{(aq)}^{z+}}^0}{\gamma_v F a(\Gamma_M)} \right] \quad (3.16)$$

And taking the partial derivative of the r.h.s. of this equation with respect to E , we get:

$$\left(\frac{\partial \mu_{M_{(aq)}^{z+}}}{\partial E_{(M_0/S)/M_{(aq)}^{z+}}(\Gamma_M)}\right)_{a(\Gamma_M)} = \gamma_v F \quad (3.17)$$

Note that in Eq. (3.17) the constant condition is $a(\Gamma_M)$, while in (3.15) it is Γ_M .

To understand the definition of the second equality in Eq. (3.15), let us consider the deposition of n moles of metal ions, requiring a charge Q_m . If charging of the double layer with the capacitance C_D is accounted by a term $C_D \Delta E$, we have the balance:

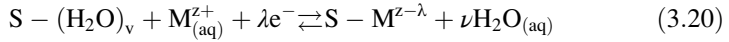
$$Q_m = -zFn + C_D \Delta E \quad (3.18)$$

And taking the derivative of the l.h.s. with respect to n :

$$\left(\frac{\partial Q_m}{\partial n} \right)_{\Delta E} = -zF \quad (3.19)$$

This equation is equivalent to the second equality of Eq. (3.15). Thus, γ_v in Eq. (3.15) controls potential dependence and charge flow during upd in very much the same way as z does in electrodeposition of bulk metals.

Going back to the modeling of Refs. [14–17], upd was described in this framework through the following equation:



where ν is the number of molecules displaced from the substrate to allow the adsorption of M.

According to Eq. (3.20), the charge transfer coefficient is the difference between the actual charge of the deposited metal $z_{\text{ads}} = z - \lambda$ and the ionic charge of the adsorbing ions z , that is, $\lambda = z - z_{\text{ads}}$. Thus, $\lambda = 0$ means no charge transfer, while $\lambda = z$ means complete charge neutralization upon adsorption. Figure 3.8 shows a scheme of the present modeling. In this Figure and for the sake of simplicity, we have neglected the potential difference between the outer Helmholtz plane and the electrolyte, assuming excess of supporting electrolyte. The profile of the electrostatic potential φ in the double layer is qualitatively shown at the bottom of this Figure. Between the substrate S and the outer Helmholtz plane there is the potential difference $\varphi_S - \varphi_e$. Upon electroadsorption, the adatoms get into the compact double layer and stay at the potential φ_{ads} . That is, the adsorbate only experiences a fraction of the potential difference $\varphi_S - \varphi_e$. The position of the adsorbed ions in the Helmholtz layer is thus described by a geometric factor g , which is defined as:

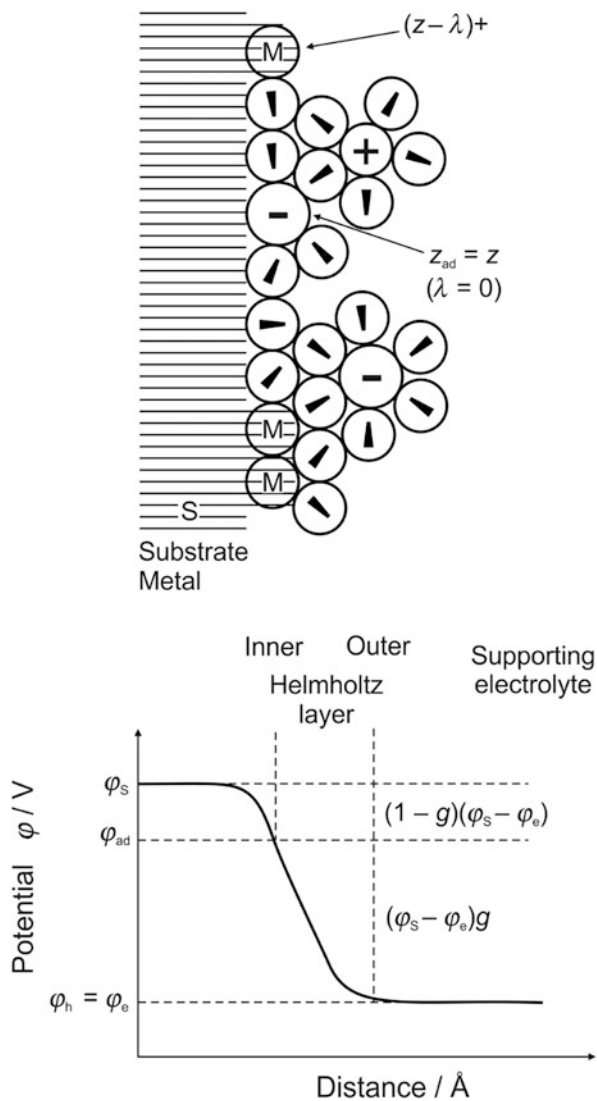
$$g = (\varphi_{\text{ads}} - \varphi_e) / (\varphi_S - \varphi_e) \quad (3.21)$$

In this way, $g = 1$ or $g = 0$ represent limiting cases where the adsorbate stays in close contact with the metal or it is located at the outer Helmholtz plane respectively.

Vetter and Schultze [15] have derived a relationship between γ_v , λ , g and dipole terms, which is given by:

$$\gamma_v = zg - \lambda(1 - g) + \kappa_{\text{ad}} - \nu\kappa_w - \int_{E_N}^E \left(\frac{\partial C_D}{\partial \Gamma_M} \right) dE \quad (3.22)$$

Fig. 3.8 Scheme of the modelling developed in Refs. [14–17] to describe electrosorption processes with partial charge transfer λ . Here, the metal M is assumed to be adsorbed at the inner Helmholtz plane with adsorption charge $(z - \lambda)$, while the anion keeps its full charge z ($\lambda = 0$) (Adapted with permission from Ref. [19])



where κ_{ad} accounts for energetic contributions from the surface dipole arising due to the formation of the adsorbate, κ_w accounts for the dipole contribution of water molecules initially adsorbed at the substrate and E_N denotes the potential of zero charge. In the case of upd, where the number of water molecules displaced from the substrate re-adsorbs on the adsorbate, $\nu = 0$.

A few comments are pertinent concerning Eqs. (3.15) and (3.22). While the derivation of Eq. (3.15) uses mainly thermodynamic calculations, Eq. (3.22) can only be derived in terms of a model, like that presented in Fig. 3.8, where non thermodynamic assumptions are made. Then, the experimental results obtained for

γ_v can be interpreted in term of the physical picture given there. From it, and if some of the terms involved in Eq. (3.15) can be calculated, inferences can be made over the remaining ones. The physics involved in this picture is relatively straightforward. On one side, we see that a deeper penetration of the adsorbate in the electrostatic potential region of the substrate ($g \rightarrow 1$) will make γ_v closer to z . On the other side, the other terms may also play a role. Vetter and Schultze have proposed for the dipole term of the adsorbed substance, κ_{ad} , the following equation:

$$\kappa_i = \pm m_i / e_0 l_i \quad (3.23)$$

where m_i is the dipole moment of the adsorbed species and $l_i = (\varphi_s - \varphi_e) / (\partial\varphi / \partial x)$ is a length of the order of magnitude of the thickness of the compact double layer. Thus, κ_i represents the ratio between two dipole lengths: that of the adsorbed species and that of the compact double layer. In the case of ionic adsorbates, κ_{ad} and κ_w are expected to be small as compared with the other charge terms [18] and at the potential of zero charge Eq. (3.22) reduces to:

$$\gamma_N \approx zg - \lambda(1 - g) \quad (3.24)$$

Within this approximation, Schultze and Koppitz [18] performed an extensive analysis of γ_v for several anionic and cationic systems.

3.4.3 Determination of the Electrosorption Valency

Equation (3.15) can be applied in various ways, since q_m and Γ_M can be determined by measurement of the double layer capacity, by measurement of the surface tension, or by coulometry and chemical analysis. We discuss here briefly the different possibilities, emphasizing on those relevant for upd.

3.4.3.1 From Capacity and Surface Tension

Measurement of the capacity or surface tension yields q_m and Γ_M as a function of the potential difference. Then q_m can be plotted versus Γ_M at constant potential difference. The slope of the curves obtained yields γ_v according to Eq. (3.15). While this method has been used to study the adsorption of different molecules and anions on mercury on the basis of electrocapillarity measurements, it cannot be used to investigate upd.

3.4.3.2 From Coverage and Charge Flow

As implicit in the equality on the right side of Eq. (3.15), γ_v may be obtained by measuring the surface concentration Γ_M of the upd metal being adsorbed, as well as the adsorption charge involved at a constant potential E . The twin-electrode thin-layer and flow-through thin layer methods developed by Schmidt and Siegenthaler [20–24], the rotating ring-disk electrode (RRDE) measurements of Bruckenstein and coworkers [25–27] and the measurements of Schultze discussed above may be mentioned as examples of this methodology. In the first type of these methods, which are described in Chap. 2,³ charge changes at the ideally polarizable electrode (called indicator electrode), where upd is achieved, are correlated with production or depletion of the electroactive species $M_{(aq)}^{z+}$ at electrodes where the formation/depletion of these species is faradaic. That is, charges are measured at the substrate electrode where upd occurs, and the same is done at other electrodes diffusionally coupled to the former, where the reaction has a precise stoichiometry. Correlation between the two charge measurements allow the determination of γ_v . For example, this method has been applied to the systems Ag(100)/Pb²⁺ and Ag(100)/Tl⁺ [24] with the finding that in both systems $\gamma_v = z$.

Concerning the application of the RRDE technique⁴ to determine γ_v , Swathirajan and Bruckenstein [27] defined a dynamic electroadsorption valency:

$$\gamma_d = -\frac{1}{F} \left(\frac{\partial q_m}{\partial \Gamma_M} \right)_E = -\frac{1}{F} \frac{(\partial q_m / \partial t)_E}{(\partial \Gamma_M / \partial t)_E} \quad (3.25)$$

where $-(\partial q_m / \partial t)_E$ is given by the instantaneous disc transient current, that is made of the substrate metal S, where the upd deposit is built. $(\partial \Gamma_M / \partial t)_E$ is obtained from the ring response. The latter electrode is made of the metal M, which is the subject of the upd study, or eventually is plated with several layers of M. The thin layer method addressed above is best suited for equilibrium studies at high solution concentrations of upd species, but not for dynamic studies, due to the high impedance of the thin layer cell. The RRDE can be employed to obtain both equilibrium and dynamic properties but the concentration of upd species in solution must be low.

3.4.3.3 From Coverage Measurements at Difference Concentration of Active Electrolyte

From Eq. (3.15), we see that $\left(\partial \log a_{M_{(aq)}^{z+}} / \partial E \right)_{\Gamma_M} RT/F = \gamma_v$. If activity coefficients are constant, the latter equation may be substituted by $\left(\partial \log c_{M_{(aq)}^{z+}} / \partial E \right)_{\Gamma_M} RT/F = \gamma_v F$,

³ See Fig. 2.10 and discussion on it.

⁴ See discussion in Chap. 2, Sect. 2.7.

where c is the concentration of M cations in solution. This corresponds to the slope of the straight lines shown in Fig. 3.7. Alternatively, the same type of plots can be made with activities provided activity coefficients are known.

3.4.3.4 From Kinetic Measurements

Although γ_v is a thermodynamic quantity, information on it can be obtained through modeling of electron transfer. With this purpose, Schultze [14] wrote the adsorption and desorption currents in an upd system as:

$$i_{\text{ad}} = -\gamma_v z F k_{\text{ad}} c_{\text{M}^{z+}(\text{aq})} \exp\left(-\frac{\beta_c B \theta}{RT}\right) \exp\left(-\frac{(1-\alpha_c)f(E)}{RT}\right) \quad (3.26)$$

$$i_{\text{des}} = \gamma_v z F k_{\text{des}} \exp\left(\frac{\alpha_c B \theta}{RT}\right) \exp\left(\frac{\alpha_c f(E)}{RT}\right) \quad (3.27)$$

where $f(E) = n_{\text{ad}} z F E - \frac{1}{2} \frac{dC_D}{d\Gamma_{\text{M}^{z+}(\text{aq})}} (E - E_R)^2$, α_c and $(1 - \alpha_c)$ are the electrochemical transfer factors, and α_c and β_c the chemical transfer factors, k_{ad} and k_{des} denote the rate constants for the adsorption and desorption respectively, and E_R is a reference potential. From Eqs. (3.26) and (3.27) it comes out that:

$$\left(\frac{\partial \log i_{\text{ad}}}{\partial E}\right)_{\theta, c} = -\frac{(1-\alpha_c)\gamma_v z F}{2.3RT} \quad (3.28)$$

$$\left(\frac{\partial \log i_{\text{des}}}{\partial E}\right)_{\theta, c} = \frac{\alpha_c \gamma_v z F}{2.3RT} \quad (3.29)$$

Subtracting Eq. (3.28) from Eq. (3.29) yields:

$$\left(\frac{\partial \log i_{\text{des}}}{\partial E}\right)_{\theta, c} - \left(\frac{\partial \log i_{\text{ad}}}{\partial E}\right)_{\theta, c} = \frac{\gamma_v z F}{2.3RT} \quad (3.30)$$

which allows the calculation of γ_v from the experimentally determined (reciprocal) Tafel-like slopes. It must be emphasized that the Schultze [14] did not perform steady-state measurements but galvanostatic ones to get the slopes (3.28) and (3.29). After obtaining the desired upd-metal coverage degree potentiostatically, he applied a constant current pulse and monitored the potential as a function of time. The short time behavior of the potential corresponded to the charging of the double layer, allowing obtaining its capacitance. Upon subtraction of the ohmic resistance, calculation of the charge-transfer overpotential was possible at constant coverage degree.

3.5 Thermodynamics of Underpotential Deposition Using the Formalism of Ideal Polarizable Electrodes

3.5.1 Formalism

Schmidt [28] has analyzed the formation of upd MLs in the framework of the thermodynamic formalism of ideally polarizable electrodes. We discuss this formulation in some detail, since it is closely related and is relevant for the formulation discussed in Sect. 3.6. In the english-written literature, Budevski et al. have revisited this problem in Appendix 8.2 of their book [29], and we advise its careful reading to grasp the details of the modeling. The scheme proposed to analyze the upd problem is depicted in Fig. 3.9. In this scheme, the substrate (S) on which upd takes place is, on one side, in contact with a connector of metal M_1 , and on the other side in contact with the electrolyte solution (sol) containing M^{z+} , K^+ , X^- ions and solvent W.

Thus, it appears an interphase (IP) between the substrate (S) and the solution (sol). The electrolyte solution is in contact with a X^-/X^* reference electrode reversible with respect to the anion X^- , which is turned in contact with a second metal connector M_1 . The phases relevant for the present analysis are the substrate (S), the interphase (IP) and the solution (sol). Each of them, say (j) is described thermodynamically by an energy equation of the type:

$$U^{(j)} = U^{(j)}\left(S^{(j)}, V^{(j)}, A^{(IP)}, N_i^{(j)}\right) \quad (3.31)$$

where the energy U is function of the extensive parameters: entropy S , volume V and particle number of the different i - species in the j -phase $N_i^{(j)}$. The total differential of $U^{(j)}$ is:

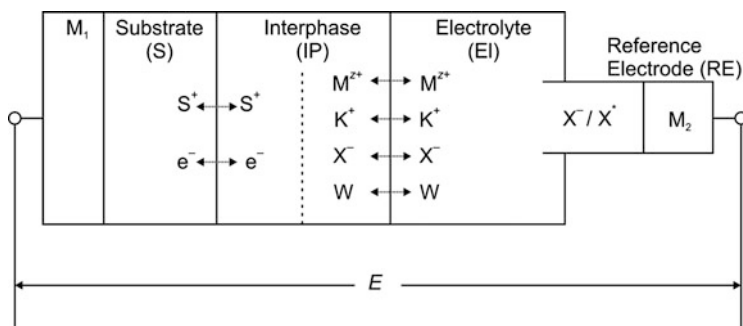


Fig. 3.9 Scheme of an electrochemical system used to model upd. It contains a substrate (S), in contact with a connector of metal M_1 , the electrolyte solution (sol) containing M^{z+} , K^+ , X^- ions and solvent W, the interphase (IP) between S and sol, and a X^-/X^* reference electrode reversible with respect to the anion X^- , which is in contact with a second metal connector M_1 (Adapted with permission from Ref. [29])

$$dU^{(j)} = T^{(j)}dS^{(j)} - P^{(j)}dV^{(j)} + \gamma^{(IP)}dA^{(IP)} + \sum_i \tilde{\mu}_i^{(j)}dN_i^{(j)} \quad (3.32)$$

where P and γ denote the pressure and specific surface energy of the (IP) respectively. The electrochemical potentials are defined as:

$$\tilde{\mu}_i^{(j)} = \mu_i^{(j)} + ze_0\varphi^{(j)} \quad (\text{with } i = M^{z+}, X^-, K^+) \quad (3.33)$$

where $\varphi^{(j)}$ is the Galvani or inner potential in the phase (j) and $\mu_i^{(j)}$ is the chemical potential. In the case of $P, T = \text{constant}$, as it is the ordinary condition of the electrochemical setup, the system is properly described by the Gibbs function, G , which is a partial Legendre transform of U :

$$G^{(j)} = U^{(j)} - T^{(j)}S^{(j)} + P^{(j)}V^{(j)} \quad (3.34)$$

So that the total free energy of the system is:

$$G = \sum_j G^{(j)} \quad (3.35)$$

Then, the total free energy change of the system will be given by:

$$\begin{aligned} dG &= dG^{(S)} + dG^{(EI)} + dG^{(sol)} \\ &= \gamma dA + \sum_j \left(\tilde{\mu}_i^{(S)} dN_i^{(S)} + \tilde{\mu}_i^{(IP)} dN_i^{(IP)} + \tilde{\mu}_i^{(sol)} dN_i^{(sol)} \right) \end{aligned} \quad (3.36)$$

With the corresponding Gibbs-Duhem conditions reading:

$$Ad\gamma + \sum_j \left(N_i^{(S)} d\tilde{\mu}_i^{(S)} + N_i^{(IP)} d\tilde{\mu}_i^{(IP)} + N_i^{(sol)} d\tilde{\mu}_i^{(sol)} \right) = 0 \quad (3.37)$$

Use of the previous equation along with electroneutrality conditions for the different phases leads to:

$$-d\gamma = \Gamma_{M_{(aq)}^{z+}} d\mu_{MX_z}^{sol} + \Gamma_{K^+} d\mu_{KX}^{sol} - q_{ion} dE \quad (3.38)$$

where $\mu_{MX_z}^{sol} = \tilde{\mu}_{M_{(aq)}^{z+}}^{sol} + z\tilde{\mu}_{X^-}^{sol}$, $\mu_{KX}^{sol} = \tilde{\mu}_{K^+}^{sol} + \tilde{\mu}_{X^-}^{sol}$, q_{ion} is the ionic surface charge density at the interphase (IP) and E is the measured potential difference. $\Gamma_{M_{(aq)}^{z+}}$ and Γ_{K^+} are the relative surface excess concentrations of $M_{(aq)}^{z+}$ and K^+ with respect to the solvent:

$$\Gamma_i := \frac{1}{A} \left[N_i^{(\text{IP})} - \frac{N_W^{(\text{IP})} N_i^{(\text{El})}}{N_W^{(\text{El})}} \right] \quad (3.39)$$

We note that Eq. (3.38) represents the total differential of the specific surface energy, as a function of the chemical potentials of the electrolytes and the measured potential difference. Thus, we have:

$$\Gamma_{M_{(\text{aq})}^{z+}} = - \left(\frac{\partial \gamma}{\partial \mu_{MX_z}^{\text{sol}}} \right)_{\mu_{KX}^{\text{sol}}, E} \quad (3.40)$$

$$\Gamma_{K^+} = - \left(\frac{\partial \gamma}{\partial \mu_{KX}^{\text{sol}}} \right)_{\mu_{MX_z}^{\text{sol}}, E} \quad (3.41)$$

$$q_{\text{ion}} = \left(\frac{\partial \gamma}{\partial E} \right)_{\mu_{MX_z}^{\text{sol}}, \mu_{KX}^{\text{sol}}} \quad (3.42)$$

Equations (3.40, 3.41, and 3.42) relate the measurable quantities $\Gamma_{M_{(\text{aq})}^{z+}}$, Γ_{K^+} and q with the variation of the surface energy with other experimental parameters (concentration of species and electrode potential). It is worth mentioning that the thermodynamic relevant parameters occurring in these equations are not the absolute surface concentrations, but the relative surface excess concentrations Γ , as defined in Eq. (3.39). For a more detailed discussion, see the Appendix 8.2 of Ref. [29].

3.5.2 Application to Sulfate Coadsorption in the Case of Cu Underpotential Deposition on Au(111)

In case of coadsorption, anions may also play a role in changing the slope of curves like those of Fig. 3.7. In fact, if anions are present in the neighborhood of the IHP, they may partially compensate the positive charge of adatoms, thus producing a lower flow of electronic charge to the surface of the substrate than expected. In the case of the Cu/Pt system illustrated there, it appears that this is the case, since the radiotracer method shows that electrosorption of copper induces a significant adsorption of HSO_4^- ions [30].

We turn now to analyze an illustrative example of the application of the formalism developed in this section. Based on it, Lipkowski and coworkers [31–34] have studied the coadsorption of SO_4^{2-} , Cl^- and Br^- in the case of Cu upd on Au (111). We discuss in some detail the studies dealing with the SO_4^{2-} anion.

Coadsorption of this anion and Cu^{2+} was analyzed using $0.1 \text{ M HClO}_4 + 10^{-3} \text{ M K}_2\text{SO}_4 + x\text{M Cu}(\text{ClO}_4)_2$ solutions ($10^{-5} < x < 5 \times 10^{-3}$). Under these condition, the electrocapillarity equation for Au(111) was written as:

$$-d\gamma = q_m dE + \left(\Gamma_{\text{HSO}_4^-} + \Gamma_{\text{SO}_4^{2-}} \right) d\mu_{\text{H}_2\text{SO}_4} + \left(\Gamma_{\text{Cu}^{2+}} + \Gamma_{\text{Cu}} \right) d\mu_{\text{Cu}^{2+}} \quad (3.43)$$

where $q_m = -q_{\text{ion}}$, is the charge density on the metal. Formally, this equation enables to get the total Gibbs excess of adsorbed copper and adsorbed anions according to:

$$\Gamma_{\text{HSO}_4^-} + \Gamma_{\text{SO}_4^{2-}} = - \left(\frac{\partial \gamma}{\partial \mu_{\text{H}_2\text{SO}_4}} \right)_{E, \mu_{\text{Cu}^{2+}}, T, P} \quad (3.44)$$

$$\Gamma_{\text{Cu}^{2+}} + \Gamma_{\text{Cu}} = - \left(\frac{\partial \gamma}{\partial \mu_{\text{Cu}^{2+}}} \right)_{E, \mu_{\text{H}_2\text{SO}_4}, T, P} \quad (3.45)$$

Since HClO_4 is present in excess, the pH of the solution remains constant so that the conditions $d\mu_{\text{H}_2\text{SO}_4} = RT d\ln(c_{\text{K}_2\text{SO}_4})$ and $d\mu_{\text{Cu}^{2+}} = RT d\ln(c_{\text{Cu}^{2+}})$ are fulfilled because the corresponding activity coefficients remain constant. The latter is also important to warranty the condition of constant chemical potential of the species not involved in the partial derivative.

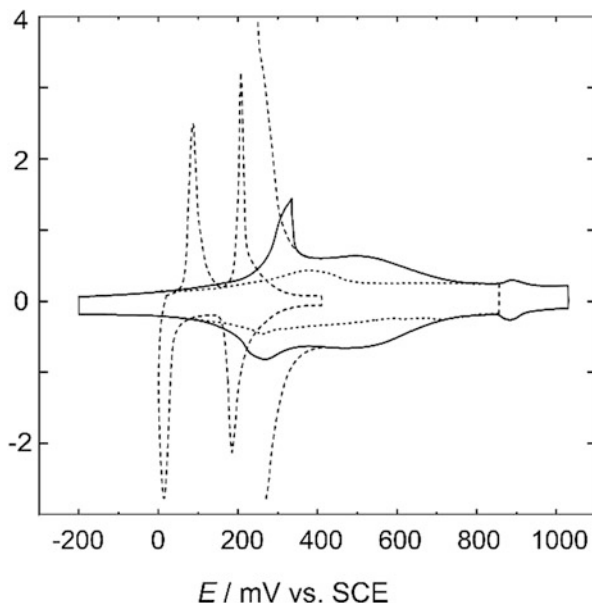
While the formalism to get the surface excesses appear is clearly defined in the Eqs. (3.44) and (3.45), the direct measurement of γ for solid electrodes appears as difficult, if not impossible. However, Shi and Lipkowski [31, 32] devised a procedure to circumvent this problem, showing a way to get *relative values* of γ as a function E from chronocoulometric measurements. The basis for this is Eq. (3.43), where it can be noticed that if charge is integrated as a function of potential for a given solution composition, changes in γ can be obtained as:

$$\Delta\gamma = \int_{\gamma_0}^{\gamma_0 + \Delta\gamma} d\gamma = \int_{E_1}^{E_2} -q_m dE \quad (3.46)$$

These authors noted that if the ionic adsorption is investigated over a wide range of potentials, it may be found a potential E , at which the adsorbed species are totally desorbed. When this condition is satisfied, relative changes in γ , and consequently, the Gibbs energy excess of the adsorbed species, can be determined from a measurement of the electrode charge, as pointed out above.

Figure 3.10 illustrates how to use cyclic voltammogram (CV) curves to find the potentials of complete desorption of anions and metal adatoms on Au(111), respectively. Let us compare for example the voltammogram in excess of base electrolyte, 0.1 M HClO_4 , dotted line, with the voltammogram with the addition of $5 \times 10^{-3} \text{ M K}_2\text{SO}_4$, given by the full line. It can be found that both voltammograms merge for potentials lower than 100 mV, indicating that below this potential the surface will

Fig. 3.10 Cyclic voltammograms recorded at an Au(111) electrode in
 (. . . .) 0.1 M HClO₄,
 (-----) 0.1 M HClO₄ +
 5 × 10⁻³ M K₂SO₄,
 (---) 0.1 M HClO₄ + 5
 × 10⁻³ M K₂SO₄ + 10⁻³ M
 Cu(ClO₄)₂. Scan rate:
 5 mV s⁻¹ (Reprinted with
 permission from Ref. [31])

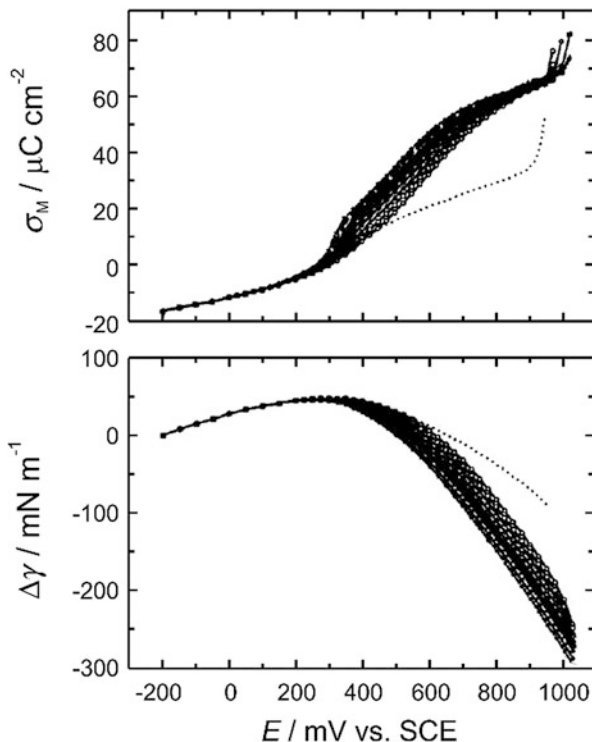


be free of sulfate adsorption. On the basis of this information, charge vs. E curves were constructed the following way: the electrode was held at a potential E , where sulfate adsorption took place for a period of time long enough to reach adsorption equilibrium. The potential was then stepped to $E_f = -0.2$ V (SCE), where sulfate species desorb, and current transients were recorded and integrated to get the charge difference between potential E and E_f .

Absolute charge densities were then calculated, using the value of the PZC, determined independently for the pure HClO₄ solution. These charge densities are shown in Fig. 3.11a. Then, the charge density data were integrated starting the integration at $E = -0.2$ V, yielding the difference between the interfacial tension at a potential E and at $E = -0.2$ V (SCE), as shown in Fig. 3.11b. It can be observed that all electrocapillary curves merge at $E < 0.1$ V (SCE) and diverge at more positive potentials, where the γ decreases with the bulk sulfate concentration.

Going back to Fig. 3.10, it can be observed that the curves corresponding to the two electrolytes containing K₂SO₄, (with and without Cu²⁺) coincide at $E > 0.4$ V (SCE), indicating that Cu is desorbed from the gold surface at these positive potentials. Thus, $E_f = +0.8$ V (SCE) can be chosen for chronocoulometric measurements carried out in the presence of Cu²⁺ into the solution. Similarly to the previous case, total charge density and electrocapillary curves can be constructed for Cu²⁺ containing solutions. For a given Cu²⁺ concentration, the total Gibbs excess of adsorbed sulfate ions may be determined by plotting the interfacial tensions at a constant E as a function of $RT \ln(c_{K_2SO_4})$ and differentiating (see Eq. 3.44). Similarly, to determine the Gibbs excess of adsorbed copper the interfacial tensions

Fig. 3.11 (a) Surface charge density-electrode potential curves and (b) electrocapillary curves for the Au(111) electrode: *dotted line*, pure 0.1 M HClO₄; *solid lines* 0.1 M HClO₄ with the addition of K₂SO₄ at different concentrations between 10⁻⁵ M and 5 × 10⁻³ M (Reprinted with permission from Ref. [31])

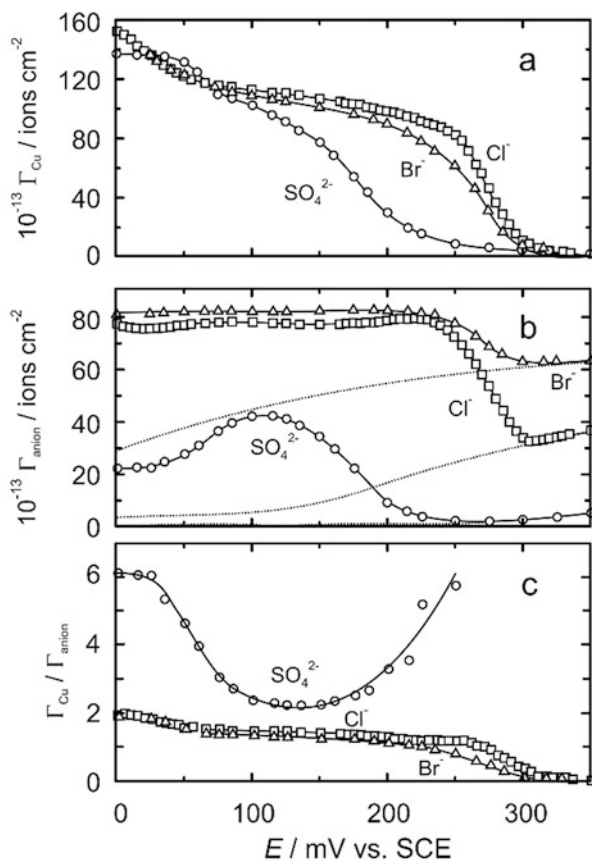


at constant E and $c_{\text{K}_2\text{SO}_4}$ may be plotted against $RT \ln(c_{\text{Cu}^{2+}})$ and differentiated (see Eq. 3.45). A similar procedure may be performed to study the excesses of other anions, as Cl^- or Br^- , as considered by Lipkowski and coworkers [33].

The methodology just described yields highly interesting information on the excesses of the different species participating in the upd of Cu in the presence of anions. Figure 3.12 shows the Gibbs excess for adsorbed copper (Fig. 3.12a) and three different coadsorbed anions: Cl^- , Br^- and SO_4^{2-} (Fig. 3.12b), as well as the relative excesses $\Gamma_{\text{Cu}}/\Gamma_{\text{anion}}$ (Fig. 3.12c).

It is interesting to correlate this thermodynamic information with the voltammograms for the different systems, shown in Fig. 3.13. Let us illustrate first the case of SO_4^{2-} containing electrolytes. Copper adsorbs epitaxially on the Au(111) surface and hence a closed packed ML of adsorbed copper atoms would correspond to the surface concentration of 1.39×10^{15} atoms cm^{-2} . The evolution of Γ_{Cu} in Fig. 3.12a with decreasing potential shows that the peak at more positive potentials in Fig. 3.13a and inset corresponds to the formation of 2/3 of a ML, while the most negative one involves the formation of a full monolayer. While Cu upd starts at potentials where $\Gamma_{\text{SO}_4^{2-}}$ is very small (Fig. 3.12b), it can be noticed that sulfate adsorption is considerably enhanced by the presence of Cu. $\Gamma_{\text{SO}_4^{2-}}$ increases rapidly with Γ_{Cu} until reaching a maximum (Fig. 3.12b) at a potential where $\theta_{\text{Cu}} = 2/3$.

Fig. 3.12 (a) Plot of the Gibbs excess of Cu in the presence of different anions, as indicated in the figure; (b) Plot of the Gibbs excess of Cl^- , Br^- and SO_4^{2-} ; (c) Plot of the ratio of the Gibbs excess of copper to the Gibbs excess of the anion adsorbed from 0.1 M KClO_4 , $+10^{-3}$ M HClO_4 $+10^{-3}$ M $\text{Cu}(\text{ClO}_4)_2$, $+10^{-3}$ M potassium salt of: (\square) Cl^- , (Δ) Br^- , and 0.1 M HClO_4 $+10^{-3}$ M $\text{Cu}(\text{ClO}_4)_2$ $+10^{-3}$ M K_2SO_4 (\circ) at a Au(111) electrode surface (Reprinted with permission from Ref. [33])



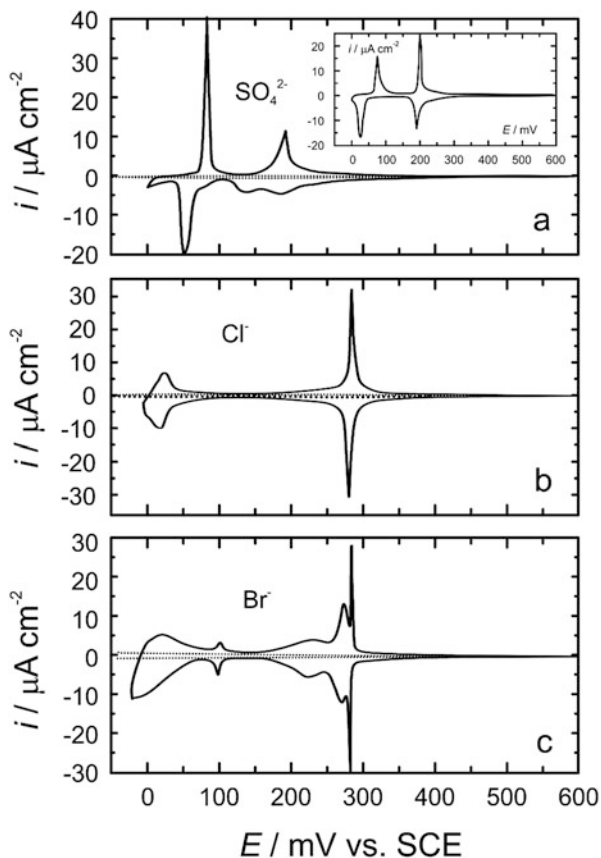
Under these conditions, $\theta_{\text{SO}_4^{2-}} = 1/3$ and $\Gamma_{\text{Cu}} + \Gamma_{\text{SO}_4^{2-}} = 1.4 \times 10^{15} \text{ ions cm}^{-2}$, thus being equal to the surface density of Au atoms. This is a clear indication that the surface is covered by a compact monolayer of coadsorbed Cu and SO_4^{2-} , as will be analyzed in Chap. 5 on the basis of theoretical modeling.

The data in Fig. 3.12a, b also show that upon completion of the Cu monolayer, SO_4^{2-} anions are not completely displaced from the electrode surface, but remain with an important surface excess, $\Gamma_{\text{SO}_4^{2-}} = 2.2 \times 10^{14} \text{ ions cm}^{-2}$. In this respect, the occurrence of SO_4^{2-} anions adsorbed on top of the Cu atoms has been proposed from EXAFS experiments [35, 36].

Turning into the consideration of Cl^- coadsorption, the Γ_{Cu} vs. E curve in Fig. 3.12a suggests first the formation of a structure with $\theta_{\text{Cu}} = 1/2$ and its subsequent transformation into another where $\theta_{\text{Cu}} = 2/3$. In the region of the small peak observed at lower potentials in Fig. 3.13b, θ_{Cu} seem to exceed unity.

The voltammetric behavior in the presence of Br^- (Fig. 3.13c) is more complex than that for Cl^- , where the five sets of peaks indicate that the Cu ML is built in a

Fig. 3.13 Cyclic voltammograms for a Au (111) electrode in 0.1 M HClO_4 , $+10^{-3}$ M $\text{Cu}(\text{ClO}_4)_2$ + 10^{-3} M potassium salt of: (a) SO_4^{2-} , and 0.1 M KClO_4 + 10^{-3} M HClO_4 + 10^{-3} M $\text{Cu}(\text{ClO}_4)_2$ + 10^{-3} M potassium salt of (b) Cl^- ; (c) Br^- . Dotted lines show CV recorded in the copper free electrolytes. Insert: CV recorded for 0.1 M HClO_4 + 10^{-3} M $\text{Cu}(\text{ClO}_4)_2$ + 5×10^{-3} M K_2SO_4 solution. Sweep rate 2 mV s^{-1} (Reprinted with permission from Ref. [33])



number of steps. Comparison with the Γ_{Cu} vs. E curves (Fig. 3.12a) indicates that the first sharp peak corresponds to $\theta_{\text{Cu}} \approx 1/5$, the second peak to $\theta_{\text{Cu}} \approx 1/2$ and the third to $\theta_{\text{Cu}} \approx 2/3$. As in the case of Cl^- , θ_{Cu} increases steadily as E approaches the bulk deposition potential, being θ_{Cu} slightly larger than one.

As a general conclusion of this section, we can state that smart analysis of coulometric measurements can yield valuable thermodynamic information on a complex upd system, as it is the case of Cu electro sorption on Au(111) in the presence of different anions.

3.6 Coverage Isotherms and Phase Transitions

On the basis of Eqs. (3.12) and (3.14), the underpotential shift may be written as [13]:

$$\Delta E^{S-M} = \left(E_{(M_\theta/S)/M_{(aq)}^{z+}} - E_{(M_\theta/S)/M_{(aq)}^{z+}}^0 \right) + \frac{RT}{F} \left(\frac{1}{\gamma_v} - \frac{1}{z} \right) \ln \left(a_{M_{(aq)}^{z+}} \right) - \frac{RT}{\gamma_v F} \ln(a(\Gamma_M)) \quad (3.47)$$

where

$$\left(E_{(M_\theta/S)/M_{(aq)}^{z+}} - E_{(M_\theta/S)/M_{(aq)}^{z+}}^0 \right) = \Delta E^{S-M,0} = \frac{\Delta G^0}{zF} - \frac{\Delta G^{\text{upd},0}}{\gamma_v F} \quad (3.48)$$

Based on the concept of submonolayer equilibrium potential, underpotential/coverage isotherms can be derived on the basis of Eq. (3.47). With this purpose, it is necessary to take into account the existence of multiple energy states and the relationship between $a(\Gamma_M)$ and Γ_M . Instead of the surface excess, it is more suitable to write this equation as a function of the coverage degree $\theta = \Gamma/\Gamma_{\text{sat}}$, where Γ_{sat} is the maximal surface excess attainable on the surface.

In the case of an ideal lattice gas, the chemical potential is given by:

$$\mu = RT \ln \left(\frac{\theta}{(1-\theta)q_p} \right) \quad (3.49)$$

where q_p is the partition function on a single adsorbed atom. Comparing the previous equation with:

$$\mu = \mu^0 + RT \ln(a) \quad (3.50)$$

We see that if we select as standard state for the monolayer $\theta = 0.5$, the activity of the monolayer is given by $a = \theta/(1-\theta)$. Thus, in the case of a langmuirian behavior of the upd layer, the relationship between the coverage degree and the equilibrium potential will be given by:

$$\Delta E^{S-M} = \left(E_{(M_\theta/S)/M_{(aq)}^{z+}} - E_{(M_\theta/S)/M_{(aq)}^{z+}}^0 \right) + \frac{RT}{F} \left(\frac{1}{\gamma_v} - \frac{1}{z} \right) \ln \left(a_{M_{(aq)}^{z+}} \right) - \frac{RT}{\gamma_v F} \ln \left[\frac{\theta}{(1-\theta)} \right] \quad (3.51)$$

In this equation, the term $\theta/(1-\theta)$ is a purely entropic one, arising from the different forms to distribute the adatoms among the adsorption sites. However, other effects like a priori surface heterogeneity or interaction between adsorbed atoms may occur [13]. A way to consider this is to introduce in Eq. (3.48) a formal dependence of $\Delta G^{\text{upd},0}$ on θ according to:

$$\Delta G^{\text{upd},0} = \Delta G^{\text{upd},\theta \rightarrow 0} + fRT\theta \quad (3.52)$$

where f is an interaction parameter accounting for these effects, so that the isotherm results in:

$$\begin{aligned} \Delta E^{\text{S-M}} = & \left(\frac{\Delta G^0}{zF} - \frac{\Delta G^{\text{upd},\theta \rightarrow 0}}{\gamma_v F} \right) + \frac{RT}{F} \left(\frac{1}{\gamma_v} - \frac{1}{z} \right) \ln \left(a_{\text{M}^{z+}(\text{aq})} \right) \\ & - \frac{RT}{\gamma_v F} \left[\ln \frac{\theta}{(1-\theta)} + f\theta \right] \end{aligned} \quad (3.53)$$

In the present adsorption phenomenon, due to the fact that adatoms are metallic, attractive interactions are expected to appear between them, so that f should be negative. Other effects have also been modeled via modification of Eq. (3.52). For example, Conway et al. [37] have included in this modeling the effect of charge polarization, in terms of an induced image dipole. This resulted in the addition of a further term to this equation, resulting:

$$\Delta G^{\text{upd},0} = \Delta G^{\text{upd},\theta \rightarrow 0} + fRT\theta + gRT\theta^{3/2} \quad (3.54)$$

And leading to [27]:

$$\begin{aligned} \Delta E^{\text{S-M}} = & \left(\frac{\Delta G^0}{zF} - \frac{\Delta G^{\text{upd},\theta \rightarrow 0}}{\gamma_v F} \right) + \frac{RT}{F} \left(\frac{1}{\gamma_v} - \frac{1}{z} \right) \ln \left(a_{\text{M}^{z+}(\text{aq})} \right) \\ & - \frac{RT}{\gamma_v F} \left[\ln \frac{\theta}{(1-\theta)} + f\theta + g\theta^{3/2} \right] \end{aligned} \quad (3.55)$$

Let us summarize the main assumption involved in this equation, limiting its potential applications: first of all, a single energy state is involved. We will find along this book that upd on single crystal faces may involve several energy states, corresponding to the formation of different structures on the metal surface. Second, it assumes additivity of adsorbate-substrate and adsorbate-adsorbate interactions. This is also a simplification to describe metal binding, where the interactions are non-additive. To account for the first of these facts Swathirajan et al. [27] have proposed to write a general isotherm for the j th state as:

$$\begin{aligned} \Delta E^{\text{S-M}} = & \Delta E_j^{\theta \rightarrow \theta_j} + \frac{RT}{F} \left(\frac{1}{\gamma_v} - \frac{1}{z} \right) \ln \left(a_{\text{M}^{z+}(\text{aq})} \right) \\ & - \frac{RT}{\gamma_v F} \left[\ln \left(\frac{\theta - \theta_{j-1}}{\theta_j - \theta} \right) + f_j(\theta - \theta_{j-1}) + g_j(\theta - \theta_{j-1})^{3/2} \right] \end{aligned} \quad (3.56)$$

where θ_{j-1} and θ_j are the initial and final coverages of j th energy states respectively. Various particular cases of this equation were discussed in Ref. [27], and the so-called Temkin parameter f was given there for several systems involving

Table 3.2 Isotherm parameters for different upd systems. f was estimated from the integral isotherms according to Eq. (3.57)

Substrate/adsorbate	f	References
Ag/Pb	16	[38]
Au/Pb	41	[39]
Pt/Pb	94	[40]
Au/Ag	25	[13]

polycrystalline substrates, as summarized in Table 3.2. The results reported in this table correspond to f values estimated from the integral isotherms as:

$$f \approx \frac{zF}{RT} \left[\frac{d(\Delta E^{S-M})}{d\theta} \right] \quad (3.57)$$

Swathirajan et al. [27] analyzed different possible reasons for the abnormally large Temkin parameters found in Table 3.2, including the polycrystalline nature of the substrate, radii mismatch between substrate and adsorbate, multiple adsorption states, lateral interactions and the variation of substrate work function with coverage. Among all these effects, they privileged the later one. As we will see below, the widespread subsequent use of single crystal surfaces in upd has largely contributed to improve our understanding on this system and we will conclude that in some cases the polycrystalline nature of the substrate may lead to a wide energy distribution yielding an abnormally large f parameter. However, we wanted to emphasize on the previous early work with polycrystalline surfaces here, since it marked interesting tracks for further research in the area. For example, besides the previous discussion on thermodynamic aspects in Ref. [27], solvent adsorption, ion adsorption and changes in the electronic properties of the upd layer were mentioned there as relevant factor influencing the observed electrochemical behavior.

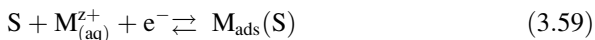
As we saw in Chap. 2, linear sweep voltammograms at a relatively low sweep rate may deliver relevant information on the adsorption isotherm of upd systems, as long as they are performed at a rate slow enough so that adsorption conditions close to equilibrium are established. These are called quasi-equilibrium conditions. Let us now discuss shortly on this point. The current density i measured in a linear voltammetric experiment can be written as:

$$i = Q_M \frac{d\theta}{dt} = Q_M \frac{d\theta}{dE} \frac{dE}{dt} = Q_M v \frac{d\theta}{dE} \quad (3.58)$$

where Q_M is the charge for generating a monolayer coverage of the adsorbate, and v is the potential sweep rate. Note that the term $Q_M d\theta/dE =: C$ has units of a capacitance. For this reason, C is called *adsorption pseudocapacitance*. If the coverage at each potential is close to that obtained under equilibrium conditions, then the current in the voltammogram is proportional to the derivative of the $\theta - E$ adsorption isotherm. Angerstein Kozłowska et al. [41] have performed computer simulations of the kinetic behavior of a single electron reaction with a single adsorbed species that can be used to described the upd phenomenon. Although

the model was meant to represent the oxidative formation of a chemisorbed species, the same set of equations may be applied to describe upd just by changing the sign of the applied potential ΔE in the original equations.

Thus, the equation describing upd through a single electron transfer according to the reaction:



can be modeled according to the following equation:

$$\begin{aligned} i &= Q_M \frac{d\theta}{dt} \\ &= Q_M \left\{ -k_1 c_{M_{(\text{aq})}^{z+}} (1 - \theta) \exp \left[-\frac{F}{2RT} \Delta E - \frac{f\theta}{2} \right] + k_{-1} \theta \exp \left[\frac{F}{2RT} \Delta E + \frac{f\theta}{2} \right] \right\} \end{aligned} \quad (3.60)$$

with $\Delta E = E_i \pm vt - E^0$, where E^0 is the standard reversible potential and E_i is the initial potential in the sweep. Steady state conditions $d\theta/dt = 0$ leads to the following adsorption isotherm:

$$\begin{aligned} E_{(M_0/S)/M_{(\text{aq})}^{z+}} &= E_{(M_0/S)/M_{(\text{aq})}^{z+}}^0 + \frac{RT}{F} \ln \left(\frac{k_1}{k_{-1}} \right) + \frac{RT}{F} \ln \left(a_{M_{(\text{aq})}^{z+}} \right) \\ &\quad - \frac{RT}{F} \left[\ln \frac{\theta}{(1 - \theta)} + f\theta \right] \end{aligned} \quad (3.61)$$

which is analogous to that described above in Eq. (3.53). We will discuss results corresponding to these conditions, which are relevant for the previous thermodynamic formulation. Figure 3.14 (left) shows adsorption isotherms for different values of the interaction parameter f .

It can be appreciated there that the isotherms with positive interaction parameters (repulsion) spread over a considerably larger potential region than that with $f = 0$, and are shifted towards positive values with respect to the standard reversible potential. On the other hand, the isotherms with negative interaction parameters become steeper and are shifted negatively with respect to E^0 . From Fig. 3.14 (left) it seems that for some negative f (close to $f = -4$) it will appear a curve with a point on it where $d\theta/dE \rightarrow \infty$. Moreover, in a E vs. θ representation of the plots, this will be inflection point at $\theta = \theta_{i,p}$, for which we now from calculus that we have the conditions $dE/d\theta = 0$ and $d^2E/d\theta^2 = 0$. From the latter condition we find $\theta_{i,p} = 1/2$, and replacing in the first condition, we find that the first derivative will be zero if $f = -4$. For interaction parameters lower than -4 , the θ vs. E curves present a potential range where they have three solutions. This behavior is analogous to the behavior of the van der Waals isotherm, and is an indication for a first-order phase transition. In the electrochemical experiment, this means that if the

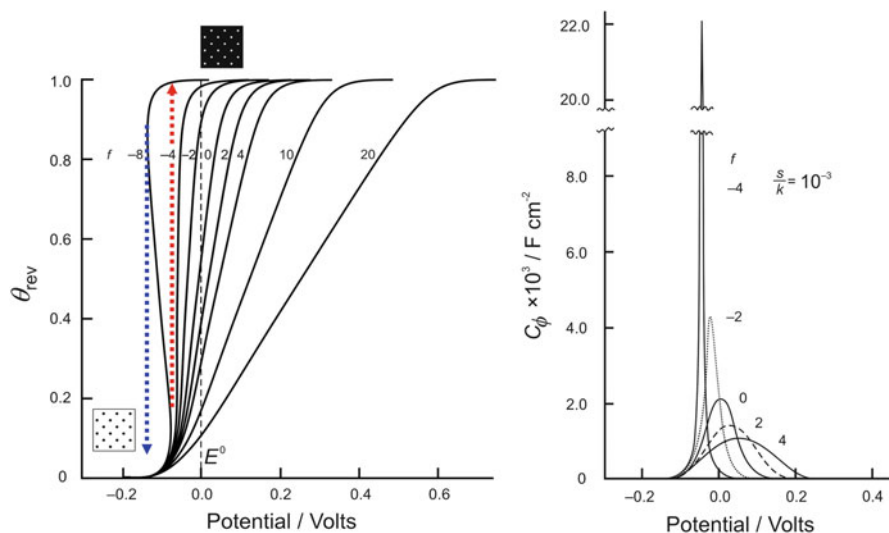


Fig. 3.14 *Left:* adsorption isotherms for the formation of M_{ad} in reaction for various positive and negative f values. *Right:* plots of the C vs. V profile for reaction (adsorption) for various positive and negative f values in Eq. (3.59) (Reprinted with permission from Ref. [41])

interaction between adsorbed particles is strong enough (by strong enough we mean in the present modeling $f < -4$), a *discontinuous change will be observed in the surface density of the adlayer*. To make this point clear, let us consider the curve in Fig. 3.14 (left) with $f = 20$. If we follow this curve from a negative up to a positive E value, we see that the coverage degree changes *continuously* (no jumps), over a potential region that exceeds 600 mV. Let us now follow the curve with $f = -8$, starting from very negative E values. There, θ will be very small, and the adsorbed atoms exist in a disperse gas-like distribution (see inset). Coverage will smoothly increase in this dilute phase, until reaching the potential marked with a red dotted vertical line. At this point, the surface coverage will change abruptly following the dotted red arrow, yielding a compact, condensed phase. Let us repeat this procedure, with the same curve $f = -8$, but now starting from a large positive E value, running in the negative direction. At large E , θ will be large, forming a condensed phase. Holes will occur in this condensed phase, until reaching the potential marked by the blue dotted vertical line. At this point, an abrupt decrease in θ will occur, following the blue arrow. Thus, the potential region between the two arrows is a metastability region, where a transition between two different phases, a condensed and a dilute one may occur. Note that all the discussion above was made along branches of the $\theta - E$ curve where $d\theta/dE$ is positive. What about the branch of the isotherm where $d\theta/dE < 0$? This corresponds to an unstable region (with a negative pseudocapacitance) and does not have a physical meaning.

Fig. 3.15 Dependence of the peak potential E_p , coverage degree at the peak θ_p , half width peak $\Delta E_{1/2}$ and standard-state coverage degree θ^0 characterizing the C vs. V profile for reversible conditions in reaction (3.58), on the f value (Reprinted with permission from Ref. [41])

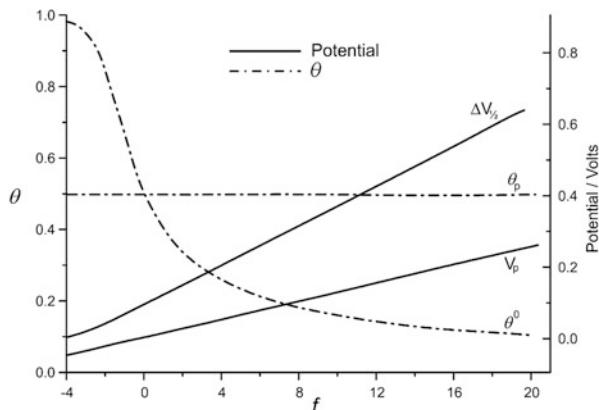


Figure 3.14 (right) shows pseudocapacitance curves, corresponding to quasi-equilibrium conditions, for some of the isotherms on the left. There we see how negative values of the interaction parameter f result in a progressive thinning of the pseudocapacitance peak, until a very sharp spike results at $f = -4$. The sharpness of the peaks may be characterized by their half-peak width $\Delta E_{1/2}$, which is the width of the peak at a C value equal the half of its maximum capacitance. $\Delta E_{1/2}$ values are shown, together with other relevant parameters, as a function of f in Fig. 3.15. It can be seen there how $\Delta E_{1/2}$ vanishes in the limit $f \rightarrow -4^+$, while it grows becoming larger than 600 mV for $f > 18$. The results of the present simulations allow to rationalize the reasons for the large f values found in polycrystalline surfaces (See Table 3.2): if an effective parameter f is fitted to an up process with extends over several hundreds of mV, due to the overlap of a series of processes in this region, a large positive value of f will result. A better way to estimate an effective f would be from the experimental $\Delta E_{1/2}$ values. However, this approach is seldom found in the literature.

In the previous discussion, we have introduced heuristically the idea of a first-order phase transition in a voltammogram. Phase transitions have been thoroughly studied in the physical literature within the so-called lattice models, which have a close relation the Ising models for magnets. Both models are illustrated comparatively in Fig. 3.16. In the upper part, we show on the left a portion of the 2-dimensional Ising model for a system of interacting dipoles, which are under the influence of an external magnetic field, H . Each of the dipoles may take either one of two states, one with spin up or +1 (blue) and another one with spin down of -1 (red). The status of the i th spin is described by the variable S_i , which may take one of these values. The interaction energy of such a dipole system takes the form:

$$U^{\text{Ising}} = -\sum_{i,j} J_{ij} S_i S_j - H \sum_i S_i \quad (3.62)$$

where the first term represents the interaction between dipoles i and j spin via the interaction J_{ij} , denominated coupling constant. In the simplest version of the model, the interaction is considered between nearest neighbors and $J_{ij} = J$ is the same for all site pairs and the hamiltonian reduces to:

$$U^{\text{Ising}} = -J \sum_{\langle i, j \rangle_{\text{neigh}}} S_i S_j - H \sum_i S_i \tag{3.63}$$

The second sum in Eq. (3.63) represents the interaction with the external magnetic field.

On the upper right part of Fig. 3.16, we represent the so called lattice gas model for adsorption. As in the Ising case, we also have a lattice but the sites may be now occupied or unoccupied by adsorbates (yellow circles) and this situation is described by an occupation variable C_i , which may take the values 1 or 0 respectively. Note that where we had “up” blue dipoles on the left, we have yellow circles on the right, so there is a one-to one correspondence between the configurations represented in the two lattices of Fig. 3.16.

The analogue of Eq. (3.63) for the lattice gas model, subject to a constant chemical potential μ is:

$$U^{\text{LG}} = -\zeta \sum_{\langle i, j \rangle_{\text{neigh}}} C_i C_j - \mu \sum_i C_i \tag{3.64}$$

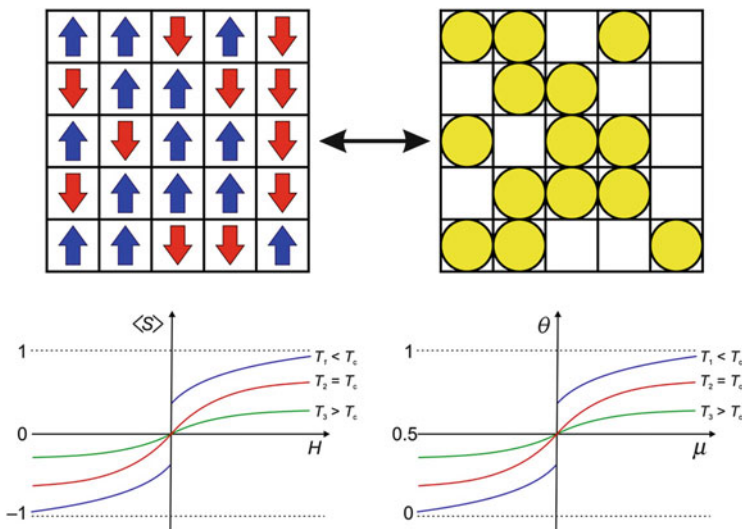


Fig. 3.16 Illustrative comparison between the Ising model for magnets (*left*) and the lattice gas model for adsorption (*right*). T_c denotes the critical temperature, below which an abrupt change in the magnetization (coverage degree) is expected as plotted as function of the magnetic field (chemical potential)

where ζ is a constant describing the interaction between two neighboring adsorbates. The interaction of the adatoms with the substrate is set arbitrarily equal to zero (see discussion below). It can be shown that Eqs. (3.63) and (3.64) are equivalent just by replacing in the first $S_i = 2C_i - 1$. This leads to the following equation:

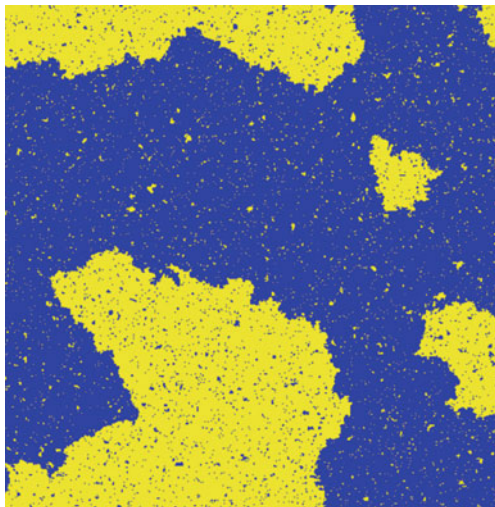
$$U^{\text{Ising}} = -4J \sum_{\langle i, j \rangle_{\text{neigh}}} C_i C_j - 2(H - J n_c) \sum_i C_i + \text{constant} \quad (3.65)$$

where n_c is the number of nearest neighbors to a given dipole. Since the additive constant is unimportant, a complete equivalence between both systems is obtained if $\zeta = 4J$ and $\mu = 2(H - J n_c)$. The mathematical equivalence between both approaches has been proved in Ref. [42]. This means that all the results derived for the Ising model can be transferred to the lattice gas model after a suitable adaptation of the corresponding equations. In the case of 2D systems, the energy Eqs. (3.63) and its equivalent (3.64) can be inserted in the statistical mechanical formalism and solved approximately or via computer simulations to evaluate properties of the system. For the present purpose, it is useful to analyze the average orientation of dipoles $\langle S \rangle$ in the magnetic system, under different chemical magnetic fields, which is the counterpart of the coverage degree under different chemical potentials. Before that, note that from Eq. (3.5), we have $\mu_M^S = \mu_M^M - ze_0 \Delta E^{S-M}$, so that in the electrochemical system, *the chemical potential of the adatoms on the substrate is determined by the potential difference applied to the cell, but a minus sign appears.*

Magnetic systems may exhibit positive or negative values of the constant J . However, since we are dealing with metal adsorbates that are expected to attract each other, ζ will be assumed to be positive in Eq. (3.64) (attractive interactions), and since $\zeta = 4J$, we will consider only positive J s in the magnetic analysis.

The application of a magnetic field to a system of dipoles will tend to align them with the field. Thus, we expect that at very large negative H (magnetic field strength) values $\langle S \rangle \rightarrow -1$, while at very large positive H values, $\langle S \rangle \rightarrow +1$. Temperature will contribute to randomize this alignment, so it is expected that the fields required to reach these limits will be larger the higher the temperature. Figure 3.16, bottom left, shows schematically $\langle S \rangle$ vs. H results obtained for three different temperatures, where it is found that this expectation is fulfilled. However, something remarkable is observed at low absolute values of H . This is a jump (discontinuity) in the $\langle S \rangle$ vs. H curve at $H = 0$, at the lowest temperature, T_1 . This discontinuity is absent at the higher temperatures, T_2 and T_3 , where it is found that $\langle S \rangle \rightarrow 0$ as $H \rightarrow 0$. This phenomenon is called spontaneous magnetization, since it happens in the absence of an applied magnetic field. It appears as a consequence of the coupling between neighboring dipoles. As we see from Eq. (3.63), the term $-JS_i S_j$ promotes alignment of neighboring dipoles in the same orientation (+1, +1) or (-1, -1). If J is large enough (or the temperature low enough), large domains of dipoles will predominate with one or other orientation when $H \rightarrow 0$.

Fig. 3.17 Illustration of phase coexistence in an Ising dipole system at $H = 0$, as obtained from a Monte Carlo simulation. *Blue points* denote $S = +1$ dipoles, *yellow points* denote $S = -1$ dipoles. The temperature is slightly below the critical temperature. ($T/T_c = 0.85$)



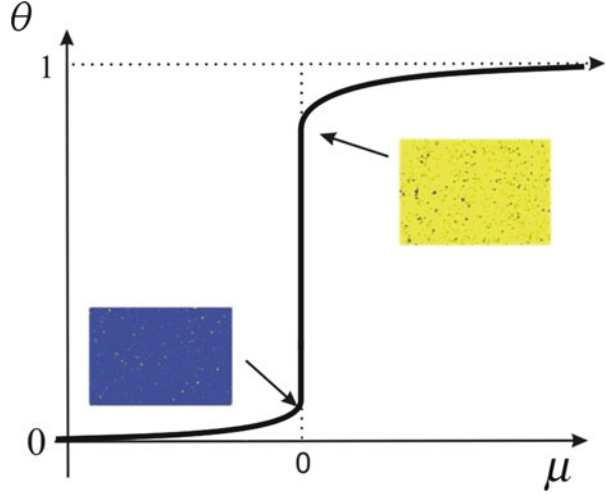
The predomination of one or the other orientation will depend whether $H \rightarrow 0^+$ or $H \rightarrow 0^-$. At $H = 0$, both phases will coexist, as illustrated in Fig. 3.17.

In the previous discussion, we stated somehow vaguely “high enough” of “low enough” temperature. Actually, it comes out that the jump in the $\langle S \rangle$ vs. H curve, as well as the phase coexistence shown in Fig. 3.17 starts to appear below a very well defined temperature, denominated “critical temperature”, T_c which depends on the strength of the coupling between de dipoles, J .

But let us turn to the problem of our interest, adsorbate formation, depicted at the bottom right of Fig. 3.16. There, we see that at a relatively low temperature a step is expected at the isotherms, as previously found in the phenomenologic model given by Eq. (3.61). Now, the step occurs at the chemical potential where the continuous isotherms yielded $\theta = 0.5$, that is $\mu = 0$. As in the case of magnetic dipoles, we see that we get different limiting coverages depending whether $\mu \rightarrow 0^+$ or $\mu \rightarrow 0^-$. In the first case, as the chemical potential approaches the point $\mu = 0$ from positive values, the configuration of the system will look like the snapshots shown on the right of Fig. 3.18. The surface will present a large coverage of the adsorbate (marked in yellow), with small blue “holes” of free sites. On the other hand, as the chemical potentials approaches the point $\mu = 0$ from lower values, the surface will be essentially empty, with isolated or small clusters of adatoms, appearing as small yellow dots on the blue substrate.

We connect now the lattice gas model with the behavior we expect to find in an electrochemical experiment, where a metal monolayer is deposited at upd. Unfortunately, due to the relationship between electrode potential difference and chemical potential via a minus sign, Eq. 3.5, the positive μ axis points into the direction of negative electrode potentials. Thus, when coming from positive electrode potentials (low μ values), the coverage presents a sudden increase at $\mu = 0$, and as sharp voltammetric peak should be observed, as it was previously noted in the

Fig. 3.18 Illustration of the behavior of the coverage vs. chemical potential curve for the lattice gas at a temperature below the critical point. Note the sudden increase in the coverage at the chemical potential $\mu = 0$



phenomenological isotherm given by Eq. (3.61) for $f < -4$. As we have shown in Fig. 3.16, in the case of the lattice gas model (and in its magnetic counterpart), the occurrence of this critical behavior depends, for a given interaction between adsorbates, on the temperature. In the case of the 2D magnetic dipolar system, the relationship between the critical temperature and the coupling parameter J has been found by Onsager [43, 44] for a square lattice and is:

$$T_c^{\text{Ising } 2\text{D}} = \frac{2J}{k_B \ln(1 + \sqrt{2})} \quad (3.66)$$

Taking into account the relationship between the magnetic coupling constant J and the pair interaction between adsorbates ζ in the lattice gas, we have that for the latter the critical temperature is:

$$T_c^{\text{lattice gas}} = \frac{\zeta}{2k_B \ln(1 + \sqrt{2})} \quad (3.67)$$

This is a very interesting result, since *from this equation we can find an order of magnitude for the interaction between adsorbates ζ required to observe a first-order phase transition in upd systems.* If we set $T_c^{\text{lattice gas}} = 298$ K, we find $\zeta = 0.04526$ eV. This is the minimal attractive interaction between pairs of adatoms on the surface required to find a first-order phase transition. We can calculate the binding energy of such a 2D layer, given by the terms $-\zeta \sum_{\langle i,j \rangle_{\text{neigh}}} C_i C_j$ in Eq. (3.64),

with $C_i = C_j = 1$. Taking into account that in a square lattice each adsorption site has four neighbors, and considering that if we sum over all atoms we count each interaction pair twice, we get $U_{\text{bind}}^{2\text{D}} = -0.09053$ eV. This is a small quantity as

compared with the cohesive energy of metals, of the order of several eV. However, we must state very clearly that this quantity represents an interaction *between adsorbates*, not with the substrate. The interaction with the substrate will determine the location of the step in the coverage on the μ axis ($\mu = 0$ so far), since the substrate-adsorbate atom interaction, say $\epsilon_{\text{subs-ads}}$, will only represent the addition of terms of the type $-\epsilon_{\text{subs-ads}}C_i$ to Eq. (3.63), to yield:

$$U^{\text{LG}} = -\zeta \sum_{(i,j)_{\text{neigh}}} C_i C_j - (\mu + \epsilon_{\text{subs-ads}}) \sum_i C_i \tag{3.68}$$

Thus, for a given ζ , the addition of the term $\epsilon_{\text{subs-ads}}$ results in the shift of the isotherm in the amount $\epsilon_{\text{subs-ads}}$ to the left, as illustrated in Fig. 3.19.

Onsager has also shown that the magnitude of the step observed at $\mu = 0$ in the isotherms on the right of Fig. 3.18 is determined by the critical temperature. If we denote the magnitude of this step in the case of lattice gas by $\Delta\theta$, we have:

$$\Delta\theta = \left\{ 1 - \left[\sinh \left(\ln \left(1 + \sqrt{2} \right) \frac{T_c}{T} \right) \right]^{-4} \right\}^{1/8} \tag{3.69}$$

which obviously becomes zero if $T = T_c$.

The plot of $\Delta\theta$ vs. T_c/T , see Fig. 3.20, shows that $\Delta\theta$ approaches very rapidly unity. A decrease of T of 10 % below the critical temperature, makes already $\Delta\theta$ larger than 0.8. In other words, the step at the adsorption isotherms should be clearly observed, as long as the system is at a temperature slightly lower than T_c .

On the basis of the previous discussion, it is worth stating the question: **are the usual upd systems candidates for a first order phase transition?** As we have seen above from the Ising model, this could occur if the binding energy of the

Fig. 3.19 Illustration of the shift of the coverage vs. chemical potential curve for the lattice gas model when the interaction energy with the substrate is changed in the amount $-\epsilon_{\text{subs-ads}}$

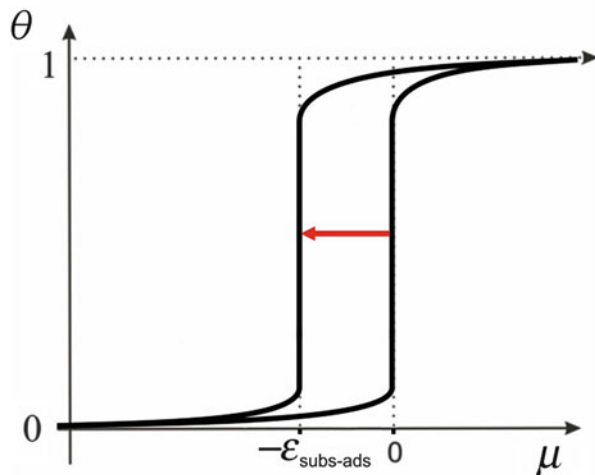
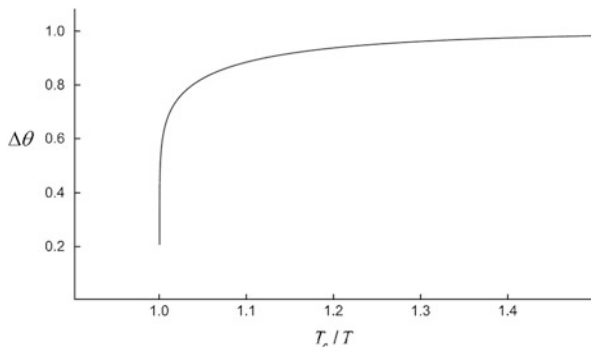


Fig. 3.20 Plot of the magnitude expected for the coverage jump $\Delta\theta$ at the adsorption isotherms due to the first-order phase transition, as a function the ratio between the critical temperature and the temperature of the system



monolayer is lower than -0.09053 eV. This Figure may only be taken as a rough indication, due to several approximations made in this model, namely:

1. Only nearest neighbor interactions are considered.
2. A square lattice is assumed for the structure of the adsorbate.
3. Vibrational effects are neglected. Thus, all vibrational entropic contributions will be absent.
4. The interactions among the components of the systems are assumed to be additive. Thus, the interactions of the adsorbates with each other and with the substrate may be separated. This is probably the strongest approximation, since metal bonding is characterized by many-body interactions.

In order to get a measure for the magnitude of the adsorbate-adsorbate interactions, we have calculated the binding energy of adatoms in the monolayer for several upd systems, which are shown in Table 3.3. The binding energy per adatom was calculated from:

$$U_{\text{bind}}^{2\text{D}} = U_{\text{M/S}}^{\theta=1} - U_{\text{M/S}}^{\theta=0} \quad (3.70)$$

where $U_{\text{M/S}}^{\theta=1}$ is the binding energy of the M adatoms in the monolayer adsorbed on the substrate S(hkl) and $U_{\text{M/S}}^{\theta=0}$ is the binding of a single atom on the surface of S.

From Table 3.3, we see that all the upd systems analyzed present a binding energy of the monolayer $U_{\text{bind}}^{2\text{D}}$ that is larger (in absolute value) than that required to observe a first-order phase transition at room temperature. Another interesting observation from this table is that the binding energy of the metal monolayers is lower (stronger binding) for adsorbates on the (100) faces.

As we have seen in Fig. 3.17, the coexistence of phases should characterize the first-order phase transitions we have analyzed so far. In principle, we have shown phase coexistence appearing only at $H = 0$ in the magnet system, or at $\mu = 0$ (eventually $\mu = -\varepsilon_{\text{subs-ads}}$) in Figs. 3.18 and 3.19. However, we represented in these Figures ideal equilibrium states, but in the real (dynamic) world, the transition from a phase to another one takes time, and the growth of a phase involves a mechanism,

Table 3.3 Monolayer binding energy and critical temperature estimated for several systems using Eq. (3.67)

Substrate/adsorbate	Monolayer binding energy/eV	Critical temperature/K
Pd(111)/Ag	-0.58	1894
Pd(111)/Au	-1.08	3541
Pd(111)/Cu	-0.91	2981
Pt(111)/Ag	-0.37	1214
Pt(111)/Au	-0.64	2110
Pt(111)/Pd	-0.90	2976
Pt(111)/Cu	-0.65	2147
Au(111)/Ag	-0.63	2061
Pd(100)/Ag	-0.45	1488
Pd(100)/Cu	-0.63	2072
Pt(100)/Ag	-0.31	1004
Pt(100)/Cu	-0.44	1445
Au(100)/Ag	-0.44	1444

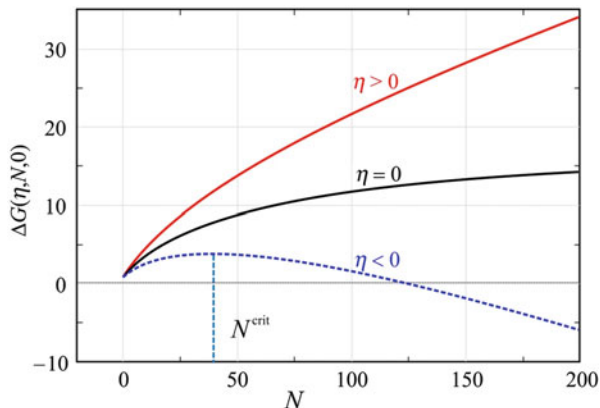
where both phases may coexist out of the equilibrium state, one being “swept out” by the other. For the sake of discussion, let us assume that we have reached equilibrium at some point $\mu < 0$ in Fig. 3.18, and we step the potential at some $\mu > 0$, defining an excess of chemical potential $\Delta\mu$. Thus, the system must evolve from a situation where the adsorbate looks very much like a gas, to another one where it has the appearance of a solid with defects. The question is: how does it evolve? The answer is not simple, since one of the important points to consider is how far from equilibrium we have driven the system. Let us assume that the final chemical potential is not much larger than 0, this would correspond to a small negative overpotential in the electrochemical system. At $\mu > 0$, small clusters of adatoms will form and dissolve, depending on their stability. Those able to grow at the chemical potential (overpotential) selected, will lead to the upd monolayer. The stability of these clusters is a function of their size and the excess of overpotential applied. The free energy to generate a cluster (nucleus) of N atoms is called the Gibbs energy of cluster formation,⁵ and is given by [45]:

$$\Delta G(N, \eta) = N\Delta\mu + \Phi(N) = -Nze|\eta| + \Phi(N) \quad (3.71)$$

where $\Delta\mu$ is the excess of chemical potential with respect to the chemical potential of phase coexistence, and $\Phi(N)$ is the excess of free energy required to generate the cluster from atoms residing in the full monolayer. This quantity can be written as function of the number of atoms of the 2D cluster as:

⁵ Also denominated work of cluster formation. Each state (N_i) does not represent a thermodynamic equilibrium state, since it does not correspond to a minimum in the free energy surface.

Fig. 3.21 Qualitative scheme of the Gibbs energy of cluster formation, as a function of the number of atoms of the conglomerate N . Note the monotonically growing behavior for $\eta \geq 0$ and the occurrence of a maximum for $\eta < 0$



$$\Phi(N) = 2\varepsilon\sqrt{b\Omega N} \quad (3.72)$$

where ε is an averaged specific edge energy, Ω is the area occupied by an adatom on the surface of the cluster and b is a geometric factor that depends on the shape of the cluster ($b = \pi$ for a circle). Thus, replacing (3.72) into (3.71) yields:

$$\Delta G = -Nze|\eta| + 2\varepsilon\sqrt{b\Omega N} \quad (3.73)$$

This equation states that the stability of a cluster has two contributions: one, the first, stemming from the driving force imposed by the overpotential, which is negative, and another, the second one in this equation, given by the fact that the cluster has edges, where the adatoms are less stable than in the complete monolayer, so it delivers a positive contribution. Equation (3.73) has a maximum at a certain $N = N^{\text{crit}}$, corresponding to the critical cluster size, see Fig. 3.21. Set at a given $|\eta|$, clusters with $N > N^{\text{crit}}$ will grow towards the infinite monolayer and clusters with $N < N^{\text{crit}}$ will dissolve. The critical cluster size may be obtained via differentiation of Eq. (3.73) to get:

$$N^{\text{crit}} = \frac{b\Omega\varepsilon^2}{ze_0|\eta|} \quad (3.74)$$

On the basis of the occurrence of growing nuclei, a theory of electrochemical phase growth under potentiostatic conditions has been developed, where the analysis of the behavior of the current as a function of time after a potential step plays a key role. This theoretical development has been widely analyzed in the literature [46–51] in term of the so-called nucleation and growth model, which been mainly focused on overpotential deposition (opd), that is, on the formation of deposits at potentials negative with respect to the Nernst reversible potential. Some typical theoretical results for potentiostatic current/time curves predicted from these theories are shown in Fig. 3.22.

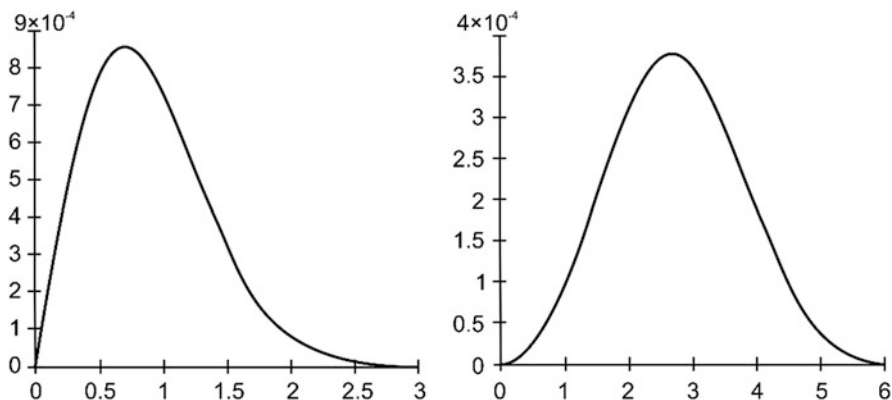


Fig. 3.22 Shape of the current/time transients for two dimensional nucleation and crystal growth, for two limiting cases: *The left* shows the so called “instantaneous” nucleation case, while the right one the “progressive” case (Adapted with permission from Ref. [51])

On the left, we see the so called “instantaneous” nucleation case, where it is assumed that the number of growing nuclei remains constant, while on the right we see the transient predicted for the “progressive” case, where the number of nuclei is assumed to increase linearly with time. Approximate equations describing the evolution of current with time have been derived for these two limiting cases, which are of the form:

$$i^{\text{instantaneous}} = A t \exp[-B t^2] \quad (3.75)$$

$$i^{\text{progressive}} = A' t^2 \exp[-B' t^3] \quad (3.76)$$

where A , A' , B , B' contain system specific parameters. The common feature for both cases is the occurrence of a maximum in the potentiostatic transients. The rising section corresponds to the growth of electroactive area as established nuclei grow and as new nuclei are formed, depending on the case. The transients reach in both cases a maximum due to overlap of the growing nuclei.

A very common diagnostic to test if the experimental data fit one or the other limiting case, consists in plotting the measured current divided the maximal current, as a function of the time divided by the time at which the maximum occurs. These plots are then compared with the corresponding version of the two curves presented in Fig. 3.22.

According to the discussion performed so far in this section, we can mention several criteria that must be met to assert for the occurrence of a first-order phase transition in an upd system:

1. Discontinuity in the adsorption isotherms.
2. Occurrence of sharp voltammetric peaks.
3. Non monotonic potentiostatic transients.
4. Appearance of growing clusters of the new phase on the surfaces.

To the previous conditions, we may also add the appearance of spikes in galvanostatic transients; large change in the slope of reflectivity vs. charge plots [63]; relative shift in the position of cathodic and anodic peaks, even at very low sweep rates; strong influence of the crystallographic nature of the substrate on the position of the peaks found for upd; influence of the supporting electrolyte on the half peak width and on the relative position of cathodic and anodic peaks and influence of the specific adsorption of foreign substances on the voltammetric features mentioned previously [52].

Although the visualization of upd as a first-order phase transition has a long history in electrochemistry [53–70], assertion of the occurrence of a first order phase transition is not trivial on the basis of the items described above, since the fulfillment of some of them is a necessary but not sufficient condition. For example, the influence of anions may generate isotherm discontinuity [71]; slope changes in the reflectivity plot may be attributed to changes in electronic states of the adsorbate [72] and non-monotonic current vs. time potentiostatic curves have been explained solving Eq. 3.60 for a potentiostatic step [73]. Concerning the diagnosis of the existence of nucleation and growth phenomena, it is worth mentioning the article by Bosco and Rangarajan [63], who gave a number of criteria for distinguishing between nucleation and adsorption processes from electrochemical measurements. Concerning experimental techniques, the advent of scanning probe microscopy (SPM) techniques, which allow direct visualization of surface structures, has made it possible the assessment of the formation of growing phases in-situ, so that in many cases the distinction between nucleation and growth phenomena and adsorption phenomena has become clearly possible. However, we will see that as a consequence of this observation, a much richer landscape, as well as new questions emerges.

An example of a system where island growth has been observed is given in Fig. 3.23, for upd of Ag on Au(100) [74, 75]. There are a number of facts that can be analyzed in these experiments, in the light of the models presented above. First, at least three sets of peaks are found in the cyclic voltammograms (see Fig. 2.1a of Chap. 2). Second, although these voltammograms do not present sharp spikes and the isotherms are rather smooth (see Fig. 2.13 of Chap. 2), in the scanning tunneling images we see clear evidence for the formation of islands, something consistent with the occurrence of a first-order phase transition. Third, islands can be detected at 200 mV, while there is no indication for their occurrence at higher potentials. However, a couple of peaks is clearly observable around 650 mV, which is labeled with A_1/D_1 in Fig. 2.1a and stable domains of an expanded quasi-hex Ag-induced overlayer structure are imaged in the range $200 \text{ mV} < \Delta E < 550 \text{ mV}$. This expanded layer is found to coexist with a quadratic overlayer, in the range $100 \text{ mV} < \Delta E < 200 \text{ mV}$, while finally only a commensurate quadratic (1×1) structure is observed at $\Delta E < 100 \text{ mV}$. The non observance of islands above 200 mV may be taken as an indication that the phases growing at higher potentials (especially that being formed at 650 mV) do not appear through a first-order phase transition. Note that the peak observed at this potential is the wider one, with a half width of about 90 mV, which according to Fig. 3.14 corresponds to $f \approx 0$. Although

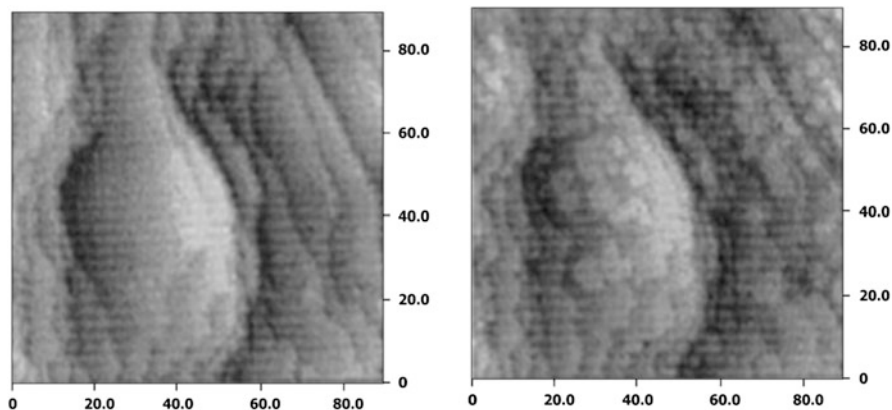


Fig. 3.23 Experimental results for Ag underpotential deposition of Ag on Au(100). In situ STM images of 2D island formation and limited growth. *Left*: $\Delta E = 500$ mV, no island formation. *Right*: $\Delta E = 200$ mV, island formation. The corresponding cyclic voltammogram and the adsorption isotherms obtained using the twin-electrode thin-layer technique is shown in Fig. 2.12 (Reprinted with permission from Ref. [75])

the other peaks (A_3/D_3) and (A_2/D_2) do not define sharp spikes, it is worth noting that they rather look like cusps, denoting some sort of blurred first-order phase transition. As can be observed in Fig. 3.23, the (100) surfaces are not perfect, but contain a number of steps and imperfections. Monte Carlo simulations performed by Gimenez et al. [76], have shown that the presence of defects smooths out adsorption isotherms. Figure 3.24 shows Monte Carlo simulations of Ag deposition on Au(111) modified by Au islands of different sizes. It is found that increasing number of defects, represented in this case by the presence of Au islands, makes the step in the isotherm less pronounced.

We conclude from the previous discussion that the strongest evidence for the occurrence of a first-order phase transition seems to be the observation of islands, while other electrochemical evidence is more difficult to interpret. We also expect that, for a given metal as a substrate, those surfaces where the adatoms are closer to each other should be more prone to show first-order phase transitions. In the case of *fcc* substrates, since the (111) surfaces exhibit adsorption sites which are closer to each other than those on the (100) surfaces, the former should exhibit sharper peaks in the voltammetric profiles, which are an indication for a first-order phase transition. An analysis of the voltammogram for upd of different metals on Ag and Au surfaces shows that this is overall valid, while in the case of Pt this is much less evident. This is illustrated for some sample systems in Fig. 3.25, where the voltammograms for several upd systems obtained with (111) and (100) single crystal surfaces are compared. As discussed below, the upd systems involving Pt present a much stronger influence of the composition of the electrolyte, and the simplistic lattice gas model cannot account for the particular behavior of these systems

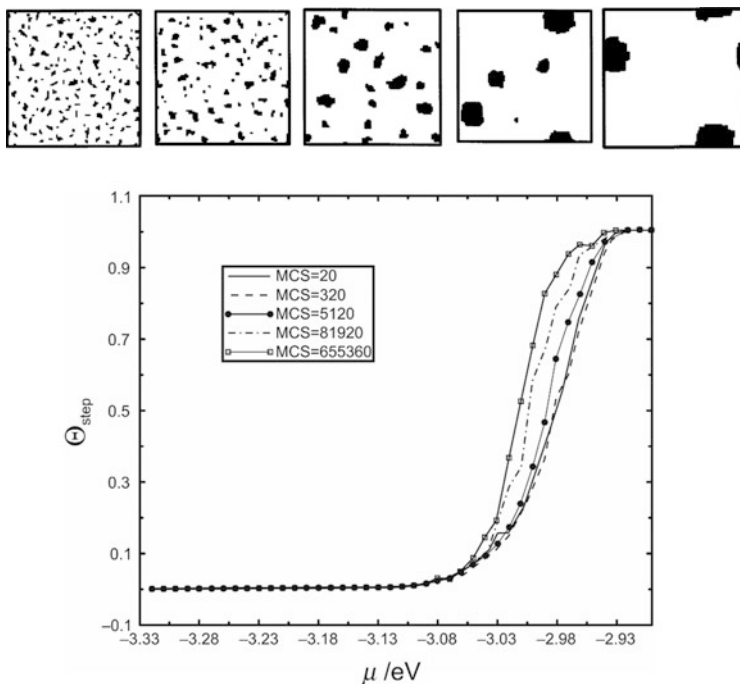


Fig. 3.24 Adsorption isotherms for Ag deposition on Au(100) in the presence of surface defects. Each *curve* corresponds to one of the five systems with Au islands on the substrate illustrated on the top (Reproduced with permission from Ref. [76])

We have compiled in Table 3.4, for the selected upd systems, experimental information concerning the observation of islands, the occurrence of non-monotonic *i/t* potentiostatic transients and appearance of sharp voltammetry peaks. It must be taken into account that this table just provides a bird-eye view on possible occurrence of first-order phase transitions in the different systems, since most of them show several voltammetric components, the occurrence of expanded phases and even bilayers. In each case, we consider that voltammetric component that appeared as the most firm candidate for a first order phase transition. We make a brief analysis of these systems.

The Ag(111)/Pb and Ag(100)/Pb systems present three voltammetric pairs of peaks (See Fig. 3.25a). In both cases, we focus on the sharpest, central component. In the first of these systems, Lorenz et al. [80] estimated an interaction parameter $f = -3.5$, that is, very close to the value expected for a first-order phase transition, and found galvanostatic *i/t* transients presenting a hump. In a more recent article, Carnal et al. [78] reported STM images showing the border of an “incomplete” Pb monolayer, coexisting with a naked Ag(111) surface. For the second of these systems, Schmidt et al. [157] found decoration of steps of the Ag(100) surface, with the subsequent formation of 2D Pb islands at lower potentials. Also step decoration has been found in the case of Tl upd on Ag(111) [78], thus indicating the formation

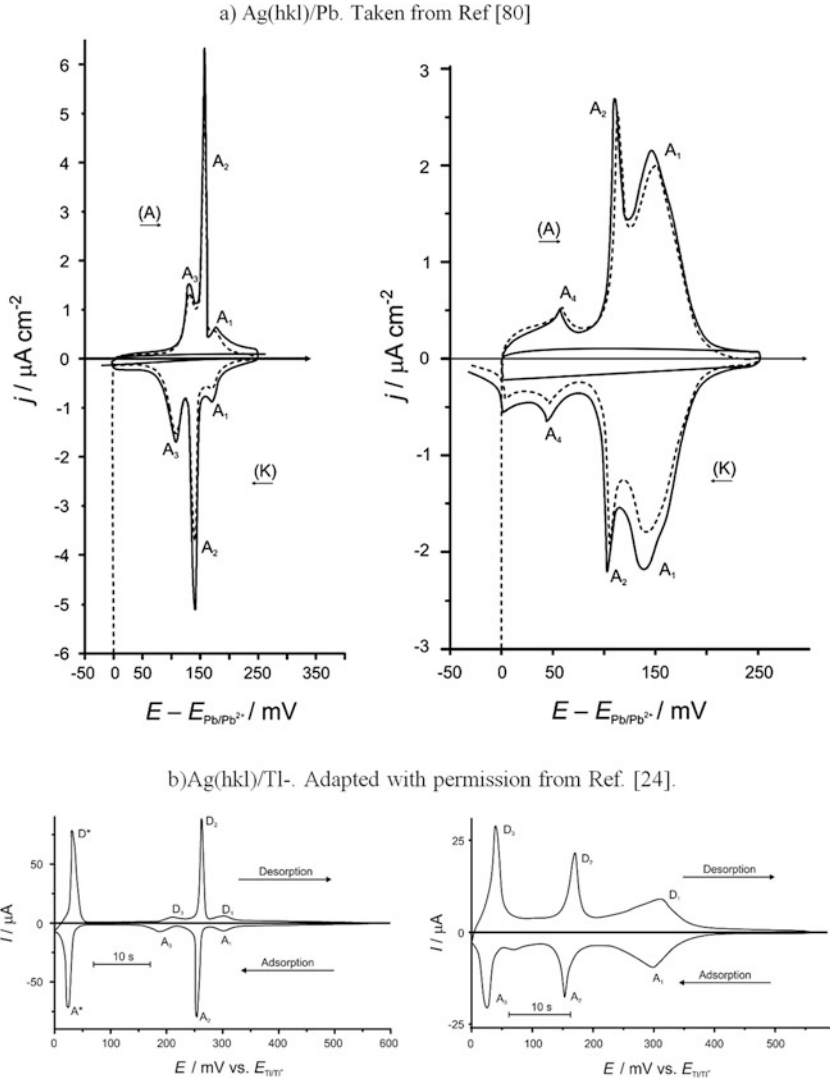
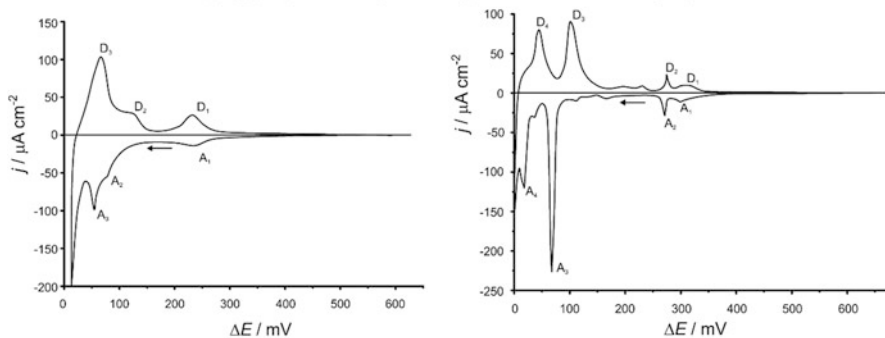
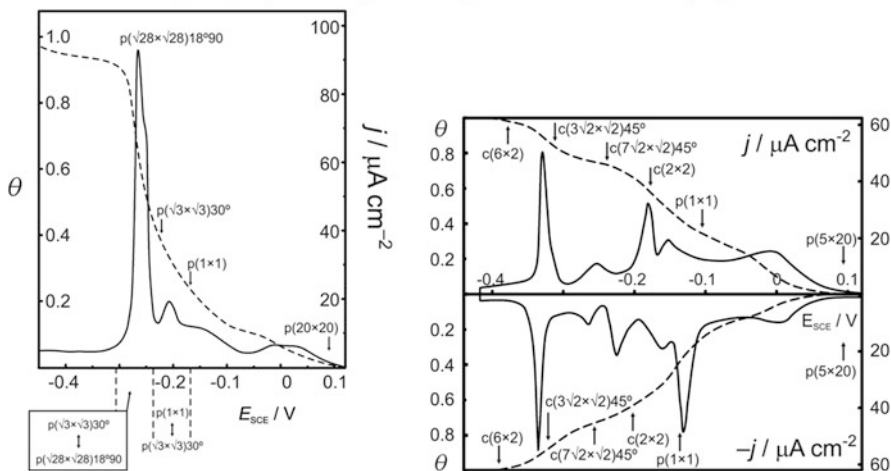


Fig. 3.25 (continued)

c) $\text{Ag}(hkl)/\text{Cd}$ -. Adapted with permission from Ref. [87].



d) $\text{Au}(hkl)/\text{Pb}$. Adapted with permission from Ref. [98].



e) $\text{Au}(hkl)/\text{Bi}$ - Left: Adapted with permission from Ref. [107]. Right: Adapted with permission from Ref. [160].

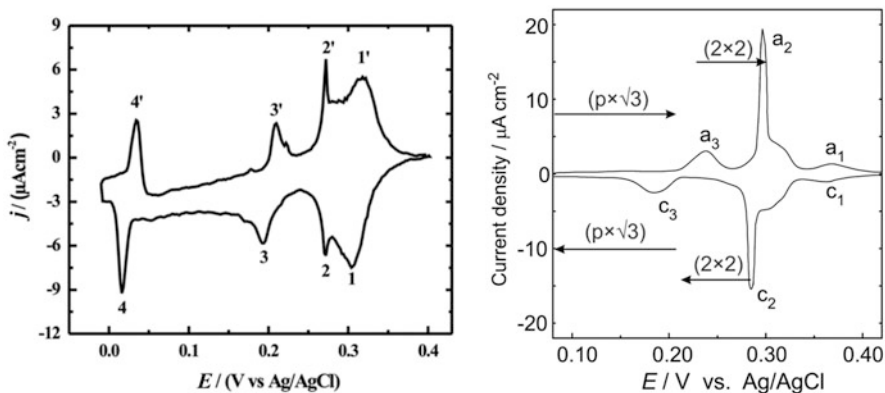


Fig. 3.25 (continued)

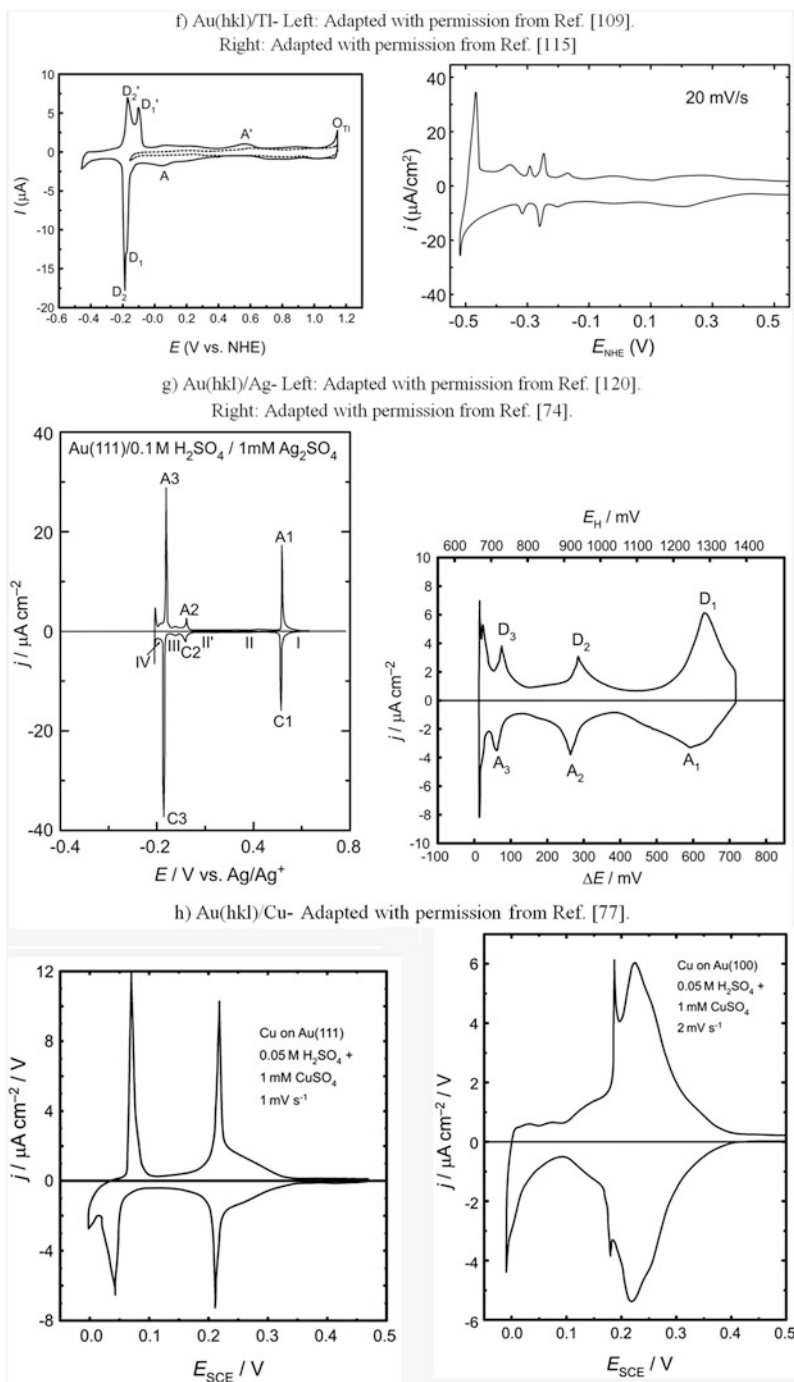


Fig. 3.25 (continued)

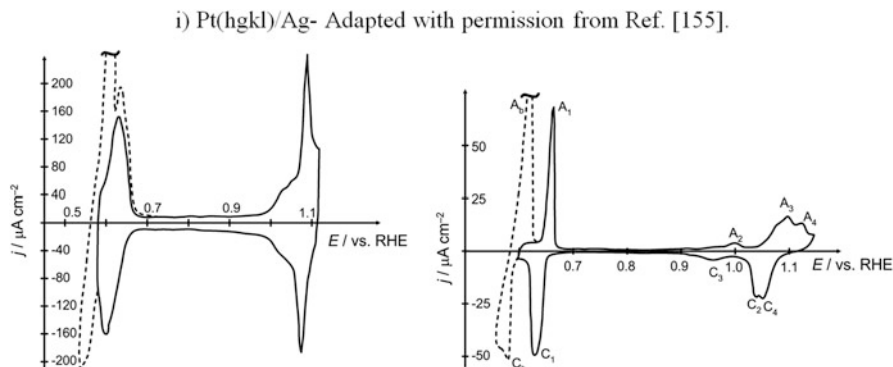


Fig. 3.25 Comparison of voltammetric profiles obtained for upd of different adsorbates on Ag, Au and Pt, (111) (*left*) and (100) (*right*) substrates. Note that as the general rule the voltammetric peaks for (111) surfaces are usually sharper than those for (100) surfaces. This can be understood in terms of the lattice gas model described above the coupling between adsorbates on (111) surfaces is stronger than on (100) ones, since they are close to each other, so they are more prone to present a first-order phase transition. (a) Ag(hkl)/Pb (Taken from Ref. [80]). (b) Ag(hkl)/Tl- (Adapted with permission from Ref. [24]). (c) Ag(hkl)/Cd- (Adapted with permission from Ref. [87]). (d) Au(hkl)/Pb (Adapted with permission from Ref. [98]). (e) Au(hkl)/Bi- (Left: Adapted with permission from Ref. [107]). (Right: Adapted with permission from Ref. [160]). (f) Au(hkl)/Tl- (Left: Adapted with permission from Ref. [109]). (Right: Adapted with permission from Ref. [115]). (g) Au(hkl)/Ag- (Left: Adapted with permission from Ref. [120]). (Right: Adapted with permission from Ref. [74]). (h) Au(hkl)/Cu- (Adapted with permission from Ref. [77]). (i) Pt(hgkl)/Ag- (Adapted with permission from Ref. [155])

of the new phase via a first-order phase transition. In the case of Tl upd on Ag(100), sharp voltammetry features were reported in Refs. [24, 67, 86], but no island formation was reported in these articles.

In the case of Cd deposition on Ag(111)(Fig. 3.25c), all three criteria for the occurrence of a first-order phase transition are met: existence of islands, non-monotonic i/t transients and sharp peaks in the case of the main reduction process [87]. However, it was noticed in the latter article that the potentiostatic transients showed a significant deviation from the theoretical transients predicted by the classical models for instantaneous and progressive 2D nucleation, shown above in Fig. 3.22, indicating that the growth of 2D Cd clusters is slower than expected from the standard models. In the case of Cd deposition on Ag(100) [87], there is also some indication for the occurrence of sharp peaks, but the different process cannot be clearly separated.

Upd of Pb on Au(111) shows a sharp main peak [90, 93, 97, 98] (Fig. 3.25d, left), as well the occurrence of island formation. On the other hand, Pb upd on Au(100) (Fig. 3.25d, right), presents at least four couples of peaks, from which we report the peak half width of the most negative component, in the anodic sweep. In the case of Ag upd on Au(100) and on Au(111), we also report the information concerning the peak located at the most negative potentials (see below).

Table 3.4 Compilation of information supporting the occurrence of first-order phase transitions in upd systems. We consider the occurrence of islands/domain boundaries, non-monotonic transients and sharp peaks. Some sample values of half-peak widths $\Delta E_{1/2}$ are given. They correspond to the upd peak closer to the bulk metal deposition or to the most important component. In the case of a langmuirian process, $\Delta E_{1/2} \approx 100$ mV

Substrate/ adsorbate	Observation of islands/ domains/step decoration	Non monotonic i/t potentiostatic transients or with shoulders	Sharp voltammetric peaks, $\Delta E_{1/2}$
Ag(111)/Pb	Yes, step decoration [78, 79]	Yes [71, 80, 81, 118]	Yes [57, 71, 79, 80, 82, 83, 118] ≈ 10 mV [83]
Ag(100)/Pb	Yes, step decoration, island formation [79, 157]	Not reported	Yes [79, 83] 12 mV [83]
Ag(111)/Tl	Yes [78]	Yes [72, 73, 84]	Yes [24, 71, 85, 96] 6 mV [24]
Ag(100)/Tl	Not reported	Not reported	Yes [24, 67, 85, 86] 9 mV [24]
Ag(111)/Cd	Yes [87, 88]	Yes [87]	Yes [89, 96] 10 mV [87]
Ag(100)/Cd	Yes [87]	Not reported [87]	No [87]
Au(111)/Pb	Yes [90–95]	Not reported	Yes [9, 95, 96, 112] 12 mV [90], 38 mV [97], 25 mV [98] 30 mV ⁹³
Au(100)/Pb	Not reported	Not reported	Yes [118] 20 mV [157], 19 mV [97], 13 mV [98]
Au(111)/Bi	Not reported	Yes [107, 99] Yes, on a Ag-Covered Au (111) surface [103]	Yes [9, 99, 100–106] 8 mV [107], 11 mV [108]
Au(111)/Tl	Not reported	Yes, shoulder [109]	Yes [9, 109–112] Yes, Br ⁻ coadsorption [113, 114]
Au(100)/Tl	Not reported	Not reported	Yes [115]
Au(111)/Ag	Yes [116–118] Step growth [119–121]	Exponential behavior [116]	Yes [117, 120, 122–131] 10 mV [132], 11 mV [133], 14 mV [10]

(continued)

Table 3.4 (continued)

Substrate/ adsorbate	Observation of islands/ domains/step decoration	Non monotonic i/t potentiostatic transients or with shoulders	Sharp voltammetric peaks, $\Delta E_{1/2}$
Au(100)/Ag	Yes [74, 75] Preferential deposition at imperfections [134] Step decoration [118]	Not reported	Yes 30 mV [119]
Au(111)/Cu	Yes [135–137] domain boundaries observed [135, 138, 139]	Yes [140–143]	Yes [62,136,140,142,144– 146,164,205] 10 mV [147], 9 mV [148]
Pt(111)/Ag	Island growth of the second up layer on the first [149]	Yes, iodine pretreated Surface [150]	Yes [149, 151] 20 mV [152] Only for the bilayer [153–155] 9 mV [156]

Bi upd on Au(111)(Fig. 3.25e, left) yields two ordered phases [158, 108]: a commensurate (2×2) -Bi phase with a quarter monolayer coverage and a close packed $(p \times \sqrt{3}) - 2\text{Bi}$ phase with the coverage varying between 0.61 and 0.67 monolayer, depending on applied potential. Studies using surface X-ray scattering and current transients [99] showed that the zero-coverage \rightarrow commensurate (2×2) phase transition occurred three orders of magnitude more rapidly than the $(2 \times 2) \rightarrow$ high-coverage incommensurate phase transition. However, while nucleation and growth kinetics was observed for transitions involving Bi desorption, langmuirian adsorption kinetics was observed both transitions involving Bi adsorption. A subsequent study on this system by Tamura et al. [107] showed that the current transient curve may not reflect the phase transitions taking place and suggested that a structural analysis by a different technique is fundamental in the phase transition studies. This conclusion is probably valid for several of the upd systems considered here. The related system, Bi upd on Au(100) (Fig. 3.25e, right) presents three superstructures that have been identified by X-ray scattering [159, 160], exhibiting sharp voltammetry features.

Tl upd on Au(111) (Fig. 3.25f, left) shows two sharp pairs of peaks [110, 111], which in alkaline solutions have been related to a phase transition between a coadsorbed OH/Tl phase and a close-packed Tl monolayer [110]. The surface X-ray scattering measurements performed in the later work also allowed finding discontinuities in the hexagonal lattice constant and in the rotation angle of the Tl incommensurate monolayer. From the behavior of this system and some of the previous discussion, we can conclude that the in the upd of Tl, Pb and Bi on Ag (111) and Au(111) adatom-adatom interactions play the major role determining the

Table 3.5 Compilation of information on the effect of solution composition on some representative upd systems on Ag, Au and Pt (111) substrates

Substrate/ adsorbate	Effect of anions on upd features
Ag(111)/Pb	In the presence of ClO_4^- the electrosorption valency is 2 [83] Peak sharpening by acetate ions [81, 111] X-ray scattering shows that acetate is not found to alter the structure of the Pb monolayer [111] Remarkable peak sharpening in the presence of acetate and small <i>negative</i> shift in peak potential [96] Peak sharpening by Cl^- ions [82]. Pb adsorption range undergoes narrowing. Citrate ions generate non-monotonic <i>i/t</i> transients [71], sharpening and small negative shift of voltammetric peaks [96]
Ag(111)/Tl	Ideal charge stoichiometry of the adsorbate reported in $\text{HClO}_4\text{--Na}_2\text{SO}_4$ [24], indicating the absence of specific anion adsorption Acetate and citrate yield slight <i>widening</i> of voltammetric peaks [96] X-ray scattering shows that acetate is not found to alter the structure of the Tl monolayer with respect to ClO_4^- solutions [111]
Ag(111)/Cd	Acetate and citrate yield slight <i>widening</i> of voltammetric peaks and small shift in peak potentials [96]
Au(111)/Pb	IR experiments show that Pb upd is not accompanied by coadsorption of electrolyte anions or associated water both in H_2SO_4 and HClO_4 solutions [187] X-ray scattering shows that acetate is not found to alter the structure of the Pb monolayer with respect to ClO_4^- solutions [111]
Au(111)/Bi	Fast Fourier transform electrochemical impedance spectroscopy studies of coadsorption ClO_4^- indicate that the surface coverage of ClO_4^- on Au would be considerably less than that of the coadsorbing Bi [188]
Au(111)/Tl	X-ray scattering shows that acetate is not found to alter the structure of the Tl monolayer with respect to ClO_4^- solutions [111]
Au(111)/Ag	Changes in the Au(111) surface morphology upon repeated upd cycling seem to be stronger in perchloric than in sulfuric acid solutions [189] An electrosorption valency of 1 is obtained in sulphuric acid, so that coadsorption or competitive adsorption of anions was excluded [74]. However, a nearly constant anion coverage in the entire Ag upd range was not excluded AES and radiotracer studies show that in fact adsorbed sulfate species are present prior to and after upd [190]. Thus, the current passed in forming the Ag adlayer does not contain a significant contribution from sulfate adsorption AFM found different structures for the overlayer in different electrolytes: (3×3) in sulfate, (4×4) in nitrate, a close-packed in acetate and an open one in perchlorate [191] LEED experiments from emmersed electrodes from HF solutions yield different surface structures [10], like (1×1) , (3×3) , (5×5) , etc., see Table 3.1 In situ STM found $(\sqrt{3} \times \sqrt{3})R30^\circ$ in H_2SO_4 and (4×4) in HClO_4 for the most positive peak couple [126]. A close packed Bi structure was found at large coverage degrees Another STM study found in H_2SO_4 a $(\sqrt{3} \times \sqrt{3})R30^\circ$, a distorted hexagonal stripe pattern, a (3×3) and a (1×1) structure [120] for a sequence of

(continued)

Table 3.5 (continued)

Substrate/ adsorbate	Effect of anions on upd features
	decreasing potentials (3 × 3) structures were found in the presence of iodine [125]
Au(111)/Cu	In H ₂ SO ₄ , there is consensus for the occurrence of a ($\sqrt{3} \times \sqrt{3}$)R30° structure, being formed at the more positive upd peak couple, consisting of 2/3 monolayer Cu and 1/3 monolayer sulfate [164, 192] which is transformed into a (1 × 1) Cu structure at lower potentials [162]. Recent experiments, however, point out towards the occurrence of an ordered sulfate p(2 × 2) [136] or ($\sqrt{3} \times \sqrt{3}$)R30° [193] structure on the pseudomorphic Cu(1 × 1) upd layer. Addition of Cl ⁻ generates, depending on its concentration, a (2 × 2) or an incommensurate “(5 × 5)” structure [137]. X-ray absorption experiments suggest that copper and coadsorbed chloride form a bilayer in which copper atoms are sandwiched in-between the top chloride and the bottom gold layers [34].
Pt(111)/Ag	Ag upd peak does not follow the Nernstian behavior of 60 mV shift per decade change in cation concentration expected [153]. Radiometric measurements show that adsorption of bisulfate is higher on silver-covered platinum than on the clean platinum substrate [194].
Pt(111)/Cu	Cu upd on Pt(111) in HClO ₄ is found to be a relatively slow process. The presence of chloride and (bi)sulfate anions facilitates upd and causes a splitting in the voltammetry peaks. This splitting was attributed to competition between the Cu adatoms and the adsorbed anions [184]. Cu is found to induce an enhanced adsorption of chloride and bromide. Exceedingly sharp voltammetric peaks are found, and a mechanism for upd was proposed involving the transient formation of a preadsorbed state consisting in a Cu-anion adlayer, yielding finally a Cu monolayer covered by an anion adlayer [166]. XANES analysis supports the idea of a partially discharged copper adlayer [195] in sulfuric acid media. LEED/RHEED studies show that the addition of different concentrations of chloride ions leads to the formation of four different superlattices on top of a pseudomorphic-grown Cu upd layer [173]. It was recognized that anion coadsorption adsorption makes a reliable evaluation of the copper coverage from charge measurements impossible [180].

structure of the monolayer. The interaction of the adsorbate with the substrate is strong, allowing upd, but its effect on determining the monolayer structure is small. This is the reason why the evidence for the existence of a first-order phase transition is strong, as expected on the basis of the lattice gas model discussed at the beginning of this Section. Surface X-ray scattering has also allowed the identification of three phases in the case of Tl upd on Au(100) [115], but the voltammetric features are considerably less pronounced for this substrate. The weaker adsorbate-adsorbate interaction in the more open (100) face is probably responsible for this behavior.

The system Au(111)/Ag (Fig. 3.25g, left) presents strong evidence for the occurrence of a first-order phase transition which is manifest by the occurrence of islands [116, 117] or step growth [119–121]. Sharp peaks are also frequently observed in voltammograms, as reported in the references given in Table 3.5.

However, the sharpness of the voltammetric peaks seems to be related to the nature of the anion present in the electrolyte. In fact, Chen et al. have studied this system in different electrolytes [124], finding sharp peaks in sulphuric acid but considerably smoother voltammetric profiles in perchloric acid. The packing densities of the different monolayers were found to change with the size of different electrolytes, showing little agreement with the expectation predicted by the coulometric measurements. This was pointed out as an indication for different amounts of charge transfer between electrolyte and adatoms. As pointed out above, the system Au(100)/Ag (Fig. 3.25g, right) shows clear evidence for island formation [74, 75], while in the case of Au(111)/Ag rather step decoration is found. This different growth type has been explained on the basis of the different time scales for Ag diffusion on Au(100) and Au(111) surfaces, using kinetic Monte Carlo simulations [161].

Cu on Au(111) (Fig. 3.25h, left) is one of the systems that probably has attracted the largest attention among upd, as it has been vastly investigated by a wealth of experimental techniques [162]. As pointed out above and can be seen in the figure, Cu upd on Au(111) present two couples of peaks. The peak pair located at about 0.27 V vs. Cu/Cu²⁺ is attributed to the formation/dissolution of the $(\sqrt{3} \times \sqrt{3})R30^\circ$ phase, which is highly reversible with almost no difference in peak potential. The second peak pair at about 0.13 V vs. Cu/Cu²⁺, is less reversible and corresponds to the transition between the $(\sqrt{3} \times \sqrt{3})R30^\circ$ phase and the (1×1) adlayer. This system shows non monotonic *i/t* transients, as studied in detail by Hölztle et al. [140–142], who have modeled satisfactorily these transients assuming that adsorption (desorption) process takes place parallel to an instantaneous nucleation and growth phenomenon, with both proceeding at different electrode sites. In a more sophisticated approach, kinetic Monte Carlo simulations along with effective lateral interactions including adsorbed cations and sulfate anions were used by Zhang et al. to reproduce these transients [163]. See discussion in Chap. 4. It must be pointed out that the interpretation of the phase transitions taking place in this system, responsible for the two couples of peaks mentioned, is considerably more involved [202–204, 164] than that given above in terms of the monatomic gas lattice model. The occurrence of islands corresponding to the different phases has been confirmed in various articles [135–137]. These systems also present relatively sharp voltammetric peaks, although the less negative pair presents always the larger irreversibility.

Upd of Ag on Pt(111) presents two main pairs of peaks (see Fig. 3.25h, left) although its deposition has been divided into four distinct steps [151, 155, 153], three of them occurring at the more positive potential, related to the formation of the upd monolayer. These upd processes, taking place at relatively high potentials, have been the subject of some controversy [162], since they appear to be sensitive to the quality of the single crystal. Furthermore, they do not follow the expected Nernstian behavior of 60 mV/decade. The most negative peak couple, close to the bulk deposition potential, is due to the formation of a bilayer, for which evidence of island formation has been observed in STM experiments [149]. Concerning the occurrence of non-monotonic potentiostatic transients, these have been measured

for metal electro sorption on a Pt(111) surface covered with a monolayer of iodine [150].

We devote here a sentence to the system Pt(111)/Cu, which has not been included in the present Table, but has been the subject of intensive research [165–186]. Cu upd on Pt(111) is extremely sensitive to the anion composition of the solution, as compared with other systems, as shown in several of these articles. For example, White and Abruña have shown that the potential for upd of Cu on Pt(111) decreases in the order of $\text{Cl}^- > \text{Br}^- > \text{I}^- > \text{S}^{2-}$, following a linear relationship with the standard reduction potential for the half-cell reaction $\text{CuX} + \text{e}^- \rightarrow \text{Cu} + \text{X}^-$. Remarkably, the sharpest voltammetric components are found in the case of the most strongly adsorbing Cl^- ions. Other systems related to Pt(111) present a singular behavior, yielding irreversible adsorbates which endure several oxidation/reduction voltammetric cycles. This is for example the case of Pt(111)/Tl, Pt(111)/Pb, Pt(111)/Bi, just to mention adsorbates close to those previously considered.

As we go along the literature involving upd on Ag, Au and Pt, we note an increasing role of anions in the upd systems on these substrates. A particular case of this situations are the just mentioned irreversible upd systems on Pt(111), which, according to experiments in UHV show that water species (HO;O) play a role in the formation of these deposits. To make this evident, we have summarized in Table 3.6 results for upd on (111) faces, where we indicate, along with the corresponding reference, the influence of anions in the different systems. Inspection of the Table shows that while in the case of upd on Ag(111) surfaces the influence of anions is usually restricted to sharpen the voltammetric upd peaks, in the case of Au new peaks appear as a consequence of the anions, while in the case of upd on Pt(111) surface the interaction with the solution is so strong that it ends in occurrence of irreversible components, in the sense that adsorption/desorption peaks appear even in the absence of cations in the corresponding solution.

Far from being an extensive analysis, the summary made in Table 3.5 for some typical upd systems shows the wide universum of behaviors concerning the influence of electrolyte on upd. The two extrema are exposed in Fig. 3.26. On one side, the addition of citrate and acetate to Tl upd on Ag(111) barely changes the shape

Table 3.6 Number of particles exchanged by the subsystem in Fig. 3.29 with the reservoir, according to Eqs. (3.77), (3.84), (3.86), (3.88), (3.90) and (3.92), which added yield the global reaction (3.79). These numbers are to be inserted in Eq. (3.81)

Equations	ΔN_e^M	ΔN_e^S	$\Delta N_{A^{a-}}$	$\Delta N_{M^{r+}}$	ΔN_{X^-}	ΔN_{K^+}	ΔN_W
(3.84)	0	Q_1/e_0	0	0	$-I_{\text{dis}}$	$-j_{\text{dis}}$	$-k_{\text{dis}}$
(3.86)	0	0	0	0	$-I_{\text{desolv}}$	$-j_{\text{desolv}}$	$-k_{\text{desolv}}$
(3.88)	0	$z - na$	n	l	0	0	0
(3.90)	0	0	0	0	I_{solv}	j_{solv}	k_{solv}
(3.92)	0	$-Q_2/e_0$	0	0	I_{ch}	j_{ch}	k_{ch}
(3.77)	$-\lambda$	0	0	$-\lambda/z$	0	0	0

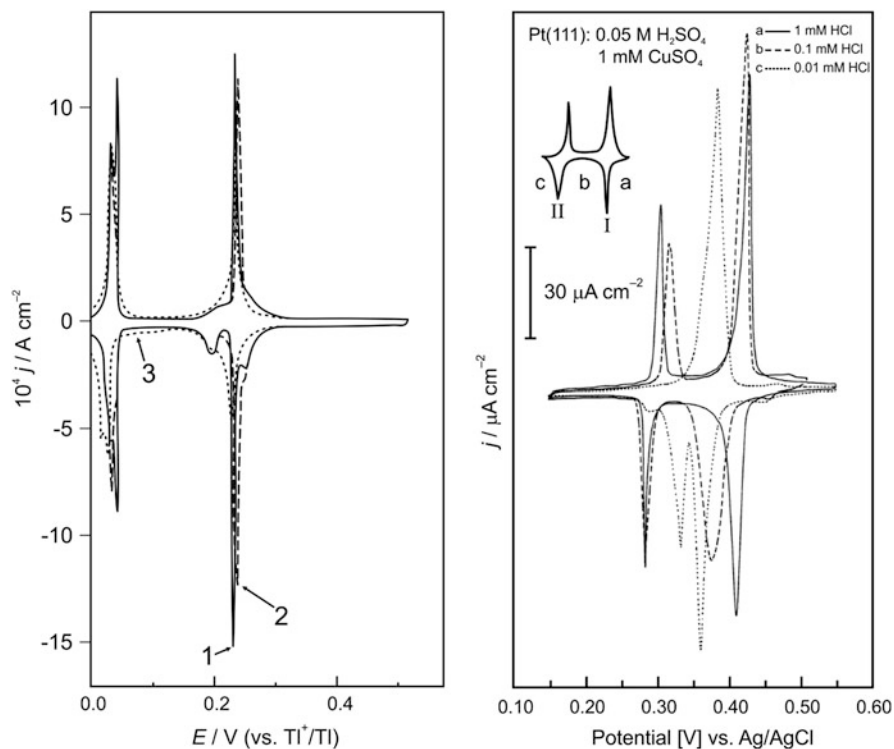


Fig. 3.26 Two extreme behaviors concerning anion effect on upd. *Left*: effect of the addition of acetate (2) and citrate (3) to Tl upd on Ag(111) (Reprinted with permission from Ref. [96]). *Right*: effect of the addition of different chloride concentrations to Cu upd on Pt(111) (a) (—) 1 mM HCl, (b) (---) 0.1 mM HCl and (c) (⋯) 0.01 mM HCl (Reprinted with permission from Ref. [173])

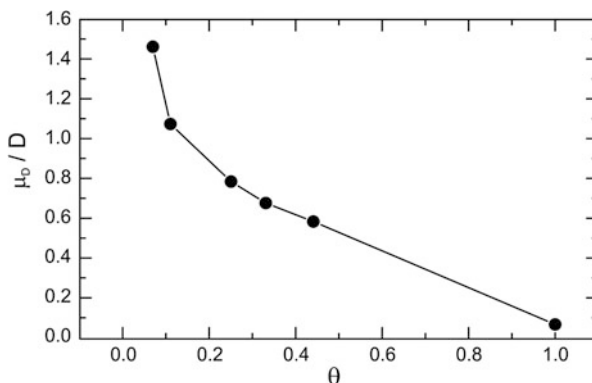
and height of the voltammetric components. On the other, the addition of chloride ions to upd of Cu on Pt(111) produces both a splitting and a strong shift of the voltammetric peaks. While the thermodynamic framework that should be used to interpret the experimental information was given in Sect. 3.5, the stability of these systems in terms of model calculations will be addressed in the next Section.

3.7 A Thermodynamic Formulation Oriented to Theoretical Modeling of Underpotential Deposition as a Phase Transition, Including Ion Coadsorption, Solvent and Double Layer Effects

We have seen above that the theory developed by Vetter and Schultze provided an interesting scope on the upd problem, emphasizing on the role that the different components of the systems play in determining the properties measured. At the time the previous modeling formulation was developed, the theoretical formulation was oriented to draw general conclusions and trends on the basis of the experimental information available. However, in the last decades the increasing computational power and the systematic application of quantum mechanics have allowed not only drawing general trends but also being able to make quantitative predictions for specific systems. This is for example the case of the prediction of electrode potentials from first-principles calculations, in some cases within a few tenths of millivolts of the experimental values [196–198]. In this respect, it would be desirable to establish a thermodynamic formulation that makes it possible to make predictions making use of these new possibilities. Before setting up this modeling, we revisit the main features of the upd system, already introduced in the models present above:

1. The metallic substrate/adsorbate system. This is the part of the system that is straightforward to treat with the modern quantum mechanical tools. As it will be discussed in Chap. 5, the underpotential shift ΔE^{upd} defined at the beginning of this chapter can be estimated from two calculations: the binding energy of the adsorbate M to the substrate S and the cohesive energy of bulk M. This is a good approximation for compact adsorbates and in those cases where the work function difference between bulk M and bulk S is small. In the first case, this so because in the case of compact upd adsorbates, adatoms present a larger depolarization [199], so that solvation effects should be smaller and may be neglected. Figure 3.27 shows effective dipole moments of Ag atoms adsorbed on

Fig. 3.27 Effective dipole moments in Debyes, as a function of the coverage degree for Ag atoms adsorbed on Au(111), as obtained from DFT calculations (Reprinted with permission from Ref. [28])



Au(111) as a function of the coverage degree, where it can be appreciated that at full coverage the effective dipole moment of Ag atoms is practically negligible. In the second case, if the work functions of M and S are similar, the shift of the potential of zero charge of the surface upon adsorbate building up will be small and potential anion coadsorption effects will be diminished.

2. The solvent. As stated in the previous paragraph, this effect may be neglected in some cases but in the case of upd in the presence of coadsorption it could become very important.
3. Coadsorbed anions. These will appear in systems with large shifts in the potential of zero charge upon adsorbate building up. A paradigmatic example is the coadsorption of sulfate with copper species on Au(111) [200–204], which defines an stoichiometric 2D compound. As will be discussed in Chap. 5, it appears that coadsorbed anions are the main responsible for the occurrence of upd in this system.
4. The electrical double layer. The effect of the electrical double layer (EDL) on the stability underpotential deposits has been seldom considered in the modern upd theories. The EDL contributes to this stability in two ways: first, the double layer of the substrate disappears upon formation of the deposit. Second, it is again rebuilt on the substrate/adsorbate system. In the case of S/M metal pairs presenting large work function differences, this contribution could become important.

The scheme used to model the upd system taking into account the features discussed in the previous points 1–4 is given in Fig. 3.28. The physical picture is very close to that presented in Sect. 3.5.1, but it deviates in some aspects that will be discussed in detail. The electrochemical cell contains a working electrode, made of the metallic substrate S on which the adsorbate M is deposited at underpotentials, but the reference electrode is now made of the bulk metal M. Thus, the potential difference measured between the two electrodes (using a proper connection) upon ML formation at equilibrium will be the underpotential shift ΔE^{S-M} . The system under consideration is now connected to an infinite reservoirs containing solvent, anions and cations at the electrochemical potentials μ_W^{sol} , $\tilde{\mu}_{X^-}^{\text{sol}}$, $\tilde{\mu}_{A^{a-}}^{\text{sol}}$ and $\tilde{\mu}_{K^+}^{\text{sol}}$, $\tilde{\mu}_{M^{z+}}^{\text{sol}}$, respectively. While $M_{(\text{aq})}^{z+}$ and A^{a-} denote species that may interact chemically with the substrate, K^+ and X^- indicate ionic species that only participate (without adsorbing) in the building up of the electrical double layer, along with the electronic charge located at the electrode. To fix ideas, if we think of Cu upd on Au(111) electrodes, $M_{(\text{aq})}^{z+}$ would be $\text{Cu}_{(\text{aq})}^{2+}$, A^{a-} would be SO_4^{2-} or HSO_4^- , K^+ could be Na^+ or another non-adsorbing cation, and X^- could be ClO_4^- or another non adsorbing anion. The latter two species should be in excess, constituting the supporting electrolyte.

We will also assume that the contributions of $M_{(\text{aq})}^{z+}$ and A^{a-} to the EDL are negligible (that is, their concentrations are negligible in comparison with that of the supporting electrolyte).

We consider the following electrochemical reactions at the electrodes:

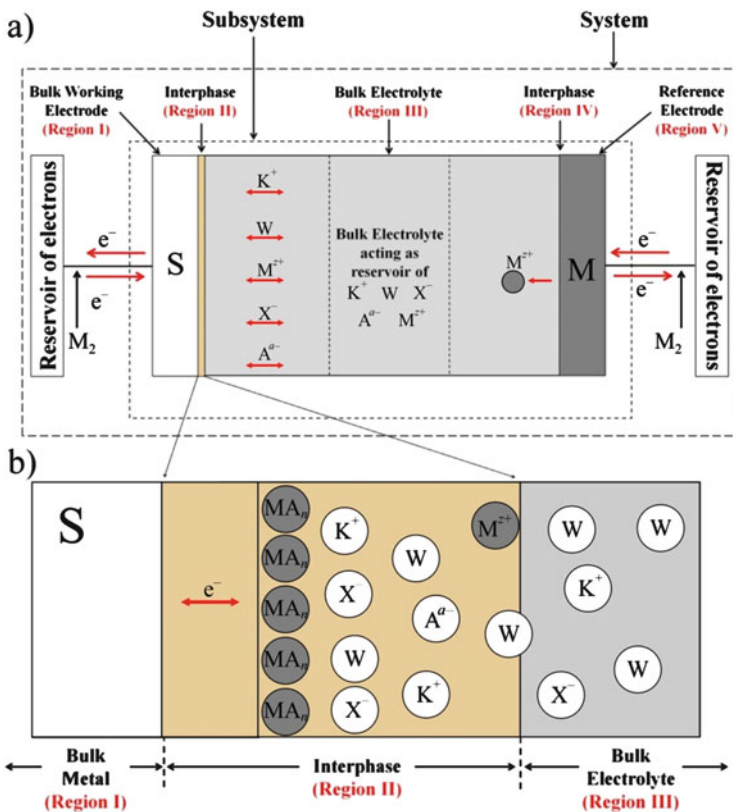
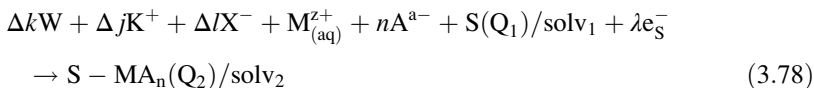
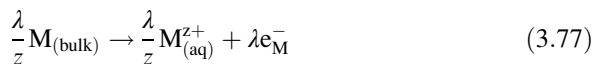


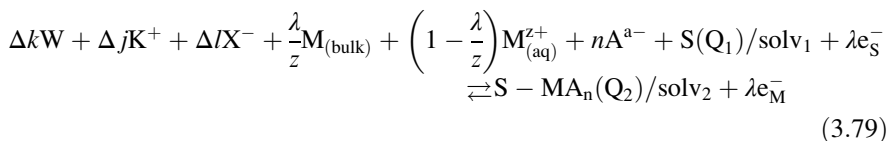
Fig. 3.28 (a) Scheme of the electrochemical system used to evaluate underpotential shift accounting for solvent, the occurrence of anion coadsorption and electrical double layer effects. The internal dotted line encloses the subsystem containing the electrodes and the electrolyte. The subsystem is connected to two electron reservoirs and to another reservoir containing solvent W, the anionic X^- , A^{a-} and cationic K^+ , $M_{(aq)}^{z+}$ species at the electrochemical potentials $\tilde{\mu}_W^{\text{sol}}$, $\tilde{\mu}_{X^-}^{\text{sol}}$, $\tilde{\mu}_{A^{a-}}^{\text{sol}}$, $\tilde{\mu}_{K^+}^{\text{sol}}$ and $\tilde{\mu}_{M^{z+}}^{\text{sol}}$, respectively. (b) zoom of the interphase under study



where Δk , Δj , and Δl denote the changes in the number of water, cationic K^+ and anionic X^- species at the interphase II upon formation of the upd deposit, λ is the number of electrons flowing to this interphase for the formation of the MA_n species, and Q_1 and Q_2 denote the charges on the surface of the electrode before and after

this process. The term “solv” indicates that the surface of the electrode is solvated in states solv_1 and solv_2 before and after upd respectively.

Addition of Eqs. (3.77) and (3.78) leads to the global reaction:



Note that in reaction (3.79), a number $(1 - \lambda/z)$ of the $M_{(\text{aq})}^{z+}$ core ions building $S - MA_n$ must come from the solution. This is to be contrasted with the reverse of the cycle shown above in Fig. 3.3. There, we see that to get *one* adsorbed $M_{(\text{S})}^{z+}$ species on S, *we just need* one $M_{(\text{M})}^{z+}$ core ion taken from bulk M. This one-to-one relationship has as a consequence that the underpotential shift $\Delta E^{\text{S-M}}$, as calculated in Eq. (3.5), is independent of the activity of $M_{(\text{aq})}^{z+}$ cations in solution. From an experimental viewpoint, this means that if the underpotential shift is measured using solutions with different activities (concentrations) of $M_{(\text{aq})}^{z+}$, always the same $\Delta E^{\text{S-M}}$ value should be obtained. We will see below that in the presence of specifically adsorbed anions, the situation is different.

Taking into account the reservoir fixing the chemical potential of the species, the thermodynamic potential describing the stability of the system can be written as:

$$\begin{aligned} \tilde{G} = G^{\text{sub}} - N_e^{\text{S}}\tilde{\mu}_e^{\text{S}} - N_e^{\text{M}}\tilde{\mu}_e^{\text{M}} - N_{\text{A}^{a-}}\tilde{\mu}_{\text{A}^{a-}}^{\text{sol}} - N_{\text{M}^{z+}}\tilde{\mu}_{\text{M}^{z+}}^{\text{sol}} - N_{\text{X}^-}\tilde{\mu}_{\text{X}^-}^{\text{sol}} \\ - N_{\text{X}^+}\tilde{\mu}_{\text{X}^+}^{\text{sol}} - N_{\text{W}}\tilde{\mu}_{\text{W}}^{\text{sol}} \end{aligned} \quad (3.80)$$

where N_i denotes the number of i species in the subsystem. The free energy change for reaction (3.79), according to Eq. (3.80) is:

$$\begin{aligned} \Delta\tilde{G} = \Delta G^{\text{sub}} - \Delta N_e^{\text{S}}\tilde{\mu}_e^{\text{S}} - \Delta N_e^{\text{M}}\tilde{\mu}_e^{\text{M}} - \Delta N_{\text{A}^{a-}}\tilde{\mu}_{\text{A}^{a-}}^{\text{sol}} - \Delta N_{\text{M}^{z+}}\tilde{\mu}_{\text{M}^{z+}}^{\text{sol}} \\ - \Delta N_{\text{X}^-}\tilde{\mu}_{\text{X}^-}^{\text{sol}} - \Delta N_{\text{K}^+}\tilde{\mu}_{\text{K}^+}^{\text{sol}} - \Delta N_{\text{W}}\tilde{\mu}_{\text{W}}^{\text{sol}} \end{aligned} \quad (3.81)$$

where ΔG^{sub} corresponds to the change of free energy of the subsystem. While this quantity appears as complicated to calculate, we will see that it is actually relatively simple. With this purpose, we divide the subsystem into five parts, as illustrated in Fig. 3.28. These five parts correspond to:

1. Bulk working electrode S. (Region I in Fig. 3.28)
2. Interphase between S and the solution (Region II in Fig. 3.28)
3. Bulk solution (Region III in Fig. 3.28)
4. Interphase between M and the solution (Region IV in Fig. 3.28)
5. Bulk M electrode (Region V in Fig. 3.28)

Thus we have $\Delta G^{\text{sub}} = \Delta G^{\text{I}} + \Delta G^{\text{II}} + \Delta G^{\text{III}} + \Delta G^{\text{IV}} + \Delta G^{\text{V}}$. Let us consider each contribution. The bulk of S remains unaltered in reaction (3.79), so $\Delta G^{\text{I}} = 0$. The reservoirs provide ions and solvent, so the bulk of the solution will remain unaltered, so $\Delta G^{\text{III}} = 0$. The only change on the M electrode is the disappearance of λ/z bulk M atoms, remaining its double layer unaltered. Thus, $\Delta G^{\text{V}} = -\lambda\mu_{\text{M}}^{\text{bulk}}/z$ and $\Delta G^{\text{IV}} = 0$ and we are only left with the calculation of ΔG^{II} , that is, the Gibbs free energy change of the substrate/adsorbate interphase. This term is equivalent to the term γdA in Eq. (3.36) and involves the formation of the upd deposit, with the corresponding EDL, as well as the disappearance of the naked substrate/solution interface. Then, we can write:

$$\Delta G^{\text{sub}} = \Delta G^{\text{II}} - \frac{\lambda}{z}\mu_{(\text{bulk})}^{\text{M}} \quad (3.82)$$

And

$$\begin{aligned} \Delta \tilde{G} &= \Delta G^{\text{II}} - \frac{\lambda}{z}\mu_{(\text{bulk})}^{\text{M}} \\ &- \Delta N_{\text{e}}^{\text{S}} \tilde{\mu}_{\text{e}}^{\text{S}} - \Delta N_{\text{e}}^{\text{M}} \tilde{\mu}_{\text{e}}^{\text{M}} - \Delta N_{\text{A}^{+}} \tilde{\mu}_{\text{A}^{+}}^{\text{sol}} - \Delta N_{\text{M}^{z+}} \tilde{\mu}_{\text{M}^{z+}}^{\text{sol}} - \Delta N_{\text{X}^{-}} \tilde{\mu}_{\text{X}^{-}}^{\text{sol}} - \Delta N_{\text{K}^{+}} \tilde{\mu}_{\text{K}^{+}}^{\text{sol}} - \Delta N_{\text{W}} \tilde{\mu}_{\text{W}}^{\text{sol}} \end{aligned} \quad (3.83)$$

Thus, we have simplified the calculation of $\Delta \tilde{G}$ by centering our attention on Region II, but we still have to deal with the problem of calculating free energy changes for this charged interphase. Let us now consider the reactions taking place at Region II in terms of Eq. (3.79), that we split in the following set of processes (reactions), as shown in Fig. 3.29, giving below each of them the corresponding free energy changes of this interphase:

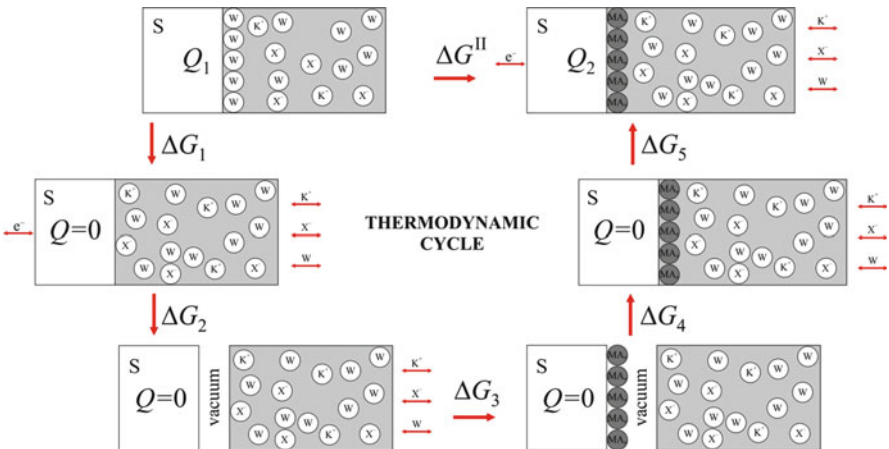
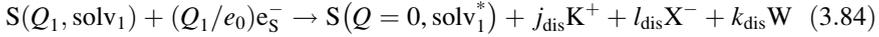


Fig. 3.29 Schematic picture of the thermodynamic cycle leading to the sequence of reactions described in (3.84), (3.86), (3.88), (3.90) and (3.92)

1. Bringing the charged substrate/solution interphase to the point of zero charge (PZC):



where j_{dis} , l_{dis} and k_{dis} represent the number of cations, anions and water molecules leaving the interphase II during the discharge process. These numbers may be positive or negative, and must be calculated with a suitable model of the EDL. Negative values of j_{dis} , l_{dis} or k_{dis} would mean that these species are not leaving but entering interphase II. In the case of a model representing the solution side of the EDL as point charges embedded in a dielectric continuum, we would have $k_{\text{dis}} = 0$. We wrote solv_1^* to emphasize that the solvation of the substrate may be different for the uncharged surface.

The Gibbs free energy change of step 1 is:

$$\Delta G_1 = G^{S(Q=0, \text{solv}_1^*)} - G^{S(Q_1, \text{solv}_1)} \quad (3.85)$$

where $G^{S(Q_1, \text{solv}_1)}$ is the free energy of the charged substrate/electrolyte interphase and $G^{S(Q=0, \text{solv}_1^*)}$ is its free energy at the PZC.

2. Desolvation of the discharged substrate:

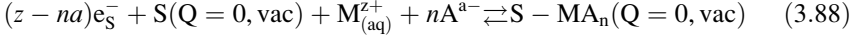


where j_{desolv} , l_{desolv} and k_{desolv} denote the number of cations, anions and water molecules leaving interphase II upon substrate desolvation. This step implies removal of the substrate from the discharged interface, creating two new interphases: the substrate/vacuum and the vacuum/solution ones. Since interphase II is here at the PZC, the number of anions leaving/entering the interface should be equal to the number of cations undergoing this process. Thus, we have the mass balance requirement $j_{\text{desolv}} = l_{\text{desolv}}$. This free energy change can be written as:

$$\Delta G_2 = G^{S(Q=0, \text{vac})} + G^{\text{sol}(Q=0, \text{vac})} - G^{S(Q_1=0, \text{solv}_1^*)} \quad (3.87)$$

where $G^{S(Q=0, \text{vac})}$ is the free energy of the substrate in vacuum and $G^{\text{sol}(Q=0, \text{vac})}$ is free energy of the solution part of the interphase exposed to vacuum, denoted by "vac". It must be stressed that this desolvation energy does not involve a pure solvent, but an ionic solution.

3. Assembling the adsorbate on the substrate in vacuum, with electrons from the reservoir attached to the substrate and ions from the reservoir attached to the solution, so that the substrate/adsorbate system remains free of a surface charge:

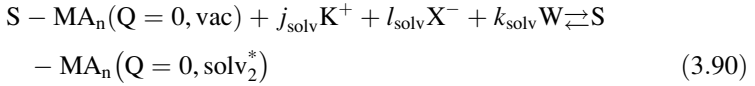


No changes take place at the solvent/vacuum interphase at this point. The free energy change of interphase II at this step amounts:

$$\Delta G_3 = G^{S-MA_n(Q=0, \text{vac})} - G^{S(Q=0, \text{vac})} \quad (3.89)$$

where $G^{S-MA_n(Q=0, \text{vac})}$ and $G^{S(Q=0, \text{vac})}$ are the free energies of the substrate/adsorbate interphase in vacuum and the substrate in vacuum, respectively. The composition of the solution side remains unaltered, since the ions are provided by the reservoir.

4. Solvation of the discharged substrate/adsorbate substrate:

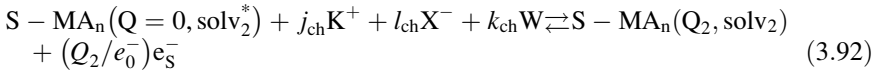


where j_{desolv} , l_{desolv} and k_{desolv} denote the number of cations, anions and water molecules getting into interphase II because of solvation of the substrate/adsorbate surface. As in step 2, we have the condition $j_{\text{solv}} = l_{\text{solv}}$ and free energy change is:

$$\Delta G_4 = G^{S-MA_n(Q=0, \text{solv}_2^*)} - G^{S-MA_n(Q=0, \text{vac})} - G^{\text{sol}(Q=0, \text{vac})} \quad (3.91)$$

where $G^{S-MA_n(Q=0, \text{solv}_2^*)}$ is the free energy of the substrate/adsorbate/solution interphase (II) at the PZC.

5. Bringing the substrate/adsorbate/solution interphase from the PZC to its final charged state:



where we have:

$$\Delta G_5 = G^{S-MA_n(Q_2, \text{solv}_2)} - G^{S-MA_n(Q=0, \text{solv}_2^*)} \quad (3.93)$$

where j_{ch} , l_{ch} and k_{ch} represent the number of cations, anions and water molecules coming into interphase II during the EDL charging process.

According to the previous equations, we thus have:

$$\Delta G^{\text{II}} = \sum_{i=1}^5 \Delta G_i \quad (3.94)$$

Table 3.6 shows the number of particles exchanged with the reservoirs for each of these steps.

From Table 3.6, we get the following equalities determining the coefficients in Eq. (3.79):

$$\Delta k = k_{\text{ch}} - k_{\text{dis}} + k_{\text{solv}} - k_{\text{desolv}} \quad (3.95)$$

$$\Delta l = l_{\text{ch}} - l_{\text{dis}} + l_{\text{solv}} - l_{\text{desolv}} \quad (3.96)$$

$$\Delta j = j_{\text{ch}} - j_{\text{dis}} + j_{\text{solv}} - j_{\text{desolv}} \quad (3.97)$$

The latter reactions are subject to the electroneutrality condition of the interphase before and after adsorbate formation. Previous to upd, the surface charge of substrate Q_1 is compensated by the charge of the double layer. We thus have:

$$Q_1 = -e_0(j_{\text{dis}} - l_{\text{dis}}) \quad (3.98)$$

After upd, and according to the sequence of Eqs. (3.82) to (3.93), we find that $\lambda = Q_1/e_0 + z - na - Q_2/e_0$ electrons, one M^{z+} ion and nA^{a-} anions have flowed to the substrate/adsorbate side of interphase II. These events set the condition:

$$Q_2 = Q_1 - e_0(\lambda + z - na) \quad (3.99)$$

On the other hand, charge balance at the substrate/adsorbate solution interphase, at the final state (r.h.s. of Eq. (3.92)) involves:

$$Q_2 = -e_0(j_{\text{ch}} - l_{\text{ch}}) \quad (3.100)$$

So, it comes out the following condition for λ :

$$\lambda = -j_{\text{dis}} + l_{\text{dis}} + z - na + j_{\text{ch}} - l_{\text{ch}} \quad (3.101)$$

Using the previous results and Table 3.6, we can replace into Eq. (3.83) to get:

$$\begin{aligned} \Delta \tilde{G} = \Delta G^{\text{II}} - \frac{\lambda}{z} \mu_{(\text{bulk})}^{\text{M}} + \lambda(\tilde{\mu}_{\text{e}}^{\text{M}} - \tilde{\mu}_{\text{e}}^{\text{S}}) - n\tilde{\mu}_{\text{A}^{a-}}^{\text{sol}} - \left(1 - \frac{\lambda}{z}\right) \tilde{\mu}_{\text{M}^{z+}}^{\text{sol}} \\ - \Delta \tilde{\mu}_{\text{X}}^{\text{sol}} - \Delta j \tilde{\mu}_{\text{K}^+}^{\text{sol}} - \Delta k \mu_{\text{W}}^{\text{sol}} \end{aligned} \quad (3.102)$$

We can use the definition of electrochemical potential of the i species $\tilde{\mu}_i^{\text{sol}} = \mu_i^{\text{sol}} + z_i e_0 \varphi^{\text{sol}}$, and use (3.94), (3.85), (3.87), (3.89), (3.91) and (3.93) to replace into (3.83) to get:

$$\begin{aligned}
\Delta\tilde{G} = & G^{S-\text{MA}_n(Q=0, \text{vac})} - G^{S(Q=0, \text{vac})} - \frac{\lambda}{z}\mu_{(\text{bulk})}^{\text{M}} - \left(1 - \frac{\lambda}{z}\right)\mu_{\text{M}^{z+}}^{\text{sol}} - n\mu_{\text{A}^{\text{a-}}}^{\text{sol}} \\
& + \Delta G_{\text{disc}}^{\text{S}} + \Delta G_{\text{ch}}^{\text{S}-\text{MA}_n} \\
& + \Delta G_{\text{desolv}}^{\text{S}} + \Delta G_{\text{solv}}^{\text{S}-\text{MA}_n} \\
& + \lambda(\tilde{\mu}_{\text{e}}^{\text{M}} - \tilde{\mu}_{\text{e}}^{\text{S}})
\end{aligned} \tag{3.103}$$

where we have defined the following quantities:

$$\Delta G_{\text{disc}}^{\text{S}} := G^{S(Q=0, \text{solv}_1^*)} - G^{S(Q_1, \text{solv}_1)} - (-l_{\text{disc}}\mu_{\text{X}^-}^{\text{sol}} - j_{\text{disc}}\mu_{\text{K}^+}^{\text{sol}} - k_{\text{disc}}\mu_{\text{W}}^{\text{sol}}) \tag{3.104}$$

$$\Delta G_{\text{ch}}^{\text{S}-\text{MA}_n} := G^{S-\text{MA}_n(Q_2, \text{solv}_2)} - G^{S-\text{MA}_n(Q=0, \text{solv}_2^*)} - (l_{\text{ch}}\mu_{\text{X}^-}^{\text{sol}} + j_{\text{ch}}\mu_{\text{K}^+}^{\text{sol}} + k_{\text{ch}}\mu_{\text{W}}^{\text{sol}}) \tag{3.105}$$

$$\begin{aligned}
\Delta G_{\text{desolv}}^{\text{S}} := & G^{S(Q=0, \text{vac})} + G^{\text{sol}(Q=0, \text{vac})} - G^{S(Q_1=0, \text{solv}_1^*)} \\
& - (-l_{\text{desolv}}\mu_{\text{X}^-}^{\text{sol}} - j_{\text{desolv}}\mu_{\text{K}^+}^{\text{sol}} - k_{\text{desolv}}\mu_{\text{W}}^{\text{sol}})
\end{aligned} \tag{3.106}$$

$$\begin{aligned}
\Delta G_{\text{solv}}^{\text{S}-\text{MA}_n} := & G^{S-\text{MA}_n(Q=0, \text{solv}_2^*)} - G^{S-\text{MA}_n(Q=0, \text{vac})} - G^{\text{sol}(Q=0, \text{vac})} \\
& - (l_{\text{solv}}\mu_{\text{X}^-}^{\text{sol}} + j_{\text{solv}}\mu_{\text{K}^+}^{\text{sol}} + k_{\text{solv}}\mu_{\text{W}}^{\text{sol}})
\end{aligned} \tag{3.107}$$

$\Delta G_{\text{disc}}^{\text{S}}$ represents the free energy change corresponding to the *discharging* of the EDL of the substrate/solution interphase, taking it to its point of zero charge, $\Delta G_{\text{ch}}^{\text{S}-\text{MA}_n}$ is the free energy change corresponding to the *charging* of the EDL of the substrate/adsorbate/solution interphase, taking it from its point of zero charge its status when the upd monolayer has been formed. $\Delta G_{\text{solv}}^{\text{S}-\text{MA}_n}$ is a solvation term corresponding to the S – MA_n surface and $\Delta G_{\text{desolv}}^{\text{S}}$ is a desolvation term corresponding to the S pristine surface (without upd layer).

Equation (3.103) contains all the physics involved in the present problem. The first line accounts for the free energy of formation of the 2D deposit MA_n on S, from ions in reservoirs ($n \text{ A}^{\text{a-}}$ anions and one M^{z+} cation) and ions stemming from the reference electrode ($\lambda/z \text{ M}^{z+}$ cations). The second line is a double layer term, accounting for the dismantlement (or discharge) of the double layer of the substrate and the building of the double layer of the upd deposit. Analogously, the third line accounts for desolvation and resolution effects. The fourth line considers electronic flow from/to the two electrodes, and is related to the potential difference that can be measured between the electrodes shown in Fig. 3.28. This the driving force for the presente electrochemical reaction.

Equation (3.103) may be used to calculate from first-principles the relative stability of different S – MA_n structures at different potentials. Alternatively, we

can set $\widetilde{\Delta G} = 0$, and in this case the difference of electrochemical potentials ($\widetilde{\mu}_e^M - \widetilde{\mu}_e^S$) will be equivalent to the desired underpotential shift ΔU^{S-M} , so we get:

$$\Delta E^{S-M} = -\frac{1}{\lambda} \left[\left(G^{S-MA_n(Q=0, \text{vac})} - G^{S(Q=0, \text{vac})} - \frac{\lambda}{z} \mu_{(\text{bulk})}^M \right) - n\mu_{A^{a-}}^{\text{sol}} - \left(1 - \frac{\lambda}{z} \right) \mu_{M^{z+}}^{\text{sol}} + \Delta G_{\text{rech}}^{\text{dl}} + \Delta G_{\text{resolv}} \right] \quad (3.108)$$

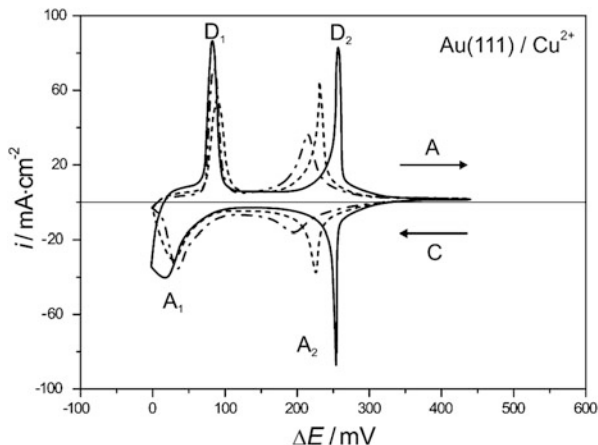
where we have defined $\Delta G_{\text{rech}}^{\text{dl}} := \Delta G_{\text{disch}}^S + \Delta G_{\text{ch}}^{S-MA_n}$, a recharging free energy and $\Delta G_{\text{resolv}} := \Delta G_{\text{desolv}}^S + \Delta G_{\text{sol}}^{S-MA_n}$ a resolution free energy. Equation (3.108) has a twofold relevance. From the theoretical point of view, this equation allows the first-principles theoretical calculation of underpotential shifts. While the quantities in the first parenthesis in Eq. (3.108) may be obtained precisely from DFT calculations, $\mu_{A^{a-}}^{\text{sol}}$ and $\mu_{M^{z+}}^{\text{sol}}$ involve ion solvation energies, which are subject to calculations errors of the order of a fraction of eV, making the result uncertain. A suitable alternative for their evaluation would be to use thermodynamic data. The penultimate term, $\Delta G_{\text{rech}}^{\text{dl}}$, could be computed from double layer theories, and will be small as long as the PZC are not markedly different, as is should be the case of metals with similar work functions. The last term, ΔG_{resolv} is probably negligible in the case of the formation of relatively compact adsorbates, where the adatoms show a large depolarization. On the other hand, this equation may be also used to interpret experimental results. Assuming that the free energy contribution due to discharging/recharging of the double layer is negligible, we have, $\lambda \approx z - na$. Thus, Eq. (3.108) results in:

$$\Delta E^{S-M} = - \left[\left(\frac{G^{MA_n/S(Q=0, \text{vac})} - G^{S(Q=0, \text{vac})}}{z - na} - \frac{1}{z} \mu_{(\text{bulk})}^M \right) - \frac{n}{z - na} \mu_{A^{a-}}^{\text{sol}} - \left(\frac{1}{z - na} - \frac{1}{z} \right) \mu_{M^{z+}}^{\text{sol}} + \frac{\Delta G_{\text{resolv}}}{z - na} \right] \quad (3.109)$$

Thus, the dependence of the underpotential shift on the activity (and thus on the chemical potential) of the different ionic species (A^{a-} and M^{z+}) could yield information on the stoichiometry of the surface compound $S - MA_n$ being formed. In fact, we see from Eq. (3.109) that the following equations apply:

$$\left(\frac{\partial \Delta E^{S-M}}{\partial \mu_{A^{a-}}^{\text{sol}}} \right)_{\mu_{M^{z+}}^{\text{sol}}} = \frac{n}{z - na} \quad (3.110)$$

Fig. 3.30 Cyclic voltammograms of Cu upd on Au(111). Current density is plotted as a function of electrode potential referred to Cu/Cu²⁺ in the same solution. The electrolyte solutions were 9×10^{-2} M H₂SO₄ + xM CuSO₄, pH = 1, $T = 298$ K. $x = 5 \times 10^{-2}$ M (-----), 5×10^{-3} M (- - - -), 5×10^{-4} M (- - .. - -) (Reprinted with permission from Ref. [205])



$$\left(\frac{\partial \Delta E^{S-M}}{\partial \mu_{M^{z+}}^{\text{sol}}} \right)_{\mu_{A^{a+}}^{\text{sol}}} = \frac{1}{z - na} - \frac{1}{z} \quad (3.111)$$

Although the present restrictions do not apply strictly to their experimental data, it is worth mentioning here the work of Omar et al. [205] for Cu upd on Au(111) in the presence of sulfate anions. Figure 3.30 shows voltammograms at a nearly constant activity of sulfate species. It is observed that while the more negative peak is relative insensitive to Cu²⁺ concentration ($\mu_{M^{z+}}^{\text{sol}}$), the more positive shows a shift $\partial \Delta E^{S-M} / \partial \mu_{M^{z+}}^{\text{sol}}$ close to 30 mV/decade, indicating that $(\partial \Delta E^{S-M} / \partial \mu_{M^{z+}}^{\text{sol}})_{\mu_{M^{z+}}^{\text{sol}}} \approx 0.5$. Using Eq. (3.110) with $z = 2$ and $a = 2$, we get $n = 0.5$, in agreement with the expected Cu (SO₄)_{1/2}/S stoichiometry expected for the $(\sqrt{3} \times \sqrt{3})R30^0$ structure predicted for this interphase.

References

1. Marinkovic NS, Wang JX, Marinkovic JS, Adzic RR (1999) J Phys Chem B103:139
2. Kolb DM, Przasnyski M, Gerischer H (1974) J Electroanal Chem 54:25
3. Kolb DM, Przasnyski M, Gerischer H (1974) Surf Sci 43:662
4. Kolb DM (1978) In: Gerischer H, Tobias CW (eds) Advances in electrochemistry and electrochemical engineering, vol 11. Wiley, New York, p 125
5. Leiva EPM (1996) Electrochim Acta 41:2185
6. Trasatti S (1975) Zeits für Phys Chem NF 98:75
7. Sudha V, Sangaranarayanan MV (2002) J Phys Chem B 106:2699
8. Sudha V, Sangaranarayanan MV (2003) J Phys Chem B 107:3907
9. Schultze JW, Dickertman D (1976) Surf Sci 54:489
10. Mrozek P, Sung Y-E, Wieckowski A (1995) Surf Sci 335:44
11. Hamm UW, Kramer D, Zhai RS, Kolb DM (1996) J Electroanal Chem 414:85

12. Hamelin A, Titanov T, Sevastyanov E, Popov A (1983) *J Electroanal Chem* 145:225
13. Swathirajan S, Mizota H, Bruckenstein S (1982) *J Phys Chem* 86:2480
14. Schultze JW (1970) *Ber Bunsenges Phys Chem* 74:705
15. Vetter KJ, Schultze JW (1972) *Ber Bunsenges Phys Chem* 76:920
16. Vetter KJ, Schultze JW (1972) *Ber Bunsenges Phys Chem* 76:927
17. Schultze JW, Vetter KJ (1973) *J Electroanal Chem* 44:63
18. Schultze JW, Koppitz FD (1976) *Electrochim Acta* 21:327
19. Szabó S (1991) *Int Rev Phys Chem* 10:207
20. Schmidt E, Gyax HR (1996) *J Electroanal Chem* 12:300
21. Siegenthaler H, Schmidt E (1969) *Helv Chim Acta* 52:2245
22. Schmidt E, Siegenthaler H (1970) *Helv Chim Acta* 53:321
23. Siegenthaler H, Schmidt E (1977) *J Electroanal Chem* 80:129
24. Siegenthaler H, Jüttner K, Schmidt E, Lorenz WJ (1978) *Electrochim Acta* 23:1009
25. Tindall GW, Bruckenstein S (1968) *Anal Chem* 40:1051
26. Swathirajan S, Bruckenstein S (1982) *J Electrochem Soc* 129:1202
27. Swathirajan S, Bruckenstein S (1983) *Electrochim Acta* 28:865
28. Schmidt E (1969) *Helv Chim Acta* 52:1763
29. Budevski E, Staikov G, Lorenz WJ (1996) *Electrochemical phase formation and growth*. VCH, Weinheim
30. Horányi G (1974) *J Electroanal Chem* 55:45
31. Shi Z, Lipkowski J (1994) *J Electroanal Chem* 364:289
32. Shi Z, Lipkowski J (1994) *J Electroanal Chem* 365:303
33. Shi Z, Wu S, Lipkowski J (1995) *Electrochim Acta* 40:9
34. Wu S, Lipkowski J, Tyliczczyk T, Hitchcock AP (1995) *Prog Surf Sci* 50:227
35. Blum L, Abruña HD, White J, Gordon JG II, Borges GL, Samant MG, Melroy OR (1968) *J Chem Phys* 85:6732
36. Melroy OR, Samant MG, Borges GL, Gordon JG II, Blum L, White J, Albarelli MJ, McMillan M, Abruña HD (1988) *Langmuir* 4:728
37. Conway BE, Angerstein-Kozłowska H (1980) *J Electroanal Chem* 113:63
38. Schmidt E, Wüthrich N (1970) *J Electroanal Chem* 28:349
39. Schmidt E, Wüthrich N (1972) *J Electroanal Chem* 34:377
40. Schmidt E, Wüthrich N (1972) *J Electroanal Chem* 40:399
41. Angerstein-Kozłowska H, Klinger J, Conway BE (1977) *J Electroanal Chem* 75:45
42. Lee TD, Yang CN (1952) *Phys Rev* 87:410
43. Onsager L (1944) *Phys Rev* 65:117
44. Yang CN (1952) *Phys Rev* 85:808
45. Budevski E, Staikov G, Lorenz WJ (1996) *Electrochemical phase formation and growth*. VCH, Weinheim
46. Bewick A, Fleischmann M, Thirsk HR (1962) *Trans Faraday Soc* 58:2200
47. Fleischmann M (1963) Thirsk HR. In: Delahay P (ed) *Advances in electrochemistry and electrochemical engineering*, vol 3. Interscience, New York
48. Bosco E, Rangarajan SK (1981) *J Chem Soc Faraday Trans* 77:483
49. Gunawardena G, Hills G, Montenegro I, Scharifker B (1982) *J Electroanal Chem* 138:255
50. Armstrong RD, Fleischmann M, Thirsk HR (1966) *J Electroanal Chem* 11:208
51. Abyaneh MY, Fleischmann M (1982) *Electrochim Acta* 27:1513
52. Pangarov N (1983) *Electrochim Acta* 28:763
53. Astley DJ, Harrison JA, Thirsk HR (1968) *J Electroanal Chem* 19:325
54. Adzic R, Yeager E, Cahan BD (1974) *J Electrochem Soc* 121:474
55. Horkens J, Cahan BD, Yeager E (1975) *J Electrochem Soc* 122:1585
56. Jüttner K, Staikov G, Lorenz WJ, Schmidt E (1977) *J Electroanal Chem* 80:67
57. Jüttner K, Lorenz WJ (1980) *Z Phys Chem NF* 122:163
58. Schultze JW, Dickertmann D (1977) *Faraday Symp Chem Soc* 12:36
59. Schultze JW, Dickertmann D (1978) *Ber Bunsenges Phys Chem* 82:528

60. Holzle MH, Zwing V, Kolb DM (1995) *Electrochim Acta* 40:1237
61. Holzle MH, Kolb DM (1994) *Ber Bunsenges Phys Chem* 98:330
62. Holzle MH, Retter U, Kolb DM (1994) *J Electroanal Chem* 371:101
63. Bosco L, Rangarajan SK (1981) *J Electroanal Chem* 129:25
64. Huckaby DA, Blum L (1991) *J Electroanal Chem* 315:255
65. Blum L, Huckaby DA (1994) *J Electroanal Chem* 375:69
66. Blum L, Legault M, Turq P (1994) *J Electroanal Chem* 379:35
67. Bewick A, Thomas B (1975) *J Electroanal Chem* 65:911
68. Bewick A, Thomas B (1976) *J Electroanal Chem* 70:239
69. Bewick A, Thomas B (1977) *J Electroanal Chem* 84:127
70. Bewick A, Jovicevic J, Thomas B (1977) *Faraday Symp Chem Soc* 12:24
71. Staikov G, Juttner K, Lorenz WJ, Schmidt E (1978) *Electrochim Acta* 23:305
72. Bewick A, Thomas B (1975) *J Electroanal Chem* 65:911
73. Juttner K, Staikov G, Lorenz WJ, Schmidt E (1977) *J Electroanal Chem* 80:67
74. García SG, Salinas D, Mayer C, Schmidt E, Staikov G, Lorenz WJ (1998) *Electrochim Acta* 43:3007
75. García SG, (1997) Ph.D. thesis, Universidad Nacional del Sur, Bahía Blanca, Argentina
76. Giménez MC, Del Popolo MG, Leiva EPM (1999) *Electrochim Acta* 45:699
77. Magnussen OM, Hotlos J, Beitel G, Kolb DM, Behm RJ (1991) *J Vac Sci Technol B* 9:969
78. Carnal D, Oden PI, Muller U, Schmidt E, Siegenthaler H (1995) *Electrochim Acta* 40:1223
79. Sackmann J, Bunk A, Poetzschke RT, Staikov G, Lorenz WJ (1998) *Electrochim Acta* 43:2863
80. Lorenz WJ, Schmidt E, Staikov G, Bort H (1977) *Faraday Symp Chem Soc* 12:14
81. Bewick A, Thomas B (1977) *J Electroanal Chem* 85:329
82. Widmer R, Siegenthaler H (2004) *J Electrochem Soc* 151, E238
83. Bort H, Jüttner K, Lorenz WJ (1978) *J Electroanal Chem* 90:413
84. Jüttner K, Siegenthaler H (1978) *Electrochim Acta* 23:971
85. Waszczuk P, Wnuk A, Sobkowski J (1999) *J Electrochim Acta* 44:1789
86. Wang JX, Adii RR, Magnussen OM, Ocko BM (1995) *Surf Sci* 344:111
87. Staikov G, García SG, Salinas DR (2010) *ECS Trans* 25:3
88. García SG, Salinas DR, Staikov G (2005) *Surf Sci* 576:9
89. Bort H, Jüttner K, Lorenz WJ (1983) *Electrochim Acta* 28:993
90. Chen C, Wasburn N, Gewirth AA (1993) *J Phys Chem* 97:9754
91. Tao NJ, Pan J, Li Y, Oden PJ, De Rose JA, Lindsay SM (1992) *Surf Sci Lett* 271:L338
92. Green MP, Hanson KJ, Scherson DA, Xing X, Richter M, Ross PN, Carr R, Lindau I (1989) *J Phys Chem* 93:2181
93. Green MP, Hanson KJ, Carr R, Lindau I (1990) *J Electrochem Soc* 137:3493
94. Green MP, Hanson KJ (1991) *Surf Sci Lett* 259:L743
95. Wang F-X, Pan G-B, Liu Y-D, Xiao Y (2010) *Chem Phys Lett* 488:112
96. Jovic VD, Jovic BM, Despic AR (1990) *J Electroanal Chem* 288:229
97. Engelsmann K, Lorenz WJ, Schmidt E (1980) *J Electroanal Chem* 114:1
98. Hamelin A, Lipkowski J (1984) *J Electroanal Chem* 171:317
99. Tamura K, Wang JX, Adzic RR, Ocko BM (2004) *J Phys Chem B* 108:1992
100. Schultze JW, Dickertmann D (1977) *Electrochim Acta* 22:117
101. Fu Y-C, Su Y-Z, Zhang H-M, Yan J-W, Xie Z-X, Mao B-W (2010) *Electrochim Acta* 55:8105
102. Nakamura M, Sato N, Hosh N, Sakata O (2010) *Langmuir* 26:4590
103. Thiel K-O, Hintze M, Vollmer A, Donner C (2010) *J Electroanal Chem* 638:143
104. Seo M, Yamazaki M (2008) *ECS Trans* 11:13
105. Sandnes E, Williams ME, Bertocci U, Vaudin MD, Stafford GR (2007) *Electrochim Acta* 52:6221
106. Jeffrey CA, Harrington DA, Morin S (2002) *Surf Sci* 512:L367
107. Tamura K, Mizuki J (2005) *J Phys Chem B* 109:12832

108. Chen C-H, Kepler KD, Gewirth AA, Ocko BM, Wang J (1993) *J Phys Chem* 97:7290
109. Niece BK, Gewirth AA (1998) *J Phys Chem B* 102:818
110. Wang JX, Adzic RR, Ocko BM (1994) *J Phys Chem* 98:7182
111. Toney MF, Gordon JG, Samant MG, Borges GL, Melroy OR (1995) *J Phys Chem* 99:4733
112. Chabala ED, Harji BH, Rayment T, Archer MD (1992) *Langmuir* 8:2028
113. Adzic RR, Wang JX (1998) *J Phys Chem B* 102:6305
114. Wang JX, Robinson IK, Adzic RR (1998) *Surf Sci* 412/413:374
115. Wang JX, Adzic RR, Magnussen OM, Ocko BM (1995) *Surf Sci* 335:120
116. Zell CA, Endres F, Freyland W (1999) *Phys Chem Chem Phys* 1:697
117. Hachiya T, Itaya K (1992) *Ultramicroscopy* 42–44:445
118. Staikov G, Lorenz WJ (1997) *Can J Chem* 75:1624
119. Garcia S, Salinas D, Mayer C, Schmidt E, Staikov G, Lorenz WJ (1998) *Electrochim Acta* 43:3007
120. Esplandiu MJ, Schneeweiss MA, Kolb DM (1999) *Phys Chem Chem Phys* 1:4847
121. Corcoran SG, Chakarova GS, Sieradzki K (1994) *J Electroanal Chem* 377:85
122. Chabala ED, Rayment T (1996) *J Electroanal Chem* 401:257
123. Chabala ED, Ramadan AR, Brunt T, Rayment T (1996) *J Electroanal Chem* 412:67
124. C-h C, Vesecky SM, Gewirth AA (1992) *J Am Chem Soc* 114:451
125. Sugita S, Abe T, Itaya K (1993) *J Phys Chem* 97:8780
126. Ogaki K, Itaya K (1995) *Electrochim Acta* 40:1249
127. Hachiya T, Itaya K (1992) *Ultramicroscopy* 42–44:445
128. Lee D, Rayment T (1999) *Phys Chem Chem Phys* 1:4389
129. Ramadan AR, Chabala ED, Rayment T (1999) *Phys Chem Chem Phys* 1:1591
130. Koost DA, Richmond GL (1992) *J Phys Chem* 96:3110
131. Uchida H, Masaru M, Watanabe M (1995) *J Electroanal Chem* 386:261
132. Chabala ED, Rayment T (1996) *J Chem Soc Faraday Trans* 92:4657
133. Ogaki K, Itaya K (1995) *Electrochim Acta* 43:3007
134. Ikemiya N, Yamada K, Hara S (1996) *Surf Sci* 348:253
135. Xia XH, Nagle L, Schuster R, Magnussen OM, Behm RJ (2000) *Phys Chem Chem Phys* 2:4387
136. Vasiljevic N, Viyannalage LT, Dimitrov N, Sieradzki K (2008) *J Electroanal Chem* 613:118
137. Hotlos J, Magnussen OM, Behm RJ (1995) *Surf Sci* 335:129
138. Hachiya T, Honbo H, Itaya K (1991) *J Electroanal Chem* 275:315
139. Manne S, Hansma PK, Massie J, Elings VB, Gewirth AA (1991) *Science* 251:186
140. Hölzle MH, Kolb DM (1994) *Ber Bunsenges Phys Chem* 98:330
141. Hölzle MH, Retter U, Kolb DM (1994) *J Electroanal Chem* 371:101
142. Hölzle MH, Zwing B, Kolb DM (1995) *Electrochim Acta* 40:1237
143. Ataka K, Nishina G, Cai W-B, Sun S-G, Osawa M (2000) *Electrochem Commun* 2:417
144. Watanabe M, Uchida H, Miura M, Ikeda N (1995) *J Electroanal Chem* 384:191
145. Ikemiya N, Miyaoka S, Hara S (1994) *Surf Sci* 311:L641
146. Akiyoshi Kuzume A, Herrero E, Feliu JM, Nichols RJ, Schiffrin DJ (2004) *J Electroanal Chem* 570:157
147. Kolb DM (1994) *Ber Bunsenges Phys Chem* 98:1421
148. Hachiya T, Honbo H, Itaya K (1991) *J Electroanal Chem* 315:275
149. Kimizuka N, Itaya K (1992) *Faraday Discuss* 94:117
150. Gibson NC, Saville PM, Harrington DA (1991) *J Electroanal Chem* 318:271
151. Zelenay P, Gamboa-Aldeco M, Horányi G, Wieckowski A (1993) *J Electroanal Chem* 357:307
152. Frank DG, Golden T, Chyan OMR, Hubbard AT (1991) *Appl Surf Sci* 48/49:166
153. Rodriguez JF, Taylor DL, Abruña HD (1993) *Electrochim Acta* 38:235
154. Wang JX, Marinkovic NS, Adzic RR, Ocko BM (1998) *Surf Sci* 398:L291
155. El Omar F, Omar L, Durand R, Faure R (1984) *J Electroanal Chem* 160:385
156. Wang JX, Marinkovic NS, Adzic RR, Ocko BM (1998) *Surf Sci* 398:L291

157. Schmidt U, Vinzelberg S, Staikov G (1996) *Surf Sci* 348:261
158. Chen CH, Gewirth AA (1992) *J Am Chem Soc* 114:5439
159. Hara M, Nagahara Y, Yoshimoto S, Inukai J, Itaya K (2004) *J Electrochem Soc* 151, E92
160. Zheng SH, Krug K, Golks F, Kaminski D, Morin S, Magnussen OM (2010) *J Electroanal Chem* 649:189
161. Giménez MC, Del Pópolo MG, Leiva EPM, García SG, Salinas DR, Mayer CE, Lorenz WJ (2002) *J Electrochem Soc* 149, E109
162. Herrero E, Buller LJ, Abruña HD (2001) *Chem Rev* 101:1897
163. Brown G, Rikvold PA, Novotny MA, Wieckowski A (1999) *J Electrochem Soc* 146:1035
164. Zhang J, Sung Y-E, Rikvold PA, Wieckowski A (1996) *J Chem Phys* 104:5699
165. Yee HS, Abruña HD (1994) *J Phys Chem* 98:6552
166. Gómez R, Yee HS, Bommarito GM, Feliu JM, Abruña HD (1995) *Surf Sci* 335:101
167. White JH, Abruña HD (1990) *J Phys Chem* 94:894
168. Gómez R, Feliu JM, Abruña HD (1994) *J Phys Chem* 98:5514
169. White JH, Abruña HD (1991) *J Electroanal Chem* 300:521
170. Finnefrock AC, Ringland KL, Brock JD, Buller LJ, Abruña HD (1998) *Phys Rev Lett* 81:3459
171. Finnefrock AC, Buller LJ, Ringland KL, Brock JD, Abruña HD (1997) *J Am Chem Soc* 119:11703
172. Wang C, Chung C-S, Chang S-C (1995) *J Electroanal Chem* 395:317
173. Zei MS, Wu K, Eiswirth M, Ertl G (1999) *Electrochim Acta* 45:809
174. Danilov AI, Molodkina EB, Polukarov YM, Climent V, Feliu JM (2001) *Electrochim Acta* 46:3137
175. Danilov AI, Molodkina EB, Rudnev AV, Polukarov Yu M, Feliu JM (2005) *Electrochim Acta* 50:5032
176. Leung L-W H, Gregg TW, Goodman DW (1992) *Chem Phys Lett* 188:467
177. Leung L-W H, Gregg TW, Goodman DW (1991) *Langmuir* 7:3205
178. Sashikata K, Furuya N, Itaya K (1991) *J Electroanal Chem* 316:361
179. Shingaya Y, Matsumoto H, Ogasawara O, Ito M (1995) *Surf Sci* 335:23
180. Michaelis R, Zei MS, Zhai RS, Kolb DM (1992) *J Electroanal Chem* 339:299
181. Tripkovic DV, Strmcnik D, van der Vliet D, Stamenkovic V, Markovic NM (2008) *Faraday Discuss* 140:25
182. Nishihara C, Nozoye H (1995) *J Electroanal Chem* 386:75
183. Markovic NM, Gasteiger HA, Ross PN (1996) *Langmuir* 11:4098
184. Markovic N, Ross PN (1993) *Langmuir* 9:580
185. Tidswell IM, Lucas CA, Markovic NM, Ross PN (1995) *Phys Rev B* 51:10205
186. Markovic NM, Gasteiger HA, Lucas CA, Tidswell IM, Ross PN (1995) *Surf Sci* 335:91
187. Futamata M (2001) *Chem Phys Lett* 333:337
188. Garland JE, Assiongon KA, Pettit CM, Emery SB, Roy D (2002) *Electrochim Acta* 47:4113
189. Whelan CM, Smyth MR, Barnes CJ, Attard GA, Yang X (1999) *J Electroanal Chem* 474:138
190. Mrozek P, Sung Y-E, Han M, Gamboa-Aldeco M, Wieckowski A, Chen C-H, Gewirth AA (1995) *Electrochim Acta* 40:17
191. Chen C-H, Gewirth AA (1992) *Ultramicroscopy* 42–44:437
192. Toney MF, Howard JN, Richer J, Borges GL, Gordon JG, Melroy OR (1995) *Phys Rev Lett* 75:4472
193. Lee JRI, O'Malley RL, O'Connell TJ, Vollmer A, Rayment T (2009) *J Phys Chem C* 113:12260
194. Zelenay P, Gamboa-Aldeco M, Horányi G, Wieckowski A (1993) *J Electroanal Chem* 357:307
195. Yee HS, Abruña HD (1993) *J Phys Chem* 97:6278
196. Reynolds CA (1995) *Int J Quantum Chem* 56:677
197. Namazian M, Almodarresieh HA, Noorbala MR, Zare HR (2004) *Chem Phys Lett* 396:424

198. Konezny SJ, Doherty MD, Luca OR, Crabtree RH, Soloveichik GL, Batista VS (2012) J Phys Chem C 116:6349
199. Sánchez CG, Dassie SA, Leiva EPM (2002) Langmuir 18:6628
200. Nakai Y, Zei M, Kolb DM, Lehmpfuhl G (1984) Ber Bunsenges Phys Chem 88:340
201. Batina N, Will T, Kolb DM (1992) Faraday Discuss 94:93
202. Huckaby DA, Blum L (1991) J Electroanal Chem 315:255
203. Blum L, Huckaby DA (1994) Electroanal Chem 375:69
204. Blum L, Legault M, Turq P (1994) J Electroanal Chem 379:35
205. Omar IH, Pauling HJ, Jüttner K (1993) J Electrochem Soc 140:2188

Chapter 4

Applications of Underpotential Deposition on Bulk Electrodes as a Model System for Electrocatalysis

4.1 Introduction

The underpotential deposition (upd) of metals may modify the catalytic activity of substrates in several ways. For the sake of simplicity, we divide the types of impacts that upd metals can produce in four types, although they all can in principle be acting on a given reaction at the same time.

1. Geometric effects. These occur due to the presence of adsorbate atoms and should not depend on their chemical nature. Examples of this are the reactions in which the adatoms inhibit the formation of a poison, or reactions where the presence of adatoms enhances the selectivity of the electrocatalyst surface toward a particular product. In the case of the oxidation of organic substances, this has often been called the “third body” effect.
2. Bifunctional Catalyst effects. In this case, the adatoms provide the active sites of preferential adsorption for the species involved in the rate-limiting step, other species that can be adsorbed on the substrate. In this case the important features of the adatoms are related to their ability to adsorb the chemically active species.
3. Direct electronic effects. In this case, the catalytic effects are related to the changes produced by the presence of the adatoms in the electronic structure of the catalyst surface. This must be important in cases in which the reaction speed is controlled by a transfer of electrons; this reaction is directly related to the electronic density of states of the catalytic converter.
4. Indirect electronic effects. We use this terminology to denote the change of the binding properties of the intermediate level (i.e., a poison) due to the presence of other co-adsorbed species.

In this chapter, we give a bird’s eye view of the some experimental results and phenomenological models derived from them that are relevant for theoretical discussion.

4.2 Catalysis of the Electrooxidation of Some C1 Molecules on Pure Pt Surfaces and Bimetallic Catalysis

4.2.1 CO

We shall analyze first the catalysis of the electrooxidation of CO on Pt surfaces because of the important role that this compound plays in electrocatalysis and in electrochemical surface science [1–4] and particularly in the electrooxidation of all C1 molecules (HCOOH, CH₃OH and HCHO) [5–7] (whether as a main reaction path or as a poison).

With the exception of few particular examples where the preadsorbed CO favors certain oxidation reactions typically [8, 9], adsorbed carbon monoxide acts as a poisoning intermediate in catalytic processes. Because of this, the ability of active sites to efficiently oxidize or destabilize this molecule at the surface is highly desirable [10].

The status of CO as an adsorbate on Pt surfaces under electrochemical conditions presents by itself quite a complex picture, as discussed by Chang and Weaver [11], a detailed picture of the CO/metal bonding being possible due to the large dynamic dipole of the C–O vibration and the sensitivity of its frequency, ν_{CO} , to the surface coordination geometry and local environment. In Table 4.1, we see the large difference in ν_{CO} for CO adsorbed in terminal (t) and bridging (b) configurations. This difference can be understood in simple bond-order terms. The larger coordination of the bridge state with the surface weakens the CO bond, delivering a smaller ν_{CO} . Not so straightforward to interpret are the corresponding dependencies of ν_{CO} with the applied potential, E . On one side, a source of this dependency can be explained via a linear Stark effect, that is, the change of the frequency of the C–O bond in the presence of an external field, E , that can be evaluated by means of first-order perturbation theory [12]. However, some of the experimental results showed a deviation from the linear ν_{CO}/E prediction that cannot be explained in terms of linear effects, and a dependency of $d\nu_{\text{CO}}/dE$ on the adsorption site geometry (terminal < twofold < threefold site) that required the consideration of the bonding to the metal surface. This was made by Mehandru and Anderson [13] in terms of the

Table 4.1 Some typical IR frequencies ν_{CO} and frequency-potential slopes $d\nu_{\text{CO}}/dE$ for CO adsorbed on Pt/aqueous interface in terminal (t) and bridging (b) geometries

Surface	Potential vs. NHE ^a (V)	θ_{CO}	$\nu_{\text{CO}}^{\text{t}}$	$d\nu_{\text{CO}}^{\text{t}}/dE$	$\nu_{\text{CO}}^{\text{b}}$	$d\nu_{\text{CO}}^{\text{b}}/dE$
Pt(111)	0.1	~0.65	2062	32	1776	58
Pt(111)	0.55	~0.65	2072	25	1844	46
Pt(111)	0.25	0.3	2055	40	1836	40
Pt(111)	0.25	0.13	2047	43		
Pt(100)	0.25	0.85	2057	36		
Pt(110)	0.05	1.0	2069	32		

Taken from Ref. [11] with permission

^aNHE normal hydrogen electrode

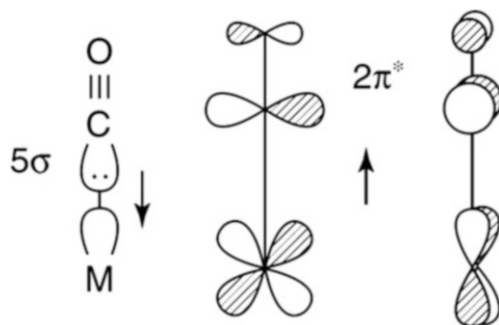


Fig. 4.1 Molecular orbital model for a CO molecule interacting with a metal surface. The *arrow* pointing towards the metal surface denotes the donation from the CO σ orbital to the metal, and the *arrows* pointing to the molecule denote the back-donation to the antibonding π^* orbital of CO (Reproduced from Ref. [14])

atom superposition and electron delocalization molecular orbital theory, and an interpretation of the effect can be made in terms of the CO-metal model shown in Fig. 4.1.

According to the didactic explanation given by Anderson [15] the CO π^* and σ orbitals act as acceptors and donors respectively relative to the metal surface. As the potential is increased, the Fermi level of the metal is shifted negatively with respect to the molecule, and the occupation of both orbitals decreases, producing on one side the strengthening of the C–O bond via the emptying of the π^* orbital, and a weakening because the same occurs with the σ one. The former effect predominates, which results in an increasing of the frequency. The theoretical calculations also predicted the correct dependence of $d\sigma/dE$ upon adsorption site geometry, and delivered the prediction that at more positive potentials linear bonded CO should predominate on the other species, a fact that was in agreement with results obtained from infrared (IR) spectroscopy experiments [16]. It is interesting to point out that the dosing with species that decrease the work function of the system also leads to an increasing coordination of CO, suggesting an “electrostatic field” approach to this phenomenon in the sense that the fields at the interface determine the nature of the CO bonding to the surface. The quantum mechanical factors that influence the potential-dependent bonding properties of CO on Pt, Ir and Pd have been analyzed in detail by Wasileski et al. [17] by means of density functional theory calculations. These authors studied the binding energetics and geometries of CO_{ad} , as well as the vibrational properties of the C/O and the metal/CO(M/CO) bonds as a function of the electric field at the interface. A remarkable feature of these calculations is the prediction of a broad maximum in the $\nu_{\text{M/CO}}$ vs. E plots. Another important conclusion was that frequency-bond lengths correlations are expected when the electric field is varied, in the sense that lower frequencies must be related to larger bond lengths and vice versa. However, these first-principles calculations showed that no clear cut correlation should be expected between $\nu_{\text{M/CO}}$ and the metal/CO binding energy when E is varied. Comparison with ultra-high vacuum (UHV)

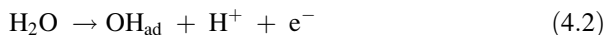
results at moderate θ_{CO} , where other species like hydrogen and water molecules may coexist with CO on the surface, allows the study of coadsorption effects [11]. The physical picture emerging of studies on Pt(111) is the appearance of CO islands, where the formation of CO patches with a higher concentration of CO is more prevalent in the presence of coadsorbed water than with hydrogen. The existence of these islands should be strongly conditioned by the way in which the associated coverage is obtained. In this way, a given CO coverage obtained by straightforward dosing from CO solutions should present island formation in much a lower extent than the same coverage obtained by partial oxidation of a saturated monolayer [18]. A thorough discussion of different studies of coadsorption in UHV and their relevance for electrochemistry is also given in Ref. [18]. Combined IR reflection-absorption spectroscopy/scanning tunneling microscopy (STM) experiments have delivered important information on the structuring of CO on Pt(111) surfaces at high coverage degrees [19], where the STM technique can be successfully applied to image adsorbed CO.

A transition from a $(2 \times 2) - 3\text{CO}$ ($\theta_{\text{CO}} = 0.75$) adlayer to a $\sqrt{19} \times \sqrt{19}R23.4^\circ - 13\text{CO}$ ($\theta_{\text{CO}} = 13/19$) structure was found at potentials close to 0 V vs. the saturated calomel electrode (SCE). Furthermore, experiments at potentials below 0.2 V vs. SCE in the absence of dissolved CO delivered the more open $\sqrt{7} \times \sqrt{7}R19.1^\circ - 4\text{CO}$ unit cell ($\theta_{\text{CO}} = 4/7$), denoting the sensitivity of the adsorbed species to the presence of CO in solution. These compressed adlayers have also been found recently to be sensitive to the long-range order of the Pt(111) surface [20].

The stoichiometry of the oxidation reaction:



or a similar one for alkaline solutions, suggests that some water species are required for this reaction to take place. It is in fact currently accepted that removal of adsorbed CO occurs through a Langmuir-Hinselwood mechanism [21] where the simplified overall reaction scheme is:



According to this scheme, and assuming a 1:1 adsorbate/substrate relationship and a random distribution of the adsorbates, optimal reaction conditions would be obtained for $\theta_{\text{CO}} = \theta_{\text{OH}} = 0.5$. However, the previous discussion shows that:

1. CO tends to segregate water molecules, so that a random distribution of reactants is not guaranteed, and reaction (4.2) would rather take place at the border of islands or negative nucleation and growth centers.
2. Reaction (4.3) is potential dependent, so that in order to obtain a reasonable θ_{OH} , a corresponding overpotential must be applied.

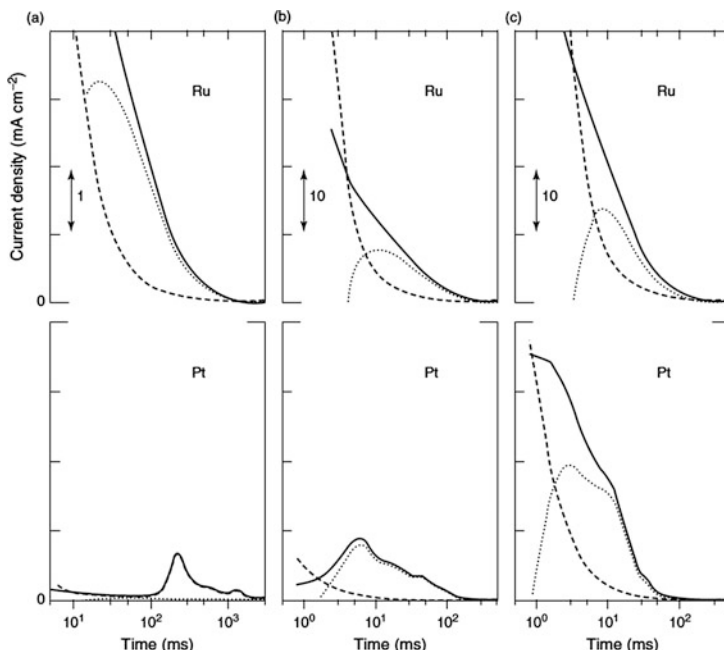


Fig. 4.2 Electrooxidation at constant potential of an adsorbed monolayer of CO on sputter-cleaned Ru and Pt electrodes. (a) 800, (b) 900 and (c) 1000 mV. (—) Currents in the presence of preadsorbed CO, (----) background currents in the absence of CO, (· · · · ·) difference between oxidation and background current. H_2SO_4 0.5 M (Reproduced from Ref. [24] with permission)

The consideration of these two points shows a way to improve the electrocatalytic behavior of the surface. It is clear that Pt constitutes a suitable adsorbent to provide CO_{ad} , so that an alternative way to improve the reaction rate of reaction (4.2) is to introduce on the surface some atomic species that are capable to provide the required OH_{ad} species at lower potentials. This opens the field of bimetallic electrocatalysis that has been analyzed in detail by Ross [22]. Two elements combine with Pt to present optimal performance for CO electrooxidation: Ru and Sn [23–27]. In the case of Pt/Ru alloys, CO is found to adsorb and oxidize on both, Pt and Ru [24]. As long as some Ru sites are set free by oxidation of CO, these sites are found to be very active for OH adsorption, enhancing the performance of the catalyst surface, as found in stripping experiments. Ross [22] has emphasized the difference between this type of mechanisms, where Ru has (as Pt) the dual role of adsorbing CO and OH, and the original bifunctional mechanism as proposed by Watanabe and Motoo in their study using Ru adatoms deposited on Pt [28]. In the latter model, each of the metals constituting the catalyst is specialized in the adsorption of only one of the reactants. However, potentiostatic experiments for CO oxidation on pure Ru and pure Pt electrodes, as shown in Fig. 4.2, clearly indicate that CO and water species adsorb and react on both surfaces.

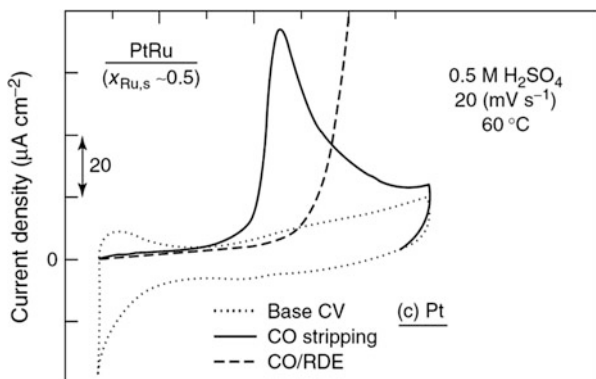


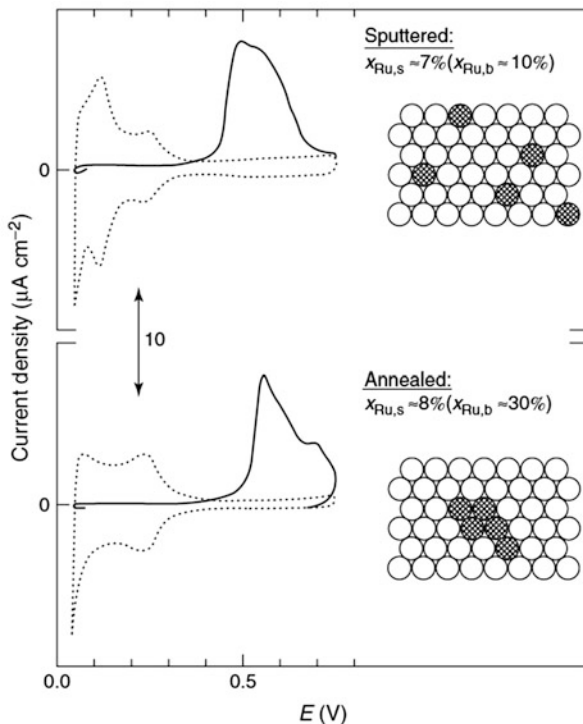
Fig. 4.3 Base voltammogram (\cdots), CO-stripping voltammogram (—) and anodic oxidation of dissolved CO (---) in a rotating disc electrode configuration for UHV sputter-cleaned surfaces. Pt/Ru alloy with a surface composition of 50 % (Reproduced from Ref. [22] with permission)

This difference should be kept in mind to explain the negative reaction order with respect to CO partial pressure. This is consistent with the fact that when dissolved CO is oxidized continuously, the oxidation currents in a voltammogram displace positively with respect to anodic stripping voltammograms, whereas only preadsorbed CO is oxidized and adsorption is avoided. This is shown in Fig. 4.3 for a Pt/Ru alloy, and similar results are obtained for pure Pt electrodes. This effect can be understood in terms of the competition of CO and OH for the same adsorption sites. In the case of dissolved CO experiments, the continuous adsorption of CO increases θ_{CO} at expense of θ_{OH} , and the oxidation rate is decreased.

The nature of the catalytic mechanism makes the performance of the catalyst very dependent on the preparation of the surface, so that sputtered bulk alloys, annealed bulk alloys or submonolayer deposits of Ru behave differently from each other. The latter two systems show a poor performance as compared with the former, and this can be explained according to the model described above in terms of a different geometrical distribution of the Ru atoms on the surface. Annealed bulk alloys and deposited Ru present a trend toward the clustering of Ru atoms, so that for a given composition the number of Pt/Ru pairs becomes smaller and the catalytic efficiency decreases. This is illustrated in the voltammetric behavior of alloys with a very similar surface composition but presenting different distributions of the atoms in the surface, as shown in Fig. 4.4.

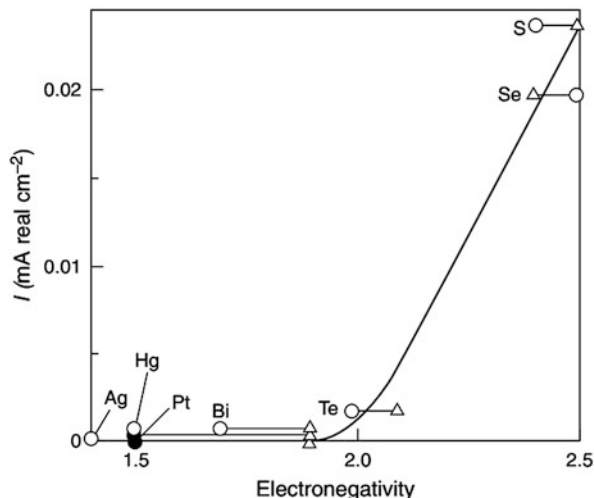
There is still one point that must be considered for complete explanation of the singular behavior of the Pt/Ru catalyst for CO oxidation, and this is the synergistic behavior with respect to pure Ru. Since CO seems to interact with Ru in a similar way to that with Pt, Gasteiger et al. [24] have proposed that the acceleration of reaction (4.2) must be due to a particular status of CO_{ad} in the alloys, making it more active for this reaction. The “pure” bifunctional mechanism could be in part responsible for the high activity of bimetallic catalysts containing Sn, as is the case

Fig. 4.4 CO stripping voltammetry of sputtered and annealed Pt/Ru alloys surfaces with a very similar surface composition as indicated in the figure but different atom distribution on the surface. (—) First-sweep CO monolayer stripping and (·····) first sweep after stripping (Reproduced from Ref. [24] with permission)



of the $\text{Pt}_3\text{Sn}(110)$ surface, since CO has not been detected to adsorb on Sn. As in the case of Ru, remarkable differences in the performance of the bimetallic catalyst are found, depending on the way in which they are prepared. In fact, Pt_3Sn alloys perform much better than deposited Sn. Summarizing on the oxidation of CO on Pt-containing surfaces, we can say that the commonly accepted reaction scheme and the study of the CO adsorbate status on these surfaces brings to the conclusion that in the case of the most active (Ru and Sn containing) catalysts, some degree of bifunctional catalysis occurs (type 2 in our classification in the initial discussion). According to this mechanism, the geometric arrangement of the active sites for CO and OH plays an important role. A first glance to reaction (4.2) suggests that if the availability of OH_{ad} is rate-determining, then the problem can be solved by locating atoms (properly distributed) on the surface that provide this species at a low potential. However, with this simple analysis we are neglecting the specific nature of the OH_{ad} and CO_{ad} species participating in the reaction. This can only be analyzed in terms of their chemical properties, and may be done using quantum mechanical tools. The importance of the quality of the CO_{ad} species is precisely one of the conclusions drawn by Wang et al. [29] in studies with Pt_3Sn alloys, where the

Fig. 4.5 Dependence of the maximum current density for CO oxidation at 0.45 V in 0.5 M H₂SO₄ on the electronegativity of adatom. Electronegativity values from Pauling's (*triangles*) and from Alfred Rochow (*circles*) (Reproduced from Ref. [30] with permission)



existence of a particularly reactive state of CO_{ad} has been postulated at high CO coverages.

Shibata and Motoo [30] studied the effect of several adatoms (S, Se, Te, Bi, Hg) on the rate of bulk CO oxidation at Pt. Figure 4.5 compares the currents measured at 450 mV for different adatoms. The catalytic effect clearly depends on the electronegativity of the adsorbed metal, increasing in the order Te < Se < S.

Recently, there have been many efforts to optimize these catalysts and improve the activity of platinum surfaces towards the oxidation of carbon monoxide. It has been suggested that one could indeed describe the change in the necessary overpotential with two reactivity descriptors: the free energies of adsorption of CO* and OH* on the surface. These adsorption energies may be adjusted by means of modifying the surface structure and composition by positioning appropriate metal atoms at the surface as overlayers or by making surface alloys and near surface alloys.

As an example of the viability of the aforementioned approach, Fig. 4.6 demonstrates how the electrocatalytic activity of the surface of the Pt(111) electrode towards the electrochemical oxidation of CO changes when there is a change in the relative position of Cu atoms [31].

According to DFT calculations, the most active surface, which would bind both *CO and *OH intermediates in an optimum way, is the Cu overlayer on Pt(111) (Fig. 4.6a). Positioning Cu in the first and second atomic layers of the host metal reveals the following theoretical activity trend (Fig. 4.6a): Cu overlayer > Cu–Pt (111) surface alloy (SA) > Cu–Pt near-surface alloy (NSA) > Pt(111).

However, in the experimental realm, the implementation of these systems shows that the electrochemical stability of the copper overlayer is not sufficient, indicating

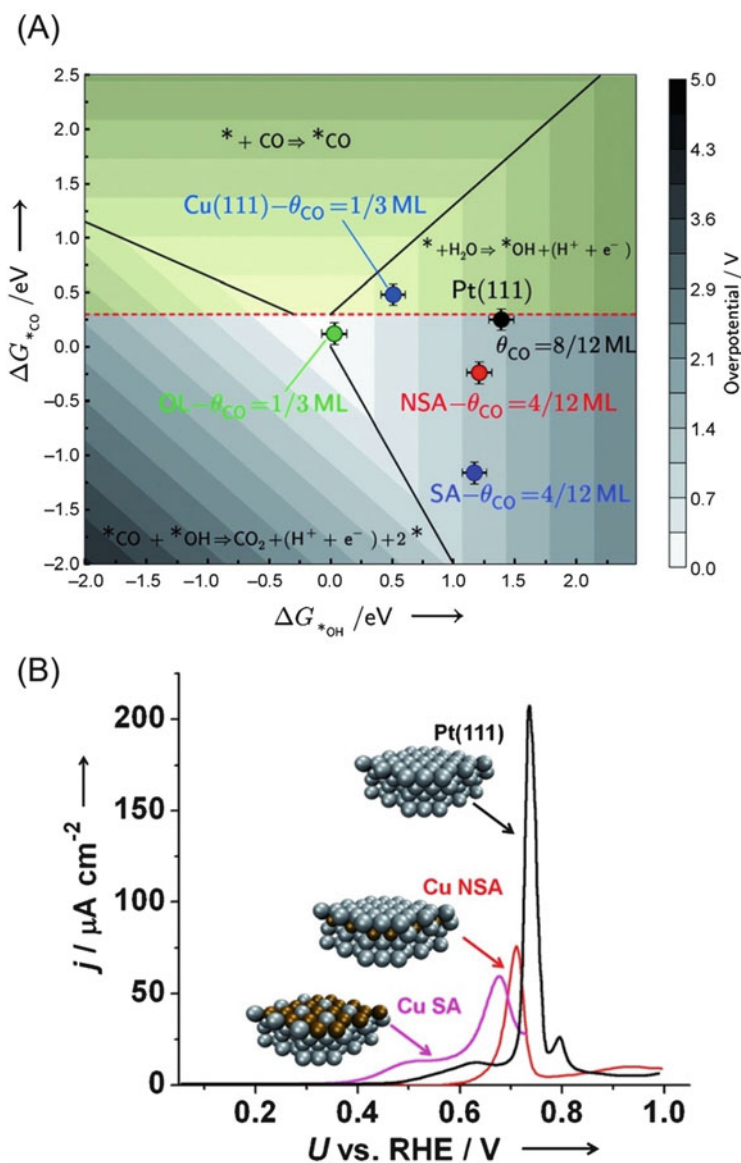
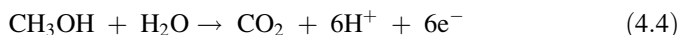


Fig. 4.6 (a) Volcano plot for CO electro-oxidation as a function of the differential free energies of adsorption of CO and OH on different surfaces: Pt(111), Cu(111), Cu/Pt(111) near-surface alloy (NSA), Cu/Pt(111) surface alloy (SA), and Cu/Pt(111) overlayer. (b) *CO stripping voltammograms for Pt(111), Cu/Pt(111) SA and Cu/Pt(111) NSA, in $HClO_4$ (CO was adsorbed at 0.05 V, whereas the voltammogram was carried out in a CO-free solution). More active surfaces enable CO oxidation at lower electrode potentials (Reproduced from Ref. [31] with permission)

the importance of performing the screenings that include stability descriptors. Nonetheless, the other materials confirm the theoretical tendency, as shown in Fig. 4.6b. It could be envisioned that screening procedures which would involve a wider set of possible material combinations and structures as well as additional stability descriptors would identify surfaces with higher CO oxidation activities than those known for the Pt alloys with Sn, Ru, Cu and some other metals.

4.2.2 CH_3OH

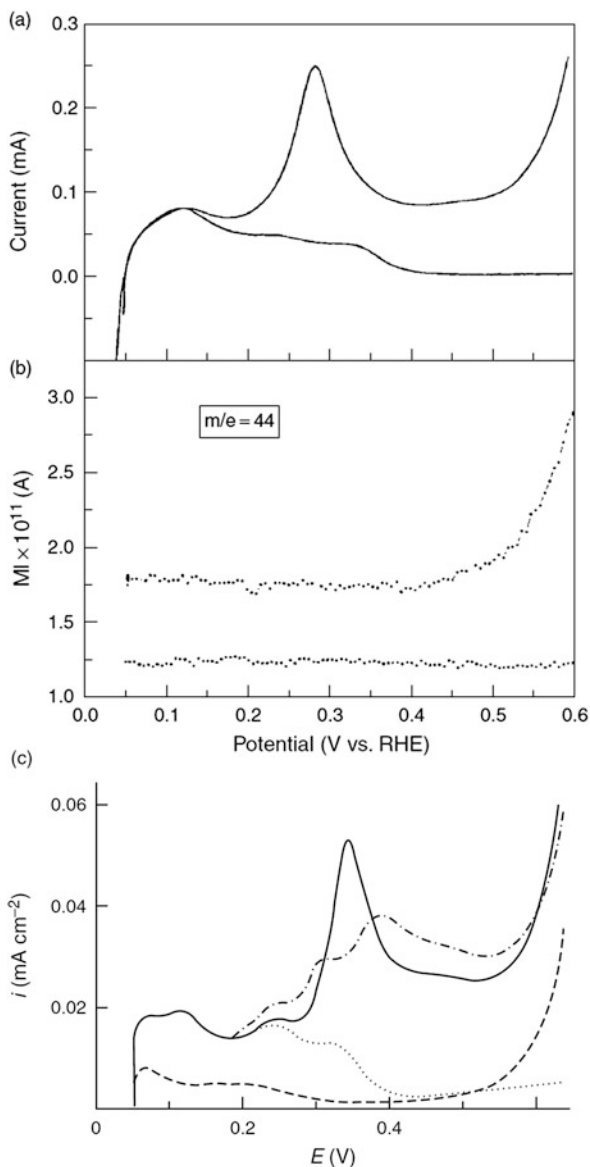
Different aspects of the electrooxidation of CH_3OH on Pt in acid electrolytes, according to the reaction,



have been subjected to extensive reviews. For example, we can mention the electrochemical reaction in relationship to vacuum studies [32], reaction mechanism [33] and the electrooxidation process in the context of direct methanol fuel cells [34]. We discuss here the more salient conclusions drawn on the basis of experimental studies that will be discussed below in the context of theoretical studies. It is out of question that the oxidation of CH_3OH on Pt surfaces starts with dehydrogenation of the molecule, as experiments using differential electrochemical mass spectrometry (DEMS) clearly show. In Fig. 4.7, we present DEMS results from Vielstich and Xia [35], showing that the current peak at ca. 0.3 V for methanol electroadsorption on a fresh Pt surface is not accompanied by a corresponding CO_2 production.

This dehydrogenation process appears to be very sensitive to the conditions of the surface, as illustrated in Fig. 4.7c, where we see that addition of small amounts of SO_4^{2-} containing electrolytes produces important changes in the voltammetric profiles [36]. It can also be concluded from the figure that this process disappears after creation of adsorbed species (i.e., 120-s adsorption at 0.5 V). The other point clear in the literature is that during the CH_3OH electrooxidation process, CO species occur on the surface, as has been found by Beden et al. [37] by means of electrochemically modulated IR spectroscopy (EMIRS). In these experiments, clear evidence was found for the presence of linear and multibonded CO species. These studies were extended to single crystal surfaces [38]. In all cases, indication of linear or multibonded CO was found. The former was found to predominate in the spectra in the cases of the more open (100) and (110) surfaces. In the case of the (100) face, a complex shaped band at low frequencies was assigned to formyl species. Quantitative analysis using photoelastically-modulated IR reflectance absorption spectroscopy showed that the predominant species was in fact linearly bonded CO, with the additional finding that for equivalent coverage degrees, the CO adsorbate from CO or CH_3OH yielded different spectroscopic behavior [39]. The monitoring of products during the electrooxidation process has been

Fig. 4.7 First potential scan starting the potential scan at 0.05 V. (a) Porous platinum electrode in 0.2 M CH₃OH with 0.1 M HClO₄, current/potential profile, sweep rate of 0.01 Vs⁻¹. (b) Simultaneously recorded mass signal CO₂ production. The lower curves correspond to blank experiments. (Reproduced from Ref. [35] with permission) (c) Smooth platinum electrode: (· · · · ·) 0.05 M HClO₄ base electrolyte, (—) 0.01 M CH₃OH/0.05 M HClO₄, (- - - - -) 0.01 M CH₃OH/0.05 M HClO₄/10⁻³ M Na₂SO₄, (----) 0.01 M CH₃OH/0.05 M HClO₄. First sweep after 120-s adsorption at 0.5 V (Reproduced from Ref. [36] with permission)



made by using substantively normalized Fourier transform IR spectroscopy. The detection of significant quantities of HCOOH during the electrooxidation process [40] may have mechanistic implications, as will be discussed below. A thorough comparison of the spectroscopic features of CO_{ad} arising from CH₃OH adsorption with that from the adsorption of dissolved CO was given in the review by Hamnett [33]. Some of the most important conclusions are:

- CO_{ad} coverages are remarkably smaller in the case of CH_3OH adsorption.
- Some indirect coulometric indication exists that other species than CO_{ad} are formed at low CH_3OH concentrations.
- CO island formation appears to occur to a lower extent in the case of CO_{ad} stemming from CH_3OH .
- No bridged CO_{ad} is found for methanol oxidation on Pt(111), for concentrations between 0.05 and 5 M.
- In contrast to adsorption from dissolved CO where only bridged CO is found, both bridged and terminal CO appear on Pt(100) when CH_3OH is adsorbed.

The fact that methanol suffers dehydrogenation and the finding of CO_{ad} in different coordinations as a stable intermediate lead to the conclusion in terms of a dehydrogenation scheme proposed by Bagotzky et al. [41] that in principle as many as eight different intermediates may occur before reaching the final CO_2 product, ranging from the first dehydrogenated version of CH_3OH , i.e., CH_2OH , to the COOH intermediate species also postulated for the oxidation of formic acid. A whole set of reaction possibilities, including the oxidative desorption of some of these species to yield formaldehyde or formic acid has been compiled by Hamnett in the review mentioned above. To the eight possible intermediates mentioned above, we should also add the methoxy (CH_3O) intermediate, assigned by Lopes et al. [42] to EMIRS vibrational spectra obtained with moderate CH_3OH concentrations. If the existence of methoxy is confirmed, multiple pathways could be suggested for methanol dehydrogenation, since isotopic studies by Franaszczuk et al. [43] indicate that this process should mainly proceed by the scission of the C–H bond. Concerning the non-methoxy dehydrogenated intermediates, Sun [44] claims having identified CH_2OH , CHOH , CHO and COH , while Nichols and Bewick assign bands observed in the potential region active for CH_3OH methanol oxidation to the species COH , CHOH or CH_2OH . However, these bands were found to disappear if the potential is lowered 0.2 V vs. SCE. More evidence for other dehydrogenated species is reported in the work of Sun [44]. The potential complexity of this reaction mechanism opened thus the hypothesis of the existence of parallel oxidation pathways. Since the firmly identified intermediate CO_{ad} proves to be a very electrochemically stable one, much effort has been devoted towards identifying a more easily oxidizable species, in order to find the way to promote CH_3OH oxidation over this “fast” pathway. The identification of the “easily oxidizable” intermediate would probably allow for deviating the reaction over this pathway, with the consequently increased reaction rate. However, at variance with the case of HCOOH addressed below, where the “fast” pathway has been identified and clearly promoted, the case of CH_3OH has proved to be an extraordinarily difficult one, and the acceleration of the electrooxidation of CH_3OH seems to be rather linked to the acceleration of the slow reaction path via CO_{ad} . Aside from CO_{ad} , the more firmly suggested candidates for alternative reaction pathways have been C–OH and H–CO out of all the intermediates that may potentially appear during CH_3OH electrooxidation. Besides the original hypothesis sustained by Bagotzky and Vassilyev [45], the assumption of an H:C:O intermediate was

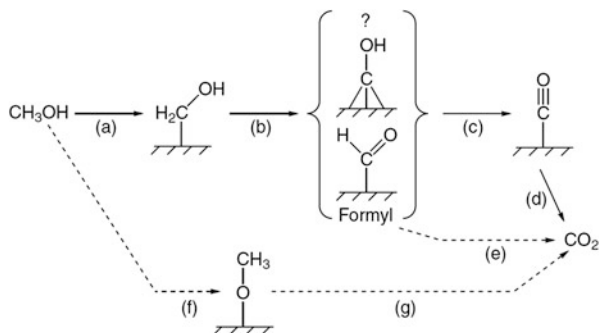


Fig. 4.8 Known (solid arrow) and possible (dashed arrow) electrooxidation pathways for methanol to form CO_2 . CO species have been identified by IR spectroscopy. Indirect evidence through differential electrochemical mass spectroscopy [46] as well as by ECDTMS [47] experiments exist for a H:C:O intermediate (Reproduced from Ref. [32] with permission)

revitalized by indirect evidence through differential electrochemical mass spectroscopy [46] as well as by ECDTMS [47] experiments, where the loss of hydrogen associated with CO desorption was detected in thermal desorption diagrams. The existence of H:C:O has also been suggested on the basis of IR spectroscopy as discussed above, but has not definitively proved until now in the sense of providing an experimental body of information capable of determining the kinetic parameters for the formation and oxidative reaction of this species.

Thus, in general, we can say that there are several traces for the existence of this intermediate but not a proper characterization as in the case of CO_{ad} . As the potential complexity of the reaction mechanism suggests, the analysis of kinetic data (i.e., Tafel plots) for CH_3OH is far from straightforward; the kinetic parameters depending on oxidation potential, methanol concentration and platinum surface morphology [33]. The bell-shaped curves obtained for the surface coverage by the adsorbed species resulting from methanol adsorption at a constant potential [48] indicate, as can also be inferred from the results shown in Fig. 4.7, that CH_3OH is not able to displace H_{ad} for its adsorption, and that an important fraction of the surface must be free for adsorption to take place.

In recent time, the kinetic modeling of methanol electrooxidation on Pt has undergone [49] renewed interest, with the aim of establishing the existence of a dual reaction pathway, like that shown in Fig. 4.8. This kinetic modeling by Sriramulu et al. [49, 50] for CH_3OH oxidation on Pt(111) is based on Langmuir–Hinselwood kinetics, and points to a H:C:O intermediate more abundant at short times and low coverages, as well as to a CO intermediate at long times and high coverages.

In contrast to the cases of CO analyzed above or the HCOOH discussed below, the activation of the electrooxidation of CH_3OH by adatom deposition or bimetallic surfaces has been in many cases found more ambiguous and rather poorly defined. As an example, we show in on the left of Fig. 4.9 the early results of Motoo and Watanabe [51] for the Pt(substrate)/Sn(adatoms) system. We can see in this figure

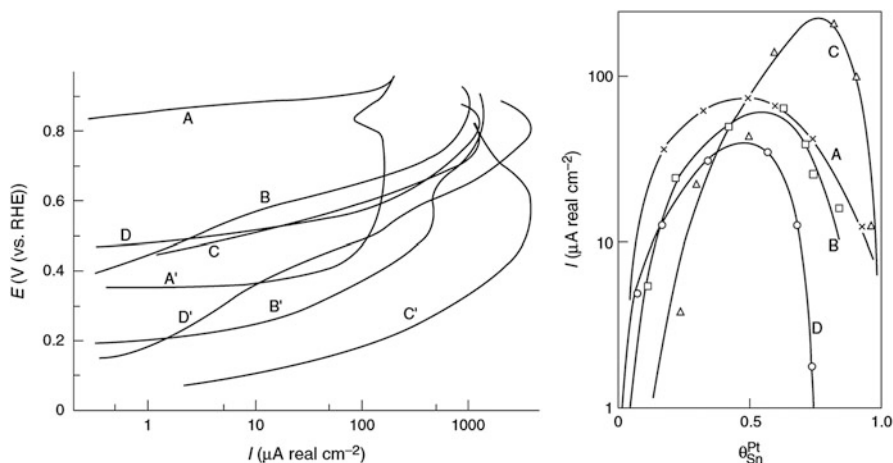
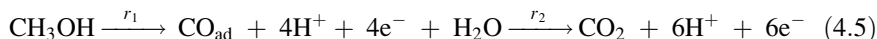


Fig. 4.9 Polarization curves for the oxidation of CO (A, A'), HCOOH (B, B'), HCHO (C, C') and CH₃OH (D, D') at 40 °C. (A, B, C, D) on pure polycrystalline Pt, (A', B', C', D') on Pt with deposited Sn atoms (Reproduced from Ref. [51] with permission)

that while the adatom effect on CO and HCHO oxidation appears as formidable, it is less important in HCOOH and modest for CH₃OH.

From all the bimetallic systems studied in the literature for improving methanol electrooxidation, the only one that has enjoyed general consensus was Pt/Ru [22, 34, 52], followed by Pt/Sn, for which much more diverse results have been obtained. We briefly give here the most relevant features found by experimentalists.

While early studies by Watanabe and Motoo [53] employing adatoms indicated that a coverage close to 0.5 by Ru would be optimal for enhancing CH₃OH electrooxidation, work using well-characterized Pt/Ru alloys [54] showed that a 10 % Ru containing alloy performed considerably better than a 50 % one. We discuss here the mechanism proposed by these authors for the reaction. The electrooxidation process was proposed to follow the series sequence:



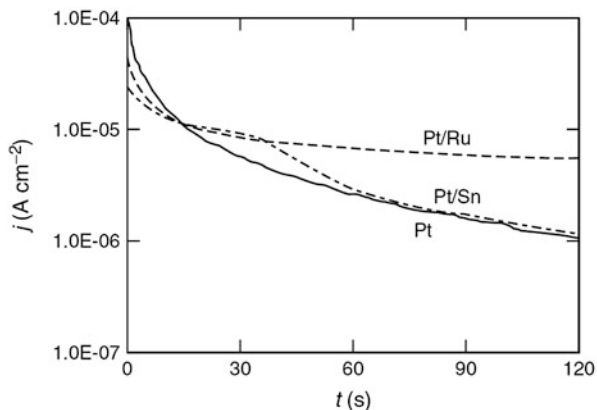
where methanol adsorption would take place only on the Pt sites on the surfaces, yielding ensembles of Pt atoms with CO_{ad}, and the Ru atoms would act as OH_{ad} providing centers. The r_1 and r_2 denote global rates assigned to these processes, although each of them involves several elementary steps. According to this, the catalytic improvement would be due to a bifunctional mechanism (type 2), as that proposed for carbon monoxide. The reason why a Pt/10 % Ru alloy may perform better than a more Ru-concentrated one can be qualitatively understood in terms of this scheme. Increasing Ru content increases r_2 by providing more adsorbed water species required to oxidize CO_{ad}. However, since dissociative electroadsorption of the organic molecule is very demanding of Pt sites, r_1 decreases with increasing θ_{Ru} .

Thus, the rate-determining step (RDS) may change from r_2 for $\theta_{\text{Pt}} = 1$ to r_1 at some intermediate θ_{Ru} , where the first step in Eq. (4.5) is strongly inhibited. In the case where CH_3OH adsorption on Ru is made possible via increasing the temperature of the cell [55], the optimal composition of the alloy was found to change to a more concentrated Pt/Ru alloy (30 % in Ru), giving also further support to the explanation given above. Interestingly, these experiments also provided information on the activation energy, E_a , for the whole electrooxidation process. It was found that while Ru-concentrated alloys presented E_a values compatible with the dissociative adsorption of the molecule (ca. 0.6 eV), the E_a values for the 10 % Ru alloy were rather compatible with those expected for CO_{ad} diffusion on the surface (ca. 0.3 eV), indicating that this CO motion on the surface plays a very important role in the electrooxidation process. More recent work by other groups on the electrooxidation of CH_3OH on Pt/Ru alloys using Fourier transform IR spectroscopy [56] or employing Pt single crystal surfaces modified by Ru adlayers [57] confirm the general bifunctional picture given above. Note that in all the previous analysis to explain the promotion found with Pt/Ru alloys, an alternative pathway for CH_3OH electrooxidation does not appear at all. In the case of Sn/Pt bimetallic catalysts, the reports on catalytic improvement are far more diverse than in the case of Ru/Pt [32, 33]. Here, we provide some of the highlights given by Haner and Ross [58], because these authors have performed a careful comparative study with Pt_3Sn alloys and Pt single crystal surfaces modified by upd of Sn. Some of the main results were:

- The Pt_3Sn (111) and (100) faces, as well as a polycrystalline 2 % Sn alloy showed no catalytic improvement with respect to pure Pt surfaces. Partial dissolution of Sn to increase Pt concentration led to a concomitant increase in methanol oxidation current.
- Pt(110) and polycrystalline Pt surfaces showed no enhanced activity for any Sn (II) concentration in solution.
- Pt(111) and Pt(110) surfaces showed enhanced activity for methanol electrooxidation at a concentration of Sn(II) ca. 10^{-6} M. In the former case, the enhancement was found to disappear if the surface was roughened via Ar^+ bombardment.

The authors concluded that tin possessed a negative electronic effect on the reaction and proposed a mechanism of action of Sn based on dissolved Sn(II) species, weakly interacting with the surface. This oxygen-containing species should react with the residues stemming from methanol adsorption to yield CO_2 , being regenerated via reaction with OH_{ad} . It was also mentioned in this work that the use of potential sweeps to study the reaction could underestimate the true kinetic enhancement due to diffusional limitations, a fact that would conciliate the results

Fig. 4.10 (a)
Cronoamperometry of
smooth (a) and high area
(b) Pt, Pt/Ru and Pt/Sn
electrodes in 3 M H₂SO₄
with 1 M CH₃OH at
500 mV vs. RHE
(Reproduced from Ref. [60]
with permission)



obtained there with others where an important activation by Sn has been reported [59]. Subsequent experiments by Morimoto and Yeager [60], presented in Fig. 4.10, indicate the sensitivity of the catalytic activity of the Pt/Sn system to the time scale in which it is measured, as well as to the roughness of the electrode. While in the case of smooth electrodes, the long-time behavior of Pt/Sn electrodes is practically the same, a marked difference is found for high area electrodes, a fact that was attributed to the dissolution of Sn from the surface.

Because of the fact that the overall activity towards methanol electrooxidation depends to a large extent on the electrochemical oxidation of CO, it can be predicted to some degree by the same descriptors as in the case of carbon monoxide oxidation (as considered in the previous section). Figure 4.11 shows the output of a theoretical screening performed by Rossmel et al., where the theoretical activity of Pt surface alloys towards CH₃OH electrooxidation was analysed [61].

As can be seen from Fig. 4.11a, the Pt–Ru combinations are situated close to the optimum region of the volcano plot. However, as the Cu–Pt surface alloys (discussed in the previous section) are active towards CO oxidation, they are also found to be very close to the theoretical optimum. In order to experimentally evaluate the effect of Cu on the oxidation of methanol, Rossmel et al. [61] did a series of measurements utilizing Cu overlayers on platinum by changing the Cu coverage (Fig. 4.11b). From this work, it was possible to estimate experimentally that the optimum Cu coverage is ~0.5 ML, giving an activity approximately three times as large as that of pure Pt surfaces, which is in qualitative agreement with theoretical tendencies. Further experiments with real Cu–Pt surface alloys would be necessary to evaluate this promising catalyst in detail.

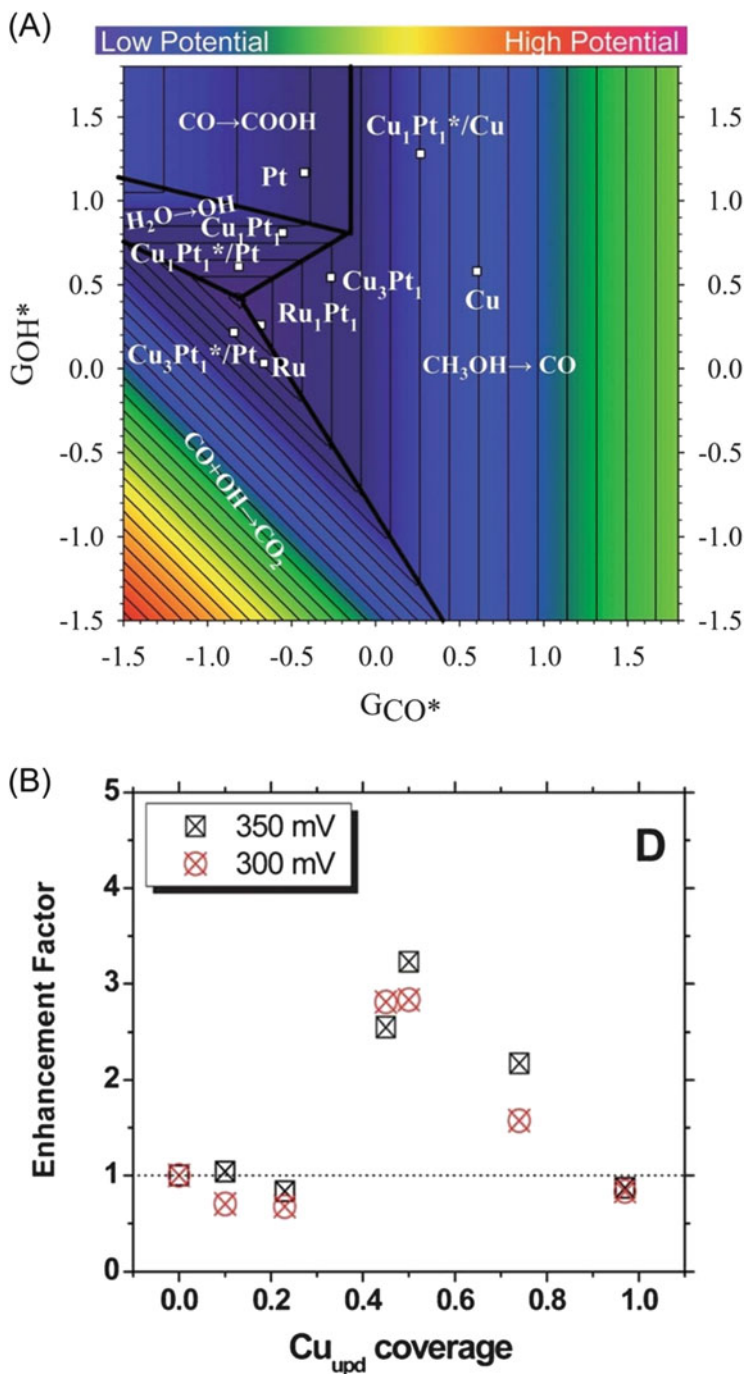
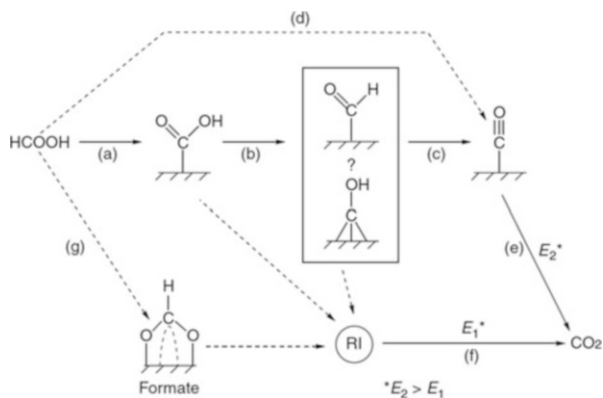


Fig. 4.11 (a) Positions of selected Pt–Ru and Pt–Cu bulk and surface alloys on the volcano plot for the methanol oxidation reaction. The potential determining step of each region (outlined in *black*) is also shown. (b) Activity enhancement factors of methanol electrooxidation activities at 0.3 V/AgCl and 0.35 V/AgCl as a function of Cu coverage (Reproduced from Ref. [61] with permission)

4.2.3 HCOOH

The most positive aspect of the electrooxidation of formic acid can be stated by saying that this molecule contains in itself all it is required to be turned into CO_2 . Thus, the only condition that a proper catalyst must fulfill is to be a good dehydrogenator, provided it is not poisoned by some species occurring during this process. As simple as it sounds, the conditions for an optimal catalyst usable with practical purposes have not been yet found. An extensive reviewing on this electrooxidation process between 1981 and 1988 was made by Parsons and VanderNoot [62] and more recent discussion has been given by Jarvi and Stuve [32]. In Fig. 4.12, we present the scheme given by these authors for the reaction pathways of HCOOH on Pt surfaces, according to the time-being knowledge on this reaction. This reaction scheme involves the complete oxidation to CO_2 (f) via a “reactive intermediate” in parallel with a pathway where adsorbed CO is formed (d). The latter behaves as a poisoning intermediate, with a very slow reaction rate (step (e)). The length ratio solid arrow/dashed arrows show that although three decades of massive extensive and intensive research on the area, our ignorance on the nature of the species occurring during this reaction is greater than our knowledge. The main problem is, as in the case of CH_3OH previously discussed, that the stoichiometry of the intermediates has been mainly inferred through indirect evidence (i.e., current and charge measurements). IR techniques, extremely powerful to identify the chemical nature of species, have pointed as a rule to the appearance of adsorbed CO as intermediate; the existence of other species being masked by the strong IR adsorbing properties of water. The potential energy picture expected for parallel reaction pathways, as suggested for HCOOH oxidation is depicted schematically in Fig. 4.13. In the present case, I_2 and I_1 would represent the reactive intermediate and the CO poison respectively. Thus, the reaction should occur mainly through intermediate I_2 . However, I_2 and I_1 are both adsorbed intermediates and compete for the same adsorption sites, so that I_2 accumulates on the surface of the electrode,

Fig. 4.12 Known (solid arrow) and possible (dashed arrow) electrooxidation pathways for formic acid to form CO_2 (Reproduced from Ref. [32] with permission)



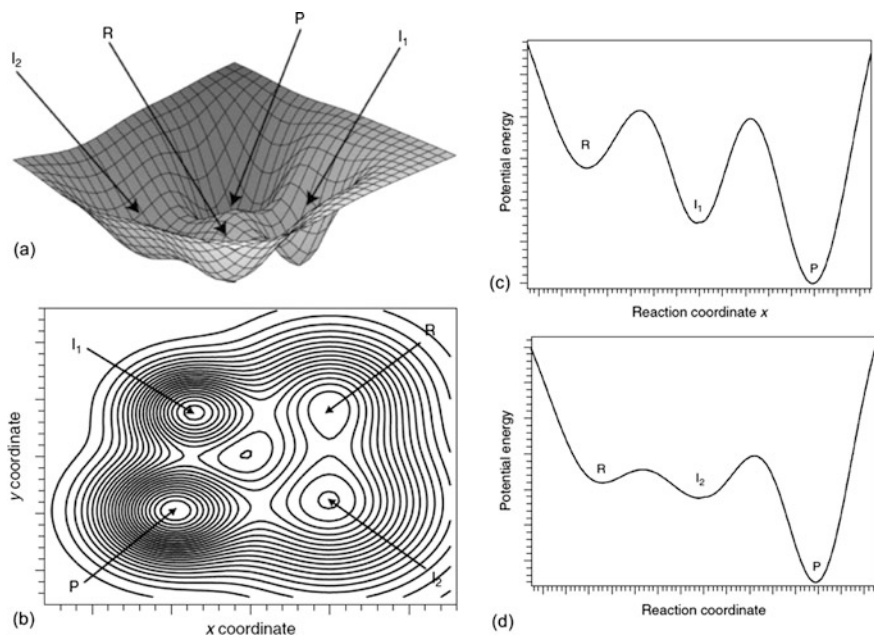


Fig. 4.13 Potential energy surface for a reaction that may proceed via two alternative intermediates: three dimensional representation (a) and contour plot (b) energy as a function of the position along the two possible minimum energy paths joining reactants and products in the shown potential energy surface: pathway through intermediate I_1 (c) and I_2 (d) (Reproduced from Ref. [63] with permission)

the concentration of I_1 decreases and the overall reaction rate is concomitantly decreased.

As in the previous cases, we briefly address here some experimental evidence that will be used in the context of the theoretical discussion.

As in the case of CH_3OH , the dehydrogenation of the HCOOH is concomitant with the appearance of CO_{ad} [5, 64], which blocks the surface of the electrode for some other surface reactions, such as the formation of adsorbed hydrogen. The blocking of several single crystal surfaces upon HCOOH adsorption has been quantified by Clavilier and Sun [65] by measuring the electrical charge for hydrogen desorption before and after formation of the poison in HCOOH 0.1 M. If we call these quantities Q_0 and Q_f respectively, the percentage of sites blocked was defined:

$$S_b = 100 \frac{Q_0 - Q_f}{Q_0} \quad (4.6)$$

S_b is shown in Table 4.2 for the Pt low index single crystal faces, and the results are compared with those obtained for the adsorption of CH_3OH . From this table it becomes clear that the site requirements for CH_3OH adsorption are larger than for

Table 4.2 Percentage of sites blocked for hydrogen adsorption on different Pt surfaces after adsorption in 0.1 M HCOOH and 0.1 M CH₃OH [0.1 M HClO₄] [65, 67]

Face	S _b (HCOOH)	n(HCOOH)	S _b (CH ₃ OH)	n(CH ₃ OH)
111	70.5	2.00	37.0	2.05
100	77.4	2.02	57.0	2.06
110	94.0	1.63	86.0	1.62
Polycrystalline	73.2	1.73	55.0	1.77

Taken from Refs. [65, 67] with permission

HCOOH and that more open surfaces show greater susceptibility to poisoning. These authors have also collected information on the number of electrons, n , transferred per hydrogen site to oxidize the poison on these and other single crystal faces. This quantity was calculated according to:

$$n = \frac{Q_p}{Q'_0 - Q_f} \quad (4.7)$$

where Q_p is the charge corresponding to the oxidation of the poison, and Q'_0 is the hydrogen charge recovered after desorption of the poison. These values are also shown in Table 4.2. The values close to two suggest that the chemisorbed poison should be essentially linearly bonded CO, while the lower values indicate the presence of other CO species with a larger coordination with the surface. The kinetics of CO poisoning during HCOOH electrooxidation on polycrystalline Pt has been followed using the single potential alteration IR technique by Corrigan and Weaver [66]. The integrated absorbance of the ν_{CO} band A_i was found to deliver a reliable measure for the coverage degree by CO_{ad}, so that following this quantity during the electroadsorption of HCOOH was equivalent to following the concentration of the poison. Figure 4.14 shows A_i as a function of time for HCOOH adsorption under different conditions.

Sun et al. [68] have also measured the kinetics of dissociative adsorption of HCOOH on Pt, employing for this purpose single crystal electrodes. A very interesting point in these studies, performed using a low concentration of HCOOH, is the existence of a maximum in the average rate of poisoning. These authors defined an average rate of dissociative adsorption, \bar{v} , as:

$$\bar{v} = \frac{Q}{t} \quad (4.8)$$

where Q is the charge corresponding to the oxidation of the dissociative adsorbate formed, and evaluated this average rate for $t = 1$ min at different adsorption potentials, as shown in Fig. 4.15 for Pt(100). While in the case of CH₃OH the maximum of poisoning is related to the onset of the oxidation of the poisoning CO_{ad}

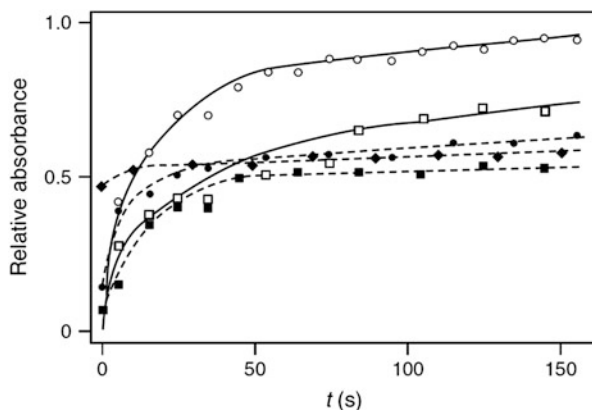


Fig. 4.14 Adsorption kinetics of formic acid at 0 V (*squares*) and 0.1 V (*circles*) vs. SCE as determined from the relative integrated absorbance of the ν_{CO} band as a function of time for various potential steps. Open symbols: previous cleaning at 1.2 V for several seconds; closed symbols: partial electrooxidative desorption at 0.35 V before stepping back to the adsorption potential; diamonds correspond to a readsorption at 0 V, with an initial surface coverage close to 0.5 (Reproduced from Ref. [66] with permission)

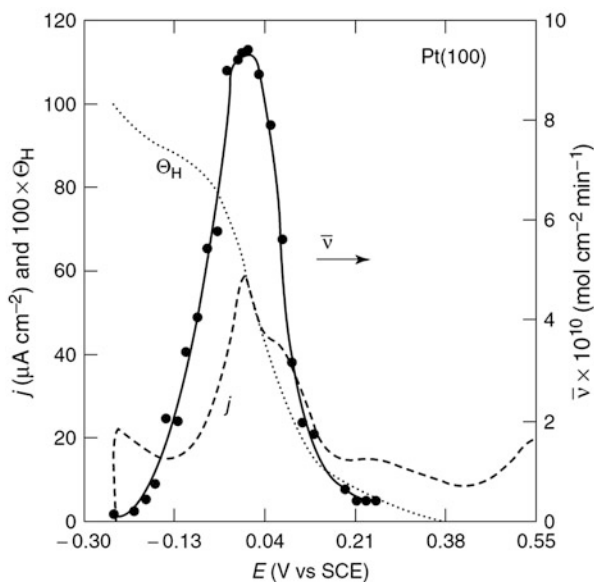


Fig. 4.15 Variation of the average rate of HCOOH dissociative adsorption $\bar{\nu}$, the coverage degree of the clean surface with hydrogen, Θ_H , and the oxidation current in base electrolyte with the potential for Pt(100) in 0.1 M HClO_4 . HCOOH concentration: 5×10^{-4} M (Reproduced from Ref. [68] with permission)

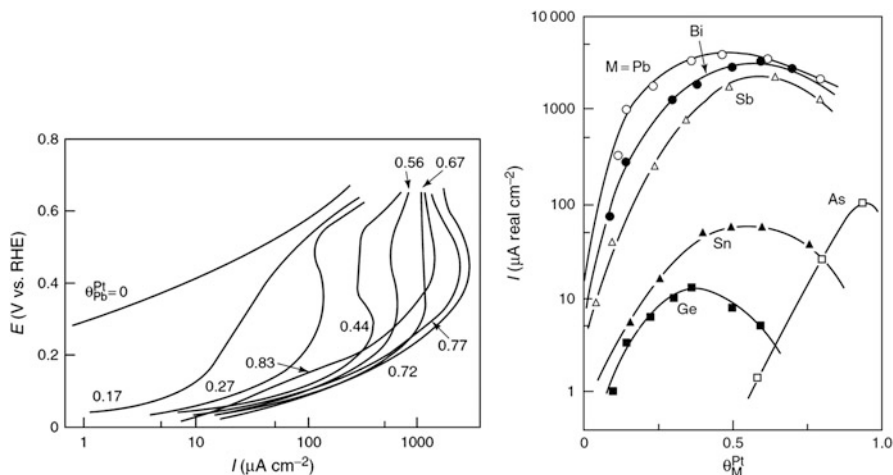


Fig. 4.16 (a) Steady state polarization curves of Pb ad-electrodes for formic acid oxidation. The number on the curves show the coverages of smooth Pt with Pb adatoms. (b) Relationship between the coverage of smooth platinum with various adatoms and the current density at 0.25 V vs. RHE. Conditions: 1 M HCOOH/0.5 M H₂SO₄, 40 °C (Reproduced from Ref. [70] with permission)

species (at ca. 0.5 V vs. the reference hydrogen electrode (RHE)), this is clearly not the case of HCOOH, where the maximum occurs at ca. 0.28 V vs. RHE. As can be seen in the Figure, this potential corresponds to a coverage of the surface of 50 % by adsorbed hydrogen, suggesting that an important source for the poisoning stems from the reactions of adsorbed organic species with adsorbed hydrogen.

Both the poisoning of the surface and the electrooxidation of HCOOH on Pt appear as very sensitive to the nature of the single crystal Pt surface employed. The most active Pt(100) surface, in the sense that the higher currents are obtained there, is the more poisonable one. The least active and poisonable (111) exhibits anyway $\theta_{CO} = 0.35$ at maximum coverage in the voltammetric experiments [69].

As advanced above in Fig. 4.9 for the case of Sn adatoms, early work with upd metals delivered very promising results for improving the electrocatalytic activity of platinum towards HCOOH electrooxidation. Watanabe et al. [70] performed polarization curves for HCOOH electrooxidation on polycrystalline Pt surfaces using fourth and fifth group adatoms at different coverage degrees. Some results from Watanabe et al. are given in Fig. 4.16. From Fig. 4.16a we see that the presence of Pb, the most remarkable case, increases the activity of Pt in several orders of magnitudes at low potentials. For other adsorbate metals the enhancement is less remarkable, as can be seen in Fig. 4.16b, but in most cases a maximum activity is found at some intermediate coverage degree by adatoms. Other promising studies involved the use of Pd [71, 72], which is itself active for HCOOH electrooxidation. Work on the catalysis by adatoms has been reviewed by Adzic [73], Kokkinidis [52], Parsons and VanderNoot [62] and more recently by Jarvi and Stuve [32]. Possible hypothesis for the activation mechanism by adatoms have been analyzed by Parsons and VanderNoot [62], and can be synthesized as follows:

- Microscopic “mechanical” effects. The motion of adatoms should increase via collisions with the poisoning species their likelihood of desorption. This is a poisoning preventing effect.
- Blocking of hydrogen adsorption. This should prevent the reaction of the HCOOH molecule or reactive intermediate with H_{ad} from forming the poison.
- Alteration of the electronic properties of the substrate.
- Blocking of the poisoning reaction (within this family is the so-called third body effect).
- Bifunctional catalysis.

Let us discuss briefly these items. The collision hypothesis could in any case work to explain the inhibition of poison formation, but not the enhanced desorption of the poison. While the kinetic energy of the atoms in the surface is of the order of $k_B T$ (0.026 eV), the binding energy of the poisoning species amounts to ca. 2 eV. Thus, eventual collisions make a negligible energetic contribution. Furthermore, mobile metallic atoms would tend to merge and grow islands on the surface, which is the most stable state for metallic adsorbates.

The second point, inhibition of the poisoning via adsorbed hydrogen, justifies part of the activation effects observed. However, experiments which avoid hydrogen adsorption also present poisoning effects if high concentrations of HCOOH are used. The third point is not well defined unless a tentative reaction mechanism for HCOOH is given. In fact, we are in the presence of a bond breaking/creating reaction, so that the influence of the electronic status of the catalyst must be accounted for in the rate-determining step of the oxidation reaction. Point five can also be considered in the context of the activation discussed for CO and CH₃OH. Given a dual reaction pathway, where the species accumulating in the slow pathway may block the fast one, removal of the blocking species will naturally lead to a global improvement of the reaction. For this to happen, the removal of blocking species must already succeed at a potential where the fast pathway is operative. Thus, we are left with the blocking of the poisoning reaction as a salient feature of HCOOH with respect to the other systems considered above.

In relation to the different mechanisms discussed above, Leiva et al. [74] developed a theoretical model to explain the effect of adatoms in the electrocatalysis of HCOOH oxidation. Assuming square or hexagonal arrays of lattice points to describe the (100) and (111) single crystal faces of Pt respectively, these authors performed simulations of the catalytic activity of these surfaces for HCOOH oxidation in the presence of different adatoms. Three different cases were considered for the role played by adatoms, which are depicted in Fig. 4.17:

- (I) Adatoms cause a true enhancement of the reaction rate, and the substrate surface is not poisoned by the organic residue. It was assumed that pairs of both free and adatom-covered sites act as centers for the reaction. Furthermore, it was assumed that the catalytic activity of such pairs is much higher than the intrinsic activity of the substrate, so that the latter can be neglected. This case is illustrated in Fig. 4.17a.

In the case of an hexagonal lattice, the mathematical form of the current (I) vs. adatom coverage (θ) relationship is:

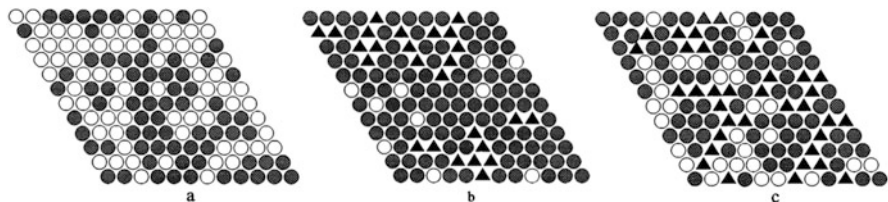


Fig. 4.17 Model of the adsorbate-covered surfaces employed by Leiva et al [74] to model electrocatalytic effects of adatoms on the oxidation of formic acid. *Empty circles* represent the substrate sites, *full circles* the adsorbed atoms, and *filled triangles* the poisoning species. (a) Only empty sites and adatoms occur on the surface. No poisoning species are built up. (b) These surfaces consist of poisoning species, adatoms, and empty sites which are free from being poisoned only because they are completely surrounded by metallic adatoms. (c) This is the more general case. The surface presents poisoning species, adatoms, free places and substrate sites which are not surrounded by adatoms but are left empty. The latter could represent those places which are left free due to oxidative removal of the poison (Taken from Ref. [74] with permission)

$$I \propto (1 - \theta)(\theta + \theta^2 + \theta^3 + \theta^4 + \theta^5 + \theta^6)$$

(II) Only third-body effects are operative. Adatoms are electrocatalytically inert and prevent the poisoning of the surface only by steric effects. Poison formation is precluded at substrate sites which are completely surrounded by adatoms and these sites are the only ones delivering a contribution to the oxidation current. This case is illustrated in Fig. 4.17b.

The mathematical form of the current (I) vs adatom coverage (θ) relationship is:

$$I \propto (1 - \theta)\theta^n$$

Where n is 6 or 8 for the hexagonal and square lattice respectively.

(III) Both, third-body and real catalytic effects are operative. The substrate surface is poisoned by the organic residue at different extents. Besides the sites which are set free because they are completely surrounded by adatoms, other sites are set free additionally, assuming that currents are measured at a potential where the poison starts being oxidized. This case is illustrated in Fig. 4.17c.

The previous modeling was applied to different experimental systems, as depicted in Fig. 4.18. Figure 4.18a depicts a system that reflects the behavior of case I. This corresponds to HCOOH electrooxidation on the Pt(111)/Bi adatoms system. The full line represents the theoretical predictions, while the filled circles are experimental results from reference [75]. In the case of the theoretical results, at zero coverage degree the current is zero because the intrinsic activity of the substrate is neglected. The current then increases almost linearly over a wide range of coverages, goes through a maximum, and finally drops when the surface becomes completely covered by adatoms. The broad linear range occurs because

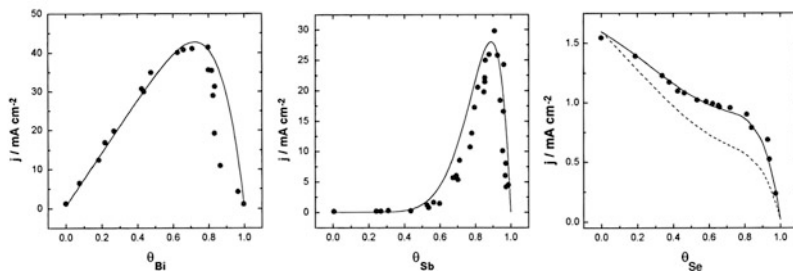


Fig. 4.18 Results from theory (*full lines*) and experiment (*filled circles*) with behaviors coming close to the three cases for electrocatalysis by adatoms of HCOOH oxidation described in the text. Current vs coverage curves for the (a) Case I. Electrooxidation of formic acid at Pt(111)/Bi 0.25 M HCOOH + 0.5 M H₂SO₄. (b) Case II. Electrooxidation of formic acid at Pt(100)/Sb 0.25 M HCOOH + 0.5 M H₂SO₄ (c) Case III. Electrooxidation of formic acid at Pt(111)/Se 0.1 M HCOOH + 0.5 M H₂SO₄ (Taken from Ref. [74] with permission)

the adatoms keep on contributing to the total current as long as they have at least one free substrate neighboring site. The linearity also denotes that the current switches on with a single unoccupied neighboring site close to an adatom, and then remains constant regardless of the number of unoccupied sites neighboring it.

Figure 4.18b shows the behavior of a system that reflects case II: HCOOH electrooxidation on Pt(100)/Sb adatoms. It has been shown that partially covering a Pt(100) electrode with Sb adatoms causes a linear decrease of the amount of CO formed in the presence of HCOOH [76, 77]. This is a typical third body effect, aside from the fact that, additionally, Sb may act as a true catalyst of the reaction. The experimental results (filled circles) show the necessity for the coverage of Sb to be above 0.4 in order to produce an increase in current. This is similar to the behavior expected for the third body effect in the theoretical model (full line). The maximum effect is obtained for an adatom coverage close to 0.90, which compares very well with the prediction of the model for the square lattice, 0.889.

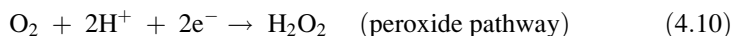
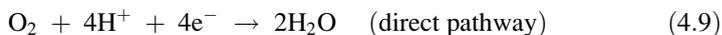
Figure 4.18c shows the behavior of a system that may be interpreted in terms of case III: HCOOH electrooxidation on Pt(111)/Se adatoms. In the presence of Se adatoms at Pt(111) a linear decrease of the poison formation with adatom coverage has been found, the total inhibition occurring at a Se coverage of 0.84 [78]. As can be seen, the model (full line) fits satisfactorily the experimental data (filled circles), assuming a linear combination between true catalytic (16 %) and third body (84 %) effects.

4.2.4 The Oxygen Reduction Reaction

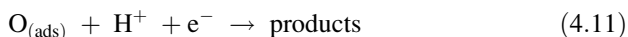
In the previous paragraph, we gave a short outline of some important anodic reactions in electrocatalysis. In the following we also give a short introduction on

one of the most important cathodic reactions, the oxygen reduction reaction (ORR), in the light of theoretical calculations. A review on the advances in the kinetics of the ORR up to 1996 has been given by Adzic [79]. Theoretical aspects of this reaction have been discussed by Leiva et al. [80].

Depending on the catalyst, ORR goes over a four-electron (direct) pathway or a peroxide pathway, involving H_2O_2 as intermediate product. In acid solutions the reactions are:



In the second case, hydrogen peroxide may further react electrochemically to yield water species or undergo chemical decomposition delivering O_2 . Several schemes have been proposed to analyze the ORR that consider these reaction pathways, as well as the coexistence in a number of combinations as in series and parallel. A discussion in terms of a general scheme proposed by Anastasijevic et al. [81], containing nearly all intermediates proposed in the literature, is given in the review mentioned above. In the case of Pt and Pt-family metals, where direct four-electron reduction is found, two main proposals exist for the first reaction step: Proton transfer simultaneous with charge transfer. According to this, the RDS should read:



Dissociative chemisorption of O_2 , probably simultaneous with charge transfer. In this case proton transfer should play no role in the reaction rate [82].

Like in the oxidation of C1 molecules mentioned above, Pt appears as a top catalyst for this reaction, together with some of its alloys involving some first-row transition metals. In the latter case, the predominant hypothesis for improved catalysis points towards the shortening of the Pt/Pt distance. However, also in these cases the reaction appears as too slow, and in acid solution it displays an amazing complexity. In spite of this, recent progress has been made in assessing the role that adsorbed non-intermediate species play in inhibiting the oxygen evolution reaction (OER). Experimental work on ORR on well-defined Pt(hkl) surfaces between 1992 and 1997 has been reviewed by Markovic and Ross [83] and the role of anions has been recently discussed (see for example Refs. [84, 85] and references therein). Anion adsorption determines indirectly the role of surface structure on the OER. For example, strong adsorption of phosphoric acid anions on Pt(111) determines the lower activity of this crystal face with respect to the other low index faces. Studies with halides show that in those cases where a strong halide-Pt(hkl) is operative, the anion blocks neighboring pairs of Pt sites needed for the cleavage of the O–O bond and hydrogen peroxide is formed in solution. A similar effect appears to take place in presence of upd adsorbed hydrogen in the most densely packed surfaces. Summarizing, in the case of electrooxidation on Pt surfaces experimental evidence support the series pathway, via the $\text{HO}_{2(\text{ad})}$ intermediate, with the RDS is suggested to be:

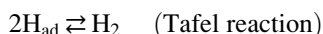
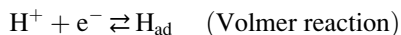


In the case of epitaxial film deposition of Pd [86], the inhibiting role of anions seems to be stimulated by the negative shift of the potential of zero charge concomitant with the decrease of the work function of the surface.

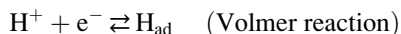
Upd of different metals on Pt has as a rule inhibiting effects on the OER. While sp metals like Tl, Bi and Pb induce H₂O₂ formation [87], Cu just presents a blocking effect with negligible peroxide formation in solution [88]. It is also relevant to mention here the catalytic effect of Pb and Bi for the ORR on Au(hkl) [89–91]. In acidic solutions, this reaction is known to occur via a two-electron reduction on clean Au single crystal surfaces [79]. However, Pb and Bi adatoms lead to a four-electron process producing water, an effect that will be analyzed in terms of a lattice model for the catalyst surface. The relevant appeal in the book by Bockris and Kahn [92] to the quantum chemical community to take up the struggle in this field has found a rather weak echo. We hope this weak response will soon strengthen in the light of the rapidly growing field of theoretical electrochemistry.

4.2.5 Hydrogen Evolution Reaction

On clean metal surfaces and in acid media, two different mechanisms have been established for the hydrogen evolution reaction (HER) (see, for example, Ref. [93]). The first one is the so-called Volmer-Tafel mechanism, which consists of a proton transfer followed by a chemical recombination reaction:



The second one is the Volmer-Heyrovsky mechanism, where the second step involves a charge transfer mechanism:

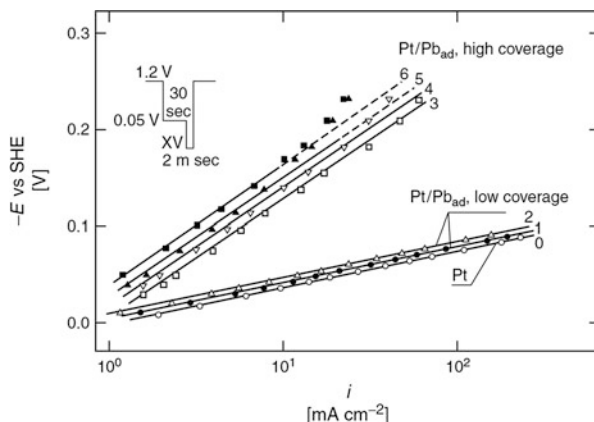


As general rule, it has been observed that upd generally is inhibited by upd deposits [94].

On the basis of the previous reactions, it comes out that adatom upd may inhibit the HER in different ways: by simple geometric blocking, by a decrease in the number of pairs of uncovered Pt atoms, which decreases the H+H recombination reaction, and for a change of electronic states of uncovered Pt atoms.

It has been found that, for several Pt/M_{ad} systems, considerable H₂ evolution takes place when the upd of H is completely blocked. This fact provides an additional proof that upd H has no connection to the intermediates in H₂ evolution [94].

Fig. 4.19 Hydrogen evolution on a rotating Pt electrode in 1 M HClO₄ in the presence of Pb adatoms. The curves 0–6 correspond to $\theta_{\text{Pb}} = 0, 0.17, 0.19, 0.56, 0.67, 0.86, 0.91$ respectively. Rotation rate 5000 rpm (Reproduced from Refs. [95, 96] with permission)

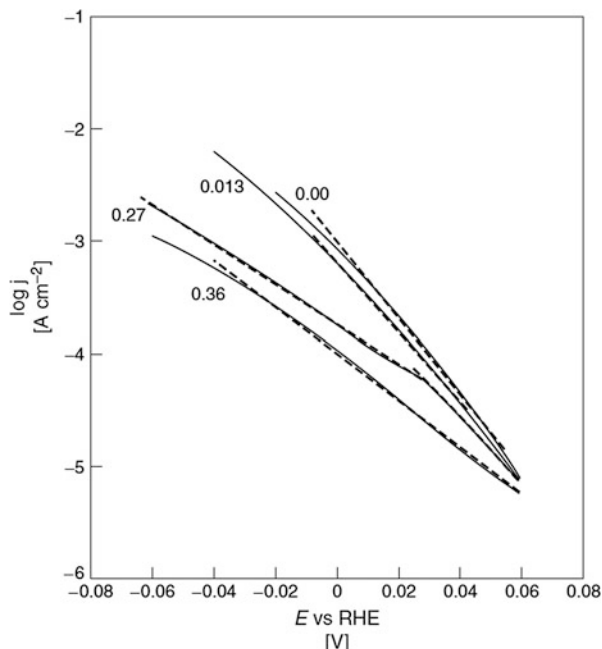


The inhibition of HER by metal adlayers is of interest for fundamental electrocatalysis and electrode kinetics, but it also of practical significance in promoting sorption of H into some metals, altering selectivity for some hydrogenation reactions, and in corrosion inhibition (the last being possible when O₂ reduction is not enhanced by metal adlayers.)

Both the chemical nature of the upd metal and the degree of coverage has notable effects on the reaction mechanism. On Pt, small coverages of Pb, Tl, and Cd cause pronounced inhibition, but the Tafel slope for the reaction remains the same as for bare Pt (–30 mV) [94]. The interpretation of this is that the recombination of two H atoms giving H₂ (H_{ad} + H_{ad} → H₂) is the rate-determining step for Pt both with and without the adlayer. At larger Pb coverages, the Tafel slope becomes –120 mV (Fig. 4.19) because there are no pairs of Pt atoms for a recombination reaction to occur, and the mechanism with the ion-plus-atom reaction (H_{ad} + H⁺ + e[–] → H₂) rate-determining step becomes operative [95, 96]. Changes of slope from –30 to –60 and –120 mV have been reported for Pt with Ge [97, 98].

No change of Tafel slope was found for H₂ evolution on Au/Pb [95, 96] since on bare Au the ion-plus-atom reaction, which requires one surface site, is the rate-determining step. Inhibition of H₂ evolution was reported for stationary single-crystal electrodes for As/Pt(111) [149], Bi/Pt(100), Sb/Pt(100), Bi/Pt(111) and + [99, 100] surfaces. For the Bi/Pt(111) system, the polarization curves have slopes of –30 to –35 mV for $\theta_{\text{Bi}} < 0.04$ (0.02), and for 0.14 (0.07) < $\theta_{\text{Bi}} < 0.33$ (0.18), the slopes are –35 and –54 mV at small and high overpotentials, respectively [99, 100] (Fig. 4.20). For Pt(100), a linear decrease of the H₂ evolution current as a function of coverage has been observed up to $\theta_{\text{Bi}} = 0.35$ (0.18), and a steep decrease has been observed above it. For Pt(111), a large decrease of H₂ evolution was observed at small Bi coverages up to 0.1 (0.03), and a linear decrease was seen for larger coverages. A similar observation was made for polycrystalline Pt with Pb [95, 96]. Small changes of Tafel slope for low Bi coverages were explained by a hypothetical mechanism in which a slow recombination and an ion-plus-atom reaction rate-determining steps occur in parallel. Inhibition effects of As, which

Fig. 4.20 H₂ evolution on a Bi/Pt(111) electrode in 0.5 M H₂SO₄. Tafel plots for different Bi coverages: $\theta_{\text{Bi}} = 0, 0.13 (0.06), 0.27 (0.13),$ and $0.36 (0.18)$ (Reproduced from Refs. [99, 100] with permission)



is a prototype catalytic poison, have been reported for polycrystalline electrodes [101, 102] and for a Pt(111) surface [103]. Surprisingly, small inhibition was observed up to $\theta_{\text{As}} = 1/3$ (1/6) for the latter system. The mechanism of significant H₂ evolution on Pt with large coverage of inhibiting metal adatoms is not clear. For Bi on Pt(100), the existence of the $c(2 \times 2)$ Bi adlayer was assumed, and it was proposed that H₂ evolution takes place through fourfold symmetry holes in the adlayer [99, 100]. This adlayer exists at Pt(100) [104, 105], but its structure still needs to be verified during H₂ evolution. In situ verification of the adlayer structure during the course of H₂ evolution has been obtained by surface X-ray scattering for Pt(111) with a Tl adlayer [106]. Figure 4.21 shows data for Tl adlayers on Pt(111) in solutions of two different pH values. A significant H₂ evolution current flows at Pt(111) despite the close-packed configuration of the Tl adlayer. The electro-compression of the Tl–Tl distance with decreasing potential is observed with this system. H₂ evolution has no effect on the structure of the Tl adlayer, but the Tl–Tl distance ceases to contract at its onset (Fig. 4.21). It is likely that in addition to defect sites, H₂ evolution occurs through hollow sites in the structure of the Tl adlayer. This prevents further compression with decreasing potential. These data seem to corroborate the assumption for the H₂ evolution through the hollow sites in the Bi adlayer on Pt(100).

Several approaches were used to quantify inhibition effects of metal adlayers. These involved calculations of currents of H₂ evolution based on the order-disorder theory of alloys [95, 96, 107], and simulations based on geometric [99, 100, 102] and long-range electronic effects [99, 100]. Verification of the models used in some

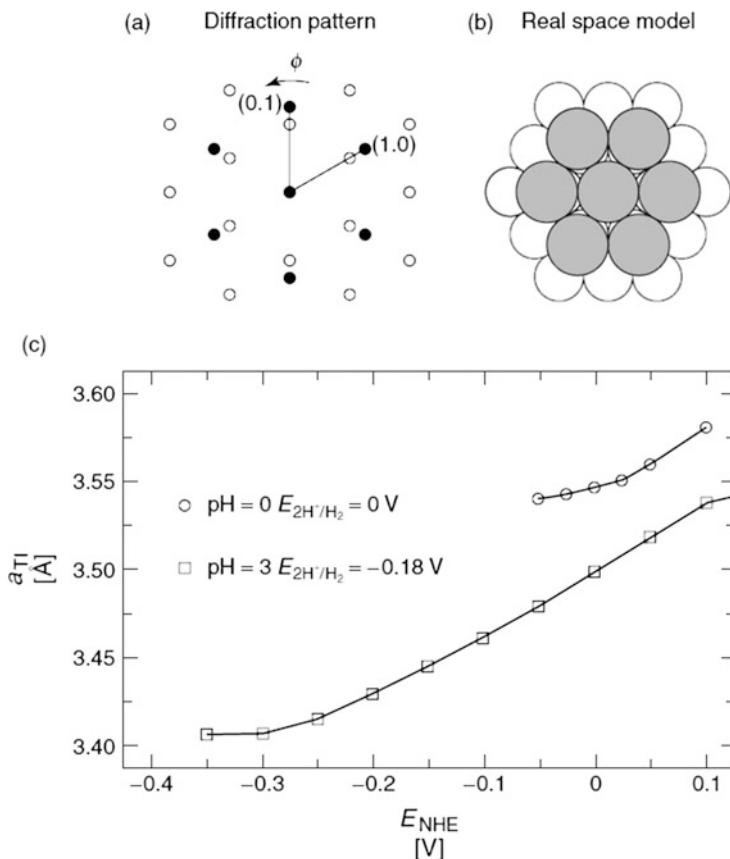


Fig. 4.21 (a) In-plane diffraction pattern from close-packed hexagonal Tl adlayer (*open circles*) on Pt(111) in 0.05 M H_2SO_4 solution with 1 mM Tl^+ . *Solid circles* diffractions from Pt(111). (b) Real space model for Tl adlayer. (c) Tl–Tl interatomic distance determined from the rocking θ scans at diffraction positions as a function of potential. The electrocompression increases in solution with pH = 3 beyond that observed at pH = 0, but it ceases to change when H_2 evolution starts (see text) (Adapted from Ref. [106] with permission)

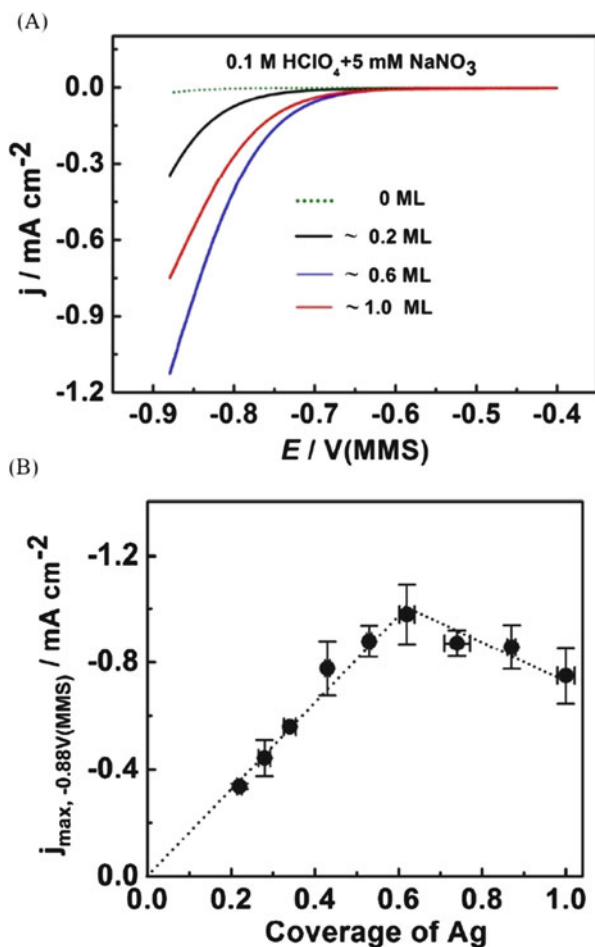
simulations seems necessary in order to obtain a more complete understanding of the inhibition effects.

Another realm where the inhibition of H_2 evolution might play a role is the effect of cations on the corrosion of iron. In the presence of Mn^{2+} , Cd^{2+} , and Zn^{2+} , there is a decrease of the corrosion of Fe in sulfuric acid. A possible interpretation of this is in terms of the inhibition of H_2 evolution by the upd of these metals [108–110]. Similar effects were observed for Pb, Tl, Ge and Ga [109–111]. In deaerated solutions, the inhibition effect can be quite pronounced. In the presence of O_2 , however, an enhanced O_2 reduction can increase corrosion rates.

4.2.6 Nitrate Reduction Reaction

It is nowadays recognized that the current imbalance in the biogeochemical cycle of nitrogen is as serious as that of carbon [112–115]. Therefore, effective catalysis of the electrochemical reduction and oxidation of nitrogen compounds is of particular importance. Electrochemical conversion of nitrogen compounds, in particular nitrate, could be done under relatively mild conditions with minimal negative impact to the environment [116, 117]. The products of nitrate reduction depend on the catalytic system. For example, Pt electrodes modified with sub-monolayer amounts of Cu reduce nitrate to NO and ammonia [118], while adsorbed Bi atoms on Pt can generate N_2O [119]. The electroreduction of nitrate to nitrite, which occurs in acidic media at Ag–Au electrodes, can be considered as a model reaction where both activity and selectivity play a critical role [120]. Figure 4.22 shows the results of the experimental activity evaluation of the Ag–Au system.

Fig. 4.22 (a) Cathodic parts of cyclic voltammograms of the Ag/Au electrode with different coverages (as deposited) of Ag in 0.1 M $HClO_4$ + 5 mM $NaNO_3$, $dE/dt = 50 \text{ mV s}^{-1}$. (b) The dependence of the activity towards nitrate-anion reduction on Ag coverage for Ag_{ad}/Au electrodes. The maximum of activity is reached at a Ag coverage of approximately 2/3 ML (Reproduced from Ref. [120] with permission)



Silver adatoms deposited on Au surfaces drastically increase the activity of gold electrodes towards the reduction of nitrate ions (Fig. 4.22a) [120]. A well-defined volcano-type curve was found that correlated the catalytic activity with the Ag coverage on the electrode surface, with the maximum activity observed approximately at 2/3 ML Ag (Fig. 4.22b). This example additionally shows how theoretical modelling and essentially empirical observations can be combined for the rational design of bimetallic catalysts.

References

1. Wieckowski A, Vayenas CE, Savinova ER (eds) (2003) *Catalysis and electrocatalysis at nanoparticle surfaces*. Marcel Dekker, New York
2. Marković NM, Ross PN (2002) *Surf Sci Rep* 45:121
3. Mayrhofer KJJ, Arenz M, Blizanac BB, Stamenković V, Ross PN, Marković NM (2005) *Electrochim Acta* 50:5144
4. Huang S, Hara K, Fukuoka A (2009) *Energy Environ Sci* 2:1060
5. Sun SG, Clavilier J, Bewick A (1988) *J Electroanal Chem* 240:147
6. Beden B, Hahn F, Lamy C, Léger JM, de Tacconi NR, Lezna RO, Arvia AJ (1989) *J Electroanal Chem* 261:401
7. Olivi P, Bulnoes LOS, Leger JM, Hahn F, Beden B, Lamy C (1994) *J Electroanal Chem* 370:241
8. Rodríguez P, Kwon Y, Koper MTM (2012) *Nat Chem* 4:177
9. Rodríguez P, Koverga AA, Koper MTM (2010) *Angew Chem Int Ed Engl* 49:1241
10. García G, Koper MTM (2011) *Chemphyschem* 12:2064
11. Chang S-C, Weaver MJ (1991) *J Phys Chem* 95:5391
12. Lambert DK (1988) *J Chem Phys* 89:3847
13. Mehandru SP, Anderson AB (1989) *J Phys Chem* 93:2044
14. Hoffmann R (1988) *Rev Mod Phys* 60:601
15. Anderson AB (1999) In: Wieckowski A (ed) *Interfacial electrochemistry*. Marcel Dekker Inc, New York
16. Kitamura F, Takahashi M, Ito M (1989) *Surf Sci* 223:493
17. Wasileski SA, Koper MTM, Weaver MJ (2001) *J Phys Chem B* 105:3518
18. Chang S-C, Weaver MJ (1990) *J Chem Phys* 92:4582
19. Villegas I, Weaver MJ (1994) *J Chem Phys* 101:1648
20. Rodes A, Gómez R, Feliú JM, Weaver MJ (2000) *Langmuir* 16:811
21. Lai SCS, Lebedeva NP, Housmans THM, Koper MTM (2007) *Top Catal* 46:320
22. Ross PN (1998) In: Lipkowski J, Ross PN (eds) *Electrocatalysis*. Wiley-VCH, New York
23. Watanabe M, Motoo S (1975) *J Electroanal Chem* 60:275
24. Gasteiger HA, Marković NM, Ross PN, Cairns EJ (1994) *J Phys Chem* 98:617
25. Liu P, Logadottir A, Nørskov JK (2003) *Electrochim Acta* 48:3731
26. Strasser P (2008) *J Comb Chem* 10:216
27. Maillard F, Lu G-Q, Wieckowski A, Stimming U (2005) *J Phys Chem B* 109:16230
28. Watanabe M, Motoo S (1975) *J Electroanal Chem* 60:267
29. Wang K, Gasteiger HA, Marković NM, Ross PR Jr (1996) *Electrochim Acta* 41:2587
30. Shibata M, Motoo S (1985) *J Electroanal Chem* 194:261
31. Bandarenka AS, Varela AS, Karamad M, Calle-Vallejo F, Bech L, Perez-Alonso FJ, Rossmeisl J, Stephens IEL, Chorkendorff I (2012) *Angew Chem Int Ed Engl* 51:11845

32. Jarvi TD, Stuve EM (1998) In: Lipkowski J, Ross PN (eds) *Electrocatalysis*. Wiley-VCH, New York
33. Hamnett A (1999) In: Wieckowski A (ed) *Interfacial electrochemistry*. Marcel Dekker Inc, New York
34. Wasmus S, Küver A (1999) *J Electroanal Chem* 461:14
35. Vielstich W, Xia XH (1995) *J Phys Chem* 99:421
36. Leiva EPM, Giordano MC (1983) *J Electroanal Chem* 158:115
37. Beden B, Lamy C, Bewick A, Kunimatsu K (1981) *J Electroanal Chem* 121:343
38. Beden B, Juanto S, Leger JM, Lamy C (1987) *J Electroanal Chem* 238:323
39. Kunimatsu K (1990) *Ber Bunsenges Phys Chem* 94:1025
40. Christensen PA, Hamnett A, Troughton GL (1993) *J Electroanal Chem* 362:207
41. Bagotzky VS, Vassilyev YB, Khazova OA (1977) *J Electroanal Chem* 81:229
42. Lopes MIS, Beden B, Hahn F, Léger JM, Lamy C (1991) *J Electroanal Chem* 313:323
43. Franaszczuk K, Herrero E, Zelenay P, Wieckowski A, Wang J, Masel RI (1992) *J Phys Chem* 96:8509
44. Sun SG (1998) In: Lipkowski J, Ross PN (eds) *Electrocatalysis*. WILEY-VCH, New York
45. Bagotzky VS, Vassilyev YB (1967) *Electrochim Acta* 12:1323
46. Willsau J, Heitbaum J (1985) *J Electroanal Chem* 185:181
47. Wilhelm S, Vielstich W, Buschmann HW, Iwasita T (1987) *J Electroanal Chem* 229:377
48. Bagotzky VS, Vassilyev YB (1966) *Electrochim Acta* 11:1439
49. Sriramulu S, Jarvi TD, Stuve EM (1999) In: Wieckowski A (ed) *Interfacial electrochemistry*. Marcel Dekker Inc, New York
50. Sriramulu S, Jarvi T, Stuve E (1999) *J Electroanal Chem* 467:132
51. Motoo S, Watanabe M (1976) *J Electroanal Chem* 69:429
52. Kokkinidis G (1986) *J Electroanal Chem* 201:217
53. Watanabe M, Motoo S (1975) *J Electroanal Chem* 60:259
54. Gasteiger HA, Marković NM, Ross P, Cairns EJ (1993) *J Phys Chem* 97:12020
55. Gasteiger HA, Marković NM, Ross PN, Cairns EJ (1994) *J Electrochem Soc* 141:1795
56. Kabbabi A, Faure R, Durand R, Beden B, Hahn F, Leger J-M, Lamy C (1998) *J Electroanal Chem* 444:41
57. Tremiliosi-Filho G, Kim H, Chrzanowski W, Wieckowski A, Grzybowoska B, Kulesza P (1999) *J Electroanal Chem* 467:143
58. Haner AN, Ross PN (1991) *J Phys Chem* 95:3740
59. Bittins-Cattaneo B, Iwasita T (1987) *J Electroanal Chem* 238:151
60. Morimoto Y, Yeager EB (1998) *J Electroanal Chem* 444:85
61. Rossmeisl J, Ferrin P, Tritsarlis GA, Nilekar AU, Koh S, Bae SE, Brankovic SR, Strasser P, Mavrikakis M (2012) *Energy Environ Sci* 5:8335
62. Parsons R, VanderNoot T (1988) *J Electroanal Chem* 257:9
63. Sánchez CG, Leiva EPM (2003) In: Vielstich W, Lamm A, Gasteiger HA (eds) *Handbook of fuel cells – fundamentals, technology and applications*, vol 2, chapter 3. Wiley, Chichester
64. Beden B, Bewick A, Lamy C (1983) *J Electroanal Chem* 148:147
65. Clavilier J, Sun SG (1986) *J Electroanal Chem* 199:472
66. Corrigan DS, Weaver MJ (1988) *J Electroanal Chem* 241:143
67. Sun SG, Clavilier J (1987) *J Electroanal Chem* 236:95
68. Sun SG, Lin Y, Li NH, Mu HQ (1994) *J Electroanal Chem* 379:273
69. Iwasita T, Xia X, Herrero E, Liess H-D (1996) *Langmuir* 12:4260
70. Watanabe M, Horiuchi M, Motoo S (1988) *J Electroanal Chem* 250:117
71. Lorca MJ, Feliú JM, Aldaz A, Clavilier J (1994) *J Electroanal Chem* 376:156
72. Baldlauf M, Kolb DM (1996) *J Phys Chem* 100:11375
73. Adžić RR (1984) In: Gerischer H, Tobias CW (eds) *Advances in electrochemistry and electrochemical engineering*, vol 13. Wiley, New York

74. Leiva EPM, Iwasita T, Herrero E, Feliú JM (1997) *Langmuir* 13:6287
75. Clavilier J, Fernandez-Vega A, Feliú JM, Aldaz A (1989) *J Electroanal Chem* 58:89
76. Fernandez-Vega A, Feliú JM, Aldaz A, Clavilier J (1989) *J Electroanal Chem* 258:101
77. Herrero E, Feliú JM, Aldaz A (1994) *J Electroanal Chem* 368:101
78. Llorca MJ, Herrero E, Feliú JM, Aldaz A (1994) *J Electroanal Chem* 373:217
79. Adžić RR (1998) In: Lipkowski J, Ross PN (eds) *Electrocatalysis*. Wiley-VCH, New York
80. Leiva EPM, Sánchez CG (2003) In: Vielstich W, Lamm A, Gasteiger HA (eds) *Handbook of fuel cells – fundamentals, technology, applications*, vol 2, chapter 5. Wiley, Chichester
81. Anastasijević NA, Vesović V, Adžić RR (1987) *J Electroanal Chem* 229:305
82. Yeager E (1984) *Electrochim Acta* 29:1527
83. Marković NM, Ross PN (1999) In: Wieckowski A (ed) *Interfacial electrochemistry*. Marcel Dekker Inc, New York/Basel
84. Climent V, Marković NM, Ross PN (2000) *J Phys Chem* 104:3116
85. Marković NM, Gasteiger HA, Grgur BN, Ross PN (2001) *J Electroanal Chem* 500:44
86. Marković NM, Gasteiger HA, Grgur BN, Ross PN (1999) *J Electroanal Chem* 467:157
87. Kokkinidis G, Jannakoudakis D (1984) *J Electroanal Chem* 162:163
88. Stamenković V, Marković NM (2001) *Langmuir* 17:2388
89. Alvarez-Rizatti M, Jüttner K (1983) *J Electroanal Chem* 144:351
90. Sayed SM, Jüttner K (1983) *Electrochim Acta* 28:1635
91. Jüttner K (1984) *Electrochim Acta* 29:1597
92. Bockris JO, Khan SUM (1993) *Surface electrochemistry. A molecular level approach*. Plenum Press, New York/London
93. Schmickler W, Santos E (2010) *Interfacial electrochemistry*, 2nd edn. Springer, Berlin/Heidelberg
94. Adžić RR (2007) In: Bard A, Stratmann M (eds) *Encyclopedia of electrochemistry*, vol 1, Wiley-VCH, Weinheim
95. Adžić RR, Spasojević MD, Despić AR (1979) *Electrochim Acta* 24:577
96. Adžić RR, Spasojević MD, Despić AR (1979) *Electrochim Acta* 24:569
97. Furuya N, Motoo S (1979) *J Electroanal Chem* 98:195
98. Furuya N, Motoo S (1979) *J Electroanal Chem* 99:19
99. Gómez R, Fernandez-Vega A, Feliú JM, Aldaz A (1993) *J Phys Chem* 97:4769
100. Gómez R, Feliú JM, Aldaz A (1997) *Electrochim Acta* 42:1675
101. Furuya N, Motoo S (1977) *J Electroanal Chem* 78:243
102. Gao LJ, Conway BE (1995) *J Electroanal Chem* 395:261
103. Clavilier J, Feliú JM, Fernandez-Vega A, Aldaz A (1990) *J Electroanal Chem* 294:193
104. Lucas CA, Marković NM, Grgur BN, Ross PN (2000) *Surf Sci* 448:65
105. Lucas CA, Marković NM, Ross PN (2000) *Surf Sci* 448:77
106. Adžić RR, Wang JX, Magnussen OM, Ocko BM (1996) *J Phys Chem* 100:14721
107. Furuya N, Motoo S (1976) *J Electroanal Chem* 72:165
108. Dražić DM, Vorkapić LŽ (1978) *Corros Sci* 18:907
109. Dražić DM, Nakić V (1978) In: 29th ISE meeting, Budapest
110. Dražić DM, Hao CS (1983) *Corros Sci* 23:683
111. Jüttner K (1980) *Materials and Corrosion* 31:358
112. Duca M, van der Klugt B, Koper MTM (2012) *Electrochim Acta* 68:32
113. Duca M, Koper MTM (2012) *Energy Environ Sci* 5:9726
114. Duca M, Cucarella MO, Rodriguez P, Koper MTM (2010) *J Am Chem Soc* 132:18042
115. Figueiredo MC, Solla-Gullón J, Vidal-Iglesias FJ, Climent V, Feliú JM (2013) *Catal Today* 202:2
116. Reyter D, Bélanger D, Roué L (2011) *J Hazard Mater* 192:507
117. Szyprkiewicz L, Daniele S, Radaelli M, Specchia S (2006) *Appl Catal B Environ* 66:40

118. Molodkina EB, Ehrenburg MR, Polukarov YM, Danilov AI, Souza-Garcia J, Feliú JM (2010) *Electrochim Acta* 56:154
119. Figueiredo MC, Souza-Garcia J, Climent V, Feliú JM (2009) *Electrochem Commun* 11:1760
120. Calle-Vallejo F, Huang M, Henry JB, Koper MTM, Bandarenka AS (2013) *Phys Chem Chem Phys* 15:3196

Chapter 5

Modelling of Underpotential Deposition on Bulk Electrodes

5.1 Introduction

As discussed in Chaps. 2 and 3, a wide variety of experimental techniques have allowed to obtain a wealth of information of upd systems. This information concerns:

- Structure of the adsorbed monolayer, as determined by GIXS, surface EXAFS, X-ray standing waves, SHG, and SPM (AFM, STM) techniques.
- Coverage degree of the different adsorbed species as a function of the applied potential, as determined from cyclic or linear sweep voltammograms under quasi-equilibrium conditions (at slow sweep rates), from the integral analysis of potentiostatic and galvanostatic transients, or from radiometric measurements.
- Kinetic information, via transient electrochemical techniques, eventually coupled to some of the other in situ techniques, as long as the time scale of the events allows it.
- Chemical information, as the oxidation state of the adsorbate, as obtained from XANES.
- Ex situ information on structure using LEED, RHEED and chemical composition (using AES).

It will come out below that depending on the type of property to be analyzed, there are different theoretical approaches that may be used with interpretative or predictive purposes.

The first attempt to understand a given problem within upd starts with a model, that is, a description of the upd problem using mathematical concepts and language.

According to quantum mechanics, the most precise description that we can get for a system, stems from its wave function $\Psi(\mathbf{r}, \mathbf{R}, t)$, which can be obtained from the solution of Schrödinger equation:

$$-\frac{\hbar}{i} \frac{\partial \Psi(\mathbf{r}, \mathbf{R}, t)}{\partial t} = \hat{H} \Psi(\mathbf{r}, \mathbf{R}, t) \quad (5.1)$$

where we have emphasized that the wave function is a function of the coordinates of the light (electrons) the heavy (nuclei) particles, and the time, which were denoted with \mathbf{r} , \mathbf{R} and t respectively. \hat{H} is the Hamiltonian of the system, which contains the kinetic energy of all the particles and the potential energy describing the interaction between them, say $U(\mathbf{r}, \mathbf{R}, t)$. To the best of our knowledge, the dynamic Eq. (5.1) has never been solved for an upd system. The closest that has been done to the problem stated in Eq. (5.1) in the upd field was the resolution of the dynamic behavior of a system of electrons, with the purpose of calculating the plasmon spectrum of Au nanoparticles decorated with upd Ag atoms [1]. In the case that \hat{H} is time independent, the previous problem reduces to the resolution of the eigenvalue equation:

$$\hat{H} \Psi(\mathbf{r}, \mathbf{R}) = E \Psi(\mathbf{r}, \mathbf{R}) \quad (5.2)$$

where E corresponds to the energy eigenvalues. In order to make the latter equation solvable, a further simplification is required: the Born-Oppenheimer approximation, where the wave function is splitted as:

$$\Psi(\mathbf{r}, \mathbf{R}) = \psi_{\text{elec}}(\mathbf{r}, \mathbf{R}) \psi_{\text{nuc}}(\mathbf{R}) \quad (5.3)$$

where ψ_{elec} and ψ_{nuc} correspond to wave function of the electrons and nucleus, respectively. The latter approximation leads to two further equations:

$$\hat{H}_{\text{el}} \psi_{\text{elec}}(\mathbf{r}, \mathbf{R}) = E_{\text{el}}(\mathbf{R}) \psi_{\text{elec}}(\mathbf{r}, \mathbf{R}) \quad (5.4)$$

$$\hat{H}_{\text{nuc}} \psi_{\text{nuc}}(\mathbf{R}) = E_{\text{nuc}} \psi_{\text{nuc}}(\mathbf{R}) \quad (5.5)$$

where \hat{H}_{el} is an operator that contains the kinetic energy of electrons and the electron–electron and electron–nuclei potential energy interactions. Thus, \hat{H}_{el} and the eigenvalues $E_{\text{el}}(\mathbf{R})$ in Eq. (5.4) contain the nuclear coordinates as parameters. Making some further approximations, many of the computer codes based on Density Functional Theory (DFT) (see Sect. 5.2 below) are able to solve Eq. (5.4) quite accurately for a few tens of atoms. Eq. (5.5) is the wave equation for the nuclei of the system, moving in a potential energy provided by the nuclei–nuclei interaction energy and the potential energy delivered by the eigenvalues E_{nuc} . In most cases, the inner electrons (core electrons) are frozen to solve Eq. (5.4), so Eq. (5.5) actually represents the motion of ion cores. For elements heavier than hydrogen and relatively high temperatures, Eq. (5.5) is usually replaced by its classical version:

$$m_i \frac{d^2 \mathbf{R}_i}{dt^2} = \mathbf{f}_i \quad (\text{with } i = 1, 2, 3 \dots N) \quad (5.6)$$

where m_i is the mass, the index i runs over the N heavy particles of the system 5 and \mathbf{f}_i is the force exerted on particle i . The \mathbf{f}_i can be calculated from the potential energy of the system $U(\{\mathbf{R}_i\})$ according to:

$$\mathbf{f}_i = -\nabla_i U(\{\mathbf{R}_i\}) = -\frac{\partial U(\{\mathbf{R}_i\})}{\partial x_i} - \frac{\partial U(\{\mathbf{R}_i\})}{\partial y_i} - \frac{\partial U(\{\mathbf{R}_i\})}{\partial z_i} \quad (5.7)$$

where (x_i, y_i, z_i) are the cartesian coordinates of particle i . As stated above, the potential energy for an arbitrary atomic configuration can be obtained from the eigenvalues E_{nuc} and the repulsive interaction between the heavy particles. Thus, the resolution of equations of motion (5.6) using the eigenvalues (5.4) along with Eqs. (5.7) and (5.4) would allow to describe the time evolution of the system. Unfortunately, such a resolution can be made, with the most powerful computers nowadays available, for times of the order of picoseconds for a reduced number of atoms. Thus, what can quantum mechanics be of aid to the upd problem? As stated above, Eq. (5.4) can be solved very efficiently with modern computer codes for a given configuration. The eigenvalues $E_{\text{el}}(\mathbf{R})$, together with the repulsive interaction between heavy particles yields the potential energy $U(\{\mathbf{R}\})$. Thus, theoreticians can obtain efficiently equilibrium configurations by solving the problem:

$$\mathbf{f}_i = -\nabla_i U(\{\mathbf{R}_i\}) = 0 \quad (5.8)$$

With the information resulting from these calculations, relevant (static) physical quantities can be obtained, like lattice constants, bulk modulus and surface energies, which can be compared with experiment to check the accuracy of the obtained results. Some first-principles results are compared with experimental values in Table 5.1, showing a reasonably good overall agreement. Similarly, the binding energy of an adatom on a foreign substrate can be obtained with a good accuracy, and underpotential shifts, as were discussed in Chap. 3, can be calculated quite

Table 5.1 Comparison between theoretical predictions from DFT first-principles calculations (th) and Experimental Results (exp) for the Lattice Constant a (in Bohr), Bulk Modulus B (in Mbar), and Surface Energies γ (in eV/Å²) of different metals of relevance in electrochemistry (Taken from Ref. [2])

Metal	a_{th}	a_{exp}	B_{th}	B_{exp}	γ_{th}	γ_{exp}
Ag	7.61	7.73	1.33	1.04	0.091	0.077
Au	7.75	7.71	2.06	1.67	0.090	0.094
Cu	6.71	6.82	1.80	1.38	0.134	0.111
Pd	7.30	7.35	2.22	1.95	0.128	0.125
Pt	7.44	7.41	2.78	2.83	0.145	0.155

accurately. A detailed discussion on the application of first-principles calculations to upd is given in the following Sect. 5.2.

To summarize this introductory discussion on the application of first-principles calculations to upd, we can state that these methods may deliver essentially information on static equilibrium properties, like lattice constants and binding energies. Other electronic properties like densities of states, partial charges of adsorbates and some basic vibrational properties, in the harmonic approximation, can also be obtained. Thus, all the analysis is usually restricted to ground-state properties (0 K) or same elementary vibrational properties.

To move forward to the prediction of other properties of upd system, like those involving a finite temperature, we get into the realm of statistical mechanics. Using the two postulates of statistical mechanics [3], it can be shown that the eigenvalues of Eq. (5.2) may be used to predict any equilibrium property of the system. For example, considering a system of N particles enclosed in a volume V at temperature T it can be shown that the average value of a mechanical property A may be calculated through:

$$\langle A \rangle = \sum_i P_i A_i \quad (5.9)$$

where the brackets denotes statistical average, the sum runs over all the i energy states of the system, say E_i ; A_i is the value of A at the state i and the probability of observing it is given by:

$$P_i = \frac{\exp[-E_i/k_B T]}{\sum_j \exp[-E_j/k_B T]} \quad (5.10)$$

The denominator of this equation is the so-called canonical partition function, usually denoted with Q . The classical versions of Eqs. (5.9) and (5.10) look very similar, but replacing the state sums by the integrals over momenta (\mathbf{p}) and configurational space (\mathbf{r}). In the case of the partition sum, we have:

$$Q = \frac{1}{N! h^{3N}} \int \exp[-\hat{H}(\mathbf{r}, \mathbf{p})/k_B T] d\mathbf{r} d\mathbf{p} \quad (5.11)$$

where $\hat{H}(\mathbf{r}, \mathbf{p})$ is the classical Hamiltonian of the system, h is the Planck constant. Thus, the probability density becomes:

$$P(\mathbf{r}, \mathbf{p}) = \frac{\exp[-\hat{H}(\mathbf{r}, \mathbf{p})/k_B T]}{\int \exp[-\hat{H}(\mathbf{r}, \mathbf{p})/k_B T] d\mathbf{r} d\mathbf{p}} \quad (5.12)$$

Since the Hamiltonian can be usually separated into space and momentum components, $\hat{H}(\mathbf{r}, \mathbf{p}) = K(\mathbf{p}) + V(\mathbf{r})$, Eq. (5.12) can be splitted as:

$$P(\mathbf{r}, \mathbf{p}) = \frac{\exp[-K(\mathbf{p})/k_B T] \exp[-V(\mathbf{r})/k_B T]}{\int \exp[-K(\mathbf{p})/k_B T] d\mathbf{p} \int \exp[-V(\mathbf{r})/k_B T] d\mathbf{r}} \quad (5.13)$$

The previous equation may be integrated over the momenta to give:

$$P(\mathbf{r}) = \frac{\exp[-V(\mathbf{r})/k_B T]}{\int \exp[-V(\mathbf{r})/k_B T] d\mathbf{r}} \quad (5.14)$$

Which yields the probability density of finding a given configuration independently from the momentum of the particles. The denominator of this equation is termed configuration integral, since the integral runs over all possible configurations of the system.

In the case where the number of particles in a system fluctuates in a constant volume V , in contact with a reservoir at the chemical potential, μ , the equations for the partition function (5.11) and probability density (5.14) must be replaced by:

$$\Xi(V, T, \mu) = \sum_N \frac{1}{N! h^{3N}} \exp\left(\frac{\mu N}{k_B T}\right) \int \exp[-\hat{H}(\mathbf{r}, \mathbf{p})/k_B T] d\mathbf{r} d\mathbf{p} \quad (5.15)$$

$$P_N(\mathbf{r}) = \frac{\exp[(-V(\mathbf{r}) + \mu N)/k_B T]}{\sum_N \int \exp[(-V(\mathbf{r}) + \mu N)/k_B T] d\mathbf{r}} \quad (5.16)$$

where we note the occurrence of a new sum over the number of particles. The present statistical mechanical description is often used to describe the electrochemical interphase, since the latter may be envisaged as an open system with respect to the particles being absorbed, while the volume under study considered encloses the immediate neighborhood of the substrate/adsorbate system.

The generalization of Eqs. (5.15) and (5.16) to multicomponents systems is relatively straightforward, involving sums over the different species involved.¹ This is the basis of the theories developed in Sect. 5.4. A word of caution is necessary here. While, as we say, the generalization of the mathematical form of the partition function and the probability density is simple, their calculation may be quite involved, if not impossible in general. There are two ways out of this problem. One of them is to introduce an extremely simplified mathematical form for the potential energy function $V(\mathbf{r})$, and thus the integral in Eq. (5.15) can be evaluated, after some simplifying assumptions. The other way out is to calculate the averages in Eq. (5.9) without going through the partition functions. Although this may sound some sort of magic, this can be done by means of the Monte Carlo methods, as explained in Sect. 5.4. For the reader who is eager to know how this incredibly useful method works, we can advance that the trick consists in making moves

¹ A example of multicomponent is given in Chapter 6 in the case of up on nanoparticles.

(create or destroy particles, displace them, etc.) on the configuration of the system, such that the probability of accepting these moves depends on a ratio of probability densities given in Eq. (5.14) or Eq. (5.16), (i.e. $P(\mathbf{r}_i)/P(\mathbf{r}_j) = \exp[-(V(\mathbf{r}_i)-V(\mathbf{r}_j))/k_B T]$) so that the denominators become simplified.

The structure of the present chapter is as follows: we start with the first-principles approaches to the study of upd. We then describe the applications of statistical mechanics and follow with Monte Carlo applications. We end describing miscellaneous theoretical approaches, not included in the previous items.

5.2 Application of Quantum Mechanical Methods to Underpotential Deposition

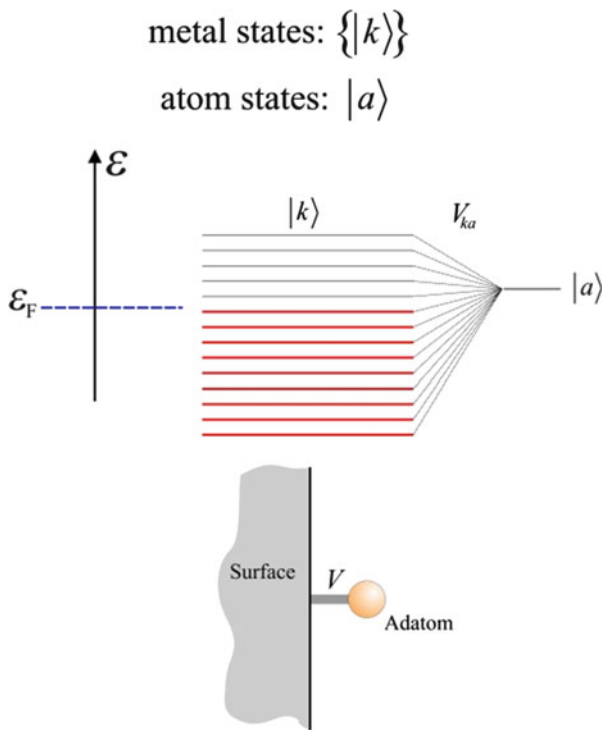
5.2.1 Quantum Mechanical Modeling of Underpotential Deposition Previous to the Application of Density Functional Theory

Pioneering modeling on metal adatom formation in electrochemistry using quantum mechanical tools is due to Schmickler [4] and Kornyshev and Schmickler [5]. These authors used a model for electrosorption based on the Anderson-Newns model for adsorption from the gas phase. The later topic has been reviewed by Muscat and Newns [6], and Gadzuk [7], and the application of this model to electrochemistry has been reviewed by Schmickler and Henderson [8]. Figure 5.1 depicts the main ideas involved in the Anderson-Newns model applied to describe an adsorbate in contact with a metal at the metal/gas interphase.

In the electrochemical approach [4, 5], the total Hamiltonian of the interface contains the contributions of the valence electrons of the adatoms, the metal electrons and the solvent molecules. To give a flavor of this model, we briefly state its components and the interactions between them, as it was discussed in detail in Ref. [9], where Schmickler considered the occurrence of charge transitions in metal adsorbates on foreign metal substrates. Assuming that only one adatom orbital is interacting with the metal, the Hamiltonian of the system was:

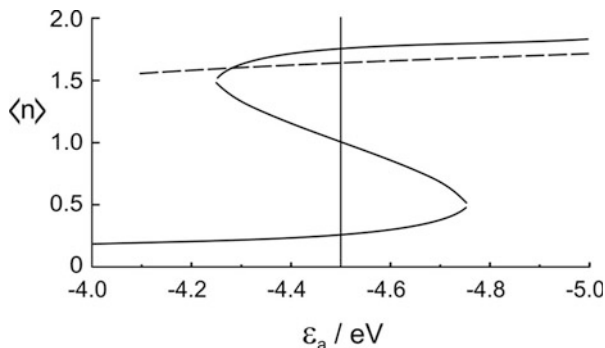
$$\begin{aligned} \hat{H} = & \sum_{\sigma} \varepsilon_a n_{a\sigma} + U n_{a\sigma} n_{a-\sigma} + \sum_k \varepsilon_k n_k + \sum_k \varepsilon_k n_k + \left(\sum_{k\sigma} V_{ka} c_{k\sigma}^+ c_{a\sigma} + V_{ka}^* c_{a\sigma}^+ c_{k\sigma} \right) \\ & + \frac{1}{2} \sum_{\nu} \hbar \omega_{\nu} (p_{\nu}^2 + q_{\nu}^2) \\ & + \sum_{\nu} \hbar \omega_{\nu} \left(z - \sum_{\sigma} n_{a\sigma} \right) q_{\nu} g_{\nu} \end{aligned} \quad (5.17)$$

Fig. 5.1 Scheme of the Anderson-Newns used model to describe the interaction of an adatom with a metal substrate. The electronic states $|k\rangle$ of the metal interact with the electronic state of the adsorbate $|a\rangle$. The interaction between them is represented by a hopping matrix V_{ka} . ϵ_F denotes the Fermi level of the metal



where ϵ denotes energy, n are number operators, c^+ and c are creation and annihilation operators, the index a denotes adsorbate, σ is the spin, k labels the electronic states in the metal, and v labels the solvent modes (vibrational, librational). According to this notation, ϵ_a is the energy level of the adsorbate, U is the repulsive interaction between two electrons in the same orbital, V_{ka} represent the off-diagonal elements for electron exchange between metal and adsorbate. The first line in Eq. (5.17) is that present in the Anderson model mentioned above. The second line contains slow solvent modes, which are represented as a set of harmonic oscillators of frequencies ω_v , momentum p_v , and coordinates q_v . The model considers, via the third line of Eq. (5.17), the coupling of the adsorbate with the slow (vibrational, librational) modes of the solvent molecules, whose interaction with the adatom is proportional to the adsorbate charge. The term g_v represents the corresponding coupling constants. The allowance of electron exchange between the substrate and the adsorbate results in a broadening of the energy levels of the latter and produces a shift of their values with respect to the bulk value. Thus, a partial charge arises naturally as a consequence of adsorption. Kornyshev and Schmickler [5] evaluated partial charge transfer coefficients for several systems, considering different broadenings of the adsorbate level and different degrees of adatom solvation. The upd couples showed an intermediate behaviour between the extreme cases of adsorption of alkali and halide ions on mercury. In the case of upd, multiple solutions were found to

Fig. 5.2 Total occupancy of the adatom orbital as a function of the adsorbate energy ϵ_a (Reprinted with permission from Ref. [9])



exist for the occupation probability $\langle n \rangle$ of the adsorbate orbital as a function of the energies of the adsorbate relative to the Fermi level of the metal (see Fig. 5.2). According to the theoretical analysis, the existence of these multiple solutions would be associated with a weak interaction of the adsorbate with the metal and a strong interaction with the solvent, behavior that would be expected in the case of adsorption on flat terraces. As discussed by Schmickler in his work, the occurrence of multiple solutions could lead to current spikes in cyclic voltammograms.

Extensions of the present model were the inclusion of the dependence of the partial charge transfer coefficient on the coverage degree [10], the consideration of two kinds of ions with opposite charge [11], the treatment of a random adsorbate layer with arbitrary coverage [Mishra AK, (1999) J Phys Chem B 103:1484] and the formulation by Schmickler of a unified approach to electrochemical electron and ion transfer reactions [12], with the subsequent inclusion of spin effects [13]. Recent work by Santos et al. [14] showed that the combination of the previous type of electron transfer theory with density functional theory calculations (see below) gives results that agree very well with experimental data for complex reaction like hydrogen evolution. In the future, this kind of modeling may provide further insight into the problem of charge transfer in upd systems.

5.2.2 *Early Applications of Density Functional Theory to Underpotential Deposition*

As stated in the Sect. 5.1, the most accurate, but computationally demanding approach to the study of upd systems is the quantum mechanical one. The early articles that applied quantum mechanics to understand the upd phenomenon based on Density Functional Theory (DFT) were those of Leiva and Schmickler [15], Schmickler [16] and Lehnert and Schmickler [17], within the so-called jellium model for a metal. In the first of these articles, the substrate was modeled as a semi-infinite positive charge background with a given charge density, and the adsorbate was represented as a slab of a different, positive charge density, see Fig. 5.3. This work

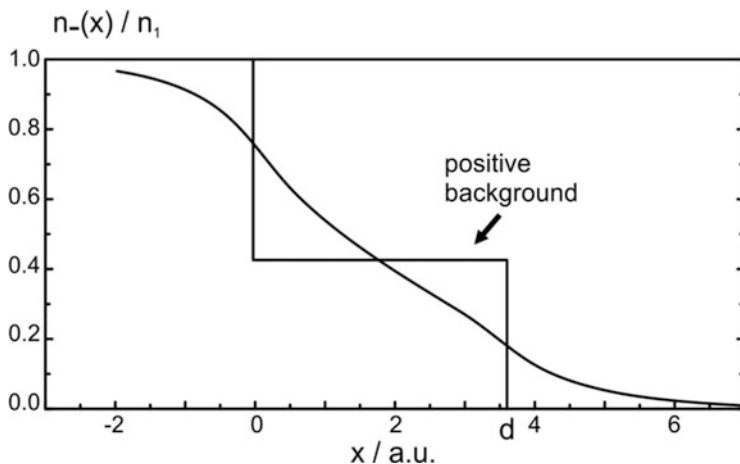


Fig. 5.3 Positive background charge and electronic density profile of the jellium model used to analyze monolayer adsorption on a foreign substrate. The substrate extends over the region $x < 0$, while the adsorbate layer is confined to the region $0 \leq x \leq d$ (Reprinted with permission from Ref. [15])

showed that two different mechanisms are operative in upd systems. One is the fact, already known, that the electrons flow from the adsorbate, usually having a lower work function, to the substrate, usually having a larger one. The other mechanism is related to the surface energy. Metals with a high work function usually tend to have a high surface energy, a behavior which is also supported by predictions of the jellium model for high electronic densities [18]. In this way, energy is gained when a substrate is covered with an adsorbate having a surface energy lower than its own. This fact explained why most substrates employed in upd have particularly high surface energies.

In the subsequent improvements of the model, the substrate was represented through a lattice of local pseudopotentials [19] appropriate to the single crystal plane, while the adsorbate layer was represented as a thin layer of jellium with a two-dimensional lattice of pseudopotentials commensurate with the substrate [16, 17]. Lehnert and Schmickler used local pseudopotentials to describe the metal ion cores, with the aim of calculating the surface dipole induced by the adsorbate, the work function of the substrate and the substrate/adsorbate system, and the relationship between the latter and the upd shift for a number of sp metals.

Subsequent DFT calculations within the jellium model used more sophisticated self-consistent calculations of the electronic density to draw general trends concerning underpotential deposition on single crystal surfaces. For example, Leiva and Schmickler [20] analyzed the average electronic density profile for Pb on Ag(111), as shown in Fig. 5.4. In the bulk of the metal (near to zero) it oscillates about its average value. There is a maximum at the positions near to the ions and there is a minimum at the interphase between the Pb overlayer and the Ag(111) surface. Since the electronic density of Pb is higher than that of Ag there is an accumulation of electronic charge in the top layer, which rapidly decays to zero

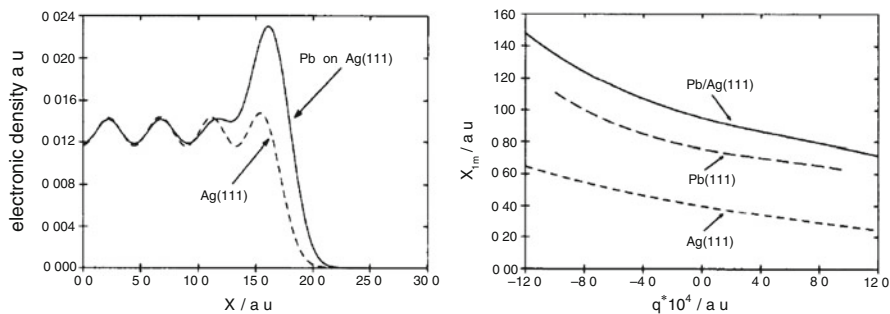


Fig. 5.4 (a) Electronic density profile and (b) position of the effective image charge as a function of the surface charge density, for a monolayer of lead on Ag(111) according to Jellium model (Reprinted with permission of Ref. [20])

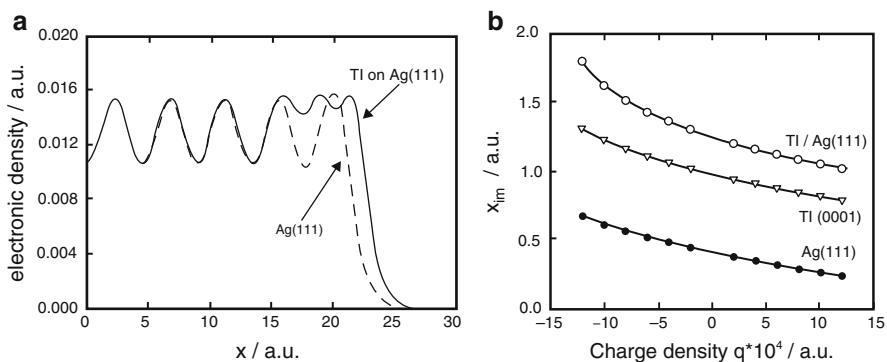


Fig. 5.5 (a) Electronic density profile and (b) position of the effective image charge as a function of the surface charge density, for a monolayer of Tl on Ag(111) according to Jellium model (Reprinted with permission of Ref. [21])

outside of the metal surface. Towards the bulk of the metal the electronic density becomes identical to that for bulk Ag after a few lattice spacing.

Figure 5.4b shows the position of the image plane, measured with respect to the metal surface, as a function of the surface charge on the metal for Ag(111), Ag(111)/Pb, and for a surface of Pb(111). The curve for Ag(111)/Pb is close to that of Pb(111) indicating that a monolayer of Pb on Ag(111) should have almost the same interfacial capacity as a surface of Pb(111). When the electrode is negatively charged the excess electrons accumulate mainly in front of the metal surface, and the image charge is pushed further away from the surface. In contrast, when the electrode is positively charged the surface electrons withdraw towards the bulk, and the image plane moves towards the surface.

The same model was used to analyze the electronic surface properties of the upd system Ag(111)/Tl [21]. Figure 5.5a shows the electronic density before and after the deposition of a Tl monolayer on Ag(111). The response of the surface electrons to an external electrostatic field is shown in Fig. 5.5b.

The jellium model was also used to analyze the lattice constants of adsorbed metallic incommensurate layers [22], corresponding to upd systems. For surfaces, the attractive interaction with the neighboring ions is missing, so the lateral pressure on the electron gas is smaller than in the bulk. Consequently the electronic density expands in the direction perpendicular to the lattice plane and contracts within the plane. This results in a shortening of the interplanar distance. When an adsorbate layer is added to the surface, the interplanar distance increases again.

5.2.3 Density Functional Theory Calculations for Underpotential Deposition Systems

While local pseudopotentials have been found to deliver reasonably good results for sp metals, they are not adequate for d metals, which are the most widely used as substrates in upd. A pioneering step to improve this situation in the field of DFT calculations applied to upd was given by Kramar et al. [23]. These authors analyzed the Pt(001)/Cu(2×2) system using the self-consistent, semirelativistic, all electron full-potential-linearized plane wave method. In the analysis they considered lattice parameter relaxation, band structure, partial density of states, electronic density and work function. This article was pioneering in determining the magnitude of the Cu-Pt bond, but the Cu cohesive energy was not considered, so that the underpotential shift was not evaluated. A next step forward was undertaken by Sánchez and Leiva [24], who analyzed both the binding energy of the adsorbate to the substrate $U_{S-M\theta}^{\text{bind}}$ ² and the cohesive energy of the adsorbate U_S^{coh} for a number of systems, thus obtaining the underpotential shift according to:

$$\Delta U_{S-M\theta}^{\text{upd}} \simeq \frac{1}{ze_0} \left[U_S^{\text{coh}} - U_{S-M\theta}^{\text{bind}} \right] \quad (5.18)$$

It is important to note that this equation is approximate and only contains energetic contributions, so that it is rigorously valid at 0 K. Figure 5.6 shows schematically the supercell used by these authors to represent the substrate/adsorbate system. The structure of the substrate was represented by a 5 (111)-planes wide atomic slab, on which an adsorbate plane was located at each side with (1×1) adsorption geometry on the threefold *fcc* adsorption sites. The supercell is periodically repeated in the three directions. Two surfaces (top and bottom) were separated by a vacuum region considered as six times the distance between (111) lattice planes.

Within DFT, the energy of the electronic system illustrated in Fig. 5.6 is given by:

² $U_{S-M\theta}^{\text{bind}}$ is calculated as: $U_{S-M\theta}^{\text{bind}} = (U_{S+M} - U_S)/N_M - U_M^{\text{vac}}$, where is U_{S+M} is the energy of substrate + adsorbate, U_S is the energy of a naked substrate, N_M is the number of M atoms in the supercell, and U_M^{vac} is the energy of a single M atom in vacuum.

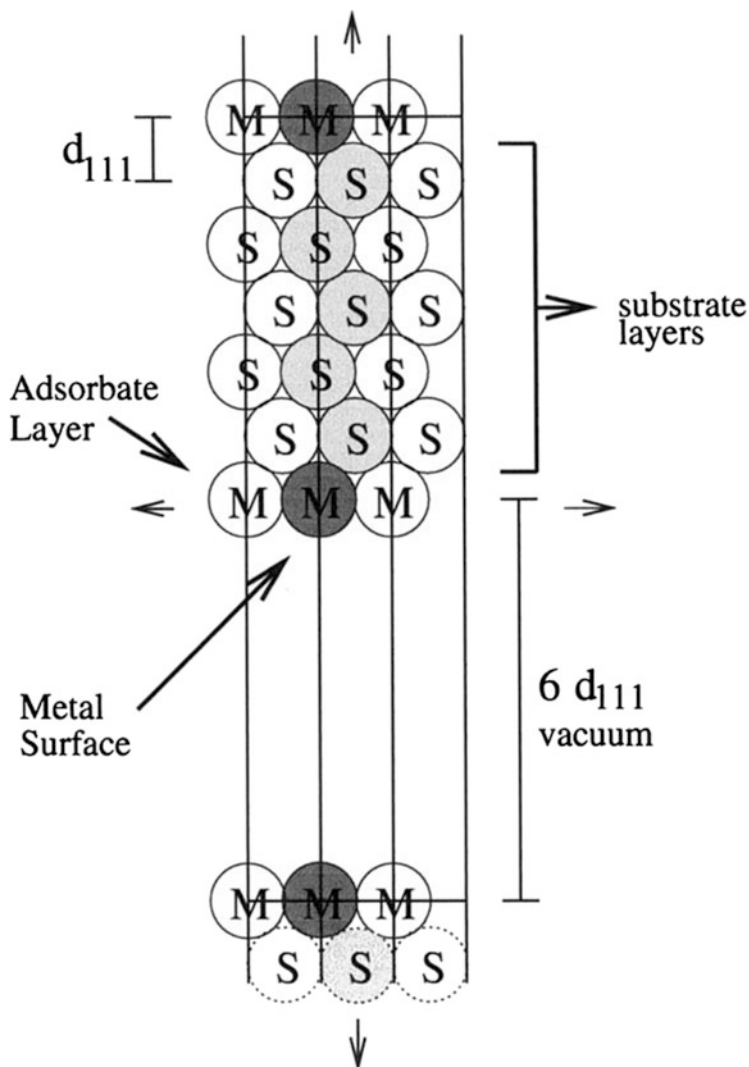


Fig. 5.6 Schematic illustration of the supercell geometry employed by Sánchez and Leiva, in order to represent the substrate/adsorbate system. d_{111} denotes the distance between (111) lattice planes. The metal slabs representing the system extend over planes perpendicular to the plane of the page (Reprinted with permission from Ref. [24])

$$U[n] = T^s[n] + U^H[n] + U^{e-nuc}[n] + U^{xc}[n] + U^{nuc-nuc} \quad (5.19)$$

where $T^s[n]$ is the functional describing the kinetic energy of a system of non interacting electrons with density $n(\mathbf{r})$, $U^H[n]$ is the Hartree energy, calculated from the corresponding potential $v_H(\mathbf{r})$ and $U^{xc}[n]$ is the exchange and correlation energy. The remaining terms correspond to the electron–nuclei ($U^{e-nuc}[n]$) and

nuclei–nuclei ($U^{\text{nuc-nuc}}$) electrostatic interactions. The electronic density $n(\mathbf{r})$ is obtained through the self-consistent solution of the corresponding Kohn-Sham equations:

$$\left[-\frac{1}{2}\nabla^2 + V_{\text{ext}}(\mathbf{r}) + V_{\text{H}}(\mathbf{r}) + V_{\text{xc}}(\mathbf{r}) \right] \psi_i(\mathbf{r}) = \varepsilon_i \psi_i(\mathbf{r}) \quad (5.20)$$

where V_{ext} , V_{H} and V_{xc} are the external potential, the Hartree and the exchange-correlation potentials, respectively, which are given by:

$$V_{\text{H}}(\mathbf{r}) = \int d\mathbf{r}' \frac{n(\mathbf{r}')}{|\mathbf{r} - \mathbf{r}'|} \quad (5.21)$$

and

$$V_{\text{xc}}(\mathbf{r}) = \frac{dE_{\text{xc}}}{dn(\mathbf{r})} \quad (5.22)$$

Thus, $n(\mathbf{r})$ is given by:

$$n(\mathbf{r}) = \sum_i^{\text{occ}} f(i) |\psi_i(\mathbf{r})|^2 \quad (5.23)$$

where $f(i)$ is the occupation number of state i . The effects of the core electrons and the nuclei on the valence electrons were replaced by suitable non local, relativistic pseudopotentials [24]. Table 5.1 shows the work functions for the substrate and substrate/adsorbate systems obtained by Sánchez and Leiva. Ag(111)/Cu(1×1) yields a work function which is lower than that of both bulk metals. This is reasonable, since the atomic density of Ag(111)/Cu(1×1) is considerably lower than that of a Cu(111) surface.

The underpotential shift, calculated according to Eq. (5.18), is also shown in the fourth column of Table 5.1. A small $\Delta U_{\text{S-M}}^{\text{upd}}(\text{theoretical})/\text{eV}$ was obtained for the Au(111)/Ag(1×1) system, in agreement with experimental results, and overpotential deposition (opd) is predicted for Ag(111)/Cu, as found in experiment [26]. However, for the Au(111)/Cu(1×1) and Ag(111)/Au(1×1) systems the theoretical predictions are at odds with the experimental results. No upd is predicted for Au(111)/Cu(1×1), while an underpotential shift of 0.12 V results for Ag(111)/Au(1×1). For the later system no upd has been reported in the literature so far. The case of Au(111)/Cu(1×1) has been the subject of a long controversy between experiment and theoretical predictions. Sánchez and Leiva [25] analyzed the application of different DFT functionals (Local Density Approximation –LDA– and Gradient Generalized Approximation –GGA) in calculations for different single crystal surfaces of the system Au(hkl)/Cu. In all cases opd was predicted. However, a strong change in the work function of the Au(hkl)/Cu(1×1) system, of

Table 5.2 Calculated and experimental work functions and calculated and experimental underpotential shift for different systems according to Sánchez and Leiva [24, 25]

System	$\Phi_{\text{theoretical}}/\text{eV}$	$\Phi_{\text{experimental}}/\text{eV}$	$\Delta U_{S-M}^{\text{upd}}(\text{theo})/\text{eV}$	$\Delta U_{S-M}^{\text{upd}}(\text{exp})/\text{eV}$
Cu(111)	5.27	4.94	–	–
Ag(111)	4.97	4.74	–	–
Au(111)	5.66	5.31	–	–
Cu/Ag(111)	4.80	–	–0.28	<0 [26]
Ag/Au(111)	5.00	–	0.03	0.04 [27]
Au/Ag(111)	5.32	–	0.12	–
Cu/Au(111)	4.63	–	–0.18	0.05 [28]

the order of 1 eV, was obtained upon metal upd monolayer formation. These authors noted the possibility that anion coadsorption, due to the concomitant shift of the potential of zero charge of the system, may be providing the extra free energy required for upd (Table 5.2).

Another important information that can be obtained from the DFT calculations are the (pseudo)electronic density profiles, and the differential electronic density plots. The latter may allow to visualize the increase or reduction of electronic density, as a consequence of bond formation. Accumulation and depletion regions should lead to an apparent increase of the corrugation of the surface when it is observed by scanning tunnel microscopy in the constant height mode, if a pure M surface is taken as a reference. The differential electronic density, $\delta\rho(\mathbf{r})$, is calculated from:

$$\delta\rho(\mathbf{r}) = \rho_{S/M} - \rho_S - \rho_M \quad (5.24)$$

where $\rho_{S/M}$, ρ_S and ρ_M correspond to the electronic densities of the substrate/adsorbate system and the separated substrate and adsorbate, respectively. Figure 5.7 presents images of the differential electronic densities, showing the charge rearrangement that takes place upon bond formation in the system. Figure 5.7a shows accumulation plots, while Fig. 5.7b shows depletion plots. It is found that charge accumulates more strongly at the plane between substrate and adsorbate, and is slightly depleted at the sites corresponding to the first substrate layer.

A further systematic calculation of upd shifts using DFT and first-principles pseudopotentials was undertaken in 2001 by Sánchez et al. [2]. The excess binding energies, corresponding to the term in brackets of Eq. (5.18), are given in Table 5.3 for different adsorbates on the *fcc* (111) face of single crystals of several substrates.

From Table 5.3 it can be observed that for a given substrate, with some notable exceptions, the excess binding energy tends to decrease for increasing surface energy of the adsorbate. Conversely, a given adsorbate usually exhibits larger excess binding energies on high surface energy substrates. These results support the same general trend already found within the framework of the jellium model, shown in the first part of this section, that represents the simplest approach to bulk metals and metal surfaces that takes into account explicitly the electronic component.

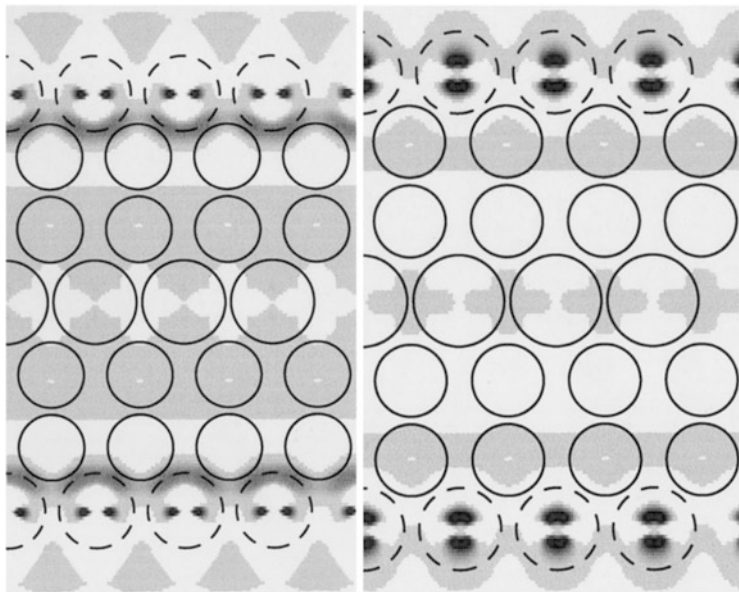


Fig. 5.7 Electronic accumulation (a) and depletion (b) plots for the Ag(111)/Cu(1 × 1) systems. In (a) the darker regions indicate the highest accumulation of the electronic density. In (b) the darker regions indicate the highest depletion of the electronic density (Reprinted with permission from Ref. [24])

Table 5.3 Excess binding energies for different adsorbates on different (111) substrates. All values are given in eV/atom. (Taken from Ref. [2] with permission)

Substrate	Adsorbate					Surface energy σ eV/Å ²
	Ag	Au	Cu	Pd	Pt	
Ag	–	0.17	–0.55	–0.13	–0.15	0.077
Au	0.00	–	–0.50	–0.24	–0.40	0.094
Cu	–0.38	–0.51	–	0.00	–0.15	0.111
Pd	0.27	0.32	–0.02	–	0.02	0.125
Pt	0.33	0.32	0.06	0.08	–	0.155

5.2.4 Relationship Between Excess Binding Energy and Surface Energy

Based on the hypothesis that the upd shift is related to the surface energy difference between substrate and adsorbate, Sánchez et al. [2] considered the thermodynamic cycle shown in Fig. 5.8. The *left* part of the figure shows two alternative ways to generate a free substrate surface and bulk adsorbate material from the substrate/adsorbate system. On one side, going through the unprimed way (I, II, III), the process involves: (I) detachment of the M adsorbate monolayer from the

substrate S, (II) disassembly of the monolayer into its constituting atoms and (III) reassembly of the isolated M atoms to yield the bulk M material. The energy change calculated along this cycle corresponds to the quantity in the bracket of Eq. (5.18). The primed path (I', II', III') has the same initial and final states as the unprimed one, but involves: (I') compression (expansion) of the adsorbed M monolayer to fit the lattice parameter of the bulk M material; (II') setting the compressed (expanded) monolayer in contact with its bulk material (III') detachment of the bulk piece of M from the substrate. The excess of binding energy, as calculated from the primed cycle, results in:

$$\Delta U_M^{\text{bind}} = \left[U_M^{\text{bind}} - U_{S-M_0}^{\text{bind}} \right] = \Delta U_{I'} + \Delta U_{II'} + \Delta U_{III'} \quad (5.25)$$

Neglecting the compression (expansion term), that is, setting $\Delta U_{I'} \approx 0$, leads to the following relationship between the binding energy excess and the difference of surface energies:

$$\begin{aligned} \Delta U_M^{\text{bind}} &= f(\gamma_M, \gamma_S) \\ &= \begin{cases} A_M(\gamma_S - \gamma_M) & \text{for } a_S > a_M \\ A_S[\gamma_S - (A_M/A_S)\gamma_M] + \gamma_M(A_S - A_M) & \text{for } a_S \leq a_M \end{cases} \end{aligned} \quad (5.26)$$

where a_S y a_M denote the lattice parameters and A_S and A_M are the atomic areas of substrate and adsorbate, respectively. Figure 5.8b shows the excess of binding energy as a function of the difference of surface energies between substrate and adsorbate, $f(\gamma_M, \gamma_S)$, as plotted according to Eq. (5.26). It is evident that the points scatter around a straight line with slope one, although the systems Cu(111)/Ag(1 × 1) and Cu(111)/Au(1 × 1) deviate strongly from this general trend. This indicates that the

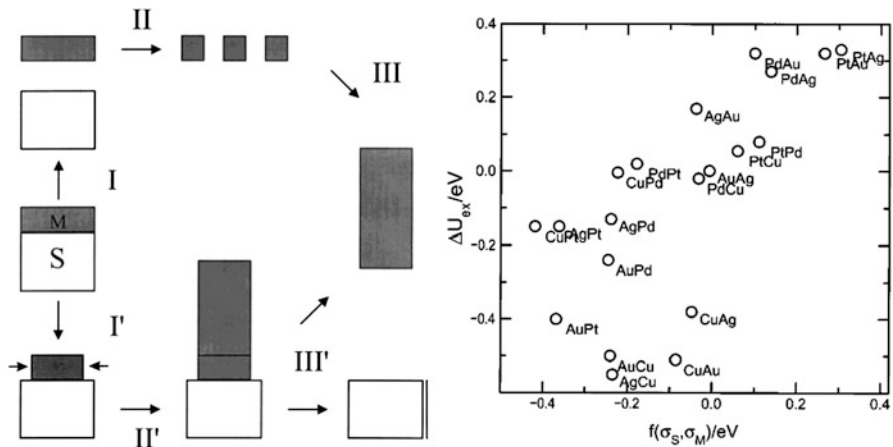


Fig. 5.8 (a) Two alternative pathways to calculate the excess of binding energy of a metal M adsorbed on a substrate S. For more details see the text. (b) Excess of binding energy vs difference of surface energies between substrate and adsorbate (Reprinted with permission from Ref. [2])

Table 5.4 DFT-Calculated underpotential shifts in Volts. The values in parenthesis are the cohesive energies of the corresponding bulk metals (in eV) [31] (Taken from Ref. [29] with permission)

Substrate	Adsorbate								
	Ir	Pt	Rh	Ni	Co	Pd	Au	Cu	Ag
Ir (6.94)	0.02	0.20	0.08	0.03	0	0.20	0.12	0.14	0.27
Pt (5.84)	-0.16	0.04	-0.16	-0.12	-0.11	0.07	0.12	0.10	0.37
Rh (5.75)	-0.03	0.13	-0.02	-0.04	-0.07	0.11	0.11	0.09	0.22
Ni (4.44)	-0.12	0.02	-0.10	0	-0.03	0.06	0.07	0.08	0.06
Co(4.39)	-0.09	0.11	-0.02	0.02	-0.02	0.09	0.08	0.04	0.04
Pd (3.89)	-0.21	-0.02	-0.16	-0.13	-0.11	-0.02	0.11	0.04	0.29
Au (3.81)	-0.31	-0.17	-0.42	-0.38	-0.39	-0.1	0.01	-0.18	-0.02
Cu (3.49)	-0.21	0.05	-0.26	-0.18	-0.26	0.01	0.07	0	0.05
Ag (2.95)	-0.29	-0.13	-0.4	-0.32	-0.39	-0.07	0.04	-0.20	-0.02

approximation $\Delta U_T \approx 0$ is not good for these systems. Less meaningful deviations are observed for the Ag(111)/Cu(1 × 1) and Au(111)/Cu(1 × 1) systems.

Recently, Greeley [29] has extended the previous work, using DFT calculations to determine periodic trends in the reversible deposition/dissolution potentials of admetals on a variety of transition metal substrates. A total of 81 systems were analyzed using the DACAPO code [30]. Greeley performed calculations involving adsorbed monomer, dimer and kink adatoms. Calculated underpotential shift results of that work are given in Table 5.4. For the sake of the analysis we perform below, we have ordered the metals in the table by increasing cohesive energy.

Since the diagonal terms correspond to metal adsorption on the same material and should be zero, they can be taken as a measure for the precision of the calculation method. On the average, we find that the error is of the order of 0.02 eV. From this table, it can be easily visualized that many of the systems over the main diagonal exhibit positive underpotential shifts. On the contrary, many systems below the main diagonal exhibit negative values, predicting overpotential deposition. Remarkable exceptions to this rule are Rh, Ni and Co adsorbates on Pt, Pt and Co adsorbates on Rh, Cu adsorbate on Au and Pt and Au adsorbates on Cu. Of all these systems, the most striking result is that of Cu on Au, where upd is not predicted, at odds with the occurrence of one of the most popular upd systems, as already discussed in the previous paragraphs.

5.2.5 Density Function Theory Calculations for Expanded Monolayers

As discussed in Sect. 3.1, and illustrated in Table 3.1, Ag upd on Au(111) yields a number of expanded structures, as determined by LEED [32]. This work motivated the study of expanded Ag adlayers adsorbed on Au(111) performed by Sánchez

Table 5.5 Results of DFT calculations for different structures involving Ag adatoms on Au(111) at different coverage degrees (θ): Underpotential shift (ΔU_{S-M}^{S-M}) and change in work function $\Delta\Phi$ produced by the adsorbate (Taken from Ref. [33])

Structure of Ag on Au(111)	θ	$\Delta U_{S-M}^{u\text{pd}}(\text{theo})/\text{eV}$	$\Delta\Phi/\text{eV}$
p(1 × 1)	1	0.03	0.98
(3 × 3)	0.44	−0.73	0.90
$p(\sqrt{3} \times \sqrt{3})\text{R}30^\circ$	0.33	−1.04	0.89
p(2 × 2)	0.25	−1.09	0.89
p(3 × 3)	0.11	−0.99	0.88
p(4 × 4)	0.07	−1.30	0.88

et al. [33]. These first-principles calculations on the stability of expanded Ag adlayers adsorbed on Au(111) were performed using the SIESTA program [34]. Different structures were considered for the adlayer: p(1 × 1), (3 × 3), $p(\sqrt{3} \times \sqrt{3})\text{R}30^\circ$, p(2 × 2), p(3 × 3), and p(4 × 4), all adsorbed on Au(111). The corresponding coverage degrees were $\theta = 1, 0.44, 0.33, 0.25, 0.11$ and 0.07, respectively. Table 5.5 reports the upd shift and changes in work function values for these systems, according to Sánchez et al. [33]. These calculations showed that in a vacuum environment, all Ag expanded monolayers are less stable than the bulk Ag phase and hence should not present upd. This is a striking discrepancy between experimental results and theoretical calculations. To rationalize this, it must be taken into account that DFT calculations consider a vacuum phase environment. The previous authors mentioned that at least three different effects, related to changes in the double layer, may contribute to stabilize these expanded structures: adsorption of anions, negative shift of the potential of zero charge [32, 35] and the influence of the electric field on the binding energy [33, 36].

Adsorption of various d-metals (Pd, Pt, Cu, Au) and p-metals (Sn, Pb, Bi) at different coverages on the Pt(111) surface was studied by means of DFT calculations by Pasti and Mentus [37] using the PWscf code of the Quantum ESPRESSO distribution [38]. The Perdew–Burke–Ernzerhof (PBE) [39] functional for the general gradient approximation (GGA) was employed. Upd shifts were determined at different coverages between 0.25 and 1, using (2 × 2) and $(\sqrt{3} \times \sqrt{3})\text{R}30^\circ$ surface structures. A (2 × 2) cell was used to model coverages of 1/4 and 1/2 of a monolayer, while a $(\sqrt{3} \times \sqrt{3})\text{R}30^\circ$ cell was used to model a clean Pt(111) surface and coverages of 1/3 and 2/3 of a monolayer.

Table 5.6 shows that the *fcc*-hollow adsorption site is generally the most stable one. For the d- and p-metals, the adsorption energy increases in the order $\text{fcc} \approx \text{hcp} > \text{bridge} > \text{atop}$.

Table 5.6 Adsorption energies (in eV) for some S/M structures on Pt(111) considering adsorption at different sites for $\theta = 0.25$, using a 2×2 motif (Reprinted with permission from Ref. [37])

Adsorbate	U^{ads}/eV (fcc)	U^{ads}/eV (hcp)	U^{ads}/eV (bridge)	U^{ads}/eV (atop)
Pd	-3.20	-3.17	-3.03	-2.27
Pt	-4.41	-4.36	-4.18	-3.17
Cu	-3.49	-3.48	-3.35	-2.71
Au	-3.15	-3.13	-3.04	-2.58
Sn	-4.65	-4.64	-4.39	-3.91
Pb	-3.84	-3.83	-3.65	-3.29
Bi	-4.38	-4.33	-4.00	-3.35

5.2.6 Analysis of Substrate and Adsorbate Interaction Energy

The adsorption energy of adatoms may be formally decomposed as [37]:

$$U^{\text{ads}}(\theta) = U_{\text{S-M}_0} + U_{\text{M-M}} \quad (5.27)$$

where $U_{\text{S-M}_0}$ is the binding of a free standing adlayer to the substrate,³ and $U_{\text{M-M}}$ is the binding energy of M atoms in a free standing adlayer, referred to isolated atoms in vacuum. Due to the nature of metallic bond, both quantities are a function of coverage degree. Figure 5.9 shows $U_{\text{S-M}_0}$ and $U_{\text{M-M}}$ as a function of θ as obtained from the DFT-GGA calculations of Pasti and Mentus [37]. The magnitude of $U_{\text{S-M}_0}$ decreases (the deposit becomes more unstable) with increasing coverages for all systems, concomitantly with the negative shift of the Pt d-band center in the formation process of the adsorbed monolayer. On the other hand, the magnitude of $U_{\text{M-M}}$ increases with increasing coverage degrees. In the case of Pd, Pt, Cu and Au the magnitude of $U_{\text{M-M}}$ increases with increasing coverage in the entire coverage range. In the cases of Sn, Pb and Bi, the magnitude of $U_{\text{M-M}}$ passes through a maximum at an intermediate coverage degree. This can be understood taking into account the appearance of pronounced repulsive forces due to the adatom sizes at high coverages.

³ Note that this quantity is different from the binding energy of an adsorbate atom, $U_{\text{S-M}_0}^{\text{bind}}$ used in Eq. (5.18), which is referred to isolated adsorbate atoms in vacuum. That is: $U_{\text{S-M}} = (U_{\text{S+M}} - U_{\text{S}} - U_{\text{adlayer}}^{\text{vac}}) / N_{\text{M}}$ where $U_{\text{S+M}}$ is the energy of substrate + adsorbate, U_{S} is the energy of a naked substrate, N_{M} is the number of M atoms in the supercell, and $U_{\text{adlayer}}^{\text{vac}}$ is the energy of a free standing adlayer in vacuum.

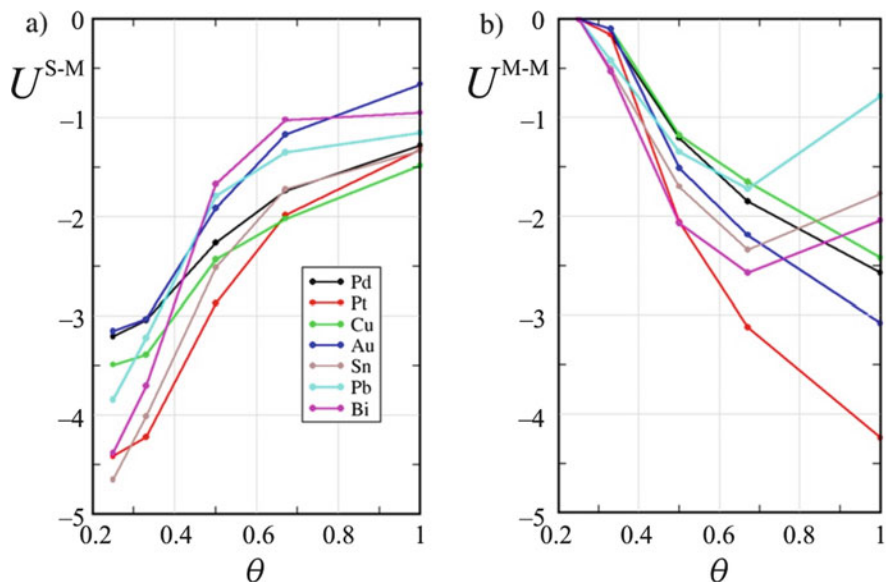


Fig. 5.9 U_{S-M} and U_{M-M} , given in Eq. (5.27) of the text, as a function of θ for different metals adsorbed on a Pt(111) surface (Results taken from Ref. [37] with permission)

5.2.7 Growth of Deposits Underpotentially formed on Stepped Surfaces

Theoretical studies of upd growth on stepped surfaces were undertaken by Danilov et al. in Ref. [40], performing DFT calculations with the Gaussian 03 program. These authors employed a scheme to construct additive pair potentials from DFT calculations. These potentials were then used to simulate the growth of Cu overlayers on different Pt stepped surfaces. The surfaces analyzed comprised (111) terraces, with (100) and (110) monoatomic steps, including some kink sites at these steps, see Fig. 5.10a. Figure 5.11 shows the evolution of the system energy as a function of the number of Cu atoms deposited onto the stepped Pt(111) surface. First, the Cu atoms are deposited onto the most active sites, that is, on the kink-positions, see Fig. 5.10a (black spheres) and step 1 in Fig. 5.11. Then, Cu atoms are deposited at the (110) and (100) steps sparsely (Fig. 5.10b). This process corresponds to step 2 in Fig. 5.11. A new plateau in the U vs. N curve (step 3 in Fig. 5.11) appears, corresponding to the formation of a continuous row of Cu atoms at the step, see Fig. 5.10c, d. Then, Cu atoms are deposited preferentially on the wide terraces as shown in Fig. 5.10e. Figure 5.10f, g displays a Cu $(\sqrt{3} \times \sqrt{3})R30^\circ$ motif on the Pt terraces. The authors pointed out that the open structures shown in

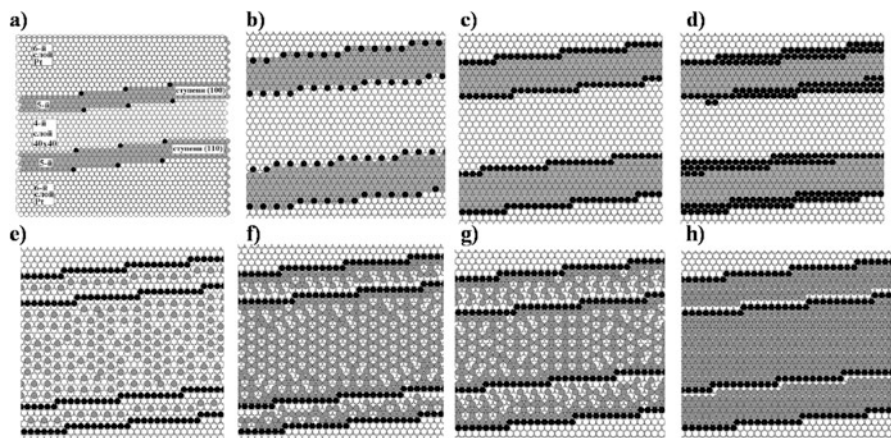


Fig. 5.10 Snapshots of the different surface structures resulting from the quantum-chemical modeling of Cu deposition onto a stepped Pt(111) single crystal surface. From (a) to (d) Cu atoms are represented as black spheres, while Pt atoms are represented with gray and white spheres. From (e) to (h) the Cu atoms at steps are represented with black spheres, while Cu atoms on terraces are represented with gray, and Pt atoms are represented as white spheres (Reprinted with permission from Ref. [40])

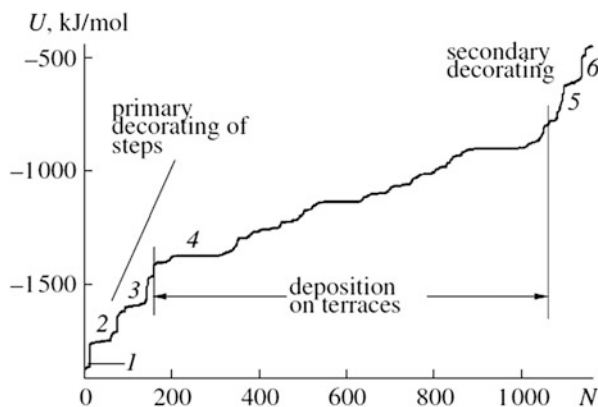


Fig. 5.11 Change in the energy of the system as copper atoms are deposited on a stepped Pt(111) surface (Reprinted with permission from Ref. [40])

Fig. 5.10f, g were formed as a result of the mutual repulsion between Cu atoms, carrying a partial positive charge. It must be emphasized that the present model leads to open adlayers, without the need of assuming the presence of anions on the surface. Finally, Cu deposition at terraces builds a Cu(1 × 1) epitaxial monolayer, as show in Fig. 5.10h.

5.3 A Statistical-Mechanical Approach to Underpotential Deposition

Blum and Huckaby developed pioneering work in the field of statistical mechanics devoted to describe chemisorption of a single type of species at the liquid/solid interface [41, 42] that was latter extended to the study of complex systems, as we analyze below.

We will not address the technical details of the models, since they are extensively explained in the corresponding papers, and a complete review on phase transitions at electrode interfaces has been given by Blum et al. in Ref. [43]. We just point out here their most relevant features, which are illustrative of the methodology employed. In this approach, a fluid of N molecules with a spherical hard core σ_C was considered interacting with a smooth, hard wall with sticky sites, each of them having q nearest neighbours. This was called sticky sites model (SSM). The sticky interaction with the wall $U^s(\mathbf{r})$ at the point $\mathbf{r} = (x, y, z)$ was defined as:

$$\exp(-U^s(\mathbf{r})/k_B T) = 1 + \lambda \delta(z) \sum_{n_1, n_2} \delta(\mathbf{R} - n_1 \mathbf{a}_1 - n_2 \mathbf{a}_2) \quad (5.28)$$

where z denotes the distance to the contact plane, located at a distance $\sigma_C/2$ from the electrode surface. $\mathbf{R} = (x, y, 0)$ is the position of the surface plane, δ represents the Dirac delta function, λ is a parameter that represents the likelihood of adsorption of an individual atom or molecule onto the sticky site. n_1 and n_2 are integer numbers, \mathbf{a}_1 and \mathbf{a}_2 are lattice vectors spanning a two-dimensional lattice L . The Hamiltonian describing the fluid was:

$$\hat{H} = \hat{H}_0 + \hat{H}_S \quad (5.29)$$

where \hat{H}_0 is the Hamiltonian of the system in the absence of the sticky sites on the hard wall, and \hat{H}_S represents the interaction with the sticky sites:

$$\hat{H}_S = \sum_{i=1}^N U^s(\mathbf{r}_i) \quad (5.30)$$

The analysis of the partition function of this model showed that the SSM maps for the adsorption on a flat surface onto a two-dimensional lattice problem with an arbitrary number of interactions. A further approximation was writing the n -body correlation $g_n^0(\mathbf{R}_1 \dots \mathbf{R}_n)$ for the smooth wall problem as a product of pair correlation functions $g_2^0(\mathbf{R}_i, \mathbf{R}_j) = g_2^0(|\mathbf{R}_i - \mathbf{R}_j|)$ according to:

$$g_n^0(\mathbf{R}_1 \dots \mathbf{R}_n) = \prod_{\langle ij \rangle} g_2^0(\mathbf{R}_i, \mathbf{R}_j) \quad (5.31)$$

The atoms in the 2-d lattice were assumed to have a nearest-neighbor interaction $w(r)$, which corresponded to the pair potential of mean force of the adsorbed species interacting at the distance r :

$$w(r) = -k_B T \ln[g_2(r)] \quad (5.32)$$

For a constant distance between lattice sites, g_2 can be visualized as an interaction parameter, which can be used to fit experimental results. If the lateral interactions between the adsorbates are attractive and $g_2 > g_2(\text{critical})$ then a first-order phase transition occurs, which is seen as a sharp spike in the voltammogram. If the interactions are repulsive then only second order (order-disorder) phase transitions can occur. Since second-order phase transitions are discontinuous in the first derivative of coverage, they should be seen as small cusps in the voltammogram.

The relationship between the contact density and the potential bias, referred to the PZC, was assumed to be given by:

$$\rho_i^0(0, E) = \rho_i^0(0, 0) \exp(-z_i(E - E_{\text{pzc}})/k_B T) \quad (5.33)$$

The coverage degree θ was written in terms of Padé approximants for low and high fugacities f . The latter was given by:

$$f = \rho_i^0(0, E) \lambda \quad (5.34)$$

Once the coverage is obtained as a function of the electrode potential, cyclic voltammograms may be constructed calculating the current from:

$$I = -\frac{d\theta}{dt} = -\frac{d\theta}{dE} \frac{dE}{dt} \quad (5.35)$$

Adsorption isotherms and cyclic voltammograms for different interaction parameters are shown in Fig. 5.12. A sharp peak results for the case $g_2 = 3.1$ which has a transition, whereas a rather broad peak occurs for the case $g_2 = 2.3$, for which there is no transition.

The previous modeling was extended to a two-adsorbate system, in order to investigate the upd of Cu on the Au(111) surface in the presence of sulfate ions [44]. According to this formulation, the following sequence of events occurs in the case of a cathodic potential sweep:

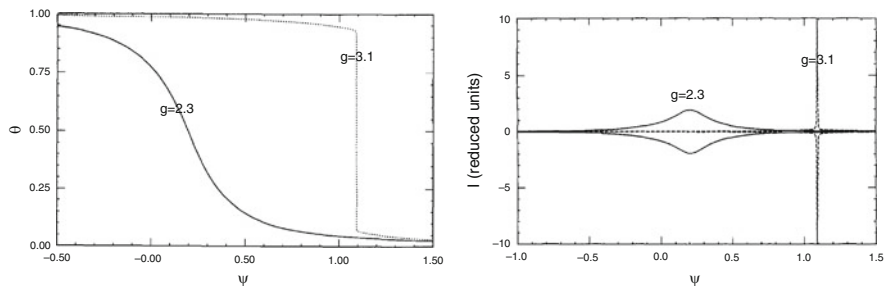


Fig. 5.12 Adsorption isotherms (*left*) and voltammograms (*right*) for two different interaction parameters as given in the figure. Ψ is a reduced potential referred to the pzc, $\Psi = (E - E_{pzc})/k_B T$ (Reprinted with permission from Ref.[43])

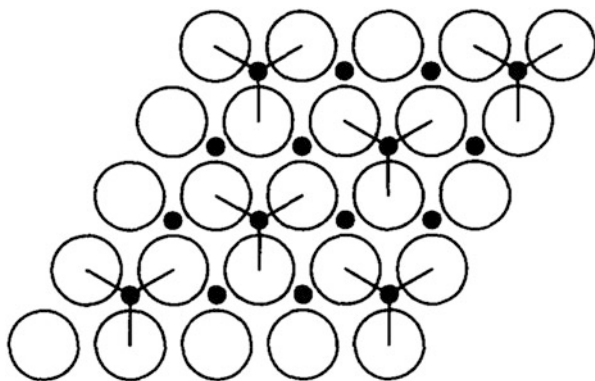


Fig. 5.13 Scheme of the geometrical model used by Huckaby and Blum for the theoretical study of upd of Cu on Au(111) in the presence of sulfate ions. Gold atoms are represented by large white disks, the adsorption sites for sulfate and copper are depicted as *small black disks*, and the adsorbed sulfate groups are depicted as sets of *three lines* emerging from the adsorption sites to the neighboring gold atoms (Reprinted with permission from Ref. [44])

- I- Formation of a $\sqrt{3} \times \sqrt{3}$ sulfate phase on the gold substrate. See Fig. 5.13.
- II- Adsorption of Cu ions on the free adsorption sites, yielding a honeycomb lattice.
- III- Replacement of adsorbed sulfate ions by Cu ions.

The mathematical model was similar to that described above, but the interaction of the copper ions with the Au(111) surface containing the $\sqrt{3} \times \sqrt{3}$ sulfate film was introduced. Denoting with λ_T , the stickiness parameter for the sites on the triangular sublattice L_T , associated with the sulfate groups, and with λ_H , the stickiness parameter for sites on the vacant honeycomb lattice L_H , the fugacities of the copper atoms on the different sites were:

$$f_T = \rho_1^0(0, E)\lambda_T \quad (5.36)$$

And

$$f_H = \rho_1^0(0, E)\lambda_H \quad (5.37)$$

and the equivalent of equation (5.32) becomes:

$$w_H = -k_B T \ln[g_2(d)] \quad (5.38)$$

for two copper atoms on neighbouring sites of L_H , and

$$w_T = -k_B T \ln\left[g_2\left(\sqrt{3}d\right)\right] \quad (5.39)$$

for two copper atoms on neighbouring sites of L_T . In this first approach, the coupling between the two lattices was ignored to make the calculations straightforward. The theoretical voltammograms, shown in Fig. 5.14, exhibited features similar to those of the experimental ones.

The previous model was then extended by Huckaby and Blum to include the dynamics of the sulfate adsorption-desorption process, assuming a strong coadsorption of copper with bisulfate [45, 46]. In these articles second nearest neighbour configurations were also included, and the foot of the voltammetric spike for Cu upd on Au(111) located at more positive potentials was explained by a second-order order-disorder hard hexagon surface phase transition. The better

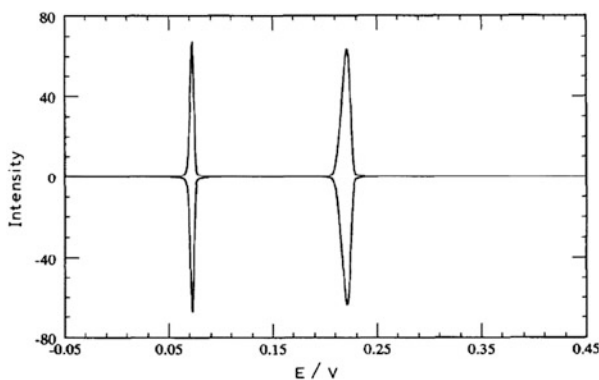


Fig. 5.14 Theoretical voltammogram from Huckaby and Blum [44] corresponding to two first-order phase transitions (Reprinted with permission from Ref. [44]). The peak couple on the right corresponds to adsorption/desorption of Cu atoms on/from the adsorption sites left free by a $\sqrt{3} \times \sqrt{3}$ sulfate phase on the gold substrate. The peak couple on the left corresponds to replacement of adsorbed sulfate ions by Cu atoms, leaving a full adsorbed Cu monolayer (or to the reverse reaction)

Fig. 5.15 Improved version of the theoretical voltammogram from Huckaby and Blum [46]. The theory includes only the copper contribution to the voltammetric current (Reprinted with permission of Ref. [46])

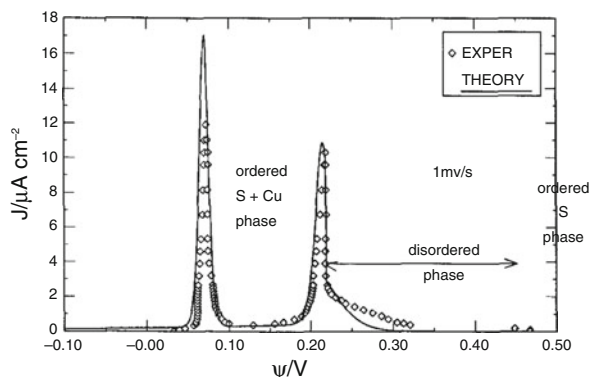
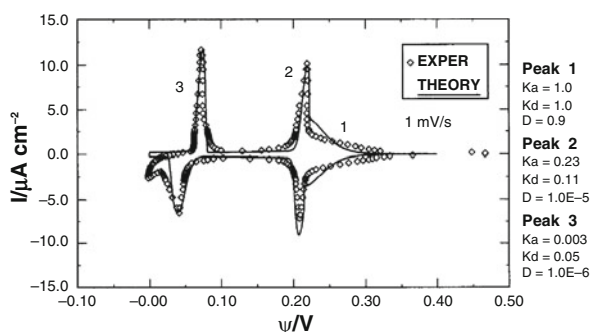


Fig. 5.16 Dynamic version of the theoretical voltammogram from Blum *et al.* [47]. The theory includes only the copper contribution to the voltammetric current (Reprinted with permission of Ref. [47])



agreement with the experiment introduced by this improved formulation can be seen in Fig. 5.15.

A further improvement of the model was achieved when kinetic features were introduced [47], including diffusion reaction kinetics. This extension of the model to the dynamic regime delivered phenomenological rate constants by fitting the theory to the experiment and produced a theoretical cyclic voltammogram that was in fairly good agreement with the experiment, in both the anodic and cathodic sweeps, as can be seen in Fig. 5.16

The subsequent approaches to upd using statistical mechanics were devoted to understand the shapes of the voltammogram spikes [48–50] since the simulated voltammetric profiles obtained from microscopic theory or computational modeling did not agree straightforwardly with the shapes of the experimental spikes. It must be reminded here that the width of the peaks in Figs. 5.14, 5.15, 5.16 and 5.17 were tuned by fitting a free parameter, introduced in an error function [44], or in a power functional form [46, 47]. Also the voltammogram simulated by lattice gas models exhibits peaks which are considerably sharper than the experimental results, see for example Fig. 5.35 of Sect. 5.4.3.2.

It was shown by Huckaby and Medved [48] that the rigorous Borgs–Kotecky theory [51, 52] of finite-size effects near first-order transitions implies that a current spike from a lattice of a “reasonable” size is about 100 times taller and sharper than

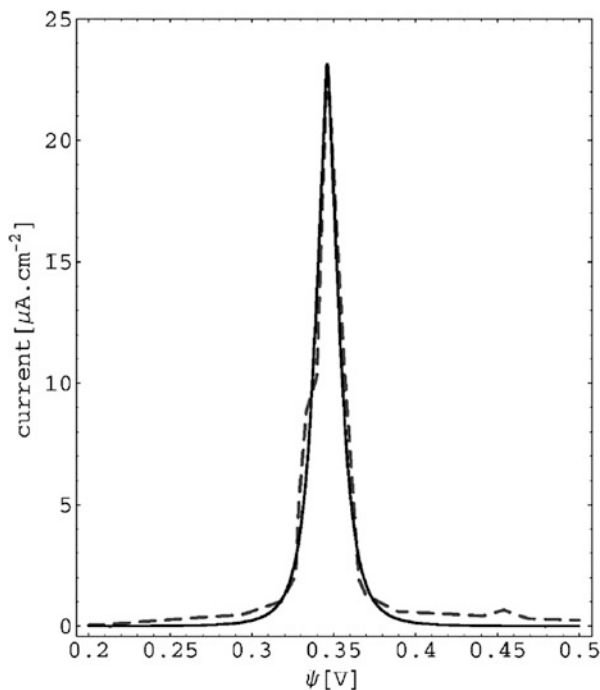


Fig. 5.17 Comparison between experimental results for underpotential deposition of Cu on Pt(111) from 1 mM Cu^{2+} and 0.1 M H_2SO_4 at a scan rate of 1 mV/s [53] (broken line) and the theoretical modeling of Huckaby and Medved [48]. The parameters fitted in the theoretical model were the effective electrovalence of the adsorbed ion $\gamma_v = 1.981$, the reference potential for the voltammogram $E_{\text{ref}} = -0.31$ V, the interaction parameter between adsorbed species $\zeta = -0.4334$ eV and the probability of occurrence of line defects $P = 0.1$. The latter quantity determines the distribution of lattice domains sizes on the surface (Reprinted with permission from Ref. [48])

experimental spikes. Although kinetic effects could be invoked to understand this discrepancy, many experiments involve very low sweep rates and there is no indication for kinetic limitations, in the sense that the current profiles obtained in the anodic and cathodic sweeps are practically the mirror image of each other. The hypothesis put forward by Huckaby and Medved is that an electrode surface is made of a huge number of domains (regular arrays of adsorption sites) separated by small areas of defects (irregular arrays of sites), so that the emerging current spike from an electrode is the addition of the current spikes from each domain. In Ref. [48] Huckaby and Medved showed that the lone use of periodic boundary conditions to simulate voltammograms fail to agree with experiment, so that boundary effects on the electrode crystals must be of real importance, and therefore, they derived expressions to obtain the total electrode current density as an average of the current densities of single crystals having a distribution of sizes and boundary interaction strengths.

Figure 5.17 shows the agreement between experimental results and the model prediction for Cu upd on Pt(111). The fitting parameters are the effective

electrovalence of the adsorbed ion, the reference potential for the voltammogram, the interaction parameter between adsorbed species (see discussion on the lattice gas model in Chap. 3, Sect. 3.6), and the probability of occurrence of line defects. The latter quantity determines the distribution of lattice domains sizes on the surface.

The previous studies were extended by the authors to consider Cu upd on Pt(100) and to the more complex system Cu upd on Au(111) [49, 50], allowing an evaluation of interaction parameters between deposited ions.

5.4 Monte Carlo Methods

5.4.1 Introduction and Generalities

The term Monte Carlo (MC) is often used to describe a wide variety of numerical techniques that are applied to solve mathematical problems by means of the simulation of *random variables* (the name MC itself makes a reference to the random nature of the gambling at MC, Monaco). These methods first emerged in the late 1940s and 1950s as electronic computers came into use.

Computer simulations generate information at a microscopic level (atomic positions and momenta, etc.) that has to be converted into macroscopic information (pressure, internal energy, etc.). As mentioned in Sect. 5.1, a thermodynamic property A may be calculated through a weighted average in which the weighting factors are the Boltzmann probabilities of each microscopic state and in which the sum runs over all of the states of the system (Eq. 5.9).

In practice, it is impossible to calculate a sum over *all of the microscopic states* of a system and, hence, we must propose a way to circumvent this problem.

In a first stage, we might be tempted to approximate the calculation of this average just by randomly generating a sufficiently large number of configurations and calculating the weighted average of the instantaneous value of the property A for each one of the generated states.

Two practical problems arise when we consider the calculation of the property A through this methodology:

1. Most randomly generated configurations will have a very low probability and, hence, a very small contribution to the average (which makes this a very inefficient approach).
2. As mentioned before in Sect. 5.1, the evaluation of these probabilities involves the calculation of the partition function which, for most systems of practical interest, is very difficult (if not downright impossible).

An elegant solution to these problems was provided by Metropolis and co-workers of the Los Alamos team [54]. In the Metropolis approach, instead of randomly accumulating configurations and then evaluating their probability-

weighed contribution to the desired average, configurations according to their Boltzmann probability can be accumulated and then a simple arithmetic average can be taken.

Thereby the problem is not solved, but merely reformulated. Now we need a way to generate a set of states in which each state appears a number of times that is proportional to its Boltzmann probability.

The way this is accomplished in the Metropolis approach can be summarized as follows:

Given a starting configuration i , a new configuration j is generated by means of a random change (which can be the simple movement, addition or removal of a particle). This new state j is accepted with a transition probability $P_{i \rightarrow j}$, which is calculated as follows:

- If the probability of state j is greater than the probability of state i , then the transition probability is equal to 1 (i.e. the new configuration is automatically accepted).
- If the probability of state j is smaller than the probability of state i , then the transition probability is equal to the ratio between the probabilities of states j and i ($P_{i \rightarrow j} = P_j/P_i$).

Or, in a compact form:

$$P_{i \rightarrow j} = \min\left(1, \frac{P_j}{P_i}\right) \quad (5.40)$$

where $\min(a,b)$ denotes the minimum value between a and b . This way of defining the transition probabilities allows us to skip the calculation of the partition function because, when evaluating the ratio between the probabilities (as defined in Eqs. (5.12) or (5.13)), the partition functions (which are in the denominators of the *r.h.s.* of such equations) become simplified.

Taking this into account, the transition probability becomes:

$$P_{i \rightarrow j} = \min(1, \exp[-(V_j - V_i)/k_B T]) = \min(1, \exp[-\Delta V_{ij}/k_B T]) \quad (5.41)$$

The chain of states constructed by this way has a limiting distribution equal to the probability distribution of the corresponding thermodynamic ensemble. This means that, at the end, a set of configurations is obtained according to Boltzmann statistics and the expectation value of the property of interest is obtained simply as the arithmetic average of values from individual accepted configurations.

So far we have said nothing about the way of generating these new configurations in order to construct the required chain of states. The different ways of doing so will be addressed in the following sections.

5.4.2 Off-Lattice Monte Carlo

In the Off-Lattice approach to the MC method, when attempting a move, the new random configurations are chosen from a continuous set, i.e., the atoms are allowed to move continuously.

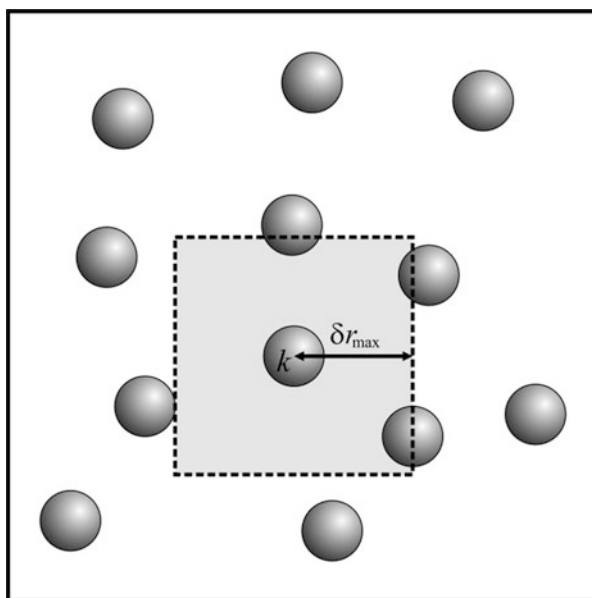
Several ways of accomplishing this condition have been proposed. One of the simplest (and the most used one) is the following one: At the beginning of a MC move, an atom is randomly selected and given a uniform random displacement along each one of the coordinate directions, as shown in Fig. 5.18. The maximum displacement, δr_{\max} , is an adjustable parameter that governs the size of the region.

After the new configuration j is generated, the transition is accepted with a probability $P_{i \rightarrow j}$ as defined in Eq. (5.41). The whole process is then repeated.

The efficiency of the exploration of the configuration space depends on the value of δr_{\max} in the following way: if it is too small, the energy changes associated with the transition will be small and a large fraction of moves will be accepted, but the configuration space will be explored slowly (i.e., consecutive moves will be highly correlated). If δr_{\max} is too large, then nearly all the trial moves will be rejected (due to the high probability of overlapping with other atoms) and, again, there is little movement through the configuration space. To maximize the efficiency of the exploration, the value of the parameter δr_{\max} is adjusted during the simulation so as to keep the acceptance ratio close to 50 %.

In the case of a simulation in the Grand Canonical Ensemble, the chemical potential is fixed while the number of molecules fluctuates. In order to construct the

Fig. 5.18 State j is obtained from state i by moving the selected atom k with a uniform probability to any point in the shaded region



chain of states, the most used method is the one proposed by Norman and Filinov [55]. In this technique there are three different types of move:

- (a) a particle is displaced.
- (b) a particle is destroyed (no record of its position is kept).
- (c) a particle is created at a random position.

The displacement of a particle is handled using the normal Metropolis method described above. If a particle is destroyed, the ratio of the probabilities of the two states is given by:

$$\frac{P_j}{P_i} = \exp[(-\Delta V_{ij} - \mu)/k_B T] \frac{N\Lambda^3}{V} \quad (5.42)$$

where N is the number of molecules initially in state i , V is the volume of the system, and Λ is the thermal de Broglie wavelength, defined as $\Lambda = (h^2/2\pi m k_B T)^{1/2}$. Similarly, for the creation of a particle, the ratio of probabilities is given by:

$$\frac{P_j}{P_i} = \exp[(-\Delta V_{ij} + \mu)/k_B T] \frac{V}{(N+1)\Lambda^3} \quad (5.43)$$

In both cases of destruction and creation, the final transition probability is calculated (like in the case of displacement), as $\min(1, P_j/P_i)$.

5.4.2.1 Off-Lattice Monte Carlo: Applications to Underpotential Deposition

Off-Lattice Monte Carlo methods were early applied not to upd but to an overpotential deposition system: Cu on Ag(111) [56]. We explain now shortly the motivation for such work. As pointed very often in the literature [57], important phenomenological criteria exist to determine if the type of deposit to be formed by metal on metal deposition is a two dimensional or a three-dimensional one. These criteria are based on the interaction energy of the adsorbate with the substrate, U_{S-M} , the interaction energy of M atoms with a substrate of the same type, U_{M-M} , and the crystallographic misfit M-S. According to this analysis, three types of growth modes of a deposit on a foreign surface can be established. In the case where $U_{S-M} \gg U_{M-M}$, crystal growth is expected to proceed via a 3D island growth or a Volmer-Weber mechanism. In the case where $U_{S-M} \ll U_{M-M}$ two possibilities may in turn be distinguished, depending on the misfit with the substrate. If the misfit is small, a layer by layer growth (Frank-van der Merwe) mode should be expected. On the other hand, if the misfit is large, a 3D growth on top of predeposited monolayers (Stranski-Krastanov) should occur. Even when a wide variety of systems appear to fit adequately into the previous scheme, the

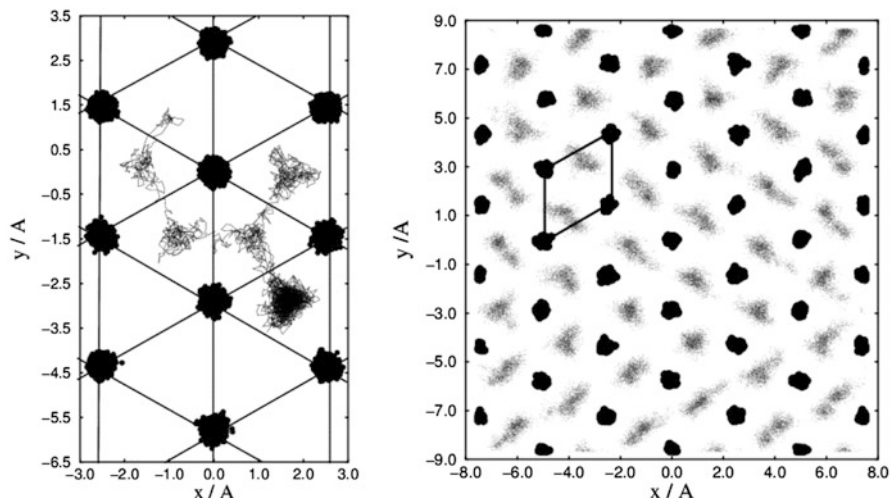


Fig. 5.19 MC simulation results for Cu deposited on Ag(111). *Left*: trajectory of a single Cu adatom indicated as a thin line; spots show the position of the first layer of Ag atoms. *Right*: Atomic positions for a monolayer of Cu adatoms (grey clouds) on a Ag(111) surface (Ag atoms in the first layer are shown as black clouds). Dashed lines show arbitrary unit cells (Reprinted with permission from Ref. [56])

measurements made by Dietterle et al. [58] on Cu deposition on Ag(111) showed that in this system a particular situation occurs, where the classical view seems to be challenged. While Cu deposition on Ag(111) presents no upd, a fact that would indicate that $U_{S-M} < U_{M-M}$, the formation of a pseudomorphic monolayer can be observed at low deposition overpotentials. On the other hand, three dimensional clusters are formed only at higher overpotentials, a situation where the deposition reaction is considerably accelerated. This fact lead Dietterle et al to suggest that a “delicate balance of adatom-adatom and adatom-substrate interactions” should take place, to explain this anomalous behavior.

Going back to the theoretical work of Cu deposition on Ag(111), it involved MC simulations where, like in most of the work discussed in this section, the interatomic potentials were those of the embedded atom method, which is discussed in more detail in Sect. 5.4.4.2. Figure 5.19 shows results from these simulations, for trajectories corresponding to the motion of a single atom (*left*) and of a full monolayer (*right*).

The binding energy of the Cu atoms was evaluated as a function of the coverage degree, as shown in Table 5.7. It is found that in all cases the binding energies of Cu are below the cohesive energy of Cu (3.54 eV), so that overpotential deposition is predicted.

Off-Lattice MC simulations using EAM potentials have been also found useful to calculate surface stress changes $\Delta\sigma_s$ upon island and monolayer formation of metal on foreign substrates. Based on a previous work devoted to study the

Table 5.7 Average binding energies of Cu adatoms on a Ag(111) surface at different coverages. The ratio $n_{\text{Cu}}/n_{\text{Ag}}$ indicates the ratio of Cu to Ag atoms in the simulation cell. The cohesive energy of Cu is 3.54 eV (Data taken from Ref. [56] with permission)

$\bar{E}_{\text{bind}}/\text{eV}$	$n_{\text{Cu}}/n_{\text{Ag}}$
2.77	1/36
3.37	36/36
3.38	39/36
3.39	42/36

properties of metallic islands [59], Rojas et al. [60] have developed a model to calculate $\Delta\sigma_s$ using a statistical mechanical argument.

Using the relationship between the Helmholtz free energy and the canonical partition function:

$$F = -k_B T \ln[Q(N, V, T)] \quad (5.44)$$

and the fact that when the stress tensor is diagonal, we can obtain the surface stress from the derivative:

$$\sigma_s = \left(\frac{\partial F}{\partial S} \right)_{N,T} \quad (5.45)$$

Rojas et al. [60] arrived to the following equation to calculate the surface stress change of the system:

$$\Delta\sigma_s = -k_B T \left(\frac{N_M}{S} \right) + \left\langle \left(\frac{\partial U_{S-M}}{\partial S} \right)_{N,T} \right\rangle - \left\langle \left(\frac{\partial U_M}{\partial S} \right)_{N,T} \right\rangle \quad (5.46)$$

where N_M is the number of adatoms, S is the surface, U_{S-M} and U_M are the interaction potential energies of the substrate-adsorbate and the substrate system respectively, and the quantities in brackets are evaluated from an isotropic stretching and compression of the simulation box in the direction parallel to the surface for each configuration of the production run.

The relaxation of islands on different substrate/adsorbate systems is illustrated in Fig. 5.20, together with a scheme of the simulation box. The *arrows* in the figure denote the displacement of the atoms in the island with respect to their pseudomorphic adsorption sites, and the colors indicate the magnitude of the displacement.

It is interesting to compare in the figure different behaviors: the homoepitaxy Ag (111)/Ag shows practically no relaxation at the center of the island, while some inwards relaxation at the borders becomes evident. On the other hand, the remaining systems present outwards relaxation.

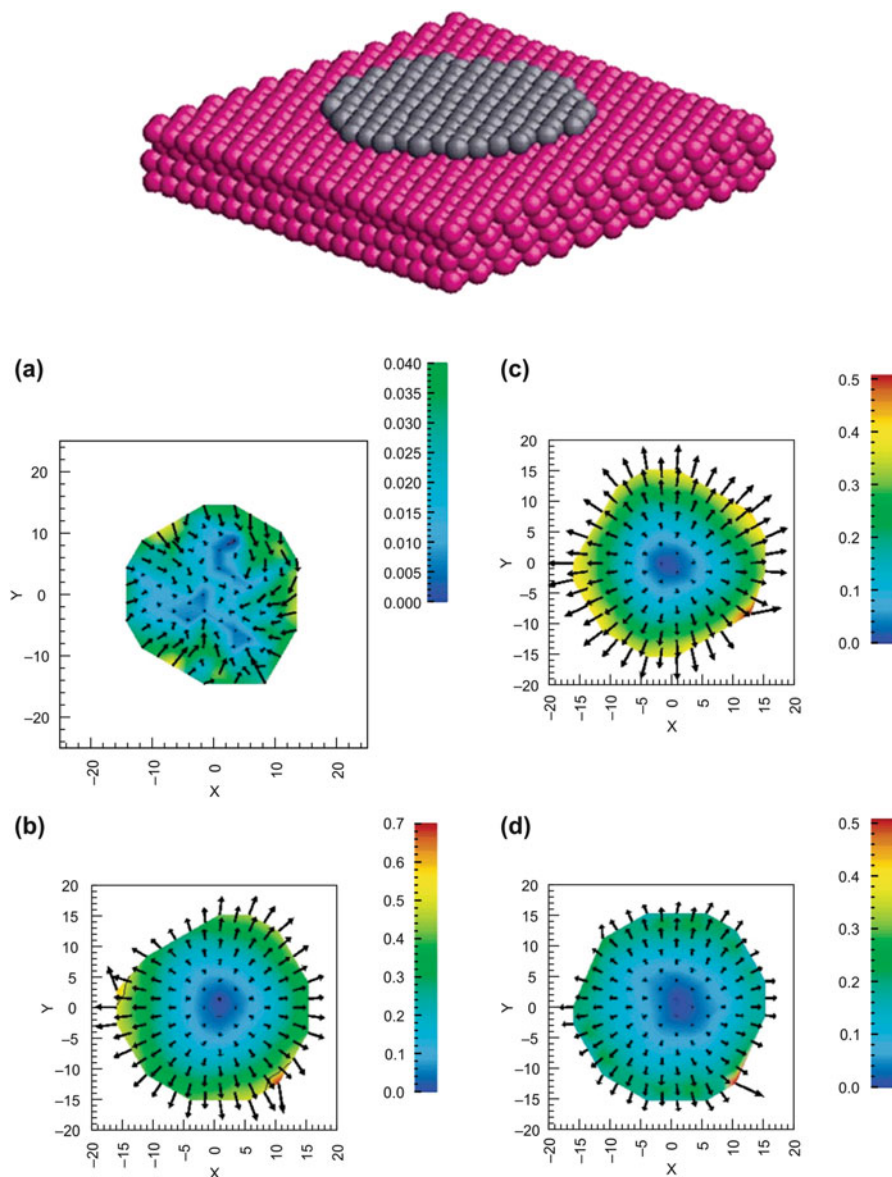


Fig. 5.20 *Top*: scheme of the simulation cell used to study the relaxation of an island of adatoms on a substrate. *Bottom*: Atom displacements in a 129-atom island for different systems adsorbate/substrate. The *arrows* represent the relaxation with respect to the (1×1) pseudomorphic configuration in Å. **(a)** Ag(111)/Ag; **(b)** Pd(111)/Ag; **(c)** Pt(111)/Ag; **(d)** Pt(111)/Ag. *Colours* also denote a displacement scale (Reprinted with permission from Ref. [60])

With quantitative purposes, a misfit may be defined according to:

$$\varepsilon_{\text{mf}} = \frac{a_{\text{subs}} - a_{\text{ads}}}{a_{\text{subs}}} \times 100 \quad (5.47)$$

where a_{subs} and a_{ads} denote the lattice constants of substrate and adsorbate respectively. The values of ε_{mf} Pd(111)/Ag, Pt(111)/Ag and Pt(111)/Au are -5.1 , -4.3 and -4.1 respectively, something that is reflected by the qualitative behavior observed in the Fig. 5.20.

The surface stress changes calculated for the adsorption of monolayers is shown in Table 5.5. In the case of Ag/Pt(111), the result of -4.9 N/m can be compared with -8.8 N/m, which is the value measured by Grossmann et al. [61]. For the systems Ag/Pd(111) and Au/Pt(111), large compressive stresses were also obtained (Table 5.8).

Rojas [62] extended the previous EAM Off-Lattice MC simulations to several systems, involving Ag, Au, Pt, Pd, and Cu. The results for stress changes are shown in Table 5.9. While the general trend is that a big adsorbate on a small substrate yields a compressive stress, and the opposite situation leads to tensile stress, there are also chemically specific effects. Comparison of these results with previous ones where relaxation of the adsorbate was not allowed [63], indicated that this effect is very important for the Cu(111)/Ag and the Cu(111)/Au systems, where misfits are very large.

Rojas also calculated underpotential shifts for all these systems, as reported in Table 5.10.

Table 5.8 Surface stress change $\Delta\sigma_s$ for the adsorption of a monolayer as obtained from Monte Carlo Simulations (Taken from Ref. [60] with permission)

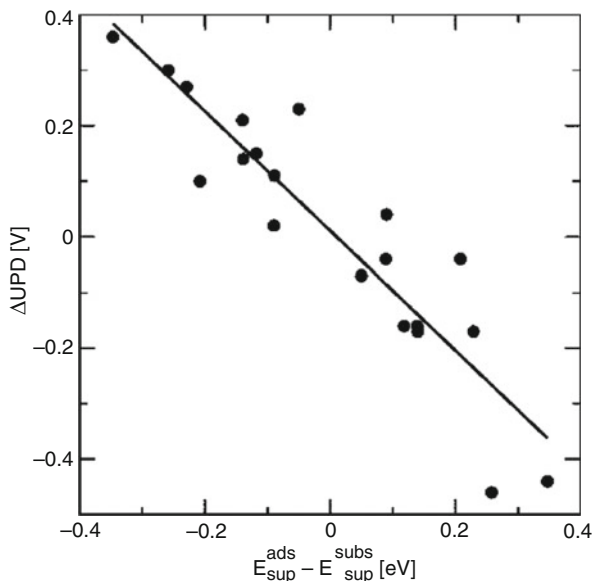
System	$\Delta\sigma_s/\text{J m}^{-2}$
Pt(111)/Ag	-4.92
Pd(111)/Ag	-4.88
Pt(111)/Au	-3.24

Table 5.9 Surface stress changes in J/m^2 for monolayer adsorption onto different (111) substrates, as calculated from Monte Carlo simulations in Ref. [62]. Columns correspond to adsorbates and rows to substrates. The notation (P), (E) or (C) indicates if the adlayer is pseudomorphic or becomes expanded or compressed with respect to the substrate lattice parameter

Substrate/adsorbate	Ag	Au	Pt	Pd	Cu
Ag(111)	0	1.1 (P)	3.8 (P)	2.1 (P)	0.6 (C)
Au(111)	-1.3 (P)	0	2.7 (P)	1.2 (P)	-0.5(C)
Pt(111)	-4.9 (P)	-3.2 (P)	0	-0.9 (P)	-0.3 (P)
Pd(111)	-4.9 (P)	-2.6 (P)	1.5 (P)	0	0.7 (P)
Cu(111)	-0.9 (E)	-1.6 (E)	-6.8 (P)	-6.2 (P)	0

Table 5.10 Deposition potential shifts for different metals on S(111) surfaces. All values are given in V. Taken from Ref. [62]. Positive values indicate upd, negative ones opd

Substrate/Adsorbate	Ag	Au	Pt	Pd	Cu
Ag(111)	0	-0.04	-0.44	-0.17	-0.16
Au(111)	0.11	0	-0.46	-0.17	-0.07
Pt(111)	0.36	0.30	0	0.15	0.10
Pd(111)	0.27	0.21	-0.16	0	0.02
Cu(111)	0.14	0.23	-0.04	0.04	0

Fig. 5.21 Underpotential deposition shifts vs difference of average surface energies between substrate and adsorbate (Reprinted with permission from Ref. [62])

When the values in Table 5.10 are plotted as a function of surface energy difference, a linear relationship results, as shown in Fig. 5.21. This follows the predictions made by the jellium model, see discussion in Sect. 5.2.2, as well as those from first-principles calculations, see discussion in Sect. 5.2.3 and Fig. 5.8 therein.

Oviedo et al. [64] used EAM Off-Lattice MC to study upd on low dimensional surface defects. They considered the energetics of the deposition of Ag, Cu and Pd atoms on a Pt(111) surface with vacancies, steps and holes, as compared with adsorption in monolayers, bilayers, etc. Some of the 0-D defects considered are illustrated in Fig. 5.22

The main results for the binding energies obtained are summarized in Table 5.11.

From these results, it can be concluded that for adsorption of a single atom on defects, the absolute value of the binding energy (bond strength) increases with the increase of the coordination ($U_{\text{step}}(0\text{D}) < U_{\text{kink}}(0\text{D}) < U_{\text{vacancy}}(0\text{D})$). On the other

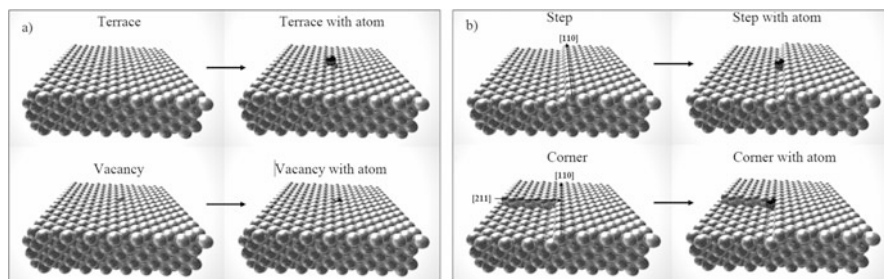


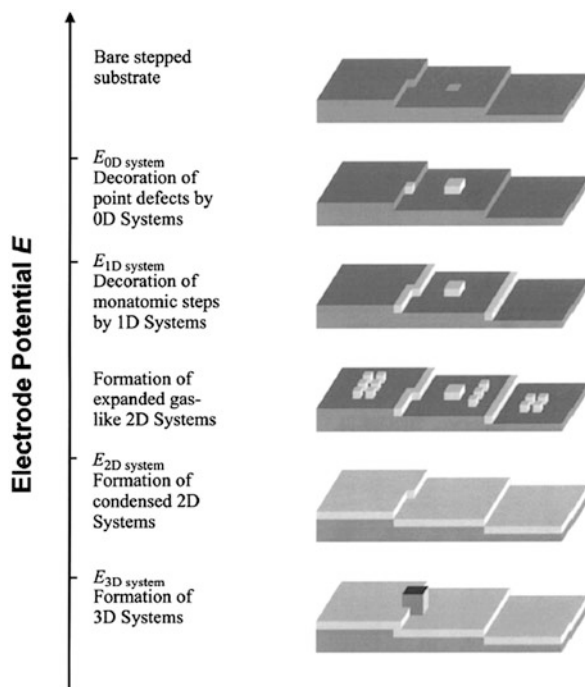
Fig. 5.22 Illustration of some of the 0-D defects considered to deposit atoms in a EAM Off-Lattice MC simulation. *Left*: terrace and vacancy sites. *Right*: Step and kink sites (Reprinted with permission from Ref. [64])

Table 5.11 Absolute value of binding energies in eV for Ag, Cu and Pd adatom adsorption on different defects/structures on a Pt(111) surface. 0-D denotes single atom adsorption. 1-D denotes adsorption along a line. 2-D denotes mono-, bi-, 3- etc layer adsorption, 3-D corresponds to the cohesive energy (Taken from Ref. [64] with permission)

Dimension of the defect/structure	Adsorption type:	Ag	Cu	Pd
0D	Terrace	2.69	3.06	3.14
	Step	3.25	3.91	3.99
	Kink	3.65	4.10	4.16
	Vacancy	4.45	4.97	5.09
1D	Step	3.47	3.99	4.12
2D	Monolayer	3.16	3.69	4.06
	bilayer	2.96	3.54	3.91
	3-layer	2.90	3.49	3.90
	6-layer	2.83	3.44	3.88
3D	bulk	2.18	3.50	3.89

hand, from the viewpoint of the dimensionality of the phase involved, the absolute value of binding energy decreases (bond strength) with the dimensionality $U_{\text{step}}(1\text{D}) > U_{\text{monolayer}}(2\text{D}) > U_{\text{bulk}}(3\text{D})$. Concerning upd, the present results indicate that, starting a negative potential sweep from a positive potential value where the substrate is naked, as the electrode potential is made more negative, the first sites to be filled with adsorbate should be the vacancies, followed by kink sites and steps. Then, monolayer formation would follow and finally the bulk deposit would appear. All these facts were found to be supported by experimental results, as discussed in Ref. [65] and shown schematically in Fig. 5.23.

Fig. 5.23 Formation of low dimensional structures in upd systems at different substrate inhomogeneities in the undersaturation range, depending on electrode potential (Reprinted with permission from Ref. [65])

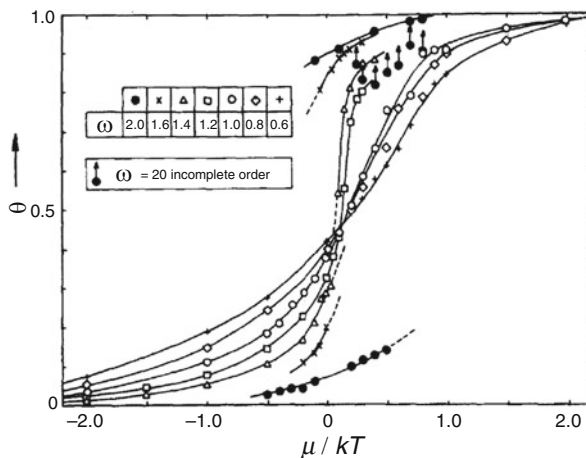


5.4.3 Lattice Monte Carlo

In the Lattice MC method, the particles constituting the system are located on the points of a lattice. This means that, in order to generate the chain of states implied by the Metropolis method, the displacement of atoms will take place between lattice points and, in the case of Grand Canonical simulations, atoms will be created or destroyed at these lattice points, as we discussed in Fig. 3.14. One of the advantages of these methods is that they allow dealing with a large number of particles at a relatively low computational cost.

These lattice models are of widespread use in studies of adsorption on surfaces. If the crystallographic misfit between the involved atoms is not important, it is a good approximation to assume that the adatoms adsorb on defined discrete sites on the surface, given by the positions of the substrate atoms. In principle, it must be kept in mind that continuum Hamiltonians should be much more realistic in those cases where epitaxial growth of an adsorbate leads to incommensurate adsorbed phases or to adsorbates with large coincidence cells. On the other hand, the use of fixed rigid lattices restricts enormously the number of possible configurations for the adsorbate and its use may be justified on the basis of experimental evidence or continuum computer simulations that predict a fixed lattice geometry.

Fig. 5.24 Simulation of adsorption isotherms for adsorption with exclusion effects on a square lattice. It is assumed that the adsorbate blocks two sites on the lattice substrate. ($n = 2$, see discussion in the text) (Reprinted with permission from Ref. [66])



5.4.3.1 Simulation of Relatively Simple Underpotential Deposition Systems

Pioneering application of lattice MC simulations to upd systems was undertaken by Van Der Eerden et al. [66]. These authors performed MC simulations using an Ising-type model (see Chap. 3), where the adsorbate atoms were assumed to have a diameter greater than the distance between two neighbouring adsorption sites on the substrate surface. Thus, each adatom is assumed to occupy only one adsorption site, but at the same time, due to exclusion effects, it blocks (first) neighbouring adsorption sites and prevents them from being occupied by other adatoms. This modeling has been denominated $1/n$ adsorption, where $n = 1/\theta_{\max}$. The cases considered were $n=2$ for a square lattice and $n=4$ for an hexagonal lattice. These authors investigated the occurrence of phase transitions as a function of the quantity $\omega = \zeta/k_B T$, where ζ is the interaction between two neighboring adsorbates, as defined in Chap. 3. Figure 5.24 shows the behavior of the isotherms for different values of ω for a square lattice with $n=2$. A smooth behaviour is found for θ vs $\mu/k_B T$ at low ω s, until $\omega = 1.4$. Above this value, a *hysteresis*, characteristic for the occurrence of a phase transition becomes evident. We use this word to denote that the isotherms present separated upper and lower branches, yielding two coverages at the same chemical potential, one of which corresponds to a metastable state.

Using this procedure, the authors determined critical ω values for the systems considered. In the case of the square lattice, the MC simulations yielded $\omega_{\text{critical}} = 1.3$. Comparison of the MC simulations with experimental results for the system Pb upd on Ag(100) are shown in Fig. 5.25, where it is found a good agreement for $\omega = 0.6$, which is a value well below the critical one, so that according to this modelling a first-order phase transition should be excluded for this system.

Fig. 5.25 Simulated isotherms for $n = 2$ adsorption on a square lattice with $\omega = 0.6$ (\circ); experimental results for upd of Tl(\bullet) and Pb(\square) on Ag (100) (Reprinted with permission from Ref. [66])

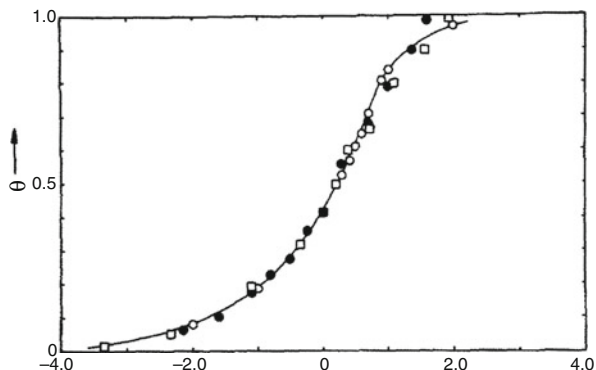
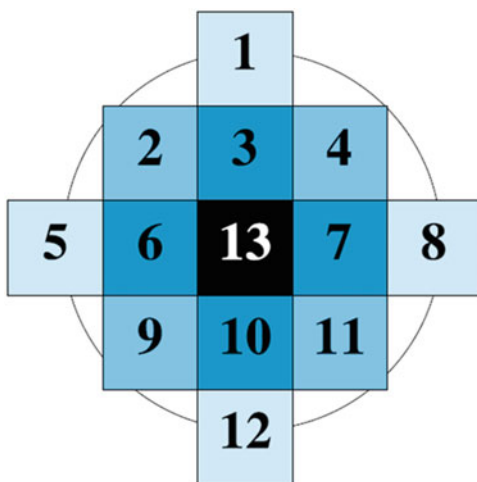


Fig. 5.26 Environment of 12 sites surrounding an adsorption site. These may be employed for the calculation of the adsorption/desorption energies of an adsorbate atom on a substrate for a cutoff radius corresponding to the distance between third-nearest neighbors. The particle is adsorbed on the central box (13) and the remaining sites may be occupied by adsorbate or substrate-like atoms. A total number of 3^{11} configurations results



As will be discussed in Sect. 5.4.4.2, the proper description of metallic binding requires the use of many-body potentials, where the embedded atom method has shown to be a reasonable alternative for many electrochemical applications. At first sight, this seems difficult to compute with a lattice model. To solve this problem in a computationally efficient way, the adsorption (desorption) of a particle may be considered at a site embedded in a certain environment surrounding it, as shown in Fig. 5.26 for a square lattice, which may be used to represent adsorption on a (100) *fcc* surface. The adsorption site for the particle is located in the central box, and the calculation of the interactions is limited to a circle of radius R . The adsorption energy for all the possible configurations of the environment of the central atom are calculated previous to the simulation, so that during the MC simulation the most expensive numerical operations are reduced to recover the index that characterizes the configuration surrounding the particle at the adsorption site.

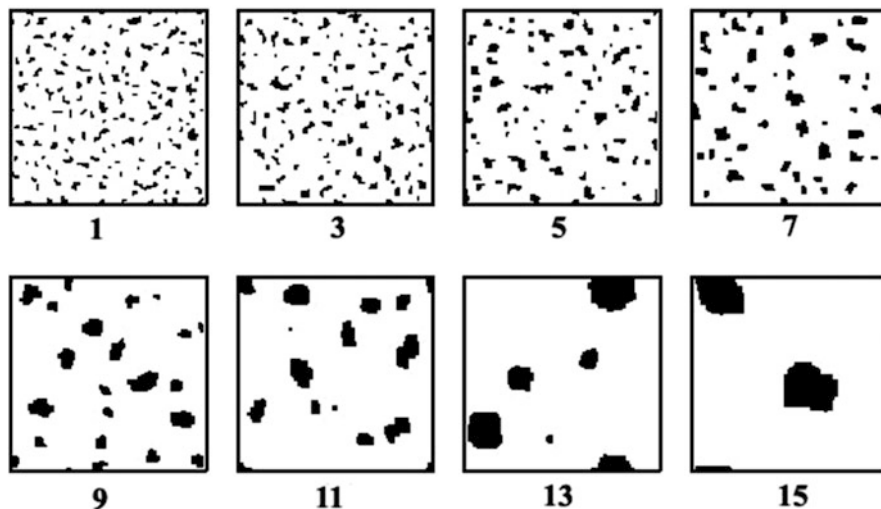


Fig. 5.27 Different island types obtained from simulated annealing simulations, used to obtain surfaces with different types of defects. The number of Monte Carlo steps N_{MCS} increases from upper left to down right. $N_{\text{MCS}} = 20 \times 2^{m-1}$, where m is the ordinal number of the configuration in the figure (Reprinted with permission from Ref. [67])

In the case of the electrochemical system, potentiostatic control is in many cases applied to fix the chemical potential of species at the metal/solution interface. Since the natural counterpart of potentiostatic experiments are Grand Canonical Monte Carlo (GCMC) simulations, where the chemical potential μ is one of the parameters fixed in the simulations, this was the methodology chosen by Giménez and Leiva [67] to study the formation and growth of low dimensionality phases on surfaces with defects. This work is somehow a lattice model version of the Off-Lattice problem analyzed in Sect. 5.4.2. To simulate (100) surfaces, the system was represented by a square lattice with N adsorption sites, as that shown in Fig. 5.26. Different arrangements of the substrate atoms allowed for the simulation of various types of surface defects. Within the procedure described in Sect. 5.4.1 (Metropolis algorithm), thermodynamic properties were obtained after proper equilibration steps as average values of instantaneous magnitudes stored along a simulation run. A key result is the average coverage degree of the adsorbate atoms $\langle \theta_M \rangle$ at a given chemical potential μ . To emulate different surface defects, substrate islands of various sizes and shapes were made by means of the MC-related technique denominated simulated annealing. Within this approach, a given number of substrate atoms is set on the surface, and a MC simulation is started at a very high initial temperature T_0 , of the order of 10^4 K. The system is later cooled down according to a logarithmic law ($T_{n+1} = T_n \alpha_a$), where α_a is a positive constant lower than one and T_n is the temperature at the n^{th} iteration step. A given number of MC steps, say N_{MCS} , are run at each temperature and the simulation is stopped when the desired T_f is reached. By setting different N_{MCS} , various kinds of structures may be obtained, as shown in Fig. 5.27.

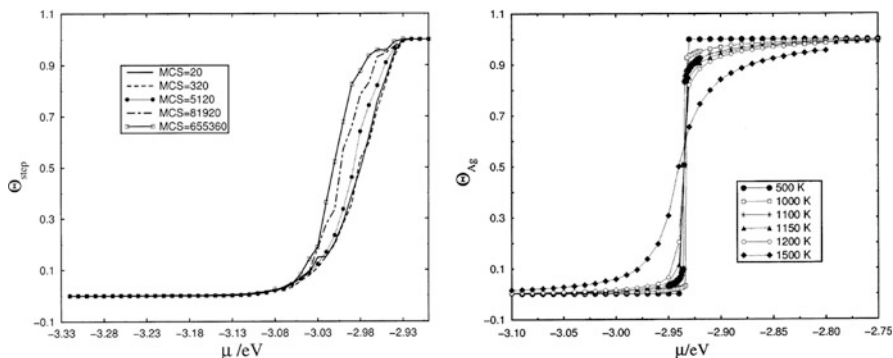


Fig. 5.28 *Left*: Adsorption isotherms for the decoration of monoatomic steps of Au defective surfaces with Ag up. The Au surface structures considered were the final states of simulated annealing runs similar to those of Fig. 5.27 with $m = 1, 5, 9, 13$ and 16 , resulting in the number of Monte Carlo Steps reported in the figure. The temperature was 300 K. *Right*: Adsorption isotherms for Ag up on a perfect Au(111) surface, at different temperatures (Reprinted with permission from Ref. [67])

Table 5.12 Excess of chemical potential $\mu_M^S - \mu_M^M$ in eV. Negative values of this quantity indicate underpotential deposition, while positive values indicate overpotential deposition, see Eq. (3.5). Values taken from Ref. [68]

Subs/Ads	Ag	Au	Pt	Pd
Ag	0.00	0.08	0.53	–
Au	–0.17	0.00	0.54	0.14
Pt	–0.55	–0.42	0.00	–
Pd	–	–0.26	–	0.00

The shape of the adsorption isotherms obtained with the different islands types turned out to be strongly sensitive to the structure of the surface, as shown on the *left* of Fig. 5.28. The isotherms obtained with more perfect surfaces (less steps) were steeper, becoming closer to the behavior expected for a first-order phase transition, which is shown on the right of the figure. We remind from the discussion performed in Chap. 3, that the voltammetric profiles are the derivatives of the isotherms, so that rounded isotherms lead to wider voltammetric peaks. Thus, we see that increasingly imperfect surfaces will lead to wider voltammograms. This is in rule with the theoretical modelling by Huckaby and Medved [48] that we presented at the end of Sect. 5.3.

In a further contribution, Gimenez et al. [68] considered several systems involving Ag, Au, Pt and Pd. It was found that, taking into account some general trends, such systems can be classified into two large groups. The first one comprises Au(100)/Ag, Pt(100)/Ag, Pt(100)/Au and Pd(100)/Au, which have favorable binding energies as compared with the homoepitaxial growth of adsorbate-type atoms, as shown in Table 5.12. These are systems where underpotential deposition is expected, see Eq. (3.5) of Chap. 3.

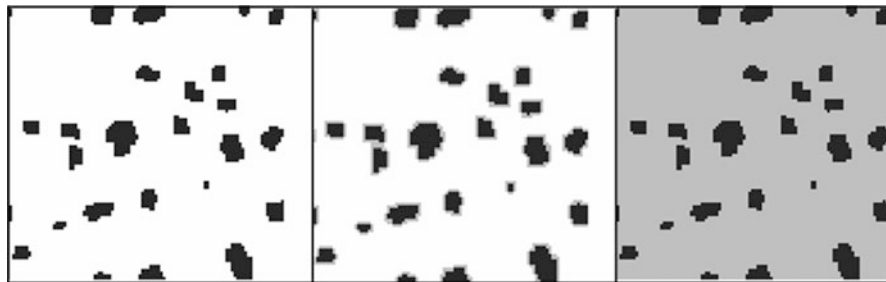


Fig. 5.29 Snapshots of the final state of the surface at three different chemical potentials (-4.27 eV, -3.44 eV, and -3.06 eV) for Ag decoration of a Pt(100) surface with Pt islands. The average island size is about 48 atoms. Note that the islands remain essentially unchanged (Reprinted with permission from Ref. [68])

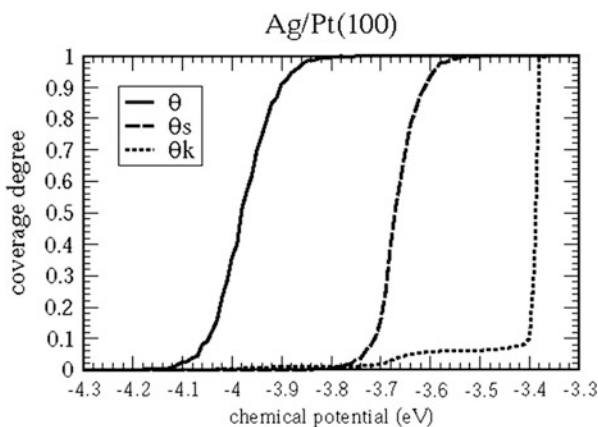


Fig. 5.30 Isotherms corresponding to the system of Fig. 5.29. θ , θ_s , and θ_k denote total, step and kink coverages respectively (Reprinted with permission from Ref. [68])

For this type of systems, when the simulations are performed in the presence of substrate-type islands emulating surface defects, the islands remain almost unchanged, and the adsorbate atoms successively occupy kink sites, step sites and the complete monolayer. This is illustrated in Fig. 5.29 for the surface atomic arrangement of Ag on a Pt(100) surface with Pt islands. The corresponding adsorption isotherms are shown in Fig. 5.30.

The partial coverage degrees for step and kink sites in Fig. 5.30 were defined relative to the total number of step and kink sites available respectively. The sequential filling of kink sites, steps and the rest of the surface can be appreciated clearly in the partial isotherms.

The second group of systems, as considered by Gimenez et al. [68] is composed of Ag(100)/Au, Ag(100)/Pt, Au(100)/Pt, and Au(100)/Pd, for which monolayer adsorption is more favorable on substrates of the same nature than on the

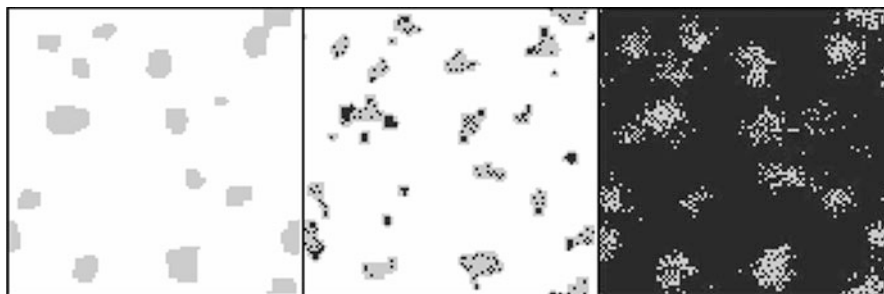


Fig. 5.31 Snapshots of the final state of the surface at three different chemical potentials (-5.74 , -5.32 and -5.21 eV) for Pt decoration of Ag islands on Ag(100). Average island size 53 atoms. Note the progressive disintegration of the Ag islands (Reprinted with permission from Ref. [68])

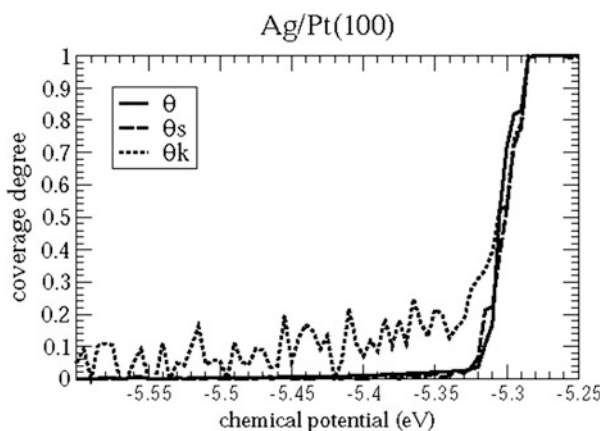


Fig. 5.32 Isotherms corresponding to the system of Fig. 5.32. θ , θ_s and θ_k denote total, step and kink coverages respectively (Reprinted with permission from Ref. [68])

considered substrates (see Table 5.11). When simulations are carried out in the presence of islands of substrate-type atoms, it is found that they tend to disintegrate, yielding 2D alloys with adsorbate atoms. This is illustrated in Fig. 5.31 for Pt deposition on Ag(100). For this second type of systems, the partial adsorption isotherms do not evidence any particular sequential filling, as can be observed in Fig. 5.32.

A detailed analysis of the environment of adatoms and substrate atoms at different adatom coverage degrees was found very helpful to understand the two types of behaviors described above.

More recently, Gimenez et al. [69] have shown that MC simulations with pair potential interactions between nearest neighbors may also yield the two types of behaviors described above, opening the way to a less demanding computational modeling. These authors have also extended this modeling to consider on-top adsorption of anions in upd systems [70].

5.4.3.2 Simulation of Cu Underpotential Deposition on Au(111) in Sulfate-Containing Electrolytes

We devote a special section to the analysis of Cu upd on Au(111) in the presence of sulfate ions, since the work developed by Zhang et al. [71] represents an interesting example of the application of the lattice MC technique to complex upd systems. As we have seen in Chap. 2, (Fig. 2.2) the voltammogram obtained for upd of Cu on Au (111) in the presence of sulfate anions presents two pairs of peaks, see also Fig. 5.35 below. From now on, the pair of peaks at more positive potentials will be labeled as #1 and the pair at more negative potentials as #2. According to experimental information [71–73], these correspond to transitions between a full monolayer (ML) of Cu at more negative potentials, an ordered ($\sqrt{3} \times \sqrt{3}$) mixed copper and sulfate phase at intermediate potentials, and a disordered low-coverage phase at more positive potentials. Inspired in the model proposed by Blum and Huckaby described in Sect. 5.3, these authors assumed that sulfate coordinates the (unreconstructed) triangular Au(111) surface through three of its oxygen atoms, with the fourth S–O bond pointing away from the surface. The Cu atoms were assumed to compete for the same adsorption sites as the sulfate. In order to obtain the configuration energies of the coadsorbed particles required for the MC simulation, the following three-state lattice-gas Hamiltonian was proposed:

$$\hat{H}(c) = -\tilde{\mu}_C \sum_i c_i^C - \tilde{\mu}_S \sum_i c_i^S - \sum_n \left[\Phi_{SS}^{(n)} \sum_{\{i,j\}} c_i^S c_j^S + \Phi_{CC}^{(n)} \sum_{\{i,j\}} c_i^C c_j^C + \Phi_{SC}^{(n)} \sum_{\{i,j\}} c_i^S c_j^C + c_i^C c_j^S \right] - \hat{H}_3 \quad (5.48)$$

where $-\tilde{\mu}_k$ denotes the change in the chemical potential of species k ($k = S$ (sulfate) or C (copper)) when one i particle is removed from the bulk solution and adsorbed on the surface, c_i^k the occupation number (0 or 1) of site i by the species k , (n) indicates the rank of neighborhood between sites (first, second, etc), and $-\Phi_{km}^{(n)}$ is the pairwise interaction energy between particles of type k and m that are first neighbors. The term \hat{H}_3 denotes three-particle interactions between sulfates, involving all second-neighbor equilateral triangles.

The lattice gas parameters were fitted by an iterative process, where they were finally fixed to yield reasonable agreement of the theoretical predictions with the shapes of the observed adsorption isotherms and voltammetric profiles, as well as with the dependences of the CV peak positions on the electrolyte composition in experiments. The interactions involved in Eq. (5.48) are shown in Fig. 5.33.

Part of the fitting involved the so-called ground-state configurations, which corresponded to the sets of most stable configurations at 0 K for given electrochemical potentials $\tilde{\mu}_C$ and $\tilde{\mu}_S$. This allowed the construction of phase diagrams as a

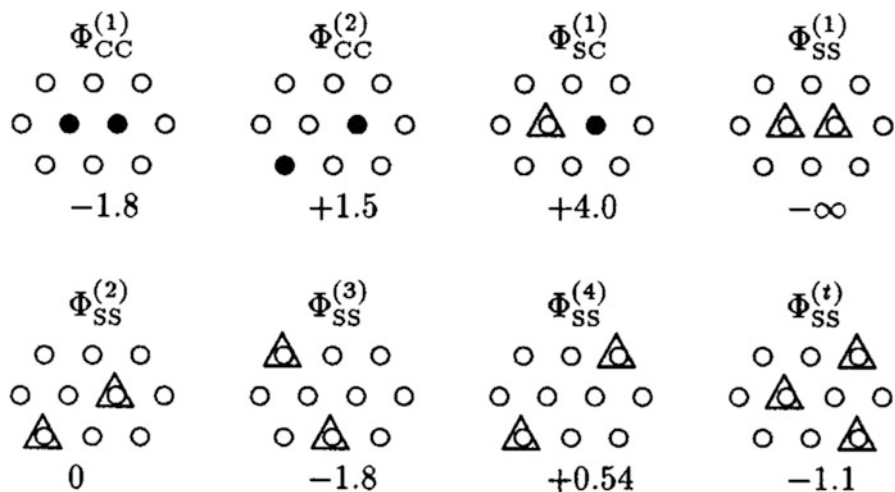


Fig. 5.33 The relative positions of Cu (●) and sulfate (Δ) corresponding to the effective interactions in Eq. (5.48). Free adsorption sites are denoted by ○. The number underneath each bond representation is the corresponding effective interaction energy used in Ref. [71], given in kJ/mol. The interactions are invariant under symmetry operations on the lattice (Reprinted with permission from Ref. [71])

function of $\tilde{\mu}_C$ and $\tilde{\mu}_S$, which are useful to interpret the results of simulations, discussed below. Figure 5.34 shows such a diagram and their corresponding ground-state configurations.

The different phases in Fig. 5.34 are identified with the notation $(X \times Y)_{\theta_C}^{\theta_S}$, where θ_C and θ_S denote the sulfate and copper coverages respectively. For example, $(1 \times 1)_0^0$ denotes an empty surface, $(1 \times 1)_1^0$ denotes a surface covered by a Cu monolayer, $(\sqrt{3} \times \sqrt{3})_{2/3}^{1/3}$ indicates a surface covered by a mixture of sulfate at $\theta_S = 1/3$ and Cu at $\theta_C = 2/3$, etc. It must be noted that the latter, which is the phase observed experimentally in the potential region between peaks #2 and #1, occupies a wide region in the ground-state diagram of Fig. 5.34. A detailed discussion of the occurrence of different phases in terms of the interactions of Eq. (5.48) is given in Ref. [71], we just point out here some general features to understand the idea behind the modeling.

The electrochemical potentials, which correspond to the axis on the *right* of Fig. 5.34, are related to the bulk concentration of species k and electrode potential E according to:

$$\tilde{\mu}_S = \mu_S^0 + RT \ln \frac{[S]}{[S]^0} - z_S F E \quad (5.49)$$

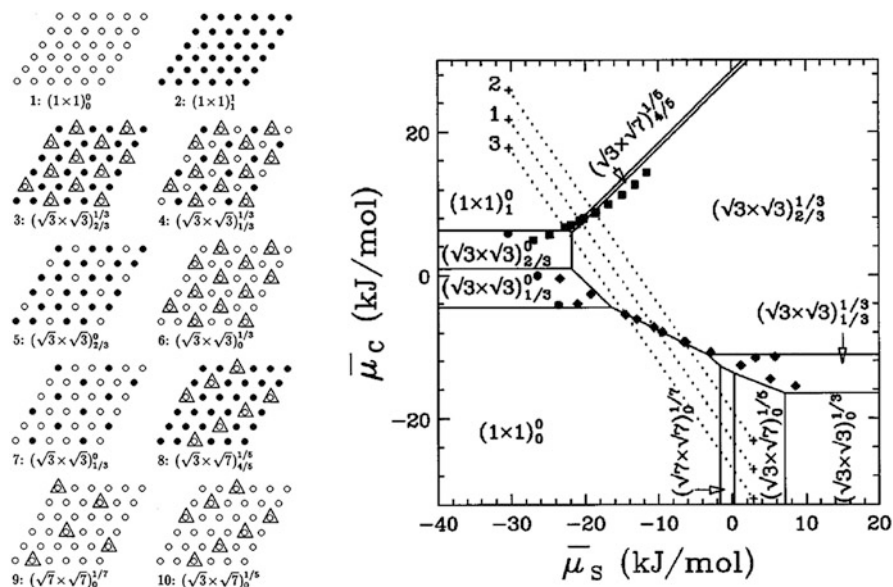


Fig. 5.34 Ground-state configurations (a) and ground-state diagram (b), as given in Ref. [71] for the system Cu/Au(111) in the presence of sulfate. The free adsorption sites are denoted by \circ , and adsorbed Cu and sulfate are denoted by \bullet and Δ , respectively (Reprinted with permission from Ref. [71])

$$\tilde{\mu}_C = \mu_C^0 + RT \ln \frac{[C]}{[C]^0} - z_C FE \quad (5.50)$$

where z_S and z_C are the effective electrovalences of sulfate and copper, respectively, and the superscript denote reference conditions. Thus, large $\tilde{\mu}_S$ positive values correspond to high sulfate concentrations or large positive potentials (z_S is a negative quantity). On the other hand, large $\tilde{\mu}_C$ positive values correspond to high Cu^{2+} concentrations or large negative potentials (z_C is a negative quantity). This is the reason why the pure Cu phase $(1 \times 1)_1^0$ appears at large positive $\tilde{\mu}_C$ values and rather negative $\tilde{\mu}_S$. The converse situation (large positive $\tilde{\mu}_S$ and negative $\tilde{\mu}_C$) leads to the pure sulfate phase, $(\sqrt{3} \times \sqrt{3})_0^{1/3}$.

According to Eqs. (5.49) and (5.50) the electrochemical potentials $\tilde{\mu}_S$ and $\tilde{\mu}_C$ are linearly related, so that when a potential scan is applied to the system, this moves along a straight line in Fig. 5.34b. Three of these lines are depicted there. The equation describing this straight line has the form $\tilde{\mu}_C = \text{constant} + \tilde{\mu}_S z_C / z_S$. Let us consider for example a trajectory along the line labeled with 1, where the potential scan is initiated on the upper left side of the plot. The system starts with the pure Cu phase $(1 \times 1)_1^0$ and ends up in the pure sulfate phase $(\sqrt{3} \times \sqrt{7})_0^{1/5}$, coming across two mixed Cu/sulfate phases. At the lines delimiting the phases, phase transitions

are expected to take place, with drastic changes in the composition of the surface structure. These changes in the surface composition are due to the electrochemical adsorption/desorption of species, involving charge transfer and eventually leading to peaks in the cyclic voltammograms, as shown in the simulation below.

Since the adsorbed particles are restricted to adsorb on N well defined lattice sites, the coverage can be easily calculated from $\theta_k = \sum_i c_i^k/N$ and the charge flowing upon adsorption of the species of type k is $q_k = -e_0 z_k \theta_k$. Sulfate coverage θ_S^2 adsorbed on top of the complete Cu monolayer in the negative-potential region was represented in terms of the Cu coverage θ_C and the sulfate coverage in the first layer θ_S by the equation:

$$\theta_S^2 = \alpha \theta_C \left(\frac{1}{3} - \theta_S \right) \quad (5.51)$$

where α was a fitting parameter, expected to be between zero and one. If the latter were the case, a full Cu monolayer would be covered by 1/3 of a monolayer of sulfate.

Considering a very low sweep rate so as to assume quasi-equilibrium conditions, the voltammetric current was calculated from the coverage degrees and their partial derivatives (obtained from coverage fluctuations [74] in the MC simulations) according to:

$$i = e_0 F \left\{ z_S^2 (1 - \alpha \theta_C) \left(\frac{\partial \theta_S}{\partial \bar{\mu}_S} \right)_{\bar{\mu}_C} + z_C \left(z_C - \frac{2}{3} \alpha z_S \theta_S \right) \left(\frac{\partial \theta_C}{\partial \bar{\mu}_C} \right)_{\bar{\mu}_S} + \left[z_S \left[2z_C + \alpha z_S \left(\frac{1}{3} - \theta_S \right) - \alpha z_C \theta_C \right] \left(\frac{\partial \theta_S}{\partial \bar{\mu}_C} \right)_{\bar{\mu}_S} \right] \right\} \frac{dE}{dt} \quad (5.52)$$

Figure 5.35 shows experimental and room-temperature simulated voltammograms. Given the complexity of the system, it can be stated that a good overall agreement is found.

Besides the simulations devoted to comparison with the experimental data, Zhang *et al.* performed a finite-size scaling analysis. This is useful at the time of identifying the order of the phase transitions involved. On the basis of the equivalence of the lattice gas hamiltonian (Eq. 5.48) with the generalized triangular-lattice model of Blume–Emery–Griffiths [75], the authors concluded that the transition at peak #1 is a first-order phase transition, while the transition at peak #2 is a second-order one. These predictions were checked performing simulations with different system sizes (finite size scaling analysis).

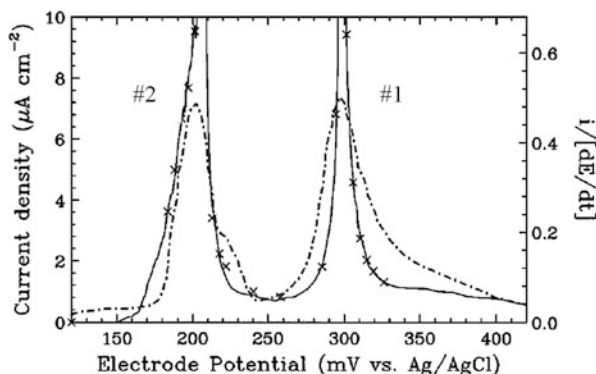


Fig. 5.35 Experimental (*dot-dashed*) and lattice MC simulated (solid) CV current densities. The left-hand vertical scale shows the current density for a scan rate of 2 mV/s, whereas the right-hand scale shows the current density normalized by the scan rate, in units of elementary charges per mV and Au(111) unit cell (Reprinted with permission from Ref. [71])

5.4.4 Kinetic Monte Carlo Applications

5.4.4.1 Introduction

Although MC methods are often used to obtain static, or equilibrium properties of model systems as described above, this technique may also be utilized to study dynamical phenomena. This leads to the formulation currently denominated dynamic Monte Carlo or kinetic Monte Carlo (KMC).

The foundations of dynamical MC simulations have been discussed by Fichthorn and Weinberg [76] in terms of the theory of Poisson processes, and we give here a bird's eye view on this methodology. There are many physical systems where the events of interest can be described at a coarse-grained, mesoscopic level, assuming that the complex microscopic behavior leads to various possible transitions that we can enumerate $\mathbf{E} = \{e_1, e_2, \dots, e_n\}$, which can be characterized by average transition rates $\mathbf{R} = \{r_1, r_2, \dots, r_n\}$.

As an example, we chose the diffusional trajectories of an adatom on a (100) single crystal surface, as shown in Fig. 5.36. We assume that we monitor a number of trajectories where the adatom is initially trapped in the central adsorption site, ending at one of the four neighboring adsorption sites. At relatively low temperatures, the trajectories will look like those on the left plot, where the adatom spends a long time (in the atomic scale) at the central site and finally diffuses to some of its four neighboring sites through trajectories close to the minimum energy path. If the experiment (eventually the simulation) is made several times, the scape of the atom from the central site to each of its neighbors will be characterized by a set average times, say $\{\tau_1, \tau_2, \tau_3, \tau_4\}$. Due to the symmetry of the system chosen for this example, all these average scape times will be equal, but they may be generally different (for instance if the environments of the various sites are different). Thus,

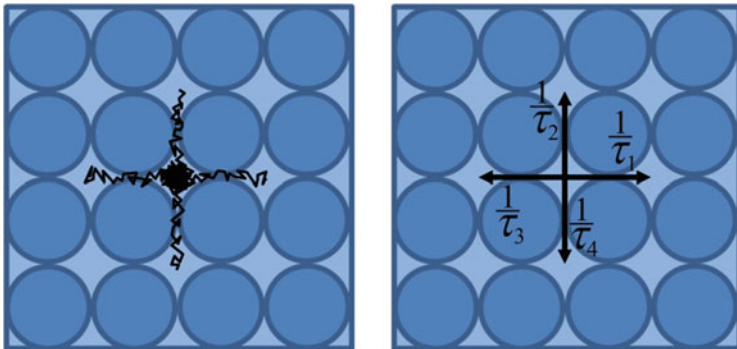


Fig. 5.36 Illustration of how the fine grained motion found in deterministic trajectories, i.e. from molecular dynamics (*left*) can be converted into effective or average rates (*right*)

the fine grain problem on the left of the figure may be replaced by coarse grain problem on the right, where the adatom may undergo four different transitions, $E = \{e_1, e_2, \dots, e_4\}$, at four different average rates $R = \{1/\tau_1, 1/\tau_2, 1/\tau_3, 1/\tau_4\}$. These ideas may be generalized to more complex problems, as long as the kind of events involved fulfills some features. If each of these events satisfies the conditions necessary to be a Poisson event,⁴ the probability density of times between successive events will have the following exponential form:

$$f(t) = \left(\frac{1}{\tau_i}\right) \exp[-t/\tau_i] \quad (5.53)$$

One interesting property of Poisson processes is that an ensemble of independent Poisson processes will behave as one, large Poisson processes. In the example of diffusion above, this means that if we have (simultaneously with diffusion) other phenomena occurring like adatom adsorption, adatom desorption, etc, that can be considered themselves as Poisson processes, the whole behavior of the system (diffusion + adsorption + desorption) may be treated as a single Poisson process. Thus, our vector of events will look like

$$\mathbf{E} = \{e_1^{\text{diff}}, e_2^{\text{diff}}, \dots, e_1^{\text{ad}}, e_2^{\text{ad}}, \dots, e_1^{\text{des}}, e_2^{\text{des}}, \dots\} \quad (5.54)$$

where the upper indices have an obvious meaning: e_1^{diff} is a diffusion event of type 1, e_1^{ad} is an adsorption event, e_2^{des} a desorption event, etc. Thus, the vector of events \mathbf{E} contains all the events that may occur at a given instant (configuration) of the system.

⁴ Poisson processes in a nutshell: if $N_i(t)$ is a random variable characterizing the observation of a number of certain events during a time interval t , Poisson processes are characterized by: (a) $N_i(0) = 0$, (b) $N_i(t_1)$ and $N_i(t_2)$ are independent if t_1 and t_2 are disjoint intervals. (c) The probability of observing a single event in the interval h increases linearly with h . (d) The probability of observing two or more events in the interval h increases with a power larger than one.

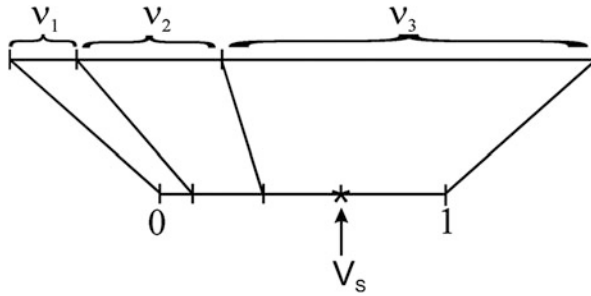


Fig. 5.37 Illustration of the way in which a given process is selected in a kinetic Monte Carlo simulation where only three processes may occur. The probability of each process to occur is represented on a straight line by a segment proportional to its rate v_i . The sum of all the segments is normalized to unit length, so that the occurrence of a process can be selected by generating a random number v_s between 0 and 1, and then choosing the process corresponding to the segment on which the random number is found to fall. Here v_s falls in the segment corresponding to the rate v_3

Similarly, the rates vector will be:

$$\mathbf{R} = \{1/\tau_1^{\text{diff}}, 1/\tau_2^{\text{diff}}, \dots, 1/\tau_1^{\text{ad}}, 1/\tau_2^{\text{ad}}, \dots, 1/\tau_1^{\text{des}}, 1/\tau_2^{\text{des}}, \dots\} \quad (5.55)$$

Or alternatively:

$$\mathbf{R} = \{v_1^{\text{diff}}, v_2^{\text{diff}}, \dots, v_1^{\text{ad}}, v_2^{\text{ad}}, \dots, v_1^{\text{des}}, v_2^{\text{des}}, \dots\} \quad (5.56)$$

where we have defined the average rates $v_i = 1/\tau_i$. A way to visualize the last equation is to draw a line, where the average rate of each process is represented by a segment on this line, as it is shown in Fig. 5.37 for three processes. Let us represent the event vector with $\mathbf{E} = \{e_1, e_2, e_3\}$ and the velocity vector with $\mathbf{R} = \{v_1, v_2, v_3\}$.

Since no two Poisson events may occur simultaneously, we can make the status (configurations) of the system advance by choosing one of the events whose rates are shown in the figure. To do that, the whole velocity segment may be applied into the interval [0,1], and a random number η may be generated to select the event to happen. It is observed from the figure that the random number resulted in the occurrence of a process whose velocity is v_3 .

Thus, what it must be done is to allow event e_3 to happen. If the processes under consideration were $e_1 :=$ diffusion of a particle, $e_2 :=$ adsorption of a new particle, $e_3 :=$ desorption of the particle, we would have to desorb the particle. The new configuration of the system would be an empty surface, and the new event vector would only contain a single element, corresponding to particle adsorption. Of course, in a real system we have many particles that may diffuse, desorb, adsorb, etc, and the event and rates vectors are very large, but this is the main idea. Upon updating the configuration of the system, we must update the time in the simulation, that is, we must add to the accumulated time a time increment representing the event that has just occurred. To do that, we appeal to an equation similar to

Eq. (5.53), but taking into account that we are considering all the events of the system. Now, the overall rate is $v_t = v_1 + v_2 + v_3$ and Eq. (5.53) turns into:

$$f(t) = v_t \exp[v_t t] \quad (5.57)$$

To generate time increments distributed according to the previous equation, we must use:

$$\Delta t = -\frac{1}{v_t} \ln(v_S) \quad (5.58)$$

where v_S is a uniform random number between 0 and 1. Note that random numbers close to zero lead to large time steps, while random numbers close to 1 yield short ones.

We see that according to the KMC method, the sampling of the system must involve transition probabilities based on a reasonable dynamic model of the physical phenomena involved. The transition probabilities should reflect a “dynamic hierarchy” related to the processes taking place in the system. With this aim, the rates v_i are usually taken from some suited version of absolute rate theory, adapted to surface diffusion, electron transfer, etc.

Since in principle *all* the processes that may potentially occur must be included in the vector \mathbf{R} , the application of KMC methods is restricted to lattice models of the system.

5.4.4.2 Electrochemical Phase Formation for an Ideal Frank-van der Merwe System

To illustrate the application of the KMC method, we discuss the system Au(hkl)/Ag. This is a typical example for M upd on a foreign substrate S, with strong M-S interaction but negligible M-S misfit (the lattice parameters are 4.09 Å and 4.08 Å for Ag and Au, respectively). Thus, the Frank-van der Merwe or layer by layer growth mechanism is expected to operate in this system, in contrast with the Stranksi-Krastanov growth mode, expected for systems with relatively large misfits [57], or the Volmer-Weber mechanism, expected for systems where the interaction with the substrate is relatively weak, as compared with the adsorbate-adsorbate interaction. As discussed in the literature [77] and in Chaps. 2 and 3 of the present book, these systems exhibit a number of complex features, like surface reconstruction, even in the absence of adsorbate, and different expanded phases. However, a simplified model as that we will discuss here, has been shown to be useful to understand some of the experimental observations, and may also be helpful to understand other upd related problems. Giménez et al. [77] have modeled nucleation and growth of Ag upd on Au(100) and Au(111) by KMC. We discuss their modeling in some detail, since it is illustrative of how this methodology may be implemented to study upd deposition phenomena.

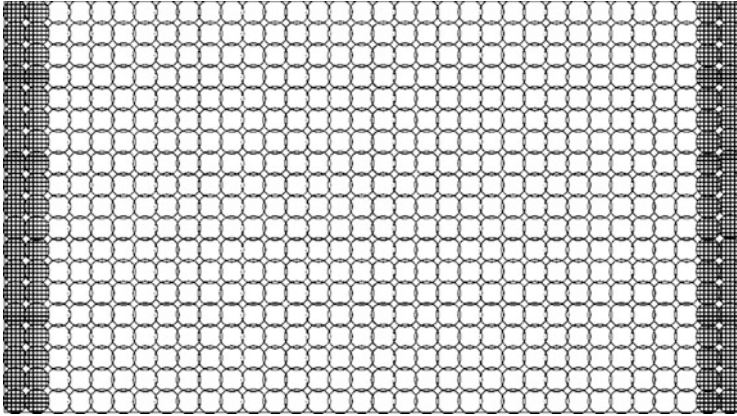


Fig. 5.38 Simulation box employed to study Ag nucleation and growth upon upd on a Au(100) surface. The system has periodic boundary conditions in the vertical direction (Reprinted with permission from Ref. [77])

Model for the Substrate

As stated above, the KMC methodology requires a finite number of processes taking place, so that a lattice model for the substrate appears as the best alternative. Thus, square and hexagonal lattices were selected to represent the Au(100) and Au(111) substrates respectively. Figure 5.38 shows the square lattice used to represent the former surface. There, the lattice consists of 1600 adsorption sites inserted between two Au steps, to simulate both island growth on a surface and at step borders. The image of the simulation cell is repeated periodically in the vertical direction (periodic boundary conditions).

Interactions Between the Particles of the System

The choice of proper interatomic potentials is a key issue in computer simulations. This is particularly the case in upd systems, which are characterized by metallic many-body interactions. Several methods are available to calculate the total energy of a many-particle metallic system, with a computational effort similar to that of a pair potential. Among them, it is worth mentioning the EAM [78], the N -body potentials of Finnis and Sinclair [79], the second-moment approximation [80] and the glue model [81]. The article here discussed used the EAM because it showed to reproduce important characteristics of the metallic binding. The EAM considers that the total energy U_{tot} of a metallic system made of N particles may be calculated as the sum of energies U_i corresponding to single particles according to:

$$U_{\text{tot}} = \sum_{i=1}^N U_i \quad (5.59)$$

U_i is written as:

$$U_i = F_i(\rho_{h,i}) + \frac{1}{2} \sum_{j \neq i} V_{ij}(r_{ij}) \quad (5.60)$$

where F_i is the so-called embedding function, which represents the energy resulting from embedding atom i in the electronic density $\rho_{h,i}$ at the position at which this atom is located. $\rho_{h,i}$ is obtained from the superposition of the individual electronic densities $\rho_j(r_{ij})$;

$$\rho_{h,i} = \sum_{j \neq i} \rho_j(r_{ij}) \quad (5.61)$$

while ρ_j represents an attractive, many-body electronic contribution, the second term in Eq. (5.60) represents the repulsion between ion cores. The latter is described through a pair potential $V_{ij}(r_{ij})$, which depends only on the distance between the cores r_{ij} with the form:

$$V_{ij}(r_{ij}) = Z_i(r_{ij})Z_j(r_{ij})/r_{ij} \quad (5.62)$$

where the $Z_i(r_{ij})$ represent an effective charge, dependent on the nature of the atom i . The functions $F_i(\rho_{h,i})$ and $V_{ij}(r_{ij})$ have been parameterized to fit experimental data for the isolated metals like cohesive energies, elastic constants, bulk lattice constants and bimetallic properties like dissolution enthalpies of binary alloys.

Dynamic Hierarchy: Calculations of Rates for the Different Events

As stated in the introduction, KMC requires establishing a dynamic hierarchy, which allows the construction of the rate vector \mathbf{R} (Eqs. 5.55 and 5.56). Thus, the rates of the events that may take place must be clearly determined. In the present case of study, surface phase formation, the following events may occur: (a) adatom formation (adsorption) (b) adatom oxidation (desorption) (c) adatom diffusion. If one is interested in the particular study of the formation/disappearance of the upd phase, processes (b) or (a) may alternatively be neglected with respect to the complementary one. For example, the study of Ref. [77] was focused on the deposition of Ag on Au(100) and Au(111), so that the dissolution rate was neglected and the deposition rate was used as a parameter. On the other hand, the diffusion rate was calculated using the EAM potentials. With this purpose, the diffusion of a Ag adatom on a Au surface was considered in different possible environments as illustrated in Fig. 5.39. The initial and the final positions of the

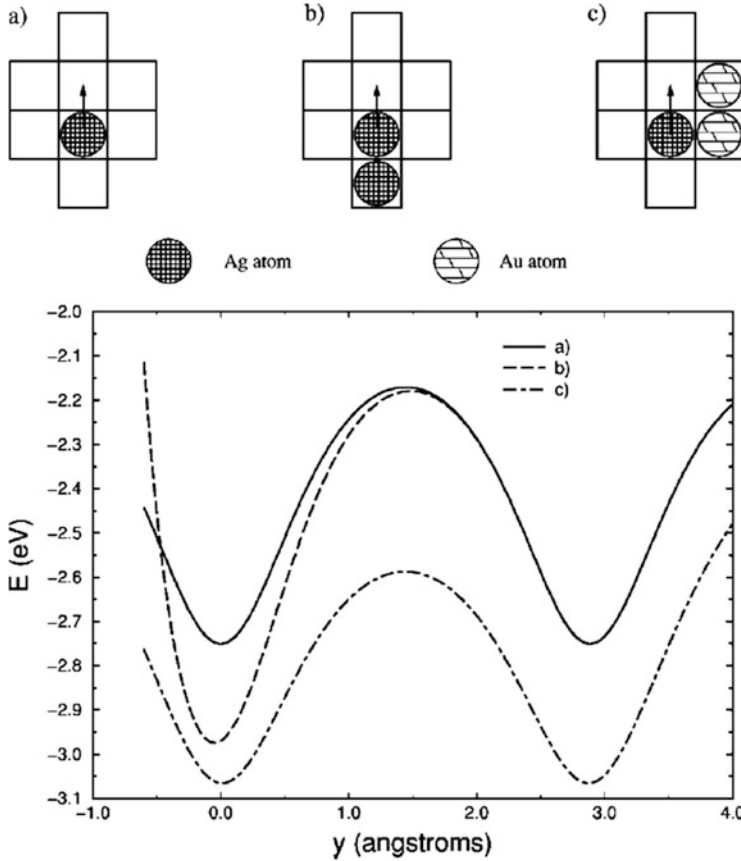


Fig. 5.39 (a)–(c) Sample environments considered for the diffusional motion of a Ag atom on a Au(100) surface. (d) Potential energy as a function of the distance along the diffusion path for the environments shown in (a)–(c) (Reprinted with permission from Ref. [77])

diffusing atom are embedded in an environment of six neighboring sites, which may be free or occupied by Ag or Au atoms, thus yielding a total number of $3^6 = 729$ configurations. Figure 5.39 shows three sample environments and the corresponding energy curves along the diffusion paths. The diffusion rates were calculated from these curves according to [82]:

$$v_{\text{diff}} = 2\nu \exp[-E_a/k_B T] \tag{5.63}$$

where ν is the attempt frequency and E_a is the activation energy as calculated from a trajectory between the initial and the final state, using the EAM potentials.

Details on the organization of the KMC procedure and a description of how the algorithm may be coded, including the storage and search algorithms that are used, are described for example in the Appendix of the manuscript by Drews et al. [83].

The steps of the KMC algorithm can then be summarized as:

1. A random number, v_{S_1} , is chosen from a uniform distribution in the range (0,1).
2. All the possible N_t events are determined and their rates v_i calculated.
3. A transition event is selected from the event vector, by selecting the first index s

$$\text{for which } \sum_{j=1}^s v_i / \sum_{j=1}^{N_t} v_i \geq v_{S_1}.$$

4. The even selected is allowed to occur.
5. All v_i that have changed as a result of making the move are updated.
6. The time in the simulations is advanced Δt where Δt is:

$$\Delta t = -\frac{1}{\sum_{j=1}^{N_t} v_i} \ln(v_{S_2}) \quad (5.64)$$

where v_{S_2} is a second random number, also chosen from a uniform distribution in the range (0,1).

The previous modeling was used to analyze the different behavior of Ag nucleation and growth found on Au(100) and Au(111) faces. The KMC simulations indicated the nucleation and growth should take place with the characteristic time of tenths of seconds in the case of the Au(100) face and of the order of milliseconds in the case of the Au(111) face. Therefore, if Ag is deposited at intermediate rates on both surfaces, island growth is predicted to occur on Au(100) but not on Au(111), as found in experiment [84, 85]. These features are illustrated in Fig. 5.40.

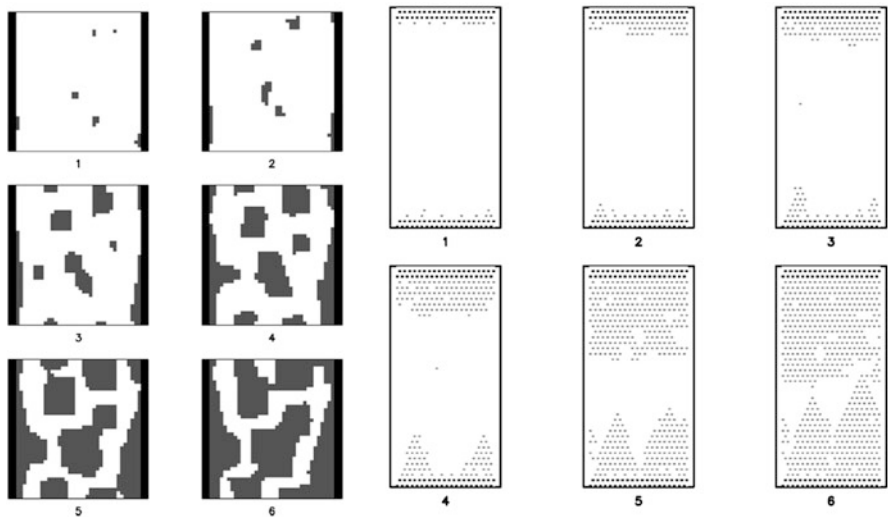
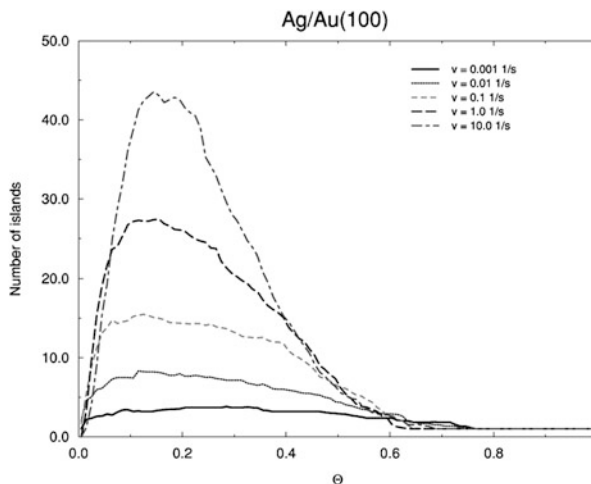


Fig. 5.40 Snapshots of Ag up-d growth on Au(100) (*left*) and Au(111) surfaces (*Right*). Note the occurrence and the absence of islands in the first and the second case respectively (Reprinted with permission from Ref. [77])

Fig. 5.41 KMC results for the number of islands as a function of the coverage degree for Ag upd on Au (100) at different deposition rates ν , as indicated in the figure. Each curve represents an average over six simulation runs (Reprinted with permission from Ref. [77])



Another valuable information that can be obtained with this simulation technique is the number of islands formed as a function of coverage degree at different adsorption rates, as illustrated in Fig. 5.41.

The present methodology has been very recently extended by Treeratanaphitak et al. [86, 87] to account for collective surface diffusion processes, in addition to nearest-neighbor hopping, including atom exchange and step-edge atom exchange, allowing the study of polycrystalline metal electrodeposition. Thus, the combination of EAM potentials with KMC appears as a very promising tool for studying the present and other related phenomena, like for example the formation of surface alloys.

5.4.4.3 Other Simple Metal Deposition Systems Involving a Foreign Substrate

The previous formalism has also been used to tackle other upd-related deposition phenomena. Rather than simulating specific systems, a useful approach is sometimes to vary one or more of the parameters of the model applied and analyze how they affect the properties emerging from the simulation. The utility of this approach is twofold: on one side, it can be expected that if a simulation reflects the experiment results, its parameters may be close to those of the experimental system. This allows getting information that is not directly available from the experiment. On the other hand, the parameters of the simulation may be tuned to get a given result, like for example a uniform distribution of islands on a substrate. In this way, the simulation becomes a useful tool for system design.

Concerning the first type of application mentioned above, Giménez et al. [88] have used KMC to analyze three different situations for adatom deposition rates, as

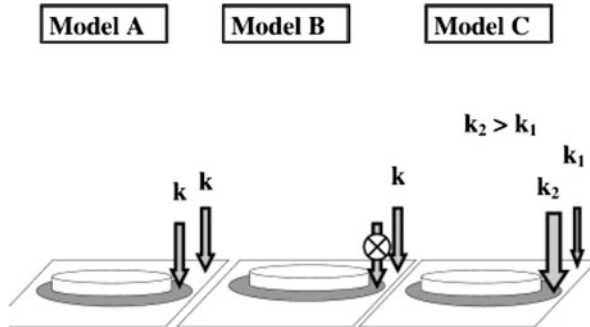


Fig. 5.42 Scheme of the mechanisms for atom deposition considered in Ref. [88]: (a) Particle adsorption occurs on all unoccupied sites at the same rate k . (b) Particle adsorption occurs only at sites without neighboring adsorbates at the rate k . (c) Particles are considered to be discharged preferably at sites with neighboring adatoms at a rate k_2 and at a lowest rate, k_1 , at those sites without neighboring adatoms (Reprinted with permission from Ref. [88])

illustrated in Fig. 5.42: (a) a case where the deposition rate is the same on any adsorbate-free sites on the substrate (Model A); (b) a case where deposition is only allowed on sites characterized by adsorbate-free surroundings (Model B); (c) a more general case where deposition at edge sites and terraces is allowed at different rates (Model C). In the last two cases, the coverage vs time curves were fitted to a stretched exponential law ($\theta = 1 - \exp[-t^\alpha/k_B T]$), with the finding that the parameter α can be used as a diagnose criterion to differentiate between the two cases. While in model B, α was found to be always smaller than 1, in model C, α was found to vary between 1.1 and 2.4, depending on the deposition rates assumed. This predictions may be contrasted with those of Avrami's model [89], where the exponent α is 2 or 3, depending on whether the nucleation is progressive or instantaneous.

Drews et al. [90] have also used KMC simulations to investigate nucleation and early stages of growth during metal electrodeposition on a foreign substrate. A negative overpotential was assumed (overpotential deposition). The authors also chose conditions where the kinetics of attachment of atoms to the electrode surface is rate-limiting, that is, low overpotentials. A negative overpotential was assumed (overpotential deposition). Adatom diffusion, characterized by a diffusion jump frequency w , was not only considered on the substrate, but also on a monolayer and on a bilayer of M. Adatom deposition was allowed on both the substrate or the metal M via a Tafel kinetics, at a deposition rate v_{dep} . Some of the information obtained from the simulation was concerned with cluster density, average cluster size, and average cluster height. It was found that the energy barrier for metal-on-substrate surface diffusion had the strongest effect on the cluster density in the parameter regimes investigated, while the energy barrier for metal-on-metal surface diffusion had a weak effect.

In a subsequent article, Drews et al. [83] have used KMC to study the influence of the presence of metal seed clusters and other parameters on the cluster size

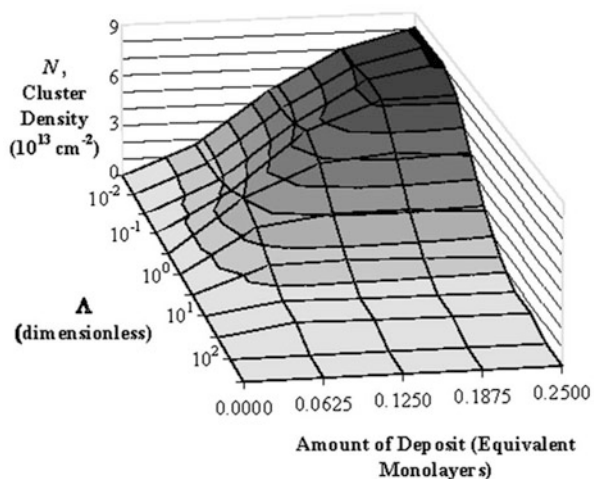
distribution of deposits. According to these simulations, it was found that the best conditions for producing a uniform size distribution is an initial high number of seed clusters, a low applied potential and a low metal-surface diffusion energy barrier.

Although metal deposition on a foreign substrate was also assumed to occur under overpotential conditions as in the previous case, it is worth mentioning here the KMC work of Stephens and Alkire [91] concerning nucleation and growth at monatomic step edges. It was found that the propensity of the deposit to grow at step edges or to form islands on the surface may be measured by the adimensional quantity Λ , which was defined as:

$$\Lambda_d = \frac{1}{L} \sqrt{\frac{D}{v_{\text{dep}}}} \quad (5.65)$$

where D is the diffusion coefficient, v_{dep} is the deposition rate of adatoms and L is half the distance between steps. Since the denominator represents a diffusion length of the incoming atoms, it can be expected that if $\Lambda_d \gg 1$, atoms being deposited will diffuse around the surface easily, with the result that most of the deposit would grow at the step edges. On the other hand, if $\Lambda_d \ll 1$, the surface diffusion rate is small in comparison to the deposition rate, so that atoms will tend to stay near the site of deposition. The results of the simulation reflected this interpretation, as can be observed for example in Fig. 5.43, which was obtained from simulations for homoepitaxial growth. There, we can see the transition from regions of instantaneous nucleation ($\Lambda_d > 1$) to progressive nucleation ($\Lambda_d < 1$). In fact, in the first case we see little formation of clusters at large values of Λ_d , since the simulations show very little formation of clusters other than the growth at the step edges. In the

Fig. 5.43 Cluster density plotted as a function of Λ_d and time. Time is represented by the amount of deposit on the surface (Reprinted with permission from Ref. [91])



second case, for small values of Λ_d , the cluster density shows an approximately linear relationship with respect to time, consistent with progressive nucleation.

Figure 5.44 shows snapshots of these simulations, for different Λ_d , as well as for different jump frequencies with different heights of the diffusion energy barriers. There, it can be observed the transition from island formation to border decoration upon Λ_d increase. On the other hand, the far left column of this figure shows results obtained with a low jump frequency and low surface diffusion energy barriers that may be contrasted with the results shown on the far right column, which shows results obtained with a high jump frequency and high energy barriers. It is apparent that in the former case large, faceted clusters are formed, while in the latter much less smooth and smaller clusters result.

Although the results we have shown above in Figs. 5.43 and 5.44 were for a homoepitaxial system, it was found that heteroepitaxial growth follows the same principles that govern the cluster density, step edge growth, and other deposit characteristics.

New advances in related KMC simulations, have been undertaken recently. As mentioned above, Treeratanaphitak et al. [86, 87] have extended the EAM-KMC methodology to include atom exchange and other phenomena. Another interesting improvement of KMC is the introduction of the first passage time algorithm [92] to replace the computationally demanding simulation of diffusion hops in KMC by larger jumps when particles are far away from step-edges or other particle. This innovation has allowed to analyze different categories of deposition systems: homoepitaxy, heteroepitaxy, multi-layer, step edge, and confined regions [93].

5.4.4.4 Kinetic Monte Carlo Analysis of Cu Underpotential Deposition on Au(111)

Similarly to the discussion done in Sect. 5.4.3.2 of this chapter, we discuss separately the work of Brown et al. [94] on the application of KMC techniques to complex upd systems. As we have seen in Sect. 5.4.3.2, an effective lattice-gas Hamiltonian was developed for the Au(111)/Cu system in the presence of sulfate anions. As pointed out above in Sect. 5.4.4.1 a dynamic hierarchy, involving the calculation of different transitions rates, is necessary for the implementation of the KMC procedure. It is illustrative to see how Eq. (5.48) can be used, along with some considerations, to construct such a hierarchy. At first, it is relevant to consider which processes are to be taken into account. In the present model these processes were, for both species, Cu and sulfate: (a) adsorption, (b) desorption, (c) one-step lateral diffusion. To proceed to assignation of rates, since these are related to processes involving single particles, it is more useful to consider the free energy associated with a single adsorbed particle of species X ($X = S$ (Sulfate) or C (Copper)) occupying site i for a specific configuration of neighbors and to formulate the lattice-gas Hamiltonian:

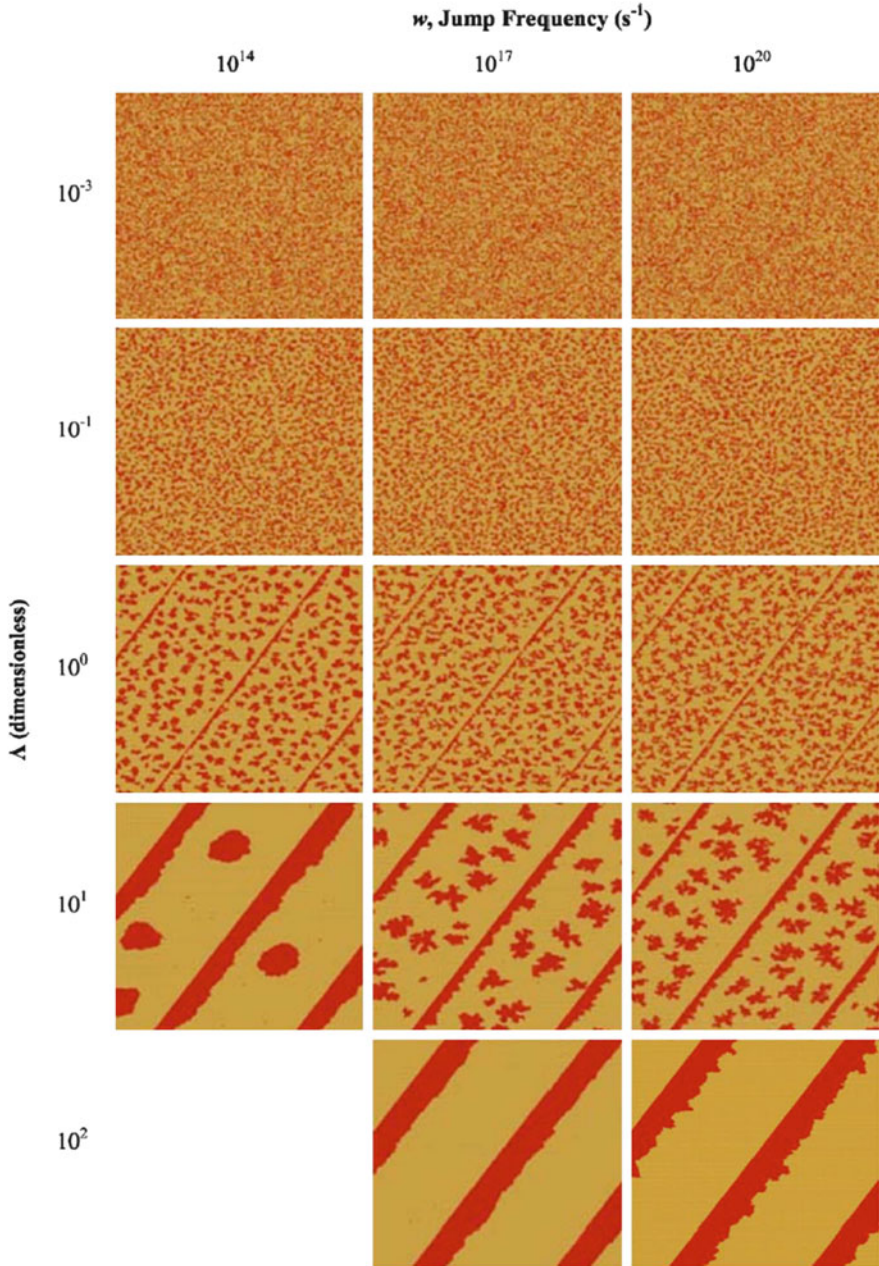


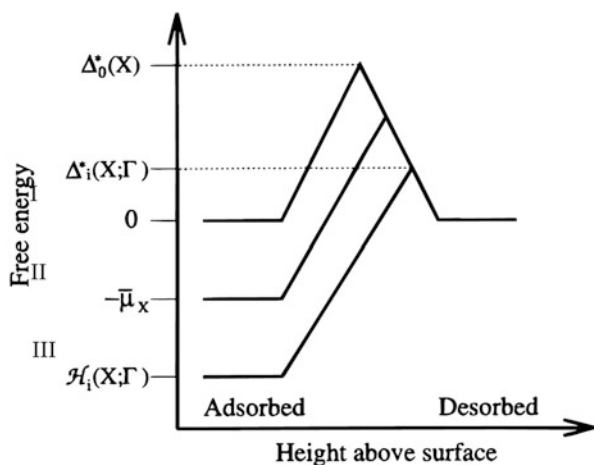
Fig. 5.44 Snapshots of simulation outputs after deposition of one-quarter equivalent monolayers of KMC simulated deposition, for several of the simulated parameter regimes. From *top to bottom*, the snapshots correspond to increasing Λ_d values. From *left to right*, correspond to increasing jump frequencies and surface diffusion energy barriers (Reprinted with permission from Ref. [91])

$$\hat{H}_i(X, \Gamma) = -\tilde{\mu}_X - \sum_n \left[\Phi_{XS}^{(n)} \sum_{j(i)}^{(n)} c_j^S + \Phi_{XC}^{(n)} \sum_{j(i)}^{(n)} c_j^C - \delta_{X,S} \Phi_{SS}^{(t)} \sum_{\Delta(i)}^{(n)} c_j^S c_k^S \right] \quad (5.66)$$

where the symbols have the same meaning as in Sect. 5.4.3.2. The sum $\sum_{j(i)}^{(n)}$ runs over all adsorption sites j that are that are n th neighbors of site X , the sum $\sum_{\Delta(i)}^{(n)}$ runs over all second-neighbor equilateral triangles involving site i , the factor $\delta_{X,S}$ is unity when $X=S$ and zero otherwise, and the index Γ runs over all possible arrangements of neighboring adsorbate particles within the maximum interaction range from site i . The index X may also take the value 0 (unoccupied site), in which case $\hat{H}_i(0, \Gamma) = 0$, regardless of the arrangement of the neighbors.

Let us now consider the desorption-adsorption process in terms of the hamiltonian (Eq. 5.66). With this purpose, we appeal to a representation of the free energy profile of the reaction in terms of the Butler-Volmer approximation [95], as depicted in Fig. 5.45. To analyze the adsorption of a particle, we move from right to left of the figure. Three different situations are considered for the ad-state. The most simple initial case, labeled with I, is an adsorbed particle without neighbors, in a condition where $\tilde{\mu}_X = 0$. Under this condition $\hat{H}_i(X, \Gamma) = 0$, the free energy profile is completely symmetric, with a free energy barrier of magnitude $\Delta_0^*(X)$. The next initial ad-case is labeled with II in the figure, and corresponds to an initial adsorbed particle without neighbors, but in the presence of an electrochemical potential $\tilde{\mu}_I \neq 0$. In this case $\hat{H}_i(X, \Gamma) = -\tilde{\mu}_I$. The most general case is that denoted with III, where the single-particle Hamiltonian is $\hat{H}_i(X, \Gamma)$. In this case, the free-energy barrier for adsorption is changed to:

Fig. 5.45 Butler-Volmer-type free-energy barrier scheme for considering adsorption/desorption of particles. Three different cases are analyzed, as discussed in the text (Reprinted with permission of Ref. [94])



$$\Delta_i^*(\mathbf{X}, \Gamma) = \Delta_0^*(\mathbf{X}) + \alpha \hat{H}_i(\mathbf{X}, \Gamma) \quad (5.67)$$

where α is the so-called symmetry factor, usually assumed to be close to 1/2. Thus, if the effective interactions of the ad-state are negative, the free energy activation barrier will be lowered by the amount given by the second term on the rhs of Eq. (5.67). Through this equation, we have solved a kinetic problem by using a thermodynamic expression, given by Eq. (5.66). A free parameter $\Delta_0^*(\mathbf{X})$, which depends on the species being adsorbed, has emerged from the ansatz (Eq. 5.67).

To get the activation energies for surface diffusion between neighboring sites i and j , the ansatz proposed was:

$$\tilde{\Delta}_{ij}^*(\mathbf{X}, \Gamma) = \tilde{\Delta}_0^*(\mathbf{X}) + \frac{1}{2} \max[\hat{H}_i(\mathbf{X}, \Gamma), \hat{H}_j(\mathbf{X}, \Gamma)] \quad (5.68)$$

where the $\max[x, y]$ is a function that selects the maximum value between x and y and $\tilde{\Delta}_0^*(\mathbf{X})$ is a new parameter to be chosen.

The parameters introduced in Eq. (5.66) to calculate $\hat{H}_i(\mathbf{X}, \Gamma)$ were not those presented in Sect. 5.4.3.2 but an improved version of them, which were also reported in Ref. [94]. The phase diagram obtained with this improved set of parameters is shown in Fig. 5.46, along with a cyclic voltammogram for Cu upd onto Au(111) surface.

Rather than on voltammograms, the KMC simulations were focused on potentiostatic transients, motivated by experimental results that were discussed in Chap. 2 [96–98]. Hölzle et al. [97] measured current transients in potential-step

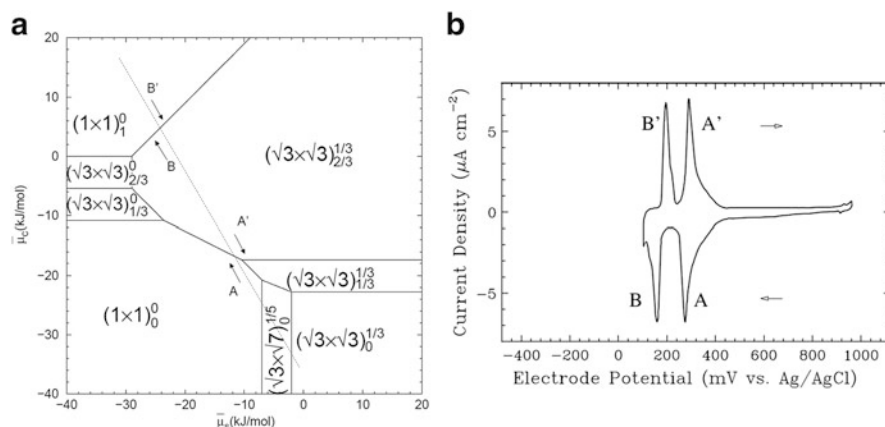


Fig. 5.46 (a) Improved ground-state phase diagram for the system Cu/Au(111) in the presence of sulfate anions, as presented in Ref. [94]. The structure of the different phases can be found in Fig. 5.35 of Sect. 5.3.2. The dotted line represents the isotherm used to simulate the potential-step experiments. It was chosen to match the transition potentials observed in experiments. (b) Cyclic voltammogram for Cu upd onto Au(111) surface, taken from Ref. [71]. Note the correlation between the peaks in the voltammograms (A/A' and B/B') in figure (b), with the crossings in the phase boundaries marked with arrows in figure (a) (Reprinted with permission from Refs. [94] and [71])

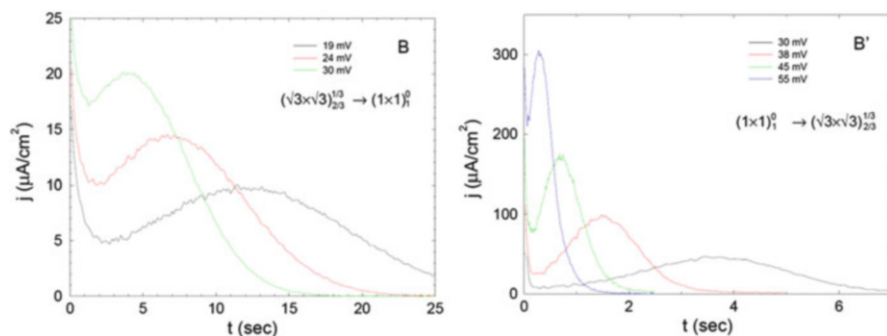


Fig. 5.47 KMC simulation of potential steps across the transition between the $(1 \times 1)_1^0$ and $(\sqrt{3} \times \sqrt{3})_{2/3}^{1/3}$ phases. *Left*: Potential step in the positive direction, as illustrated by the *arrow B'* in Fig. 5.46a. *Right*: Potential step in the negative direction, as illustrated by the *arrow B* in Fig. 5.46b (Reprinted with permission from Ref. [94])

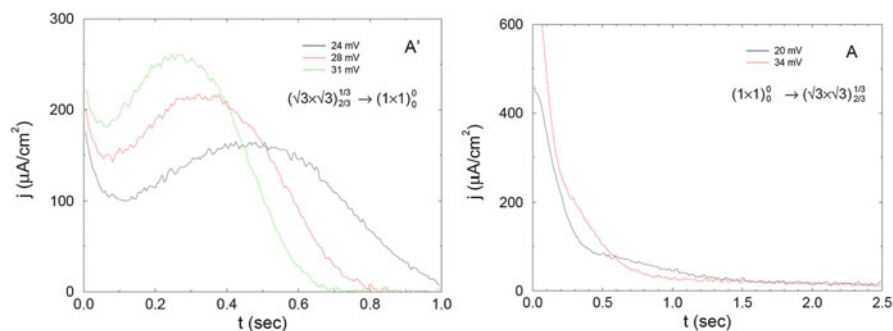


Fig. 5.48 KMC simulation of potential steps across the transition between the $(\sqrt{3} \times \sqrt{3})_{2/3}^{1/3}$ and $(1 \times 1)_0^0$ phases. *Left*: Potential step in the positive direction, as illustrated by *arrow A'* in Fig. 5.46a. *Right*: Potential step in the negative direction, as illustrated by *arrow A* in Fig. 5.46b (Reprinted with permission from Ref. [94])

experiments performed at both transitions marked with A/A' and B/B' in Fig. 5.46a, with both positive-going and negative-going steps. Figures 5.47 and 5.48 show simulated potential steps for the B/B' and A/A' transitions respectively. In the first case, it must be remarked that both transients reflect nucleation and growth mechanisms. As observed in the experimental data, the broad maximum becomes stronger and it shifts to shorter times as the size of the step is increased. In the second case, Fig. 5.48, it is remarkable that the transients are very different for positive and negative potential steps. While the positive step present current transients that are non-monotonic (*left*), the negative steps lead to monotonically decreasing transients, which do not present to a simple functional form. Snapshots of a simulation of this type of negative step shows that equilibration after the step occurs in a disordered phase with a relatively high sulfate coverage (see Fig. 5.49).



Fig. 5.49 Series of snapshots after a negative-going potential step to 20 mV below the transition between the low coverage and mixed layers, see *arrow A* in Fig. 5.46a. Note the high concentration of sulfate species at 0 s, the predominance of phase $(\sqrt{3} \times \sqrt{3})_{1/3}^{1/3}$ at 0.25 s and the predominance of the $(\sqrt{3} \times \sqrt{3})_{2/3}^{1/3}$ at 1 s. The *circles* were drawn to focus on some compact, representative domains (Reprinted with permission from Ref. [94])

The sulfate present collapses first with incoming copper atoms to form a domain of the phase $(\sqrt{3} \times \sqrt{3})_{1/3}^{1/3}$, metastable at the potential where the step was made (see Fig. 5.46a). This phase is filled later with Cu to yield finally the stable $(\sqrt{3} \times \sqrt{3})_{2/3}^{1/3}$ phase (see Fig. 5.49).

The authors pointed out that the fact that different dynamic paths can give current profiles qualitatively similar to those observed experimentally indicates that more study of the copper upd system is desirable. However, it must be recognized that these studies represented an important step forward in the understanding of this puzzling system.

5.5 Miscellaneous Models Applied to Underpotential Deposition

We devote this section to different models that have been applied to model upd, but which have not yet evolved to develop a wide branch of theoretical work.

5.5.1 Quantum Mechanical Semiempirical Calculations

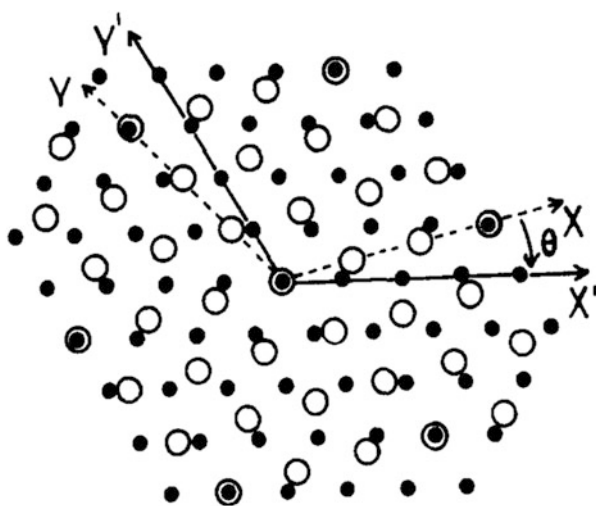
Before the availability of DFT programs, much quantum mechanical work was based on semiempirical approximations. This was for example the case of the semiempirical atom superposition and electron delocalization molecular orbital (ASED-MO) technique [99, 100]. This method became very popular at the end of the 1980s and the beginning of the 1990s, and found a number of applications to upd. Mehandru and Anderson [101] used this method to consider the behavior of quarter of a monolayer and a half-monolayer of Pb atoms adsorbed on Au(100) in relationship to the binding and orientation of the oxygen molecule on these surfaces.

Lopez et al. calculated the stability of different Ni upd structures as a function of surface coverage and electric potential applied to the Pt(111) surface [102], and they also investigated the influence of different surface structures on coadsorbed water decomposition [103]. In the first case, the information obtained was related to the most favorable binding site and the growth mechanism of the metal deposit, which was accompanied by a molecular orbital analysis. Lopez et al. used the same methodology to consider the possible structures of copper electrodeposits on Pt (100) and Pt(111) clusters under different applied electric potentials [104].

5.5.2 Orientational Ordering of Adsorbed Monolayers

We have seen in Chaps. 2 and 3 that Tl and Pb monolayers adsorbed on Ag(111) surfaces form incommensurate, hexagonal monolayers that are compressed compared to the bulk metals by 0.1–3.2 % and rotated from the substrate [011] direction in several degrees. A similar observation has been made for Tl and Pb adsorbed on Au(111). To study these systems, Mola and Blum [105] and Mola *et al.* [106, 107] have set up a model for the adsorption energy of a hexagonal close packed monolayer deposited on a substrate surface of the same structure but different lattice constant as a function of the epitaxy angle between the principal axis. The underpotentially deposited Pb on the (111) surface of silver was the subject of these studies, but the model could easily be extended to other similar cases of different geometry. Figure 5.50 shows the geometrical arrangement that these authors employed to represent this system. The substrate S was considered to be described as a hexagonal lattice with lattice constant a , set equal to 1 for convenience, while the adsorbate defined a superimposed hexagonal arrangement of

Fig. 5.50 Portion of a geometric arrangement as that used by Mola and Blum [105] to study the upd deposition of Pb on Ag (111). *Filled circles*: points of the substrate lattice. *Open circles*: points of the adsorbate lattice (Reprinted with permission from Ref. [105])



lattice constant b . Coordinate systems (x,y) and (x',y') were defined for A and S, respectively so that the vectors (m,n) and (r,s) with integer components define the positions of the point lattices A and S. Assuming a common origin for both coordinates, the angle θ defines the epitaxy angle.

The representation of a lattice point $\mathbf{X} = (m, n)$ of the adsorbate lattice on the substrate system, say $\mathbf{X}' = (x', y')$ is given by:

$$\mathbf{X}' = b\mathbf{M}(\theta)\mathbf{X} \quad (5.69)$$

where the matrix relating the components in the two systems, which are shown in Fig. 5.50, has a simple form:

$$\mathbf{M}(\theta) = \frac{2}{\sqrt{3}} \begin{bmatrix} \sin(\pi/3 + \theta) & \sin(\theta) \\ \sin(\theta) & \sin(\pi/3 - \theta) \end{bmatrix} \quad (5.70)$$

The points at which the two lattices in Fig. 5.50 overlap define a coincidence lattice. These points, that we label within the adsorbate lattice with $\mathbf{R}_c = (x_c, y_c)$, fulfill the relationship:

$$d(x_c, y_c) = (x_c^2 + y_c^2 - x_c y_c)^{1/2} = hb \quad (5.71)$$

where $d(x_c, y_c)$ is the distance of the point \mathbf{R}_c to the center of the coordinates and h is an integer number. Using Eqs. (5.69), (5.70) and (5.71) we get:

$$\begin{bmatrix} x_c \\ y_c \end{bmatrix} = b \frac{2}{\sqrt{3}} \begin{bmatrix} \sin(\pi/3 + \theta) & \sin(\theta) \\ \sin(\theta) & \sin(\pi/3 - \theta) \end{bmatrix} \begin{bmatrix} h \\ 0 \end{bmatrix} \quad (5.72)$$

which leads to the angle:

$$\theta = \sin^{-1} \left[\frac{2x_c - y_c}{2(x_c^2 - y_c^2 + x_c y_c)^{1/2}} \right] \quad (5.73)$$

Considering the approximate experimental value of $b = 1.2010$, Mola and Blum [105] calculated the values of h , x_c and y_c compatible with it, as well as the corresponding θ , finding the best agreement with experiment for $h=28$, $b=1.2000$ and $\theta = \pm 4.43^\circ$.

Extensions of this model were developed by Mola et al. [106, 107], expanding the potential energy per surface atoms in a Fourier series:

$$V(\mathbf{R}) = \sum_{\mathbf{G}} V_{\mathbf{G}} \exp(i\mathbf{G} \cdot \mathbf{R}) \quad (5.74)$$

where \mathbf{G} denotes 2-dimensional reciprocal lattice vectors and \mathbf{R} indicates the position of an adatom.

The binding energy per adatom was evaluated considering up to three or four harmonics in Eq. (5.74), finding a good agreement between the calculated θ values and the experimental ones.

5.5.3 Entropic Contribution to Underpotential Deposition Shift: Lattice Dynamics Analysis

Entropic contributions to underpotential shift (see definition in Chap. 1) have been seldom considered in the literature [108]. Pioneering work in the modeling of entropic contributions to underpotential shift was undertaken by Oviedo et al. [109] by means of lattice dynamics. In this approach, the Hamiltonian of the system, which takes into account potential and kinetic contributions to the energy of the system in normal coordinates ξ and momentum $\dot{\xi}$ is written as:

$$\hat{H}(\xi, \dot{\xi}) = U(0) + \frac{1}{2} \sum_i f_i \xi_i^2 + \frac{1}{2} \sum_i M_i \dot{\xi}_i^2 \quad (5.75)$$

where $U(0)$ is the energy of the system when all atoms are in their equilibrium positions, f_i denotes an effective force constant and M_i represents the effective mass of particle i . The energy of the system was calculated using the EAM, as discussed in Sect. 5.4.4.2, and the quasi-harmonic lattice dynamic method (EAMLD) developed by Barrera and co-workers [110]. Within this approximation, it is assumed that the Helmholtz energy of a crystal at a temperature T can be written as the sum of static and vibrational contributions:

$$F = U_{\text{stat}} + F_{\text{vib}}(T) \quad (5.76)$$

where U_{stat} is the potential energy of the static lattice in a given configuration and F_{vib} is the sum of the harmonic vibrational contributions from all normal modes. For a periodic structure, the vibrational frequencies $\nu_j(\mathbf{q})$ (\mathbf{q} being a wave vector defined in the reciprocal lattice of the system) are obtained by diagonalization of the dynamic matrix, so that F_{vib} is given by:

$$F_{\text{vib}} = \sum_{j=1}^{3N} \sum_{\mathbf{q}} \left[\frac{1}{2} h \nu_j(\mathbf{q}) + k_B T \ln \left(1 - \exp \left(- \frac{h \nu_j(\mathbf{q})}{k_B T} \right) \right) \right] \quad (5.77)$$

where the first term is the zero-point energy at $T = 0$ K. For a macroscopic crystal, the sum over \mathbf{q} becomes an integral over a cell in reciprocal space, which can be evaluated by taking successively finer uniform grids until convergence is achieved. The normal mode frequencies $\nu_j(\mathbf{q})$ depend on the interactions among the atoms in the solid, as described by the EAM.

The vibrational contribution to the entropy is in turn given by:

$$S_{\text{vib}} = k_B \sum_{j=1}^{3N} \sum_q \left[-\ln \left(1 - \exp \left(-\frac{h\nu_j(\mathbf{q})}{k_B T} \right) \right) + \frac{h\nu_j(\mathbf{q})/k_B T}{\left[\exp \left(-\frac{h\nu_j(\mathbf{q})}{k_B T} \right) - 1 \right]} \right] \quad (5.78)$$

The specific heat at constant volume may be obtained from the previous equation considering the thermodynamic relationship $(\partial S/\partial T)_V = C_V/T$. Figure 5.51 shows the supercells used to perform the lattice dynamics analysis for several systems, including the (111), (100) and (110) faces of different substrate/adsorbate combinations containing Ag, Au, Pt, Pd and Cu. A 1×1 commensurate structure was assumed for all systems.

Figure 5.52 shows the entropic contribution to underpotential shifts for the systems analyzed, as function of the crystallographic misfit. The misfit was defined as in Eq. (5.47), but without the factor 100, so that the systems included in this figure are in the range $12\% < \varepsilon_{\text{mf}} < 14\%$. The first relevant information concerns the magnitude of the entropic contribution to upd shift, where it is found that this quantity is rarely larger than 20 meV, which translated into the electrochemical scale means changes at the most of the order of 20 mV. It can be observed that plots for all single crystal faces present a positive slope, so that negative and positive misfits roughly correspond to negative and positive entropic contributions, respectively. This has the following physical explanation: when an adsorbate is

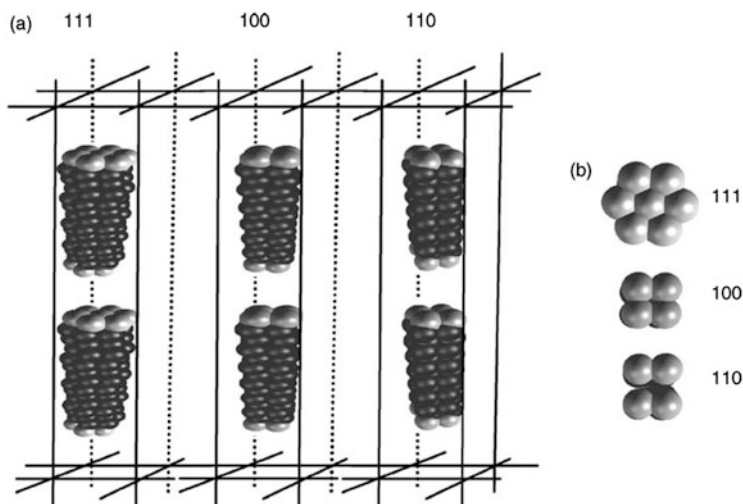


Fig. 5.51 Diagram of the supercells employed to represent the substrate (single crystal face) + adsorbate system for the lattice dynamic analysis described in the text. It consists of a 14-layer basis (12 inner substrate layers plus two external adsorbate ones). (a) Slabs and their images in the z-direction. (b) Top view of the surface. Periodic boundary condition in x-, y- and z-directions were applied (Reprinted with permission from Ref. [109])

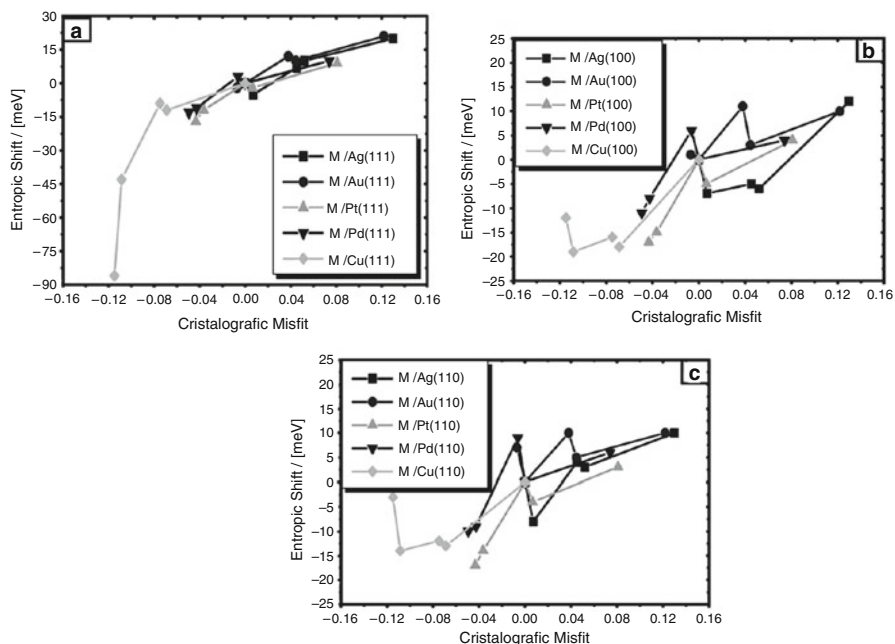


Fig. 5.52 Entropic contribution to the underpotential shift as a function of the crystallographic misfit. The adsorption of M (M = Ag, Au, Pt, Pd, Cu) is considered on different substrates. (a) (111), (b) (100) and (c) (110) corresponding to the three single crystal surfaces studied. The inset shows the symbols employed to represent the different adsorbates on a given substrate. On each line representing a substrate, the adsorbates were, from left to right: Ag, Au, Pt, Pd and Cu (Reprinted with permission from Ref. [109])

compressed to fit on a smaller substrate, its motion becomes more restricted delivering a negative contribution to upd shift. This general trend is modulated by specific chemical effects, but it seems to be valid in a first approximation. Experimental entropy shifts will very likely differ quantitatively from the values reported in Fig. 5.52, since the calculations assumed pseudomorphic structures, and real systems with a large misfit will relax this condition either by adopting incommensurate structures or via the occurrence of surface defects in the monolayer.

5.5.4 Application of Molecular Dynamics and Related Techniques to Underpotential Deposition

Molecular Dynamics (MD) is a computer simulation technique that allows generating trajectories in the phase space of a given system. This procedure is performed by numerically solving the classical equations of motion (Eq. 5.6) and (Eq. 5.7), presented in the introduction of this chapter and can be summarized as:

$$m_i \frac{d^2 \mathbf{R}_i}{dt^2} = \mathbf{f}_i \quad \text{with} \quad \mathbf{f}_i = -\nabla_i U(\{\mathbf{R}\}) \quad (5.79)$$

In the quantum mechanical approach we took in the introduction of this chapter the set $\{\mathbf{R}_i\}$ represented the position of nuclei or core ions, which were in principle treated separately from electrons. In a more approximate description often used, the $\{\mathbf{R}_i\}$ represent the position of the atoms, viewed as a whole. Each atom is not viewed as composed of a nucleus and electrons, but considered as a whole entity, which interacts with other atoms via an effective potential. This is, for example, the case of the Lennard-Jones interaction potential, where the interaction between particles 1 and 2 is given by:

$$v_{12}^{\text{LJ}}(R_{12}) = 4\varepsilon_{\text{LJ}} \left[\left(\frac{\sigma_{\text{LJ}}}{R_{12}} \right)^{12} - \left(\frac{\sigma_{\text{LJ}}}{R_{12}} \right)^6 \right] \quad (5.80)$$

where ε_{LJ} is the depth of the potential well, σ_{LJ} is the finite distance at which the inter-particle potential is zero and $R_{12} = |\mathbf{R}_2 - \mathbf{R}_1|$. The potential energy for such a system can be written as $U(\mathbf{R}) = \frac{1}{2} \sum_{i \neq j} v_{ij}^{\text{LJ}}(R_{ij})$. In order to continue the discussion

of the method, we introduce the atomic momenta $\mathbf{p} = (\mathbf{p}_1, \mathbf{p}_2, \mathbf{p}_3, \dots, \mathbf{p}_N)$. Thus, the kinetic energy of the system (K) can be written as:

$$K(\mathbf{p}) = \sum_{i=1}^N \frac{|\mathbf{p}_i|^2}{2m_i} \quad (5.81)$$

The total energy may then be written as a sum of kinetic and potential terms $H = K + U$. The time integration algorithm most commonly used in molecular dynamics is probably the so-called Verlet algorithm. The general idea behind this algorithm is to write third-order Taylor expansions for the positions $\mathbf{r}_i(t \pm \Delta t)$, in different time directions. If we consider that, for particle i , \mathbf{v}_i is the velocity, \mathbf{a}_i is the acceleration, and \mathbf{b}_i is the third derivative of \mathbf{r}_i with respect to t , we can write:

$$\mathbf{R}_i(t + \Delta t) = \mathbf{R}_i(t) + \mathbf{v}_i(t)\Delta t + \frac{1}{2}\mathbf{a}_i(t)\Delta t^2 + \frac{1}{6}\mathbf{b}_i(t)\Delta t^3 + O(\Delta t^4) \quad (5.82)$$

$$\mathbf{R}_i(t - \Delta t) = \mathbf{R}_i(t) - \mathbf{v}_i(t)\Delta t + \frac{1}{2}\mathbf{a}_i(t)\Delta t^2 - \frac{1}{6}\mathbf{b}_i(t)\Delta t^3 + O(\Delta t^4) \quad (5.83)$$

By adding the two expressions, we obtain:

$$\mathbf{R}_i(t + \Delta t) = 2\mathbf{R}_i(t) - \mathbf{R}_i(t - \Delta t) + \mathbf{a}_i(t)\Delta t^2 + O(\Delta t^4) \quad (5.84)$$

Since we are dealing with Newton's equations of motion, $\mathbf{a}_i(t)$ is just the force divided by the mass, and the force is, in turn, a function of the complete set of atomic coordinates $\{\mathbf{R}_i\}$, as established in Eq. (5.79).

Molecular or atom dynamics simulation as discussed above is a deterministic technique that allows the prediction of the “real” trajectories of motion at real time. However, to capture many relaxation processes, the integration time step must be very small, of the order of 10^{-15} s, and therefore the period of time explored cannot usually overcome the nanoseconds, something that makes the technique not suited for many physical problems involved in crystallization. Furthermore, in some cases not all the degrees of freedom considered are relevant for the process under study. Taking metal deposition as an example, in some cases the simulator may be interested in the structure of the deposit being formed. While the coordinates of the discharged metal atoms are relevant for this purpose, not so the coordinates of the solvent molecules, since they rather participate as thermal bath where the depositing ions are immersed. One of the options to solve this situation was discussed in Sect. 5.4.4. Another, intermediate possibility is Langevin dynamics (LD), which was developed to follow the trajectories of ions or neutral atoms in a fluid at relatively low computational cost. The algorithm for LD is closely related to MD and is conceptually simple: the motion of the i -th atom with mass m_i is governed by Langevin equation:

$$m_i \frac{d^2 \mathbf{R}_i}{dt^2} = \mathbf{f}_i - \gamma_i \frac{d \mathbf{R}_i}{dt} + \mathbf{f}_{\text{rand}}^i \quad (5.85)$$

where the terms on the rhs of Eq. (5.85) denote: \mathbf{f}_i is the force as calculated in ordinary MD, the second term corresponds to an average frictional force with a macroscopic friction coefficient given by γ_i , and $\mathbf{f}_{\text{rand}}^i$ is a random Gaussian force obeying the fluctuation-dissipation theorem [111]. Ermak’s algorithm [112] provides a way to treat properly both the systematic dynamic and the stochastic elements of Langevin equation.

Schmickler et al. [113, 114] have developed a simulation method combining MD and LD to study systems of interest in upd. A scheme of this simulation method is shown in Fig. 5.53. The simulation system consists of three principal parts. The bottom part, labelled A, contains several layers of metal atoms arranged in an *fcc* lattice (or similar) containing 400 atoms per layer; the three bottom layers are kept fixed, the others are mobile and obey ordinary deterministic MD. The interaction between these metal atoms is calculated from the EAM [78]. In the electrolyte solution, only the metal ions are modeled explicitly as particles contained in the regions B and C. Their motion is described using LD. In region C, the concentration of the particles is kept constant by adding or removing particles, as required. In contrast, region B contains a variable number of particles and can thus represent a depletion layer for metal deposition. The particles in the solution do not interact with each other, but experience a constant background. Switching between LD and MD occurs at the interface B and A, allowing atom adsorption/desorption at rates that depend on the background chemical potential μ_0 .

Schmickler et al. [113] used the present methodology to study Ag upd on Au (111) surfaces and Pt upd on Au(111) surfaces. In a subsequent work, Mariscal et al. [114] used this methodology to analyze the decoration of Au islands on

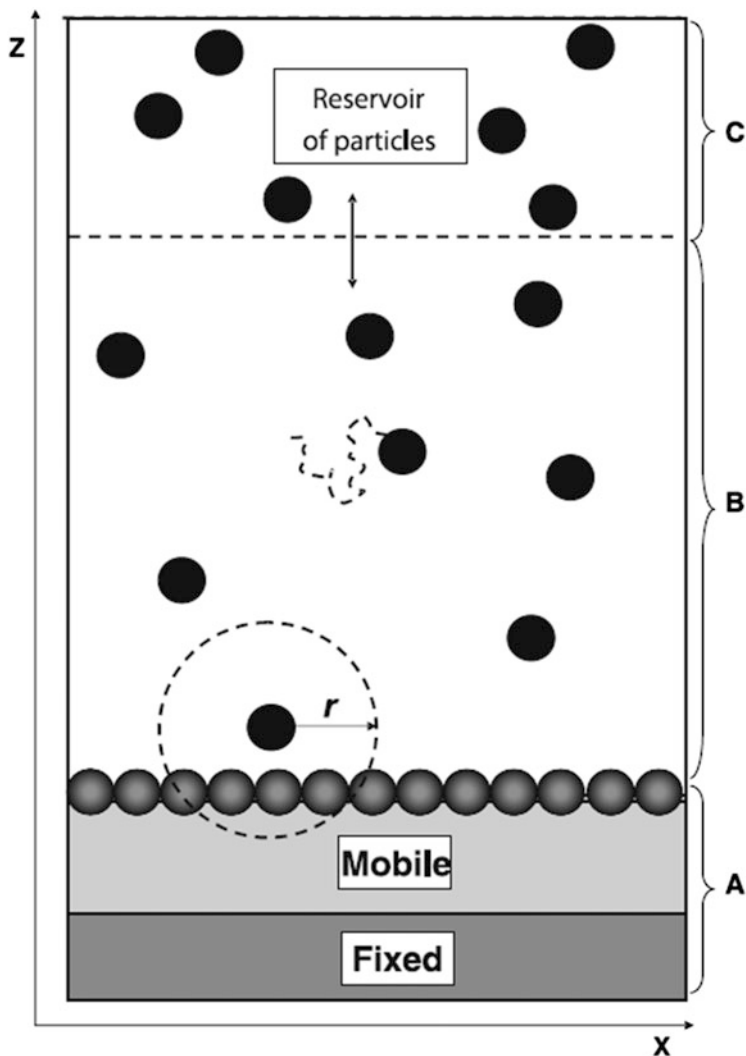


Fig. 5.53 Scheme of the simulation method developed in Ref. [113] to study the deposition of metal atoms on a foreign surface, as described in the text (Reprinted with permission from Ref. [113])

Au(111) surface by Ag atoms, and the deposition of Ni on Au(111) and Pt(111) surfaces. Snapshots of a simulation of the former system are shown in Fig. 5.54

Very recently, MD simulations have also been used along with the two-phase thermodynamic (2PT) method to study the entropic contribution to monolayer up formation [115]. We explain briefly the idea behind this application. In the canonical thermodynamic ensemble, all thermodynamic functions can be calculated from

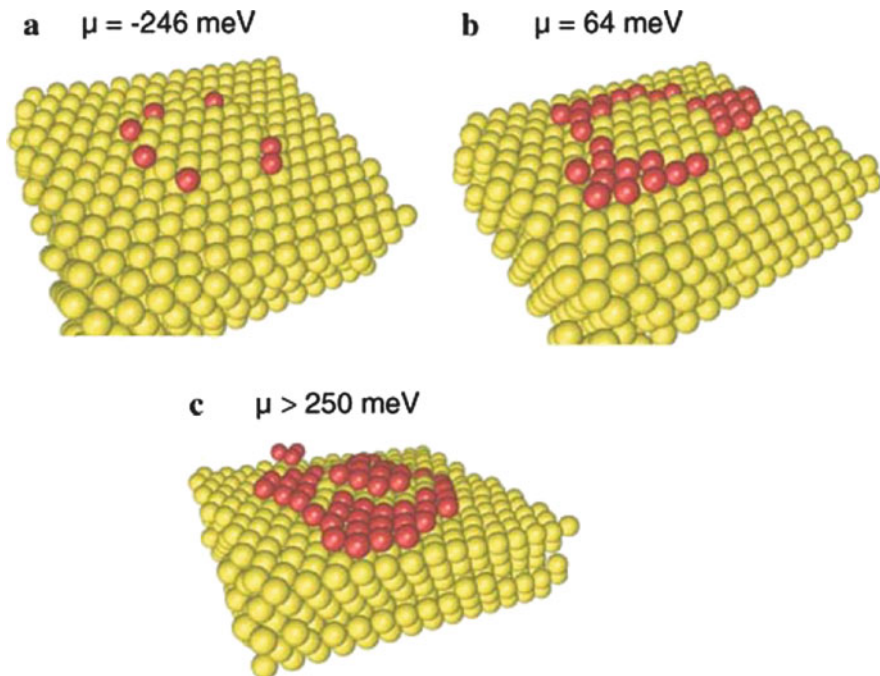


Fig. 5.54 Snapshots of a MD-LD simulation of Ag decoration of a Au island on a Au(111) surface (Reprinted with permission from Ref. [114])

the partition function Q . In the case of entropy, the relationship between entropy and the partition function is given by:

$$S = k_B T \frac{\partial \ln Q}{\partial T} + k_B \ln Q \quad (5.86)$$

The thermodynamic properties of pure metals are in many cases calculated on the basis of a harmonic oscillator model using statistical mechanics [116]. Within the harmonic approximation, the partition function can be obtained from the vibrational density of states $\text{DOS}(\nu)$ of the system according to:

$$\ln Q = \int_0^\infty \text{DOS}(\nu) W(\nu) d\nu \quad (5.87)$$

where ν is the frequency of normal modes and $W(\nu)$ corresponds to a weighting function given by $W(\nu) = -h\nu/2k_B T - \ln[1 - \exp(-h\nu/2k_B T)]$. The density of states (DOS) may be calculated from the Fourier transform of the velocity auto-correlation function [117]. The harmonic approximation may be a reasonable approach for bimetallic systems with negligible mobility and misfit [109]. However, in bimetallic up systems like Pb/Au, characterized by a high adatom diffusivity

and misfit, this approach may no longer be valid because of the significant anharmonic nature of the frequency modes. Furthermore, in very small bidimensional clusters the translational contribution may become important. This is the reason for the development of a more sophisticated approach including translational contributions, like the 2PT model. Within this model, the thermodynamic properties are determined from the sum of static, translational, and vibrational contributions. In the case of entropy:

$$S = S^{\text{tras}} + S^{\text{vibra}} \quad (5.88)$$

This is possible by dividing the DOS distribution into solid-like and gas-like components:

$$\text{DOS}(\nu) = \text{DOS}^{\text{solid}}(\nu) + \text{DOS}^{\text{gas}}(\nu) \quad (5.89)$$

The gas component is determined based on the DOS at zero frequency and ensures that all of the diffusive modes are included in this component. Once the gas-like component is determined, the solid-like component can be obtained from the difference between the total DOS and the gas-like DOS. So, the 2PT method allows the computation of anharmonic effects explicitly. The studies of Ref. [115] demonstrated that very small Pb clusters on Au(111) surfaces show an entropic contribution to their stability. This is expected from the observation of their DOS, as shown in Fig. 5.55, where the increasing translational contribution for smaller clusters is marked with *arrows* in the figure.

The entropic contribution of small clusters to underpotential shift, calculated using the 2PT method is shown in Table 5.13, together with the energetic and free energy contributions. It can be observed that the largest contribution to the upd shift stems from the vibrational part, being the translational practically negligible, even for the smallest clusters.

Fig. 5.55 Density of states corresponding to Pb clusters of different sizes on a Au (111) surface at 300 K as is indicated in the legend. The curves have been normalized by dividing by the number of Pb atoms (Reprinted with permission from Ref. [115])

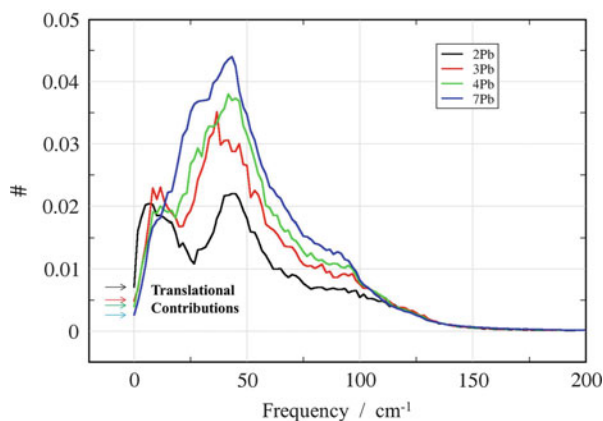


Table 5.13 Entropic, energetic and free energy contributions to the underpotential shift for bidimensional Pb clusters of different sizes. The entropic contributions are divided into translational ($TS_{\text{Pb}}^{\text{tras}}$) and vibrational ($TS_{\text{Pb}}^{\text{vib}}$) ones. $T\Delta S^{\text{upd}}$ and ΔU^{upd} correspond to entropy and potential energy differences referred to the Pb atoms in the bulk state. All values are in eV per atom. Taken with permission from Ref. [115]

Cluster (2d)	$TS_{\text{Pb}}^{\text{tras}}$	$TS_{\text{Pb}}^{\text{vib}}$	$-T\Delta S^{\text{upd}}$	ΔU^{upd}	ΔA^{upd}
2-Pb	0.0203	0.089	0.076	0.084	0.160
3-Pb	0.0154	0.123	0.047	0.037	0.084
4-Pb	0.0145	0.139	0.032	-0.016	0.016
5-Pb	0.0151	0.149	0.021	-0.031	-0.010
6-Pb	0.0203	0.152	0.013	-0.013	0.00
7-Pb	0.0111	0.162	0.012	-0.055	-0.043

References

- Oviedo OA, Negre CFA, Mariscal MM, Sánchez CG, Leiva EPM (2012) *Electrochem Commun* 16:1
- Sánchez CG, Leiva EPM, Kohanoff J (2001) *Langmuir* 17:2219
- Hill TL (1960) *An introduction of statistical mechanics*. Addison-Wesley Publishing Company Inc, Reading
- Schmickler W (1979) *J Electroanal Chem* 100:533
- Kornyshev A, Schmickler W (1985) *J Electroanal Chem* 185:253
- Muscat JP, Newns DM (1978) *Prog Surf Sci* 9:1
- Gadzuk JP (1975) *Surface physics of materials*, vol 2. Academic, New York
- Schmickler W, Henderson D (1986) *Prog Surf Sci* 22:4
- Schmickler W (1985) *Chem Phys Lett* 115:216
- Kornyshev A, Schmickler W (1986) *J Electroanal Chem* 202:1
- Newmark AR, Schmickler W (1992) *J Electroanal Chem* 329:159
- Schmickler W (1995) *Chem Phys Lett* 237:152
- Schmickler W (1996) *Electrochim Acta* 41:2329
- Santos E, Quaino P, Schmickler W (2012) *Phys Chem Chem Phys* 14:11224
- Leiva EPM, Schmickler W (1989) *Chem Phys Lett* 160:75
- Schmickler W (1990) *Chem Phys* 141:95
- Lehnert W, Schmickler W (1991) *J Electroanal Chem* 310:27
- Lang ND, Kohn W (1970) *Phys Rev B* 1:4555
- Ashcroft NW (1966) *Phys Lett* 23:38
- Leiva EPM, Schmickler W (1994) *Electrochim Acta* 39:1015
- Leiva EPM (1995) *Surf Sci* 335:83
- Leiva EPM, Schmickler W (1995) *Electrochim Acta* 40:37
- Kramar T, Podlucky R, Neckel A, Erschbaumer H, Freeman AJ (1991) *Surf Sci* 247:58
- Sánchez CG, Leiva EPM (1998) *J Electroanal Chem* 458:183
- Sánchez CG, Leiva EPM (1999) *Electrochim Acta* 45:691
- Dietterle M, Will T, Kolb DM (1995) *Surf Sci* 342:2937
- Ogaki K, Itaya K (1995) *Electrochim Acta* 40:1249
- Kolb DM (1994) *Ber Bunsenges Phys Chem* 98:1421
- Greeley J (2010) *Electrochim Acta* 55:5545
- Hammer B, Hansen LB, Nørskov JK (1999) *Phys Rev B* 59:7413
- Kittel C (2005) *Introduction to solid state physics*, 8th edn. Wiley, London
- Mrozek P, Sung Y-E, Wieckowski A (1995) *Surf Sci* 335:44

33. Sánchez CG, Dassie SA, Leiva EPM (2002) *Langmuir* 18:6628
34. Soler JM, Artacho E, Gale J, García J, Junquera J, Ordejón J, Sánchez-Portal D (2002) *J Phys Condens Matter* 14:2745
35. Esplandiu MJ, Schneeweiss MA, Kolb MA (1999) *Phys Chem Chem Phys* 1:4847
36. Feibelman P (2001) *Phys Rev B* 64:125403
37. Pasti I, Mentus S (2010) *J Alloys Compd* 497:38
38. Giannozzi P, Baroni S, Bonini N, Calandra M, Car R, Cavazzoni C, Ceresoli D, Chiarotti GL, Cococcioni M, Dabo I, Dal Corso A, Fabris S, Fratesi G, de Gironcoli S, Gebauer R, Gerstmann U, Gougoussis C, Kokalj A, Lazzeri M, Martin-Samos L, Marzari N, Mauri F, Mazzarello R, Paolini S, Pasquarello A, Paulatto L, Sbraccia C, Scandolo S, Sclauzero G, Seitsonen AP, Smogunov A, Umari P, Wentzcovitch RM (2009) *J Phys Condens Matter* 21:395502
39. Perdev JP, Burke K, Ernzerhof M (1996) *Phys Rev Lett* 77:3865
40. Danilov AI, Nazmutdinov RR, Zinkicheva TT, Molodkina EB, Rudnev AV, Polukarov YM, Feliu JM (2008) *Russ J Electrochem* 44:697
41. Blum L, Huckaby DA (1990) *J Chem Phys* 92:2646
42. Blum L, Huckaby DA (1991) *J Chem Phys* 94:6887
43. Blum L, Huckaby DA, Legault M (1996) *Electrochim Acta* 41:2207
44. Huckaby DA, Blum L (1991) *J Electroanal Chem* 315:255
45. Huckaby DA, Blum L (1993) *Proc Electrochem Soc* 93:232
46. Blum L, Huckaby DA (1994) *J Electroanal Chem* 375:69
47. Blum L, Legault M, Turq P (1994) *J Electroanal Chem* 379:35
48. Huckaby DA, Medved I (2002) *J Chem Phys* 117:2914
49. Huckaby DA, Medved I (2006) *Rom J Phys* 51:603
50. Medved I, Huckaby DA (2010) *Fluid Phase Equilib* 290:21
51. Borgs C, Kotecky R (1990) *J Stat Phys* 61:79
52. Borgs C, Kotecky R (1995) *J Stat Phys* 79:43
53. White JH, Abruña HD (1990) *J Phys Chem* 94:894
54. Metropolis N, Rosenbluth AW, Rosenbluth MN, Teller AH, Teller E (1953) *J Chem Phys* 21:1087
55. Norman GE, Filinov VS (1969) *High Temp* 7:216
56. Del Popolo MG, Leiva EPM (1997) *J Electroanal Chem* 440:271
57. Budevski E, Staikov G, Lorenz WJ (1996) *Electrochemical phase formation and growth*. VCH, Weinheim
58. Dietterle M, Will T, Kolb DM (1995) *Surf Sci* 342:29
59. Rojas MI, Amilibia GE, Del Popolo MG, Leiva EPM (2002) *Surf Sci Lett* 499:L135
60. Rojas MI, Del Popolo MG, Leiva EPM (2004) *Langmuir* 20:4279
61. Grossmann A, Erley W, Hannon JB, Ibach H (1996) *Phys Rev Lett* 77:127
62. Rojas MI (2004) *Surf Sci* 569:76
63. Leiva EPM, Del Pópolo MG, Schmickler W (2000) *Chem Phys Lett* 320:393
64. Oviedo OA, Rojas MI, Leiva EPM (2005) *Electrochem Commun* 7:472
65. Lorenz W, Staikov G, Schindler W, Wiestbeck W (2002) *J Electrochem Soc* 149:K47
66. Van Der Eerden JP, Staikov G, Kashchiev D, Lorenz WJ, Budevski E (1979) *Surf Sci* 82:364
67. Giménez MC, Leiva EPM (1999) *Electrochim Acta* 45:699
68. Giménez MC, Leiva EPM (2003) *Langmuir* 19:10538
69. Giménez MC, Ramirez-Pastor AJ, Leiva EPM (2006) *Surf Sci* 600:4741
70. Giménez MC, Ramirez-Pastor AJ, Leiva EPM (2010) *J Chem Phys* 132:184703
71. Zhang J, Sung YE, Rikvold PA, Wieckowski A (1996) *J Chem Phys* 104:5699
72. Hachiya T, Honbo H, Itaya KJ (1991) *J Electroanal Chem* 315:275
73. Magnussen OM, Hotlos J, Beitel G, Kolb DM, Behm RJ (1991) *J Vac Sci Technol B* 9:969
74. Binder K (1986) In: Binder K (ed) *Monte Carlo methods in statistical physics*, 2nd edn. Springer, Berlin

75. Blume M (1966) *Phys Rev* 141:517; Capel HW (1966) *Physica* 32:966; Blume M, Emery VJ, Griffiths RB (1971) *Phys Rev A* 4: 1071
76. Fichthorn KA, Weinberg WH (1991) *J Chem Phys* 95:1090
77. Giménez MC, Del Pópolo MG, Leiva EPM, García SG, Salinas DR, Mayer CE, Lorenz WJ (2002) *J Electrochem Soc* 149, E109
78. Foiles SM, Baskes MI, Daw MS (1986) *Phys Rev B* 33:7983
79. Finnis MW, Sinclair JE (1984) *Philos Mag A* 50:45
80. Carlsson AE (1990) In: Ehrenreich H, Seitz H, Turnbull D (eds) *Solid state physics*, vol 43. Academic, New York
81. Ercolessi F, Tosatti E, Parrinello M (1986) *Phys Rev Lett* 57:719
82. Hill TL (1960) *An introduction to statistical thermodynamics*. Addison-Wesley Publishing Company Inc., London
83. Drews TO, Braatz RD, Alkire RC (2007) *Z Phys Chem* 221:1287
84. García SG (1997) Ph.D. thesis. Universidad Nacional del Sur, Bahía Blanca, Argentina
85. García S, Salinas D, Mayer C, Schmidt E, Staikov G, Lorenz WJ (1998) *Electrochim Acta* 43:3007
86. Treeratanaphitak T, Pritzker MD, Abukhdeir NM (2014) *Electrochim Acta* 121:407
87. Treeratanaphitak T, Pritzker MD, Abukhdeir NM (2014) *Electrochem Commun* 46:140
88. Giménez MC, Del Pópolo MG, Leiva EPM (2002) *Langmuir* 18:9087
89. Schmickler W (1996) *Interfacial electrochemistry*. Oxford University Press, New York
90. Drews TO, Radisik A, Erlenbacher J, Braatz RD, Searson PC, Alkire RC (2006) *J Electrochem Soc* 153:C434
91. Stephens RM, Alkire RC (2007) *J Electrochem Soc* 154:D418
92. Bezzola A, Bales BB, Alkire RC, Petzold LR (2014) *J Comp Phys* 256:183
93. Bezzola A, Bales BB, Petzold LR, Alkire RC (2014) *J Electrochem Soc* 161, E3001
94. Brown G, Rikvold PA, Novotny MA, Wieckowski A (1999) *J Electrochem Soc* 146:1035
95. Bard AJ, Faulkner LR (1980) *Electrochemical methods: fundamentals and applications*. Wiley, New York
96. Hölzle MH, Kolb DM (1994) *Ber Bunsenges Phys Chem* 98:330
97. Hölzle MH, Retter U, Kolb DM (1994) *J Electroanal Chem* 371:101
98. Hölzle MH, Zwing B, Kolb DM (1995) *Electrochim Acta* 40:1237
99. Anderson AB (1975) *J Chem Phys* 62:1187
100. Anderson AB, Grimes RW, Hong SY (1987) *J Phys Chem* 91:4245
101. Mehandru S, Anderson AB (1989) *Surf Sci* 216:105
102. Lopez MB, Estiu GL, Castro EA, Arvia AJ (1990) *J Mol Struct (Theochem)* 210:353
103. Lopez MB, Estiu GL, Castro EA, Arvia AJ (1990) *J Mol Struct (Theochem)* 210:365
104. Lopez MB, Estiu GL, Castro EA, Arvia AJ (1992) *Surf Sci* 277:184
105. Mola EE, Blum L (1989) *Int J Quantum Chem Quantum Chem Symp* 23:687
106. Mola EE, Vicente JL (1992) Blum L (1992) *Int J Quantum Chem Quant Chem Symp (Proc Int Symp At Mol Condens Matter Theory. Comput Methods* 26:621
107. Mola EE, Appignanesi G, Vicente JL, Blum L (1993) *Proc Electrochem Soc* 93–5:186
108. Conway BE, Chacha JC (2004) *J New Mater Electrochem Syst* 7:231
109. Oviedo OA, Leiva EPM, Rojas MI (2006) *Electrochim Acta* 51:3526
110. Isoardi EP, Allan NL, Barrera GD (2004) *Phys Rev B* 69:24303
111. Reif F (1965) *Fundamentals of statistical and thermal physics*. McGraw-Hill Kogakusha, Tokyo
112. Allen MP, Tildesley DJ (1987) *Computer Simulation of Liquids*. Oxford University Press, Oxford
113. Schmickler W, Mariscal MM, Pötting K (2006) *Chem Phys* 320:149
114. Mariscal MM, Leiva EPM, Pötting K, Schmickler W (2007) *Appl Phys A* 87:385
115. Farigliano LM, Villarreal MA, Oviedo OA, Leiva EPM (2014) *ECS Trans* 58:3
116. Kittel C (2004) *Introduction to solid state physics*, 8th edn. Wiley, New York
117. Haile JM (1992) *Molecular dynamics simulation*. Wiley, New York

Chapter 6

Underpotential Deposition and Related Phenomena at the Nanoscale: Theory and Applications

6.1 General Aspects

Macroscopic materials composed by transition metals such as Ag, Au, Cu, Pd, and Pt are ductile, malleable, besides displaying excellent electrical and heat conductivity and high optical reflectivity. These properties have allowed these materials to be widely used in several areas, such as electronics (electrical contacts and conductors) and the catalysis of chemical reactions. When the size of these materials decreases to the nanometric scale, these particles show unique properties, which cannot be observed in macroscopic-sized materials. The number of synthesis methods of these nanomaterials and their new and possible technological applications has increasingly grown during the last decade. This progress has inevitably led to the commercialization of several nanomaterials. For example, Ag nanoparticles (NPs) have been used as a type of antimicrobial reactive of broad spectrum in medicine, mass consumer products, antiseptic aerosols of domestic use, antimicrobial water filters coatings, etc. [1]. Apart from these commercial applications, nanomaterials are largely used in the field of research, e.g. plasmonics, medicine, reactivity, combustion cells, etc. [2, 3].

These last decades have witnessed important advances in the development, the characterization and the way to assemble and/or produce molecular-scale devices. Nanoscience and Nanotechnology are the branches of science in charge of these advances. Nanotechnology consists of production, manipulation, and integration of devices at the nanoscale while Nanoscience provides the basic theoretical support for these achievements [4, 5].

Many construction processes, artificial as well as natural, occur at the nanoscale; this has inspired many different researchers all over the world to deepen into the fundamental study of matter at this scale. The new properties possible to be reached manipulating the matter at these size orders are unprecedented and for this reason, different authors predict that this technology will lead to a third industrial revolution much deeper than its predecessors.

Several examples clearly show that the physical parameters of nanomaterials such as size, shape, surface coating, and surrounding environment strongly influence their properties and, therefore, their performance in the applications. Different shapes of metallic nanomaterials are synthesized in a routine way; these include spheres, spheroids, cubes, cuboctahedrons, octahedrons, tetrahedrons, decahedrons, icosahedrons, thin plates, ribs or wires, stars, etc. To this aim, a great number of techniques, protocols, and manufacturing routines can be summarized in two types of strategies:

- (a) Top-Down, also known as conventional manufacturing: it starts from the big objects which are then broken down into smaller objects. This type of strategy has characterized the technological advances of the last century. Some common examples are the technologies used for the manufacture of microprocessors, hard disks based on giant magnetoresistance, focused ion beams, atomic force microscope tips used as a writing device, etc.
- (b) Bottom-up, also known as molecular manufacturing: small individual elements are linked together in order to form bigger components with a superior hierarchy, which then in turn are linked to each other until an even bigger system is formed. For instance, the manufacturing processes that utilize the specificity of Watson-Crick base pairing to build DNA and other nucleic acids well-defined structures, the chemical and/or electrochemical synthesis (organic and inorganic synthesis) aim to design molecules with well-defined shape, molecular self-assembly for automatic ordering, etc. It is expected that this type of strategy will prevail in the present century.

Bottom-up methods allow smaller geometries than Top-Down ones and are generally more economical. Today we face a dramatic transition stage between these two strategies [1–6].

But, what makes nanotechnology or nanoscience scientifically interesting? This question has many answers, but perhaps the one of greater importance is that many of the nanosystems properties can be tuned by controlling the size, shape and composition of nanosystems. Such is the importance of this topic that a complete book has been devoted to it [7]. In general, nanomaterials properties separate from the macroscopic laws of Physics; however, these properties can be rationalized considering quantum mechanics and/or nanothermodynamics. Ligand molecules generally coordinate small metallic clusters, commonly less than 1 nm in diameter, and their behavior is similar to that of a single molecule. In contrast, properties of metallic NPs, greater than 1 nm in diameter, can be considered as intermediate cases between the properties of a single molecule and the properties of bulk material. The following example can help to a better understanding of this situation. The melting point of a solid is, in a classical way, a constant, an intensive property of the matter; it is even utilized in the laboratories initial lessons at chemistry university studies as a method of identification. This picture may not occur at the nanoscale. It is well-known that the melting point of a bulky piece of Au is approximately 1337 K, but Au-NPs of approximately 20 nm in diameter start melting at lower temperatures. The melting point dramatically falls in sizes ranging

from 3 to 4 nm [8], while for a Au nanocluster of 1.5 nm, it can fall down to 775 K [7].

What effect does nano-size have on the chemical properties of materials? The answer will be given through another example. The chemical potential of a component's system, μ , is defined as the differential change of Gibbs free energy, G , given the addition of a new particle to the system, N , maintaining all the other variables constant. Mathematically speaking this corresponds to:

$$\left(\frac{\partial G}{\partial N}\right)_{P,T} = \frac{G}{N} = \mu \quad (6.1)$$

If the system is infinite (bulk), both equalities in Eq. (6.1) are then fulfilled. In other words, the chemical potential is only a function of pressure (P) and temperature (T), that is, we can write $\mu(P, T)$. Let us consider now a NP of the same material, at the same P and T conditions. The NP chemical potential, called μ^{NP} , is:

$$\left(\frac{\partial G}{\partial N}\right)_{P,T} \approx \mu + \alpha N^{-1/3} \approx \mu^{\text{NP}} \quad (6.2)$$

where α is a surface free energy per atom, $N^{-1/3}$ appears as a consequence that the number of surface atoms is proportional to N to the power $2/3$. It is worth mentioning that Eq. (6.2) is a first approach to the chemical potential of a NP. If the NP was of a smaller size or free standing, other contributions should be added to Eq. (6.2), such as curvature and rotational terms. The mathematical expression for μ^{NP} depends on the model used to describe it. The most used version consists in assuming a spherically-shaped NP where $\alpha N^{-1/3} = (2M\gamma)/(zF\rho r)$ where M , γ , z , F , ρ and r correspond to the molar mass, surface energy, cation charge, Faraday constant, specific mass and NP radius, respectively. This is known in the literature as Gibbs-Thomson Model. As the NP gets smaller, the second term on the right hand side of Eq. (6.2) becomes relatively more important and subsequently, major deviations from the bulk behavior will appear. It is intuitive to infer from Eq. (6.2) that at the nanoscale, the chemical potential is not only a function of both: P and T , but also of the NP size as well, that is $\mu^{\text{NP}}(P, T, N)$.

What effect does nano-size have on the electrochemical properties of materials? We will attempt an answer by analyzing the effect on the Fermi level of a metal (ε_{F}). The latter magnitude is defined as the electrochemical potential of the electrons inside a metal ($\tilde{\mu}_{\text{e}}$). The work function (Φ), is the minimum work necessary to remove an electron from the Fermi level to the vacuum:

$$\Phi = -\varepsilon_{\text{F}} - e_0\phi \quad (6.3)$$

where ϕ is the electrostatic potential right outside of the metal. The vacuum level is the energy of an electron at rest at a point far enough from the surface that the electrostatic image force can be despised – typically at 10 nm from the surface [9].

If the electrode is infinitely large, then Φ has a well-defined value for a given metal and surface structure. Conversely, for spherical metal NPs of intermediate sizes, the electron removal energy has been found to scale as [10]:

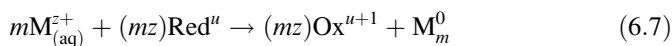
$$\Phi^{\text{NP}} = \Phi - \left[\frac{2M\gamma}{zF\rho} - \frac{5e_0^2}{8} \right] \frac{1}{r} \quad (6.4)$$

where Φ^{NP} corresponds to the NP work function. The term $2M\gamma/(zF\rho)$, appears from considering the change of the NP chemical potential according to the Gibbs-Thomson model [11], as presented in the discussion following Eq. (6.2). The term $5e_0^2/8$ corresponds to the corrections of the image-charge contributions according to a classical model introduced by Wood and Plieth [12, 13]. Thus, work function size dependence may be considered as the addition of two terms: first, the chemical potential change of the electrons in the metal particle and second, the image force change. If a NP is used as a nanoelectrode, the position of its Fermi level regarding the molecular orbitals of the redox species in solution may change; consequently, its electrochemical behavior may be different. In general for a metal, the dipolar contribution is greater than chemical contribution, so extracting an electron from a NP sometimes involves a larger work than taking it out from the corresponding bulk material and the smaller the NP is, the larger this work will become. Thus, this early work showed that “nano” effects might become important in electrochemical processes where the work function is known to play a key role, for example in determining the potential of zero charge of the electrode. For instance, Schnipper et al. [14] showed that the work function of Ag particles, $\Phi_{\text{Ag}}^{\text{NP}}$ increased from (5.29 ± 0.05) to (5.53 ± 0.05) eV as the particle size decreased ranging from 35 to 4 nm. These values are approximately 1.01 to 0.55 eV higher than for monocrystalline Ag surfaces (4.74, 4.64, and 4.52 eV for [111], [100], and [110] surface, respectively [8]). As it is mentioned by the authors, this great difference is also partly attributed to the surface dipole induced by the link citrate-Au (surface) (about 0.2 eV) and the presence of an oxide film on the Ag-NPs surface. However, disregarding these contributions, the tendency to increase $\Phi_{\text{Ag}}^{\text{NP}}$ with the size is still clear.

6.2 Kinetics and Thermodynamic Driving Force

6.2.1 Reduction Mechanism

The reduction of aqueous metallic oxidized species, $M_{(\text{aq})}^{z+}$, leads to neutral atoms and these constitute the construction blocks of clusters and metallic NPs. This process is the result of consecutive redox reactions in which the electrons of a reducing agent, Red^u , are transferred to the metal according to the following electrochemical equations:



where Ox^{u+1} is the oxidized species. The driving force of the process is the difference between the redox potentials, ΔE , between reactions (6.5) and (6.6). The magnitude of ΔE determines the value of the equilibrium constant, K , of reaction (6.7) according to:

$$\ln K = \frac{zF}{RT} \Delta E \quad (6.8)$$

The reduction reaction of $M_{(\text{aq})}^{z+}$ is thermodynamically possible only if ΔE is positive, which implies that the redox potential of the reducing agent must have a more negative value than that of the metallic species. From a practical viewpoint, this difference must be greater than about 0.4 V, otherwise, it will not be able to start, or it will proceed at a very slow speed. For example, for the Au or Pt cases, two metals with high reduction potentials ($E_{\text{Au}^+/\text{Au}}^0 = 1.692$ V and $E_{\text{Pt}^{2+}/\text{Pt}}^0 = 1.18$ V), the reduction process may occur with weak reducing agents. On the contrary, metals with low reduction potentials such as Cr ($E_{\text{Cr}^{2+}/\text{Cr}}^0 = -0.913$ V) require stronger reducing agents and more extreme reaction conditions.

If the metal ion intervening in reaction (6.5) is complexed in aqueous solution or if it is part of a compound, the standard redox potential, E^0 will be smaller. The decrease of redox potential depends on the stability of these complexes; for instance, Table 6.1 shows the changes occurring in the Ag ion standard potential due to the formation of complexes with an increase in the stability. These different stabilities limit the selection of the reducing agents.

Another alternative to modify E^0 is the use of the acid–base reactions, which are generally coupled to the reduction reactions. The reaction pH has a strong impact on the solute redox potentials and this impact can be quantified by Nernst equation. Both, complexing and pH effects, can be condensed in the so-called “redox diagrams”. These provide detailed information about the way to manipulate the reaction conditions in order to generate metallic NPs with the desired structure and size. As an example, Fig. 6.1 shows the redox diagram of Pd^{2+} , Ag^+ and hydrazine when the pH of the solution is adjusted with ammonia, which strongly makes both cations complexed. The corresponding redox reactions are inserted in the Figure.

According to Eq. (6.8) an increase in the value of ΔE will translate into a more spontaneous reaction, leading to smaller sized metal particles due to the generation of a larger number of nuclei. The size of the metal particles decreases as ΔE of the reaction increases. So, reduction reactions with very large ΔE must be employed to generate nanosized metal particles, which implies the selection of uncomplexed

Table 6.1 Changes on the Ag^+ redox potential as the result of the formation of different complexes in aqueous solution

Redox system	E^0/V
$\text{Ag}^+ + e^- \rightarrow \text{Ag}^0$	0.799
$[\text{Ag}(\text{NH}_3)_2]^+ + e^- \rightarrow \text{Ag}^0$	0.38
$[\text{Ag}(\text{SO}_3)_2]^{3-} + e^- \rightarrow \text{Ag}^0 + 2\text{SO}_3^{2-}$	0.29
$[\text{Ag}(\text{S}_2\text{O}_3)_2]^{3-} + e^- \rightarrow \text{Ag}^0 + 2\text{S}_2\text{O}_3^{2-}$	0.01
$[\text{AgI}_4]^{3-} + e^- \rightarrow \text{Ag}^0 + 4\text{I}^-$	-0.09
$[\text{Ag}(\text{CN})_3]^{2-} + e^- \rightarrow \text{Ag}^0 + 3\text{CN}^-$	-0.51

Reedited with permission from Ref. [15]

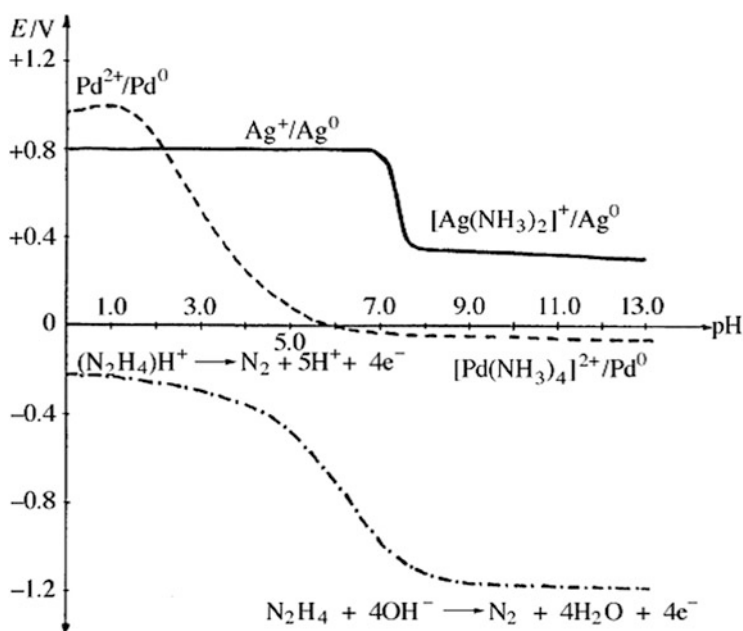


Fig. 6.1 pH effect on the hydrazine redox potential and the complex ammonium-Metallic of palladium and silver (Reprinted with permission from Ref. [56])

metal ions coupled with very strong reducing agents. The requirement of a large ΔE is a necessary, but not sufficient condition to achieve such monodispersed small particles. We can infer from Fig. 6.1 that the Pd-NP formation reaction by hydrazine oxidation may occur without kinetic hindrances at low and high pH. However, at pHs about 5, ΔE has a small (but positive) value, indicating according to Eq. (6.8) that the Pd-NP formation is thermodynamically driven but kinetically hindered. A similar argument cannot be given for the formation of Ag-NPs with hydrazine.

Another example of manipulation of redox potential with pH can be found in the article by Sánchez-Iglesias et al. [17]. These authors grew a Ag layer at room temperature through the reduction of Ag-ions with quinone/hydroquinone on a

Au-NP surface. The coupling of an acid–base equilibrium, allowed these authors to modify the hydroquinone redox potential with pH [18]. At a pH of 7.4 or higher, the hydroquinone redox potential is enough to reduce Ag, even if Au-NPs were present or absent. At pH values below 7 the redox potential becomes less negative and no reaction occurs even when Au-NPs are present. At intermediate pH values, it is possible to reduce Ag only on the Au-NPs surface.

Solvents play an important role on the NPs electrochemical synthesis [19]. These can play a multiple role on the preparation; for example, primary alcohols (methanol, ethanol) can work as solvent as well as reducing agents in the preparation of Pd, Pt and Au NPs, while the polyols (glycerol, diethylene glycol) can perform a triple function: as solvents, stabilizing and reducing agents, in the preparation of Cu and Ni NPs [20].

6.2.2 Strong Versus Weak Reducing Agents

The reducing agents that produce the metallic reduction reaction in Eq. (6.7) can be classified as weak or strong. However, as discussed in the previous section, this depends on the reaction conditions.

One of the most common reducing agents is hydroquinone (H_2Q). This agent is widely used for reducing Ag-ions for photo developing. In the photographic processing, the BrAg film exposed to light creates small Ag metallic clusters, which are too small to be visible with naked eyes. This constitutes what is commonly denominated as a photographic negative. The fogging process consists in provoking a growth in these metallic clusters through the addition of a solution containing H_2Q and additional Ag-ions. This makes the initial clusters grow until they become visible. H_2Q is incapable of reducing Ag-ions isolated in photographic film, but it is capable of reducing Ag-ions in the presence of pre-existent metallic clusters. Fayet et al. [21] proposed that these clusters should be composed of at least four atoms. The reason for this selection lies in its reduction potential. The energy used to reduce several Ag-ions to create a precursor seed is markedly different from the energy used to reduce ions on a pre-formed metallic cluster. This is the difference between homogeneous and heterogeneous nucleation, as we will discuss later. Table 6.2 shows estimates of the redox potential of different Ag metallic clusters [18]. From Table 6.2, we can observe that the hydroquinone redox potential is $E_{Q/H_2Q}^0 = -0.7$ V for pH = 1 and it is incapable of exceeding the highly negative redox potential required to produce an isolated Ag atom, $E_{Ag^+/Ag_1^0}^0 = 1.8$ V. However; it is enough to reduce Ag^+ -ions if there are previously existing clusters made of four or more atoms, on which the redox potential for Ag^+ is $E_{Ag^+/Ag_4^0}^0 = -0.4$ V or higher. It is worth mentioning that the Ag^+ ions could also be reduced on solid Ag, because $E_{Ag^+/Ag_\infty^0}^0 = 0.8$ V. An analogous situation should occur in the formation of the Ag-NPs in solution.

Table 6.2 Redox Potential required to produce an Ag cluster of a given size

Redox system	E^0/V
$\text{Ag}^+ + \text{e}^- \rightarrow \text{Ag}_1^0$	-1.8
$\text{Ag}^+ + \text{e}^- + \text{Ag}_3^0 \rightarrow \text{Ag}_4^0$	-0.9
$\text{Ag}^+ + \text{e}^- + \text{Ag}_4^0 \rightarrow \text{Ag}_5^0$	-0.4
$\text{Ag}^+ + \text{e}^- + \text{Ag}_{\infty-1}^0 \rightarrow \text{Ag}_{\infty}^0$	0.799
$\text{Q} + 2\text{H}^+ + 2\text{e}^- \rightarrow \text{H}_2\text{Q}$	-0.699 (pH = 1)
$\text{Q} + 2\text{H}^+ + 2\text{e}^- \rightarrow \text{H}_2\text{Q}$	-0.3 (pH = 7)
$\text{H}_2\text{BO}_3^- + 5\text{H}_2\text{O} + 8\text{e}^- \rightarrow \text{BH}_4^- + 8\text{OH}^-$	-1.24 (pH = 14)
$\text{C}_6\text{H}_6\text{O}_6 + 2\text{H}^+ + 2\text{e}^- \rightarrow \text{C}_6\text{H}_8\text{O}_6$	0.13

Values taken from Ref. [18]

Borohydride (BH_4^-) is one of the strongest reducing agents widely utilized in the generation of NPs and in many other applications in organic and inorganic chemistry. The redox potential, at $\text{pH} = 14$, is $E_{\text{H}_2\text{BO}_3^-/\text{BH}_4^-}^0 = -1.24\text{ V}$. Borohydride reacts quickly with Ag^+ -ions in solution to create Ag-NPs. Given its high reduction potential, this agent is used in the formation of initial clusters of almost all transition metals. In the particular case of Ag, and when observing the reduction potentials shown in Table 6.2, it seems contradictory that the (BH_4^-) may reduce Ag^+ -ions. Nevertheless, it should be taken into consideration that in general, for a reaction to take place in solution, the Ag^+ -ions are complexed, a fact that reduces the free energy necessary (or the potential) to form the precursor seed, as it can be observed in Table 6.1. To thoroughly analyze this problem, we can resort to the experiment by Gentry et al. [18], whose results are represented in Fig. 6.2. There, we see the absorption spectra for Ag nanoparticles grown using as reducing agents (a) H_2Q and (b) (BH_4^-)/ H_2Q . Figure 6.2a shows the spectrum when the solution containing Ag-ions is exposed to reduction of H_2Q ; no formation reaction is observed. On the contrary, when (BH_4^-) is added to the electrolyte solution, Ag-ion reduction starts and a shoulder near 400 nm (Fig. 6.2b) starts to appear in the absorption spectrum. After the whole (BH_4^-) has reacted, then authors proceed to add H_2Q observing an increase in the absorption spectrum intensity, thus indicating the growth of the Ag-NPs previously formed (Fig. 6.2b). In other words, H_2Q is useful as a weak reducing agent (incapable of forming initially Ag) once a strong reducing agent such as (BH_4^-) is employed to start the formation process. A similar discussion is valid with stronger and weaker reducing agents other than borohydride and hydroquinone.

6.2.3 Formation Mechanism of Monoatomic Nanoparticles

Metallic atoms generated by reduction according to Eq. (6.7) are substantially insoluble in aqueous media and, therefore, they become gradually added in groups called embryos. Embryos are dynamic entities that intervene in the process of

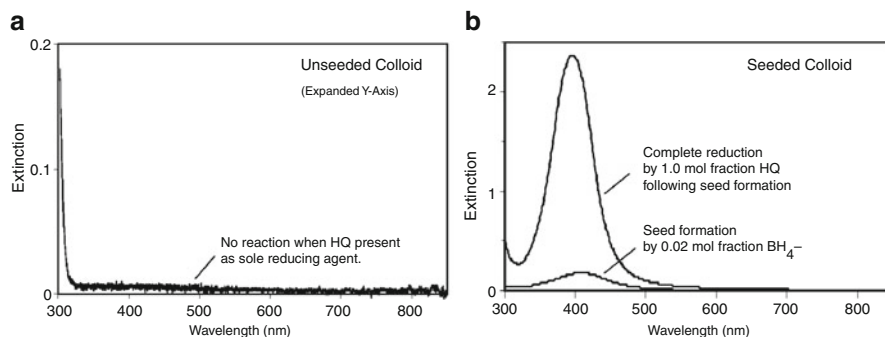


Fig. 6.2 Extinction spectra on (a) unseeded and (b) seeded samples. The unseeded colloid contained 1.0 mol fraction HQ relative to the number of moles of AgNO_3 , but no NaBH_4 . The seeded colloid was initially charged with 0.02 mol fraction NaBH_4 . HQ (6.0 mol fraction) was added to the seeded sample after 3 min. All samples contained 0.2 mM AgNO_3 and 0.2 mM sodium citrate (Reprinted with permission from Ref. [18])

continuous dissociation-condensation. As new metallic atoms are generated, embryos grow until they reach a determined size, called precursor seed. The nuclei size depends on several reaction parameters such as the solubility constants, solute concentration, redox potential, temperature, nature, and concentration of surfactants, of solvent viscosity and surface tension. These nuclei are, as a rule, metastable since they represent a system of relatively large free energy. These nuclei can grow through two different mechanisms: reduction of material on the seed surface and through addition of other nuclei in themselves. To produce NPs of practically the same size (monodispersity), the coalescence process among nuclei must be hindered at the early stages. This objective can be fulfilled by manipulating the electrostatic and/or steric effects of each NP. Electrostatic stabilization, strictly based on manipulating the equilibrium between attractive and repulsive forces, has little impact on the concentrated systems. There, the double layer is compressed due to the high ionic strength and, consequently, the NPs can get closer and undergo aggregation. By contrast, in dilute systems, the impact of the double layer is quite effective and has the advantage of leading to stable dispersions because the extension of the double layer is large. Electrostatic stabilization consists in the adsorption of surfactant, polymers, or polyelectrolytes, which counterbalances the van der Waals forces. The efficiency of both types of hindrance significantly depends on the system under study.

Let us consider for simplicity the free energy of formation of a monoatomic, naked, free-standing nanoparticle at an overpotential η , which is given by:

$$\Delta\tilde{G}^{\text{form}} = [G^{\text{NP}} - N_{\text{M}}\mu_{\text{M}}^{\text{bulk}}] + ze_0N_{\text{M}}\eta \quad (6.9)$$

where G^{NP} is the free energy of the NP, N_{M} is the number of its constituent atoms, and $\mu_{\text{M}}^{\text{bulk}}$ is the chemical potential of the atoms in the bulk metal, since we are

considering this material as the reference. Following Eq. (6.2), at first approximation, $[G^{\text{NP}} - N_M \mu_M^{\text{bulk}}]$ term is positive and proportional to the number of surface atoms, so $[G^{\text{NP}} - N_M \mu_M^{\text{bulk}}] \approx \alpha N_M^{2/3}$. Then Eq. (6.9) may be approximated by:

$$\Delta \tilde{G} = \alpha N_M^{2/3} + ze_0 N_M \eta \quad (6.10)$$

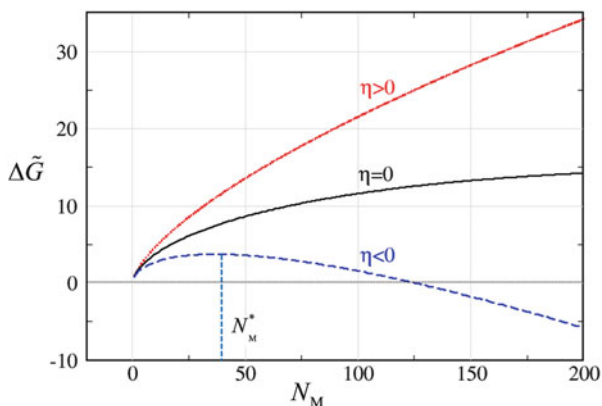
This equation has been widely used to analyze nucleation and growth phenomena. Note that the first chemical term is proportional to $N_M^{2/3}$ and the second one, the electrochemical term, is proportional to N_M . Thus, the electrochemical factor has a larger power dependence in $\Delta \tilde{G}$ than the surface term and the former will predominate in the limit $N_M \rightarrow \infty$. Thus, the behavior of $\Delta \tilde{G}$ will be of two different types, depending on whether $\eta > 0$ or $\eta < 0$. This situation is illustrated in Fig. 6.3.

In the first case, $\eta > 0$, the electrochemical factor will add the monotonic growing function $ze_0 N_M$ to the surface energy term, so that $\Delta \tilde{G}$ becomes always positive for all N_M . This behavior is the natural consequence of the increasing area of the growing NPs, and shows that, subject to the chemical potential of the bulk metal M, particles of all sizes will tend to dissolve.

In the second case, where $\eta < 0$, the electrochemical contribution will add a monotonic decreasing term to the monotonic increasing surface term, so that a maximum will appear at $N_M = N_M^*$, corresponding to the critical cluster size. This situation is illustrated qualitatively in the broken line of Fig. 6.3, and corresponds to systems where the thermodynamic stable state is the bulk material. Particles of size N_M^* are in an unstable equilibrium. Smaller particles will dissolve, and larger particles will grow towards the bulk condition. The application of a more negative overpotential, $\eta \ll 0$, shifts N_M^* to lower values, but the maximum still persists.

Figure 6.4 shows the energetic contribution to $\Delta \tilde{G}$ for the growth of an Au-NPs with two different crystalline structures, as obtained from computer simulation based on semiempirical embedded atom potentials [22–24]. It can be observed that the overall behavior is qualitatively similar to that described in Fig. 6.3 and

Fig. 6.3 Qualitative scheme of the excess of Gibbs energy, $\Delta \tilde{G}$, as a function of the number of atoms of the NP, N_M . Note the monotonically growing behavior for $\eta > 0$ and the occurrence of a maximum for $\eta < 0$, corresponding to an unstable state



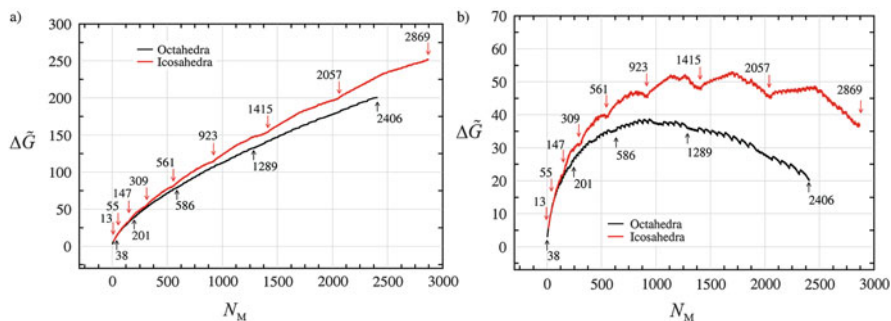


Fig. 6.4 Potential energy excess as a function of the number of atoms N_M for octahedral (black lines) and icosahedral (red lines) Au nanoparticles. The plots correspond to overpotentials of (a) $\eta = 0$ and (b) $ze_0\eta = -75$ mV. Some selected numbers of atoms, corresponding to closed shells, are marked with arrows

Eq. (6.9). However, the presence of a crystalline structure generates a sawtooth behavior of the curve, something that is characteristic of this type of systems [25, 26]. While the minima marked by arrows in Fig. 6.4 correspond to the completion of full shells in the NP, the fine structure is due to growth of individual facets. The latter are a consequence of the local minimization method employed in [27, 28] and could disappear if global optimization methods are used [3]. The layer-by-layer growth characteristic of these metastable systems [7, 27], may be understood in terms of the presence of local minima, separated by barriers of the order of the eV, we will later return to this issue. The beginning of crystal growth (nucleation) takes place under supersaturation conditions. That is, the electrochemical potential of the metal ions must be larger than that corresponding to the bulk phase ($\eta < 0$). Under supersaturation conditions any NP size is unstable and, consequently, the NP should grow ad infinitum or dissolve. This “grand canonical” picture (in the sense of an open system) of NP growth actually occurs in the synthesis in a rather short period of time. As the NP grows, the concentration of ions in solution starts to decrease, the system approaches equilibrium and subsequently the $\mu_M^{\text{NP}} \rightarrow \mu_M^{\text{bulk}}$. The later conditions correspond to a rather “canonical” picture of growth. Both pictures regarding NP growth coexist in the literature. As it will be further seen, a canonical view is useful to understand the processes of nucleation and growth, while a grand canonical view allows understanding stabilities in the processes of NP formation via upd.

A consequence of the fact that $\mu_M^{\text{NP}} > \mu_M^{\text{bulk}}$, making the NP unstable with respect to the bulk material, is that most of the methods of NP synthesis must control their size and morphology using kinetic strategies to block their growth. In order to understand this, a scheme was proposed by LaMer in the 1950s [28] and it is known as the “burst nucleation” concept. As it was mentioned in the above paragraphs, most of the methods employed in the formation of NPs require a supersaturation to proceed. In this process, many nuclei are generated at the same time, and then these nuclei start to grow. Because all of the particles nucleate almost simultaneously,

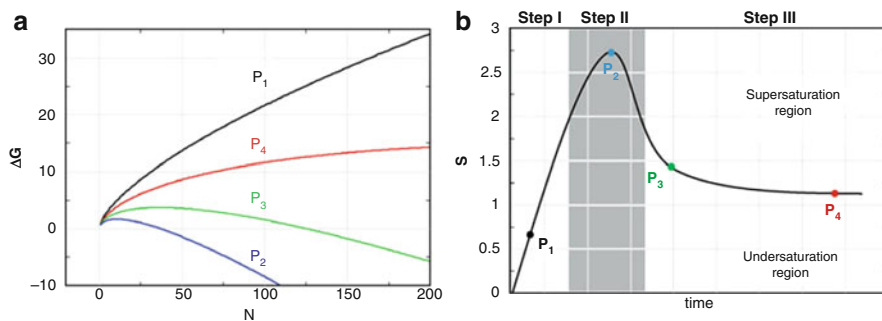


Fig. 6.5 (a) Typical free energy profile for the growth of a NP according to Eq. (6.9). (b) LaMer plot, change of saturation as a function of reaction time

their growth histories are nearly the same. This is the essence of the “burst-nucleation” process, which makes it possible to control the size distribution of the ensemble of NPs as a whole during growth. “Burst nucleation” has been adopted as an important concept in the synthesis of monodisperse NPs. As a synthetic strategy, this method is often referred to as “the separation of nucleation and growth”. In this homogeneous nucleation process, there exists a high free energy barrier, mainly due to the appearance of a new interface between the new (growing) phase and the original one (precursor).

How does burst nucleation work? At a given moment, the precursor agent starts to be injected. Let us further assume that diffusion is infinitely fast, so that matter is uniformly dispersed all over the volume of the system, and that its temperature remains unchanged. As the initial concentration of precursor is small, $\mu_M^{\text{NP}} > \mu_{M(\text{aq})}^{z+}$, where $\mu_{M(\text{aq})}^{z+}$ is the chemical potential of M^{z+} in solution. A typical point in this region would be for example point P_1 in Fig. 6.5b. The work of nucleation should be similar to that described in curve P_1 in Fig. 6.5a. This condition is generally called subsaturation region. Upon further addition of matter, $\mu_M^{\text{NP}} < \mu_{M(\text{aq})}^{z+}$, locating the system in the supersaturation region. Supersaturation increases continuously until the injection of matter stops. This point corresponds to step II, called “the nucleation stage”. At this moment, the amount of metallic precursor is maximal, so that metal activity and the solubility coefficient take their largest value. This corresponds to the point marked as P_2 in Fig. 6.5b. The work of nucleation under these conditions will look like the curve P_2 in Fig. 6.5a. At this time, the critical nucleus size reaches its lowest value. As the system is under supersaturation conditions, very frequently growth nuclei are formed; many of them being unstable, but occasionally large fluctuations are produced so that these fluctuations overcome the above-mentioned critical nuclei. These NPs are stable and begin their growth. At the same time these nuclei grow, other new nuclei are formed, and the precursor concentration drastically decreases. The situation at this intermediate period is for example that of point P_3 in Fig. 6.5b, and its work of nucleation is described by curve P_3 in Fig. 6.5a. In LaMer’s curves, this corresponds to the third stage of the

process, and the latter is generally called the “growth stage”. When the precursor concentration decreases, the critical nucleus size displaces toward larger values. At this stage, the probability of nucleation is relatively low. This prevents the formation of new nuclei and favors the growth of those already existing. Growth continues and μ_M^{NP} decreases asymptotically to $\mu_{M^{+}}^{\text{(aq)}}$. At this moment, the critical nucleus size has reached a very large value; a typical point for this situation has been marked as P4 in Fig. 6.5a, b. At this stage, the nucleation process is practically suppressed and only the growth of nucleus previously formed is observed. The experiment described above is the essence of the separation between the nucleation and growth processes. As the transition time between stages I and II becomes faster, the monodispersity of the NPs formed increases.

In systems with a rather low speed of metal reduction, the formed nuclei can fluctuate between crystal structures and twinned crystals [29]. This frequency of structural exchanges decreases when the NP size increases, until the point in which the NPs are trapped in one of these structures. These structures will serve as a guide for growth. Many applications need to be able to select some of these structures. A solution to this may be including new components to the system, which allow differentiating them even more in energy and finding a way to separate selectively nuclei from each other to obtain a better monodispersity of the NPs structures synthesized. For example, this is the case of adding to the reactants small quantities of oxygen and chloride ions to select the Ag-NP type to be obtained. In presence of these two components, the twinned structures can be dissolved because the twinning sites provide active sites for NP oxidation (little coordination). This corresponds to an etching process, where chloride acts as a coordinator causing also oxidation of these sites. As a result, the final NPs present only crystal structures with {111} and {100} type facets [30].

The differences between theoretical predictions and experimental results suggest that the nucleation process of NPs in aqueous solution does not proceed via the classical pathway from LaMer’s point of view; but it follows ways that are more complex and it involve several steps. For example, little nuclei can be linked together to form bigger and more stable nuclei. In order to understand this phenomenon, two models have been proposed: the Lifshitz-Slyozov-Wagner model [31, 32] and the two-stage model [33]. There is evidence that clusters of smaller sizes than the critical one, are sufficiently stable to the extent that successive aggregation of these units cause a rise in the speed of NPs formation [34]. The interaction (coordination) between solvent and/or surfactants molecules with small clusters can stabilize the molecules enough time so that these little units can be added to form a single big group, which eventually nucleates towards the bulk phase. Then, the presence of other components in the thermodynamic formulations is necessary to allow analyzing the effect of anions, solvents, surfactants, and so on. Important advances on the influence of these contributions on the formation of upd monolayers have been the pivot of the discussion in Chap. 3 of the present book. However, its extrapolation to the nanoscale still corresponds to a vacant issue in current literature.

6.2.4 Statistical Mechanic Formulation on the Stability and Metastability of Nanoparticles

In the present Section we will focus on the problem of stability of homoatomic nanosystems, with the aim of extending later these concepts to the study of upd on nanoparticles. To this purpose, we will use the Hill and Chamberlin model (HC) [35] originally developed to study the conversion of metastable (nanometric) drops of a liquid into its bulk phase. Important similarities arise for the formation of NPs in solution. This formalism was based on nanothermodynamics rules. For an introductory view, we address the readers to the first chapter of Hill's book on small systems [36].

The partition function of an incompressible, completely open system may be written as follows:

$$Y(\mu, T) = \sum_{N_M=1}^{\infty} Q(N_M, T) \exp[\mu N_M / k_B T] \quad (6.11)$$

where $Q(N_M, T)$ corresponds to the canonical partition function of an N -atoms sized cluster at temperature T . If we further consider that the system is made of a spherical cluster, $Q(N_M, T)$ takes the form:

$$Q(\mu, T) = c(T) N_M^4 \exp \left[-\alpha(T) N_M^{2/3} + \mu_M^{\text{bulk}} N_M / k_B T \right] \quad (6.12)$$

The term $c(T) N_M^4$ corresponds to rotational and translational contributions, $\alpha(T)$ is proportional to the surface tension and the term $\mu_M^{\text{bulk}} N_M / k_B T$ is related to the partition function of N_M particles in the bulk. Replacing Eq. (6.12) into Eq. (6.11) yields:

$$Y(\mu, T) = c(T) \sum_{N_M=1}^{\infty} N_M^4 \exp \left[-\left(\varphi N_M + \alpha(T) N_M^{2/3} \right) \right] \quad (6.13)$$

where the coefficient of saturation has been defined as $\varphi = (\mu_M^{\text{bulk}} - \mu) / k_B T$. If $\varphi > 0$ the system is in a subsaturation region; if $\varphi < 0$ it is in supersaturation conditions. If $\varphi = 0$ the system is right at the saturation limit. The probability density of observing a cluster made of N atoms may be written as follows:

$$P_{N_M}(\mu, T) = \frac{c(T) N_M^4 \exp \left[-\left(\varphi N_M + \alpha(T) N_M^{2/3} \right) \right]}{Y(\mu, T)} \quad (6.14)$$

The main idea in the HC model is to analyze stability in terms of the numerator of $P_{N_M}(\mu, T)$, since $Y(\mu, T)$ is fixed for the given μ and T . Then, a plot of $f(N_M, \mu, T)$

defined as $f(N_M, \mu, T) = P_{N_M}(\mu, T)Y(\mu, T)$ will present the same behavior as $P_{N_M}(\mu, T)$ out of a constant factor. A more suitable form to represent f is to make the changes of variables $n = \alpha^{3/2}N_M$ and $\delta = \alpha^{-3/2}\varphi$, to get:

$$f(N_M, \mu, T) = f(n) = n^4 \exp[-\delta n] \exp\left[-n^{2/3}\right] \quad (6.15)$$

Figure 6.6a shows a contour plot of $f(n)$ as a function of δ and $\log(n)$ at 300 K. We have selected four representative iso-saturation lines to this purpose: $\delta = 0, -0.04, -0.07$, and -0.09 , which are plotted in Fig. 6.6b–e. Each of the factors in Eq. (6.15) has been marked in Fig. 6.6b–e to illustrate the different contributions to $f(n)$. We can mention that the surface component is always a decreasing quantity (green curve), and that its value depends on the surface energy of the NP being formed. The rotational-translational contribution (red curves) is always a monotonically increasing function. The product of the two former components (the case of $\delta = 0$, black curve) determines a maximum of $f(n)$ around $\log(n) \approx 2.6$ (Fig. 6.6b). This maximum indicates a finite probability of finding nanoclusters of a given size at $\delta = 0$ and it is a consequence of the rotational-translational contribution. Turning into our focus of interest, that is, metallic NPs, the previous results a rather awkward prediction, since this would mean the occurrence of stable NPs at zero overpotential. On the contrary, we are aware from experiment that always overpotential is required for the growth of a new phase, to overcome the critical nucleus size, as analyzed above in Fig. 6.3. One of the points to be considered is that the traditional electrochemical conditions are usually not with free-standing NPs but deposited on a substrate, where the rotational-translational contribution, responsible for the maximum in Fig. 6.7b, vanishes. The other point to consider is the magnitude of the parameter α . An estimation of α yields in the range of $31 < \alpha < 57$ and $53 < \alpha < 55$ at room temperature for Au and Ag, respectively [38]. So the “drop” size would yield between $7 < N_{\text{Au}} < 13$ and $N_{\text{Ag}} \approx 8$, that is, very small values. It must be emphasized that such a prediction is absent in the formulation leading to Fig. 6.3, where the rotational-translational considerations were absent. At moderate supersaturation conditions, for example $\delta = -0.04$, the term containing the chemical potential (blue curve) starts to be noticeable, and the maximum of $f(n)$ is shifted towards larger n values, while its value increases (see Fig. 6.6c). At larger supersaturations, for example $\delta = -0.07$, Fig. 6.6d, the behavior remains the same and a steep increase is found in $f(n)$ above $\log(n) \approx 7$. This sudden increase in $f(n)$ after the maximum denotes the mathematical divergence of the probability density for $n \rightarrow \infty$, because of the fact that the supersaturation term is dominating the probability density for large nanodrop sizes. This divergence is associated to the occurrence of the bulk phase.

In Fig. 6.6d, it can be noted that in the region $5.7 < \log(n) < 7$ the probability density of finding a nanocluster is practically negligible. This area of low probability acts as a bottleneck for the transition of n -sized drops towards the bulk phase. However, this situation reaches a limit at larger supersaturations. For example,

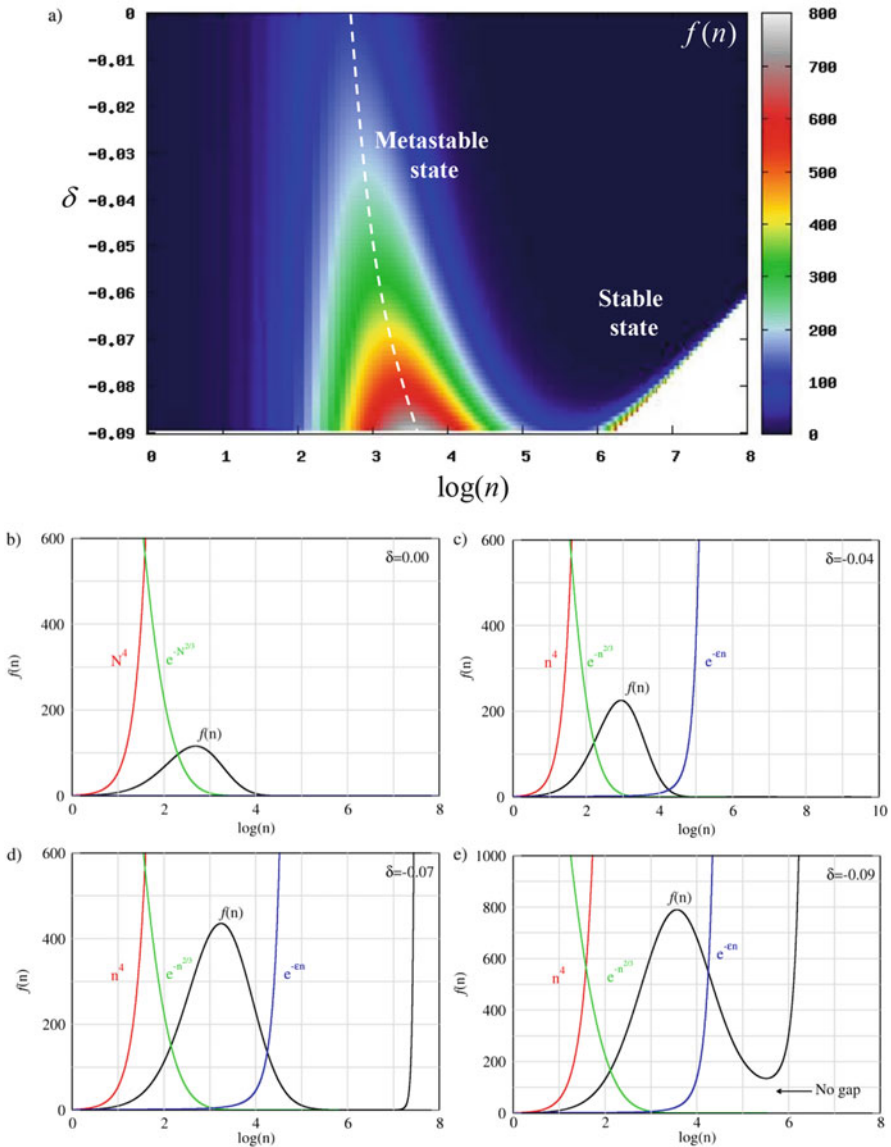


Fig. 6.6 (a) Contour plot of the function $f(n)$ at a constant temperature. Contributions of the different factors in Eq. (2.10) at diverse values of the normalized supersaturation δ . (b) $\delta = 0$, (c) $\delta = -0.04$, (d) $\delta = -0.07$, and (e) $\delta = -0.09$. In (b–e) the green curve has been multiplied by a factor 10^4 to fit into scale. See discussion in the text

Fig. 6.6e shows that at $\delta = -0.09$ the region where $f(n) \sim 0$ has disappeared, and it can be expected that small fluctuations, even of one particle, may lead to the transition to the bulk liquid. At very large supersaturations (not shown here), the

metastable nanocluster should no longer be observed, remaining only a monotonic growth towards the bulk phase. In Fig. 6.6a it can be observed how the region corresponding to the bottleneck progressively becomes thinner with increasing supersaturation. The rate at which the steep increase in $f(n)$ moves towards small n for decreasing δ is larger than the rate at which the metastable state moves towards large n . White broken lines in Fig. 6.6a represent this. The broken line on the left shows the position of $f(n)$ maximum, while the broken line on the right shows the evolution of a point at which $f(n) = 10^3$. Although the two lines have not converged into a representative point in the region analyzed in Fig. 6.6a, it can be seen that the dark blue region (bottleneck), i.e., the one with a negligible probability, has disappeared for $\delta = -0.09$, so that the system will no longer be confined to a metastable state at this supersaturation value.

The bottleneck in Fig. 6.6 represents a kinetic hindrance for the phase transition under consideration. The size of the gap may be related to an activation energy [39], in the sense that if this activation energy is large enough (wide probability gap), the transition will not take place at the timescale of experiment. This “confination” allows the computation of the thermodynamic properties of the nanoclusters, even when their structures do not correspond to a global minimum of the free energy of the system.

The idea of what Hill and Chamberlin called physical convergence of the probability density emerged from the previous analysis [25]. When the mathematical divergence is shifted onto large drop sizes ($\delta \rightarrow 0^-$, to denote that we are approaching the zero from small negative values), and we are interested in the calculation of properties of the metastable NP, the sum in Eq. (6.13) may be truncated to give:

$$Y(\mu, T) = c(T) \sum_{N_M=1}^{N_0} N_M^4 \exp \left[- \left(\varphi N_M + \alpha(T) N_M^{2/3} \right) \right] \quad (6.16)$$

where N_0 corresponds to a value of N at the minimum of the argument of the sum. Please note that $N_0 = N_0(\mu, T)$ is a function of chemical potential and temperature. As it is always the case, knowledge of the partition function allows calculation of all properties related to the metastable nanocluster.

When the system is in undersaturation conditions ($\delta > 0$), no divergence is found in the probability density, since under these conditions the sum (6.16) always converges. At moderate undersaturations ($\delta \rightarrow 0^+$, to denote that we are approaching the zero from small positive values), $f(n)$ presents a maximum and the nanocluster properties may be evaluated straightforwardly, since the local maximum in $f(n)$ is also a global one. Despite the simplicity of the model, Hill and Chamberlin showed that just at the saturation point (and at small subsaturation coefficients), clusters can be thermodynamically stable. That means that a supersaturation is not necessary to form initial clusters. Rotational and translational contributions are responsible for this “extra stability” not considered in Eq. (6.10).

6.2.5 Bimetallic Nanoparticles

Preparation of bimetallic NPs, from its precursors, is relatively more complex than the homoatomic synthesis. In general terms, this can be divided into two alternatives: a co-reduction or a successive reduction.

Co-reduction is the simplest method, where two or more precursors are simultaneously reduced. Morphology and space distribution of species within the NP, mainly depend on the velocity constants of the NP intrinsic processes: reduction potentials, self-diffusion, exchanges, etc. When the redox potentials of the two metals are similar, ($E_1^0 \sim E_2^0$) and ΔE is big (see Eq. (6.8), predominantly alloyed NPs are obtained [40, 41]. When the redox potentials of the two metals are different and are moderately big, the metallic species with the higher redox potential will precipitate first, forming the NP nucleus, followed by co-solubility of the second component, which prevails on the surface. It is worth mentioning that the solubility sequence can be reverted by the formation of complexes with ligands that creates a complex significantly stronger with the core formation metal. For example, in Fig. 6.1 it can be observed that Pd oxidizes at a more positive potential than Ag, so that attempt of reduction of both materials under similar conditions should prioritize mainly a core of Pd and an external layer rich in Ag. Nevertheless; when ammonia is added to the solution (at a relatively high pH), the reduction potentials are inverted, modifying the reduction priorities. In this last case, we should expect a core rich in Ag and a Pd shell.

In the *successive reduction* method, each reduction stage is carried out in different periods. The second reduction is carried out on the pre-formed NP surface (called seed-NP). This kind of growth implies a second nucleation stage. The temporary phase-lag of the stages is special for the NP posterior growth or the formation of core@shell NP. This kind of growth mechanism has been known from the beginning of the last century. It has also been used for the growth of homoatomic NPs as well as for bimetallic ones [42, 43]. We will discuss this kind of deposition in Sect. 6.4, where a model to describe the stability of preformed NPs will be set out.

Getting into the electrochemical field, it comes out that various strategies, originally used for the modification of flat surfaces, are nowadays successfully applied to design and modify nano-sized structures. Among these, it is of great interest the modification of a metal surface by upd, which as discussed in previous chapters consists in metal deposition on a foreign substrate at potentials positive with respect to the Nernst thermodynamic prediction. The potential utility of upd is due to the relatively rapid, simple, and precise modification of the reaction conditions, which allow controlling the degree of coverage of the adsorbate metal on the substrate surface. The main obstacle to the implementation of upd for a large number of systems is the fact that this phenomenon is usually limited to the deposition of a less noble metal on a nobler one. In the case of electrocatalytic applications, this situation is right the opposite to the desired one. One way to circumvent this problem is to use a technique denominated galvanic replacement

(gr). In this method, the substitution of a sacrificial upd sub/monolayer by the desired noble metal atop in circuit allows to obtain the desired catalyst. Applied together, upd and gr allow reducing the quantity of noble metal used to a minimum amount, thus reducing the economic costs of the final product. This is a key objective for potential industrial applications. Thus, both upd and gr appear as attractive bottom-up methods, with great prospects for the development of novel nanomaterials. Upd and gr are considered particular types of successive reduction methods.¹

6.2.6 Deposition Mechanisms at the Nanoscale

In analogy with metallic deposition mechanisms on planar surfaces [44], three types of growth at the nanoscale have been described:

- “Volmer-Weber” or three-dimensional island growth,
- “Frank-van der Merwe” or layer-by-layer growth,
- “Stranski-Krastanov” or three-dimensional island growth on a pre-formed layer.

In the first mechanism, the binding energy between the adsorbate and the substrate is smaller in absolute value than the binding energy of the native metal. This type of growth is common in systems presenting overpotential deposition (opd). In the second and third mechanisms the binding energy between the adsorbate and the substrate is larger than the binding energy of the native metal. Thus, two-dimensional phases can be formed driven by this magnitude. These growth types are typical of systems presenting upd. The difference between the second and the third growth types lays in the crystallographic mismatch between the adsorbate and the parameters of the substrate. For systems displaying a fairly small difference between their lattice parameters, it is expected that they follow a layer-by-layer growth type. On the other hand, for systems displaying a fairly large difference between their network parameters, it is expected that they follow the Stranski-Krastanov mechanism. As the number of deposited layers increases, a tension (caused by the crystallographic mismatch) accumulates so that the shell breaks on top and the growth method changes from layer-by-layer to three-dimensional island growth. Clearly, this division of growth mechanisms is a rather simplified picture of the real situation. It is well known that for a NP of a single material, the lattice parameter of the subsequent layers composing the NP varies according to size. The definition of crystallographic mismatch, as it is taken from flat surfaces makes no sense; at the nanoscale, this parameter is function of size. These deformations generate instability. There are two types of instabilities at the nanoscale [45]. The first one is that produced inherently by the geometry of the NP, which may deviate in its inner structure from that expected for the bulk material. This is for example

¹ See discussion on Sect. 7.1 in Chap. 7.

the occurrence of icosahedral structures in the case of metals with bulk *fcc* structure. This instability increases when the number of the layers of the nanoparticle grows. The second type of instability appears in the case of substrate/adsorbate systems, where the lattice mismatch between the adsorbate and the substrate leads to the Stranski-Krastanov growth type.

6.3 Towards Electrochemical Control in Synthetic Routines for Free-Standing Nanoparticles

In the early 2000s, detailed electrochemical studies on nanoparticles were carried out by Park and Weaver [37, 46], who investigated by voltammetric experiments the upd of Cu on Au NPs of different sizes. Figure 6.7a schematically shows Park and Weaver experimental design [37, 46]. Here, the NPs are placed above a conductive film that is in contact with the electrolytic solution containing ions Cu^{+2} ; the NPs surface potential was controlled by a potentiostat. Figure 6.8a shows the voltamperometric profile obtained for the deposition of Cu on 13 nm-in-diameter NPs (solid trace) in the presence of sulfate ions. Cathodic and anodic sweeps show the presence of two pairs of reversible processes, a-a' and b-b', associated with the electrodeposition of upd-Cu and of bulk Cu (see also Fig. 6.8). The curve represented in a dotted line corresponds to the potential sweep in the absence of NPs, thus indicating that the conductive film is not permeable to Cu^{+2} ions. So, these authors concluded that the measured current is produced only by the reduction of Cu^{+2} on Au NPs.

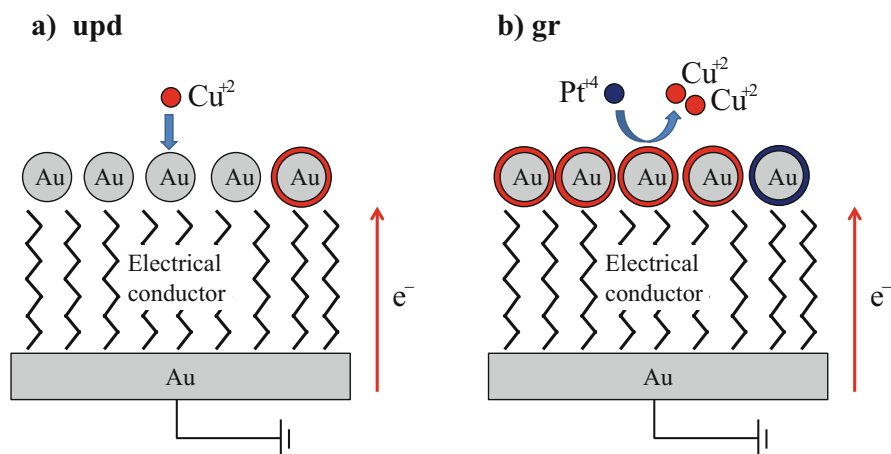


Fig. 6.7 Schematic representation of the process used by Park and Weaver to produce core@shell NPs of Au@Cu and Au@Pt using (a) underpotential deposition and (b) underpotential deposition in conjunction with galvanic replacement (Adapted with permission from Ref. [37])

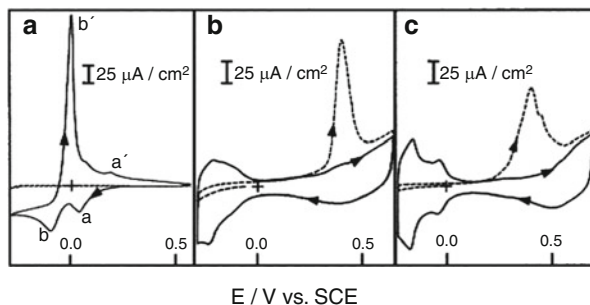
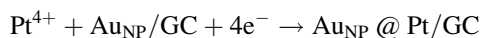


Fig. 6.8 Voltammograms (a) at (5 mV s^{-1}) for Cu deposition on Au-NPs ($d_{\text{NP}} \approx 13 \text{ nm}$) in $0.1 \text{ M H}_2\text{SO}_4 + 1 \text{ mM CuSO}_4$ (Solid trace). Baseline (dashed trace) was obtained in the absence of Au-NPs. (b) Solid trace: cyclic voltammogram (50 mV s^{-1}) for Pt modified Au-NPs in $0.05 \text{ M H}_2\text{SO}_4$; dashed trace is for electrooxidation of irreversibly adsorbed CO. (c) Similarly to (b), but for Pt-NPs ($d_{\text{NP}} \approx 6 \text{ nm}$) in absence and presence of a CO adlayer (Reprinted with permission from Ref. [37])

Similarly, Fig. 6.7b shows a scheme of the model used by Park and Weaver in Reference [37] for the fabrication of Au@Pt NPs using Cu upd and subsequent galvanic replacement of the upd deposit by Pt^{4+} . Figure 6.8b shows the voltammogram for Au@Pt NPs in absence (continuous curve) and in the presence (dotted lines) of CO. The current peak in the dotted line curve appearing between 0.4 and 0.5 V corresponds to the CO irreversible electrooxidation characteristic for Pt surfaces. Figure 6.8c shows the voltammogram for Pt NPs of 6 nm diameter, in the presence and absence of CO. The comparison of Fig. 6.8b, c shows that the electrochemical behavior, concerning CO electrooxidation, of the Au@Pt core-shell is similar to that of pure Pt.

In a different approach, Zhang et al. and Lu et al. [47, 48] presented a synthesis protocol where the electrons needed for the metallic reduction process are released by a molecule which is in solution, see Fig. 6.9a, thus avoiding the use of a potentiostat as electrons source. These authors seeded Au-NPs of 12 nm diameter on graphitic carbon (GC) and grew a Pt layer on the surface of the Au-NPs using ascorbic acid as reducing agent.

The reduction equation that represents this growth is:



where electrons are provided by the oxidation reaction of ascorbic acid. Figure 6.9b shows cyclic voltammograms obtained with 12 nm diameter Au NPs and Au@Pt NPs, both deposited on GC. The Au-NPs/GC electrode shows the electrochemical behavior of a typical Au electrode. However, when substituted by a Au(core)@Pt(Shell)/GC system, the CVs resemble the one of a pure Pt electrode. This can be visualized in the CV in the characteristic peaks of hydrogen adsorption/desorption between -0.3 and $+0.1 \text{ V}$, as well as in platinum oxide formation and reduction at higher potentials. The absence of the peak corresponding the

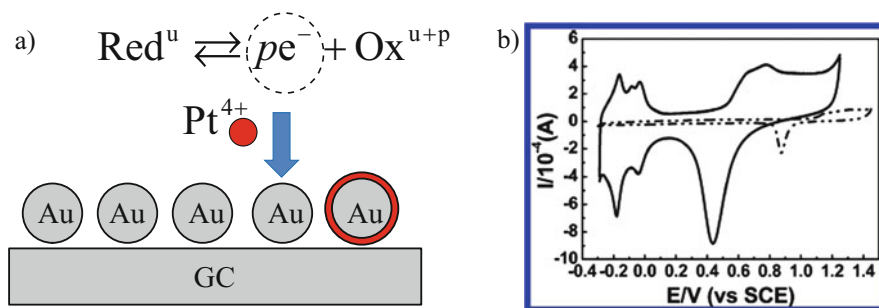
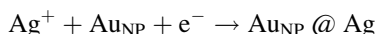


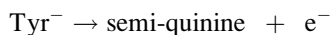
Fig. 6.9 (a) Schematic representation of the process of NP formation of core@shell type using molecules with redox activity as reducing agent. (b) Cyclic voltammogram (50 mV/s) corresponding to Au NPs of 12 nm (*dotted line*) and Au(core)@Pt(shell) NPs of 50–60 nm in 0.5 M of H₂SO₄ (Reprinted with permission from Ref. [47])

Au oxidation (~ 0.9 V) indicates that the Au cores are completely covered by Pt. Pt deposition on Au surfaces is a typical system with opd growth. Consequently, in Zhang's et al. experiment previously described, it is not possible to control the thickness of the Pt layer thermodynamically. These authors obtained a Pt layer between 38 and 48 nm thick. It should be noticed that in this type of experiments the potential (fixed by the reductant, here ascorbic acid) may be considered as constant during all the reaction. Thus, Zhang's experiment can be compared with an electrochemical growth at a constant potential in the overpotential region.

Selvakannan et al. [15] showed that tyrosine can be used as reducing agent in alkaline conditions, to reduce Ag⁺ ions on the surface of Au-NPs without the need of a support. The reduction process of the Ag⁺ ions can be represented as follows:



where Au_{NP}@ Ag denotes a free standing NP in solution. The electrons necessary for the reduction process come from the oxidation of tyrosine, according to the following oxidation reaction:



in which semi-quinine refers to the structure obtained after tyrosine oxidation. The global electrochemical equation is:



Tyrosine presents acid–base activity:

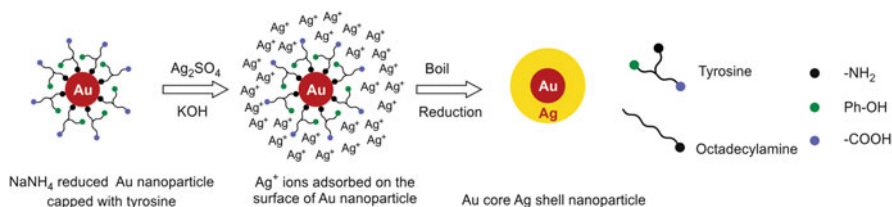


Fig. 6.10 Formation scheme of a core-shell Au@Ag NP according to Selvakannan's method (Reprinted with permission from Ref. [15])

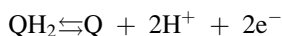


where we note that the species which causes the Ag reduction reaction is Tyr⁻ but not Tyr. At high pH values the ionization of the tyrosine phenolic group is produced, leading to a semi-quinone structure. Figure 6.10 shows the NPs formation scheme by Selvakannan method [15].

At intermediate or acid pH values, this ionization is hindered and consequently Ag reduction does not take place. Thus, the pH of the solution was used as a switch (on/off), to control the occurrence of the reaction. Other amino acids such as tryptophan and aspartic acid, allow the reduction of Au ions, but do not allow the reduction of Ag⁺ ions [49, 50].

Fonticelli et al. showed in 2007 [51] that p-benzoquinone (a molecule with similar characteristics to those of tyrosine) can be used to reduce Ag⁺ ions on the surface of a Au-NP coated with thiol molecules. The main difference between the experiments of Selvakannan et al. and those of Fonticelli et al. is that in the first case, the reducing molecules were on the surface of the NP while in the second, they were free in solution. This is a slight but significant difference, since the reducing molecules on the surface of the NP may be influenced by the presence of a second material, thereby affecting the deposition process.

The equation of oxidation for the reducing agent in the case of Fonticelli et al. is:

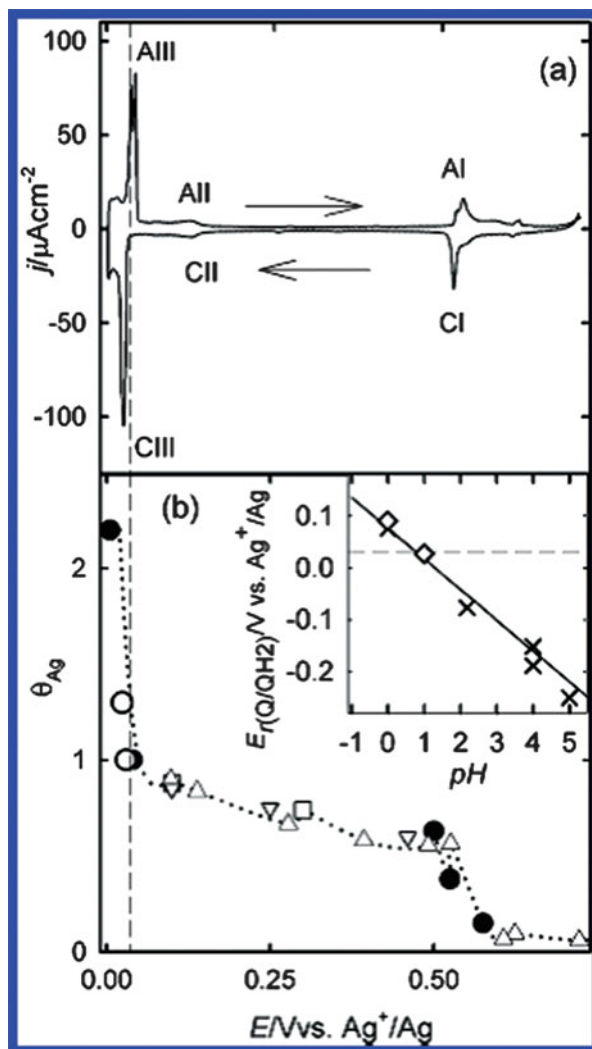


in which QH₂ and Q represent p-benzoquinone and p-hydroquinone, respectively. The equilibrium potential (Nernst) of the couple is:

$$E_{\text{Q/QH}_2}^r = E_{\text{Q/QH}_2}^0 + \frac{RT}{2F} \ln \left(\frac{a_{\text{Q}} a_{\text{H}^+}^2}{a_{\text{QH}_2}} \right)$$

in which $E_{\text{Q/QH}_2}^0 = 0.6992$ V vs NHE is the standard potential of the couple. It is clear that $E_{\text{Q/QH}_2}^r$ is a function of pH, as illustrated in the inset of Fig. 6.11b. If the pH of the solution is selected lower than 1, the deposition potential (controlled by the redox couple) is moved to more positive values than the Ag bulk deposition

Fig. 6.11 (a) voltammogram for Ag deposition on the surface of Au(111) (b) θ_{Ag} vs. E plot obtained from different data. Circles correspond to coverage obtained using the Q/QH₂ redox couple. Inset: $E_{r(Q/QH_2)}$ vs. pH plot for the redox couple (concentration = 1×10^{-3} M). The horizontal dashed lines indicate the potential selected for depositing Ag by using the Q/QH₂ redox couple (Reprinted with permission from Ref. [51])



potential $E_{Ag^+/Ag}^r$ and consequently Ag^+ reduction takes place in upd region. Figure 6.11b shows an adsorption isotherm obtained for Ag deposition on Au-NPs, as obtained from measurements from different authors, as reported in the work mentioned. The vertical dotted line indicates the potential fixed by the redox couple, at which the Au@Ag NP synthesis took place. For the sake of comparison, a voltammogram for Ag deposition on the surface of Au(111) can be observed in Fig. 6.11a, under similar conditions. We conclude that this work showed that the electric potential for metal deposition on free standing NPs suspended in solution can be continually tuned using reducing molecules (and their oxidized counterpart) with acid–base activity, in very much the same way that a potentiostat is used to

control the surface potential of an electrode. Thus, within this picture, the NP resembles a nanoelectrode that can be wired to a desired potential via a redox system.

We end the section stating that in analogy with the definition given for flat surfaces in section Chap. 3, metal deposition on NPs that are free in solution, can also be classified into:

- underpotential deposition (upd) for $E_{Q/QH_2}^r > E_{M/M^{z+}}^0$,
- overpotential deposition (opd) for $E_{Q/QH_2}^r < E_{M/M^{z+}}^0$.

This classification is relevant for the discussion given in the following section.

6.4 Thermodynamics of Underpotential Deposition at the Nanoscale

We will begin our analysis by considering a modelling similar to the one exposed in Sect. 6.2.3 of this chapter (see Fig. 6.3), with the difference that the analysis of thermodynamic stability will be made for a metal deposited on a NP, yielding a core@shell type NP. The model is shown in Fig. 6.12 and it consists of a typical

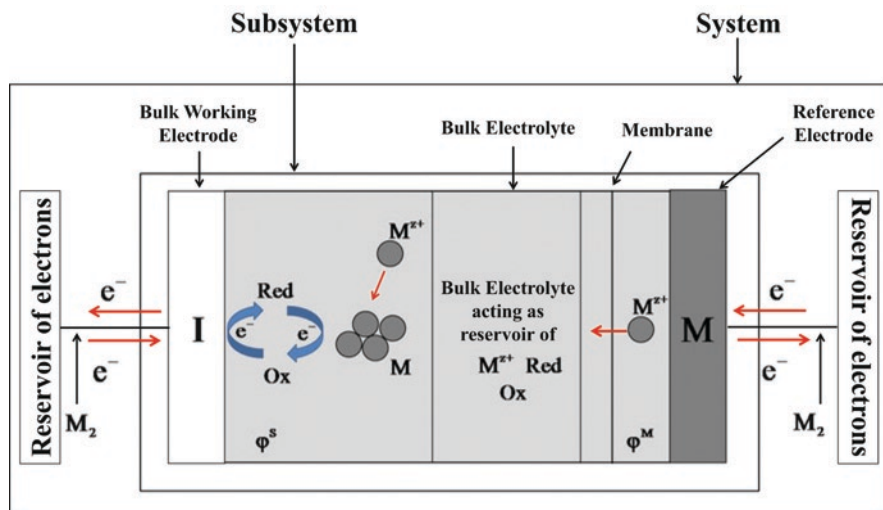


Fig. 6.12 Scheme of the electrochemical system used to analyze underpotential deposition on freestanding nanoparticles, where a redox system is used to set the potential applied to the metal nanoparticles. The broken line encloses the subsystem containing the electrodes, the nanoparticles, and the electrolyte. The broken line denotes a membrane that is permeable to all components of the system, with exception of the molecular species involved in the redox couple. The inner electrostatic potentials at both sides of the membrane are in principle different due to the presence of the redox system (Readapted with permission from Ref. [135])

electrochemical cell containing two infinitely large electrodes: the working electrode (W) and the reference electrode (R). The chemical species found in the electrolytic solution are metal ions to be deposited ($M_{(aq)}^{z+}$), the NPs made of a metal S, and the redox couple. The electrochemical cell is large enough so that the bulk properties of the electrolyte are not affected by the reactions on the surface of the NPs. We will denote this cell, that is, the electrolytic solution plus the two electrodes with the term “sub system” (see internal dotted line in Fig. 6.12). The later, together with the reservoirs will be called “system”. While the subsystem is open, exchanging electrons and heat with the reservoirs; the complete system is isolated.

Let us consider for this system the free energy change due to the transfer of N_M atoms from the bulk electrode on the right to the surface of a NP on the left compartment.

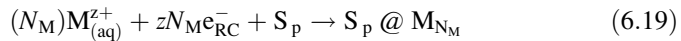
First, N_M cations are generated at the electrode R and the electrons stemming from the metal oxidation go to electron reservoir, e_R^- :



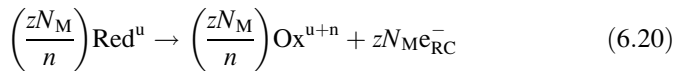
These cations go through the membrane towards the left compartment:



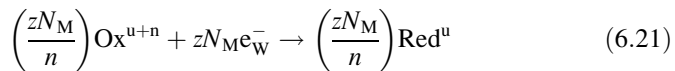
Since we assume that the membrane is permeable to the $M_{(aq)}^{z+}$ cations, the free energy change for this step is zero. Then, these cations are deposited on the surface of a NP made of p metallic atoms of S:



The electrons, e_{RC}^- , required for their reduction are provided from the simultaneous oxidation of the redox couple:



Then, an electron exchange is allowed to take place on the surface of the I electrode (inert surface), returning the redox system to its reduced original state:



The electrons, e_W^- , required for this process are provided by the electron reservoir on the left. As result of this process, M deposition on the surface of the S-NP occurs. The electrochemical global reaction that takes place is:



The related free energy of this reaction may be obtained using the free energy differences of products and reactants:

$$\Delta \tilde{G} = [G^{Sp} @ M_{N_M} - G^{Sp} - N_M \mu_M^{bulk}] + zN_M [\tilde{\mu}_e^R - \tilde{\mu}_e^W] \quad (6.23)$$

As shown above, when electronic equilibrium establishes at the left compartment, the electrochemical potentials of electrons at the NP, the redox system and the I electrode are equal. Thus, electrons from the reservoir on the left may reach the surface of the NP without the need of an electrical work.

In Sect. 3.1 of this book, it has been stated that the difference of the electrochemical potentials of electron corresponds to $(\tilde{\mu}_e^R - \tilde{\mu}_e^W) = ze_0 \eta$, so that the previous Eq. (6.23) reduces to:

$$\Delta \tilde{G} = [G^{Sp} @ M_{N_M} - G^{Sp} - N_M \mu_M^{bulk}] + ze_0 N_M \eta \quad (6.24)$$

Equation (6.24) looks very much like Eq. (3.71) of Chap. 3 for flat surface. We write, “looks very much like” because the contributions in Eq. (6.24) involve a number of subtleties not present in the case of upd on flat surfaces. The first is that the presence of the redox couple generates a difference between the inner potentials of the solution in the left and right compartments, say $\Delta\varphi$. Since the membrane separating the compartments of the cell has been assumed to be permeable to the $M_{(aq)}^{z+}$ cations, the electrochemical potential in both compartments is the same. Thus, the activities of the cations must be different. Alternatively, if the membrane had been impermeable to the $\alpha_{M_{(aq)}^{z+}}$ cations and the same activity had been introduced in both compartments, a extra term $(-ze_0 N_M \Delta\varphi)$ would appear in Eq. (6.24).

The other difference between flat and curved surfaces concerning the free energy of formation of structures, is that ΔG in Eq. (3.71) involves an infinitely large surface, while in Eq. (6.24) the term in brackets corresponds to a finite system. Even more, since the present system is of nanoscopic size, the correct formalism to deal with it is nanothermodynamics, as established by Hill [35, 36]. To state these differences shortly, we can say that in the flat surface formulation ΔG is extensive with respect to the number of adatoms, in the sense that if we multiply the number of adatoms by a constant all the properties of the system will be scaled accordingly. In Eq. (6.24), this is not the case. This can be better understood if we consider the effects of the curvature. As the NP becomes of a smaller size, curvature effects become more important and in general, this fact gradually weakens the metallic bound. Thus, the properties of this type of systems are not extensive.

Figure 6.13 shows the qualitative behavior of $\Delta \tilde{G}$ as a function of the number of M atoms, N_M deposited on a NP for systems presenting (a) opd and (b) upd. In the case of opd, Fig. 6.13a, the behavior of $\Delta \tilde{G}$ looks very much like that usually found in the analysis of classical models of nucleation and growth, see discussion in

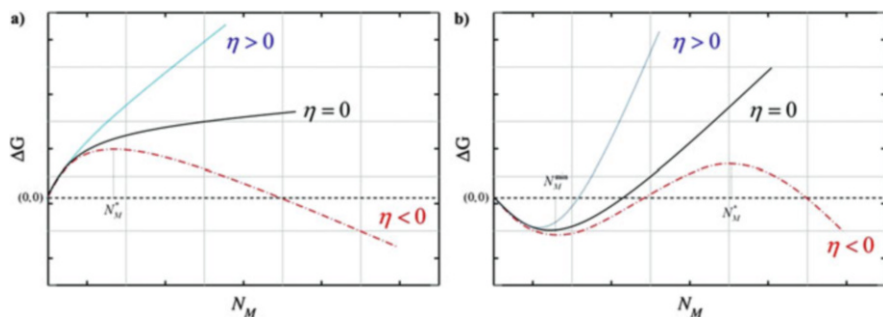


Fig. 6.13 Qualitative scheme of the excess Gibbs energy $\Delta\tilde{G}$ as a function of the number of atoms N_M for the electrochemical formation of a core@shell nanostructure. (a) Corresponds to a situation where the interaction of the deposited atoms with the substrate, is weaker than the interaction with each other (opd). (b) Opposite case of (a), (upd) (Reprinted with permission from Ref. [136])

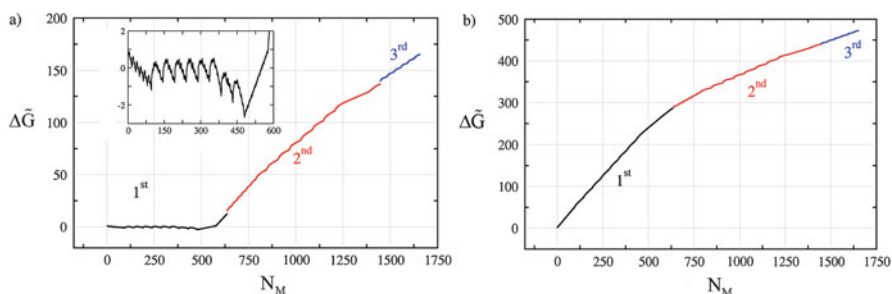


Fig. 6.14 Energy excess as discussed below Eq. (6.24) for the deposition of (a) Ag atoms and (b) Pd atoms on an Au NP made of 1289 atoms with octahedral structure. The different coloured lines denote in both cases the completion of a monolayer (Reprinted with permission from Ref. [26])

Sect. 6.2 (Fig. 6.3). The behavior for upd systems, shown qualitatively in Fig. 6.13b, is strikingly different. There, we find a minimum in the $\Delta\tilde{G}$ vs. N_M curve for a number of adatoms that we denote with N_M^{\min} . As discussed below, several minima may eventually occur. This minimum will eventually subsist at zero or slightly positive overpotentials, defining a global extremum. On the other hand, this minimum could also remain for slightly negative overpotentials, thus defining a local minimum or metastable state. This would imply the existence of core@shell nanostructures under overpotential conditions where bulk-growth should occur. The height of the free energy barrier, occurring at N_M^* , depends on overpotential, and so will the lifetime of the metastable state.

The qualitative picture presented in Fig. 6.13 has been verified by Grand Canonical Monte Carlo computer simulations [26]. Alternatively, Fig. 6.14 shows the behavior of $\Delta\tilde{G}$ approximated from static energy calculations, as a function of the amount of metal atoms, which constitute the shell. The results shown are for the deposition of Ag atoms on an Au (1289) truncated octahedral NP and for the deposition of Pd atoms on an Au (1289) NP. We note that the general behavior is

similar to Fig. 6.13. However, the discrete atomic nature and the packing of atoms in the NP produce deviations from the simplified behavior shown there. A magnification of Fig. 6.14a (see inset) shows a more complex sawtooth behavior, with 14 maxima, grouped into two families (6 + 8). These maxima correspond to a 2D nucleation and growth phenomenon located on each of the facets of the truncated octahedron. However, this saw motif should be wiped out by thermal effects at 300 K. While decoration of the NP is expected at zero overpotentials for the system Au(1289)@Ag (Fig. 6.14a), no spontaneous decoration is predicted for the system Au(1289)@Pd (see Fig. 6.14b).

Equation (6.24) can also be obtained from statistical mechanical considerations [26]. The partition function $Y(\mu_M, S_p, T)$ of the nanosystem shown in Fig. 6.12 is:

$$Y(\mu_M, S_p, T) = \sum_{N_M=0}^{\infty} Q(N_M, S_p, T) \exp[\beta N_M \mu_M] \quad (6.25)$$

where $Q(N_M, S_p, T)$ corresponds to the canonical partition function and $\beta = (k_B T)^{-1}$. Using Eq. (6.24), Eq. (6.25) can be rewritten in term of excess quantities:

$$Y(\mu_M, S_p, T) = A \sum_{N_M=0}^{\infty} \exp[-\beta \Delta G^{\text{sub}}] \exp[-zF\beta N_M \eta] \quad (6.26)$$

where $A = \exp[-\beta G^{S_p}]$. According to statistical mechanics, this equation contains all we need to calculate the thermodynamic properties of the NP system, since from it, all equilibrium properties may be calculated. However, there are at least two handicaps for such a calculation. One is the calculation of the free energy change ΔG^{sub} which in turn implies knowledge of the canonical partition function $Q(N_M, S_p, T)$. This calculation involves the sum over all energy states compatible with N_M , S_p and T . Even assuming a lattice model, and thus restricting the positions of the M and S atoms to a finite number of point in the configurational space, such a calculation appears as computationally extremely demanding due to the number of possible permutations. The other additional problem is the existence of infinite many terms in the sum of Eq. (6.26).

In Sect. 6.2.2, we presented the Hill-Chamberlin Model applied to understand supersaturated metastable states. It is possible to apply the same formalism to the case of under/over potential deposition. To show this, let us consider the probability of having N_M metallic atoms deposited on a NP made of S_p atoms at the overpotential η and temperature T :

$$p_{N_M}(\eta, S_p, T) = \frac{\exp[-\beta \Delta G^{\text{sub}} - zF\beta N_M \eta]}{Y(\mu_M, S_p, T)} \quad (6.27)$$

Since for given conditions the $Y(\mu_M, S_p, T)$ is a constant, we have that the product $p_{N_M}(\eta, S_p, T) Y(\mu_M, S_p, T)$ is monotonic with $p_{N_M}(\eta, S_p, T)$ and also its $(k_B T)^{\text{th}}$ power:

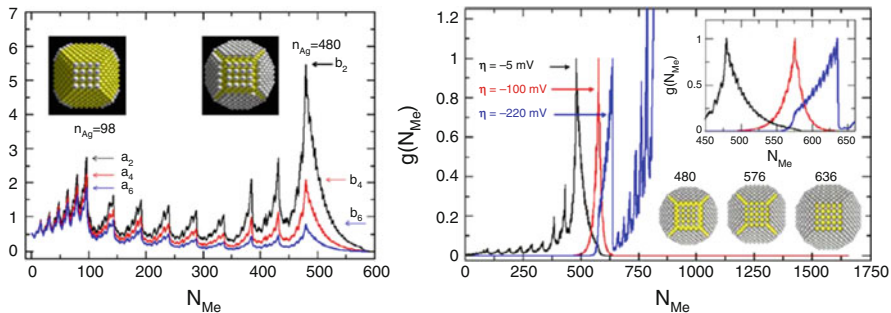


Fig. 6.15 Probability density of observing N_M Ag atoms deposited on a truncate octahedral Au (1289) core as a function of the number of atoms that conform the shell at different (a) underpotentials and (b) overpotentials (Reprinted with permission from Ref. [26])

$$f(N_M) = [p_{N_M}(\eta, S_p, T) Y(\mu_M, S_p, T)]^{k_B T} \quad (6.28)$$

thus, plot representation of $f(N_M)$, that can be calculated from Eq. (6.24), yields a straightforward visualization of minima and maxima in $p_{N_M}(\eta, S_p, T)$ without knowledge of $Y(\mu_M, S_p, T)$.

Figure 6.15a shows the $f(N_M)$ representation for the underpotential region ($\eta > 0$) for a NP of Au(1289) with truncated octahedral shape at 300 K, obtained for computer simulations [26]. We can note the convergence of the sum, for $N_M > 600$. For η close to the bulk deposition potential of M, $0 < \eta < 4$ mV, the system presents the highest probability at $N_M \approx 480$ (note $a_2 < b_2$ in Fig. 6.15a). In this region an ensemble of systems should be mainly composed of core-shell NPs with a coverage close to 75%. At $\eta \approx 4$ mV the system has $a_2 \approx b_2$ and therefore we would observe the coexistence of particles with two different coverages. At larger η , for example in the range of $4 \text{ mV} < \eta < 13 \text{ mV}$, the highest probable density is for a coverage close to 15%, where $N_M \approx 98$. This value corresponds to the decoration of all {100} facets.

In the overpotential region, the sum (6.26) will diverge and some physical considerations must be made to get physical insight into the present problem in spite of this mathematical divergence. Figure 6.15b shows the normalized $f(N_M)$ (to its maximum value) for the same conditions as in Fig. 6.15a but for $\eta < 0$ (overpotential). The local maximum is shifted from $N_M \approx 480$ to $N_M \approx 636$ for $-5 \text{ mV} < \eta < -220 \text{ mV}$ (See inset in Fig. 6.15b). Similarly to the observation within the HC model, as the overpotential becomes more negative (oversaturation), the mathematical divergence of the probability function is shifted towards lower N_M .

We must note that for the present system the core-shell structure is not completely formed at underpotentials, and due to border effects, it requires large negative overpotentials to occur. However, large negative overpotentials will make the monolayer eventually unstable and a multilayer will appear.

6.5 Atomistic Model for Underpotential Deposition on Nanoparticles

In order to make a qualitative analysis, a simplified model can be set up that allows describing ΔG^{sub} in terms of the geometry of the NP. Figure 6.16 shows a scheme of the simplified model we address here. We define three regions in the system: an inner part (inner), an intermediate part (intermediate), and an external part (monolayer). The former two belong to the pre-existing seed and they build the core of a core@shell structure in the case of heteroatomic growth.

We will characterize the energy of the inner atoms by the chemical potential of the bulk S atoms, μ_S^{bulk} and define two types of atoms in the intermediate region: those located on the facets, characterized by the free energy g_S^{facet} , and those located at border sites, with the free energy g_S^{border} . In the case of the monolayer, we also differentiate between facet and border adatoms, with their free energies given by $g_{S/M}^{\text{facet}}$ and $g_{S/M}^{\text{border}}$ respectively, see Fig. 6.16.

According to the model mentioned before, the Gibbs free energy of the core (initial state) may be approximated as:

$$G^{\text{S}_p} = N_S^{\text{core}} \mu_S^{\text{bulk}} + N_S^{\text{facet}} g_S^{\text{facet},0} + N_S^{\text{border}} g_S^{\text{border},0} \tag{6.29}$$

As we will analyze later, the second term of the right side of the equality (6.29) may be interpreted as the “surface” effects while the third term can be interpreted as “curvature” effects. On the other hand, the Gibbs free energy of the core@shell NP may be estimated as:

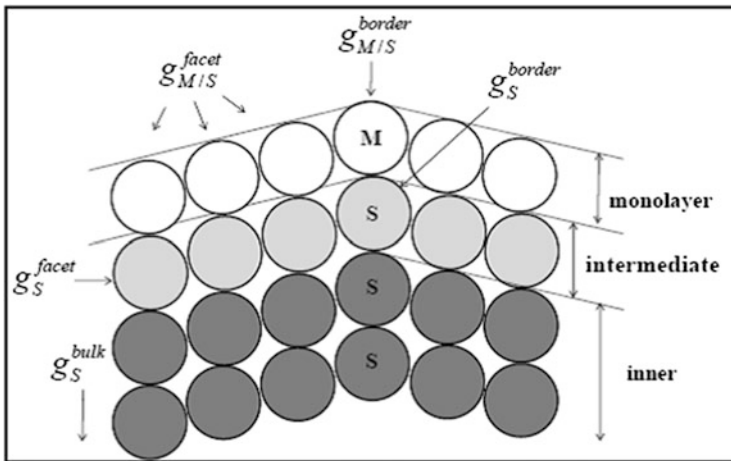


Fig. 6.16 Schematic representation of the simplified model used to analyze upd on NPs, described in terms of five different atom types

$$G^{S_p @ M_{NM}} = N_S^{\text{core}} \mu_S^{\text{bulk}} + N_S^{\text{facet}} g_S^{\text{facet},0} + N_S^{\text{border}} g_S^{\text{border},0} + N_{S/M}^{\text{facet}} g_{S/M}^{\text{facet}} + N_{S/M}^{\text{border}} g_{S/M}^{\text{border}} \quad (6.30)$$

We should notice that $g_S^{\text{facet},0} \neq g_S^{\text{facet}}$ and that $g_S^{\text{border},0} \neq g_S^{\text{border}}$ given that the presence of the shell modifies the configuration (and the energy) of the core surface layer. The difference of formation energy may be estimated by subtracting Eq. (6.30) from Eq. (6.29), so that:

$$G^{S_p @ M_{NM}} - G^{S_p} = N_S^{\text{facet}} (g_S^{\text{facet}} - g_S^{\text{facet},0}) + N_S^{\text{border}} (g_S^{\text{border}} - g_S^{\text{border},0}) + N_{S/M}^{\text{facet}} g_{S/M}^{\text{facet}} + N_{S/M}^{\text{border}} g_{S/M}^{\text{border}} \quad (6.31)$$

Equation (6.31) indicates that the free energy change $G^{S_p @ M_{NM}} - G^{S_p}$ only depends on the energetic of the two more external layers. ΔG^{sub} can be estimated as:

$$\Delta G^{\text{sub}} = N_S^{\text{facet}} (g_S^{\text{facet}} - g_S^{\text{facet},0}) + N_S^{\text{border}} (g_S^{\text{border}} - g_S^{\text{border},0}) + N_{S/M}^{\text{facet}} (g_{S/M}^{\text{facet}} - \mu_M^{\text{bulk}}) + N_{S/M}^{\text{border}} (g_{S/M}^{\text{border}} - \mu_M^{\text{bulk}}) \quad (6.32)$$

It can be noticed that N_S^{facet} and $N_{S/M}^{\text{facet}}$ are linearly related, such as $N_S^{\text{facet}} = \kappa N_{S/M}^{\text{facet}}$, where κ is a geometrical coefficient (generally $\kappa > 1$). The same occurs for N_S^{border} and $N_{S/M}^{\text{border}}$. We can rewrite the previous equation as:

$$\Delta G^{\text{sub}} = N_{S/M}^{\text{facet}} (g_{S/M}^{\text{facet,eff}} - \mu_M^{\text{bulk}}) + N_{S/M}^{\text{border}} (g_{S/M}^{\text{border,eff}} - \mu_M^{\text{bulk}}) \quad (6.33)$$

Then, $\Delta \tilde{G}$ may be estimated from:

$$\Delta \tilde{G} = N_{S/M}^{\text{facet}} (g_{S/M}^{\text{facet,eff}} - \mu_M^{\text{bulk}} + ze_0\eta) + N_{S/M}^{\text{border}} (g_{S/M}^{\text{border,eff}} - \mu_M^{\text{bulk}} + ze_0\eta) \quad (6.34)$$

The present model implies that the excess of energy has at least two components: one related to the facets and other related to the borders. If $N_{S/M}^{\text{border}} \ll N_{S/M}^{\text{facet}}$ as it is the case for relatively large NPs, $\Delta \tilde{G}$ is reduced to the behavior of an infinitely flat surface.

The generalization of model for NPs formed by different types of facets and borders is straightforward:

$$\Delta\tilde{G} = \sum_i^{\text{sites}} N_{S/M}^i \left(g_{S/M}^{i,\text{eff}} - \mu_M^{\text{bulk}} + ze_0\eta \right) \quad (6.35)$$

6.6 Strengthening and Weakening of Underpotential Deposition at the Nanoscale. Underpotential Deposition-Overpotential Deposition Transition

To analyze a little more in detail how curvature effects play a role in favor or against upd, we can consider a relationship between $N_{S/M}^{\text{border}}$ and $N_{S/M}^{\text{facet}}$, within a given family of NPs, that is, with a particular geometry. In a general way, we can define $N_{S/M}^{\text{border}} = \delta \left(N_{S/M}^{\text{facet}} \right)^{1/2}$ where $\delta > 0$ is a geometrical factor that depends on the shape of the NP. In this way, the number of variables in Eq. (6.34) can be reduced. In this context, we can find from the later equation that [52]:

$$\Delta\tilde{G} = 0 \quad \Rightarrow \quad N_{S/M}^{\text{facet},*} = \left[\delta \frac{\left(g_{S/M}^{\text{border,eff}} - \mu_M^{\text{bulk}} + ze_0\eta \right)}{\left(g_{S/M}^{\text{facet,eff}} - \mu_M^{\text{bulk}} + ze_0\eta \right)} \right]^2 \quad (6.36)$$

$N_{S/M}^{\text{facet},*}$ must be interpreted as a threshold value that must be overcome for a thermodynamically spontaneous deposition, with $\Delta\tilde{G} < 0$. The number $N_{S/M}^{\text{facet},*}$ is straightforwardly related to the total number of atoms in the shell N_M , since $N_M = N_{S/M}^{\text{border}} + N_{S/M}^{\text{facet}}$.

The reason for the system to present a $\Delta\tilde{G} < 0$ lays on the strong interaction between adsorbate and substrate in the facets. In the case of infinite planar surfaces, this is the interaction responsible for upd. If metal atoms deposited on a facet of S are more stable than in the bulk state, $g_{S/M}^{\text{facet,eff}}$ will be more negative than μ_M^{bulk} and we will have the inequality $\left(g_{S/M}^{\text{facet,eff}} - \mu_M^{\text{bulk}} \right) < 0$. Let us analyze the consequence of this condition in Eq. (6.34), for $\eta = 0$, which becomes equal to Eq. (6.33). Since the second term in Eq. (6.33) is usually positive, the condition $\Delta\tilde{G} = 0$ will be fulfilled at some $N_{S/M}^{\text{facet},*}$. Thus, the adsorbate atoms will subsist on the surface of S at more positive potentials than the Nernst reversible potential for bulk M deposition. This reminds us the occurrence of the upd phenomenon on flat metal surfaces. The reverse situation will take place when $\left(g_{S/M}^{\text{facet,eff}} - \mu_M^{\text{bulk}} \right) > 0$, since ΔG^{sub} in Eq. (6.33) will be always positive. The latter is clearly an unsuitable condition for size and shape control of nanosystems since when $\eta < 0$, the bulk deposit can be formed so that the application of an overpotential allowing the deposition on S should inevitably drive it to M-bulk growth, at least from a thermodynamic viewpoint. In the model described in Fig. 6.16 and Eqs. (6.28), (6.29), (6.30),

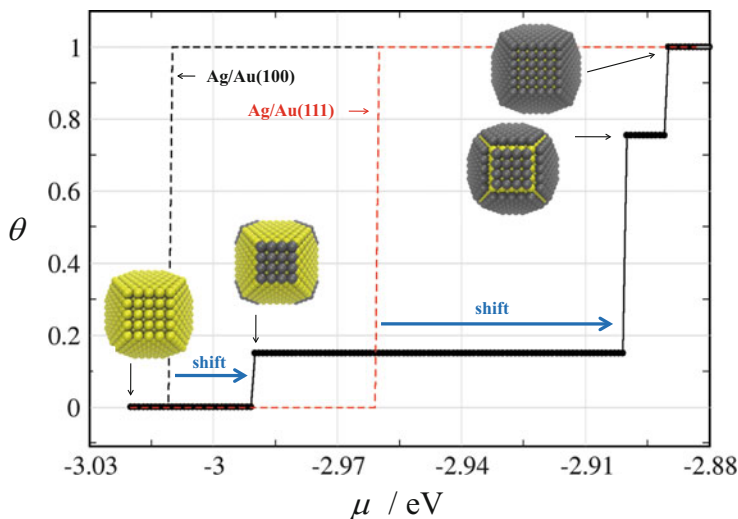


Fig. 6.17 Adsorption isotherms for Ag deposition on a Au truncated octahedral nanoparticle made of 1289 atoms. For comparison, the isotherms corresponding to Ag deposition on Au(100) (black dashes) and Au(111) (red dashes) are shown

(6.31), (6.32), (6.33), (6.34), and (6.35), $g_{S/M}^{\text{facet}}$ and $g_{S/M}^{\text{border,eff}}$ have been assumed to be constant. In the real case, these quantities are a function of NP size.

Figure 6.17 shows adsorption isotherms for Ag adsorption on a Au NP of octahedral shape, as well as on planar Au(111) and Au(100) surfaces. These were obtained from lattice Grand Canonical Monte Carlo simulations using embedded atom potentials. It is illustrative to compare the potentials at which the {111} and {100} facets are filled, in comparison with the decoration of the infinite surfaces. It is found that in the case of the NP, curvature plays a destabilizing role concerning upd. It can be noted that while upd on (111) and (100) faces occur at $\mu_{\text{Au}\{111\}/\text{Ag}}^{\text{bulk}} \approx -2.968$ eV and $\mu_{\text{Au}\{100\}/\text{Ag}}^{\text{bulk}} \approx -3.018$ eV, the related processes on the facets of the NP take place at $\mu_{\text{Au}\{111\}/\text{Ag}}^{\text{NP}} \approx -2.907$ eV and $\mu_{\text{Au}\{100\}/\text{Ag}}^{\text{NP}} \approx -2.990$ eV. These values correspond to shifts in the deposition chemical potentials of $\Delta\mu_{\text{Au}\{111\}/\text{Ag}}^{\text{NP}} \approx 61$ mV and $\Delta\mu_{\text{Au}\{100\}/\text{Ag}}^{\text{NP}} \approx 28$ mV for the {111} and {100} facets respectively. Thus, these simulations clearly show the existence of a positive shift of metal deposition towards larger chemical potentials for nanoparticles, thus weakening upd. We remind that more positive chemical potentials correspond to more negative electrode potentials in the electrochemical scale.

Going back to Eq. (6.36) for NPs, we find that the stronger the border effects, given by the $\left(g_{S/M}^{\text{border,eff}} - \mu_M^{\text{bulk}}\right)$ term, the larger the NP size at which the upd-opd transition occurs will be. On the opposite, systems with large upd shifts in flat surfaces, involving a large $\left(g_{S/M}^{\text{faceta,eff}} - \mu_M^{\text{bulk}}\right)$ contribution, will present the upd-opd transition at smaller NP sizes. According to computer simulations, upd has been predicted to disappear for small particles sizes in the Au(core)/Ag(shell)

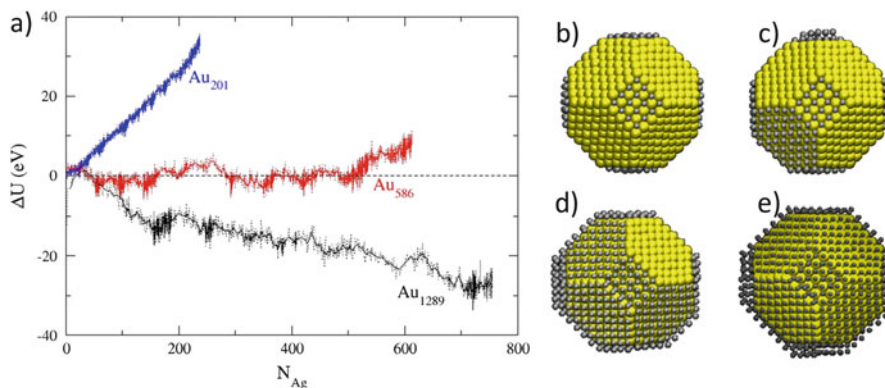


Fig. 6.18 (a) Excess energy as a function of the number of deposited Ag atoms for Au nanoparticles of different sizes at $\eta = 0$. Representative atomic configurations taken for Au (1289) at (b) $\eta = -220$ mV, (c) $\eta = -40$ mV, (d) $\eta = -20$ mV, and (e) $\eta = 0$ (Reprinted with permission from Ref. [136])

[25, 26, 136, 137] and Au(core)/Pd(shell) systems [52]. In the experimental field, there is evidence that upd may disappear for Pb and Cd deposition on Ag NPs [138, 139, 140]. Figure 6.18 shows Off-Lattice Grand Canonical Monte Carlo (GCMC) simulations for the system Au(core)@Ag(shell), where it comes out that the upd phenomenon disappears for core sizes smaller than 512 atoms. Representative snapshots of GCMC simulations, corresponding to different overpotentials, are presented on the right of Fig. 6.18b–e, where selective decoration of some facets of the NP becomes evident.

In the case of systems with relatively strong substrate-adsorbate interactions, it is possible to obtain an adsorbate bilayer at underpotentials, as was discussed in Chaps. 2 and 3. Following the preceding discussion, bilayer upd may also be weakened (strengthened) by the occurrence of positive (negative) curvatures. According to theoretical predictions, this should be the case of the system Pd@Au(bilayer). For this system, we have calculated the excess potential energy using Pd-seed NPs of icosahedral structure with different sizes, on which different numbers of atomic layers of Au-adsorbate were located. These excesses are shown in Fig. 6.19. When analyzing Fig. 6.20, it must be taken into account that the curves connect systems with the same number of layers. For example, the black curve connects Pd(13)@Au(42), Pd(55)@Au(92), Pd(147)@Au(162), Pd(309)@Au(252), Pd(561)@Au(362) and Pd(923)@Au(492), that is, increasing Pd core sizes, always covered by a Au monolayer. As can be observed, the free energy excess for small NPs is positive. However, the excess of free energy for monolayer formation turns negative for Pd(309)@Au(252) and remains negative for larger cores, indicating that upd could be possible for larger NPs. It is also remarkable that the curve for the formation of the bilayer presents a maximum, indicating that for larger NP sizes bilayer formation could be spontaneous at $\eta = 0$.

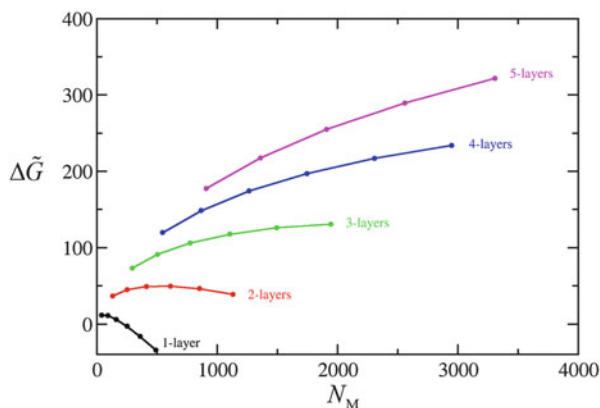


Fig. 6.19 Excess of binding free energy for the formation of a Pd(core)@Au(shell) nanoparticle as a function of the number of atoms forming the shell. Each curve corresponds to a given number of adlayers deposited on different core sizes (Reprinted with permission from Ref. [141])

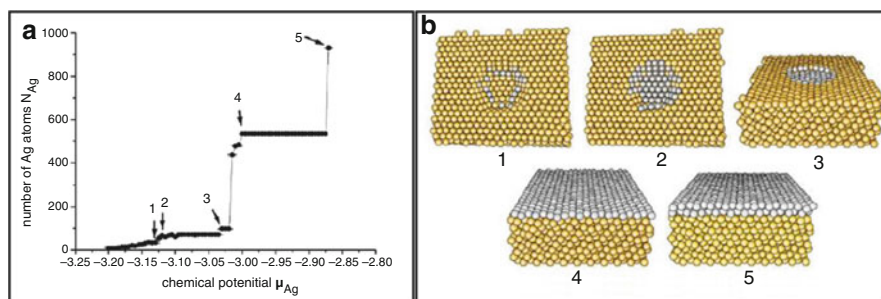


Fig. 6.20 Number of deposited Ag atoms as a function of the chemical potential for decoration of a nanocavity on a Au(111) surface. (b) Snapshots of the simulation showing the different stages of nanohole decoration, corresponding to the numbers of part (a). The chemical potentials were $\mu_{\text{Ag}} = -3.155$ eV, $\mu_{\text{Ag}} = -3.12$ eV, $\mu_{\text{Ag}} = -3.03$ eV, and $\mu_{\text{Ag}} = -3.00$ eV (Reprinted with permission from Ref. [53])

Going back to the nanohollow case, computer simulations of this phenomenon were undertaken by Luque et al. [53] using the Off-Lattice GCMC methodology. These studies showed that depending on the interaction between the adsorbate and the substrate as compared with the adsorbate–adsorbate interactions, the deposit may grow defining a cluster over the surface level, like Au(111)/Cu or heal the damage on the surface with the subsequent formation of a monolayer, like Au(111)/Ag. In the former case, Cu deposition remains confined to the defects generated on the surface, since the formation of clusters on the Au(111) is disfavoured. On the contrary, Ag deposition on the flat Au(111) surface occurs after the filling of the nanocavity.

Figure 6.20 shows the results from Off-Lattice GCMC atomistic simulations for the decoration of nanocavities on Au(111) with Ag atoms. The decoration of the

nanocavity starts at $\mu_{\text{Ag}} = -3.155$ eV at its bottom, being the first Ag atoms deposited on the border sites. The basis of the nanocavity becomes completely covered at $\mu_{\text{Ag}} = -3.12$ eV and its filling occurs at $\mu_{\text{Ag}} = -3.03$ eV. All these processes take place at chemical potentials more negative than that corresponding to the bulk Ag metal, $\mu_{\text{Ag}} = -3.00$ eV. These atomistic simulations showed for the first time that negative curvatures allow metal deposition at more negative chemical potentials (more positive electrode potentials on the electrochemical scale) than those corresponding to upd on planar surfaces with the same crystal orientation.

6.7 Experimental Research

Although a bimetallic nanocrystal consists of only two elements, it may exist in many different structures depending on the spatial distributions of these two elements. We will describe some techniques of electrochemical origin that allow the manipulation of this degree of freedom, as follows:

6.7.1 Seed-Mediated Growth

The growth of NPs or nanorods (NRs) mediated by seeds has demonstrated to be an easy and versatile route for metallic nanocrystal formation with well-defined size and shape [16, 54–57]. Originally, Zsigmondy called this technique “nuclear method” [58] and its origin dates from the beginning of last century. In 1920, Svedberg stated that any reducing agent (known at that time) could produce Au-NPs from HAuCl_4 [59]. The technique is very versatile and can be applied in aqueous systems as well as in organic systems [60, 70] at different temperatures and for a large number of systems that include Au, Ag, Pd and Pt [30, 48, 61–71]. The first step consists in the production of clusters and/or NPs which may be used as growth seeds. Generally, this process is called “first nucleation”. Metallic salts may be reduced at room temperature with a strong reducing agent (for example, borohydride). It is necessary to overcome the large barrier of homogenous nucleation for the formation of a new phase. In a second stage, this preformed seeds are put into a solution to serve as preferential sites for a new process of nucleation and growth. This second step is called “growth stage”. The growth of a second metal can be involved in this second stage, or not. In Sect. 6.2.2 we discussed these topics and we presented the LaMer model to understand the behavior of the phases in this stage.

The driving force for NP growth is the difference between the redox potentials (ΔE) of the two reactions (metallic reduction and oxidation of the reducing agent). A larger ΔE means a more spontaneous reaction. Reagent concentration,

temperature, and pH influence the growth kinetics as well as the size, shape and structure of the final NPs. For example, a strong reducing agent such as NaBH_4 or phosphorus can be used for the production of small size Au NPs, while ascorbic acid – a weak reducing agent – produces larger NPs. NP aggregation can be avoided through a strong shaking or by adding stabilizing agents.

Homogeneous nucleation and growth generally produces irregularly shaped particles and a wide size distribution. The activation energy for the process of heterogeneous nucleation is significantly lower than the activation energy for the process of homogeneous nucleation. As a result, heterogeneous nucleation is thermodynamically favored with respect to homogeneous nucleation. While homogeneous nucleation and growth can be described in terms of a curve like that shown in Fig. 6.13a, its heterogeneous counterpart can be represented by Fig. 6.13a or Fig. 6.13b, depending on the effective interactions between the elements that constitute the core and the shell. In practice, seed-mediated growth takes place at a relatively slow rate in soft conditions, such as those provided by a weak reducing agent and/or low temperatures. The reduction on the surface of the seed can be viewed as an autocatalytic process. As the NP acquires a larger size, the nucleation barrier becomes smaller.

In general, metals tend to nucleate and grow in thermodynamically stable nanoparticles, which exhibit a compact shape. These NPs expose facets of low energy in order to minimize the total energy of the surface. Highly anisotropic shapes are not favorable from the thermodynamic point of view, but can be obtained by inserting agents that can alter the surface energies of the different crystallographic faces [71]. Carbó-Argibay et al. [61] analyzed in detail the growth of Au nanorods (NRs) using well-characterized Au-NPs as growth seeds. Initially, see Fig. 6.21a, the NRs present eight $\{110\}$ and $\{100\}$ facets, alternated in their lateral parts. Their tips consist of $\{001\}$, $\{110\}$ and $\{111\}$ facets. The first step in the

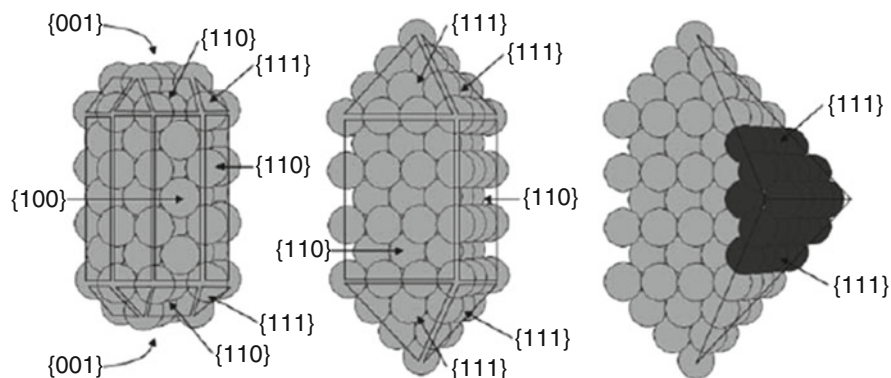


Fig. 6.21 Structural model of Au nanorod growth. *Left*: Original nanorod with octagonal cross-section and $\{100\}$, $\{110\}$, $\{111\}$ facets. *Center*: Rod with sharp tips, square cross-section, $\{110\}$ and $\{111\}$ facets. *Right*: Growth of a sharpened rod into an octahedral particle by deposition of Au atoms (*dark spheres*) along the $\{110\}$ facets (Reprinted with permission from Ref. [61])

growth consists in the preferential deposition of Au atoms on the 4 {100}-type facets from the lateral part and on the 2 {100}-type facets at the tips (see Fig. 6.21b). As a result, 4 lateral {110} facets were obtained, as well as sharp tips made from 4 {111} facets (Fig. 6.21b). The second growth stage consisted in a morphological transition to become an octahedron. This is produced by means of a delicate balance between the growth rates on facets {110} and {111}. Fig. 6.21c shows schematically the growth on {110}-type facets, forcing facets {111} to grow until they join in the final octahedral structure.

The mechanism described in Fig. 6.21, is based on the preferential growth of certain crystal facets. It could be formally correlated with the sequence of surface energies in the following order: $\{100\} > \{110\} > \{111\}$. This does not agree with the sequence of surface energies of Au, which follows the order: $(110) > (100) > (111)$. However, as these authors noted in Reference [61], the effective values of surface energies can be affected by the adsorption of chemical species such as ions and molecules in a significant way and thus, they can be assumed to be responsible for such changes and could explain such a tendency. Although there is no concrete evidence to support these assumptions, these results show that the crystallographic structure of the seeds, together with the chemical nature of the bath where they grow, play a key role in the determination of the NPs final structure and shape. Thus, these results present a strong indication that surfactant ions and molecules can affect the growth kinetics and can help to control the final shape of the NPs. For example, citrate binds strongly to Pd {111}-type facets, leading the synthesis towards octahedra and icosahedra formation [72]. In contrast, polyvinylpyrrolidone is a protecting agent, which binds stronger to Pd {100}-type facets, favoring the formation of truncated cubes [73, 74]. Besides, bromide ions promote Pd-NP formation exposing {100} facets [75].

A versatile approximation to the formation of bimetallic NPs core@alloy type is called co-reduction mediated by seeds [76–78]. In this technique, two metallic precursors are simultaneously reduced on a NP used as growth seed. This technique allows control of the NP morphology, obtaining branched NPs commonly called nanodendrites. DeSantis et al. [76] made a systematic study on the influence of synthesis conditions on the morphology of nanodendrites. These authors analyzed the role of the concentration of precursors (ratio Au/Pd), reaction pH, and concentration of NP protecting agent. For example, Fig. 6.22 shows the structural variation of Au/Pd NPs at different pH values for otherwise the same reaction conditions. The pH was adjusted by adding different amounts of HCl to the system (from A up to F corresponds to 2 mL of 0.0, 12.5, 25.0, 37.5, 50.0, and 62.5 mM HCl, respectively). Pd became dispersed all over the surface of the octopods and became localized along the tips of the branched nanostructures, with Au predominating in the interior of the particles (Fig. 6.22 4A, 4B). We note that Pd-rich regions appear lighter in TEM and STEM images, as $Z_{\text{Au}} > Z_{\text{Pd}}$. With decreasing pH, the SEM images reveal regions of negative curvature associated with the absence of {100} facets of what would otherwise be cuboctahedral particles (Fig. 6.22 4C–4E). Finally, a perfect octahedral NP was obtained at a relatively low pH (Fig. 6.22 4F). At a larger content of HCl (lower pH) the inner part of the NPs becomes more abundant in Au and

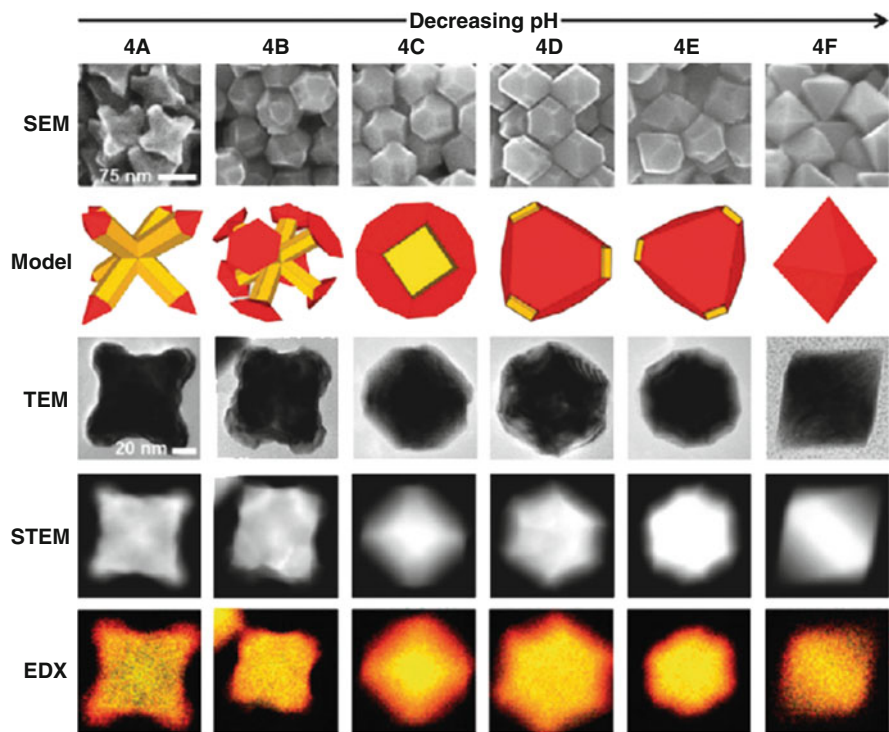


Fig. 6.22 From *top to bottom*, AuPd nanocrystals characterized by higher magnification SEM as well as 3D models (yellow represents Au-rich and red represents Pd-rich regions), TEM, STEM, and STEM-EDX mapping (yellow indicates Au and red indicates Pd). Note: all SEM images are at the same magnification. Similarly, TEM, STEM, and STEM-EDX mapping are at the same magnification (Reprinted with permission from Ref. [76])

show cuboctahedral or octahedral structures. These are thermodynamically favored structures. In opposite conditions, at high pHs, the amino acid reducing capacity is larger; consequently, the reduction velocity is faster and the system has not enough time to re-adapt, thus obtaining structures very different from the ones predicted by thermodynamics (kinetic control). Another way to control morphological changes is the formation of complexes with CTAB by etched Au. It is known that the Au oxidation rate under these conditions depends on pH, so that the regions with larger curvature are more prone to oxidation [79].

As a corollary to this section and the following, we can state that all the information gained through research about the effect of solution composition (ions, molecular adsorbates) on the stability of upd deposits on single crystal surfaces is worth being analyzed with the aim of their application to the synthesis of NPs. Alternatively, many of the questions arising in the synthesis of nanoparticles may probably be answered by means of electrochemical studies of metal upd (and the related galvanic replacement technique) on single crystal surfaces.

6.7.2 *Shape Control of Nanoparticles Synthesis by Underpotential Deposition*

Liu and Guyot-Sionnest [80] proposed, in 2005, an explanation for the role of Ag ions in the directed growth of Au NPs. They suggested that upd of metallic silver occurs at different extents on the different crystal facets of Au NPs, leading to symmetry breaking and rod formation. It is known that upd of Ag is stronger on more open surfaces, involving the sequence stability $\{111\} < \{100\} < \{110\}$. In fact, electrochemical measurements yielded underpotential shifts of 0.24 and 0.07 V for Ag upd on Au $\{100\}$ and Au $\{111\}$ surfaces, respectively [81, 82]. The same trend has been found in theoretical calculations, predicting that the upd shift should be 0.14 V for Ag on Au(100) and 0.10 V for Ag on Au(111) [83]. As a consequence of this, an appropriate tuning of the deposition potential would allow decorating selectively facets (see Figs. 6.17 and 6.18). Similarly, a silver monolayer on the Au $\{110\}$ facet acts as a strong binding agent, inhibiting further growth, so that other low index faces grow faster and become dominant in the final structures. The $\{100\}$ and $\{111\}$ facets are only partially covered by silver or remain adsorbate free, and therefore grow faster than $\{110\}$. This leads to a one-dimensional growth along one direction. The growth rate ratio between $\{100\}$ and $\{110\}$ facets is adjustable by varying the Ag^+ concentration. Then, upd provides a general mechanism to control shape evolution in metallic nanostructures [84].

Seo et al. [85, 86] determined the major influencing factor for shape conversion of cuboctahedral NPs. Cuboctahedral NPs are built from $\{100\}$ and $\{110\}$ facets, as shown in Fig. 6.23a (middle picture) and Fig. 6.23c. Ag^0 reduced from Ag^+ was preferentially deposited onto the $\{100\}$ facet to form silver layers, which suppressed epitaxial overgrowth of the gold layers during the reaction. The $\{111\}$ facets grew producing changes in the NP morphology. This change transformed the NPs from octahedral shapes to cuboctahedral and then to cubic shapes (Fig. 6.23a, d). In the absence of silver ions, the addition of Au^{3+} precursor enhances $\{100\}$ growth to increase the surface fraction of $\{111\}$ facets. That process makes cuboctahedral NPs to become octahedral ones, where only $\{111\}$ facets are present (Fig. 6.23a, b). This procedure was also applied for redirecting and controlling Pt NPs growth [87].

Mirkin and coworkers [88] have also shown that a fine control of NP shape is possible using Ag upd to direct the growth of different Au-NPs morphologies: for example, octahedrons with $\{111\}$ facets, rhombic dodecahedrons with $\{110\}$ facets, truncated ditetragonal prisms with $\{310\}$ facets, and concave cubes with $\{720\}$ facets. In a later work, Mirkin and coworkers [89] analysed in detail the effect of including other additives like chloride, bromide and iodide on NP growth under Ag-upd control. These authors showed how different sets of NP shapes can be obtained via kinetic control, surface passivation, or a combination of both. A number of important findings emerged from this work, some of them are:

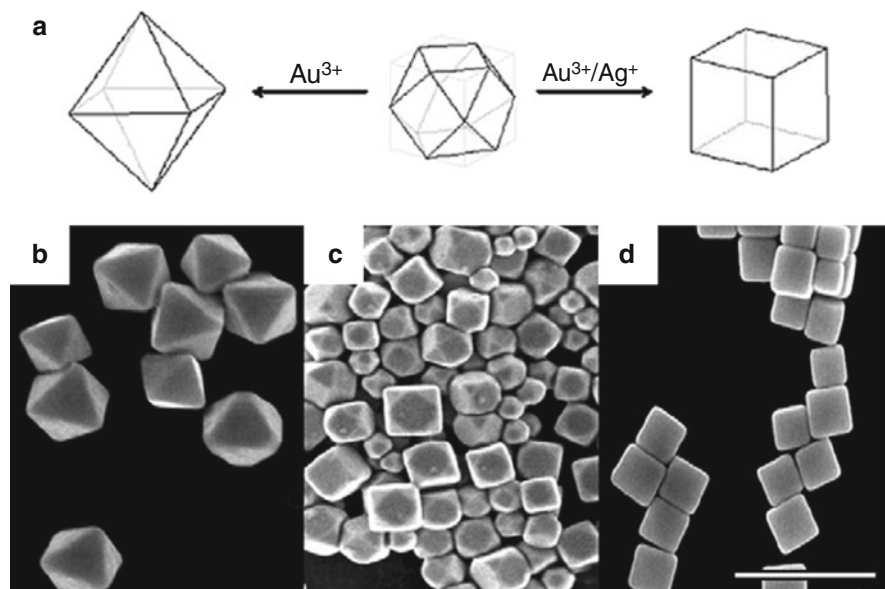


Fig. 6.23 (a) Shape evolution of cuboctahedral seeds by changing the growth solutions. SEM images of (b) large octahedra grown by addition of the gold precursor, (c) cuboctahedral seeds, and (d) cubes grown by addition of Ag^+ and the gold precursor. The bar represents 500 nm (Reprinted with permission from Ref. [86])

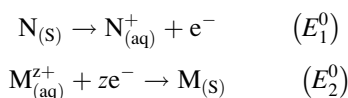
- (a) In the absence of bigger halides (bromide and iodide), increasing concentrations of silver ions stabilize particles with a larger number of exposed surface atoms per unit surface area, enabling the formation of high-index nanostructures.
- (b) In the presence of silver ions as a shape-directing additive, the addition of a large amount of the bigger halides (bromide and iodide) greatly decreases the stability of the Ag upd layer and blocks silver deposition, limiting the number of particle shapes that can be formed.
- (c) The enhanced stability of the Ag-upd layer in the presence of chloride causes growing Au-NPs to become kinetically “trapped” or “locked” into a particular facet structure early in their growth, enabling the formation of a wide variety of shapes as well as concave particles.

6.7.3 Galvanic Replacement and Underpotential Deposition

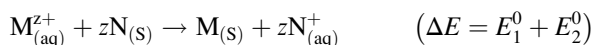
The main obstacle for the implementation of upd to a large quantity of systems is the fact that this phenomenon is usually limited to the deposition of a less noble metal on a more noble one, as it is for example the case of the Au(hkl)/Cu and Pt (hkl)/Cu systems. In the case of electrocatalytic applications, the situation is right

the opposite to the desired one, for example Cu(hkl)/Pt structures are wished. One way to circumvent this problem is to use a technique denominated galvanic replacement (gr). In 2001, Brankovic et al, followed by other groups, reported a facile route to the synthesis of Pt monolayers on Pd as base metal via gr of an upd Cu monolayer on a Pd core with a Pt precursor [46, 90, 91]. A year later, the first example of gr involving nanoscale objects was reported by Sun et al. [92]. The gr reaction is driven by the difference in electrochemical potentials, between a sacrificial template made of one metal and the ions of another metal in a solution phase [93, 94].

In the case of pure metals, galvanic corrosion is a redox process, in which a metal N is corroded by the ions of a second metal $M_{(aq)}^{z+}$ when they are in contact, in a solution phase [95]. The corrosion process can be represented by:

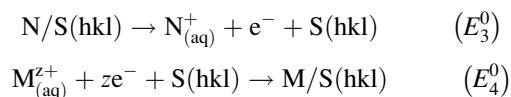


giving the global reaction:



where the N metal is dissolved in solution, simultaneously with M deposition. According to Eq. (6.8), if ΔE is positive, then the corrosion reaction is driven thermodynamically.

In the case of the denominated galvanic replacement applied to upd systems, it involves oxidation and dissolution of an upd template accompanied by reduction of the ions of a second metal and deposition of the resultant atoms on the template:



giving the global reaction:



here, a monolayer of N initially deposited (via upd) on a S surface is dissolved simultaneously with M deposition. By manipulating stoichiometry of the participant species, it is possible to control the degree of coverage of the metal being deposited. For example, a upd monolayer of Cu deposited on a $Au(111)$ surface may generate [90]:

- In the presence $[PtCl_4]^{2-}$, a Pt monolayer on $Au(111)$.
- In the presence $[PtCl_6]^{2-}$, half a Pt monolayer on $Au(111)$.

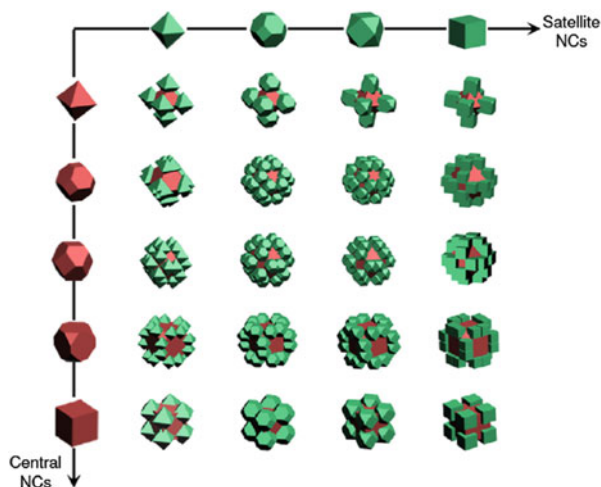
- In the presence of Ag^+ , up to a bilayer of Ag on Au(111).

Galvanic corrosion and upd clearly present similarities but also important differences. Among the later, the most relevant is related to the ΔE value. The reduction couples $E_1^0-E_3^0$ and $E_2^0-E_4^0$ are different, due to the presence of the S surface.

When a metallic substrate occurs at the nanometric scale, gr can be used as a versatile and powerful method for the generation of core@shell type NPs. Park et al. in 2002 [46] (see Fig. 6.7) showed the possibility of the formation of Au@Pd and Au@Pt core@shell type NPs via gr, starting from Au@Cu NPs. Besides its employment for the formation of core@shell type NPs [46, 96–102], gr is widely used today to obtain reversed NPs, hollow particles, hollow nanorods, nanorattles, nanoboxes, alloys and dealloys, among others nanomaterial shapes [103–109]. We will return to this later.

Yu et al. [110] have reported that the electrons which are generated in the gr reaction, may accumulate mainly over specific regions of the NP. The electronic distribution that depends on geometry can be used to direct facet growth. These authors used two metallic precursors: Ag and Pd with a colloidal solution of polyhedral Au NPs. Ag reduced fast on Au-NPs to make an upd layer. Then, this core@shell was subjected to a gr process with Pd^{2+} ions. The electrons in the galvanic replacement reaction accumulate mainly at high curvature regions of the NP such as corners and borders. This preferential accumulation of electrons, which is spatially heterogeneous, directs the deposition to those regions rich in electrons. The distribution of electrons can be altered by controlling the kinetics of electron generation. A slow electron generation rate allows the electrons to accumulate only in regions of the highest curvature, that is, corners of the polyhedral NPs. On the other hand, a fast electron generation rate can disperse the electrons over a wider area, although regions of high curvature are still preferred. In this case, the electrons

Fig. 6.24 Schematic illustration of the architectural diversity of the NP configurations that can be obtained by tuning the shapes of the central NP (*vertical axis*) and satellite NPs (*horizontal axis*) by method described in reference (Reprinted with permission from Ref. [113])



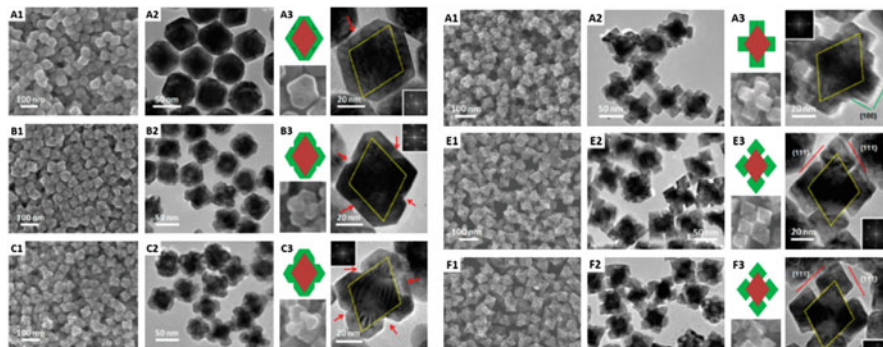


Fig. 6.25 Images obtained for the selective growth of Ag-Pd on Au NPs at different concentrations of AgNO_3 : (a) $1 \mu\text{M}$, (b) $3 \mu\text{M}$, (c) $6 \mu\text{M}$, (d) $10 \mu\text{M}$, (e) $60 \mu\text{M}$ and (f) $80 \mu\text{M}$. The H_2PdCl_4 concentration was $70 \mu\text{M}$. Column 1 shows images obtained by SEM, column 2 images obtained by TEM and column 3 shows cut profiles of the geometrical models along the direction $\langle 110 \rangle$. The red arrows show the V-shape grooves projected from the gaps and depressions (Adapted with permission from Ref. [110])

may congregate along the edges [111]. Fig. 6.24 schematically illustrates some complex nanostructures that can be obtained by using the present synthetic scheme.

The first step consists in controlling the amount of Ag adsorbed on the surface of a NP. A variable amount of Ag deposited allows a galvanic replacement variable process, as shown in SEM and TEM images for relatively low (Fig. 6.25a–c) and high (Fig. 6.25d–f) AgNO_3 concentrations. The Ag layer formed by “in situ” upd, is consumed by the galvanic substitution reaction and it is continuously regenerated by supplying Ag^+ . This Ag-regenerative layer provides a continuous supply of electrons to the corners of the NP in order to support island growth there. A lower AgNO_3 concentration directs a slow formation of Ag upd, thus island growth is restricted. This is the basis of the difference between semicorner-selective deposition and full-corner-selective deposition, schematically shown in Fig. 6.26.

Figure 6.26 shows that the accumulation of electrons, and consequently the deposition along the border regions instead of corners is possible by adjusting the growth kinetics of Au and Pd in combination. Since the growth kinetics of Pd atoms favors the exposure of $\{100\}$ facets and the growth kinetics of Ag atoms favors the increase in the proportion of $\{111\}$ facets (see for example Fig. 6.21), each of these facet types would be preferentially exposed if the growth kinetics were dominated by that of Pd atoms or Ag atoms, respectively. With the increase of the Ag/Pd ratio, the combined growth kinetics can be modified from Pd dominance to Ag dominance. Figure 6.27 shows SEM and TEM images of core(Au)@shell(Ag-Pd) NPs at different relations of $\text{Ag}^+/\text{Pd}^{2+}$. At relatively low relations $\text{Ag}^+/\text{Pd}^{2+}$, the NP shape is truncated octahedral, showing that in synthesis conditions the exposition of facets $\{100\}$ type has been favored. Under these conditions, Pd directs the growth. As the Ag^+ concentration increases, an increase in the size of facets $\{111\}$ type is gradually observed indicating that Ag upd plays the key role.

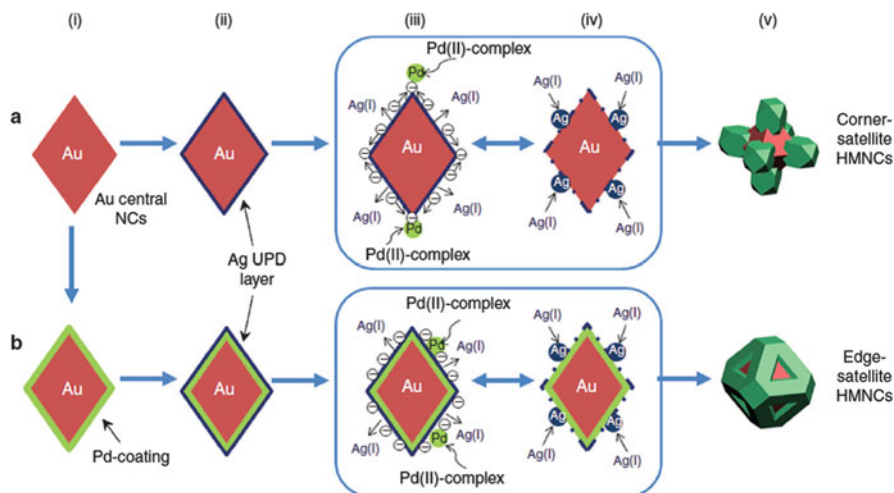


Fig. 6.26 Schematic illustrations of corner- and edge-selective depositions. The corner- and edge-selective depositions are shown in rows a and b, respectively. (i) Au central nanocrystal (NC) with a well-defined morphology. (ii) The Ag precursor is reduced first due to upd and a Ag monolayer is quickly formed on the central NCs. (iii) This in situ formed Ag layer then undergoes galvanic replacement reaction with the Pd precursor due to the difference in their reduction potentials. The electrons released by the galvanic oxidation of the Ag layer then travel and accumulate at the corners (a) or the edges (b) of the Au central NCs because of the high curvatures there. The Pd precursor is reduced and deposited preferentially on those electron-rich regions. (iv) The Ag layer is self-sustaining due to the swiftness of upd, that is, once the Ag atoms in the Ag layer are oxidized and dissolved, upd of Ag immediately occurs to replenish the Ag atoms lost by oxidation. The newly formed Ag upd layer is then be oxidized and regenerated. The cycle goes on (the boxed regions in iii and iv). (v) This cyclic process ensures a continuous supply of electrons to the corners of the central NC to sustain the reduction there. For the preparation of edge-satellite HMNCs, the surface of the Au central NCs was modified by Pd-coating (b(i)), and a Ag layer was formed on the Pd-coated Au NCs (b(ii)) (Reprinted with permission from Ref. [111])

6.7.4 Hollow Nanoparticles Through Galvanic Replacement

NPs are usually defined as polyhedra formed by facets of $\{111\}$ and $\{100\}$ type such as cubes, tetrahedra, octahedra, prisms, cuboctahedra, etc. [112]. Hollow NPs (H-NPs) are nanometric scale crystals formed by facets with Miller indices $\{hkl\}$ larger than the unit [88, 89, 113–116]. H-NPs surfaces are characterized by a great density of steps with low coordinated atoms, which confer large surface energy. Nanocrystals with hollow interiors and porous walls are of great interest and importance for catalytic and electrocatalytic applications, as they can provide high specific surface areas and enhanced activities relative to their solid counterparts. Galvanic replacement offers a facile and versatile approach to the generation of metal nanocrystals with hollow interiors and porous walls.

Figure 6.28 shows the main stages involved in a galvanic replacement reaction for the formation of H-NPs. When a small amount of HAuCl_4 is added to an

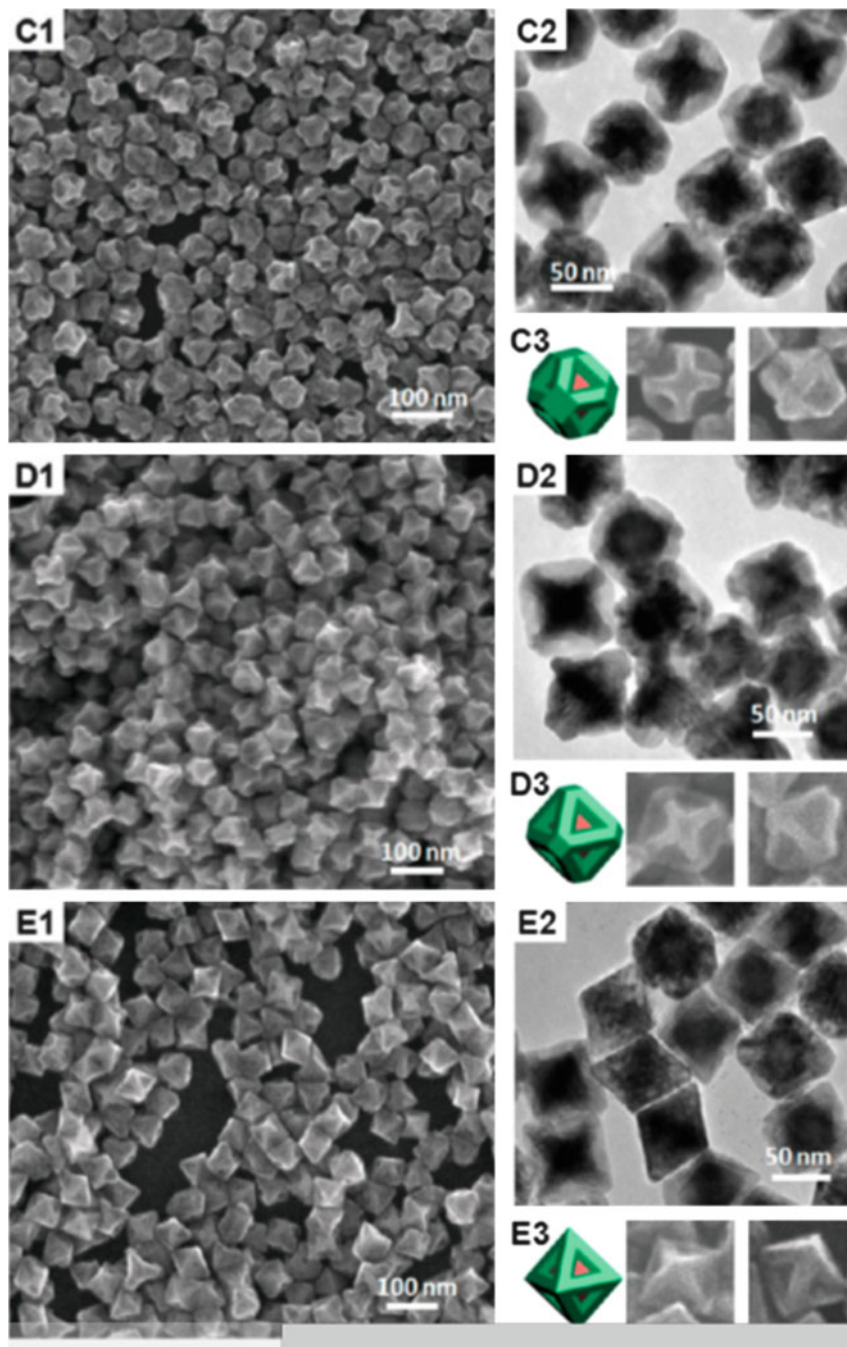


Fig. 6.27 images obtained for the selective growth at the borders shown in Fig. 6.24 and 6.26. The concentrations of AgNO_3 are (c) $20 \mu\text{M}$, (d) $40 \mu\text{M}$ and (e) $60 \mu\text{M}$ H_2PdCl_4 concentration was $100 \mu\text{M}$. Snapshot 1 shows images obtained by SEM, snapshot 2 images obtained by TEM and snapshot 3 shows cut profiles of the geometric models along the direction $\langle 110 \rangle$ and $\langle \bar{1}\bar{1}0 \rangle$ (Adapted with permission from Ref. [110])

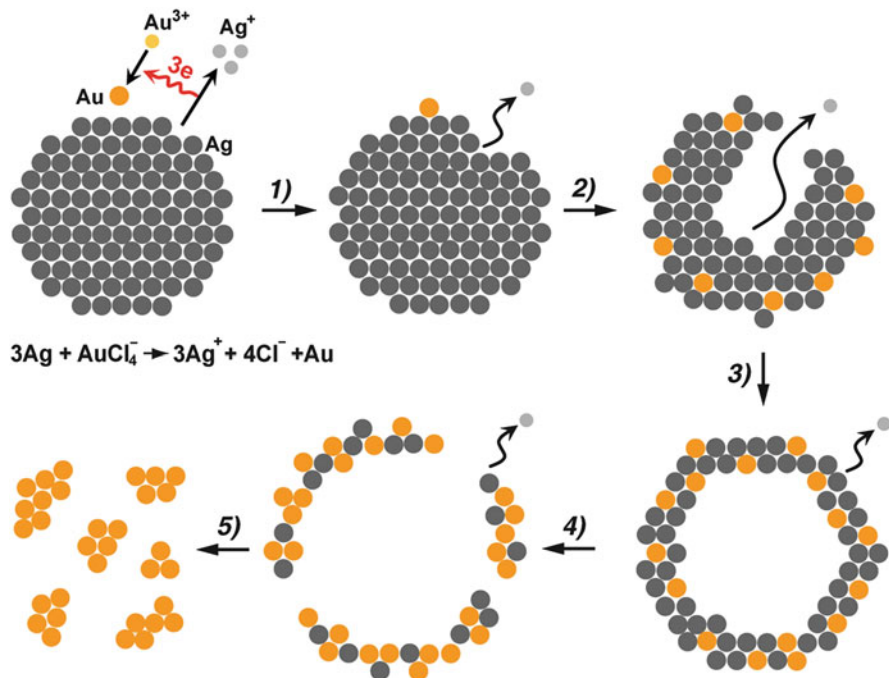


Fig. 6.28 Schematic illustration of the morphological and structural changes at different stages of the galvanic replacement reaction between a Ag nanoparticle and HAuCl_4 in an aqueous solution (Reprinted with permission from Ref. [124])

aqueous solution containing Ag NPs, the galvanic replacement of Ag by Au will start in the regions with large surface energy (for example, imperfections, vertex, corner regions). As a result, Ag atoms oxidize and dissolve into the solution; this generates a small hollow in the NP facet. At the same time, electrons migrate rapidly to the NP surface and are taken by AuCl_4^- to generate Au atoms through a reduction reaction. Due to their similar crystal structures and lattice constants (4.086 Å vs. 4.078 Å for Ag and Au, respectively), the recently formed Au atoms tend to deposit epitaxially on the surface of the NP (step 1 in Fig. 6.28). The deposition will lead to the formation of a thin and complete Au layer on the facets of each NP that prevents the reaction of other Ag atoms with AuCl_4^- below this layer, thus physically blocking the reaction. However, the small hollow generated at the beginning serves as preferential region for the continuous dissolution of Ag atoms. This hollow must have certain size that allows the income of other species allowing the galvanic replacement to take place inside the NP.

The exchange processes and/or surface diffusion may lead to a mixing of the atoms (step 2 in Fig. 6.28), since a homogeneous alloy is thermodynamically more stable than a mixture of segregated Au and Ag phases. In an intermediate state of the galvanic replacement reaction, a hollow interior and an alloy shell (step 3 in Fig. 6.28) characterizes this nanostructure. The thickness of the shell depends on

the size of the initial Ag-NP as seed (sacrificial template) as well as on the stoichiometry of the reacting Au complex. The addition of large amounts of HAuCl_4 to the reaction system, drives a dealloying process by selective elimination of Ag atoms from the alloy shell. This process generates many uncoordinated atoms, vacant regions, etc. which lead to a large increase in the surface free energy. These vacant regions join together, generating small hollows that coalesce and form hollow NPs. The dealloying process can also cause defragmentation of the NP into small Au clusters (step 5 in Fig. 6.28). Different SEM images can be observed in Figs. 6.29b–d, showing the different stages previously described. The addition of a chelate like $\text{Fe}(\text{NO}_3)_3$ is an alternative to favor the process of dealloying of the Au-Ag NP. This chelate dissolves Ag, generating pores in the facets, thus yielding NPs with hollow structures as can be observed in Fig. 6.29. The size of the pores can be controlled by adding a larger amount of $\text{Fe}(\text{NO}_3)_3$ as shown in the SEM images in Figs. 6.29e–g.

In 2011, Gonzáles et al. [117], reported a new application of the traditional concepts of corrosion at the nanoscale. They showed that gr together with the Kirkendall effect can be used to form hollow Au-NPs of many layers. The Kirkendall effect occurs in systems where the diffusion velocities of one on the other material are markedly different, such as Ag diffusion on Au that is larger than Au diffusion on Ag. The process begins with a picture similar to that exposed in Fig. 6.28a, b. The galvanic replacement has generated a hollow Ag cube covered by an external Au layer. Since Ag diffusion on Au is faster than Au diffusion on Ag, this produces a net flow of vacancies from the surface to the core. The concentration of vacancies increases until they coalesce in bubbles that grow at the metallic interface and join, forming a continuous cavity parallel to the cube wall. This allows the interior walls to be coated with Au. These “empty boxes” increase significantly the area/volume ratio of the material and could be used to transport or protect molecules, thus providing important applications in the fields of medicine and energy storage [118] (see Fig. 6.30a).

Trimetallic Ag-Au-Pd structures may also be produced by using the gr method together with the Kirkendall effect. The final product is a double wall nanobox with a Ag nucleus situated between the walls (see Fig. 6.30b), coated with a PdAu alloy or a Au-Pd layer, depending on the addition of the precursors being simultaneous or sequential. In the nanoboxes shown in Fig. 6.30b, Au and Ag form an alloy with interior parts richer in Ag while Pd is preferentially found at the wall surfaces.

6.7.5 Nanoparticles Growth Inside Dendrimers

In the early 2000s, Crooks and coworkers developed a technique for the generation of metallic NPs, denominated “dendrimer-encapsulated nanoparticles (DENS)” [119–121]. A scheme of this procedure is shown in Fig. 6.31.

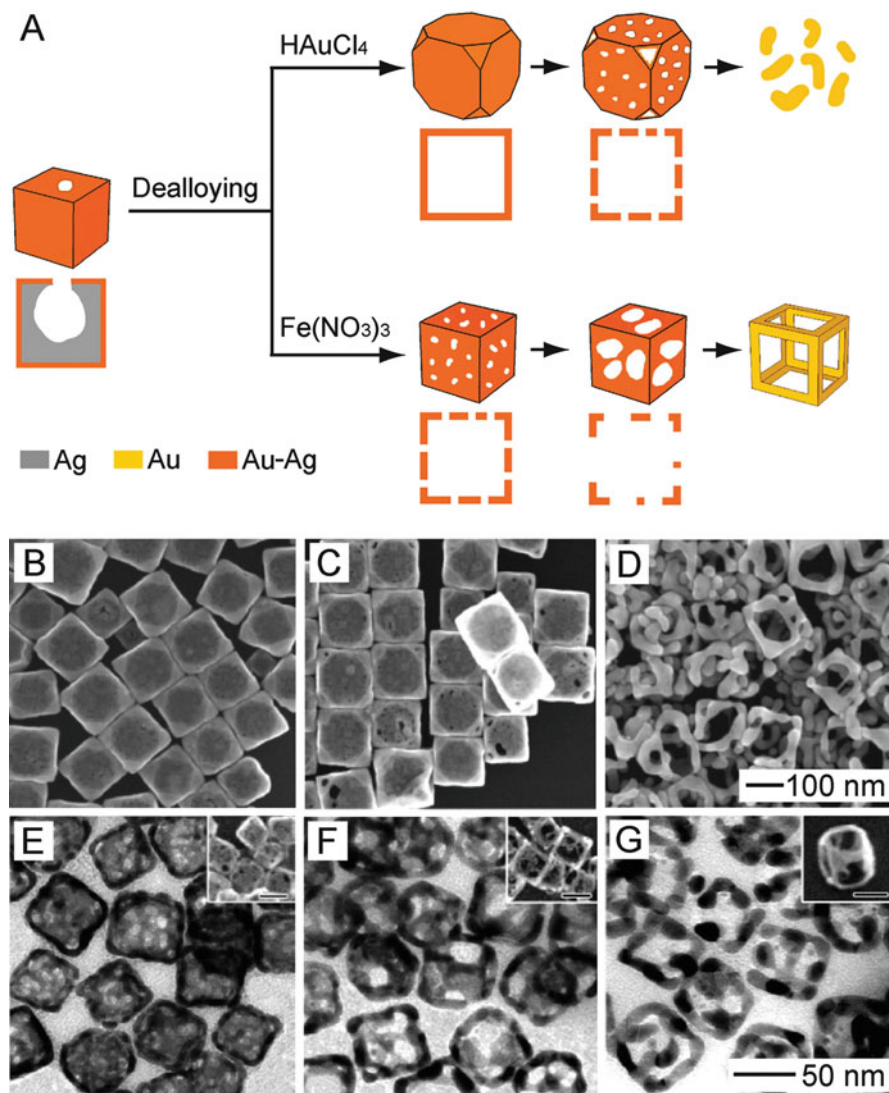


Fig. 6.29 (a) Schematic illustration of two different methods for dealloying involving the use of HAuCl_4 and $\text{Fe}(\text{NO}_3)_3$, respectively, as the etchant. (b–d) SEM images of samples obtained by de-alloying 120 nm partially hollow Au-Ag nanoboxes with increasing amounts of HAuCl_4 . The 100 nm scale bar in (d) applies to (b) and (c). (b–d) are reproduced with permission from Ref. [142]. (e–g) TEM and SEM (insets) images of samples obtained by de-alloying 50-nm partially hollow Au-Ag nanoboxes with increasing amounts of $\text{Fe}(\text{NO}_3)_3$. The 50 nm scale bar in (g) applies to (e) and (f). The scale bars in the insets of (e–g) are 50 nm. (e–g) are reproduced with permission [107] (Reprinted with permission from Ref. [124])

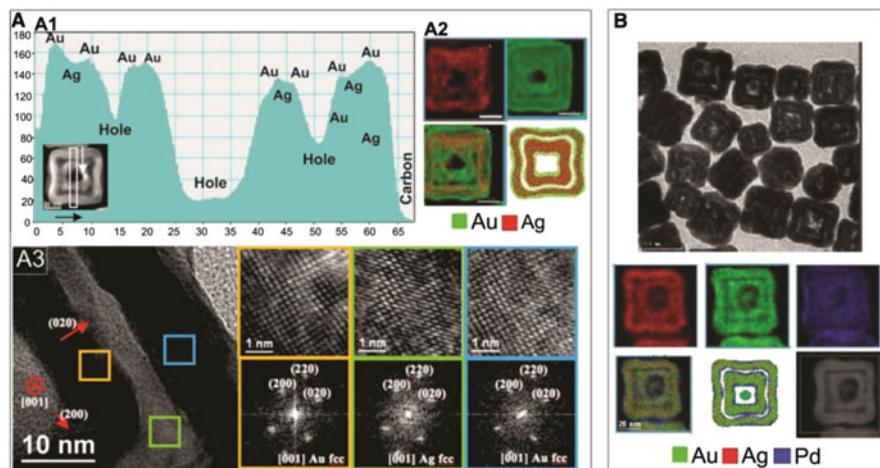


Fig. 6.30 Characterization of double wall nanoboxes. (A1) Intensity profile obtained on the z-contrast image of AuAg double-walled nanoboxes. (A2) EDX elemental map, together with a scheme of the elemental distribution. (A3) HRTEM characterization. (b) TEM image and EDX elemental maps for trimetallic PdAuAg nanoboxes (Reprinted with permission from Ref. [117])

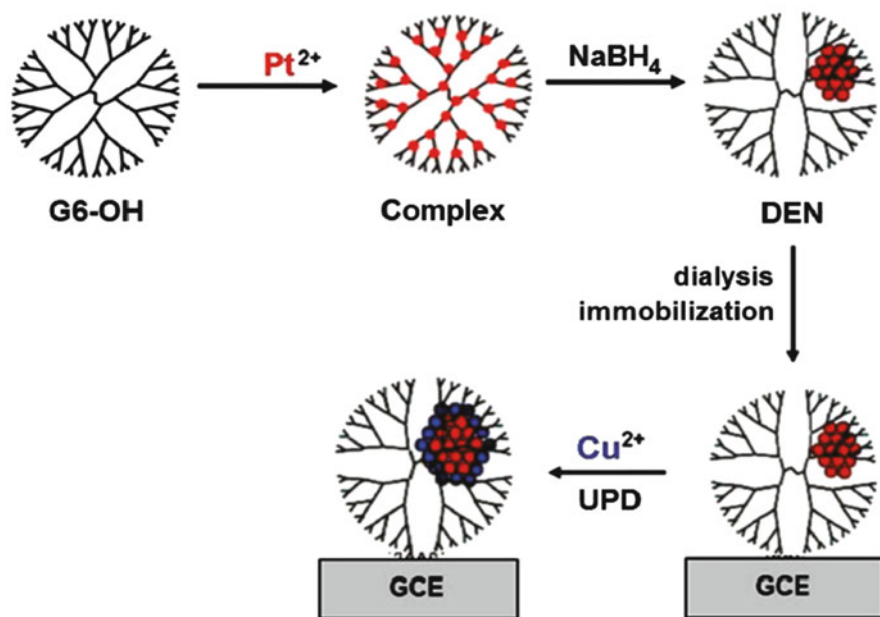


Fig. 6.31 Scheme of the dendrimer-encapsulated nanoparticles method (Reprinted with permission from Ref. [132])

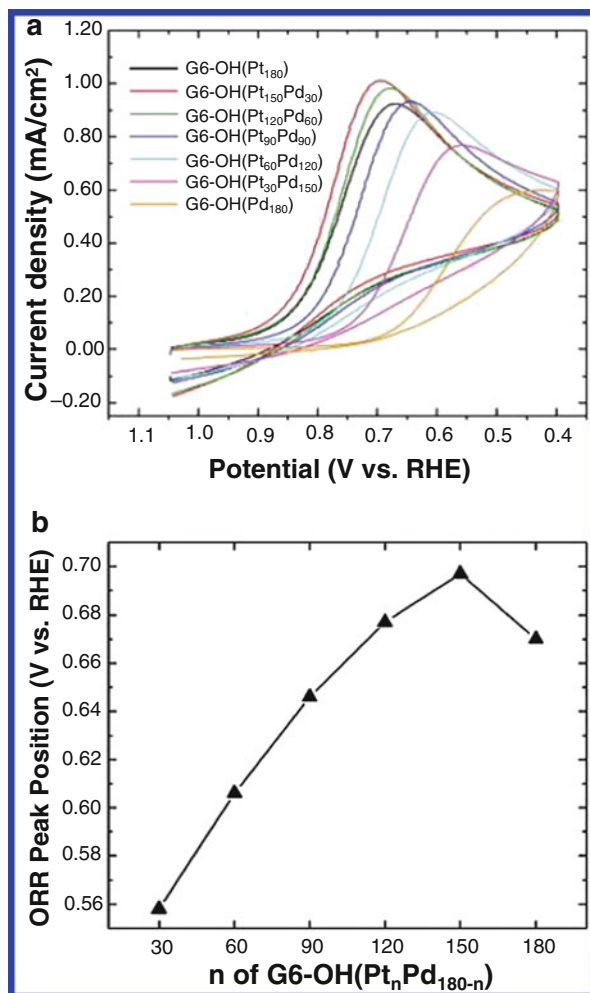
In a first step, S^{2+} cations are embedded into the dendrimer matrix, yielding a complex $[G6 - OH(S^{2+})_n]$, where $G6 - OH$ is a sixth-generation, hydroxyl-terminated polyamidoamine (PAMAM) dendrimer, and n is the amount of ions encapsulated in the dendrimer. The driving force for encapsulation of metal ions within dendrimers is usually based on covalent bond formation, electrostatic interactions, complexation reactions, or a combination thereof [119]. In a second step, the cations are completely reduced by using borohydride. In this way, metallic NPs were obtained within the cavities of the dendrimers. The DENs synthesis offers some significant advantages over other methods for preparing nanoparticles in very a small size range [122]. Since the cations are embedded in the polymeric matrix, the later determines the NP size. The cation/dendrimer ratio allows the adjustment of the amount of cations in the matrix and consequently, the adjustment of the final NP size. Typically, this strategy yields a NP size distribution having standard deviations of 0.3 nm [123]. This process leads to stable, nearly size-monodisperse NPs composed of Pt, Pd, Au and Cu [125–129]. It is also possible to prepare alloyed and core@shell bimetallic DENs using a slight variation of the basic approach [130, 131]. For example, PtPd bimetallic NPs containing an average of 180 atoms and being composed of seven different Pt/Pd ratios have been prepared within sixth-generation, hydroxyl-terminated, polyamidoamine dendrimers [130]. Figure 6.32a shows how the electrochemical response can be manipulated by changing the composition of a PtPd NP. For example, the current peak for oxygen reduction on the electrode modified with $G6-OH(Pt_{180})$ is found at 0.67 V, but the electrodes coated with bimetallic PtPd DENs having low percentages of Pd exhibit oxygen reduction reaction peaks at more positive potentials (e.g., 0.70 and 0.68 V for $G6-OH(Pt_{150}Pd_{30})$ and $G6-OH(Pt_{120}Pd_{60})$, respectively). Figure 6.32b summarizes the voltammetric data by showing the potential of the current peak for the oxygen reduction reaction as a function of increasing Pt percentage in each electrocatalytic particle. A maximum is reached when the NP is composed of $G6-OH(Pt_{150}Pd_{30})$.

In a further step, a monolayer of a less noble metal may be electrodeposited onto the DENs by upd to yield $[G6 - OH(S_n @ M_m)]$. Subsequent galvanic replacement of the upd monolayer may yield different core@shell NPs. For example, Carino et al. [132] have analyzed the voltammetric behavior of Cu deposition on Pt-DENs of 55, 147, and 255 atoms, see Fig. 6.33. Their results indicate that a single atomic monolayer of Cu is deposited onto Pt DENs cores containing an average number of 147 and 225 atoms, while more than one monolayer deposits onto Pt DEN cores containing an average of 55 atoms. Two remarkable features emerge from the voltammetry of these systems:

- (a) As NP size decreases, the peak potentials of anodic and cathodic processes show a shift towards lower potentials, that is, Cu upd weakens for relatively small NPs.
- (b) Deposition and stripping peaks become splitted into two components.

The first behavior can be analyzed in terms of NP size. The smaller the NPs, the more important become surface effects, and the deposition potential moves to lower

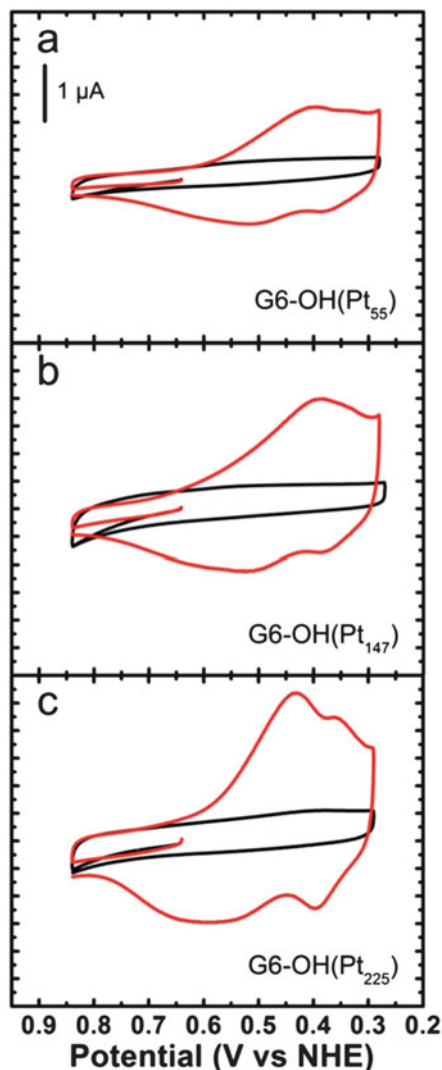
Fig. 6.32 (a) Cyclic voltammograms of G6-OH ($\text{Pt}_n\text{Pd}_{180-n}$) with $n = 180, 150, 120, 90, 60, 30,$ and 0 . (b) A plot of the current peak position for the oxygen reduction reaction as function of n for G6-OH ($\text{Pt}_n\text{Pd}_{180-n}$). Scan rate: 50 mV/s ; electrolyte solution: aqueous $0.5 \text{ M H}_2\text{SO}_4$ saturated with O_2 (Reprinted with permission from Ref. [130])



potentials. This is an evidence for the extinction of the upd phenomenon at the nanoscale, analyzed in Sect. 6.7. The second behavior, the occurrence of two shoulders in the voltammograms, was assigned to the presence of different facets and/or the different behavior of borders and facets. It is known that for a very small NP it is not possible to differentiate the superficial regions into facets and borders. However, when the NP is of a bigger size, these regions may be differentiated and this fact becomes evident through this wave splitting. Very recent results by Plowman and Compton [133] confirm the extinction of Cu upd for Au NPs of 1.8 nm in citrate media.

As mentioned at the beginning of the present section, the development of NP synthesis by means of dendrimers presents two appealing aspects. On the one side, it allows the generation of metallic NPs with a very sharp size distribution. On the

Fig. 6.33 Cyclic voltammograms obtained using G6-OH(Pt_n) DENs in aqueous electrolyte solutions containing 0.10 M H₂SO₄ + 0.010 M CuSO₄. The scans started at 0.64 V and were initially swept in the positive direction at a rate of 10 mV/s (Reprinted with permission from Ref. [132])



other side, this method allows the generation of metal NPs with very small sizes, between 1 nm and 2 nm. These two factors allow correlating straightforwardly experimental results with theoretical predictions. In this respect, it is worth mentioning the work of Yancey et al. [134] and Carino et al. [132]; they contrasted experimental results of electrochemical deposition with density functional (DFT) calculations for NP of similar sizes. Carino et al. [132] showed that upd of Cu onto Pt-NP(147) occurs in two steps: first onto the {100} facets (partial deposition) and then onto the {111} facets (full deposition). The partial and full shell structures were characterized by voltammetry and the experimental results were compared

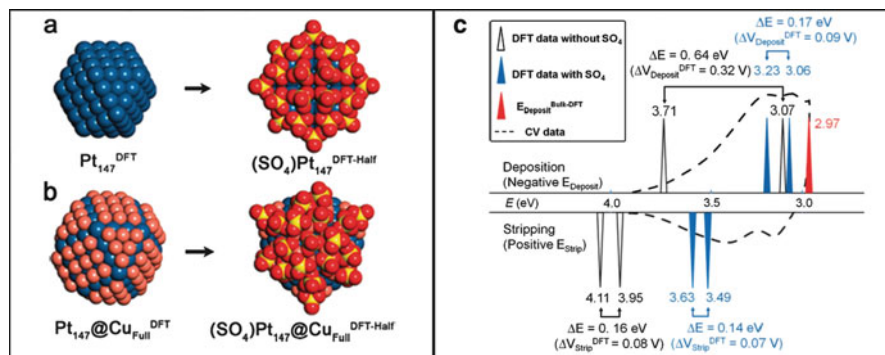


Fig. 6.34 Different models used to consider the adsorption of sulfate ions on (a) a Pt NP made of 147 atoms. (b) A core@shell NP Pt(147)@Cu(full). *Left and right* images show the NP without and with adsorbed SO₄ molecules respectively (c) DFT-calculated Cu deposition and stripping energies, as compared with the experimental voltammogram obtained for Cu upd on Pt NPs (black dashed line) (Reprinted with permission from Ref. [143])

with computational models generated by using DFT and molecular dynamics (MD) simulations. Figure 6.34a shows the different models used by Carino et al. [143] to emulate the Cu upd phenomena. Binding energies were calculated using DFT for Cu adsorbed on Pt{100} and Pt{111} facets of a “solvated” NP, in which SO₄ ligands were adsorbed on the surface to mimic the solvent – surface interactions existing in the experiments. The calculated binding energies were found to correspond well with the peaks observed in the CVs of Cu upd onto Pt NPs(147) (see Fig. 6.34b). In contrast, the same calculations performed on a naked, SO₄-free (solvent free) NP model did not fit the electrochemical data.

References

1. <http://www.nanotechproject.org/cpi/products/>. Consulted Sept 2014
2. Marie-Christine D, Didier A (2004) Chem Rev 104:293
3. Ferrando R, Jellinek J, Johnston RL (2008) Chem Rev 108(3):845
4. Drexler KE (1986) Engines of creation: the coming era of nanotechnology, Anchor Books Editions, New York
5. Drexler KE (1992) Nanosystems: molecular machinery, manufacturing, and computation. Wiley, New York
6. Ratner M, Ratner D (2003) Nanotechnology, a gentle introduction to the next big idea. Prentice Hall, Upper Saddle River
7. Corain B, Schmid G, Toshima N (2008) Metal nanocluster in catalysis and materials science. Elsevier, The Netherlands
8. Castro T, Reifemberger R, Choi E, Andres RP (1990) Phys Rev B 13:8548
9. Kittel C (2005) Introduction to solid state physics, 8th edn. Wiley, Hoboken
10. Wong K, Vongehr S, Kresin VV (2003) Phys Rev B 67:035406
11. Plieth WJ (1985) Surf Sci 156:530

12. Wood DM (1981) *Phys Rev Lett* 46:749
13. Plieth WJ (1982) *J Phys Chem* 86:3166
14. Schnippering M, Carrara M, Foelske A, Kötzc R, Fermín DJ (2007) *Phys Chem Chem Phys* 9:725
15. Selvakannan PR, Swami A, Srisathiyarayanan D, Shirude PS, Pasricha R, Mandale AB, Sastry M (2004) *Langmuir* 20:7825
16. Jana NR, Gearheart L, Murphy CJ (2001) *J Phys Chem B* 105:4065
17. Sánchez-Iglesias A, Carbó-Argibay E, Glaria A, Rodríguez-Gonzalez B, Pérez-Juste J, Pastoriza-Santos I, Liz-Marzán LM (2010) *Chem Eur J* 16:5558
18. Gentry ST, Fredericks SJ, Krchnavek R (2009) *Langmuir* 25:2613
19. Jiang XC, Pileni MP (2007) *Colloids Surf A Physicochem Eng Asp* 295:228
20. Fievet F, Lagier JP, Figlarz M (1989) *MRS Bull* 14:29
21. Fayet P, Granzer F, Hegenbart G, Moisar E, Pischel B, Wöste L (1985) *Phys Rev Lett* 55:3002
22. Foiles SM, Baskes MI, Daw MS (1986) *Phys Rev B* 33:7983
23. Li JH, Dai XD, Liang SH, Tai KP, Kong Y, Liu BX (2008) *Phys Rep* 455:1
24. Xiao L, Tollberg B, Hu X, Wang L (2006) *J Chem Phys* 124:114309
25. Oviedo OA, Mariscal MM, Leiva EPM (2010) *Phys Chem Chem Phys* 12:4580
26. Oviedo OA, Mariscal MM, Leiva EPM (2010) *Electrochim Acta* 55:8244
27. Perez MA (2007) In: Mariscal MM, Dassie SA (eds) *Recent advances in nanoscience. Research Signpost, Trivandrum*
28. LaMer VK, Dinegar RH (1950) *J Am Chem Soc* 72:4847
29. Iijima S, Ichihashi T (1986) *Phys Rev Lett* 56:616
30. Wiley B, Herricks T, Sun Y, Xia Y (2004) *Nano Lett* 4:1733
31. Lifshitz IM, Slyozov VV (1961) *J Phys Chem Solids* 19:35
32. Wagner C (1961) *Zeitschrift für Elektrochemie, Berichte der Bunsengesellschaft für physikalische Chemie* 65:585. (German)
33. Erdemir D, Lee AY, Myerson AS (2009) *Acc Chem Res* 42:621
34. Davey RJ, Allen K, Blagden N, Cross WI, Lieberman HF, Quayle MJ, Righini S, Seton L, Tiddy GJT (2002) *CrystEngComm* 4:257
35. Hill TL, Chamberlin RV (1998) *Proc Natl Acad Sci* 95:12779
36. Hill TL (1964) *Thermodynamics of small systems, part I and II*. Dover Publications, New York
37. Park S, Yang P, Corredor P, Weaver MJ (2002) *J Am Chem Soc* 124:2428
38. Skriver HL, Rosengaard NM (1992) *Phys Rev B* 46:7157
39. Frisch HL (1957) *J Chem Phys* 27:90
40. Henglein A, Giersig M (1994) *J Phys Chem* 98:6931
41. Mulvaney P, Giersig M, Henglein A (1993) *J Phys Chem* 97:7061
42. Zsigmondy R, Anorg Z (1917) *Allg Chem* 99:105
43. Schmid G, West H, Malm J-O, Bovin J-O, Grenthe C (1996) *Chem Eur J* 2:1099
44. Budevski E, Staikov G, Lorenz WJ (1996) *Electrochemical phase formation and growth – an introduction in the initial stages of metal deposition*. VCH, Weinheim
45. Bochicchio D, Ferrando R (2013) *Phys Rev B* 87:165435
46. Park S, Weaver MJ (2002) *J Phys Chem B* 106(34):8667
47. Zhang B, Li J-F, Zhong Q-L, Ren B, Tian Z-Q, Zou S-Z (2005) *Langmuir* 21:7449
48. Lu L, Wang H, Xi S, Zhang H (2002) *J Mater Chem* 12:156
49. Selvakannan PR, Mandal S, Phadtare S, Gole A, Pasricha R, Adyanthaya SD, Sastry MJ (2004) *J Colloid Interface Sci* 269:97
50. Mandal S, Selvakannan PR, Phadtare S, Pasricha R, Sastry M (2002) *Proc Indian Acad Sci Chem Sci* 114:513
51. Fonticelli MH, Corthey G, Benitez GA, Salvarezza RC, Giovanetti LJ, Requejo FG, Shon YS (2007) *J Phys Chem C* 111:9359
52. Oviedo OA, Reinaudi L, Leiva EPM (2012) *Electrochem Comm* 21:14

53. Luque NB, Reinaudi L, Serra P, Leiva EPM (2009) *Electrochim Acta* 54:3011
54. Sharma V, Park K, Srinivasarao M (2009) *Mater Sci Eng R* 65:1
55. Zhang H, Jinb M, Xia Y (2012) *Chem Soc Rev* 41:8035
56. Goia DV, Matijevic E (1998) *New J Chem* 22:1203
57. Jiang XC, Brioude A, Pileni MP (2006) *Colloids Surf A Physicochem Eng Asp* 58277:201
58. Zsigmondy R (1917) *The chemistry of colloids*. Wiley, New York
59. Svedberg T (1921) *The formation of colloids*. D. Van Nostrand Company, New York
60. Sun Y (2013) *Chem Soc Rev* 42:2388
61. Carbó-Argibay E, Rodríguez-González B, Pacífico J, Pastoriza-Santos I, Pérez-Juste J, Liz-Marzán LM (2007) *Angew Chem Int Ed* 46:8983
62. Zhang L, Wang L, Jiang Z, Xie Z (2012) *Nanoscale Res Lett* 7:312
63. Sánchez-Iglesias A, Pastoriza-Santos I, Pérez-Juste I, García de Abajo FJ, Liz-Marzán LM (2006) *Adv Mater* 18:2529
64. Elechiguerra JL, Reyes-Gasga J, Yacaman MJ (2006) *J Mater Chem* 16:3906
65. Gai PL, Hammer MA (2002) *Nano Lett* 2:771
66. Johnson CJ, Dujardin E, Davis SA, Murphy CJ, Mann S (2002) *J Mater Chem* 12:1765
67. Germain V, Li J, Ingert D, Wang ZL, Pileni MP (2003) *J Phys Chem B* 107:8717
68. Lu LH, Wang HS, Zhou YH, Xi SQ, Zhang HJ, Hu JW, Zhao B (2002) *Chem Commun*
69. Lu LH, Sun GY, Zhang HJ, Wang HS, Xi SH, Hu JQ, Tian ZQ, Chen RJ (2004) *J Mater Chem* 14:1005
70. Zhang H, Mingshang J, Wang J, Li W, Camargo PHC, Kim MJ, Yang D, Xie Z, Xia Y (2011) *J Am Chem Soc* 133:6078
71. Berhault G, Bausach M, Bisson L, Becerra L, Thomazeau C, Uzio D (2006) *J Phys Chem C* 111:16
72. Xiong Y, McLellan JM, Yin Y, Xia Y (2007) *Angew Chem Int Ed* 46:790
73. Sun Y, Mayers B, Herricks T, Xia Y (2003) *Nano Lett* 3:955
74. Xiong Y, Chen J, Wiley B, Xia Y, Yin Y, Li Z-Y (2005) *Nano Lett* 5:1237
75. Xiong Y, Cai H, Wiley BJ, Wang J, Kim MJ, Xia Y (2007) *J Am Chem Soc* 129:3665
76. DeSantis CJ, Sue AC, Bower MM, Skrabala SE (2012) *ACS Nano* 6:2617
77. DeSantis CJ, Peverly AA, Peters DG, Skrabalak SE (2011) *Nano Lett* 11:2164
78. Huang J, Zhu Y, Lin M, Wang Q, Zhao L, Yang Y, Yao KX, Han Y (2013) *J Am Chem Soc* 135:8552
79. Long R, Zhou S, Wiley BJ, Xiong Y (2014) *Chem Soc Rev* 43:6288
80. Liu M, Guyot-Sionnest P (2005) *J Phys Chem B* 109:22192
81. Ikemiya N, Yamada K, Hara S (1996) *Surf Sci* 348:253
82. Ogaki K, Itaya K (1995) *Electrochim Acta* 40:1249
83. Oviedo OA, Leiva EPM, Rojas MI (2006) *Electrochim Acta* 51:3526
84. Grzelczak M, Pérez-Juste J, Mulvaney P, Liz-Marzán LM (2008) *Chem Soc Rev* 37:1783
85. Seo D, Park JC, Song H (2006) *J Am Chem Soc* 128(46):14863
86. Seo D, Yoo CI, Park JC, Park SM, Ryu S, Song H (2008) *Angew Chem* 47:763
87. Grzelczak M, Pérez-Juste J, Rodríguez-González B, Liz-Marzán LM (2006) *J Mater Chem* 16:3946
88. Personick ML, Langille MR, Zhang J, Mirkin CA (2011) *Nano Lett* 11:3394
89. Langille MR, Personick ML, Zhang J, Mirkin CA (2012) *J Am Chem Soc* 134:14542
90. Brankovic SR, Wang JX, Adzic RR (2001) *Surf Sci* 474:L173
91. Mrozek MF, Xie Y, Weaver MJ (2001) *Anal Chem* 73:5953
92. Sun Y, Mayers BT, Xia Y (2002) *Nano Lett* 2:481
93. Skrabalak SE, Chen J, Sun Y, Lu X, Au L, Cogley CM, Xia Y (2008) *Acc Chem Res* 41:1587
94. Lu X, Chen J, Skrabalak SE, Xia Y (2008) *Proc Inst Mech Eng N* 221:1
95. Hack HP (1988) *Galvanic corrosion*. ASTM International, West Conshohocken
96. Jin Y, Shen Y, Dong S (2004) *J Phys Chem B* 108(24):8142
97. Huang M, Jin Y, Jiang H, Sun X, Chen H, Liu B, Wang E, Dong S (2005) *J Phys Chem B* 109(32):15264

98. Zhai J, Huang M, Dong S (2007) *Electroanalysis* 19:506
99. Wang L, Guo S, Zhai J, Hu X, Dong S (2008) *Electrochim Acta* 53:2776
100. Park Y-K, Yoo S-H, Park S (2008) *Langmuir* 24(8):4370
101. Peng Z, Yang H (2009) *Nano Today* 4:143
102. Hu J-W, Li J-F, Ren B, Wu D-Y, Sun S-G, Tian Z-Q (2007) *J Phys Chem C* 111(3):1105
103. Yin Y, Erdonmez C, Aloni S, Alivisatos A (2006) *J Am Chem Soc* 128:12671
104. Seo D, Song H (2009) *J Am Chem Soc* 131:18210
105. Sun Y, Wiley B, Li ZY, Xia Y (2004) *J Am Chem Soc* 126:9399
106. Chen J, Wiley B, McLellan J, Xiong Y, Li ZY, Xia Y (2005) *Nano Lett* 5:2058
107. Lu X, Au L, McLellan J, Li ZY, Marquez M, Xia Y (2007) *Nano Lett* 7:1764
108. Hong X, Wang D, Cai S, Rong H, Li Y (2012) *J Am Chem Soc* 134:18165
109. Wang Y, Wan D, Xie S, Xia X, Huang CZ, Xia Y (2013) *ACS Nano* 7:4586
110. Yu Y, Zhang Q, Yao Q, Xie J, Lee JY (2013) *Chem Mater* 25:4746
111. Yu Y, Zhang Q, Xie J, Lee JY (2013) *Nat Commun* 4:1454
112. Wales D (2004) *Energy landscapes applications to clusters, biomolecules and glasses*. Cambridge Molecular Science. Royal Society of Chemistry. http://pubs.rsc.org/en/journals/journalissues/fd?_ga=1.53658280.1007409239.1445285929#!:recentarticles&adv
113. Tian N, Zhou Z-Y, Sun S-G, Ding Y, Wang ZL (2004) *Science* 316:732
114. Tian N, Zhou Z-Y, Sun S-G (2008) *J Phys Chem C* 112:19801
115. Zhou Z-Y, Tian N, Huang Z-Z, Chen D-J, Sun S-G (2008) *Faraday Discuss* 140:81
116. Hong JW, Kim M, Kim Y, Han SW (2012) *Chem Eur J* 18:16626
117. González E, Arbiol J, Puentes VF (2011) *Science* 334:1377
118. Liu J, Qiao SZ, Chen JS, Wen X, Lou D, Xing X, Lu GQM (2011) *Chem Commun* 47:12578
119. Crooks RM, Zhao M, Sun L, Chechik V, Yeung LK (2001) *Acc Chem Res* 34:181
120. Crooks RM, Chechik V, Lemon BI III, Sun L, Yeung LK, Zhao M (2002) *Synthesis, characterization, and applications of dendrimer-encapsulated metal and semiconductor nanoparticles*. In: Feldheim DL, Foss CA Jr (eds) *Metal nanoparticles- synthesis, characterization, and applications*. Marcel Dekker, New York
121. Scott RWJ, Wilson OM, Crooks RM (2005) *J Phys Chem B* 109:692
122. Myers VS, Weir MG, Carino EV, Yancey DF, Pande S, Crooks RM (2011) *Chem Sci* 2:1632
123. Ye H, Crooks RM (2007) *J Am Chem Soc* 129:3627
124. Xia X, Wang Y, Ruditskiy A, Xia Y (2013) *Adv Mater* 25:6313
125. Zhao M, Crooks RM (1999) *Angew Chem Int Ed* 38:364
126. Ye H, Crooks RM (2005) *J Am Chem Soc* 127:4930
127. Wilson OM, Knecht MR, Garcia-Martinez JC, Crooks RM (2006) *J Am Chem Soc* 128:4510
128. Garcia-Martinez JC, Lezutekong R, Crooks RM (2005) *J Am Chem Soc* 127:5097
129. Zhao M, Sun L, Crooks RM (1998) *J Am Chem Soc* 120:4877
130. Scott RWJ, Wilson OM, Oh S-K, Kenik EA, Crooks RM (2004) *J Am Chem Soc* 126:15583
131. Wilson OM, Scott RWJ, Garcia-Martinez JC, Crooks RM (2005) *J Am Chem Soc* 127:1015
132. Carino EV, Crooks RM (2011) *Langmuir* 27:4227
133. Plowman BJ, Compton RG (2014) *ChemElectroChem* 1:1009
134. Yancey DF, Zhang L, Crooks RM, Henkelman G (2012) *Chem Sci* 3:1033
135. Oviedo OA, Vélaz P, Macagno VA, Leiva EPM (2014) *Surf Sci* 631:23
136. Mariscal MM, Oviedo OA, Leiva EPM (2012) *J Mater Res* 27:1777
137. Oviedo OA, Leiva EPM, Mariscal MM (2008) *Phys Chem Chem Phys* 10:3561
138. Campbell FW, Zhou Y, Compton RG (2010) *New J Chem* 34:187
139. Campbell FW, Compton RG (2010) *Int J Electrochem Sci* 5:407
140. Zhou Y, Rees NV, Compton RG (2012) *ChemPhysChem* 12:2085
141. Oviedo OA, Reinaudi L, Mariscal MM, Leiva EPM (2012) *Electrochim Acta* 76:424
142. Sun Y, Xia Y (2004) *J Am Chem Soc* 126:3892
143. Carino EV, Kim HY, Henkelman G, Crooks RM (2012) *J Am Chem Soc* 134:4153

Chapter 7

What Is Coming Next?

In the following sections we will discuss on some tendencies and prospects concerning underpotential deposition (upd) research, related to both theoretical and experimental work.

7.1 Underpotential Deposition as a Precision Design Tool

Tuning of size, shape, and properties of nanomaterials is of primarily importance for the development of basic science and technological progress in view of multiple applications. In this context, a peculiarity of upd makes this phenomenon an extraordinary tool as a bottom-up method: *it allows a strict morphological control at the nanoscale*. Such a level of control has up to date not been achieved by other techniques in the solution phase. In the case of techniques applied under vacuum conditions, the Atomic Layer Deposition (ALD) method has been able to achieve similar results, but using ultra high vacuum conditions, which require a costly and relative involved infrastructure. Along Chaps. 2, 3, 4, 5 and 6 we have analyzed numerous examples of various systems where it is possible to obtain deposits whose width varied between one and two atomic monolayers. It is even possible to reach monolayer fractions, expanded structures with different stoichiometries, etc. Furthermore, it is possible to achieve selective decoration of step borders, with one, and eventually two adsorbate rows. In most cases, this surface control may be achieved in a fast, reversible and reproducible way, even under several experimental conditions. Thus, from the point of view of the so-called bottom-up nanostructuring methodology, upd has shown to be a powerful tool as “building technique”. A relevant example of this upd application are the studies of Mirkin and coworkers on Au nanoparticles (NPs) growth controlled by Ag upd [1, 2] in the presence and in the absence of anions, as illustrated in Fig. 7.1, and discussed more in detail in

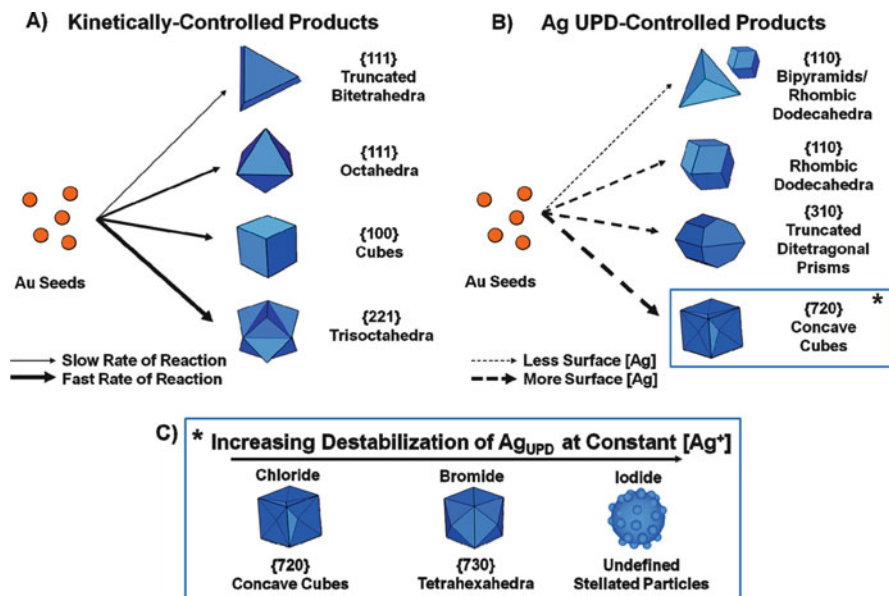


Fig. 7.1 Schematic representation of the two growth pathways on Au nanoparticles (Reprinted with permission of Ref. [1])

Chap. 6. There, we can see the three types of NP growth that appear as a result of different procedures. They are:

- Kinetically controlled products. Here the control of the rate of Au^+ reduction directs NP shape.
- Upd controlled products. Here, the upd of Ag onto the Au-NP surface blocks the growth of particular facets and thus dictates NP shape.
- Different products arising from the increasing destabilization of upd by anions.

We turn now to do a little of bibliometric analysis concerning upd. Figure 7.2a shows the number of published articles as a function of the year, using the Scopus [3] searching engine, under the keyword “underpotential deposition”, using the “Articles title, Abstract and Keywords” filter. Modulated by an oscillating function, the plot shows a roughly linear growth in the period (1976–2014), with a slope that amounts about 2 articles/year. From the 1802 publications found in this search, 16 correspond to patents which are homogeneously distributed (1 or 2 per year) in the interval 1989–2014. The year 2013 stands out with four patents. These results show that the relationship between patenting and overall publications amounts a 0.9 %. The previous figures indicate that even in the current times, where the “nano” world floods internet, magazines and even sci-fi movies, upd does not

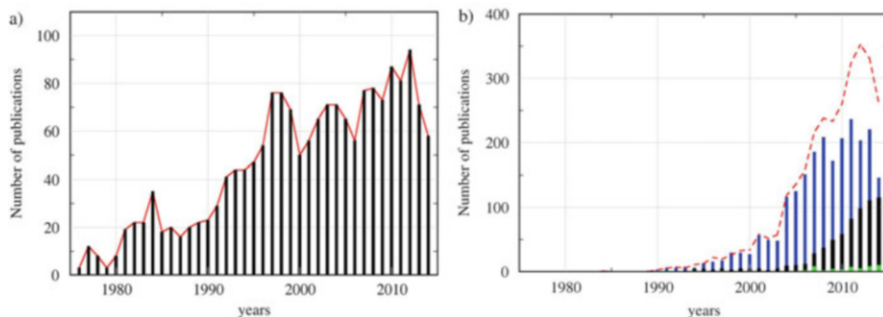


Fig. 7.2 Evolution of the number of publications as a function of the year according to the Scopus search engine with the strings (a) “underpotential deposition” and (b) black “galvanic replacement”, blue “electrochemical atomic layer deposition” and green “surface limited redox replacement” plus “Electrochemical Atomic Layer Epitaxy”. In (b) red broken line corresponds to the sum of all searches

seem to show up meaningfully in publications, all this in spite of the great possibilities it has to manage surface control as stated above. Which is the reason for this unnoticed of upd in the scientific community? Far from having the definite answer to this question, we can put forward a (not-very-chemical) hypothesis to explain this. As a general rule, upd is restricted to metal couples where the substrate is a more noble metal than the adsorbate. We have shown and analyzed in numerous experiments how Au or Pt are covered by less noble metals like Ag, Cu, Pb, Tl, etc. These actions are just in the opposite direction of the driving force that makes the world go round: *economy*. This may explain in part the low patenting rate found in relationship to upd at present times. For this reason, we come now to consider the wealthy brothers of upd: Galvanic Replacement (*gr*), Surface Limited Redox Replacement (SLRR) and Electrochemical Atomic Layer Deposition (E-ALD) also knew as Electrochemical Atomic Layer Epitaxy (ECALE).

Galvanic replacement [4] is an electrochemical corrosion process,¹ which involves the oxidation of a compound or metal (usually denominated sacrificial template) by another one, which has a more positive reduction potential. This process allows the oxidation of the template and its corresponding dissolution, while the second metal or compound is reduced and deposited onto the template. On its side, SLRR, E-ALD and ECALE [5] are referred to the experimental strategy based upon multiple applications of a protocol for submonolayer or monolayer surface modification via *gr*. Figure 7.2b shows the time evolution of articles including the terms “Galvanic Replacement”, “Surface Limited Redox Replacement”, “Electrochemical Atomic Layer Deposition” and “Electrochemical Atomic Layer Epitaxy” under analogous conditions to those of the upd search addressed above. For the sum of the search results (red broken line), the number of publications in the field before 2003 grew at a rate lower than 3 publications/year. After

¹ Galvanic corrosion is a phenomenon known since the nineteenth century.

2003, the number of publications acquired renewed impetus, mirrored in an increase in the slope of the plot up to 23 publications/year. The analysis of the four most cited articles found in 2003–2004 (582 cites for [6], 253 cites for [7], 244 cites for [8] and 174 cites for [9]) shows a common denominator: the articles report on the formation of *nanocages*, *nanohollows*, *hollow nanoparticles*, *nanotubes*, *nanocubes*, *nanoshells*, etc. Thus, the most straightforward conclusion is to associate this new impulse with the emerging activity in *nanoscience*. However, these applications of galvanic corrosion at the nanoscale did not use the upd technique as a previous step, as originally proposed by Brankovic et al. in 2001 [4] for planar surfaces and later extended by Park et al. to NPs [10]. Currently, research is going in this direction, where the joint use of upd with gr allows to design new materials at the nanoscale, with completely new properties and construction details never found before by other techniques. Synergy between upd and gr allows on one side to use the fine control of nanostructures that may be achieved by upd to build substrates with a well-controlled morphology (template), and on the other, the great versatility of gr to modify the latter [11]. The simultaneous application of both techniques offers a simple and versatile way to the fabrication of multifunctional nanostructures like hollow-NPs and many other appealing characteristics. Upd and gr may also be coupled with other methods, as sequential reduction, co-reduction and Kirkendall effect to generate nanostructures with much greater complexity [12] as was shown in Chap. 6. Combination with other physicochemical processes or synthetic techniques will allow the fabrication of nanomaterials with unexplored structures and properties. Great experimental progress is taking place right now on these topics. However, many questions remain open and new ones arise, and even many aspects of upd remain unclear, as will be addressed below. For example, it has been shown theoretically [13] and then experimentally [14] that at the nanoscale the redox equilibrium potential of an upd adsorbate changes with the size of the NPs on which it is formed, so that the driving force for gr should be sensitive to the size of the nanosystem as well. Thus, a unified theoretical framework is necessary for the understanding of all these processes, something which is still in progress. No doubt that the basic theoretical tools for such an achievement will be nanothermodynamics, statistical mechanics and/or quantum mechanics.

7.2 Towards an Accurate and First-Principles Modeling of Metal Underpotential Deposition/Dissolution

We have discussed in Chap. 5 different ways to model the kinetics of upd through Kinetic Monte Carlo methods, which allow performing calculations of reactions in a time scale which approaches the experimental one. In some cases, different kinetics were assumed for atom deposition in different environments [15]. On the other hand, Brown et al. [16] modeled adsorption/desorption of particles on the basis of the Butler-Volmer description of electrochemical charge transfer.

In this approach, the deposition ($v_{\text{dep},x}(E)$)/dissolution ($v_{\text{dis},x}(E)$) rates of the atomic species are calculated from an equation of the type [17]:

$$v_{\text{dep},x}(E) = k_{\text{dep},x} a_{\text{M}^{z+}} \exp\left(-\frac{\Delta G_{\text{dep},x}^{\#(0)}}{RT}\right) \exp\left(\frac{(1-\alpha)zFE}{RT}\right) \quad (7.1)$$

$$v_{\text{dis},x^*}(E) = k_{\text{dis},x^*} \exp\left(-\frac{\Delta G_{\text{dis},x^*}^{\#(0)}}{RT}\right) \exp\left(\frac{\alpha zFE}{RT}\right) \quad (7.2)$$

where the indices x and x^* label the type of sites where the adatom is deposited on (desorbed from), the $\Delta G^{\#(0)}$ values are the activation free energies for the ion transfer from the solution to the crystal, or vice versa, at $E = 0$, $k_{\text{dep},x}$ and k_{dis,x^*} are rate constants for deposition and dissolution reactions at sites x and x^* , respectively. α is the charge transfer coefficient and the remaining symbols have their usual meaning. This type of modeling introduces environment-depending rates, where adatom deposition/dissolution rate depends on the type of site where it is incorporated or dissolved from. The usual way to do this is to approximate the dynamic property $\Delta G^{\#(0)}$ by some simple function of the related thermodynamic quantity, as it is the corresponding free energy.

The next step to improve the modeling would consist in obtaining the rates $v_{\text{dep},x}$ and v_{dis,x^*} using first principles calculations and computer simulations. In this respect, it is worth mentioning an important step in this direction taken by Pinto et al. concerning the electrochemical deposition of Ag [18] and the deposition/dissolution of divalent metal ions [19]. The modelling by these authors consists of a combination of:

- (a) electron-transfer theory with spin polarization [20],
- (b) density functional theory (DFT) calculations and
- (c) molecular dynamics (MD) simulations.

The general idea of the former was introduced in Chap. 5, where we saw that the Hamiltonian of the system includes not only adatom-substrate but also adatom-solvent interactions. The DFT calculations are used to investigate the electronic interactions between the adatom and the metal surface, and allow to fit the coupling constants between the relevant orbitals of the adatom and the respective surface. The third ingredient, the MD simulations, provide information on the potential of mean force of the interaction of the ion with the solvent, and play a key role to understand the stability of ions with different charges and thus different solvation energies. Such a modeling allows obtaining detailed information on the free energy surface, as can be observed in Fig. 7.3 for the reaction:



The methodology used to calculate the information of Fig. 7.3 could be used to analyze upd in different systems and environments, and could become a powerful tool to simulate these systems.

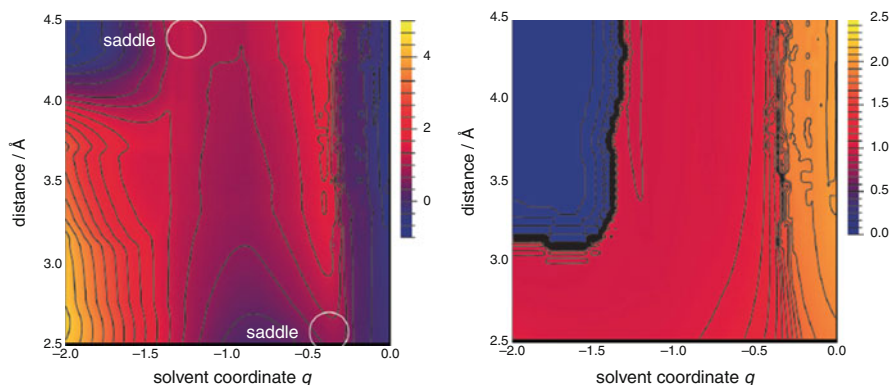


Fig. 7.3 Free energy surface (*left*) and occupation of the Zn 4s orbital (*right*) for the reaction $\text{Zn}^{2+} + 2\text{e}^- \rightarrow \text{Zn}$, where the final state is a Zn atom deposited on the terrace. The initial state for the deposition reaction is a Zn^{2+} ion located at the *upper left* region of these plots. This ion undergoes a first one-electron reduction at the saddle point at the *top-left* of the Figure, and a second electron transfer at the saddle point at the *bottom-right* of the Figure (Reprinted with permission of Ref. [18])

7.3 Computer Experiments

In relation to the previous item, it can be stated that the increasing computational power, the development of semiempirical potentials [21] and the improvement of electronic structure calculation methods (DFT) [22] have opened a new way to compare the predictions of theoretical models with calculations: the performance of *computer experiments*. In fact, it is nowadays possible to simulate on a PC the thermodynamic properties of different systems in the same size scale as those in experiments. These computer experiments allow to save time and money, and in many cases they may orientate and design experimental strategies. As an example for the present problem under consideration, it may be mentioned that in 2008 computer experiments showed that upd should vanish for some systems in the nanoscale [12]. Although there is some indication that this happens [13], more laboratory experiments are still necessary to check the general validity of this prediction.

DFT calculations stand out over other calculation methods, since they allow to obtain information on electronic structure, something that is very important to analyze in the case of electrochemical systems. In principle, DFT calculations would allow to involve in the calculation all the components of the upd system: substrate, adsorbate, adsorbed ions, capping molecules, base electrolyte, water, etc. We say “in principle” because even with the current computational power the inclusion of all these elements in the simulations is a formidable task. Computer experiments have earned nowadays an important place in almost every research work, and upd is of course not an exception. Recently, Anderson et al. [23] have shown the power of DFT to analyze the energetics of Pd, Pd@Cu and Pd@Pt NPs

made of up to 309 atoms. Another example, analyzed in detailed in Chap. 6, is the joint work of the experimental group of Crooks and the theoretical group of Henkelman on the deposition of Cu on Pt-NPs [24] in the presence of adsorbed sulfate ions. These authors used the symmetry properties of the NP to reduce the DFT-computational cost associated with the large number of atoms involved in the calculations. The error associated with this approximation was lower than 0.1 eV for the binding energy of Cu atoms. For example, the model labeled with $(\text{SO}_4)\text{Pt}(147)@\text{Cu}(\text{full})^{\text{DFT-half}}$ contained 19 sulfate molecules surrounding the half-NP.

7.4 Curvature Effects in Underpotential Deposition at the Nanoscale

Recent years have witnessed relevant progress concerning modeling of upd [25]. These advances have contributed to understand the role of substrate nature and structure and in some cases the effect of anions, for the case of planar surfaces. In the case of upd at the nanoscale, the situation is more complex, since the formation of core@shell bimetallic nanostructures appears to be very sensitive to a number of parameters, like temperature, pH, capping agents, strength of reducing agent, precursor concentration, reactant injection rate, physical properties of the seeds (this concerns size, shape, faceting, composition), and to the characteristics of the interfacial region resulting from differences of lattice constants, electronegativities and binding energies. Some of these topics have been addressed in the present book. The large degrees of curvature of NPs and nanocavities lead to a weakening or strengthening of the substrate/adsorbate interaction, with consequences for upd, to such a point that systems presenting upd on planar surfaces may not show it at the nanoscale, for small enough NPs sizes, as discussed in the previous Chapter. Conversely, systems not showing upd on planar surfaces could present this phenomenon in small nanocavities, with a large enough negative curvature, like those present in hollow NPs. While there is experimental evidence for the occurrence of the first phenomenon, the second one has not been observed so far. This is clearly a pending issue to be addressed through experiments. Cu deposition on Ag concave nanostructures is a good candidate to be addressed.

7.5 Role of Protective Molecules in Underpotential Deposition

The role played by surfactants or protecting agents in upd is an ongoing research field, involving a relatively large complexity. Chemisorption of a capping agent may alter the surface energy of the different facets of NPs, so as to revert the ordering of their stability [26]. As we have analyzed in detail in Chap. 6, recent

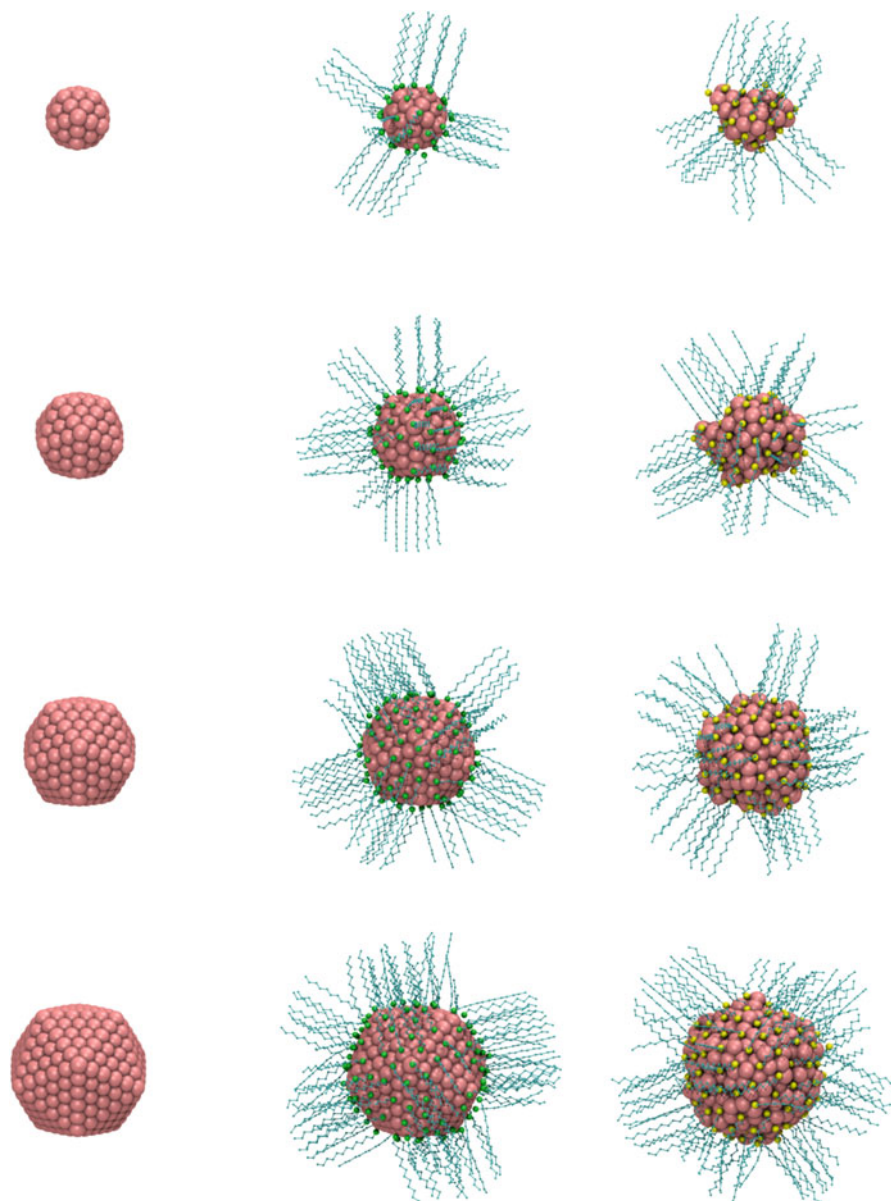


Fig. 7.4 Atomic configuration taken from molecular dynamic simulations for ligand attachment to Au NPs of different sizes. (Left) bare Ico Au NPs containing 55, 147, 309, and 561 atoms, (middle) amine-protected Au NPs, (right) thiolate-protected Au NPs. (Pink spheres: Au, Green: NH₂, Yellow: S, Cyan: Alkyl chains) (Reprinted with permission of Ref. [30])

experiments are oriented to control site selectivity for adatom deposition, by means of the application of a proper capping agent. As a consequence, the study of new protecting agents that bind selectively to a given facet type may be a promising research field deserving exploration. In this respect, experience accumulated in the study of upd on planar surfaces may provide useful information to take the initial steps in such a research. Protecting or capping molecules may play several simultaneous roles in the synthesis of nanomaterials: they may prevent NP aggregation [27], act as reducing agents and may favor (or not) the occurrence of the upd phenomenon [28, 29]. Theoretical studies in this area are still in their infancy and doubtless there is still much work to do. In this respect, it is worth mentioning the work of Olmos-Asar et al. [30], who have developed a semiempirical potential to analyze the role of surfactants on the morphology of Au-NPs. Figure 7.4 shows different configurations obtained from a MD simulation for naked and amine- and thiol-capped Au-NPs, where the role of the surfactants can be appreciated in the final morphology of the NPs. The atomic structure of the amine-protected NP does not seem to be appreciably affected by the ligands, while in the case of the thiol-protected NPs, a strong deformation on the geometry is evident, in particular for the smallest NPs, where crystallinity has disappeared. Similar conclusions were drawn by Yancey et al. using MD-DFT calculations [31] for very small NPs.

7.6 New Models of Nucleation and Growth at the Nanoscale

In spite of the important progress in the synthesis of metallic nanocrystals with well defined structures, it is necessary to deepen into the understanding of the nucleation and growth mechanisms of the synthesis of these new structures. We have mentioned in the previous paragraphs that the structural control of NPs is not a trivial task. For this reason, more studies are necessary for a proper understanding of nanocrystal growth. Such knowledge will provide a feedback to experimental work and thus allow improved synthetic routines. A new scheme has been proposed recently to handle electrochemical nucleation and growth at the nanoscale [12, 24]. This model addresses the possibility of growing a new phase without the need of surmounting the free energy barrier corresponding to the nucleation stage. This bears deep implications, opening the way to a thermodynamic control of nanostructure growth, instead of the kinetic route traditionally employed. While this proposal has been made on the basis of computer simulations for the Au@Ag and Pd@Au systems, its experimental trial is still missing. To mention work going in this direction, we show in Figs 7.5 and 7.6 two growth types at the nanoscale, as obtained by Gilroy et al. [32]. These authors analyzed the formation of bimetallic Au-Ag NPs in Ag growth-solutions under three different kinetic regimes: slow, moderate and fast. These regimes were obtained via different injection rates and different amounts of the reducing agent (ascorbic acid). While slow kinetics leads

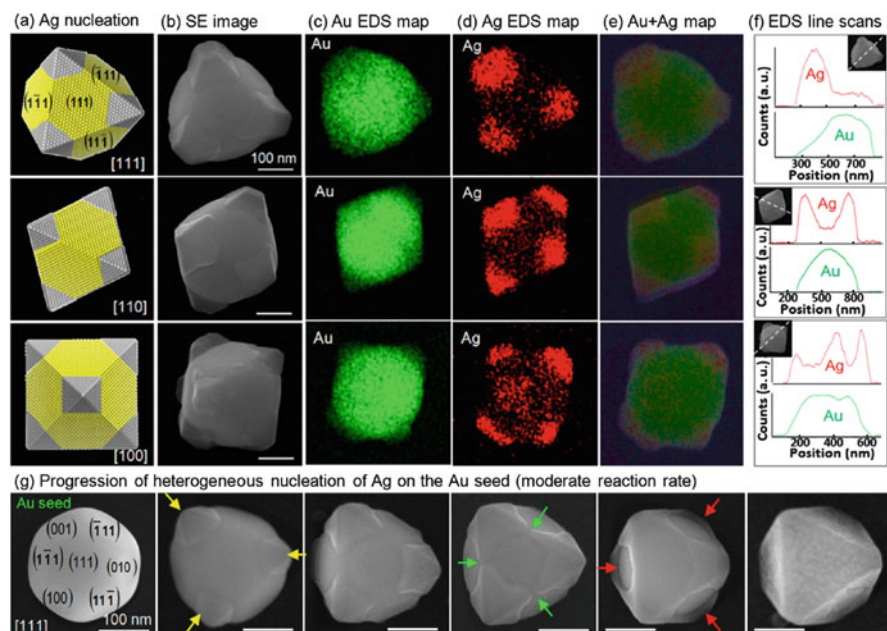


Fig. 7.5 Early stage morphological and elemental characterization of bimetallic Au–Ag structures formed in the regime of moderate kinetics. (a) Schematic depictions of the topography expected for bimetallic structures formed after the deposition of Ag on the {100} facets of [111]-, [110]-, and [100]-oriented Au seeds. (b) SEM images of the structures formed in the early stages of the reaction and their corresponding (c) Au, (d) Ag, and (e) Au + Ag elemental maps and (f) line scans. (g) SEM images showing the early to late stage progression in morphology which reveals a Au seed being overgrown with Ag to the point of encapsulation (Reprinted with permission of Ref. [31])

to a bimetallic Au–Ag heterodimer of Janus type, moderate kinetics yields an octahedral Au@Ag NP and rapid kinetics also lead to a Au@Ag NP but with a growth that follows closely the shape of the seed. The moderate regime shows that the nucleation and growth process takes place on the {100} facets of the Au-NP, yielding a pyramidal Ag growth (see yellow arrows in Fig. 7.5g). Ag growth then continues through the edges of the NP, connecting the six {100} facets (see green arrows in Fig. 7.5g). At the end, the {111} facets are decorated (see red arrows in Fig. 7.5g). The core@shell NP obtained under these conditions presents a tetragonal structure. SEM images, elemental maps and scan lines support the sequence mentioned.

The fast regime, as defined by the previous authors, shows that nucleation takes places on the {100} facets, but not with a pyramidal shape but in layer-by-layer steps. This growth rapidly reaches the edges of the NP (yellow and green arrows in Fig. 7.6g). Growth continues on the {111} facets (red arrows in Fig. 7.6g) and the final core@shell NP presents the shape of a truncated octahedron.

a very sharp peak in the corresponding voltammogram (spike). The argument for the previous statement is based on:

- (a) Phenomenological equations in terms of an effective interaction parameter, given in Sect. 3.6 of Chap. 3.
- (b) Theoretical considerations on the basis of mechanical statistical arguments, like those given in References [33–35] and discussed in Chap. 5 and also discussed qualitatively in Chap. 3 on the basis the Onsager's equation.
- (c) Monte Carlo (MC) simulations of the lattice gas models, as those performed in Reference [36], which show that steps occur in the isotherms, as was presented on the right of Fig. 5.28, Chap. 5. In this Figure it was shown that a stepwise isotherm behaviour is expected for Ag deposition on Au(111), even if the experiment could be performed for temperatures as high as 500 K.

While the theory exposed in Refs. [33–35] proposed an explanation for the widening of the experimental peaks in terms of the occurrence of a large collection of crystals on the electrode surface, with various sizes, shapes, and boundary conditions, we propose here the opposite verification, via the realization of experiments with many, as identical as possible, small systems. This ensemble of systems should be small enough so as to present as few defect as possible, but be large enough so as not to present finite size effects. Such a collection should show the spikes characteristic for the first-order phase transition, or at least, should show an indication for its occurrence as the monodispersity of the isolated systems is approached. This experiment will be challenging, but its performance would be useful to shed light into the essence of the upd phenomenon.

7.8 The Puzzling Occurrence of Low-Density Structures and the Need to Improve the Underpotential Deposition Modeling to Consider Electrochemical Features of the System

Going back to Chap. 3, and with the insight gained in Chap. 5, we notice that the results shown in Fig. 3.5 and Table 3.1 [37] of the former represent a challenge for all theoretical efforts to understand upd. These results show, under conditions where anion adsorption is minimized, the ex-situ occurrence of several Ag upd structures on the Au(111) surface, which correlate with different silver coverages. Remarkably, it is found that structures obtained at low coverage degrees are the most stable (the $p(3 \times 3)$ followed by the $p(5 \times 5)$). These results cannot be understood in terms of pure metallic binding, as described by DFT calculations, which predicts that the most stable structure should be Ag (1×1) on Au(111)

(See Chap. 5, Table 5.4). A number of points addressed by Mrozek et al. [37] should be kept in mind when modeling the present system:

- The formation of the $p(3 \times 3)$ and $p(5 \times 5)$ structures in both fluoride and sulfate media indicates that their occurrence is relatively insensitive to the type of anion coadsorbed with silver adatoms.
- The Au-Ag chemical bond is polar and, in consequence, an effective positive charge resides on a Ag adatom. This polarization is evidenced by the shift of almost one eV in the work function of the Au(111) surface upon Ag monolayer formation (See Chap. 5, Table 5.4).
- Fluoride may interact with the positively charged localized surface sites.
- Coadsorbed solvent molecules may have a strong influence on the upd adlattice stability.

Thus, the former discussion leads to the conclusion that the proper prediction of the stability of this (relatively) simple upd system, will require from first-principles calculations where the nature of the solvent, as well as the characteristic of the anions participating at the metal/solution interphase, must be taken into account. Something similar can be stated concerning many other more complex upd systems, where there is clear evidence for an important participation of anions in the upd phenomenon, where solvent effects obviously cannot be excluded. Furthermore, also the rest of the double layer should be accounted for in terms of a more simplistic model, since charging effects of the electrostatic double layer will be important due to the shift of the potential of zero charge that takes place upon upd monolayer formation (See discussion in Chap. 5, Sect. 5.2.3).

However, not all the job should be left to theoreticians concerning the present issue. The discussion given in Chap. 3, Sect. 3.5.2 showed that the thermodynamic analysis of electrochemical data yielded extremely valuable information on the composition of the upd adlayer for the Cu/Au(111) system, so that a similar attempt should be undertaken for many other upd systems.

References

1. Langille MR, Personick ML, Zhang J, Mirkin CA (2012) *J Am Chem Soc* 134:14542
2. Personick ML, Mirkin CA (2013) *J Am Chem Soc* 135:18238
3. <http://www.scopus.com/>
4. Brankovic SR, Wang JX, Adzic RR (2001) *Surf Sci* 474:L173
5. Viyannalage LT, Vasilic R, Dimitrov N (2007) *J Phys Chem C* 111:4036
6. Choy KL (2003) *Prog Mater Sci* 2:57
7. Sun Y, Wiley B, Li Z-Y, Xia Y (2004) *J Am Chem Soc* 126(30):9399
8. Elam JW, Routkevitch D, Mardilovich PP, George SM (2003) *Chem Mater* 15(18):3507
9. Sun Y, Xia Y (2003) *Nano Lett* 3(11):1569
10. Park S, Yang P, Corredor P, Weaver MJ (2002) *J Am Chem Soc* 124:2428
11. Gilroy KD, Farzinpour P, Sundar A, Hughes RA, Neretina S (2014) *Chem Mater* 26:3340
12. Xia X, Wang Y, Ruditskiy A, Xia Y (2013) *Adv Mater* 25:6313
13. Oviedo OA, Leiva EPM, Mariscal MM (2008) *Phys Chem Chem Phys* 10:3561

14. Zhou Y, Rees NV, Compton RG (2011) *ChemPhysChem* 12:2085
15. Giménez MC, Del Pópulo MG, Leiva EPM, García SG, Salinas DR, Mayer CE, Lorenz WJ (2002) *J Electrochem Soc* 149, E109
16. Brown G, Rikvold PA, Novotny MA, Wieckowski A (1999) *J Electrochem Soc* 146:1035
17. Budevski E, Staikov G, Lorenz WJ (1996) *Electrochemical phase formation and growth*. VCH, Weinheim
18. Pinto LMC, Spohr E, Quaino P, Santos E, Schmickler W (2013) *Angew Chem* 125:8037
19. Pinto LMC, Quaino P, Santos E, Schmickler W (2014) *ChemPhysChem* 15:132
20. Schmickler W (1996) *Electrochim Acta* 41:2329
21. Li JH, Dai XD, Liang SH, Tai KP, Kong Y, Liu BX (2008) *Phys Rep* 455:1
22. Laurent AD, Jacquemin D (2013) *Int J Quantum Chem* 113:2019
23. Anderson RM, Zhang L, Loussaert JA, Frenkel AI, Henkelman G, Crooks RM (2013) *ACS Nano* 7:9345
24. Carino EV, Kim HY, Henkelman G, Crooks RM (2012) *J Am Chem Soc* 134:4153
25. Oviedo OA, Vélez P, Macagno VA, Leiva EPM (2015) *Surf Sci* 631:23
26. Murphy CJ, Sau TK, Gole AM, Orendorff CJ, Gao J, Gou L, Hunyadi SE, Li T (2005) *J Phys Chem B* 109C:13857
27. Tao AR, Habas S, Yang P (2008) *Small* 4:310
28. Selvakannan PR, Swami A, Srisathiyarayanan D, Shirude PS, Pasricha R, Mandale AB, Sastry M (2004) *Langmuir* 20:7825
29. Zhu C, Zeng J, Tao J, Johnson M, Schmidt-Krey I, Blubaugh L, Zhu Y, Gu Z, Xia Y (2012) *J Am Chem Soc* 134:15822
30. Olmos-Asar JA, Ludueña M, Mariscal MM (2014) *Phys Chem Chem Phys* 16:15979
31. Yancey DF, Chill ST, Zhang L, Frenkel AI, Henkelman G, Crooks RM (2013) *Chem Sci* 4:2912
32. Gilroy KD, Hughes RA, Neretina S (2014) *J Am Chem Soc* 136:15337
33. Huckaby DA, Medved I (2002) *J Chem Phys* 117:2914
34. Huckaby DA, Medved I (2006) *Rom J Phys* 51:603
35. Medved I, Huckaby DA (2010) *Fluid Phase Equilib* 290:21
36. Giménez MC, Leiva EPM (1999) *Electrochim Acta* 45:699
37. Mrozek P, Sung Y-E, Wieckowski A (1995) *Surf Sci* 335:44

About the Authors



Silvana G. García is Professor of Chemical Engineering since 2005 at the Universidad Nacional del Sur, Bahía Blanca (Argentina). She performed her doctoral thesis in the Instituto de Ingeniería Electroquímica y Corrosión (INIEC), Bahía Blanca and the Institut für Physikalische Chemie und Electrochemie III, Universität Karlsruhe (Germany), obtaining in 1997 her Ph.D. in Chemistry. At present, she is part of INIEC and leads two research projects. She has taught in undergraduate and specialist post-graduate courses and she is supervisor of six doctoral theses (four completed and two in progress). She has benefited by seven D.A.A.D. (Deutscher Akademischer Austauschdienst) scholarships in the period 1992–2006. Her working areas are mainly the electrochemical formation of metallic thin films and nanostructures (nanoparticles, nanowires), involving the nucleation and growth mechanisms, and the analysis of the electrocatalytic effect of such structures for reactions of technological interest. Prof. García has published more

than 60 research papers including a book chapter about Nanoelectrochemistry, and participated in many national and international conferences. She is a local/external reviewer for research projects and for scientific journals in the areas of Physical Chemistry, Electrochemistry and Materials Science.



Ezequiel Leiva is Professor at the National University of Córdoba, Argentina, and Principal Researcher of CONICET, at the Instituto de Investigaciones en Físico-Química de Córdoba (INFIQC). After his studies of physical chemistry at the National University of Córdoba, he obtained PhD in Physical Chemistry there in 1982. Between 1984 and 1987 he worked with Professor W. Schmickler at the University Bonn, Germany. His main interest is in theoretical aspects of electrochemistry. He has published more than 150 scientific papers and 18 book chapters in the field of electrocatalysis and computer simulations devoted to understand the formation and properties of electrochemical nanostructures. He has actively participated in different organizations promoting and supporting science, like CONICET at the national level and the International Society of Electrochemistry at the international one. A key achievement was the coordi-

nation of a project that led to the design and installation of the fastest computer of Argentina, where about 20 % of the computer time is devoted to projects related to electrochemistry. In recent times, he devoted considerable effort to extend the concept of underpotential deposition to the nanoscale, using nanothermodynamics, statistical mechanics and Monte Carlo simulations. Several of these new concepts are embodied in the present book.



Oscar A. Oviedo is Assistant Professor in Instituto de Investigaciones en Físico-Química de Córdoba (INFIQC-CONICET) at the University of Córdoba, Argentina. He followed studies of Chemistry at this University and got his PhD in 2004. He has been part of the Theoretical Electrochemistry and Computer Simulation Group directed by Professor Leiva since 1997. He is author of more than 20 research papers. His scientific contributions include a theoretical formulation to describe the phenomenon of underpotential deposition (upd) at the nanoscale through nanothermodynamics and statistical mechanics. An interesting prediction of this modelling is the occurrence of an upd-opd transition taking place at small nanoparticle sizes. He has been the co-editor of the book called “Metal Clusters and Nanoalloys: From Modeling to Applications” of the serie: “Nanostructure Science and Technology”. He has also co-authored other two chapters,

including “Modelling of Metal Electrodeposition at the Nanoscale” in a Nano-Electrochemistry Handbook (Niknam, Ed). His research areas are theoretical electrochemistry, electrocatalysis and in computer developments in physical chemistry.



Luis Reinaudi works as a Professor at the National University of Córdoba (Argentina), and a Researcher at the Instituto de Investigaciones en Físico-Química de Córdoba (INFIQC-CONICET). He obtained his PhD Thesis in 2000, working on the subject of crystal structure determination through computer simulations. He has several research papers and co-authored a book on the subject. After his post-doctoral studies, his field of interest shifted to the study of metallic nanostructures (such as nanoparticles and nanowires), their formation, and their thermal and electrochemical stability. As such, he is a member of the Theoretical Electrochemistry and Computer Simulation Group directed by Professor Leiva. His other fields of interest include renewable energies (particularly the study of fuel cells and lithium batteries), and computer simulations of complex and non-linear systems.

About the Editor



Fritz Scholz is Professor at the University of Greifswald, Germany. Following studies of chemistry at Humboldt University, Berlin, he obtained a Dr. rer. nat. and a Dr. sc. nat. (habilitation) from that University. In 1987 and 1989 he worked with Alan Bond in Australia. His main interest is in electrochemistry and electroanalysis. He has published more than 300 scientific papers, and he is editor and co-author of the book “Electroanalytical Methods” (Springer, 2002, 2005, 2010, and Russian Edition: BINOM, 2006), coauthor of the book “Electrochemistry of Immobilized Particles and Droplets” (Springer 2005), co-editor of the “Electrochemical Dictionary” (Springer, 2008; 2nd ed. 2012), and co-editor of volumes 7a and 7b of the “Encyclopedia of Electrochemistry” (Wiley-VCH 2006). In 1997 he has founded the *Journal of Solid State Electrochemistry* (Springer) and serves as Editor-in-Chief since that time. In 2014 he has founded the journal *ChemTexts –The Textbook Journal* (Springer). He

is the editor of the series “Monographs in Electrochemistry” (Springer) in which modern topics of electrochemistry are presented. Scholz introduced the technique ‘Voltammetry of Immobilized Microparticles’ for studying the electrochemistry of solid compounds and materials, he introduced three-phase electrodes to determine the Gibbs energies of ion transfer between immiscible liquids, and currently he is studying the interaction of free oxygen radicals with metal surfaces, as well as the interaction of liposomes with the surface of mercury electrodes in order to assess membrane properties. In the last years, his research also comprises the interaction of electrode surfaces with free oxygen radicals.

Index

A

- Abelès, F., 61
Abruña, H.D., 17, 144
Adatom, 2–4, 7, 17, 19, 30, 36, 45, 70, 73, 91, 95, 97, 102, 104, 111, 112, 117, 118, 124–126, 128–130, 133, 142, 143, 146, 155, 170, 175, 185–187, 189, 201, 204–206, 217, 230, 235, 237, 242, 247, 248, 252, 255, 265, 266, 272, 304
Adlayer, 45, 121, 166, 190–192, 216, 217, 233
Adsorbate, 2
Adsorbate-adsorbate interactions, 128
Adsorption isotherms, 120, 127, 128, 131, 133, 221
Adsorption pseudocapacitance, 119
Adžic, R.R., 17
Adzic, R.R., 184, 188, 319
Ag, 10, 11, 19, 24, 30, 31, 34–38, 42–45, 48, 51–57, 59–67, 69–73, 75–77, 80, 91, 92, 97–99, 119, 129, 132–134, 138–146, 200, 201, 207, 208, 211–216, 229–231, 233–235, 237, 238, 240, 241, 250, 252, 254, 264, 267, 270, 277, 280–284, 289, 291, 294, 298–300, 304, 306, 310–313, 317–322, 324–326, 335–337, 339, 341, 343–347
 nanoparticles, 277, 284
Ag(100), 65, 139
Ag(111), 70, 73, 134, 138–141, 144, 145, 207, 208, 211–213, 215, 229–231, 233, 234, 264
Ag(111)/Au(1 × 1), 211
Ag(111)/Cu, 211, 213
Ag(111)/Cu(1 × 1), 211, 213, 215
Ag/Pd(111), 233
Agafonovas, G., 25
Alkire, R.C., 257
Alloy formation, 65–67
Anastasijevic, N.A., 188
Anderson, A.B., 164, 165, 340
Anderson-Newns model, 204
Angerstein-Kozłowska, H., 119
Aramata, A., 17
As, 71
As/Pt(111), 190
Atomic force microscopy (AFM), 20, 40, 47–49
Atomic layer deposition (ALD), 335
Atomic resolution, 42, 44
Au, 10, 11, 35, 36, 80, 82, 119, 138, 200, 201, 211–217, 221–223, 226, 233, 234, 240, 241, 243–246, 250–252, 254, 258–264, 267, 270, 272, 273, 277, 278, 280–283, 286, 287, 291, 296–300, 304, 306, 310–322, 324–326, 328, 329, 335–337, 342–347
 nanoparticles, 200, 335
 polycrystalline, 59
Au(001), 57
Au(100), 19, 21, 22, 30–33, 42–45, 48, 66, 129, 132–134, 138–140, 142, 143
Au(100)/Ag, 240
Au(111), 19, 20, 22–24, 26–28, 30–32, 36, 38, 39, 41–43, 45–49, 51–57, 61, 66–68, 70, 97–99, 111–116, 129, 133, 138–143, 146, 147, 156
Au(111)/, 39
Au(111)/Cu(1 × 1), 211, 215
Au(1289)@Ag, 305
Au(1289)@Pd, 305

- Au(332), 21, 23
 Au(554), 21, 23
 Au(775), 21, 23
 Au(core)@Ag(shell), 311
 Au@Ag nanoparticles, 299, 300
 Au@Pt nanoparticles, 297
 Au{100}, 317
 Au{111}, 317
 Auger electron spectroscopy, 20, 48–52
 AuPd nanocrystals, 316
- B**
- Bagotzky, V.S., 174
 Barrera, G.D., 266
 Behm, R.J., 21, 45
 Bertocci, U., 68
 Bewick-Fleischmann-Thirsk (BFT) model, 27
 Bi, 11, 23, 28, 37, 71, 72, 75, 80, 138–141, 144, 170, 186, 187, 189–191, 193, 216, 217
 Bi/Pt(111), 190, 191
 Bilayer, 235, 256
 Bimetallic nanoparticles, 294, 313, 315, 328
 Binding energy, 128
 Binnig, G., 40, 47
 Bisulfate, 58
 Blum, L., 220, 223, 243, 264, 265
 Blume–Emery–Griffiths model, 246
 Bockris, J.O., 189
 Bode plot, 73
 Boltzmann probabilities, 226
 Bondarenko, A.S., 73
 Borensztein, Y., 61
 Borgs–Kotecky theory, 224
 Born–Oppenheimer approximation, 200
 Borohydride, 284
 Bowles, B.J., 10
 Brankovic, S.R., 69, 70, 338
 Broda, E., 79
 Brown, G., 338
 Bruckenstein, S., 33, 34, 37, 107
 Budevski, E., 109
 Bulk modulus, 201
 Butler–Volmer, 338
- C**
- Canonical partition function, 290, 305
 Capacitance, 119
 measurements, 68
 Carbó-Argibay, E., 314
 Carbon monoxide (CO), 164–178, 180, 182, 185, 187, 297
- Carino, E.V., 328, 330
 Carnal, D., 134
 Cd, 10, 11, 23, 35, 37, 40, 65–67, 69, 138, 139, 141
 CdTe, 71
 Ce, 11
 Chamberlin, R.V., 290, 293, 305
 Chemical potential, 93–95, 103, 110, 112, 117, 123–127, 129, 149, 155, 203, 228, 237, 239, 240, 243, 270, 279, 280, 285, 286, 288, 291, 293, 307, 312
 Chen, C.-H., 143
 Cluster, 129, 130, 278, 280, 283, 284, 286, 290, 312
 Coadsorption effect, 166
 Coincidence lattice, 265
 Compton, R.G., 329
 Conway, B.E., 118
 Core@alloy, 315
 Core@shell nanoparticles, 294, 296, 298, 301, 304, 307, 320, 328, 331
 Co-reduction, 294
 Corrosion, 190, 192
 Cottrell equation, 27
 Coverage isotherms, 116–145
 Critical cluster size, 130
 Critical temperature, 126
 Crystallographic misfit, 17
 Cu, 11, 20–23, 25, 26, 28, 34–39, 43, 45–49, 51, 52, 56–61, 63, 69, 70, 72–75, 80–82, 100–102, 111–116, 129, 138, 140, 142–145, 147, 156, 172, 201, 209, 211–218, 221–223, 225, 226, 229–231, 233–235, 243–246, 258–263, 267, 277, 283, 296, 297, 312, 318–320, 328–331, 337, 340, 341, 347
 Cu(1 × 1) epitaxial monolayer, 219
 Cu(111)/Au(1 × 1), 214
 Cu/Pt(111), 171
 Cu-adlayer, 38
 Curvature, 279, 303, 307, 309, 310, 315, 320, 322
 effects in upd, 341
 Cyclic voltammetry, 18
- D**
- Danilov, A.I., 218
 Davies, P.W., 76
 de Broglie wavelength, 229
 Deakin, M.R., 37
 Defective surface, 7
 Density functional theory, 200, 206–209, 339
 DeSantis, C.J., 315

Desorption, 3, 28, 91, 98, 108, 112, 140, 143, 144
Dickertmann, D., 28, 97
Dietterle, M., 230
Differential reflectance spectroscopy (DRS), 60–61
Dissolution charges densities, 35
Double layer capacitance, 74
Double layer effects, 102
Drews, T.O., 253, 256

E

Eichler, B., 79, 82
Electrical double layer (EDL), 147
Electrocapillary curve, 113
Electrocatalysis, 164, 167, 185, 187, 190
Electrochemical atomic layer deposition (E-ALD), 337
Electrochemical atomic layer epitaxy (ECALE), 71, 337
Electrochemical impedance spectroscopy, 73–75
Electrochemical potential, 91, 93, 153
Electrochemical quartz crystal microbalance (EQCM), 37, 45
Electrocompression, 192
Electrocrystallization, 1
Electron delocalization molecular orbital technique, 263
Electron diffraction, 20
Electroneutrality conditions, 110
Electrooxidation, 164, 167, 172, 174–180, 182, 184, 188
Electroreduction, 193
Electrosorption, 12
Electrosorption valency, 12, 30, 33, 100–108, 141
Electrostatic work, 95
Entropy, 266, 267, 271, 273, 274
Epitaxial film, 70
Epitaxial growth, 71
Equilibrium-coverage-potential isotherms, 28
Ermak's algorithm, 270
Extended X-ray absorption fine structure (EXAFS), 39, 52, 53, 55, 115

F

Fayet, P., 283
Fermi level, 205, 206
Fichthorn, K.A., 247
Filinov, V.S., 229
Finnis, M.W., 251
First-order phase transition, 122, 126–128, 131–134, 138, 142

Fleischmann, M., 65
Fonticelli, M.H., 299
Formaldehyde, 164, 176
Formic acid, 164, 173–176, 180–187
Fourier transform infrared spectroscopy (FTIRS), 58–59, 173, 177
Franaszczuk, K., 174
Frank-van der Merwe growth, 229, 250–255, 295
Free energy, 94, 95, 97, 101, 110, 129, 149–152, 154, 155
Fugacity, 221, 222
Fujishima, A., 72, 73

G

Gadzuk, J.P., 204
Galvanic replacement, 318–325, 337
García, S., 43, 65, 66
Gentry, S.T., 284
Gerischer, H., 11, 12
Gewirth, A.A., 30, 43, 47, 48, 51
Gibbs energy of cluster formation, 129
Gibbs excess, 113–115
Gibbs free energy, 97, 150, 151, 279, 307
Gibbs–Duhem condition, 110
Gibbs–Thomson model, 279
Gilroy, K.D., 343, 345
Giménez, M.C., 239–242, 250, 255
Girija, T.C., 72
Glow discharge optical emission spectroscopy (GDOES), 77–79
Gold, 19
González, E., 325
Grand Canonical Ensemble, 228
Grand Canonical Monte Carlo (GCMC) simulation, 239
Grand Canonical Monte Carlo (GCMC) computer simulations, 304
Graphite, 11
Grazing incidence X-ray diffraction, 55–57
Greeley, J., 215
Green, M.P., 69
Grossmann, A., 233
Growth stress, 68–69
Gruenbaum, E., 11
Guyot-Sionnest, P., 317

H

Haenny, C., 10
Haissinsky, M., 10
Hamiltonian, 123, 200, 202, 204, 220, 243, 258, 260, 266, 339
Hamnett, A., 173, 174
Hansma, P.K., 40

- Hanson, K.J., 69
 Hassium, 83
 Helmholtz free energy, 231
 Helmholtz plane, 96, 104, 105
 Henderson, D., 204
 Herrero, E., 45, 56
 Herzfeld, K.F., 10
 Heteroepitaxy, 258
 Hg, 11, 80
 Hill, T.L., 290, 293, 303, 305
 Hölzle, M.H., 143
 Homoepitaxy, 231, 258
 Huckaby, D.A., 220, 223–225, 240, 243
 Hummrich, H., 80–82
 Hydrogen evolution reaction, 189
- I**
 Ideal polarizable electrode, 109–116
 Ikeda, N., 38
 Ikemiya, N., 43
 In situ infrared spectroscopy (IRS), 58
 Incommensurate structure, 268
 In-situ surface differential X-ray diffraction (SDD), 53–54
 In-situ surface X-ray scattering (SXS), 55
 Instantaneous nucleation, 131, 257
 Interaction parameters, 120
 Interfacial tensions, 113
 Interferometry, 47, 68
 Interphase, 94, 109, 110, 148–154, 156
 Ising dipole system, 125
- J**
 Jarvi, T.D., 180, 184
 Jellium model, 206, 207, 209, 212, 234
 Jüttner, K., 36
- K**
 Khan, S., 189
 Kink, 235
 decoration, 7
 Kirkendall effect, 325, 338
 Kohn-Sham equation, 211
 Kokkinidis, G., 17, 184
 Kolb, D.M., 11, 12, 17, 43, 51, 60, 91, 93–95, 97, 98
 Kolthoff, I.M., 10
 Koos, D.A., 61
 Koppitz, F.D., 106
- Kornyshev, A., 204, 205
 Kramar, T., 209
 Kratz, J.V., 79, 82
- L**
 LaMer, V.K., 287–289, 313
 Langevin dynamics, 270
 Langmuir–Hinselwood kinetics, 175
 Langmuir-Hinselwood mechanism, 166
 Langmuirian behavior, 117
 Langmuirian process, 139
 Laser beam deflection, 68
 Lattice constant, 201
 Lattice gas model, 123–125, 127, 133, 138, 142
 Lee, 54
 Legendre transform, 110
 Lehnert, W., 206
 Leiva, E.P.M., 17, 185, 186, 188, 206, 207, 209, 211, 212, 239
 Lennard-Jones interaction potential, 269
 Lifshitz-Slyozov-Wagner model, 289
 Lipkowski, J., 111, 112, 114
 Liu, M., 317
 Lopes, M.I.S., 174
 Lorenz, W.J., 12, 17
 Low-energy electron diffraction (LEED), 20, 49–52, 97
 Luque, N.B., 312
- M**
 Magnetic coupling constant, 126
 Magnetic field strength, 124
 Magnussen, O.M., 45
 Mariscal, M.M., 270
 Markovic, N.M., 188
 Medved, I., 224, 240
 Mehandru, S.P., 164
 Melroy, O.R., 37, 53
 Mentus, S., 216, 217
 Methanol, 164, 172–178, 180–182, 185
 Metropolis, 226, 227, 229, 236, 239
 Mills, T., 10
 Mirkin, C.A., 317, 335
 Mola, E.E., 264, 265
 Molecular dynamics, 339
 Monolayer, 6, 235
 formation, 7
 Monte Carlo (MC) simulations, 125, 133, 143, 346
 Motoo, S., 167, 170, 175, 176

- Mrozek, P., 97, 347
 Multimetallic nanoclusters, 71
 Muscat, J.P., 204
- N**
 Nanocages, 338
 Nanocubes, 338
 Nanohollows, 338
 Nanoparticles, 335, 338
 Nanoshells, 338
 Nanothermodynamics, 303, 338
 Nanotubes, 338
 Newman, R.C., 11
 News, 204, 205
 Ni, 11, 80–82
 Nicholson, M.M., 11
 Nitrate, 193, 194
 Norman, G.E., 229
 Nuclear chemistry, 79–83
 Nucleation and growth, 17, 286–289, 303, 305, 313, 314, 343–345
 Nyquist plot, 73
- O**
 Olmos-Asar, J.A., 343
 Omar, I.H., 156
 Onsager, L., 126
 Optical second harmonic generation (SHG), 61–62
 Overpotential, 285, 286, 291, 295, 298, 301, 304–306, 309
 Oversaturation, 5
 Oviedo, 234, 266
 Oxygen evolution reaction (OER), 188
- P**
 Padé approximants, 221
 Park, S., 296, 297, 320, 338
 Parsons, R., 180, 184
 Pasti, I., 216, 217
 Pauling's electronegativity, 95
 Pb, 10, 11, 28, 37, 56, 61, 65, 68–70, 72, 73, 75, 78, 80–82, 119, 134, 138–141, 144, 184, 189, 190, 192, 207, 208, 216, 217, 237, 238, 263, 264, 272–274, 337
 p-benzoquinone, 299
 Pd, 80–82, 184, 216, 277, 282, 283, 294, 304, 311–313, 315, 316, 319–322, 325, 328
 Pd(111), 129
 Pd(13)@Au(42), 311
 Pd(55)@Au(92), 311
 Pd(100)/Au, 240
 Pd(147)@Au(162), 311
 Pd(309)@Au(252), 311
 Pd(561)@Au(362), 311
 Pd(923)@Au(492), 311
 Perdew–Burke–Ernzerhof (PBE) functional, 216
 Phase transitions, 116–145
 Photoacoustic (PA) technique, 72–73
 Photographic negative, 283
 Pinto, L.M.C., 339
 Plieth, W.J., 8, 280
 Plowman, B.J., 329
 Po, 80
 Poisson processes, 247, 248
 Polycrystalline surface, 122
 Pośkus, D., 25
 Potential-dependent infrared spectra, 58
 Potential of zero charge (PZC), 102, 113, 212, 216, 221
 Potential step technique, 26
 Progressive nucleation, 122, 131, 138, 257
 Przasnyski, M., 11, 12
 Pseudocapacitance, 74, 122
 Pseudoresistance, 74
 Pt, 10, 11, 70, 80, 82, 119, 138, 201, 209, 213, 215–218, 225, 226, 233–235, 240, 241, 264, 267, 270, 277, 281, 283, 296–298, 313, 317–320, 328, 330, 331, 337, 340
 Pt(110), 177
 Pt(111), 76, 91, 129, 177, 216–218, 225, 233–235, 264, 271
 Pt(553), 76
 Pt(100)/Ag, 240
 Pt(100)/Au, 240
 Pt(111)/Bi adatoms, 186
 Pt(001)/Cu(2 × 2), 209
 Pt(100)/Sb adatoms, 187
 Pt/Ru, 176
 Pt/Sn, 176
 Pt₃Sn, 169, 177
- Q**
 Quantum mechanics, 338
 Quartz crystal microbalance (QCM), 20
 Quasi-equilibrium conditions, 119
 Quasi-harmonic lattice dynamic method, 266

R

Radiotracer, 23–26
 Ragoisha, G.A., 73
 Rayment, T., 53, 54
 Redox potential, 281–285, 294
 Reflectance, 60
 Richmond, G.L., 61
 Rogers, L.B., 10, 79
 Rohrer, H., 40
 Rojas, M.I., 231, 233
 Ross, P.N., 167, 177, 188
 Rossmeisl, J., 178
 Rotating ring-disk electrode (RRDE), 33
 Ru, 167–169, 172, 176, 178, 179

S

S, 71
 Sánchez, C.G., 209, 211–213, 215, 216
 Sánchez-Iglesias, A., 282
 Sangaranarayanan, M.V., 17, 72, 96
 Santos, E., 206
 Sauerbrey, 37
 Sb, 71
 Sb/Pt(100), 190
 Scanning probe microscopy (SPM), 40
 Scanning tunneling microscopy (STM), 20, 40–46
 Schmickler, W., 204–207, 270
 Schmidt, E., 29, 107, 109, 134
 Schnippering, M., 280
 Schönfeld, T., 79
 Schrödinger equation, 199
 Schultze, J.W., 97, 100, 103, 104, 106–108, 146
 Schulze, J.W., 12, 28
 Se, 71
 Selvakannan, P.R., 298, 299
 Semiconductors, 71
 Seo, D., 317
 Shay, M., 37
 Siegenthaler, H., 107
 Sieradzki, K., 45
 Sinclair, J.E., 251
 Single crystal surfaces, 97–100
 6-layer, 235
 Sn, 11, 23, 172, 184, 216, 217
 Sobkowski, J., 24
 Solvent effects, 102–106
 Sonnenfeld, R., 40
 Spin polarization, 339
 Sriramulu, S., 175
 Stafford, G.R., 68
 Standard submonolayer potential, 100

Statistical mechanics, 338
 Step, 235
 Step decoration, 7
 Stephens, R.M., 257
 Stickiness parameter, 222
 Stickney, J.L., 71
 Sticky interaction, 220
 Stranski-Krastanov growth, 229, 295, 296
 Stuve, E.M., 180, 184
 Submonolayers, 6
 Subsaturations, 288, 290, 293
 Substrate-adsorbate atom interaction, 127
 Successive reduction, 294, 295
 Sudha, V., 17, 96
 Sulfate, 58
 Sun, S.G., 174
 Sun, Y., 319
 Supersaturation, 287, 288, 290–293
 Surface energies, 201
 Surface free energy, 279, 325
 Surface-enhanced Raman Spectroscopy (SERS), 62–65
 Surface-limited redox replacement (SLRR), 70, 337
 Surface SEXAFS, 199
 Surface stress, 68–69, 233
 Surface tension, 106
 Svedberg, T., 313
 Swathirajan, S., 37, 107, 118, 119
 Szabó, S., 17, 103

T

Tamura, K., 140
 Te, 71, 75
 Temkin parameter, 118, 119
 Temperature programmed desorption (TPD), 75
 Terrace, 235
 Thermal desorption spectroscopy, 75–77
 Thermodynamic cycle, 150, 213
 Thiol-capped Au-NPs, 343
 3-layer, 235
 Tian, Z.-Q., 65
 Tl, 11, 23–25, 28, 61, 65, 72, 80, 134, 138–141, 144, 145, 337
 Transmission X-ray surface differential diffraction, 54
 Trasatti, S., 96
 Treeratanaphitak, T., 255, 258
 Twin-electrode thin-layer (TTL) technique, 29
 Two-phase thermodynamic method, 271

U

Uchida, H., 38
Undersaturation, 5
Undervoltage, 2

V

Vacancy, 235
Van Der Eerden, J.P., 237
van der Waals, 8, 48
van der Waals forces, 285
van der Waals isotherm, 120
VanderNoot, T., 180, 184
Vassilyev, Y.B., 174
Velocity autocorrelation function, 272
Vetter, K.J., 104, 146
Vielstich, W., 172
Vijh, A.K., 11
Volmer-Tafel mechanism, 189
Volmer-Weber mechanism, 229, 250, 295
Volta potential, 95

W

Walters, M.J., 62
Wang, K., 169
Watanabe, M., 167, 175, 176, 184
Weaver, M.J., 63, 296, 297

Weinberg, W.H., 247

White, J.H., 144

Wood, D.M., 280

Work function, 92, 95–98, 100, 119, 147, 155,
207, 209, 211, 216

X

Xia, Y., 172

X-ray diffraction (SDD), 53

X-ray photoelectron spectroscopy (XPS),
49–52

X-ray scattering, 140, 199

X-ray standing waves, 199

Y

Yancey, D.F., 330, 343

Yu, Y., 320

Z

Zhang, B., 143, 243, 246

Zhang, J., 297, 298

Zn, 10

ZnSe, 71

Zsigmondy, R., 313